

CONTRIBUTION À LA CARACTÉRISATION ET À LA MODÉLISATION MÉCANIQUE DES ASSEMBLAGES MULTI-MATÉRIAUX

Claudiu Badulescu

▶ **To cite this version:**

Claudiu Badulescu. CONTRIBUTION À LA CARACTÉRISATION ET À LA MODÉLISATION MÉCANIQUE DES ASSEMBLAGES MULTI-MATÉRIAUX. Sciences de l'ingénieur [physics]. Université Bretagne Occidentale, 2023. ⟨tel-04606374⟩

HAL Id: tel-04606374

https://hal.science/tel-04606374v1

Submitted on 12 Jun 2024

HAL is a multi-disciplinary open access archive for the deposit and dissemination of scientific research documents, whether they are published or not. The documents may come from teaching and research institutions in France or abroad, or from public or private research centers.

L'archive ouverte pluridisciplinaire **HAL**, est destinée au dépôt et à la diffusion de documents scientifiques de niveau recherche, publiés ou non, émanant des établissements d'enseignement et de recherche français ou étrangers, des laboratoires publics ou privés.



HAL Authorization

HABILITATION À DIRIGER DES RECHERCHES

Domaine :

MÉCANIQUE – GÉNIE MÉCANIQUE – GÉNIE CIVIL

Présentée à

L'UNIVERSITÉ DE BRETAGNE OCCIDENTALE

par

Claudiu BADULESCU

Titre :

CONTRIBUTION À LA CARACTÉRISATION ET À LA MODÉLISATION MÉCANIQUE DES ASSEMBLAGES MULTI-MATÉRIAUX

Soutenue publiquement le 8 décembre 2023 devant le jury composé de :

M. Pascal CASARI	GeM / IUT de Saint-Nazaire	*Rapporteur*
M. Franck LAURO	LAMIH / UPHF	*Rapporteur*
Mme. Aude SIMAR	iMMC / Université Catholique de Louvain	*Rapporteur*
M. Michel GREDIAC	Institut PASCAL / Université Clermont Auvergne	*Examinateur*
M. Eric MAIRE	MATEIS / INSA Lyon	*Examinateur*
M. Blaise NSOM	IRDL / Université de Bretagne Occidentale	*Examinateur*
M. David THEVENET	IRDL / ENSTA Bretagne	*Examinateur*
M. Eric LOLIVE	IRDL / Université de Bretagne Occidentale	*Invité*

Institut de **R**echerche **D**upuy de **L**ôme, UMR CNRS 6027
UBS / **ENSTA Bretagne** / UBO / ENIB
2 rue François Verny, 29806 Brest Cedex 9

Table des matières

Préambule **1**

Résumé **3**

Remerciements **5**

I Notice Individuelle **7**
Notice synthétique 9

1 Curriculum Vitæ **11**
1.1 Situation actuelle 11
1.2 Formation 11
1.3 Statut professionnel 12
1.4 Collaborations académiques et industrielles 13
1.5 Responsabilités 13

2 Activités d'enseignement **15**

3 Activités de recherche **17**
3.1 Synthèse des actions menées 17
3.2 Co-encadrements 20

4 Liste des publications et communications **23**
Bilan complet des publications 23
Articles à comité de lecture 23
Chapitres d'ouvrages scientifiques 26
Communications internationales 26
Communications nationales 30

5 Détails des projets de recherche **33**

II Document scientifique 41

1 Introduction 43
1.1 Contexte industriel . . . 44
1.1.1 Secteur astronomie et spatial . . . 44
1.1.2 Secteur aéronautique . . . 45
1.1.3 Secteur automobile . . . 47
1.2 Contexte scientifique . . . 48
1.2.1 Phases, constituants, défauts dans le joint . . . 48
1.2.2 Investigation multi-échelle volumique . . . 49
1.2.3 Mécanismes d'endommagement . . . 51
1.3 Plan du document . . . 52

2 Caractérisation et modélisation des assemblages structurels par collage 53
2.1 Introduction . . . 53
2.2 Dispositifs expérimentaux et multi-instrumentation . . . 54
2.3 Contraintes résiduelles et contraintes thermiques . . . 100
2.4 Influence de l'environnement à différentes échelles . . . 122
2.5 Origine de défauts et mécanismes d'endommagement . . . 178
2.6 Modèles de comportement thermomécanique . . . 228
2.7 Etudes en cours et perspectives . . . 261

3 Caractérisation des assemblages soudés par friction malaxage 265
3.1 Introduction . . . 265
3.2 Estimation des paramètres optimaux du procédé de soudage FSW par des stratégies numériques . . . 267
3.3 Identifications des défauts et de leur effet sur les joints FSW . . . 285
3.4 Etudes en cours et perspectives . . . 306

4 Synthèse et présentation des projets à 4 ans 309
4.1 Principaux objectifs atteints . . . 310
4.1.1 Adhésifs structuraux époxy bi-composants . . . 310
4.1.2 Joints soudés par friction malaxage . . . 310
4.2 Principaux thèmes de développement . . . 311
4.2.1 Approfondissement de la caractérisation de l'effet de l'hygrométrie sur les joints collés avec de l'adhésif époxy bi-composants . . . 311
4.2.2 Utilisation des outils de mesure de champs, pour la compréhension fine de mécanismes de comportement élémentaires de joints de colle311
4.2.3 Compréhension de mécanismes de distribution des différents alliages en aluminium dans les joints FSW à l'aide de la tomographie aux rayons X . . . 311
4.3 Présentation des projets à 4 ans . . . 312

4.3.1 Caractérisation des défauts et de leur effet dans les assemblages multi-matériaux collés 312
4.3.2 Identification expérimentale des mécanismes d'endommagement 313
4.3.3 Caractérisation d'assemblages collés à base de bio-colles et colles auto-cicatrisantes 314

Bibliographie **315**

Table des figures

1.1 Telescope extra-large (The Extremly Large Telescope - ELT) [12] 45
1.2 Microstructure de l'adhésif époxy bi-composant Araldite 420 A/B **a)** - constituants (porosités et billes de verre) observés au microscope dans l'adhésif Araldite 420 A/B, à l'état *'liquide'*, juste après la phase de mélange de la matrice et du durcisseur ; **b)** - présence de gouttelettes d'eau dans un échantillon de colle Araldite 420 A/B de 400 μm d'épaisseur , après l'immersion de 30 jours dans eau déminéralisée, à 22^{o}C ; **c)** - distribution de pores dans un joint d'adhésif, après un cycle de polymérisation de 110 ^{o}C pendant 1 heure 50

Préambule

Mon parcours professionnel se décompose en deux étapes majeures, qui sont *i)* ma thèse de doctorat au sein du l'Institut Français de Mécanique Avancée (IFMA, devenu SIGMA Clermont) à Clermont-Ferrand et *ii)* mon poste actuel de Maître de Conférences de l'ENSTA Bretagne. La rédaction de ce mémoire d'Habilitation à Diriger des Recherches (HDR) représente pour moi l'occasion de faire le point sur mes activités de recherche, dans ce métier passionnant, mais qui laisse parfois peu de temps pour cela. En conséquence, je me focaliserai dans ce manuscrit sur les principales activités de recherche développées à l'ENSTA Bretagne. Ainsi, l'objectif de ce manuscrit est de dresser un bilan des activités que j'ai menées depuis ma thèse de doctorat, lorsque j'ai rejoint l'ENSTA Bretagne, il y a un peu plus de dix ans. Généralement, un manuscrit d'HDR pourrait se présenter sous différentes formes : compilation de publications, seconde thèse de doctorat ou bien comme un document de synthèse mêlant état de l'art et contributions personnelles, etc. La vocation d'un tel document est, bien sûr, la validation par des pairs des compétences scientifiques et d'encadrement, mais c'est aussi et avant tout l'occasion de prendre un peu de temps pour discuter des problématiques de recherche abordées et du recul sur ses propres activités. Dans cette optique, j'ai cherché à proposer plusieurs niveaux de lecture, notamment une vision globale des activités, démarches et outils, ainsi que des présentations plus détaillées, basées sur les articles publiés.

Le choix d'une rédaction basée sur les articles permet, à mon sens, un compromis intéressant : synthétiser dans un premier temps les éléments marquants de mes recherches puis guider le lecteur tout en lui laissant le soin de creuser les différents aspects plus en détail. C'est donc le choix qui est fait pour la structure de ce document.

De façon classique, le manuscrit se compose :

- d'une synthèse de mon parcours professionnel
- d'un curriculum vitæ détaillé décrivant mon parcours ainsi que les grandes lignes de mes activités d'enseignement, d'encadrement et de recherche
- d'une synthèse des travaux de recherche menés à l'ENSTA Bretagne, plus particulièrement au LBMS, devenu IRDL au 1er janvier 2016.

Bonne lecture !

Résumé

La première partie de ce document décrit mon parcours professionnel et la deuxième présente de manière synthétique les activités de recherche menées depuis 2012. Celles-ci portent sur la caractérisation et la modélisation du comportement mécanique des assemblages multi-matériaux. La qualité, la tenue à long terme et la durabilité des structures complexes multifonctionnelles de dernière génération sont principalement liées à la qualité des liaisons créées entre les différents constituants, souvent fortement hétérogènes. Si le soudage par friction malaxage est aujourd'hui une technique avec un niveau de maturité satisfaisant, permettant de joindre principalement des matériaux métalliques de nature différente, difficilement réalisable au moyen de techniques de soudage classiques, les assemblages structurels par collage permettent, quant à eux, de répondre à un très large spectre de liaisons avec des natures de substrats très différentes (métallique, composite, plastique, céramique, etc).

L'objectif principal de mes activités de recherche est double. D'abord *i)* des outils et des démarches de caractérisation expérimentale performants ont été proposés, assurant un spectre de sollicitations de l'assemblage très étendu, et permettant ainsi d'investiguer l'influence de différentes conditions environnementales (température, humidité). La caractérisation quantitative des défauts présents dans ces assemblages ainsi que l'effet de ces derniers sur le comportement mécanique ont été abordés, en utilisant des moyens non destructifs, in situ, de type tomographie aux rayons X. Ensuite, *ii)* à des fins de dimensionnement et de prédiction du comportement à long terme, des stratégies de modélisation ont été mises en place, permettant d'intégrer les différents comportements élémentaires (élastique, visqueux, plastique) ainsi que la dépendance du comportement à différents facteurs représentatifs, comme la température, l'humidité, ou les populations de défauts.

Mots-clefs :

— Adhésifs structuraux ; Vieillissement hydrique ; Température ; Polymère

— Caractérisation expérimentale ; Défauts ; Tomographie aux rayons X

Remerciements

Famille, Equipe, jury, collègues, doctorants, partenaires académiques, partenaires industriels, financeurs.
(à finaliser ...)

Première partie

Notice Individuelle

Notice synthétique

Claudiu BADULESCU, 42 ans
Maître de conférences de l'ENSTA Bretagne, section 60
Chercheur à Institut de Recherche Dupuy de Lôme, UMR CNRS 6027

Formation et diplômes

2010 Thèse de doctorat de l'Université Blaise Pascal - Clermont-Ferrand II
2006 DEA « Science des Matériaux, Nanomatériaux, Multimatériaux »
2005 Licence « Technologie des Constructions de Machines - (Génie Industriel) »
2000 Baccalauréat « Sciences pour l'Ingénieur »

Activités d'enseignement

Depuis 2012 ENSTA Bretagne (Licence, M1 et M2 ~ 220 h/an)
Université de Pitesti / Roumanie (M1 et M2 ~ 40 h/an), depuis 2014

Activités de recherche et d'encadrement

Résumé Mes activités de recherche portent sur l'étude du comportement mécanique des assemblages multi-matériaux collés et soudés par friction malaxage. La durabilité des assemblages collés est principalement influencée par des facteurs intrinsèques à l'assemblage (comportement de l'adhésif, présence de défauts, taux de polymérisation, etc.) et par des facteurs extrinsèques (température, l'hygrométrie, nature de sollicitation), avec des conséquences non négligeables sur la réponse à court ou à long terme de l'adhésif et donc de l'assemblage. L'objectif, dans un premier temps, est de pouvoir caractériser l'intensité de ces facteurs, d'investiguer leur effet sur le comportement de l'assemblage et de proposer et valider des lois de comportement incluant ses dépendances. Ensuite, ces modélisations seront intégrées dans des stratégies de dimensionnement adaptées tant pour des sollicitations élémentaires que pour des sollicitations complexes.

Mots-clefs *Assemblages mullti- matériaux, Adhésives, tomographie, soudage FSW*
Encadrement Thèses (7), Master 2 (12), Post-doctorat (3)

Responsabilités collectives

Responsable du Mastère Spécialisé IMANO / INO
Responsable des projets **COSICO** (ANR, 2014 - 2018, coordinateur du projet), **CARMEN**(Région Bretagne, 2020-2022), **MODESIM-FSW** (PHC - FR/ROU, 2019-2021, coordinateur en France)

PUBLICATIONS

Publications dans des revues à comité de lecture :	30
Publications dans des congrès nationaux et internationaux :	50
Chapitres dans des ouvrages internationaux :	1

CHAPITRE

1 Curriculum Vitæ

Nom :	BADULESCU
Prénom :	Claudiu
Date et lieu de naissance :	le 23/09/1981 à Pitesti (Roumanie), 42 ans
Nationalité :	Roumaine
Adresse personnelle :	11, Impasse du Temps des Cerises, 29830, Plouguin
Téléphone professionnel :	02 98 34 89 77
E-mail :	claudiu.badulescu@ensta-bretagne.fr
Fonction actuelle :	Maître de Conférences de l'ENSTA Bretagne
Etablissement :	ENSTA Bretagne
	2, Rue Francois Verny 29806 Brest Cedex 9

1.1 Situation actuelle

Depuis 2012 Maitre de conférences de l'ENSTA Bretagne
Membre de l'Institut de Recherche Dupuy de Lôme, UMR CNRS 6027

1.2 Formation

2007-2010 Thèse de doctorat de l'Université Blaise Pascal - Clermont-Ferrand II intitulée : *Calcul précis des déformations planes par la méthode de la grille. Application à l'étude d'un multicristal d'Aluminium*
Soutenue le 8 Janvier 2010 à l'IFMA devant le jury composé de : F. Pierron (Président), B. Wattrisse (Rapporteur), J. Molimard (Rapporteur), H. Haddadi (Examinateur), X. Balandraud (Examinateur), M. Grédiac (Directeur de thèse), J.D. Mathias (Co-encadrant)

2005-2006 Master 2 Recherche franco-roumain, double diplôme entre l'INP Toulouse et l'Université de Pitesti/Roumanie, intitulé : *Science des Matériaux, Nanomatériaux, Multimatériaux*

2000-2005 Ingénieur de l'Université de Pitesti/Roumanie, option « Technologie des Constructions de Machines - (Génie Industriel) »

2000 Baccalauréat « Sciences pour l'Ingénieur »

1.3 Statut professionnel

Depuis 08/2012 Enseignant-Chercheur à l'ENSTA Bretagne, Brest
Enseignements : environ 220h en moyenne par an, sur les trois années de formation du cycle d'ingénieur et du cycle d'ingénieur par alternance

02/2011 - 07/2012 Post-Doctorat au Laboratoire Brestois de Mécanique et des Systèmes, EA4325, ENSTA-Bretagne, Brest

02/2010 - 01/2011 Post-Doctorat au Laboratoire de Mécanique et d'Acoustique, UMR 7031, Marseille

01/2007 - 01/2010 Doctorant à l'Université Blaise Pascal - Clermont-Ferrand II et L'Institut français de mécanique avancée (IFMA)

1.4 Collaborations académiques et industrielles

- CEA Saclay / Irfu (2011)
- PSA - Peugeot Citroen (2012)
- RENAULT (2012)
- Université Polytechnique Hauts-de-France (2012)
- IFREMER (2014)
- RESCOLL (2014)
- Safran Composites (2015)
- Safran AE (2015)
- Safran Reosc (2017)
- Thales DMS (2020)
- MATEIS - INSA Lyon (2015)
- Université de Pitesti / Roumanie (2013)

1.5 Responsabilités

- Responsable des équipements "Mesure sans contact" du Centre d'Essais de l'IRDL (site ENSTA Bretagne), depuis le 01/09/2021
- Responsable du Mastère Spécialisé "**Ingénierie Marine, Architecture Navale et Offshore**", option "**Ingénierie Navale et Offshore**"
- Coordinateur du projet ANR ***CO****mportement, modélisation et* ***SI****mulation du* ***CO****llage structural sous une large gamme de température et de vitesse de déformation, effets du vieillissement* - ***COSICO***
- Chairman à des conférences internationales (ICEM15, COMPLAS XII).
- Reviewer pour différents journaux : Mechanics of Materials/Elsevier, Composite Structures / Elsevier, Journal of Adhesion Science and Technology / Taylor & Francis , Journal of Materials Research and Technology / Elsevier, Journal of Manufacturing Processes / Elsevier, Materials & Design / Elsevier, Journal of Materials Science & Technology / Elsevier
- Gestion de contrats industriels et de recherche
- Participation à l'organisation du CFM 2019
- Participation aux comités de sélection d'enseignants-chercheurs et d'ingénieurs de recherche
- Participation à des comités de thèse
- membre des jurys de 6 thèses (H. ALFONSO, A. ILIONI, J. DESTOUESSE, V. DUMONT, L.DUFOUR et A. TINTATU)
- membre de jurys de Master 2 et de Projets de Fin d'Etudes (ENSTA Bretagne).

CHAPITRE

2 Activités d'enseignement

Je suis, depuis août 2012, enseignant-chercheur à l'ENSTA Bretagne. A ce titre, je dispense en moyenne 250 h de cours dans les différents cycles de formation de l'école. Depuis mars 2014 j'exerce en moyenne 40 h à l'Université de Pitesti / Roumanie . Quelques détails sur les principales activités d'enseignement dispensées sont donnés dans le tableau 2.1.

Les interventions peuvent prendre différentes formes : simple intervenant, création de cours (de manière collégiale dans le cas des cours-TD), proposition de nouveaux sujets, etc. J'assure la responsabilité du Mastère Spécialisé Ingénierie Marine / Architecture Navale et Offshore . J'assure également le suivi de projets étudiants de 3^e année (entre 2 à 4 projets par an), de stages de 3^e année (1 à 2 stages en moyenne par an) et participe aux différentes soutenances qui peuvent avoir lieu tout au long de l'année.

Année	Matière	Établissement	Niveau	Type
2014 - présent	Structures Navales	ENSTA Bretagne	M2	BE (33h)
2012 - 2022	Mécanique des Solides Indéformables	ENSTA Bretagne	L3	cours (18h)+ TD (18h)
2012 - présent	Mécanique des Solides Déformables	ENSTA Bretagne	L3	TD (20h)
2012 - présent	Analyse technologique	ENSTA Bretagne	L3	cours (9h)+ TD (15h)
2012 - présent	Matériaux	ENSTA Bretagne	L3	TD (18h)
2016 - présent	Matériaux	ENSTA Bretagne	M1	cours (9h)+ TD (9h)
2013 - 2021	Eléments Finis	ENSTA Bretagne	M1	TD (8h)
2016 - présent	Mesure des champs cinématiques sans contact	ENSTA Bretagne	M2	cours (3h)
2016 - présent	Architecture Navale et Offshore	ENSTA Bretagne	M2	BE (9h)
2016 - présent	Plasticité et Éléments Finis	Université de Pitesti	M2	cours (7h)+ TD (7h)
2016 - présent	Optimisation paramétrique	Université de Pitesti	M1	cours (20h)+ TD (8h)

TABLE 2.1 – Bilan des activités d'enseignement

CHAPITRE

3 Activités de recherche

3.1 Synthèse des actions menées

Mes activités de recherche portent principalement sur le développement d'outils expérimentaux et numériques afin d'améliorer la durabilité des assemblages. Plus précisément, mes préoccupations en matière de recherche s'articulent autour de la caractérisation expérimentale et de la modélisation du comportement mécanique des assemblages, avec un focus sur les assemblages collés, et, plus récemment, sur des assemblages soudés par friction malaxage. L'objectif principal était la caractérisation du comportement mécanique d'assemblages collés utilisés dans des conditions environnementales spécifiques : température très basse, humidité, etc., tout en utilisant des montages expérimentaux pertinents développés au sein de l'équipe *« Mécanique des Matériaux et des Assemblages »*. Sur la base de ces caractérisations expérimentales, des modèles de comportement thermomécanique ont pu être construits, identifiés et validés. Les différentes études menées autour de l'objectif principal sont réalisées en étroite collaboration avec le tissu industriel, et dont la finalité est le développement d'outils directement utilisables en bureau d'études. La plupart de mes activités de recherche présentées dans cette synthèse ont été menées au LBMS (EA4325), devenu IRDL (UMR - CNRS 6027) au 1er janvier 2016, et au sein de l'équipe « Mécanique des Matériaux et des Assemblages », devenue pôle thématique de recherche « Assemblage Multi-matériaux ». D'une manière générale, différentes thématiques principales se dégagent de mes activités.

Caractérisation et modélisation des assemblages collés

Le collage structural est un mode d'assemblage qui offre de nombreux avantages vis-à-vis d'autres méthodes dites conventionnelles tel le boulonnage, le rivetage ou le soudage. En effet, il permet d'assembler des matériaux au moyen d'une procédure simple, de minimiser le poids de la structure ainsi que la dégradation des matériaux. L'utilisation du collage pour l'assemblage d'éléments de structures s'est donc démocratisée dans de nombreux domaines industriels, tels que l'automobile, la construction navale ou encore l'aéronautique. Dans ce contexte de transport en particulier, un dimensionnement fiable

est essentiel et constitue donc un enjeu majeur pour les industriels, compte tenu de l'intérêt porté à la réduction de masse des véhicules. La caractérisation expérimentale du comportement mécanique de l'adhésif représente un premier axe de recherche ayant comme finalité la prédiction fiable du comportement de l'assemblage ou de la structure collée. Découpler les différents phénomènes physiques qui peuvent se superposer lors d'un essai de caractérisation normalisé (comportement mécanique, amorçage ou propagation de fissures) permet de caractériser séparément chaque mécanisme et ainsi prédire de manière robuste le comportement de l'assemblage. En conséquence, des montages d'essais, par exemple le dispositif Scarf modifié, ont été développés afin de minimiser les effets de bord lors de la caractérisation expérimentale de l'adhésif. Ce montage, facilement utilisable en milieu industriel, assure à la fois, la minimisation des effets de bord et l'obtention de différents états de sollicitation (traction, traction-cisaillement) dans le joint. Sur la base de ces résultats, des modèles de comportement ont été construits et identifiés. Leur complexité s'étale sur un large spectre, partant des comportements mécaniques simples de type élasto-plastique 2D et 3D, jusqu'à des modèles sophistiqués qui intègrent des comportements de type viscoélasticité ou viscoplasticité.

Contraintes résiduelles et contraintes thermiques

Le collage structural s'appuie principalement sur l'utilisation de colles dites thermodurcissables. Cela implique naturellement des cycles de polymérisation caractérisés par des températures relativement élevées et qui peuvent facilement conduire à des dilatations thermiques des substrats à assembler. Après refroidissement de l'assemblage à la température de service, des contraintes résiduelles peuvent apparaître. De plus, si la température de service évolue tout au long du cycle de fonctionnement, on peut voir apparaître des contraintes thermiques. Mon deuxième axe de recherche a abordé l'étude et l'analyse de ces aspects avec comme objectif principal la prise en compte de ces contraintes résiduelles et thermiques dans les modèles de dimensionnement assurant ainsi une plus grande robustesse de la prédiction du comportement de l'assemblage.

Prise en compte des effets de l'environnement

Les propriétés des adhésifs dépendent bien évidemment de la nature de ses composants. Les colles époxy sont avant tout des matériaux polymères, caractérisés par leur sensibilité aux conditions environnementales (humidité, température, etc.). L'hygrométrie est un facteur qui doit être pris en compte lors du dimensionnement des assemblages et des structures collées. Des outils sont développés pour caractériser finement l'effet que peut avoir l'hygrométrie sur le comportement mécanique des assemblages, en passant tout d'abord par une phase de caractérisation et de modélisation du comportement sur des échantillons massiques. La présence de l'humidité dans l'adhésif est souvent accompagnée d'une altération des propriétés mécaniques de celui-ci. Il est également connu que la présence de l'humidité génère une variation de volume de l'adhésif. Ainsi, des contraintes hygrométriques peuvent s'ajouter à la dilatation thermique provoquée par la variation de température. L'analyse fine de ces facteurs passe par une phase

expérimentale longue et coûteuse en termes de moyens d'investigation. On peut alors s'orienter vers des équivalences temps - température - hygrométrie, qui pour certains adhésifs et plages de variations s'adapte très bien. Ces facteurs ont été intégrés dans les stratégies de dimensionnement développées, permettant ainsi l'amélioration de la prédiction. Alors, ces outils ont permis de construire des stratégies de dimensionnement « adaptées » pour différentes applications industrielles en intégrant uniquement les ingrédients représentatifs de l'assemblage utilisé (la température, l'humidité, etc.)

3.2 Co-encadrements

J'ai co-encadré **7 thèses** (dont 4 soutenues) et participé à l'encadrement de 11 stages de Master 2 et de 3 Post-docs.

Thèses

Claudiu Ionut MALEA (30%, thèse en co-direction, entre l'ENSTA Bretagne et l'Université de Pitesti/Roumanie , début octobre 2020). *Caractérisation expérimentale et modélisation numérique du procédé de fraisage par enlèvement de copeaux.* Co-encadrement avec Eduard NITU - directeur de thèse (Université de Pitesti / Roumanie).

Mihai Octavian CRACANEL (30%, thèse tripartite en co-direction, entre l'ENSTA Bretagne, l'Université de Pitesti/Roumanie et l'Université Polytechnique de Bucarest - Roumanie, début septembre 2020). *Processus et systèmes de soudage innovants avec élément actif rotatif* Co-encadrement avec Younes DEMMOUCHE (ENSTA Bretagne), directeur de thèse : Eduard NITU de l'Université de Pitesti / Roumanie .

Andreea TINTATU (33%, financement DGA et Thales DMS, début mars 2020). *Modélisation simplifiée d'assemblages collés pour la caractérisation mécanique d'adhésifs, des interfaces colle-substrat et l'analyse de leur vieillissement.* Co-encadrement avec Philippe Le Grognec (directeur de thèse) et Pierre Bidaud (ENSTA Bretagne).

Vincent DUMONT (40%, contrat CIFRE Safran Reosc, début thèse :novembre 2016-fin thèse : décembre 2019). *On the durability of structural adhesive bonds in thermal environments : application to space-oriented optical Systems.* Co-encadrement avec Georgios Stamoulis (IUT Brest) et David Thévenet, directeur de thèse (ENSTA Bretagne). Rapporteurs : F. Lauro et E. Toussaint. Examinateurs : S. Roux, E. Maire. Invité : A. Lefèvre. Soutenue le 11 fevrier 2020. Vincent est maintenant Ingénieur synthèse technique chez Safran REOSC.

Jaime DESTOUESSE VILLA (30%, contrat CIFRE Safran Composites, début octobre 2015, fin octobre 2018). *Caractérisation et modélisation des joints de colles sous sollicitations bi-axiales statiques.* Co-encadrement avec Malick Diakhaté (IUT de Morlaix) et David Thévenet - directeur de thèse (ENSTA Bretagne). Rapporteurs : Lucas F.M. DA SILVA et Z. ABOURA. Examinateurs : N. GODIN, F. JACQUEMIN. Invité : N. CARRERE. Soutenue le 16 novembre 2018. Jaime est actuellement Ingénieur R&D mécanique, LATTICE MEDICAL, Lille, France.

Alin ILIONI (40%, projet ANR COSICO, début octobre 2014, fin novembre 2017). *Influence of seawater ageing on the behaviour of adhesives : a rapid characterization of the evolution of mechanical properties of bonded joints.* Co-encadrement avec Peter Davies (IFREMER - Brest) et David Thévenet - directeur de thèse (ENSTA Bretagne). Rapporteurs : J. GALY et J.C. GRANDIDIER. Examinateurs : R. ADAMS, F. JACQUEMIN, S. MALLARINO. Invité : N. CARRERE. Soutenue le 27 novembre 2017. Alin est

actuellement Ingénieur R&D mécanique chez Astroparticle and Cosmology Laboratory, Paris, France.

Hugo Leonardo ALFONSO (50%, financement ADEME, projet Assemblage FAST-LITE , début octobre 2013, fin décembre 2016). *Caractérisation et modélisation des assemblages multi-matériaux sous sollicitations mixtes quasi-statiques pour la conception des structures automobiles.* Co-encadrement avec Nicolas CARERRE - directeur de thèse (ENSTA Bretagne). Rapporteurs : F.LAURO et F. LACHAUD. Examinateurs : B. CASTANIE, F. LAURIN, S. CALLOCH, G. STAMOULIS. Invité : L. TOLLIER. Soutenue le 14 decemmbre 2016. Hugo est actuellement Chef de Projet R&D chez ArcelorMittal, Paris, France.

Stage de Master 2

Lina Marcela RIANO VELEZ (50%, 2015). *Effet des différents paramètres sur la tenue d'assemblages collés.* Co-encadrement avec N. CARRERE. Stage réalisé en collaboration avec CETIM Nantes.

Gratiela Narcisa CALIN (100%, 2016). *Evolution et modélisation des contraintes résiduelles au sein d'un assemblage collé acier-aluminium sous un chargement thermo-mécanique.*

Elena VANGLAR (100%, 2016). *Simulation du soudage par friction éléments finis (MEF).*

Emanuel BADULESCU (50%, 2016). *Développement d'un essai pour caractériser le comportement jusqu'à rupture d'un assemblage collé sous taux de tri-axialité variable.* Co-encadrement avec G. STAMOULIS.

Mihai-Octavian CRACANEL(60%, 2018). *Caractérisation expérimentale d'un assemblage en alliage d'Aluminium obtenu en utilisant le procédé de soudage par friction malaxage.* Co-encadrement avec Malick DIAKHATE.

Diana SCIRLOI (100%, 2018). *Effet des défauts sur le comportement mécanique d'un joint de soudure FSW bout à bout en cuivre.*

Mihaita PIRVU (50%, 2019). *Influence des paramètres du procédé de soudage FSW sur le comportement mécanique de l'assemblage.* Co-encadrement avec Malick DIAKHATE.

Andreea TINTATU (100%, 2019). *Effet des porosités sur le comportement mécanique d'un joint de colle.*

Claudiu MALEA (100%, 2019). *Simulation numérique de l'usinage par enlèvement*

de copeaux, avec la méthode des éléments finis.

Roxana OPRESCU (100%, 2020). *Caractérisation expérimentale et numérique d'un assemblage en alliage de cuivre, obtenu par le procédé de soudage par friction malaxage.*

Madalina LUPU (100%, 2020). *Caractérisation des mécanismes d'endommagement pour un joint de colle, en utilisant la tomographie par absorption de rayons X.*

Raducu BULACU (100%, 2023). *Prise en compte de la source de chaleur de type TIG dans la simulation du procédé de soudage par friction malaxage.*

Post-docs

Aurelian Denis NEGREA (50%, 2017, 2 mois, financement Campus FRANCE). *Caractérisation expérimentale d'un assemblage metal-metal, obtenu par le procédé de soudage 'friction-malaxage'*. Co-encadrement avec E. NITU de l'Université de Pitesti/Roumanie

Jan Cristian GRIGORE (50%, 2018, 2 mois, financement Campus FRANCE). *Caractérisation expérimentale par DIC 3D d'un assemblage métallique sandwich, obtenu par le procédé de soudage 'friction-malaxage'*. Co-encadrement avec E. NITU, Université de Pitesti/Roumanie

Marina BUNEA (70%, 2021, 18 mois, financement Région BRETAGNE - SAD). *Caractérisation et modélisation des mécanismes d'endommagement dans des assemblages collés à l'aide d'un essai mini-Scarf*. Co-encadrement avec M. DIAKHATE, UBO, IUT de Morlaix

CHAPITRE

4 Liste des publications et communications

Bilan complet des publications

Nombre de publications dans des revues à comité de lecture :	**30**
Nombre de publications dans des congrès nationaux et internationaux avec actes :	**34**
Nombre de publications dans des congrès nationaux et internationaux sans actes :	**16**
Nombre de chapitres dans des ouvrages internationaux :	1
Nombre total de citations :	**773**
H index (d'après les données de Google Scholar) :	**17**

Articles à comité de lecture

1. Andreea Tintatu, Claudiu Badulescu, Pierre Bidaud, Philippe Le Grognec, Jérôme Adrien, Eric Maire, Hervé Bindi and Corentin Coguenanff, **Understanding of water uptake mechanisms in an epoxy joint characterized by pore-type defects**, The Journal of Adhesion, Vol. (–), 2023, https ://doi.org/10.1080/00218464.2023.2187293

2. E. L. Nitu, M. Diakhaté, C. Badulescu, M. Grédiac, B. Blaysat, D. M. Iordache, A. Bosneag, J. Adrien, E. Maire, M. Dhondt, and Y. Demmouche, **Analyzing defects and their effects on the strength of a three-layer FSW joint by using X-ray microtomography, Localized Spectrum Analysis, and Acoustic Emission** , Materials Characterization, Vol. (190), 2022, https ://doi.org/10.1016/j.matchar.2022.112069

3. Juan Pablo Marquez Costa, Julien Jumel, Georgios Stamoulis and C. Badulescu, **Self-Similar Crack Propagation Along Viscoelastic Interface during Double Cantilever Beam Test**, Mechanics of Time-Dependent Materials, Vol. (yyy) 2022, https ://doi.org/10.1007/s11043-022-09559-8

4. V. Dumont, G. Stamoulis, C. Badulescu, A. Lefèvre, and D. Thévenet, **Investigation of the influence of the temperature on the fracture properties of**

adhesive joints, Engineering Fracture Mechanics, Vol. (269) 2022, https ://doi.org/10.1016/j.engfracmech.2022.108524

5. Eduard Laurentiu Nitu, Monica Daniela Iordache, C. Badulescu, **Numerical investigation of the radial cold rolling process of the grooves**, Journal of Engineering Manufacture :Part B, mai, 2021.
6. Monica Daniela Iordache, Claudiu Badulescu, Malick Diakhate, Marius Adrian Constantin, Eduard Laurentiu Nitu, Younes Demmouche, Matthieu Dhondt and Denis Negrea, **A numerical strategy to identify the FSW process optimal parameters of a butt-welded joint of quasi-pure copper plates : modeling and experimental validation**, The International Journal of Advanced Manufacturing Technology, Vol. 115(7), pages : 2505-2520, 2021.
7. Nicolas Leconte, Benjamin Bourel, Franck Lauro, Claudiu Badulescu, and Eric Markiewicz, **Strength and failure of an aluminum/PA66 self-piercing riveted assembly : experiments and modeling**, International Journal of Impact Engineering, Volume 142, avril, 2020.
8. V. Dumont, C. Badulescu, G. Stamoulis, J. Adrien, E. Maire, D. Thévenet, and A. Lefèvre, **Investigating the influence of the curing cycle on the creation of porosities in structural epoxy adhesives joints by means of X-ray microtomography**, The Journal of Adhesion,Vol. 97(12), pages : 1073-1106, 2021,
9. V. Dumont, C. Badulescu, G. Stamoulis, J. Adrien, E. Maire, A. Lefèvre, and D. Thévenet, **On the influence of mechanical loadings on the porosities in structural epoxy adhesives joints by means of in-situ X-ray microtomography**, International Journal of Adhesion and Adhesives,2020
10. V. Dumont, C. Badulescu, J. Adrien, N. Carrere, D. Thévenet, and E. Maire, **Experimental Investigation of Porosities Evolution in a Bonded Assembly by means of X-ray Tomography**, The Journal of Adhesion, 2019
11. Alin ILIONI, Pierre-Yves LE GAC, Claudiu BADULESCU, David THÉVENET, Peter DAVIES, **Prediction of mechanical behaviour of a bulk epoxy adhesive in a marine environment**, The Journal of Adhesion,Vol. 95, pages 64-84, 2019
12. Destouesse, J ; Diakhate, M ; Badulescu, C ; Thévenet ; Stackler, M ; Albouy, W ; Carrere, N, **Cluster analysis of acoustic emission data to investigate the damage evolution in modified scarf joint under bi-axial loading**, The Journal of Adhesion, 2018
13. Alin ILIONI, Claudiu BADULESCU, Nicolas CARRERE, Peter DAVIES, David THÉVENET, **A Viscoelastic-Viscoplastic Model to Describe Creep tnd Strain Rate Effects on the Mechanical Behaviour of Adhesively-Bonded Assemblies**, International Journal of Adhesion and Adhesives,Vol. 82, pages 184 - 195, 2018.
14. L. Alfonso, C. Badulescu, N. Carrere, **Use of the modified Arcan fixture to study the strength of bonded assemblies for automotive applications : effect of different parameters**, International Journal of Adhesion and Adhesives, Vol. 80, pages 104 -114, 2018.

15. G. Stamoulis, N. Carrère,J.-Y. Cognard, P. Davies, C. Badulescu, **Investigating the fracture behavior of adhesively bonded metallic joints using the Arcan fixture**, International Journal of Adhesion and Adhesives, Vol. 66, pages 147 - 159, 2016.
16. L. Alfonso, A. Uguen, C. Badulescu, J.-Y. Cognard, T. Bonnemains, E. Lolive and N. Carrere, **Determination of the 3D failure envelope of a composite based on a modified Arcan test device**, Composite Structures, Vol. 131, pages 185-193, 2015.
17. N. Carrere, C. Badulescu, J.-Y. Cognard, D. Leguillon, **3D models of specimens with a scarf joint to test the adhesive and cohesive behavior of adhesives**, International Journal of Adhesion and Adhesives, Vol. 62, pages 154-164, 2015.
18. C. Badulescu, C. Germain, J.Y. Cognard, N. Carrère **Characterisation and modelling of the viscous behaviour of adhesives using the modified Arcan device**, Journal of Adhesion Science and Technology, Vol. 29, 5, pp. 443-461, 2015.
19. C. Badulescu, Noel Lahellec, Pierre Suquet **Field statistics in linear viscoelastic composites and polycrystals** , European Journal of Mechanics A / Solids, Vol. 49, (329-344), 2015, 10 pages.
20. G. Stamoulis, N. Carrere, J.Y. Cognard, P. Davies, C. Badulescu **On the experimental mixed-mode failure of adhesively bonded metallic joints**, International Journal of Adhesion and Adhesives, Vol. 51, (148-158) , 2014, 11 pages.
21. R. Moutou Pitti, C. Badulescu, M. Grédiac **Characterization of a cracked specimen with full-field measurements : direct determination of the crack tip and energy release rate calculation** , International Journal of Fracture, Vol. 187(109 - 121), 2014, 14 pages.
22. J.Y. Cognard, C. Badulescu, J. Maurice, R. Créac'hcadec, N. Carrère, P. Vedrine **On modelling the behaviour of a ductile adhesive under low temperatures**, International Journal of Adhesion and Adhesives, Vol. 47, (46-56) , 2013, 10 pages.
23. Michel Grédiac, Frédéric Sur, Claudiu Badulescu, Jean-Denis Mathias, **Using deconvolution to improve the metrological performance of the grid method**, Optics and Lasers in Engineering, Vol.51(6), 2013, 19 pages.
24. J.Y. Cognard, L. Sohier, P. Davies, N. Carrère, R. Créac'hcadec, C. Badulescu, **Analysis of the mechanical behaviour of composites and their bonded assemblies under out-of-plane loads using a modified Arcan apparatus**, Composite and nanostructures, Vol.1 (19-36), 2013
25. C. Badulescu, M. Bornert, J.-C. Dupré, S. Equis, M. Grédiac, J. Molimard, P. Picart, R. Rotinat, et V. Valle, **Demodulation of Spatial Carrier Images : Performance Analysis of Several Algorithms**, Experimental Mechanics, Experimental Mechanics 53, 8 pp.1357-1370, 2013, 14 pages.
26. C. Badulescu, J.Y. Cognard, R. Créac'hcadec, P. Vedrine, **Analysis of the temperature - dependent behaviour of a ductile adhesive under monotonic tensile / compression-shear loads**, International Journal of Adhesion and Adhesives, Vol.36, 2012, 9 pages.

27. D. Delpueyo, M. Grédiac, X. Balandraud et C. Badulescu, **Investigation of martensitic microstructures in a monocrystalline Cu-Al-Be shape memory alloy with the grid method and infrared thermography**, Mechanics of Materials, Vol. 45, 2012, 18 pages.
28. C. Badulescu, M. Grédiac, H. Haddadi, J.-D. Mathias, X. Balandraud et H.-S. Tran, **Applying grid method and infrared thermography to investigate plastic deformation in aluminium multicrystal** , Mechanics of Materials, Vol. 43(1), 2011, 18 pages.
29. C. Badulescu, M. Grédiac et J.-D. Mathias, **Investigation of the grid method for accurate in-plane strain measurement**, Measurement Science and Technology, Vol.20(1), 2009, 13 pages.
30. C. Badulescu M. Grédiac J.D. Mathias et D. Roux, **A Procedure for accurate one-dimensional strain measurement using the grid method**, Experimental Mechanics, Vol.49(6), 2009, 14 pages.

Chapitres d'ouvrages scientifiques

1. R. Moutou Pitti, C. Badulescu, M. Grediac **Experimental and Numerical Fracture Analysis of a Pre-cracked Aluminum Specimen Using the Grid Method** 01/2014 ; DOI :10.1007 978-3-319-00765-6 12 ISBN : 978-3-319-00765-6 In book : Fracture and Fatigue, Volume 7, Edition : Sandia National Laboratories, Publisher : Springer International Publishing, Editors : Carroll Jay, pp.79-84

Communications internationales

1. C. Badulescu, M. Diakhaté, B. Blaysat, M. Grédiac, J. Adrien, A. Bosneag, M. Iordache, E. Nitu, **Characterization of failure mechanisms in a FSW joint by using the Localized Spectrum Analysis, Acoustic Emission and X-ray microtomography**, PhotoMechanics IDICs Conference, Nantes, 2021
2. Daniela-Monica Iordache, Roxana Oprescu, Claudiu Malea, Eduard-Laurentiu Nitu, Mihai Cracanel, Claudiu Badulescu, **Determination of Johnson-Cook material constants for copper using traction test and inverse identification**, International Conference - Modern Technologies in Industrial Engineering, 23-26 Juin, Eforie Nord, Romania, 2020
3. M. Bunea, M. Diakhate, C. Badulescu, **Different strategies for measuring the volume displacement field of an epoxy adhesive**, 6^{rd} International Conference on Adhesive Bonding, Porto, 2021
4. A. Tintatu, P. Bidaud, C. Badulescu, P. Le Grognec, **Understanding of water uptake mechanisms in an epoxy joint characterized by pore-type defects**, 6^{rd} International Conference on Adhesive Bonding, Porto, 2021

5. M A Constantin, M D Iordache, E L Nitu, M Diakhaté, Y Demmouche, M Dhondt, and C Badulescu, **An efficient strategy for 3D numerical simulation of friction stir welding process of pure copper plates**, International Conference - Modern Technologies in Industrial Engineering, 23-27 Juin, Constanta, Roumanie 2020
6. V. Dumont, C. Badulescu, D. Thévenet and G. Stamoulis, **Investigation of the influence of the curing cycle on the creation of porosities in adhesively bonded assemblies using X-ray microtomography** , International Conference on Structural Adhesive Bonding, 11 - 12 Juillet, Porto, 2019
7. V. Dumont,G. Stamoulis, C. Badulescu, D. Thévenet and A. Lefèvre, **Influence of the temperature on the fracture properties of adhesive joints**, International Conference on Advanced Computational Engineering and Experimenting, 1-5 Juillet, Athènes, 2019
8. C. Badulescu, V. Dumont and David Thévenet, **Effect of temperature on a bi-compound epoxy adhesive in metal-composite assemblies**, International Congress on Advanced Materials Sciences and Engineering, Osaka, 22-24 juillet, 2019
9. J. Destouesse,M. Diakhate, C. Badulescu, David Thévenet, M. Stackler, W. Albouy, N. Carrère, **Methodology to characterize the mechanical behavior within the adhesive joints**, 12th European Adhesion Conference and 4th Luso-Brazilian Conference on Adhesion and Adhesives, Lisbone, 5-7 septembre, 2018
10. C Badulescu,B. Blaysat, M. Grédiac, **Measuring in-plane displacement and strain fields with the grid method. A feasibility study on superconducting magnet**, The workshop #2 on Nb3Sn technology for accelerator magnets, Paris, 2018
11. J Destouesse, M Diakhate, C Badulescu, D Thevenet,M Stackler, W Albouy, N Carrere, **Methodology to characterize the mechanical behavior within the adhesive joints**, 12th European Adhesion Conference and 4th Luso-Brazilian Conference on Adhesion and Adhesives, Lisbon, 2018
12. Badulescu C., Carrere N., Adrien J., and Maire E., **3D Experimental Analysis of a Scarf Test Joint by means of X-ray Tomography** , 4^{rd} International Conference on Structural Adhesive Bonding, Porto,2017
13. J. Destouesse, C. Badulescu, M. Diakhate, David Thévenet, M. Stackler, W. Albouy, N. Carrère, **Characterization of Damage Mechanisms in Adhesive Bonding after Acoustic Emission Data** , 4^{rd} International Conference on Structural Adhesive Bonding, Porto,2017
14. J. Destouesse, C. Badulescu, M. Diakhate, M. Stackler, W. Albouy, N. Carrère, **Modified Scarf joints : A new methodology to test adhesive joints** , the eleventh European Adhesion Conference- Euradh 2016, Glasgow, Scotland, septembre 2016
15. A. Ilioni D. Thevenet, C. Badulescu, P. Davies, P.-Y. Le Gac, **Influence of ageing on the behaviour of adhesives - a rapid characterisation of the evolution**

of mechanical properties of bonded joints, the eleventh European Adhesion Conference - Euradh 2016, Glasgow, Scotland, septembre 2016

16. Badulescu C., Carrere N., Adrien J., and Maire E., **3D experimental analysis of a bonded assembly by means of x-ray tomography**, ICEM17, Rhodes, Greece, July 2016

17. Leonardo ALFONSO, Claudiu BADULESCU, Nicolas CARRERE, **Proposition of a characterization procedure of the out-of-plane behavior of bonded thermoplastic composite assemblies** , 3^{rd} International Conference on Structural Adhesive Bonding, Porto,2015

18. Uguen, C. Badulescu, T. Bonnemains, E. Lolive, N. Carrère, **Characterization of composite bonded assemblies using a three-point bending test**, 3^{rd} International Conference on Structural Adhesive Bonding, Porto,2015

19. A. Ilioni, N. Carrere, C. Badulescu, **Developing a viscoelastic model capable of describing the effects of strain rate and temperatures of the adhesives ?s mechanical behavior**, 3^{rd} International Conference on Structural Adhesive Bonding, Porto,2015

20. C. Badulescu, J.Y. Cognard, J. Maurice, R. Créac'hcdec, N. Carrère, P. Vedrine **Modelling of the low temperature-dependent behaviour of a ductile adhesive under monotonic tensile/compression-shear loads using a non associated pressure dependent model** International Conference on Computational Plasticity - COMPLAS 2013, Barcelona/Espagne, septembre 2013

21. N. Carrere, C. Badulescu et J.-Y. Cognard, **Determination of the failure envelop on an adhesive using a modified Arcan tests device - role of the plasticity and of the residual stresses**, 2^{nd} International Conference on Strctural Adhesive Bonding ,Porto/Portugal, juillet 2013

22. M. Grédiac, F.Sur, C. Badulescu, et JD. Mathias, **Deconvolution of strain maps obtained with the grid method**, SEM 2013 Annual Conference - Exposition on Experimental and Applied Mechanics, Lombard (Ireland), juin 2013

23. R. Moutou Pitti, C. Badulescu et M. Grédiac, **Experimental and numerical fracture analysis of a pre-cracked aluminum specimen using the grid method**, SEM 2013 Annual Conference - Exposition on Experimental and Applied Mechanics, Lombard (Ireland), juin 2013

24. M. Grédiac, F.Sur, C. Badulescu, et JD. Mathias, **Improving the spatial resolution of the grid method with deconvolution**, Photomechanics 2013, Montpellier (France) mai 2013

25. Cognard J.Y., Badulescu C., Carrère N., Créac'hcadec R., Vedrine P. **Numerical analysis of stress concentrations in adhesively-bonded assemblies under elastic thermo-mechanical loads - Application to the characterisation of the adhesive behaviour**, The Eleventh International Conference on Computational Structures Technology, Dubrovnik, Croatia, septembe 2012

26. C. Badulescu, J.Y. Cognard, R. Créac'hcadec, P. Vedrine, **Experimental analysis of the temperature dependent behavior of a ductile adhesive under tensile/compression-shear load**, 15th International Conference on Experimental Mechanics, Porto/Portugal, juillet 2012

27. Q. H. Vu, R. Brenner, O. Castelnau, C. Badulescu, N. Lahellec, H. Moulinec et P. Suquet, **An incremental method for the homogenization of thermo-viscoelastic polycrystals**, 2nd International Conference on Material Modelling, Paris, France, septembre 2011

28. D. Delpuyo, M.Grédiac, X. Balandraud et C. Badulescu, **Metrological analysis of several algorithms used to demodulate images with spatial carrier**, Sem Annual Conference & Exposition on Experimental and Applied Mechanics, Mohegan Sun, Uncasville, Connecticut, USA, juin 2011

29. O. Castelnau, C. Badulescu, R. Brenner, P. Duval, F. Grennerat, N. Lahellec, M. Montagnat, H. Moulinec, P. Suquet et Q. H. Vu, **The transient creep of polycrystalline ice inferred from theoretical, numerical and experimental micromechanical approaches**, The Minerals, Metals and Materials Society 2011, Annual Meeting & Exhibition, San Diego, California, USA, fevrier 2011

30. J. Molimard, C. Badulescu, M. Bornert, J.C. Dupré, S. Equis, M. Grédiac, P. Picart, R. Rotinat, V. Valle dans le cadre du GDR CNRS 2519, **Metrological analysis of several algorithms used to demodulate images with spatial carrier**, ICEM14 (International Conference On Experimental Mechanics), Poitiers,France, juillet 2010

31. C. Badulescu, M. Grédiac, J.-D. Mathias, X. Balandraud, H. Haddadi, H.-S. Tran, **Investigating the mechanical response of an aluminum multicrystal with full-field measurement techniques**, SEM Annual Conference and Exposition on Experimental and Applied Mechanics, Indianapolis, Indiana, USA, Juin 2010

32. Suquet P., Labé A., Lahellec N., Moulinec H. et Badulescu C., **Elasto-viscoplastic behavior of polycrystals : a comparison between full-field simulations and a micromechanical model based on "effective" internal variables**, IV European Conference on Computational Mechanics (ECCM 2010), Paris : France, mai 2010

33. A. Deheeger, C. Badulescu, JD. Mathias et M. Grédiac, **Experimental study of thermal stresses in a bonded joint**, International Conference on Modern Practice in Stress and Vibration Analysis, Cambridge (Grande-Bretagne) septembre 2009

34. C. Badulescu, M. Grédiac et JD. Mathias, **Accurate strain measurement with the grid method** ,4th International Conference on Optical Measurement Techniques for Structures and Systems, Anvers, Belgique, mai 2009

Communications nationales

1. Claudiu BADULESCU, Malick DIAKHATE, Vincent DUMONT, Jérôme ADRIEN, Marina BUNEA, David THEVENET, **Effet du cycle de polymérisation sur la création de pores dans les joints adhésifs structuraux de type époxy**, 4ème Colloque - Assemblages Mécaniques, Saint-Ouen, 2021
2. C Badulescu , M A Constantin, M D Iordache, E L Nitu, M Diakhaté, D Negrea, Y Demmouche et M Dhondt, **Une stratégie numérique efficace pour identifier les paramètres optimaux du procédé FSW, d'un assemblage soudé bout à bout de plaques en cuivre quasi-pur : validation expérimentale** , Réunion commission FSW/P de la SF2M et AFM, visio, 2021
3. Diana Scarloi, Marius Adrian Constantin, Claudiu Badulescu, Denis Negrea, Malick Diakhate, Eduard Nitu, Monica Iordache, **Influence des défauts de soudage FSW sur le comportement mécanique d'un assemblage bout à bout en Cu-DHP : analyse microscopique et par corrélation d'images numériques**, Le 24ème Congrès Français de Mécanique, 26-30 Août, Brest, 2019
4. Mihai-Octavian Cracanel, Ana Bosneag, Malick Diakhate, Claudiu Badulescu, Eduard Nitu, Monica Iordache, Jan Grigore, **Influence des paramètres du procédé de soudage FSW sur le comportement mécanique de l'assemblage : analyse par émission acoustique et corrélation d'images numériques**, Le 24ème Congrès Français de Mécanique, 26-30 Août, Brest, 2019
5. Vincent Dumont, Claudiu Badulescu, Jérôme Adrien, Eric Maire, Georgios Stamoulis, David Thévenet, Anthony Lefèvre, **Mesure volumique de champs de déplacements dans des joints collés par microtomographie aux rayons X**, Le 24ème Congrès Français de Mécanique, 26-30 Août, Brest, 2019
6. Claudiu BADULESCU et David THEVENET, **Effet de la température dans les assemblages métal-composite avec une colle structurelle de type époxy bi-composant**, 3-ème Colloque de l'association SUPMECA- Les Assemblages Mécaniques, 2-3 Juillet, Saint-Ouen, 2019
7. Claudiu BADULESCU, Alin ILIONI, David THEVENET, **Modélisation du comportement des assemblages collés : une stratégie de caractérisation**, 2e Colloque de l'association SUPMECA- Les Assemblages Mécaniques, 4-5 Juillet, Saint-Ouen, 2017
8. BADULESCU Claudiu (IRDL - Brest), CARRÈRE N., ADRIEN J., MAIRE E., **Caractérisation expérimentale d'un assemblage collé en utilisant la microtomographie. Mesure de champs de déplacement volumiques**, Journée Mesures de Champs à l'échelle micro, Juin 2016, Paris
9. Leonardo ALFONSO, Claudiu BADULESCU, Nicolas CARRERE, **Proposition d'une méthode de caractérisation de la résistance hors-plan des assemblages collés à matrice thermoplastique**, Les Journées Nationales sur les Composites, Lyon, 2105

10. C. Badulescu, N. Carrère **Modélisation du comportement viscoélastique des assemblages collés à différentes températures**, Journée Scientifique et Technique JST - AMAC / AFM Bordeaux novembre, 2013
11. Quoc Huy Vu, C. Badulescu, R. Brenner, O. Castelnau et H. Moulinec **Une méthode incrémentale pour l'homogénéisation de polycristaux thermo - viscoélastiques**, Congrès Français de Mécanique, Besançon, août 2011
12. D.Delpuyeo, X.Balandraud, M. Grédiac et C. Badulescu **Etude de la transition de phase d'un monocristal d'AMF en Cu-Al-Be par techniques de mesures de champs**,Congrès Français de Mécanique, Besançon, août 2011
13. C. Badulescu, J.-D Mathias et M. Grédiac **Calcul direct de champs de déformations avec la méthode de la grille : principe et applications**, Congrès Français de Mécanique Marseille , août 2009
14. J. Molimard, C. Badulescu, M. Bornert, J.C. Dupré, S. Equis, M. Grédiac, P. Picart, R. Rotinat, V. Valle dans le cadre du GDR CNRS 2519 **Méthodologie d'analyse métrologique d'algorithmes de traitement d'images à porteuse : résolution et résolution spatiale**, Congrès Français de Mécanique Marseille , août 2009
15. J. Molimard, C. Badulescu, M. Bornert, J.C. Dupré, S. Equis, M. Grédiac, P. Picart, R. Rotinat, V. Valle, B. Wattrisse **Caractérisation métrologique du décodage de l'information dans les méthodes optiques de champ : application à l'intercomparaison de méthodes à codage périodique**, 9eme Congres Francophone MTOI Nantes, novembre 2008
16. C. Badulescu, J.-D Mathias et M. Grédiac **Détermination de champs de déplacements cinématiques par la méthode de la grille associée a un traitement d'images par ondelettes**, Congrès Français de Mécanique,Grenoble, août 2007.

CHAPITRE

5 Détails des projets de recherche



Projet FASTLITE Assemblage (ADEME 2013 - 2017) et thèse de H. L. ALFONSO

Rôle : Co-encadrant de la thèse (avec N. CARRERE).

Titre : Solutions technologiques industrielles pour l'assemblage structural de composants multimatériaux

Partenaires industriels : Renault et PSA - Groupe (coordonnateurs), Laser Cheval, ARaymond, Böllhoff, Plastic Omnium, Solvay, CETIM, ESI Group, Altair

Partenaires académiques : ENSTA Bretagne et Université de Valenciennes

Montant : 6,7 M€ (3,3 M€ financés)

Résumé : Les objectifs du projet portent sur l'émergence de solutions d'assemblages multi-matériaux à un coût compétitif et compatibles avec des cadences automobiles. Le caractère innovant du projet s'appuie sur *i)* la Recherche de techniques d'assemblage multi-matériaux pour l'industrie automobile et *ii)* la modélisation numérique de la tenue des assemblages de pièces multi-matériaux. L'atteinte des objectifs du projet se traduira par la définition de règles de conception d'assemblages multi-matériaux, des outils de modélisation des assemblages ou règles d'assemblage, d'une évaluation des coûts d'industrialisation et d'une évaluation de la recyclabilité.

Mots-clefs : *Assemblage multi-matériaux ; Collage ; Industrie automobile ; Modélisation numérique*



Projet COSICO (ANR 2014 - 2018) et thèse de A. ILIONI

Rôle : Coordinateur du projet et co-encadrant de la thèse (avec D. THEVENET)

Titre : Comportement, modélisation et simulation du collage structural sous une large gamme de température et de vitesse de déformation, effets du vieillissement

Partenaires industriels : FMC Florian Madec Composite, Brest
RESCOLL, Pessac

Partenaires académiques : ENSTA Bretagne (porteur du projet) ; ENSAM - Paris ; ICube - UMR 7357 ; IFREMER et RESCOLL

Labelisations : Pôle de compétitivité Mer Bretagne Atlantique

Montant : 1950 k€ (533 k€ financés)

Résumé : Les structures de type pâles d'éoliennes off-shore et d'hydroliennes sont réalisées en plusieurs parties et ensuite assemblées en utilisant des solutions collées. Toutefois, une problématique majeure concerne la durabilité de ces assemblages en milieu marin avec des objectifs de durée vie très élevés. Afin de permettre une meilleure exploitation de ces systèmes, il apparaît indispensable de disposer d'outils permettant de prévoir leur durée de vie et le cas échéant aider à définir les délais de maintenance. Le but de ce projet est d'utiliser la complémentarité entre des moyens de caractérisation et de modélisation à différentes échelles (échelle de la microstructure, échelle de l'adhésif et échelle de l'assemblage) en prenant en compte les effets du vieillissement en eau de mer. L'objectif final est de développer et d'identifier des lois de comportements prenant en compte le vieillissement pour le dimensionnement de structures collées. L'avantage de cette approche, appliquée aux structures collées, est de permettre une évaluation plus rapide des propriétés à long terme des structures Énergies Marines Renouvelables (EMR) et ainsi permettre un retour plus rapide vers le dimensionnement des structures et la formulation de colles. En effet, l'approche classique consiste à effectuer des essais de validation sur les structures dans les conditions de vieillissement les plus sévères. L'approche proposée ici permettra grâce aux essais de caractérisation à petites échelles couplés à des essais de vieillissement accéléré de prévoir le comportement de la colle dans la structure assemblée.

Mots-clefs : *Collage structural ; Vieillissement hydrique ; Durabilité ; Modélisation numérique*



Thèse de J. DESTOUESSE VILLA (CIFRE avec SAFRAN Composites, 2015-2018)

Rôle : co-encadrant de la thèse (avec D. THEVENET et M. DIAKHATE)

Descriptif : Le collage structural se présente comme une alternative intéressante aux méthodes classiques d'assemblages par ajout d'éléments mécaniques pour alléger les structures aéronautiques. Cependant, l'utilisation de cette méthode soulève de nombreuses questions en termes de conception, caractérisation ou modélisation. Ce travail, à fort caractère expérimental, vise deux grands objectifs : *i)* sélectionner les moyens d'instrumentation les plus adaptés pour la caractérisation du comportement jusqu'à rupture des assemblages collés et *ii)* prédire le comportement des assemblages collés à partir d'une caractérisation et d'une modélisation complète sous chargements quasi-statiques biaxiaux, en utilisant un type d'essai simple et industrialisable. Dans un premier temps, pour atteindre ces objectifs, un nouvel essai appelé Scarf modifié a été proposé, afin de caractériser le comportement mécanique du joint de colle, en minimisant les effets de bord par la présence de becs. La deuxième partie du projet a porté sur le développement d'une stratégie de caractérisation simplifiée du comportement de joint de colle, sous certaines hypothèses (états de contraintes/déformations, continuité du champ de contraintes). Cette stratégie a permis d'obtenir le comportement intrinsèque de l'adhésif sous la forme de courbes $\sigma = f(\varepsilon)$. La dernière partie abordée dans ces travaux s'intéresse quant à elle à l'identification et la sélection des moyens de métrologie les plus appropriés, pour accompagner la caractérisation expérimentale et le suivi de santé de la matière.

Mots-clefs : *Assemblage collés, Essai Scarf modifié, systèmes d'instrumentation*



Thèse de V. DUMONT
(CIFRE avec SAFRAN Reosc, 2017-2020)

Rôle : co-encadrant de la thèse (avec D. THEVENET et G. STAMOULIS)

Descriptif : Le collage structural est une technique d'assemblage se retrouvant dans de nombreux secteurs industriels du fait de ses divers avantages. Il est entre autres possible de réaliser aisément des assemblages multimatériaux grâce à ce procédé, ce qui est un avantage certain dans la conception de structures de haute technologie, comportant de nombreux éléments de tailles, matériaux et fonctions variables. Les systèmes optiques présents dans les télescopes (actuels comme futurs) sont autant d'exemples parlants de ce type d'applications, nécessitant à la fois fiabilité dans le temps et connaissance précise des propriétés des adhésifs utilisés. Ces systèmes optiques sont soumis à des chargements thermomécaniques variés, impliquant divers phénomènes à diverses échelles du comportement des adhésifs. Pour apporter de nouveaux éléments de réponse à ces questionnements opérationnels et scientifiques, une caractérisation des propriétés mécaniques d'assemblages collés sous différents environnements thermiques a été réalisée, de manière à étudier l'influence de la température sur les propriétés élastiques, viscoélastiques et viscoplastiques d'un adhésif. Les paramètres d'une loi viscoélastique-viscoplastique spectrale ont ainsi été identifiés. Par ailleurs, les taux de restitution d'énergie critiques dans le plan mode I / mode II ont également été étudiés en fonction de la température via une méthode alternative aux standards ISO et ASTM. Enfin, une étude poussée de la microstructure de joints collés a été réalisée au moyen de mesures de microtomographie aux rayons X, mettant en évidence divers phénomènes liés à la polymérisation et à la croissance de porosités.

Mots-clefs : *Assemblages collés ; Loi de comportement ; Mécanique de la rupture ; contraintes résiduelles et thermiques ; Caractérisation microstructurale ; Tomographie aux rayons X in-situ*



Projet MODESIM - FSW (PHC BRANCUSI 2019 - 2021)

Rôle : Responsable du projet en France

Titre : Modelisation numérique et simulation du procédé soudage par friction malaxage avec élément actif rotatif-FSW

Partenaire : l'Université de Pitesti / Roumanie

Résumé :

Le projet collaboratif entre l'Université de Piteşti (Roumanie) et l'ENSTA – Bretagne (France) s'est déroulé du juillet 2019 au décembre 2021. Ce projet avait pour objectif le développement des modèles numériques pour simuler le processus de soudage par friction malaxage (FSW) afin d'améliorer l'assemblage bout-à-bout d'échantillons de cuivre quasi-pur. La modélisation numérique du procédé de friction-malaxage a été initiée dès le début du projet, en développant des modèles numériques *« simples »*. Ceux-ci ont été continuellement améliorés tout au long du projet, *i)* en identifiant les valeurs des coefficients dans la loi décrivant le comportement thermo-mécanique (Johnson-Cook), *ii)* en appliquant la stratégie « mass scaling » pour diminuer le temps de calcul et *iii)* en modélisant efficacement le frottement (dépendance à la température). À partir des joints FSW réalisés sous différentes conditions technologiques, plusieurs échantillons ont été prélevés, instrumentés et caractérisés. Des analyses microstructurales ont été réalisées (pour mettre en évidence la structure et les défauts éventuels des joints), des mesures de dureté (pour mettre en évidence l'influence des déformations et des températures lors du procédé de soudage), des analyses aux rayons X (pour mettre en évidence les défauts dans le joint) et des essais de traction (qui, grâce à des techniques d'investigation complexes telles que les mesures de champs cinématiques sans contact ont permis d'identifier le comportement mécanique macroscopique et microscopique de ces structures soudées). La nouveauté dans ce projet est liée à deux avancées interconnectées : *1)* un modèle numérique du procédé d'assemblage bout-à-bout par friction - malaxage sur des structures en cuivre a été développé. Il permet la simulation du procédé de friction - malaxage, avec un temps de calcul raisonnable et avec une précision suffisamment élevée (l'erreur sur le champ de température reste inférieure à 10 %) ; *2)* une stratégie a été développée pour identifier les paramètres technologiques optimaux du procédé FSW, connaissant, *a priori*, la température optimale de soudage.

Mots-clefs : *Soudage par friction-malaxage ; Modélisation numérique ; Microstructure, Cuivre*



Projet CARMEN (SAD - Région BRETAGNE 2019 - 2021)
Stage post-doctoral de BUNEA Marina

Rôle : Responsable du projet

Titre : Caractérisation et Modélisation des mécanismes d'endommagement dans des assemblages collés à l'aide d'un essai mini-Scarf

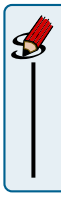
Partenaire : Région BRETAGNE

Montant : 100 k€

Résumé :

L'objectif du projet CARMEN, financé à hauteur de 75 % par la Région Bretagne et 25% par l'ENSTA Bretagne, s'est concentré principalement sur la compréhension des mécanismes d'endommagement, jusqu'alors peu étudiés. La finalité de ces investigations a été de proposer un outil de dimensionnement qui permettra de prendre en compte la présence et l'évolution de ces défauts, améliorant ainsi l'efficacité mécanique du joint sous différents cas de sollicitation. On retient que les pores et les inclusions dans un joint d'adhésif époxy jouent un rôle primordial dans l'endommagement de l'adhésif. Sur la base des données tomographiques disponibles au sein de l'équipe d'encadrement, des volumes synthétiques ont été construits, avec une connaissance exacte de l'ensemble de caractéristiques : distribution de pores, leur forme géométrique, fraction volumique globale, etc. Ces volumes synthétiques ont permis de mettre en place des outils numériques pour la détection de 3 principaux mécanismes conduisant à la dégradation des joints de colle, à savoir : *i)* ouverture, *ii)* croissance et *iii)* coalescence. Il a été constaté que des artefacts dans le traitement des données pourront potentiellement faire apparaître des mécanismes fictifs. De plus, ces volumes synthétiques ont permis de voir l'influence de la qualité des données (bruit de mesure, contraste entre les différentes phases, variation de l'intensité au voisinage de l'interface, etc.). Les zones dégradées sont souvent accompagnées de fortes concentrations de déformation. Alors, la présence de défauts et d'inclusions a permis de développer trois stratégies de mesure du champ de déplacement volumique. Chacune de ces stratégies présente des caractéristiques spécifiques (temps de calcul, efficience, robustesse) et permet de s'adapter aux différentes phases d'analyse. La validation de ces stratégies de mesure de champs de déplacement 3D a pu être faite sur des volumes synthétiques sous l'hypothèse que la forme et la taille des défauts n'évoluent pas. Pour prendre en compte la déformation des pores, des volumes spécifiques plus réalistes, basés sur un calcul par la méthode des éléments finis ont été utilisés. Ces volumes hybrides ont grandement aidé à l'évaluation de l'efficacité de ces outils. La dernière étape du projet a permis de mettre à l'épreuve ces stratégies de détection de mécanismes de dégradation du joint de colle sur des assemblages réels, pour lesquels des analyses tomographiques ont pu être réalisées.

Mots-clefs : *Mécanismes d'endommagement ; Tomographie aux rayons X ; Adhésif époxy ; Emission acoustique*



Thèse de A. TINTATU (CIFRE avec THALES (Sophia Antipolis) DMS, 2020-2023)

Rôle : co-encadrant de la thèse (avec P. LE GROGNEC et P. BIDAUD)

Descriptif : L'objectif du projet est d'étudier la diffusion de l'eau dans un matériau adhésif époxy bicomposant et de proposer une stratégie de modélisation simplifiée du comportement mécanique d'un tel adhésif au sein d'un assemblage collé de type joint à simple recouvrement, en prenant en compte les effets du vieillissement hydrique.
Tout d'abord, une analyse expérimentale de l'absorption d'eau dans l'adhésif est réalisée par gravimétrie et tomographie aux rayons X. La présence de pores dans le joint polymère permet une compréhension locale de l'évolution de la cinétique de diffusion. En effet, deux mécanismes de diffusion sont identifiés : le premier lié à la migration des molécules d'eau dans la matrice adhésive et le second lié à la pénétration de l'eau dans les pores. Cette cinétique en deux régimes peut être caractérisée par un des deux modèles : Dual-Fick ou Langmuir, présentant des résultats similaires à l'échelle macroscopique. Cependant, à l'échelle locale, les réponses de ces deux modèles diffèrent, en particulier après de longues périodes. Une attention particulière est donc accordée au second mécanisme d'absorption et à la détection des fronts d'eau par l'analyse du remplissage des pores, ce qui conduit au choix final et à la validation du modèle Dual-Fick.
Ensuite, sur la base d'essais expérimentaux, le comportement à long terme de l'adhésif étudié est caractérisé pour différents niveaux d'absorption d'eau. Une loi de comportement élastoplastique de type Mahnken-Schlimmer est retenue, dont les paramètres matériaux dépendent de la teneur en eau. Un modèle de type éléments finis 1D enrichi est ensuite développé, permettant la modélisation multi-physique d'un joint à simple recouvrement, de manière robuste et efficace. Un tel modèle permet de décrire les états de déformations et de contraintes au sein du joint de colle avec précision et à moindre coût, vis-à-vis de modèles standard 2D ou 3D. Des simulations par éléments finis 2D et des essais sur assemblages sont enfin réalisés à des fins de validation.

Mots-clefs : *Assemblages collés ; Vieillissement hydrique ; Porosité ; Modèle EF 1D enrichi ; Tomographie aux rayons X, in-situ*

Deuxième partie

Document scientifique

CHAPITRE

1 Introduction

Sommaire

1.1 Contexte industriel 44
1.1.1 Secteur astronomie et spatial 44
1.1.2 Secteur aéronautique 45
1.1.3 Secteur automobile 47
1.2 Contexte scientifique 48
1.2.1 Phases, constituants, défauts dans le joint 48
1.2.2 Investigation multi-échelle volumique 49
1.2.3 Mécanismes d'endommagement 51
1.3 Plan du document 52

La conception et la réalisation de structures multifonctionnelles de dernière génération [1], [2] (forte rigidité, résistance en milieu agressif, assemblages de matériaux de natures différentes) reposent systématiquement sur le respect strict de la réglementation très spécifique (environnementale, dimensionnelle, tenue mécanique à long terme, coût, masse, etc.). Dans ce contexte extrêmement exigent du fait de normes de plus en plus contraignantes, l'obtention d'une telle structure fait appel à des techniques d'assemblage [3] de plus en plus complexes et variées [4]. Le choix judicieux [5] de ces assemblages est indispensable pour respecter rigoureusement le cahier des charges du produit et ainsi aboutir à des structures performantes, et dimensionnées au plus juste tout en assurant sa durabilité à long terme. De par la complexité de ces structures et la variété croissante des milieux de fonctionnement, une caractérisation fine de son comportement, couplée à une modélisation pertinente [6], [7] au sens large, est requise. Ainsi, les activités de recherche que je mène depuis un peu plus de 10 ans visent à améliorer les stratégies de caractérisation et de modélisation pour un dimensionnement efficace, en identifiant les facteurs clés qui pilotent la tenue en service de telles structures.

La démarche proposée repose sur deux éléments fondamentaux :

1. proposer des stratégies de caractérisation expérimentale à différentes échelles du comportement thermomécanique de l'assemblage au moyen d'une multi-instrumentation pertinente. Ces stratégies doivent être capables de mettre en évidence l'influence de différents facteurs tels : les chargements complexes, l'effet de l'environnement (température, humidité, procédé d'assemblage, etc.) [8], [9].
2. sur la base de ces caractérisations fines, on souhaite proposer des modélisations à différentes échelles permettant d'intégrer les influences les plus représentatives qui pourraient jouer un rôle sur la tenue en service de l'assemblage, tout en ne perdant pas de vue l'applicabilité de ces outils dans un contexte industriel.

J'ai choisi d'illustrer cette démarche en me focalisant sur les différentes thèses qui ont été soutenues. Les résultats présentés seront de ce fait restreints à certaines techniques d'assemblage et familles de matériaux utilisés.

Ces activités de recherche ont été menées en étroite collaboration avec le milieu industriel. Pour comprendre la stratégie d'étude adoptée, il est nécessaire de bien appréhender les enjeux et les problématiques industriels. C'est pourquoi il paraît opportun de donner quelques éléments sur le contexte dans lequel s'inscrivent mes activités de recherche.

1.1 Contexte industriel

La grande majorité de mes activités de recherche a été menée en collaboration avec des partenaires industriels évoluant dans des secteurs très variés et dont les principaux sont les suivants : *i)* astronomie et spatial (Safran Reosc), *ii)* aéronautique (Safran Aircraft Engines, Safran Composites), *iii)* automobile (Renault, PSA Groupe) et leurs partenaires industriels (Laser Cheval, ARaymond, Bôllhoff, Plastic Omnium, Solvay, CETIM, ESI Group, Altair), mais également dans le secteur médical avec *iv)* CEA-Paris-Saclay.

1.1.1 Secteur astronomie et spatial

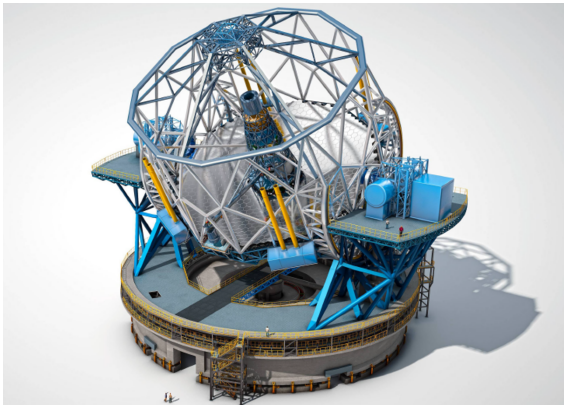
De manière concrète, le projet dans lequel j'étais impliqué visait la conception d'un télescope à réflexion (voir la figure 1.1) avec un miroir primaire segmenté d'un diamètre de 39,3 mètres et un miroir secondaire de 4,2 mètres de diamètre. Il s'appuie sur une optique adaptative, huit unités d'étoiles guides laser et de nombreux équipements scientifiques. Grâce à la grande surface du miroir primaire, ce télescope devrait recueillir 100 millions de fois plus de lumière que l'œil humain. De plus, il pourra corriger la distorsion atmosphérique. Par conséquent, les images fournies par l'ELT (Extremely Large Telescope) [10], [11] devraient être 16 fois plus nettes que celles fournies par le télescope spatial Hubble.

Les objectifs de ce télescope sont vastes et d'un grand intérêt scientifique :

1. L'ELT sera utilisé pour rechercher des planètes en dehors du notre système solaire, par des mesures directes et indirectes.



a) - Vue artistique du télescope



b) - Structure mécanique du télescope

FIGURE 1.1 – Telescope extra-large (The Extremly Large Telescope - ELT) [12]

2. Grâce à son important pouvoir de collecte de lumière, l'ELT sera utile pour observer des objets très lointains, c'est-à-dire des objets dans leur état. Il sera ainsi possible de mieux comprendre les mécanismes du fonctionnement de notre univers, grâce à l'observation des étoiles, des galaxies et des trous noirs, aidant ainsi à la compréhension des lois de la physique telles qu'elles sont énoncées aujourd'hui.

En raison des matériaux utilisés et de la complexité du type de la structure [13], il n'est évidemment pas possible d'utiliser les techniques d'assemblage traditionnelles. Le collage structural est alors l'une des rares techniques d'assemblage permettant de satisfaire la plupart des contraintes imposées aux assemblages de ces miroirs [14], [15], [16]. Il est alors d'une nécessité absolue de mettre en place des stratégies de caractérisation expérimentale et des outils prédictifs qui permettent de statuer sur la pertinence d'une ou plusieurs solutions. L'objectif final est de proposer un dimensionnement adéquat pour une durée de vie d'environ 30 ans sous conditions de chargement cyclique en fonctionnement, mais également en prenant en compte des situations extrêmes comme des tremblements de terre.

1.1.2 Secteur aéronautique

L'industrie aéronautique montre une croissance constante, car elle représente un secteur stratégique pour le développement de l'économie et de la technologie. Peu de secteurs exigent une vérification et une validation exhaustive des normes de qualité pour la certification des structures comme celui de l'aéronautique. Dans ce secteur, la volonté de réduction de masse [17], [18] qui anime cette industrie depuis ses débuts reste toujours présente comme en témoigne l'utilisation de plus en plus intensive des matériaux composites [19], [20] depuis 40 ans. Aujourd'hui, de nouvelles techniques innovantes d'assemblage [21] de différentes pièces sont déjà implémentées dans la chaîne de production, et d'autres sont en phase d'étude. Ces derniers sont caractérisés par des géométries complexes pour répondre aux contraintes des environnements agressifs (température, humidité, etc.) dans lesquels ils vont évoluer. Avant d'être en mesure

de produire ces assemblages, ils doivent être certifiés par les organismes accrédités, impliquant une justification du dimensionnement [22], [23] par le calcul et des validations sur bancs d'essai. La démarche de conception profiterait à la fois d'outils prédictifs performants (comportement et critères de dimensionnement) [24] et de méthodologies de caractérisation reproduisant des états de sollicitation de plus en plus proches de ce que les structures vont subir durant leur exploitation réelle, mais également le regard attentif sur la compréhension des mécanismes de dégradation à différentes échelles [25], [26].

L'objectif principal de ces travaux menés en collaboration avec Safran Composites se focalise sur la mise en place d'une méthodologie de caractérisation mécanique simple et efficace. Celle-ci doit donc permettre de comprendre les mécanismes d'endommagement et de caractériser le comportement mécanique d'un assemblage en vue de sa modélisation. Il s'agira donc de mettre en place les éléments théoriques, numériques et expérimentaux, ainsi que de sélectionner le moyen le plus adapté pour caractériser la rupture des assemblages collés sous chargements quasi-statiques biaxiaux. Les éléments méthodologiques proposés concernent à la fois des technologies expérimentales, des modèles, leur processus d'identification et des outils de calculs destinés à être mis à disposition des filiales du groupe.

Pour atteindre l'objectif fixé, ces travaux ont dû lever des verrous scientifiques majeurs identifiés à plusieurs niveaux. Tout d'abord, d'un point de vue expérimental : *i)* choix des configurations optimales d'essais, *ii)* instrumentation des essais permettant des mesures locales, mais également d'un point de vue théorique et numérique *iii)* modéliser le comportement mécanique des adhésifs.

Le premier point du volet expérimental traite du choix d'un essai de caractérisation mécanique. Il s'agit ici de développer et d'exploiter un ensemble d'essais uniaxiaux et multiaxiaux pour caractériser le comportement mécanique et la rupture des adhésifs sous sollicitations quasi-statiques. Ces essais doivent limiter au maximum les effets de bords dans les joints de colle. Le deuxième point est lié à la difficulté d'obtenir des informations locales sur la répartition des contraintes. Cette difficulté est inhérente au caractère « fin » des joints de colle. Les mesures traditionnellement employées sur ce type d'essais ne donnent accès qu'à des informations globales qui moyennent les informations locales. Il s'agit donc d'intégrer dans une ou plusieurs configurations d'essai, une instrumentation capable de renseigner des informations liées aux grandeurs mécaniques locales (contraintes et déformations), sans pour autant modifier significativement le comportement du milieu qui les entoure. Il est également nécessaire d'exploiter l'information liée aux mécanismes d'endommagement et de rupture du joint de colle. De ce fait, une analyse approfondie de l'adhésif étudié est essentielle.

Le volet théorique et numérique ont pour objectif la modélisation du comportement de l'adhésif au sein d'un assemblage et qui peut être divisée en deux régimes : linéaire et non-linéaire. Il s'agit donc de proposer une démarche d'identification des paramètres d'une loi de comportement en utilisant la méthode des éléments finis. Cette approche permettra de déterminer le comportement macroscopique de l'assemblage, à partir de la description des mécanismes de chaque élément constituant (adhésif, substrats) : la mise en place de ce dernier point étant rendu complexe du fait des difficultés d'observation.

1.1.3 Secteur automobile

Depuis une vingtaine d'années, l'Agence De l'Environnement et de la Maîtrise de l'Énergie (ADEME) ne cesse de suivre de très près les émissions de CO_2/km des véhicules particuliers fabriqués. Plus précisément, en 2021, les réglementations stipulaient pour ces véhicules des émissions maximales qui ne devraient pas dépasser 95 grammes de CO_2/km. Ces émissions correspondent à une consommation de 4,1 L/100 km pour un véhicule essence et de 3,6 L/100 km pour un véhicule diesel. De plus, les nouvelles normes environnementales en vigueur (REACH et EURO6) [27], [28] contraignent davantage le processus de conception en restreignant l'utilisation de certains composés chimiques qui interviennent dans la formulation de certains matériaux.

Un axe essentiel d'amélioration en vue de respecter ces exigences est la réduction de la masse des véhicules grâce à l'utilisation de matériaux plus légers [29], [30] (comme les matériaux composites), mais également une optimisation des techniques d'assemblage de manière à assurer une compatibilité entre ces nouveaux matériaux tout en assurant une durabilité à long terme de ces liaisons [31], [32]. Pour répondre à ces exigences, il est indispensable de se pencher sur le développement de nouvelles techniques d'assemblage, leur caractérisation expérimentale pertinente pour des sollicitations complexes. Enfin, des propositions de modélisation de ces techniques d'assemblage, applicables autant que possible dans le contexte industriel sont indispensables afin de trouver le meilleur compromis entre un dimensionnement fiable et des temps de calcul raisonnables, et cela pour réduire les délais de développement.

Il est évident que les techniques d'assemblage utilisées classiquement telles que le rivetage, le boulonnage ou la soudure posent des problèmes de compatibilité avec l'utilisation de ces matériaux [33]. Il est alors impératif, avant de pouvoir les utiliser, de mettre au point et de maîtriser de nouveaux procédés d'assemblages multi-matériaux métal-composite. Afin d'y parvenir, les fabricants automobiles français (Renault et PSA-groupe) et leurs partenaires industriels (Laser Cheval, ARaymond, Böllhoff, Plastic Omnium, Solvay, CETIM, ESI Group, Altair) se sont réunis dans le cadre du projet «FASTLITE Assemblage» financé par l'ADEME. L'objectif global de ce projet est l'émergence de solutions d'assemblage mixte à des coûts compétitifs et compatibles avec les cadences de production de l'industrie automobile.

Dans le cadre du projet FASTLITE les assemblages multi-matériaux visés sont les matériaux métalliques (aluminium et acier), et composites (à fibres de verre ou de carbone et à matrices thermodurcissables ou thermoplastiques). Les travaux dans lesquels j'étais impliqué avaient deux objectifs principaux :

1. La caractérisation de techniques d'assemblage multi-matériaux sous sollicitations quasi statiques de traction-compression/cisaillement.

2. La modélisation de la technique d'assemblage la plus prometteuse afin de réduire le temps de conception des structures automobiles.

1.2 Contexte scientifique

Le contexte industriel actuel, relatif à la conception des assemblages multi-matériaux (collage, soudage par friction – malaxage, etc.), doit répondre à des problématiques de plus en plus complexes, et cela dans des délais de plus en plus réduits. À ces éléments s'ajoutent les normes environnementales extrêmement contraignantes qui impactent indirectement, mais significativement les stratégies de caractérisation et de dimensionnement de ces liaisons. Pour des structures complexes [34], où les phases de maintenance [35] sont très coûteuses, les stratégies de dimensionnement doivent s'appuyer sur des démarches fiables, raisonnables en temps de calcul et compatibles avec les pratiques des bureaux d'études. Alors ces stratégies à vocation applicative forte soulèvent des problématiques scientifiques nombreuses à différentes échelles. Tout d'abord, si on s'intéresse à la durabilité à long terme des assemblages collés [36], [37], [38], [39], on identifie deux éléments clés sur lesquels repose la qualité de ces liaisons : l'interface et le joint. Les aspects liés à l'interface qui se crée naturellement entre l'adhésif et les substrats reposent sur les mécanismes de l'adhésion (adhésion chimique, adhésion par diffusion, adhésion électrostatique ou ancrage mécanique) et la préparation spécifique de la surface à coller. Si les aspects d'adhésion sont largement investigués [40], [41], [42], [43], [44] de manière à assurer une cohésion satisfaisante, le comportement de l'adhésif à différentes échelles (micrométrique, mésoscopique, macroscopique) montre des aspects encore peu étudiés en profondeur.

La difficulté pour ces adhésifs vient principalement de la complexité des mécanismes élémentaires (élasticité, viscoélasticité, viscoplasticité) [45], [46], [12] qui gouvernent leur comportement mécanique, activés simultanément, pour les environnements de service considérés, mais également de la présence de différents constituants présents dans l'adhésif : charges, pores, impuretés et qui peuvent rendre encore plus complexe le comportement du joint de colle [47], [48]. Enfin, les conditions environnementales agressives : humidité, haute température ou différents couplages entre ces ingrédients apportent une complexité supplémentaire dans la compréhension du comportement à différentes échelles [49]. Il est par conséquent ardu de comprendre, modéliser, identifier les liens entre les mécanismes pilotant le comportement et la ruine de ces matériaux à des échelles intermédiaires et les manifestations macroscopiques. La réponse à ces questions passe par une combinaison des démarches de prédiction ou d'identification.
Avant de décrire les travaux de recherche réalisés en respectant une certaine logique thématique, il m'a paru intéressant de dresser un panorama des aspects investigués aux différentes échelles pertinentes pour les assemblages collés et les assemblages soudés par friction malaxage.

1.2.1 Phases, constituants, défauts dans le joint

Le triplet : substrat - préparation de surface – adhésif, détermine de manière fondamentale l'efficacité et la qualité d'un assemblage par collage [50]. Dans la plupart des applications, la nature des substrats ainsi que leurs techniques de préparation sont

imposées par des protocoles respectant les exigences spécifiques à l'application finale de manière à assurer une bonne adhésion (résistance mécanique satisfaisante et rupture cohésive). Toutefois, le choix de l'adhésif (sous l'hypothèse de ruptures cohésives) peut influencer significativement le comportement de l'assemblage. Pour des applications structurelles, les adhésifs époxy sont les plus réputés en termes de résistance mécanique, adaptabilité et stabilité [51]. Ces adhésifs sont souvent formulés avec des charges et d'autres constituants de différentes natures. Ces formulations sont motivées par des fonctionnalités technologiques et pratiques (assurer une épaisseur minimale, conférer une résistance mécanique plus importante, etc.) mais complexifient grandement le comportement macroscopique des assemblages [52]. À ces différentes phases constitutives de l'adhésif (figure 1.2) s'ajoute la présence de défauts de différentes natures (pores, hétérogénéités des mélanges de composants, gradient de polymérisation, variation d'épaisseur, etc.) [53]. Cette vue d'ensemble questionne inévitablement sur la mise en place de stratégies expérimentales efficaces pour la détection de ces phases (distribution, formes géométriques), leurs conséquences sur le comportement mécanique, mais également leur contribution sur l'initiation de l'endommagement ou l'amorçage et propagation d'une fissure conduisant tôt ou tard à la rupture de la liaison [54], [55]. La compréhension de l'origine des défauts [56], leur détection robuste pour des dimensions caractéristiques avec une résolution de quelques µm, ainsi que leur influence sur la tenue mécanique de l'assemblage, pourrait représenter un élément déterminant dans l'établissement des stratégies cohérentes et efficaces de dimensionnement. De par la taille très variée de ces constituants et défauts, s'étalant sur une plage dimensionnelle très étendue, cela me paraît approprié d'investiguer de manière expérimentale et par modélisation leur influence sur le comportement mécanique.

1.2.2 Investigation multi-échelle volumique

Il est alors indispensable de choisir des moyens d'investigation adéquats et cohérents avec les caractéristiques des populations de constituants et de défauts à identifier. Pour des épaisseurs de joint classiquement observées dans une large gamme d'applications industrielles (variant entre 100 µm et 1000µm), il nous a paru judicieux d'investiguer ces joints à différentes échelles. Alors le choix du moyen d'investigation est essentiel dans ce cadre. Une première approche déjà largement utilisée ([57], [58]) s'appuie sur la microscopie optique qui permet d'observer à des échelles micrométriques les différents constituants observés sur des tranches d'échantillons collés ou à travers un échantillon massique s'il est légèrement transparent. Même si ces observations apportent des réponses intéressantes sur la complexité du joint, elles restent incomplètes, car ces observations sont faites sur une surface (2D). La tomographie aux rayons X, largement utilisée dans des domaines très variés ([59], [60], [59], [61]), est une alternative très intéressante, car elle permet de détecter de manière quantitative la plupart des constituants [62]. Autrement dit, cette technique, appliquée judicieusement permet d'établir pour un rapport résolution / volume investigué raisonnable et représentatif, la distribution 3D des pores, charges minérales (bille de verre par exemple), impuretés, etc. Il s'agit essentiellement ici d'une échelle de compréhension des phénomènes qui peut, de ce fait,

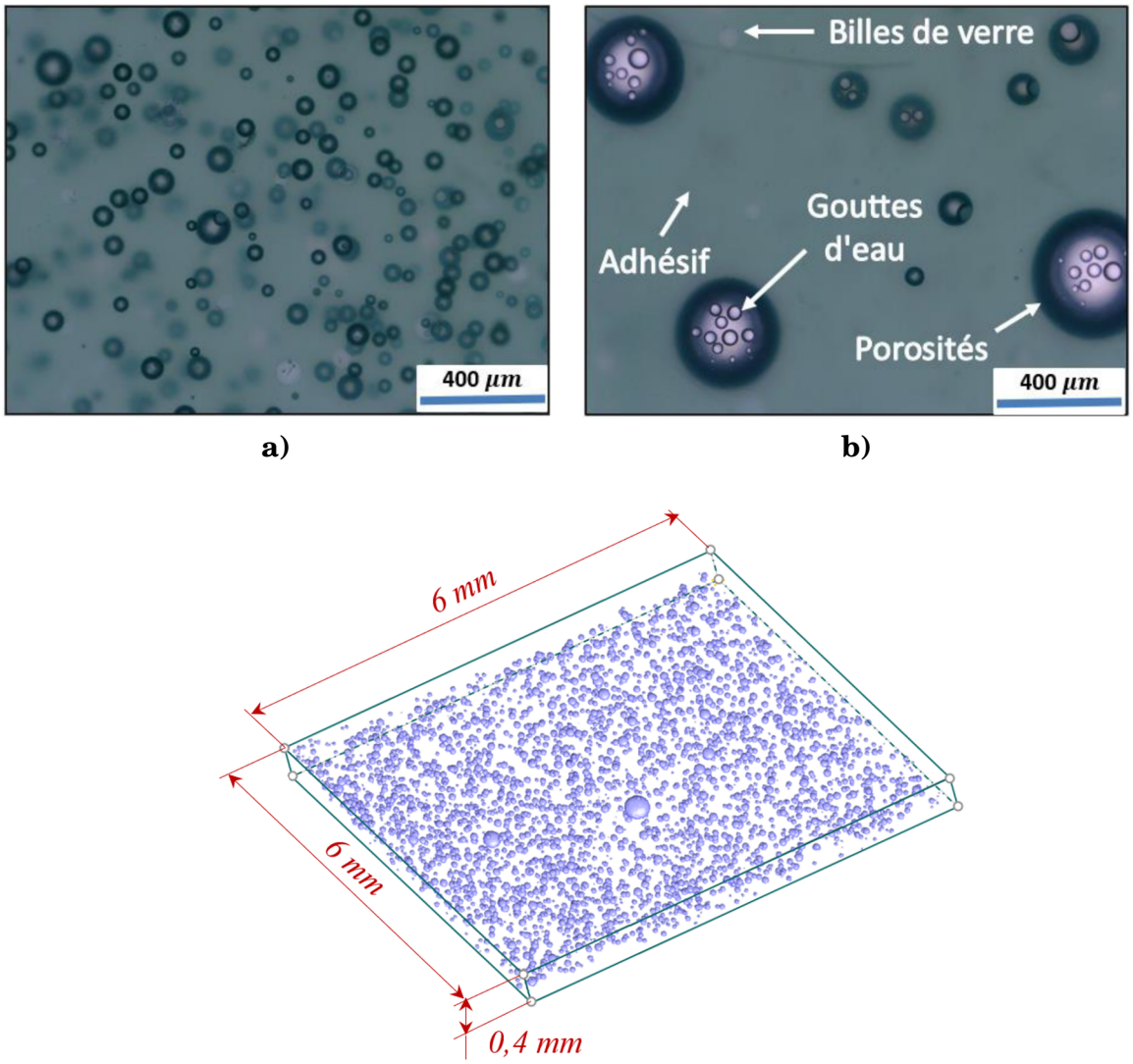


FIGURE 1.2 – Microstructure de l'adhésif époxy bi-composant Araldite 420 A/B

a) - constituants (porosités et billes de verre) observés au microscope dans l'adhésif Araldite 420 A/B, à l'état *'liquide'*, juste après la phase de mélange de la matrice et du durcisseur ;

b) - présence de gouttelettes d'eau dans un échantillon de colle Araldite 420 A/B de 400 μm d'épaisseur , après l'immersion de 30 jours dans eau déminéralisée, à 22^{o}C ;

c) - distribution de pores dans un joint d'adhésif, après un cycle de polymérisation de 110 ^{o}C pendant 1 heure

servir à alimenter la modélisation. Les résultats bruts issus de cette analyse permettent par segmentation, en utilisant des stratégies adaptées et développées dans ce contexte, de s'affranchir d'un certain nombre des artefacts [63]. Il est donc possible de proposer une distribution tridimensionnelle de ces populations, ouvrant ainsi la voie à des analyses

multi-échelles. Il est alors question de statuer sur les populations d'inclusions et de défauts les plus pertinentes à intégrer dans les stratégies de modélisation, leur effet sur le comportement du joint au voisinage de l'interface colle substrat ou au milieu du joint. Plusieurs directions d'investigation jusqu'alors peu étudiées sont alors proposées. Tout d'abord, la tomographie aux rayons X permet d'identifier ces populations [48], [64] de manière quantitative [62], les localiser dans le volumique, à l'état initial, mais également leur évolution sous sollicitation mécanique. Les effets des conditions environnantes sur l'état du joint sont également détectables (température, humidité). Enfin, ces défauts seront utilisés comme des marqueurs volumiques pour pouvoir aboutir à la mesure des champs cinématiques volumiques (déplacement, déformation). Ce dernier aspect aidera à la compréhension des états de sollicitation, a priori, très hétérogènes à des échelles micrométriques, montrant des concentrations de sollicitations non négligeables avec des effets significatifs sur l'endommagement localisé du joint. Ces observations sont systématiquement complétées par des analyses au Microscopie Électronique à Balayage (MEB), laissant sous-entendre des pistes de compréhension concernant l'endommagement relativement hétérogène.

1.2.3 Mécanismes d'endommagement

Au regard des observations mentionnées précédemment, il est légitime de se poser des questions sur les scénarios d'endommagement de l'adhésif en présence d'une microstructure fortement hétérogène. Pour les colles époxy bi-composantes, il a été clairement observé que même pour des sollicitations légèrement supérieures au seuil de pseudo-plasticité, des déformations confinées, mais parfois très intenses peuvent apparaître au voisinage des nucléations de pores ou des pores de taille importante, en d'autres termes là où la compacité reste très faible et l'état de sollicitation complexe [65]. Même si le volume affecté peut rester relativement petit, sous des sollicitations cycliques, ces déformations s'accumulent favorisant non seulement la nucléation et le grossissement des cavités et des pores, mais également l'augmentation du volume de l'adhésif dégradé [66] , favorisant ainsi l'initiation des fissures. Le fort contraste entre les propriétés mécaniques de la matrice d'adhésif et les charges peut représenter également une source d'initiation de dégradation. Dans ce cadre, le choix judicieux de diverses techniques expérimentales telles que : le suivi de la fissuration par acquisition et traitement d'images [67], la photoélasticimétrie, l'analyse fractographique des surfaces fissurées est primordiale. Mais ces observations sont souvent réalisées en surface, réduisant drastiquement la compréhension volumique complète. Alors, la tomographie aux rayons X pourrait apporter un certain éclairage sur l'initiation et l'évolution de ces d'endommagements. Sur la base de toutes ces observations expérimentales, on peut construire des modèles pertinents et représentatifs des phénomènes physiques identifiés, et qui permettent au final de développer des stratégies efficaces d'investigation du comportement jusqu'à la rupture et par conséquent d'aboutir à une prédiction plus efficace.

1.3 Plan du document

Le plan de la deuxième partie du document suit une logique naturelle et cohérente dans laquelle s'inscrivent ces travaux. Le document est composé de 4 chapitres.

Le premier chapitre est dédié à une introduction dense, permettant de décrire le contexte industriel et leurs problématiques associées, mais également les collaborations avec différents partenaires. Ensuite, le contexte scientifique est présenté, afin de mettre en évidence les concepts et les outils scientifiques nécessaires, pour répondre aux défis industriels.

Le deuxième chapitre concerne la caractérisation et la modélisation des assemblages structurelles par collage. L'effet de l'environnement marqué principalement par la température et l'hygrométrie de différents milieux (eau de mer, eau déionisée, etc.) est également investigué, pris en compte dans des stratégies de modélisation pertinentes, et utilisé dans des approches de dimensionnement. Les défauts présents dans les joints de colle, leur origine et surtout leur effet sur l'intégrité structurelle de l'assemblage ont également été abordés en s'appuyant sur des investigations tomographiques.

Le troisième chapitre a pour objectif l'investigation des joints obtenus par soudage de type friction-malaxage. Une stratégie numérique pertinente est alors proposée afin d'identifier les valeurs optimales des paramètres du procédé. Cette stratégie repose sur le développement de modèles de simulation basés sur une approche de type *coupled eulerian-lagrangian*, permettant de s'affranchir, dans une certaine mesure, des problèmes inhérents aux calculs numériques par éléments finis. Enfin, les défauts de type pores ont pu être caractérisés par des méthodes non destructives et leur effet sur le comportement macroscopique et local a été investigué.

Enfin, cette partie du document se termine par une conclusion étoffée qui dresse un bilan des activités de recherche menées et présentées succinctement dans les chapitres précédents. Elle présente également quelques pistes sur les actions en cours et les projets à 4 ans.

CHAPITRE

2 Caractérisation et modélisation des assemblages structurels par collage

Sommaire

2.1 Introduction 53
2.2 Dispositifs expérimentaux et multi-instrumentation 54
2.3 Contraintes résiduelles et contraintes thermiques 100
2.4 Influence de l'environnement à différentes échelles 122
2.5 Origine de défauts et mécanismes d'endommagement 178
2.6 Modèles de comportement thermomécanique 228
2.7 Etudes en cours et perspectives 261

2.1 Introduction

L'assemblage d'éléments constitutifs de systèmes mécaniques représente une étape fondamentale dans le développement et la fabrication de nouvelles structures. Au fil du temps, de nombreuses techniques d'assemblage ont été développées puis largement employées, telles que le boulonnage, le rivetage et le soudage. Cependant, aujourd'hui, dans le cadre du développement d'applications de dernière génération [68], il est difficile, voire parfois impossible, d'utiliser ces différentes techniques à cause de la nature des matériaux mis en jeu ou de la complexité des configurations à assembler. Alors, une alternative à ces méthodes traditionnelles aux multiples désavantages (ajout de masse, dégradation des matériaux, etc.) est représentée par des procédés innovants tels que le collage structural [69], [70]. D'un point de vue matériau, l'adhésif peut être considéré comme un polymère confiné entre deux ou plusieurs substrats de nature différente ou identique, en héritant des aspects spécifiques aux polymères (comportement visqueux, dépendance à la température et à l'humidité, taux de polymérisation atteinte, etc.) [71]. La difficulté est donc de comprendre, d'identifier et de modéliser les liens entre

les mécanismes pilotant le comportement mécanique et la ruine de ces matériaux à des échelles intermédiaires et les observations macroscopiques. C'est dans ce cadre que mes travaux de recherche s'inscrivent avec comme ligne directrice l'amélioration de la durabilité de ces liaisons par collage et en s'appuyant sur deux volets distincts : caractérisation expérimentale et modélisation numérique.

2.2 Dispositifs expérimentaux et multi-instrumentation

La première nécessité est de proposer un cadre d'investigation cohérent et en bon accord avec les objectifs. D'abord, compte tenu de la sensibilité des adhésives à la nature de la sollicitation [72], [73], [74] (sensibilité à la pression hydrostatique, par exemple), il est indispensable que lors de la phase de caractérisation expérimentale les dispositifs d'essais choisis génèrent des états de sollicitation, dans l'adhésif, proches de ceux subit par la structure collée en exploitation réelle. Même si des essais normalisés pourront répondre de manière satisfaisante à un grand éventail de situations, il est donc question de proposer des montages d'essais spécifiques pour une meilleure caractérisation. Pour répondre à ces défis, on privilégie les essais de type Arcan modifié [75], [76], [77], [78] car il permet un large spectre de sollicitations (traction, traction cisaillement, cisaillement et compression cisaillement) avec comme finalité, non seulement le comportement de l'adhésif jusqu'à rupture, pour des sollicitations préalablement définies, mais également les enveloppes élastiques et de rupture [79], [80]. De plus, ce montage favorise, grâce à une géométrie spécifique des substrats [75], la diminution de la concentration des contraintes, minimisant ainsi les ruptures prématurées, retrouvées systématiquement sur les essais de type simple recouvrement par exemple. Même si ce montage suscite un intérêt grandissant, il n'est cependant pas le plus adapté dans le milieu industriel, car complexe à mettre en œuvre (dispositif de laboratoire). En conséquence, dans le contexte industriel où la variabilité des résultats expérimentaux doit être maîtrisée au mieux, on s'oriente vers un autre essai appelé Scarf Modifié [81], [82]. Cet essai a été développé au sein de l'équipe comme une alternative au montage Arcan modifié. Caractérisé par sa simplicité de mise en œuvre dans l'environnement l'industriel, il permet de manière simple (à travers un serrage de l'échantillon collé dans les mors de la machine de traction) de déterminer le comportement de la colle. Le spectre des sollicitations de type traction-cisaillement présente des ratios plus restreints par rapport au montage Arcan modifié, car le joint ne peut se positionner par rapport à l'axe de sollicitation que dans un intervalle d'angle, compris entre 0° et 45° [82]. Ce type d'échantillon a été également utilisé pour des caractérisations à des échelles plus petites notamment, quand on souhaite des investigations fines au moyen d'une multi-instrumentation [64].

De par leur géométrie complexe, les échantillons Arcan modifié ou Scarf pourront être considérés comme des mini structures et leur sollicitation pourrait nécessiter des éléments d'interface pour appliquer le chargement. Ainsi, il paraît judicieux d'instrumenter ces essais afin de s'affranchir de différentes sources d'incertitude pouvant polluer le

comportement mécanique propre à l'adhésif ou de la structure collée sollicitée. Pour ces essais on s'oriente quasi systématiquement vers de la mesure des champs cinématiques sans contact [83], [84], en surface (plane ou gauche) à différentes échelles, en utilisant différents types de codage (mouchetis, codage périodique, etc). Ces mesures sans contact sont d'autant plus nécessaires lorsqu'on réalise des essais dans des environnements contrôlés, en utilisant des enceintes climatiques.

Le suivi en temps réel de la santé de la liaison représente un défi majeur pour les assemblages, surtout lorsque l'élément de liaison est un adhésif pour lequel le comportement mécanique évolue dans le temps (vieillissement physique), sous l'action de différents facteurs. Deux moyens adaptés à ce type d'environnement expérimental ont été mis en œuvre : la fibre optique à réseau de Bragg et l'émission acoustique. Si le premier permet de déterminer avec une grande précision la déformation au sein de l'adhésif tant lors de la phase de polymérisation qu'au cours de la sollicitation mécanique, elle reste toutefois intrusive pour des joints fins (épaisseur inférieure à 100µm). En ce qui concerne l'émission acoustique, la technique apporte des éléments intéressants dans l'optique d'identifier des indicateurs pertinents permettant de prédire le passage d'un régime de comportement à un autre (élastique vers le non linéaire par exemple),ou bien d'alerter sur l'initiation des endommagements et/ou l'amorçage de microfissures ainsi que leur propagation.

Toutes ces observations sont systématiquement complétées par des analyses microscopiques à différentes échelles des échantillons post-mortem, afin de confirmer et valider le comportement mécanique identifié antérieurement.

Enfin, ces dernières années, je me suis intéressé de près à l'étude de la présence des défauts au sein de l'adhésif et de l'effet de ses défauts sur le comportement mécanique à long terme de l'assemblage. Pour identifier la structure interne d'un adhésif (les phases constituantes, les défauts, etc.) on s'appuie principalement sur un moyen d'investigation de pointe qui est la µ-tomographie aux rayons X afin de comprendre, de manière quantitative l'origine de ces défauts, leur morphologie et leur distribution spatiale. Ces éléments permettent alors de statuer sur leur degré de préjudiciabilité sur la tenue mécanique de l'assemblage au sens large. Pour répondre à ces objectifs, on s'appuie sur des essais in situ, afin de comprendre l'évolution de ces défauts sous sollicitations mécaniques.

Publications jointes

- J. Destouesse , M. Diakhate , C. Badulescu , D. Thévenet , M. Stackler , W. Albouy and N. Carrere, **Cluster analysis of acoustic emission data to investigate the damage evolution in modified scarf joint under bi-axial loading**, *The Journal of Adhesion*, 96 :11, 969-987,(2020), DOI : 10.1080/00218464.2018.1552854

- V. Dumont, C. Badulescu, J. Adrien, N. Carrere, D. Thévenet and E. Maire, **Experimental investigation of porosities evolution in a bonded assembly by means of X-ray tomography**, *The Journal of Adhesion*, 97 :6, 528-552,(2021), DOI : 10.1080/00218464.2019.1685984

Références associées : Bibliographie des publications

THE JOURNAL OF ADHESION
2020, VOL. 96, NO. 11, 969–987
https://doi.org/10.1080/00218464.2018.1552854

Taylor & Francis
Taylor & Francis Group

Check for updates

Cluster analysis of acoustic emission data to investigate the damage evolution in modified scarf joint under bi-axial loading

J. Destouesse[a,b], M. Diakhate [c], C. Badulescu[b], D. Thévenet[b], M. Stackler[a], W. Albouy[a], and N. Carrere[a]

[a]Safran Composites, Itteville, France; [b]ENSTA Bretagne, IRDL-UMR CNRS 6027, Brest, France; [c]Univ. Bretagne Occidentale, IRDL-UMR CNRS 6027, Morlaix, France

ABSTRACT

Non-destructive monitoring of damage evolution within material or bonding assembly becomes an essential tool to better understand its mechanical behavior, and therefore to prevent failure risks of engineering structures that involve adhesive bonding matters. This paper presents the experimental results of monotonic tests that were conducted firstly to investigate the effects of bi-axial loadings (with different shear/peel ratios) on the mechanical damage evolution of metal/metal bonded joint, and secondly to both detect and identify the acoustic emission (AE) signatures of the different failure mechanisms involved in the bonded joint damage. Results from specimens with modified scarf joint show that the loading configuration (shear/peel ratio) strongly influences the normal stiffness of the adhesively-bonded joint. For each loading configuration, repetitive tests were performed, and loading rate effects on the mechanical behavior of adhesively-bonded joint were analyzed. In addition to these results, a k-means++ algorithm was used to achieve a cluster analysis of AE data, and to allow AE events that were generated by damage evolution of the bonded joint to be identified. A particular AE signature is highlighted since it allows monitoring damage evolution of the adhesively-bonded joint. Test results also show that the highest value of acoustic energy is detected when the slope of the mechanical behavior curve (macroscopic scale) drastically changes. This finding is used to perform a real-time detection of the adhesive yield strength.

ARTICLE HISTORY
Received 17 September 2018
Accepted 23 November 2018

KEYWORDS
Modified scarf joint; bonded joints; acoustic emission; non-destructive testing; adhesion; failure mode; joint design

1. Introduction

Over the last decades adhesive bonding has found many engineering applications such as marine, automobile, aerospace and construction.[1–3] The joining of two or more components allows for structures to perform their operational requirements, transferring forces from one surface to another.

CONTACT J. Destouesse jaime.destouesse@ensta-bretagne.org Safran Composites, 33 Avenue de la Gare, Itteville 91760, France

Color versions of one or more of the figures in the article can be found online at www.tandfonline.com/gadh.

© 2018 Taylor & Francis Group, LLC

The choice of this assembly method is mainly due to the advantages that adhesive bonding provides over traditional mechanical fixing techniques (bolting, welding, and screwing) including weight reductions, lower manufacturing cost, the variety of materials that can be bonded, a uniform stress distribution of the load, better fatigue properties, etc.

To further improve the performance and safety of adhesively bonded joints, a deeper understanding of their behavior in relation to the loading conditions is crucial. From literature, two major failure types are usually observed at the surface of the bonded joint: adhesion failure, slick failure at the interface between the adhesive and the adherent surface, and cohesion failure, fracture within the adhesive material itself.

In a mechanical structure, the adhesive joint may be subjected to multiaxial loadings. In laboratory, investigating the adhesive joint mechanical properties under this stress state led some researchers to propose specific test devices such as the modified Arcan fixture.[4,5] However, it's not easy to use such devices in an industrial environment, and the use of a large range of non-destructive techniques is limited. This study consists in the development of the modified scarf test which allows the implementation of different monitoring techniques. It has the advantage that it can be easily performed with a tensile test machine in an industrial environment, and it also allows applying multiaxial loadings without having high stress concentrations near the edges.

Although many monitoring procedures have been used in field or lab conditions in order to analyze appears failure within adhesive joints, such as radiography, infrared spectroscopy[6–9] and ultrasonic method, which is widely used for monitoring the structural health of components,[1,10,11] only few of them have proven their efficiency. In addition, the ultrasonic sensors must be coupled to the structure following a specific procedure, which can be time-consuming. Acoustic emission (AE) method can be used to detect transient elastic waves emitted by a growing crack within the material.[12–16] AE can be used in the identification of failure at extremely early stages, thus preventing severe structural damage. Several authors have attempted to identify AE signal signatures from various fracture mechanisms of materials[8,17–20] or adhesive composite joints,[21,22] using computational pattern recognition approaches, the studies showed that the AE signal were directly related to failure mechanism.

The aim of this study is, on the one hand, to investigate the mechanical behavior of a thin thickness adhesively-bonded joint under multiaxial loadings using a new specimen, showing that this test might also be used for the characterization of the adhesive behavior considering time effects (fatigue or creep), and on the other hand, to build a monitoring protocol (based on the AE method) that allows real-time detection and identification of the different failure mechanisms associated with the mechanical behavior of bonded

joints. An unsupervised classification method (based on k-means++ algorithm) is proposed to identify AE signatures of those failure mechanisms.

2. Experimental procedure

This section describes the mechanical tests conducted to investigate the mechanical behavior of an adhesively-bonded joint under bi-axial loadings, but also the ability of using the AE technique to detect, locate, and monitor the different failure mechanisms within the adhesive material. The experimental conditions (specimen preparation, instrumentation techniques, and mechanical loading conditions) are described.

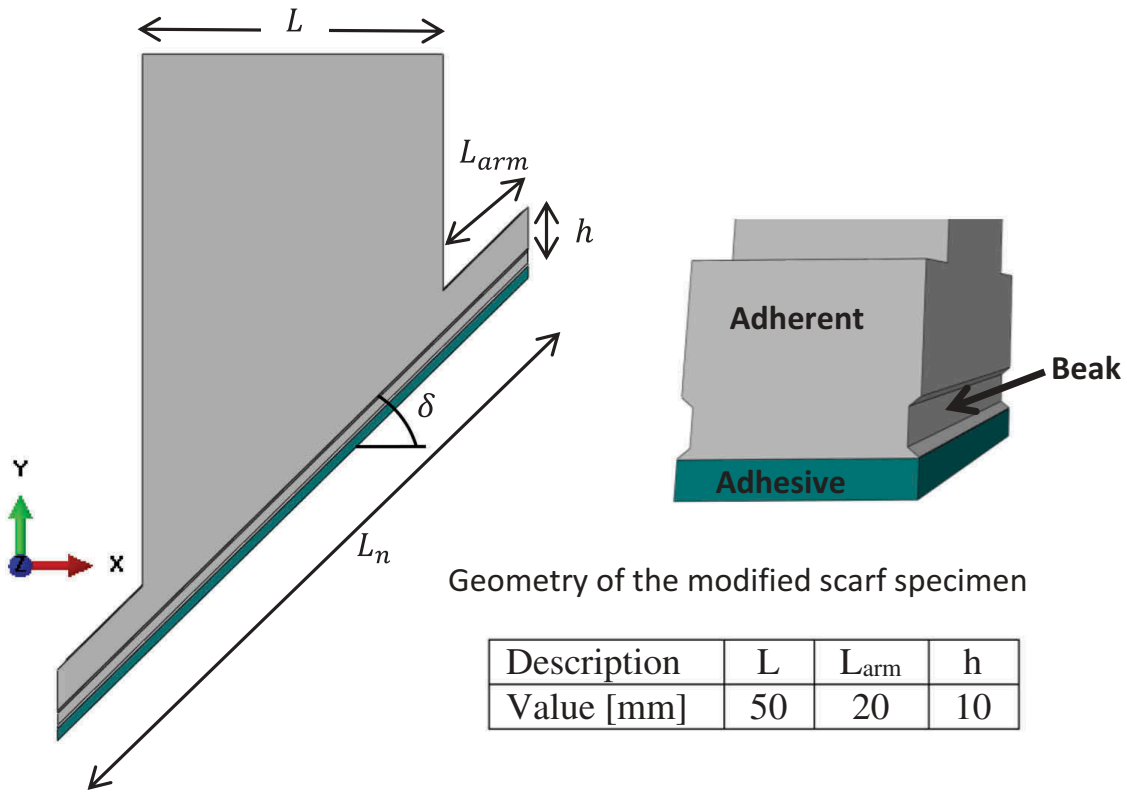
2.1. *Modified scarf specimen*

Figure 1 presents the geometry of the modified Scarf specimens inspired from Scarf joints.[23] Arms and beaks have been added in order to have homogeneous stress distributions along the surface and to reduce the stress concentrations near the free edges as proposed by Cognard *et al.* for the Arcan fixture.[5] The overlap length (L_n) is a function of the angle δ of the modified Scarf joint, and is equal to $L_n = \frac{L}{Cos\ (\delta)} + 2 \times L_{arm}$. The angle δ at the middle branch of modified Scarf specimens can be changed in order to apply different bi-axial loadings within the adhesive joint. In this work, three loading configurations (different angles δ, Figure 1) were tested: δ= 0°, 22.5°, and 45°. Table 1 presents the stress (tensile and shear) levels that are associated with each loading configuration.

2.2. *Materials and specimen preparation*

The modified scarf joint specimens are manufactured using Aluminum alloy AW7075 T6 and high pressure water jet cutting. Surfaces to be bonded were ground with a 220 SiC abrasive paper and cleaned with acetone solution to remove the remaining residues; a structural epoxy adhesive film was applied over the surfaces. In order to ensure the better positioning of substrates (two half-scarf specimens), a bonding device has been designed and manufactured (Figure 2).

The planarity of the specimen (z direction) is ensured thanks to the bonding table. The top cylinders and the top grid ensure the right positioning of the top substrates. The bottom substrate is positioned thanks to the bottom cylinder. The adhesive joint thickness is ensured using a calibrated metal wire of 200μm, which is located at the right and left extremities of the arms (where the stresses tend to zero). Finally the modified scarf joint specimen was cured following the manufacturer recommended cycle of the adhesive material.



Geometry of the modified scarf specimen

Description	L	L_{arm}	h
Value [mm]	50	20	10

Figure 1. Shape of the improved scarf joint proposed in [20].

2.3. *Instrumentation techniques: DIC and AE*

In this work, stereo Digital Image Correlation (DIC) method was used for measuring both the normal and the tangential relative displacements as a function of the applied load, along the adhesively-bonded joint. The DIC equipment (GOM Optical Measuring Techniques ARAMIS 3D (Widen, Switzerland)) consists of two 5M digital CCD cameras (Figure 3), a lighting system, and a data acquisition system. Calibration of CCD cameras was performed using a 25mm × 20mm standard to obtain a resolution deviation of less than 0.01μm. In this study, the images were recorded at a sampling frequency of 2Hz. The computation of the displacement field in both directions was accomplished as the difference between two zones close to the adhesive joint and symmetrical about the midplane of the bonded layer (Figure 4a). Each displacement is obtained in a local coordinate system that depends on the angle δ of the modified Scarf specimen Figure 4b.

Under mechanical loading, cracking within the adhesive bond generates transient elastic waves, referred in this paper as AE waveforms. Thus, in addition to the DIC equipment, a four-channel AE system designed by MISTRAS Group (New Jersey, United States) was used to record the AE waveforms within the adhesive joint during the tests. Since the crack path within the adhesively bonded joint is known in advance, two AE channels

Table 1. Summary of the stress distribution and levels with respect to the loading angle.

Angle δ (°)	Tension stress level	Shear stress level
0	++++ (high)	Not applicable
22.5	+++ (medium)	+ (low)
45	++ (medium)	++ (medium)

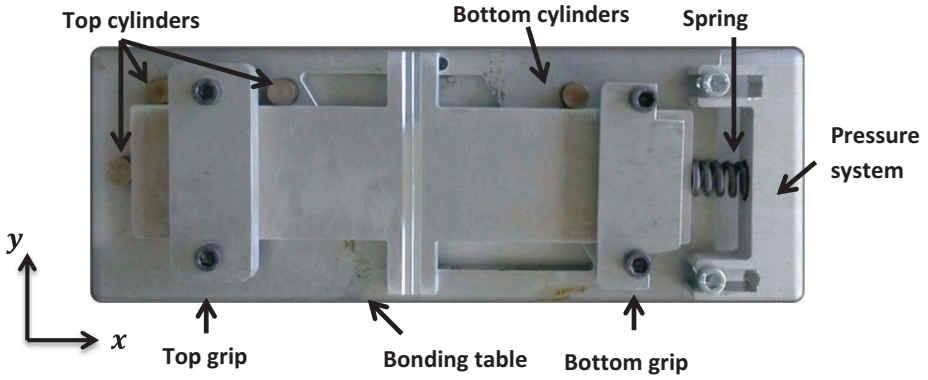


Figure 2. Device for bonding the two half-scarf specimens.

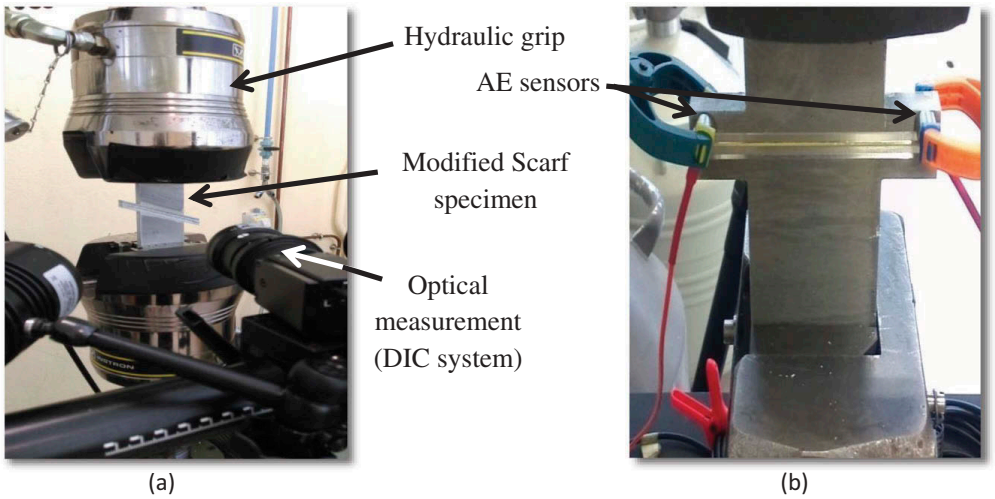
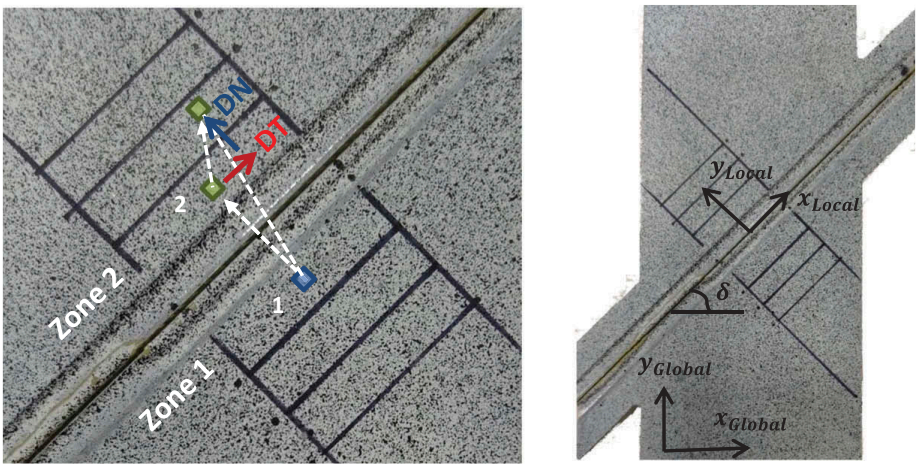


Figure 3. Instrumentation techniques: (a) DIC and (b) AE systems.

were used in order to perform a linear localization of the acoustic sources (or AE events). These two AE sensors (Figure 3), with optimum frequency range from 125 – 750kHz and a resonant frequency of 300kHz, were connected to two preamplifiers, which were connected to the acquisition system. The AE sensors were coupled to the specimen upon the static adherent with silicon grease and held fixed in position with clamps. This procedure ensures a good acoustic coupling and also allows performing a linear localization (as shown in Figures 10 and 12) of the acoustic sources within the overlap length (L_n).

As a result of using an Instron servo-hydraulic testing machine, hydraulic grips, and samples made of aluminum (Figure 3), acoustic signal acquisition



(a) (b)

Figure 4. (a) Representative DIC image – (b) Scarf local coordinate system.

threshold was set at 55dB in order to filter out vibrations induced by the testing machine. The sampled rate of AE waveforms was set at 40MHz. Before mechanical tests, pencil lead breaking test was used to evaluate the acoustic wave propagation velocity along the bonding joint.[24,25] The wave propagation velocity of 4000m/s was used in the linear localization of the AE sources within the adhesive joint.

Both systems were fully synchronized with the tensile machine so that, for each recorded image and for each acoustic emission event, the corresponding value of the applied force was also registered.

2.4. *Experimental protocol*

In order to investigate the adhesive mechanical behavior under different loading configurations (0, 22.5, and45°), and at different loading rates (0.02, 0.2, and2kN/s), three specimens of each modified scarf joint were tested under force control until failure.

3. Mechanical behavior of modified scarf joints

In this section, experimental results on the effects of loading configuration and loading rates are presented and discussed. For confidentiality reasons, experimental results (relative displacements and force values) are normalized.

3.1. *Effects of loading configuration*

Experimental results showed that the highest load machine value is obtained with the 45° modified scarf joint, whereas the highest normal relative displacement is obtained with the 0° modified scarf joint.

Figure 5 presents the normalized load as a function of the normalized normal relative displacement. The normal stiffness value of the adhesively-bonded joint can be computed from this curve. For each loading configuration, the applied load is normalized with respect to the highest load value (45° modified scarf); the relative normal displacement value is normalized with respect to the highest one (0° modified scarf).

It can be seen from Figure 5 that the loading configuration strongly influences the normal stiffness value of the bonded joint. This is probably due to the stress ratio (shear/peel) associated with each loading configuration (Table 1). In addition, differences in normal stiffness values may be due to the fact that the adhesive bonded surface (Figure 1) varies with the loading configuration. Specimen's geometries as well as experimental results have led to the following correlations (1):

$$\frac{S_{22.5^\circ}}{S_{0^\circ}} \approx \frac{F_{e22.5^\circ}}{F_{e0^\circ}} \approx \sqrt{1.09} \; and \; \frac{S_{45^\circ}}{S_{0^\circ}} \approx \frac{F_{e45^\circ}}{F_{e0^\circ}} \sqrt{2} \qquad (1)$$

Where S_{δ° *and* $F_{e\,\delta^\circ}$ represent the adhesively-bonded surface and the yield strength values associated with the loading configuration δ.

Repetitive tests were performed at 0.2kN/s for each loading configuration. For each specimen, the load machine as well as the relative displacement is normalized with respect to their corresponding value at failure. Figure 6 presents the mechanical behavior of the adhesively-bonded joint under each loading configuration. Results show a good reproducibility of the test and also a low

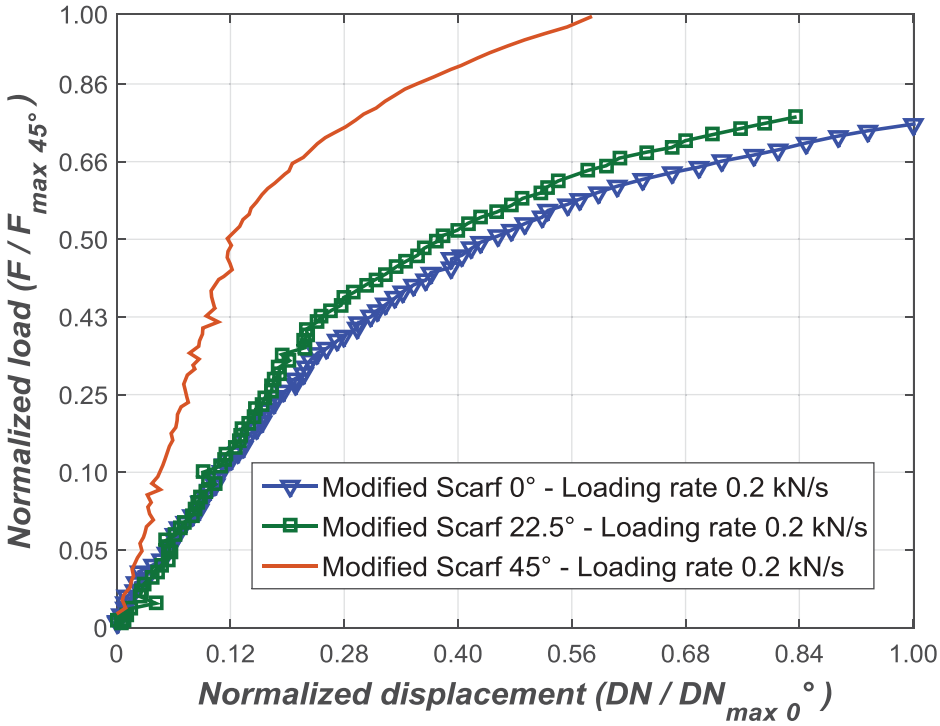


Figure 5. Effect of loading configuration on mechanical behavior of the modified scarf joint.

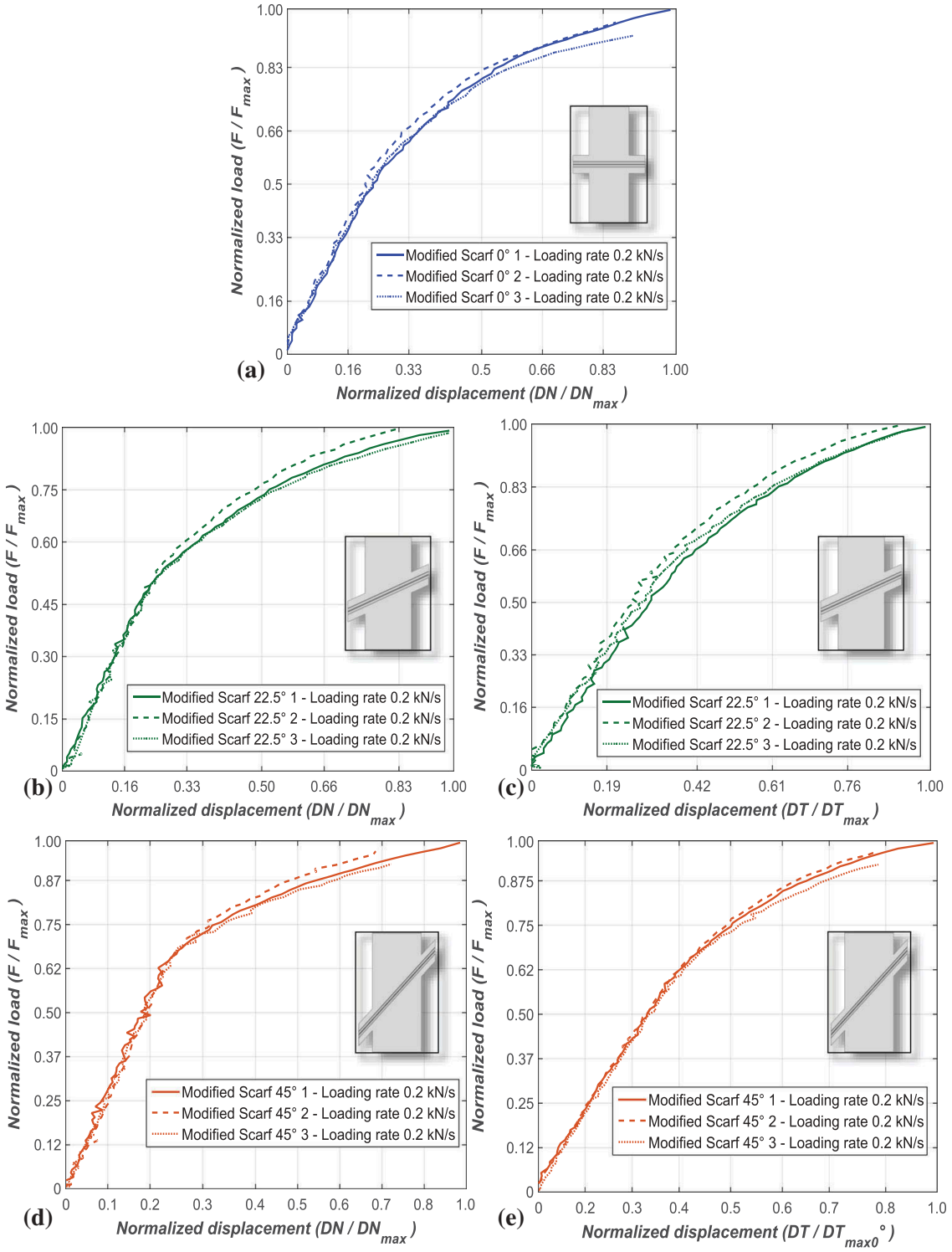


Figure 6. Repetitive tests at a loading rate of 0.2kN/s: (a) Modified scarf 0° – (b and c) Modified scarf 22.5° – (d and e) Modified scarf 45°.

scatter (< 2%) at each configuration of the modified scarf joint. The overall mechanical behavior shows two distinctive parts: the first one is characterized by a linear dependency between relative displacements and force machine, and the second one by a non-linear regime until the failure of the bonded joint.

3.2. *Effects of loading rate*

As previously stated, the effect of loading rate on the adhesive mechanical behavior is investigated (Figure 7). For each specimen, load machine and relative displacements are normalized with respect to their corresponding values at failure. Experimental results show that the elastic behavior is not affected by the loading rate, whereas the non-linear regime as well as the load

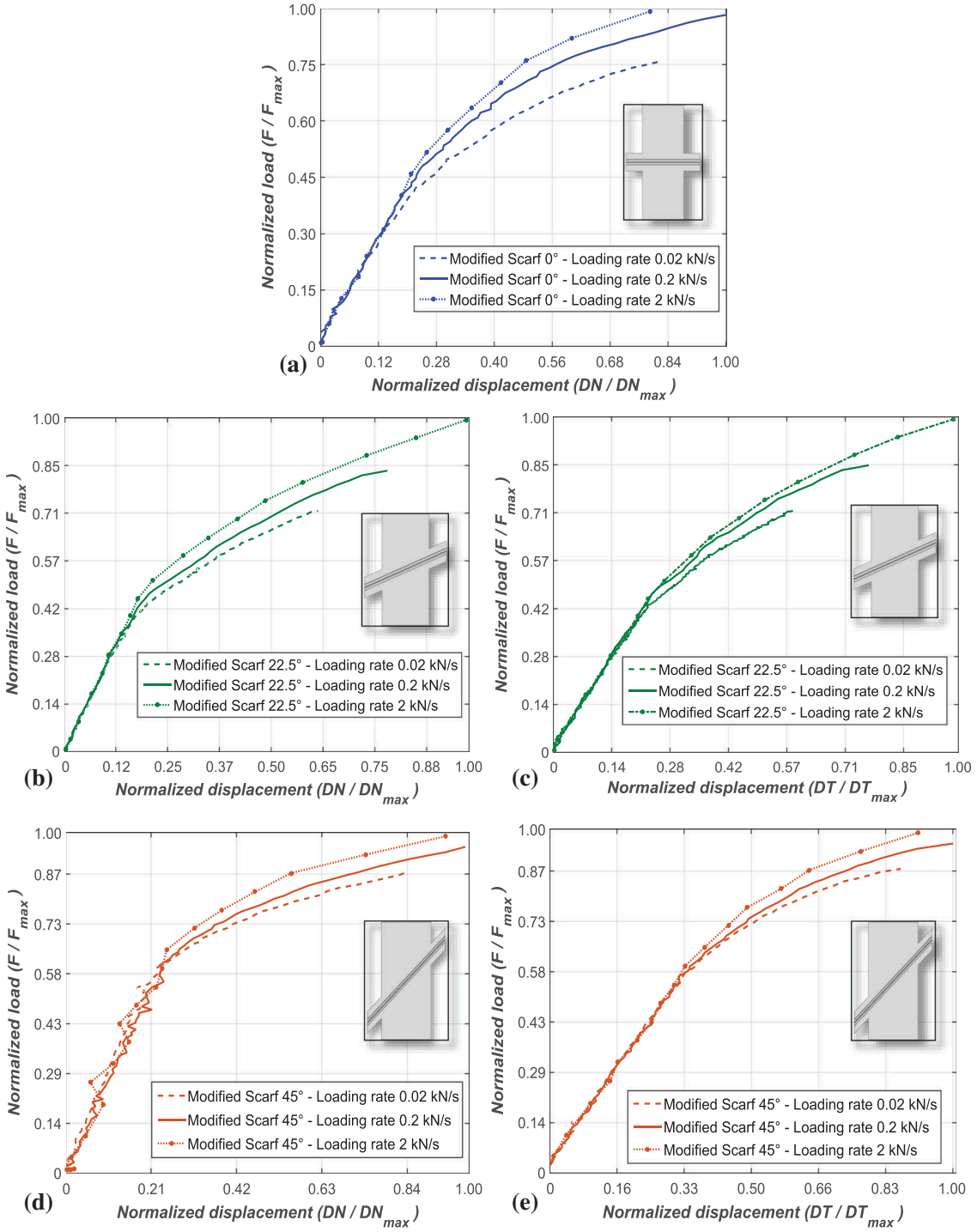


Figure 7. Effects of loading rate on mechanical behavior: (a) Modified scarf 0°– (b and c) Modified scarf 22.5°– (d and e) Modified scarf 45°.

machine at failure is strongly affected by the loading rate. In addition, it can be seen that the yield strength of the adhesively-bonded joint is not affected by the loading rate. Further on, we will discuss how the yield strength generates a particular acoustic signature (*cf.* paragraph 5.2).

3.3. *Fracture surfaces*

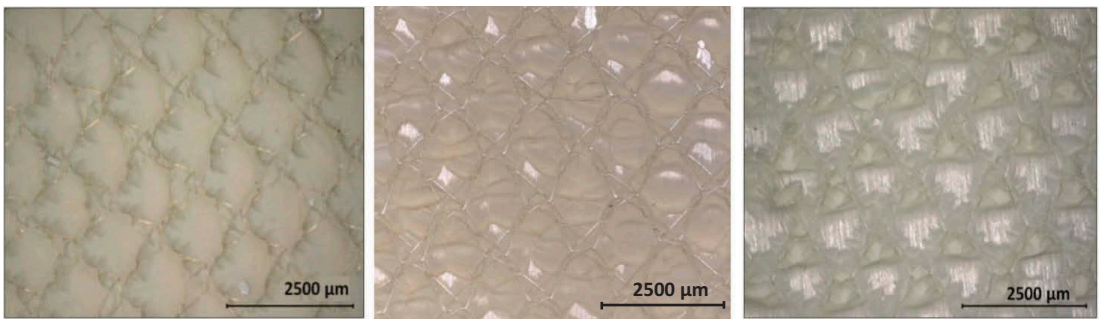
Representative fracture surfaces of two loading configurations (0° and 45° modified scarf joint) are presented in Figure 8. Optical observations using Keyence microscope pointed out cohesive failures for each 0° modified scarf joint (Figure 8a), whereas 22.5° and 45° modified scarf exhibit a mixed mode (cohesive and adhesive failures at the bonded surface, Figure 8b–c), and sharp ridges are locally observed.

4. Damage mechanisms detection based on AE signatures

As stated previously, cracking within the adhesive bond generates acoustic activity. This latter is analyzed with the aim of better understanding the failure mechanisms involved in the bonding joint damage. In a first part, the unsupervised classification method, which is used to both evaluate the number of failure mechanisms and identify their acoustic signatures, is detailed. In a second part, effects of loading configuration as well as mechanical loading rates on acoustic signatures of those failure mechanisms are investigated.

4.1. *Unsupervised classification method*

This method shows how the use of statistical tools (cluster algorithms) can help in gathering AE events into clusters (Figure 9). Among cluster algorithms, the most commonly used are k-means, self-organized map combination and fuzzy-C means algorithms. The K-means method is the most effective method for AE signal clustering, considering that the cluster



(a): Scarf 0° (cohesive fracture) **(b) : Scarf 22.5°** (adhesive /cohesive fractures) **(c) : Scarf 45°** (adhesive / cohesive fractures)

Figure 8. Effects of bonding configuration on the fracture surfaces.

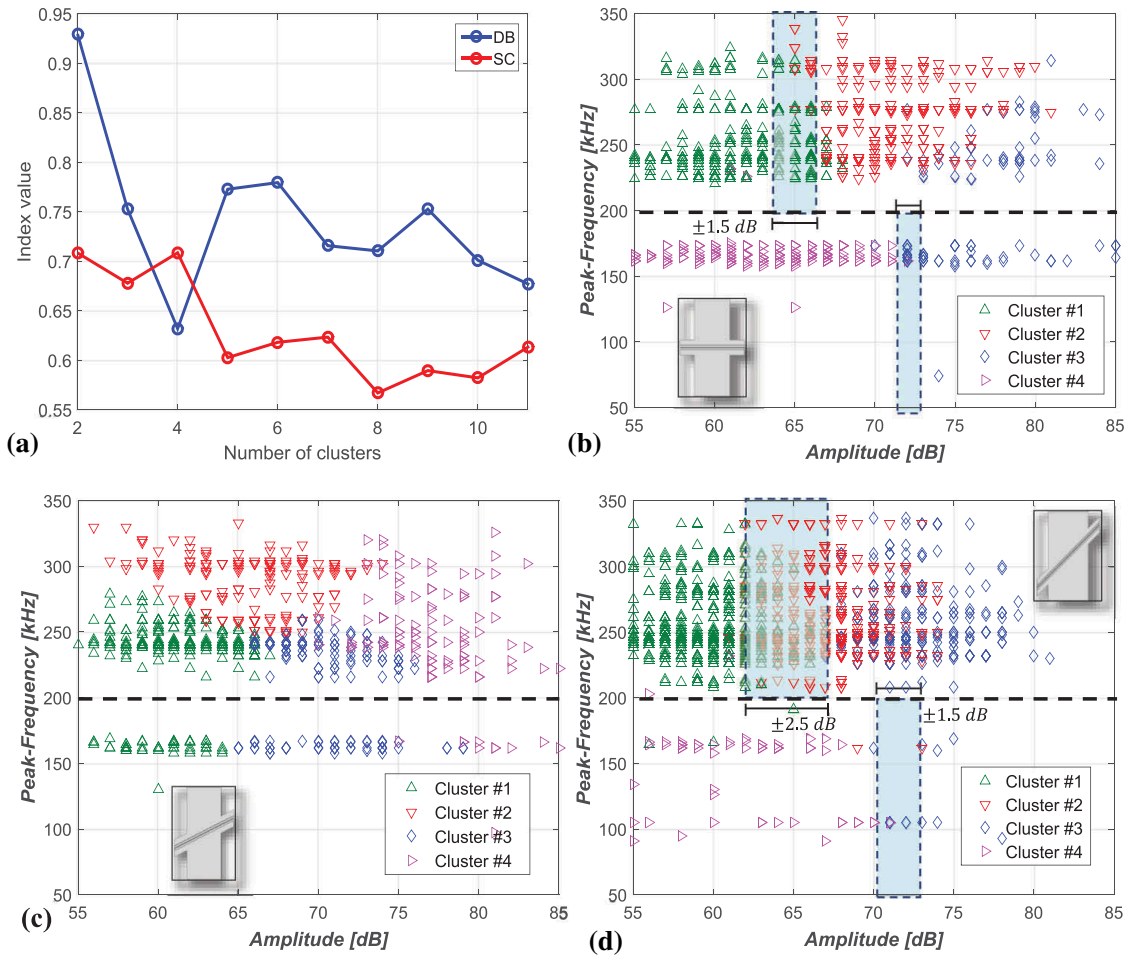


Figure 9. Clustering of AE events using two AE features: (a) optimal number, effect of loading configuration (b) $\delta = 0°$, (c)$\delta = 22.5°$, (d)$\delta = 45°$.

number is defined in advance from clustering evaluation indices (as discussed in section 4.2).[26] This fact leads to more accurate minimization of the average squared distances between the points and the cluster center. In order to gather similar AE events into clusters, the k-means++ algorithm is combined with the statistical tool called Principal Component Analysis (PCA).[17,18]

4.2. *Cluster analysis results*

The first analysis to consider before gathering AE data into clusters is to eliminate the irrelevant and redundant signals from the AE features (amplitude, duration, energy, number of counts, rise time, and rise-amplitude, i.e. rise time divided by amplitude, the peak-frequency, the centroid-frequency, i.e. the center of gravity frequency, and the weighted-frequency). The selection of the most representative AE features for data clustering was achieved using the Laplacian score and the correlation coefficients. A detailed description of the Laplacian score is available in.[16]

In this study, the selection of the optimal number of clusters is based on the values of two clustering evaluation indices, the Davies-Bouldin index (DB) and the Silhouette Coefficient (SC). Additional details on both the DB and SC criteria are available in.[17,18] The evaluation of these indices show that the optimal number of clusters is four [27] (Figure 9a), which means that four cracking mechanisms with different acoustic signatures can be identified from the acoustic activity within the adhesive bonded joint.

For each loading configuration Scarf 0° (Figure 9b), Scarf 22.5° (Figure 9c), and Scarf 45° (Figure 9d) a projection of the four clusters of AE events onto a two-dimensional plot is proposed. Results show that the loading configurations Scarf 0° and Scarf 45° allow identifying the clusters boundaries. Cluster analysis of AE events from Scarf 22.5° do not allow obtaining well separated clusters.

Figure 9b–d show that amplitude and peak frequency show a good separation of the clusters points in the space. However, it should be kept in mind that peak frequency values of AE events are influenced by the resonant frequency of AE sensors. On this basis, Figure 9b–d led to classify the AE events into three main clusters. Separated by two borders at 65 ± 1.5dB and 73 ± 0.5dB for 0° modified Scarf (for 45° modified Scarf the borders are slightly larger): AE events of Cluster#1 exhibit amplitude values lower than 65 ± 1.5dB; AE events of Cluster#2/Cluster #3 (which are merged) exhibit amplitude values greater than 65 ± 1.5dB; AE events of Cluster#4 exhibit amplitude values lower than 73 ± 0.5dB (peak frequency within the range from 50 to 200 kHz).

Figure 10 shows the linear localization (between the two AE sensors, Figure 3) of AE events of the four clusters during the mechanical test for each loading configuration. It can be seen from these figures that the very first AE events belong to Cluster#1 and Cluster#2, and appear when the resulting force reaches half of its maximum value. AE events of Cluster#3 start appearing when the resulting force reaches $0.6 \times F_{Max}$. Beyond this force value (60% of F_{max}), AE events of all the clusters appear continuously along the adhesive bonded joint. It can also be seen from these figures that localization of Cluster#3 (for Scarf 0° and 45°) or Cluster#4 (for Scarf 22.5°) AE events along the bonding joint and during the mechanical test follows a specific shape that is discussed in section 5.1.

4.3. *Effects of loading rates on AE activity*

Since mechanical tests with 0° modified scarf joint generate acoustic activity with well separated clusters (Figure 9b), force-controlled tensile tests were performed on 0° modified scarf specimens, and at different loading rates (Figure 11). This aims to investigate effects of these testing conditions on cluster analysis results of AE events.

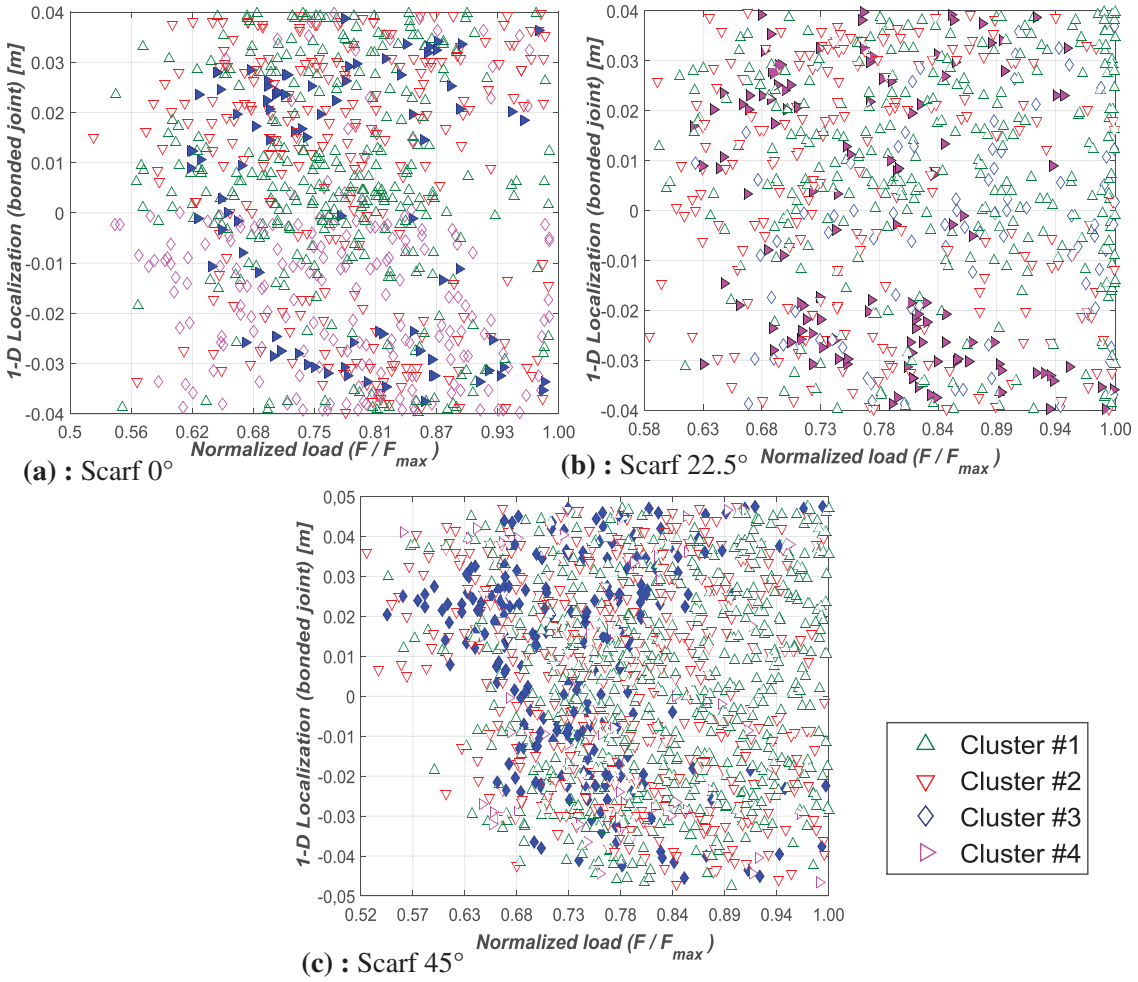


Figure 10. Linear localization of AE events within the bonded joint: Effect of loading configuration.

When focusing on AE events with peak frequency within the range from 200 to 350 kHz, cluster analysis results show that under a low loading rate (0.02kN/s) two main cracking mechanisms with different acoustic signatures can be identified (Figure 11a), and are differentiated by the amplitude level of AE events (lower or greater than 70dB).

5. Correlation between AE activity and mechanical behavior

In this section, the main goal is to perform an in-depth analysis of AE data in order to identify any acoustic signature allowing a detection of the mechanical behavior change during the modified scarf test. This change in the mechanical behavior (macroscopic) may be due to microstructural changes occurring within the adhesively-bonded joint.

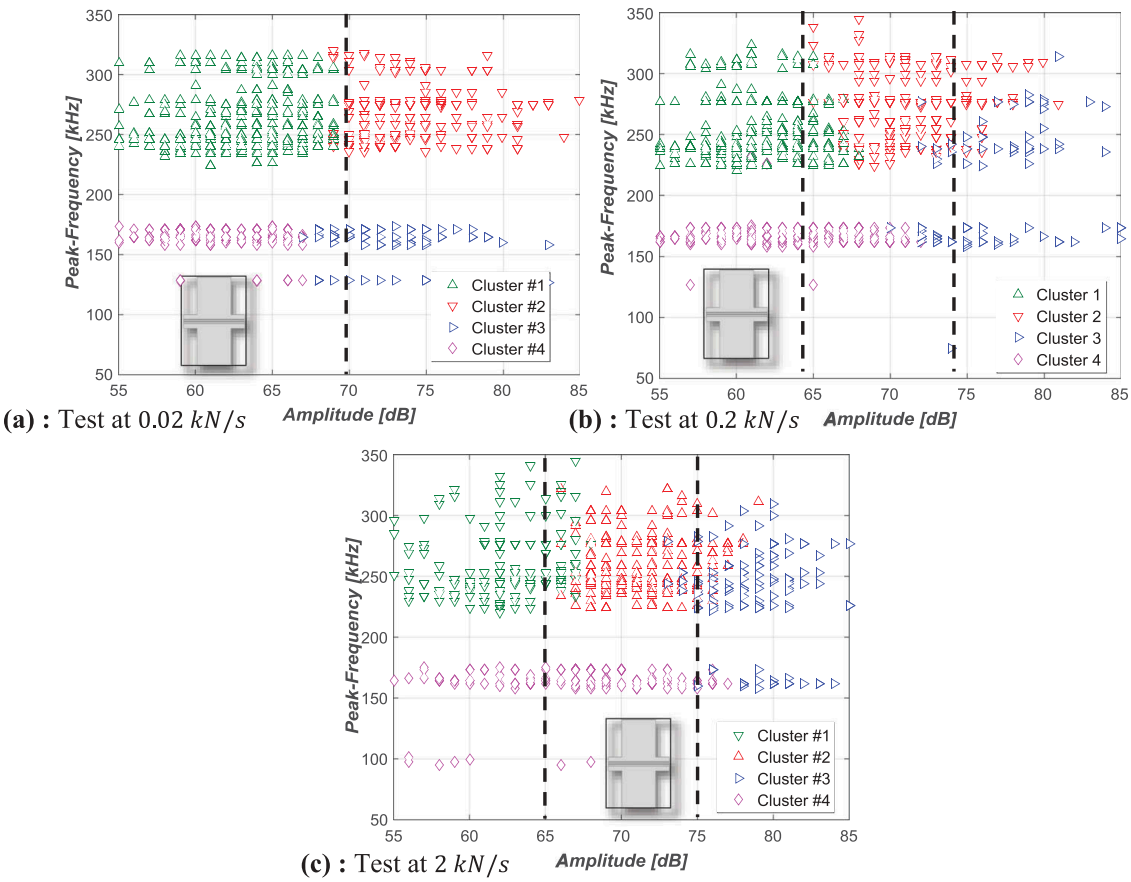


Figure 11. Clustering of AE events using two AE features: Effect of loading rate.

5.1. *Damage propagation monitoring*

As stated previously, the appearance of cluster#3 AE events during mechanical test and along the adhesive bonding follows a specific shape (Figure 10). In particular, under loading configuration scarf 0°, a bell-shape distribution of cluster#3 AE events is clearly noticeable (Figure 10a). This finding is used to evaluate the damage progress within the adhesive (Figure 12). As shown in Figure 12 damage levels of the bonded surface can be evaluated at different force values.

5.2. *Yield strength/damage detection*

This section will focus on the analysis of both the macroscopic mechanical behavior of the modified scarf joints and the acoustic emission activity within the adhesively-bonded joint. Acoustic energy is considered to be the AE feature that is highly correlated with mechanical strain energy.[17]

AE data that was recorded during mechanical tests on each loading configuration and at 0.2kN/s is analyzed in terms of acoustic energy evolution (cumulative energy divided by cumulative number of events). As long as the yield strength of the material or the structure is not reached, the material

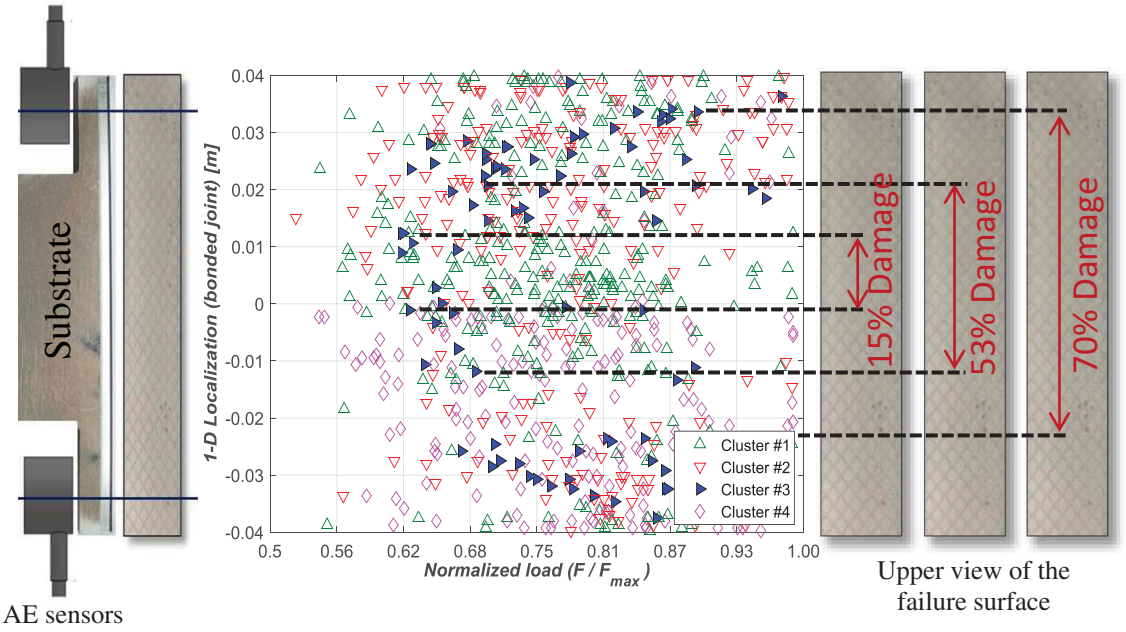


Figure 12. Damage surface evaluation by monitoring specific AE events.

continues to store mechanical energy. Once it is reached, the released strain energy is accompanied by transient elastic waves that are highly energetic, which can be related to permanent strain or micro-damage within the adhesive joint. During the test, AE software records the wave signals, and instantaneously computes and plots the corresponding acoustic energy values. This allows a real-time monitoring of acoustic energy evolution. Based on this evolution one can see from Figure 13 that the highest value of acoustic energy is detected when the slope of the mechanical behavior curve (macroscopic scale) drastically changes. This radical change in slope is generally assumed to correspond to the yield strength of the material.

In addition, it can be seen from Figure 13 that the very first AE events appear just before the adhesive bonded joint reaches its yield strength. These first AE events may be considered as warning signals. In order to identify the link between AE signals and permanent strain or damage, cyclic tests were performed using 0° modified scarf specimens. The test was conducted by applying ten cycles with a step of 0.09 F_{Max}. Figure 14a shows the overlap between the linear localization of AE events and the applied load. It can be seen from these figures that the first big package of AE events appears after the 6 first cycles (0.57 F_{Max}). Also from Figure 14b it can be seen that the unloading of the 6 first cycles has no permanent deformation, which leads to the conclusion that these events are related to micro-damage. Further analysis using tomography scans will allow identifying the defects that generate these particular acoustic signatures.

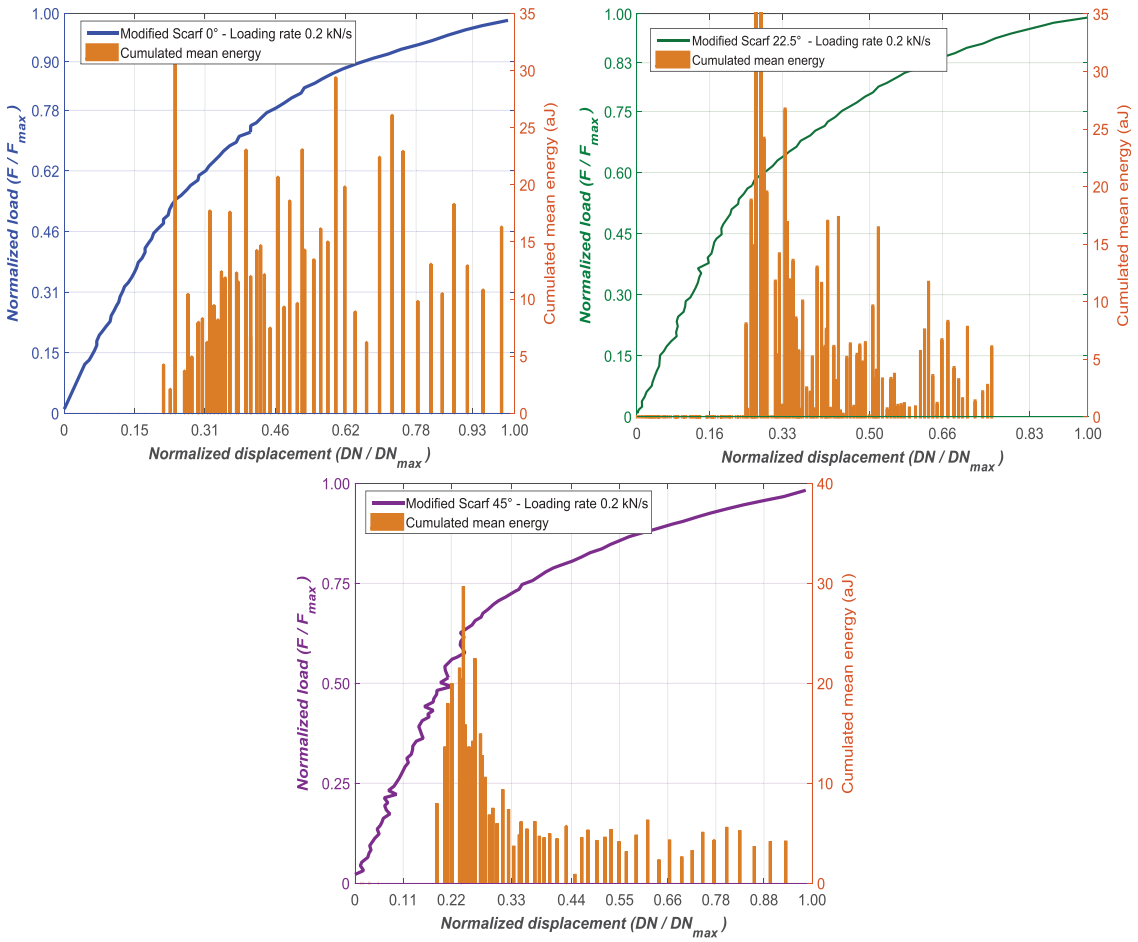


Figure 13. Real-time yield strength detection by means of acoustic emission energy.

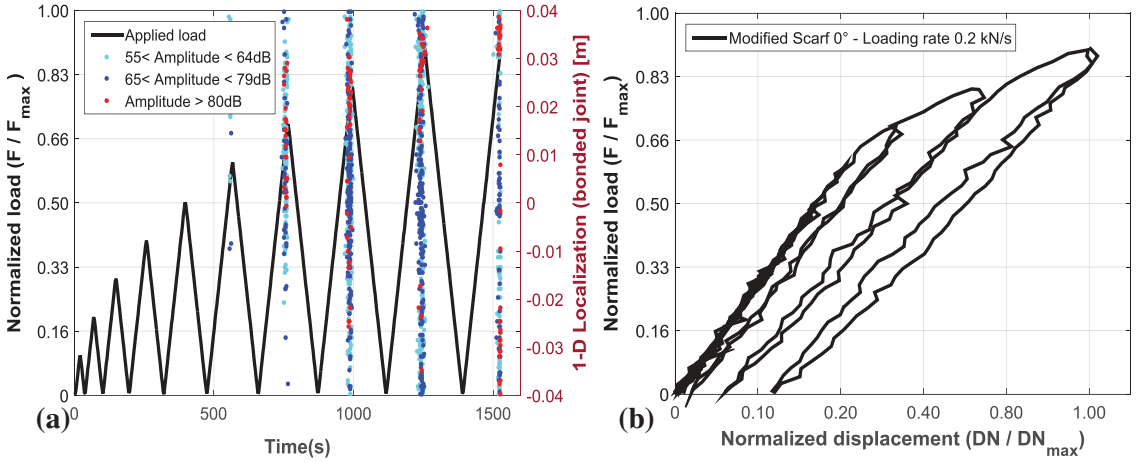


Figure 14. Cycle quasi-static test (a) applied load, (b) mechanical behavior.

6. Conclusions

In this study, monotonic tests were conducted in order to firstly investigate the damage evolution of a metal-to-metal adhesively-bonded joint under bi-axial loadings (different shear/peel ratios), and secondly to both detect and

identify acoustic emission (AE) signatures of the different failure mechanisms involved in the bonded joint damage. Specimens with modified scarf joint were manufactured. Three loading configurations were tested (three values of joint angle). In addition to the AE technique, Digital Image Correlation (DIC) method was used for measuring both the normal and the tangential relative displacements along the adhesively-bonded joint.

Experimental results show that the highest load machine value is obtained with the 45° modified scarf joint since this loading configuration leads to the highest adhesive bonded surface. Mechanical results also show that the loading configuration strongly influences the normal stiffness value of the bonded joint. These differences in normal stiffness values may be due to the fact that the adhesive bonded surface varies with the loading configuration. The effects of loading rate on the mechanical behavior of adhesive are investigated. Experimental results show that the pseudo-elastic behavior is not affected by the loading rate, whereas the nonlinear regime as well as the load machine at failure is strongly affected by the loading rate.

AE data was analyzed, and the cluster analysis shows that four cracking mechanisms with different acoustic signatures can be identified from the acoustic activity within the adhesively-bonded joint. However, three main acoustic signatures (cracking mechanisms) were retained. Additional tests by means of tomographic microscopy at different loading stages are in progress in order to identify the defects that generate these particular acoustic signatures.

Finally, an in-depth analysis of AE data was performed in order to try to identify any acoustic signature allowing a detection of the mechanical behavior change during the modified scarf test. The real-time acoustic energy evolution is analyzed, and results show that the highest value of acoustic energy is detected when the slope of the mechanical behavior curve (macroscopic scale) drastically changes. This radical change in slope curve is generally assumed to correspond to the yield strength of the material. Also, the cyclic test showed that the preliminary AE signals (with the highest value of acoustic energy) were linked to an abrupt change of slope which can be related to micro-damage within the adhesive joint. Again, this will be confirmed by RX scans.

Acknowledgements

The authors thank Li Li (Donghua University, China) and Stephan Lomov (KU Leuven, Belgium) for the cluster analysis tool.

ORCID

M. Diakhate http://orcid.org/0000-0002-7722-6388

References

[1] Vijaya Kumar, R. L.; Bhat, M. R.; Murthy, C. R. L. Some Studies on Evaluation of Degradation in Composite Adhesive Joints Using Ultrasonic Techniques. *Ultrasonics*. 2013, *53*, 1150–1162. DOI: 10.1016/j.ultras.2013.01.014.

[2] Dukes, W. A.; Kinloch, A. J. Non-Destructive Testing of Bonded Joints. *Non-Destr. Test*. 1974, *7*, 324–326. DOI: 10.1016/0029-1021(74)90054-1.

[3] Adams, R. D.; Cawley, P. Defect Types and Non-Destructive Testing Techniques for Composites and Bonded Joints. *Constr. Build. Mater*. 1989, *3*, 170–183. DOI: 10.1016/0950-0618(89)90011-1.

[4] Cognard, J. Y.; Davies, P.; Sohier, L.; Créac'hcadec, R. A Study of the Non-Linear Behaviour of Adhesively-Bonded Composite Assemblies. *Compos. Struct*. 2006, *76*, 34–46. DOI: 10.1016/j.compstruct.2006.06.006.

[5] Cognard, J. Y.; Créac'hcadec, R.; Sohier, L.; Davies, P. Analysis of the Nonlinear Behavior of Adhesives in Bonded assemblies—Comparison of TAST and Arcan Tests. *Int. J. Adhes. Adhes*. 2008, *28*, 393–404. DOI: 10.1016/j.ijadhadh.2008.04.006.

[6] Droubi, M. G.; Mcafee, J.; Horne, R. C.; Walker, S.; Klaassen, C.; Crawford, A.; Prathuru, A. K.; Faisal, N. H. Mixed-Mode Fracture Characteristics of Metal-To-Metal Adhesively Bonded Joints: Experimental and Simulation Methods. *Procedia Struct. Integr*. 2017, *5*, 40–47. DOI: 10.1016/j.prostr.2017.07.059.

[7] Nieminen, A. O. K.; Koenig, J. L. Macroscopic and Modern Microscopic NDE Methods for Adhesive-Bonded Structures. *Int. J. Adhes. Adhes*. 1991, *11*, 5–10. DOI: 10.1016/0143-7496(91)90054-L.

[8] Hamdi, S. E.; Le Duff, A.; Simon, L.; Plantier, G.; Sourice, A.; Feuilloy, M. Acoustic Emission Pattern Recognition Approach Based on Hilbert–Huang Transform for Structural Health Monitoring in Polymer-Composite Materials. *Appl. Acoust*. 2013, *74*, 746–757. DOI: 10.1016/j.apacoust.2012.11.018.

[9] Schliekelmann, R. J. Non-Destructive Testing of Adhesive Bonded Metal-To-Metal Joints 1. *Non-Destr. Test*. 1972, *5*, 79–86. DOI: 10.1016/0029-1021(72)90099-0.

[10] Korzeniowski, M.; Piwowarczyk, T.; Maev, R. G. Application of Ultrasonic Method for Quality Evaluation of Adhesive Layers. *Arch. Civ. Mech. Eng*. 2014, *14*, 661–670. DOI: 10.1016/j.acme.2013.10.013.

[11] Krause, M.; Dackermann, U.; Li, J. Elastic Wave Modes for the Assessment of Structural Timber: Ultrasonic Echo for Building Elements and Guided Waves for Pole and Pile Structures. *J. Civ. Struct. Heal. Monit*. 2015, *5*, 221–249. DOI: 10.1007/s13349-014-0087-2.

[12] Diakhaté, M.; Larcher, N.; Takarli, M.; Angellier, N.; Petit, C. Acoustic Techniques for Fatigue Cracking Mechanisms Characterization in Hot Mix Asphalt (HMA). In *7th RILEM International Conference on Cracking in Pavements*; Springer Netherlands: Dordrecht, 2012; Vol. 4, pp 771–781. ISBN 9789400745650.

[13] Kowalski, S. J.; Molinski, W.; Musielak, G. The Identification of Fracture in Dried Wood Based on Theoretical Modelling and Acoustic Emission. *Wood Sci. Technol*. 2004, *38*, 35–52. DOI: 10.1007/s00226-003-0211-7.

[14] Huguet, S.; Godin, N.; Gaertner, R.; Salmon, L.; Villard, D., Use of Acoustic Emission to Identify Damage Modes in Glass Fibre Reinforced Polyester. *Compos. Sci. Technol*. 2002, *62*, 1433–1444. DOI: 10.1016/S0266-3538(02)00087-8.

[15] Hwang, H. Y.; Kim, B. J.; Chin, W. S.; Kim, H. S.; Lee, D. G., Prediction of Crack Length and Crack Growth Rate of Adhesive Joints by a Piezoelectric Method. *J. Adhes. Sci. Technol*. 2005, *19*, 1081–1111. DOI: 10.1163/156856105774382453.

[16] Chen, Z.; Adams, R. D.; Da Silva, L. F. M. Prediction of Crack Initiation and Propagation of Adhesive Lap Joints Using an Energy Failure Criterion. *Eng. Fract. Mech.* 2011, *78*, 990–1007. DOI: 10.1016/j.engfracmech.2010.12.004.
[17] Diakhate, M.; Bastidas-Arteaga, E.; Moutou Pitti, R.; Schoefs, F. Cluster Analysis of Acoustic Emission Activity within Wood Material: Towards a Real-Time Monitoring of Crack Tip Propagation. *Eng. Fract. Mech.* 2017, *180*, 254–267. DOI: 10.1016/j.engfracmech.2017.06.006.
[18] Li, L.; Lomov, S. V.; Yan, X.; Carvelli, V. Cluster Analysis of Acoustic Emission Signals for 2D and 3D Woven Glass/Epoxy Composites. *Compos. Struct.* 2014, *116*, 286–299. DOI: 10.1016/j.compstruct.2014.05.023.
[19] Diakhate, M.; Angellier, N.; Moutou Pitti, R.; Dubois, F. On the Crack Tip Propagation Monitoring within Wood Material: Cluster Analysis of Acoustic Emission Data Compared with Numerical Modelling. *Constr. Build. Mater.* 2017, *156*, 911–920. DOI: 10.1016/j.conbuildmat.2017.09.065.
[20] Droubi, M. G.; Stuart, A.; Mowat, J.; Noble, C.; Prathuru, A. K.; Faisal, N. H. Acoustic Emission Method to Study Fracture (Mode-I, II) and Residual Strength Characteristics in Composite-To-Metal and Metal-To-Metal Adhesively Bonded Joints. *J. Adhes.* 2018, *94*, 347–386. DOI: 10.1080/00218464.2017.1278696.
[21] Dzenis, Y. A.; Saunders, I. On the Possibility of Discrimination of Mixed Mode Fatigue Fracture Mechanisms in Adhesive Composite Joints by Advanced Acoustic Emission Analysis. *Int. J. Fract.* 2002, *117*, 23–28. DOI: 10.1023/A:1022636512843.
[22] de Freitas, S. T.; Zarouchas, D.; Poulis, J. A. The Use of Acoustic Emission and Composite Peel Tests to Detect Weak Adhesion in Composite Structures. *J Adhes.* 2018. DOI:10.1080/00218464.2017.1396975.
[23] Carrere, N.; Badulescu, C.; Cognard, J.-Y.; Leguillon, D. 3D Models of Specimens with a Scarf Joint to Test the Adhesive and Cohesive Multi-Axial Behavior of Adhesives. *Int. J. Adhes. Adhes.* 2015, *62*, 154–164. DOI: 10.1016/j.ijadhadh.2015.07.005.
[24] Sause, M. G. R. Investigation of Pencil-Lead Breaks as Acoustic Emission Sources. *J. Acoust. Emiss.* 2011, *29*, 184–196.
[25] Nielsen, A. *Acoustic Emission Source Based on Pencil Lead Breaking*; Svejsecentralen, 1980.
[26] Godin, N.; Huguet, S.; Gaertner, R.; Salmon, L. Clustering of Acoustic Emission Signals Collected during Tensile Tests on Unidirectional Glass/Polyester Composite Using Supervised and Unsupervised Classifiers. *NDT E. Int.* 2004, *37*, 253–264. DOI: 10.1016/J.NDTEINT.2003.09.010.
[27] Li, L.; Lomov, S. V.; Yan, X. Correlation of Acoustic Emission with Optically Observed Damage in a Glass/Epoxy Woven Laminate under Tensile Loading. *Compos. Struct.* 2015, *123*, 45–53. DOI: 10.1016/j.compstruct.2014.12.029.

THE JOURNAL OF ADHESION
2021, VOL. 97, NO. 6, 528–552
https://doi.org/10.1080/00218464.2019.1685984

Taylor & Francis
Taylor & Francis Group

Check for updates

Experimental investigation of porosities evolution in a bonded assembly by means of X-ray tomography

V. Dumont [a], C. Badulescu[a], J. Adrien[b], N. Carrere[c], D. Thévenet[a], and E. Maire[b]

[a]ENSTA Bretagne, UMR CNRS 6027, IRDL, Brest, France; [b]Univ. Lyon, INSA Lyon, CNRS UMR 5510, Laboratoire MATEIS, Villeurbanne Cedex, France; [c]Safran Composites, Itteville, France

ABSTRACT

Structral bonding is a very advantageous technique for lots of application fields such as aeronautics or marine industry, which require both advanced performances and lightweight structures. Nonetheless, adhesive joints are often subject to bonding defects: kissing bonds, uneven polymerisation, or pores within the material, for instance. These pores, depending on their sizes and distributions, could jeopardise the mechanical strength of the assembly. Moreover, it is legitimate to hypothesise that these voids in the medium could be influenced by the application of a mechanical stress. In order to investigate this assertion, bonded samples are loaded by various tensile stress levels, and the pores within the joint are visualised and characterised using *in-situ* X-ray microtomography. This paper deals with the evolutions of various quantities such as the number of pores or their volumetric ratio along with the increasing load and with the diverse phenomena (nucleation, growth, coalescence, *etc.*) experienced during the testings. These results are extracted from the microtomographic data using a custom processing tool, whose parameters and performances are discussed.

ARTICLE HISTORY
Received 26 July 2019
Accepted 24 October 2019

KEYWORDS
Porosity; adhesively bonded assemblies; X-ray tomography; coalescence

1. Introduction

Structural bonded joints[1] represent today a promising technique due to its main advantages such as: obtaining lightweight and complex structures, its simplicity of implementation, the possibility of unification of elements of different nature (in particular composite and metal), and providing a more homogenous distribution of the loading state in the two bonded elements. In recent years, a large number of studies[2–6] were carried out in the bonded joints field, both in terms of experimental characterisation and numerical modeling of the mechanical behaviour of adhesive.

Experimental characterisation of adhesive requires the use of different types of tests dedicated to this area. Among the most common, one may

CONTACT V. Dumont vincent.dumont@ensta-bretagne.org ENSTA Bretagne, UMR CNRS 6027, IRDL, F-29200 Brest, France

Color versions of one or more of the figures in the article can be found online at www.tandfonline.com/gadh.

© 2019 Taylor & Francis Group, LLC

include: (i) single lap joint test (SLJ), (ii) standardised thick adherend shear test (TAST) or (iii) modified Arcan test.[5,7]

SLJ is characterised by the simplicity of its samples and of the test, which only requires a simple test machine. However, this test is accompanied by significant stress concentrations at the ends of the overlap length, which may cause a significant scattering of the experimental results.

An alternative to this problem is the modified Arcan test, which diminishes drastically the stress concentrations close to the free edges of the adhesive. Also this test can generate different loading states in the joint such as: pure tensile, tensile-shear, pure shear or compressive-shear. However putting into practice the modified Arcan test involves a certain degree of difficulty, which makes it less usable in industrial environments. An alternative for the modified Arcan test is the modified Scarf test.[8] This test setup allows to generate tensile or tensile-shear loads on an adhesive joint. The sample tested in this case is simple and can be used on standard tensile test machines without any additional devices. Moreover, this test is perfectly adapted for the fatigue tests investigation in the industrial environment.

Full field measurement of the displacement or strain by optical non-contact measurement systems, are increasingly being used in order to obtain the kinematic information necessary to characterise the mechanical behaviour.[9] In most cases, the information obtained using non-contact measurement systems are obtained on the surface of the sample. Notwithstanding, it is necessary to get information inside the sample for the understanding of failure mechanisms and of their evolutions during the test.

In the last decade, several studies have been conducted, which highlight the major advantages of observations using X-ray tomography (XRT).[10–12] This tool is very advantageous because it allows to access the details of the microstructure of a material without its destruction. An original methodology is proposed[13] to estimate 3D displacement fields from pairs of images from X-ray computed microtomography. Contrary to local approaches, a global approach is followed herein that evaluates continuous displacement fields. Fast tomography combined with local crack driving force analysis has been employed to analyse crack-tip stress/strain singularities in an aluminium alloy.[11] The application of fast microtomography has made possible to observe real crack initiation and propagation behaviours without intermediate unloading. The anisotropy of fracture toughness in AA2139 (AlCuMg) alloy sheet has been investigated via synchrotron radiation computed tomography of arrested cracks in Kahn tear test pieces for different loading cases.[14] More recent work[15] in the field of bonded joints have investigated the quantitative penetration of three coldset wood adhesives under hydraulic pressure into different types of modified wood using fluorescence microscopy and the results were compared to these of a previous study without pressure on adjacent wood samples. The three-dimensional visualisation of

the penetration of the adhesive into heat-treated Scots pine was also examined by X-ray tomography. X-ray microtomography is used in[16] to visualise the distribution of melamine-urea-formaldehyde adhesive in the wood composite, particle board, and to examine changes in adhesive distribution on wood particles (flakes) before and after pressing. Also X-ray computed microtomography (XCT) was used to analyse the 3D adhesive penetration behaviour of different wood-adhesive bondlines.[17]

However, there are only few papers that analyse quantitatively the information that can be achieved using X-ray tomography in the field of structural bonded assemblies. It should be noted that the damage mechanisms are linked mainly by the presence of defects such as: pores, lack of glue, the presence of several phases in the adhesive structure, *etc.*

The present paper focuses on the quantitative analysis at the micrometric scale of bonded joints (epoxy adhesive and aluminium alloy). The main objective is to obtain the 3D microstructure of the adhesive after polymerisation process (*i.e.* to identify the phases in the glue and their distribution) and to monitor the evolution of these phases when the sample is subjected to a tensile loading. In the first section, the experimental procedure will be presented, followed by the development and the validation of the adequate processing tool. Finally, the results will be outlined and discussed in the last section.

2. Experimental procedure

2.1. *X-ray tomography setup*

Since its first applications in the medical field,[18] X-ray tomography has been the subject of many studies both from a theoretical and applied point of view. A brief description is therefore given here in order to introduce the concepts, which will be used further in the text. Various experimental setups can be used to perform X-ray tomography, but the basic principles of the technique remain the same (see Figure 1). Tomography measurements are based on the variation of the linear X-ray attenuation coefficient, hereafter written μ, through the volume of a material. For a perfectly isotropic material this μ coefficient is a constant with respect to the spatial coordinates (x, y, z). However, for non-homogenous material, such as porous environments, μ is a function of these coordinates. It is possible to obtain the spatial distribution of this μ coefficient by sending a source X-rays beam through the bulk of the studied sample, from different angles, and by collecting the transmitted beam. Hence, the sample is mounted on a rotator included in the tomograph chamber, and for each angular step, a X-ray beam is emitted, attenuated by the internal structure of the sample, and gathered by a detector. The attenuation phenomenon is described by a Beer – Lambert law depending on $\mu(x, y, z)$:

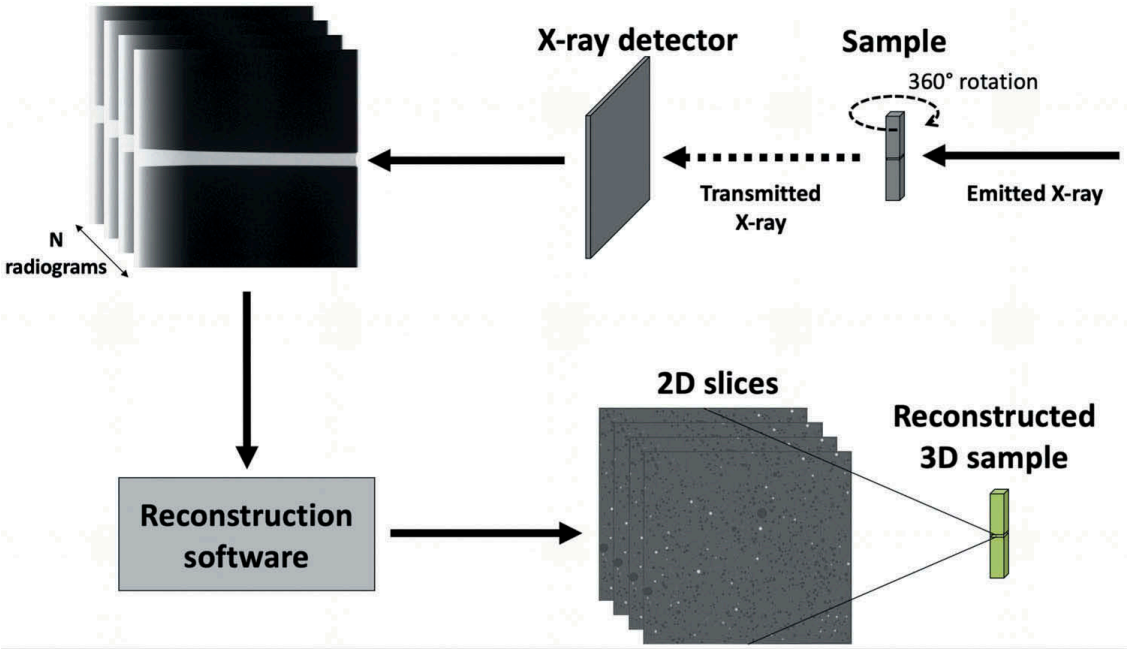


Figure 1. X-ray tomography principle.

$$\frac{I}{I_0} = \exp\left(\int_{x_0}^{x_{max}} \mu(x,y,z)dx\right) \tag{1}$$

where I_0 represents the source intensity (emitted), I is the detected intensity (transmitted and collected by the X-ray detector) and x represents distance along the transmission path $[x_0; x_{max}]$.

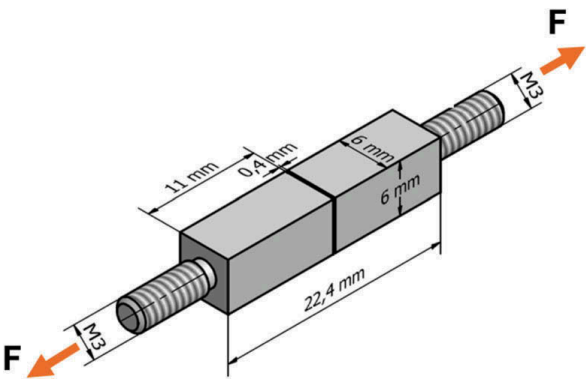
A series of N radiograms, or radios, is obtained through the complete acquisition process (Figure 1). A reconstruction algorithm is then used to build the 3D internal structure of the sample (*i.e.* the spatial distribution of $\mu(x,y,z)$) from the radiographs series.

Those algorithms may be based on two different approaches: the software may either solve a set of linear equations to compute $\mu(x,y,z)$ (algebraic approach) or use a backprojection of the detected intensity by a Fourier transformation (analytical approach). Although the analytical approach is faster to compute, it requires a full dataset with no missing views from the radiographs series. This method is referred to as filtered backprojection reconstruction. For more details about these techniques and about their theoretical backgrounds, see.[10,19] The results presented in this paper were obtained by a filtered backprojection approach. Those algorithms depend on the X-ray source used to perform the measurements, being either a synchrotron or a laboratory tomograph, for the emitted beam itself depends on the underlying technology. For laboratory devices, the emitted beam is produced into a cone shape, rather than being constituted by parallel rays (which is the case for synchrotron X-ray sources). This has to be taken into account during the Fourier transformation backprojection.[10] Although the formalism of the algorithm shall not be

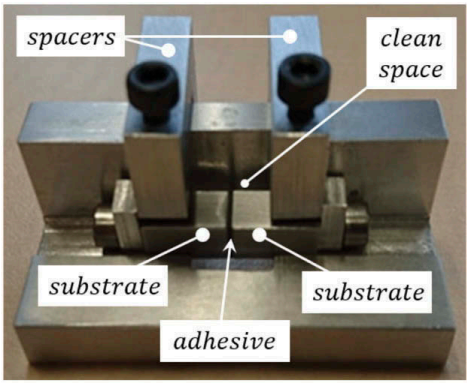
discussed here, the reader could find more information about this particular matter in various reference works.[10,19,20] The reconstruction step provides the 3D structure of the observed sample (Figure 1), defined with a given voxel size, in a similar fashion as pixels constitute a picture. It is worth noticing that the voxel size is related to the spatial resolution of the measurement, but is not equivalent. An empirical relationship between those quantities may be established, the spatial resolution being then twice the voxel size.[10] It is obvious that the spatial resolution of the experimental set-up depends not only on the voxel size, but also on various external parameters relative to the whole experimental set-up, and that the resolution must be in compliance with the characteristic sizes of the microstructure defects to observe. Some laboratory tomographs allow the operator to perform *in-situ* measurements during mechanical and/or thermal loadings.[21] These kinds of experiments are though complex to handle due to the measurement artifacts it may produce. It is hence possible to access the microstructure of the sample, which is now a function of time, as opposed to classical, one-shot experiments delivering a unique radios series. The acquisition time for each radiographs series comes into play and defines the time resolution of the measurement, which has to be negligible when compared to the characteristic time of the observed phenomena. The following results in this paper are gathered using such an experimental set-up.

2.2. *Sample preparation*

The samples consist of two Aluminium (2017A) substrates adhesively bonded by an epoxy resin layer of a given thickness. A simple, butt joint-like, geometry is designed as presented in Figure 2a. The area of the bonded section is set to $6 \times 6 = 36$ mm^2. A non-uniform stress state is then expected within the bulk of the adhesive joint, along with stress concentration effects due to the influence of the edges of the substrates during the mechanical loading.[1]



(a) Sample geometry



(b) Sample mounted in the bonding apparatus with controlled joint thickness

Figure 2. Samples and bonding apparatus.

The assemblies are obtained by bonding the substrates described above with the epoxy adhesive *Huntsman*^{TM} *Araldite 420 A/B*. The adhesive thickness is set to a value of 400μ m and is controlled by a system of spacers. This system, and the specially designed corresponding apparatus, are presented in Figure 2a. This system enables both the control of the thickness of the adhesive joint and the correct alignment of the substrates. A clear space is also preserved in order to clean the adhesive joint once the substrates are assembled, and thus to obtain a neatly defined sample.

In order to guarantee the good adhesion between the adhesive layer and the substrates, a classical (chemical and mechanical) surface treatment is performed on the bonding surfaces to remove any greasy byproducts that may remain after the machining of the substrates and to create an adequate surface roughness for the desired mechanical interlocking between the substrates and the adhesive. In a first step, the substrates are placed in an acetone bath for several hours to degrease the surfaces. They are then treated with grade 180 sandpaper to remove the remaining impurities and to eliminate any oxide layer that could have formed due to the exposition of the Aluminium to the ambient environment. Moreover, this mechanical treatment creates the aforementioned surface roughness required for a good adhesion. Lastly, the surfaces thusly treated are cleaned with acetone to remove the impurities and Aluminium particles created with the mechanical treatment. The adhesive joint is then prepared by applying the mixed epoxy resin and hardener on both substrates, which are assembled and installed in the apparatus (Figure 2b) carefully adjusted to obtain the desired joint thickness. The samples are finally placed in a *Secasi Technologies 100/60* thermal enclosure at 115°C for 1 hour to ensure a fully polymerised material. Due to the very limited volume of the adhesive joints, it is assumed that the thermal field in the material is homogeneous, and that there is no significant influence of possible curing degree gradients in the adhesive. It can be seen in Figure 2a that threaded holes are machined at each end of the samples to allow the positioning of the rods necessary to the installation of the samples in the clamping jaws of the tensile machine to be used. Those holes are also used during the gluing process to control the relative positioning of the substrates.

2.3. *Test procedure*

The samples are placed inside a *Phoenix*^{TM} *VtomeX* tomograph equipped with a *Varian*^{TM} *Paxscan* X-Ray detector featuring a resolution of 1920 × 1536 pixels. This detector outputs a 14-bits coded grayscale picture of the attenuation. The chamber of the tomograph includes a 3kN tensile machine, which allows to perform X-ray tomography measurements while applying a mechanical load to the sample (Figure 3).

The voxel size obtained using this experimental set-up is 6 μm x 6 μm x 6 μm. The corresponding spatial resolution is expected to be in compliance with the

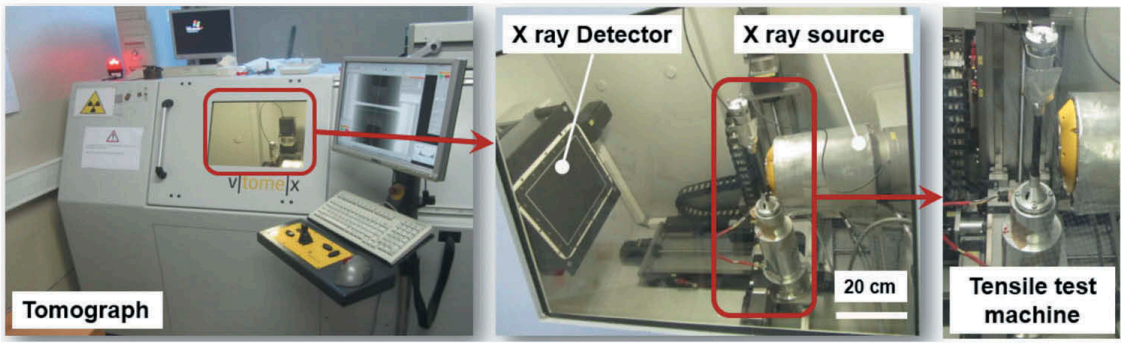
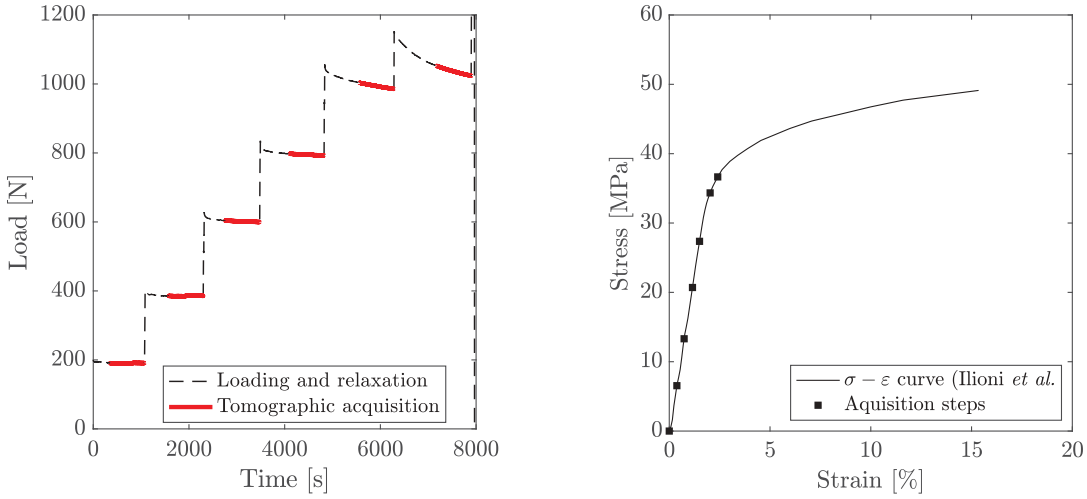


Figure 3. Standard laboratory *Phoenix*^{TM} *VtomeX* tomograph.

characteristic size of the pores to be observed. Also, the adhesive contains 0.16% (weight ratio, according to manufacturer data) of glass beads, whose diameters are about 80 m, i.e. more than 10 times greater that the resolution of the device. The measurements are assumed to occur for a quasi-static state of the samples, and therefore the corresponding characteristic time overshadows the acquisition time for a radiographs series. Hence, it is concluded that the experimental set-up is well-suited to the measurements to be performed. In order to reconstruct the full observed volume, the acquisition is performed along with a rotational motion of the sample. A total of 912 pictures are taken throughout the rotation, for a complete acquisition time of 12 min. These series are then used as previously mentioned by an algorithm based on the results presented in[4], in the perimeter of an analytical approach of the computation of the spatial field $\mu(x, y, z)$. The full volume of the samples, visualised by means of the variation of the values of the attenuation coefficient $\mu(x, y, z)$, is then broken into a series of slices (Figure 5).

An amount of 96 slices is obtained for the adhesive joint only, from the tomographs series. As already mentioned, the tensile test machine included in the tomograph chamber allows us to perform these measurements while applying a mechanical loading to the samples. The decision has been made to incrementally increase the applied load with a 200 N step (Figure 8). The ramps between the steps are displacement-controlled (0.5 mm/min). A stress-strain curve for the considered material is given in Figure 4b along with the stress states corresponding to each aquisition step (Figure 4a). In addition, the elastic properties of the adhesive are presented in Table 1.

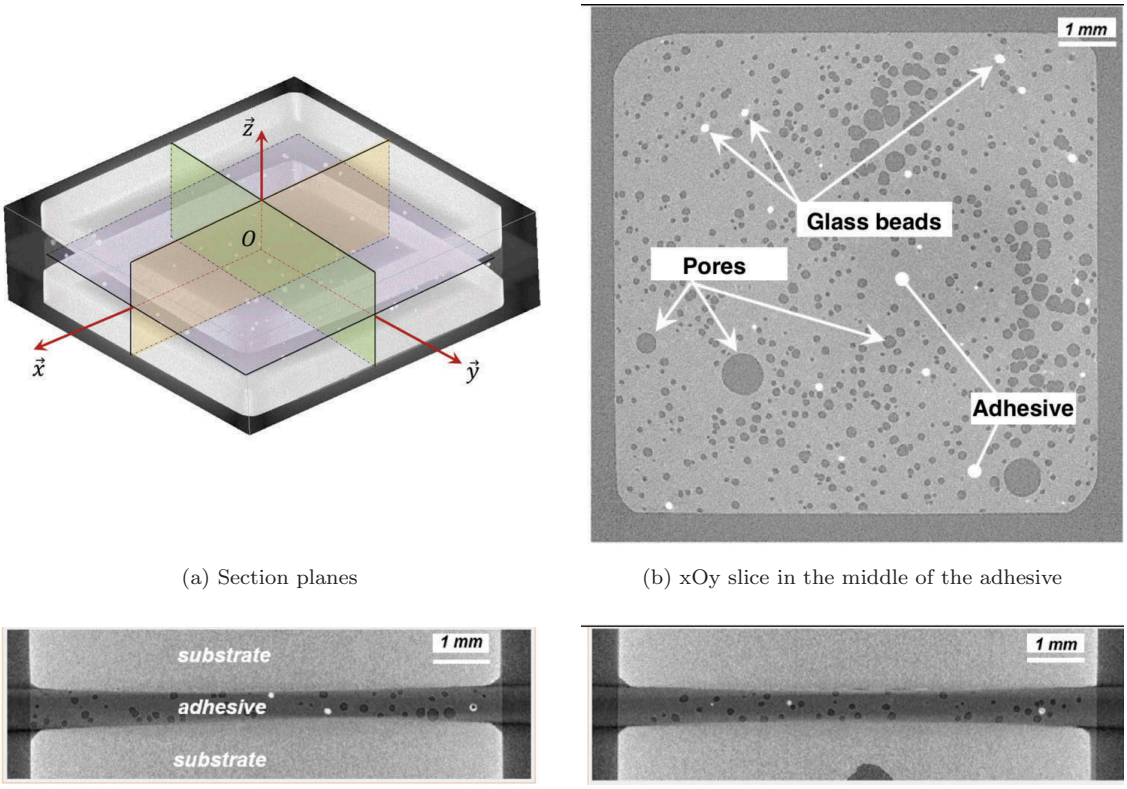
The process goes on until the failure of the sample. It is clear from Figure 4a that stress relaxation phenomena are occurring during these steps, especially for the high loads. For each step, the corresponding displacement is therefore maintained for a certain time, in order to let these phenomena occur. Otherwise, the measurement would be disturbed by the on-going relaxation, due to the similarity between the acquisition time and the relaxation characteristic time. By considering significantly longer load steps, it is possible for the load to reach an asymptotical value and hence to obtain a relatively steady state



(a) Load applied to the sample

(b) Tensile stress-strain curve of the considered adhesive [22]

Figure 4. Mechanical loading and properties of the adhesive.



(a) Section planes

(b) xOy slice in the middle of the adhesive

(c) xOz slice in the middle of the adhesive

(d) yOz slice in the middle of the adhesive

Figure 5. Reconstructed volume of the sample obtained from tomography investigation.

Table 1. Elastic parameters of the adhesive[22].

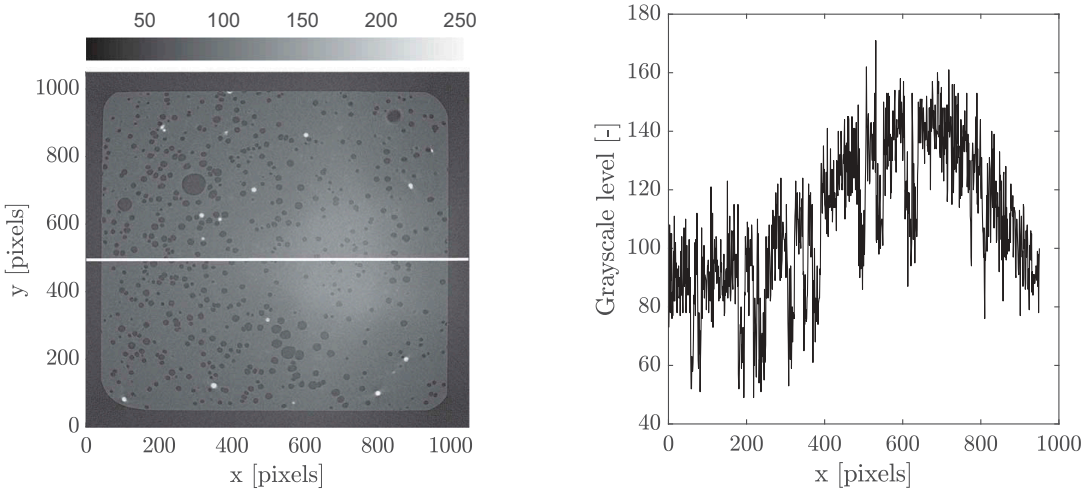
Parameter	Value
E [MPa]	2000 ± 50
ν [-]	0.41 ± 0.01

during the 12 minutes necessary to complete a full rotation of the sample. The aforementioned asymptotical value is harder to reach in a reasonable time the higher the load is, and may even not be reachable in some cases (loads greater than 800 N, Figure 4a). This may lead to blurry acquisition data, as those measures are critically sensitive to any disturbances, which cause significant artifacts. It is then possible to acquire a snapshot of the 3D microstructure of the adhesive joint for several loads. In other words, given the adequate post-processing tools, it is possible to follow the evolution, along with the applied load, of the microstructure, in a non-destructive *in-situ* fashion.

3. Postprocessing tool

A time series of radiographs sets is delivered by the experiments detailed above. The reconstructed volume of the central part of the sample for the initial state of load is shown in the Figure 6a. Those raw grayscale images, display 3 visible phases (see Figure 5b–d): the adhesive, the air pores and the glass beads introduced by the manufacturer.

The raw data is initially encoded in 16 bits. In order to reduce the volume of data and thus facilitate post-processing steps, the raw 16-bits data were converted to 8-bits grayscale levels. This step results in a lighter dataset and in faster processing steps without damaging excessively the quality of the data to observe. The data obtained with X-ray tomography were then post-processed in order to extract the following information: the spatial distribution and rate of each phase as well as their evolution during the different load applied. The complete study of the microstructure with respect to the applied load requires the development of a processing tool, which will: (i) eliminate unwanted artifacts from the



(a) Unprocessed volume slice close to the substrate adhesive

(b) Grayscale values along a path (white line in Fig.6a)

Figure 6. Slice of raw data.

reconstructed slices of adhesive and extract the mean intensity; (ii) filter the signal to remove the noise and (iii) detect the microstructural entities observed (here, pores and glass beads) from a grayscale intensity threshold.

This processing tool should allow to automatically detect the requested microstructural entities from the raw signal presented in Figure 6b.

3.1. *Creation of synthetic microtomographic data*

In order to design the processing tool, a preliminary study is performed using synthetic microtomographic data. The main advantage of this technique is that every property of the microstructure is accurately known, since it is imposed. The grayscale levels of the voxels for a 2D slice taken in this synthetic volume are given in Eq.2.

$$S_{z_j}(x,y) = I_{0,Z_j}(x,y) + \gamma_i \cdot p_i(x,y) + b_{z_j}(x,y) \tag{2}$$

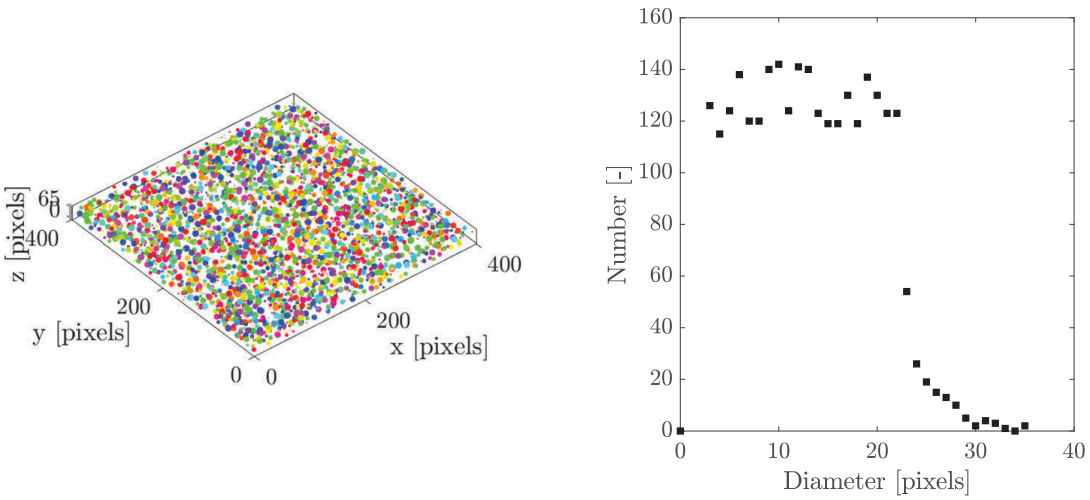
where $S_{z_j}(x,y)$ are the grayscale levels of the slice j in the Z direction with $j \in [1,65]$, $I_{0,Z_j}(x,y)$ is the mean grayscale level, γ_i is the contrast for each phase i, $p_i(x,y) = N_i$ with $N_i \in [0, 2^8 - 1]$ are 8-bits grayscale levels for each phase i, and $b_{z_j}(x,y)$ is a 8-bits grayscale level correspondong to Gaussian measurement noise.

The intensity of the measurement noise is assumed to be independant of the position. Therefore, the standard deviation of the Gaussian distribution used to generate the measurement noise is the same in the entire volume. The value of the standard deviation σ is experimentally obtained, by subtracting two microtomographic acquisitions of the same volume. The properties of the generated volume are displayed in Table 2.

The spatial distribution of the generated pores can be visualised in Figure 7a. Moreover, the distribution of their corresponding diameters is available in Figure 7b. One may notice that the diameters distribution is not perfectly uniform. This is due to the non-overlap condition for the pores used during the generation of the volume. Therefore, a few of the randomly generated diameters (mainly the largest ones) were programmatically modified or discarded in order to comply with this constraint.

Table 2. Synthetic data properties.

Property	Value
Size	960x960x65 voxels
Pores number $n_{p_{th}}$	3114 (non-overlapping)
Pores ratio p_{th}	9.69%
Pores diameters	Uniformly distributed between 1 and 35 voxels
Noise intensity	Standard deviation $\sigma = 9.62$



(a) Spatial distribution of pores

(b) Equivalent diameters distribution in the synthetic volume

Figure 7. Artificially generated volume for known pores amount, pore ratio and pores locations.



Figure 8. Processing tool architecture.

3.2. *Postprocessing tool architecture*

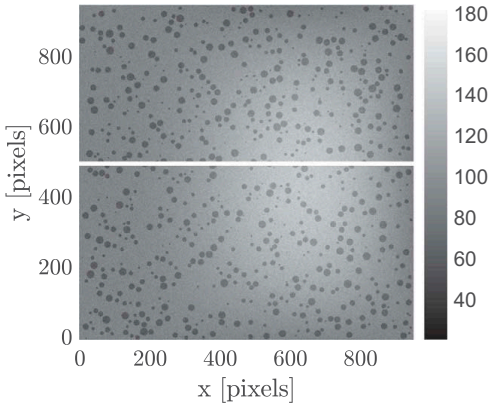
In order to characterise the pores located in a volume, it is necessary to segment the tomographic data. To do so, a processing tool is designed and programmed using $Matlab^{TM}$ software. The scheme of treatment of the raw data is shown in Figure 8.

3.2.1. *Preprocessing*

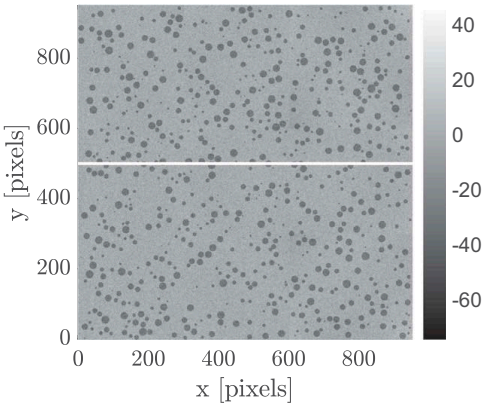
As it may be seen in Figure 5b–d, the radiograms include a large part of the substrates and some blank space around the samples. Hence, the reconstructed volume also contains these elements, resulting in some useless volume slices (with only Aluminium showing). The adhesive being absent from these pictures, they are removed from the dataset. By doing so, it is possible to reduce the number of slices to be analysed from several hundreds to 65.

3.2.2. *Subtraction of* I_0

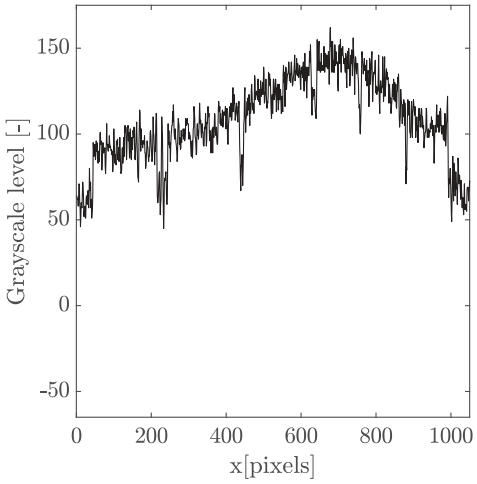
The mean grayscale intensity is assumed to follow a polynomial expression, as in Eq.3. The degree of this polynomial surface is left undetermined in Eq.3. In pratice, $m = 3$ was enough for the study presented in this paper. The value of m may be adjusted accordingly with the shape of I_0.



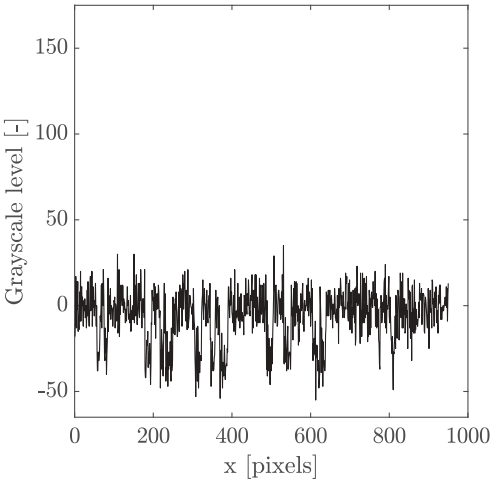
(a) Artificially generated adhesive slice before subtraction of I_0



(b) Artificially generated adhesive slice after subtraction of I_0



(c) Grayscale levels along $y = 500$ px for the raw signal (white line in Fig.9a)



(d) Grayscale levels along $y = 500$ px for the flattened signal (white line in Fig.9b)

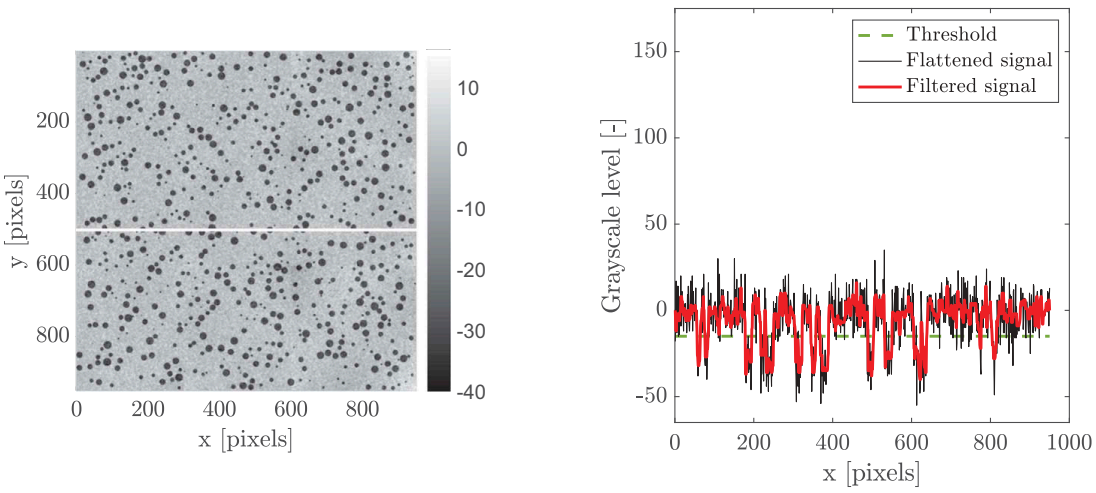
Figure 9. Subtraction of I_0.

$$I_0(x,y) = \sum_{j=0}^{m} \sum_{i=0}^{j} c_{i,j-i} x^i y^{j-i} \tag{3}$$

The coefficients $c_{i,j-i}$ in Eq.3 are identified using the grayscale levels of each reconstructed volume slice (Figure 9a). The obtained values of I_0 are then subtracted to the grayscale levels of the volume (Figure 9b), in order to obtain a flattened signal (Figure.9c and d).

3.2.3. *Filtering and thresholding*

The filtering and the thresholding steps are designed to smooth the signal (*i.e.* remove as much noise as possible from the flattened signal) and to identify precisely the transition between the adhesive and the pores in terms of



(a) Artificially generated slice after filtering

(b) Artificial grayscale levels along $y = 500$ px for the flattened signal

Figure 10. Filtering of the synthetic data.

grayscale levels (Figure 10). To correctly tune the corresponding parameters (t_f and n_s, see Figure 8), an optimisation loop is performed using $Matlab^{TM}$. The filter used in the process is a classical 2D median filter,[23] characterised by its size t_f. The main advantage of this formulation is that it is edge-preserving[24] (*i.e.* it will preserve the edges between the adhesive and the pores), which is paramount to accurately detect the pores included in the adhesive.

The threshold n_s is trivially defined as the minimal grayscale level shift to consider to detect a microstructural phase switchover. Those values are then adjusted in order to minimise an error function, characterising the performance of the tool. It is possible to consider two different shapes for this error function: Err_{M1} which takes into account only the difference between the pore ratios p_i (method M1, Eq.4) and Err_{M2} which takes into account the difference between the pore ratios p_i and the difference between the number of pores detected n_{p_i} (method M2, Eq.5).

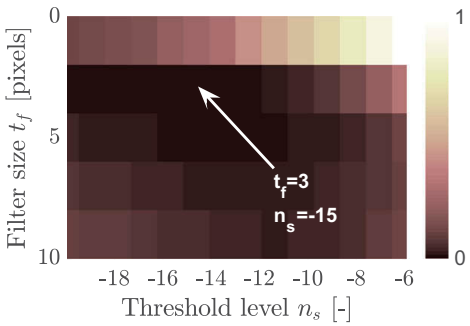
$$Err_{M1}(t_f, n_s) = \left[\frac{p_{th} - p_{obt}(t_f, n_s)}{p_{th}}\right]^2 \tag{4}$$

$$Err_{M2}(t_f, n_s) = \alpha_1 \left[\frac{p_{th} - p_{obt}(t_f, n_s)}{p_{th}}\right]^2 + \alpha_2 \left[\frac{n_{p_{th}} - n_{p_{opt}}(t_f, n_s)}{n_{p_{th}}}\right]^2 \tag{5}$$

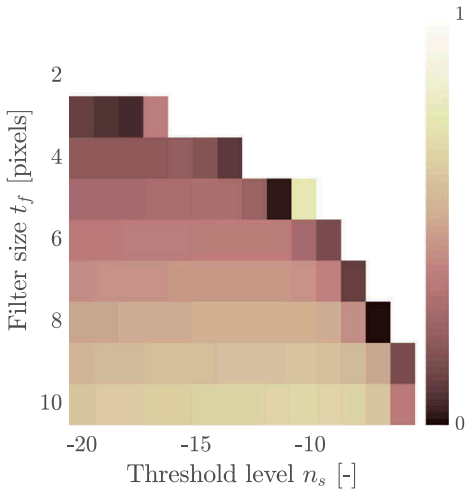
where p_{th} and p_{obt} are respectively the imposed pore ratio and the detected pore ratio for a given (t_f, n_s) couple, and $n_{p_{th}}$ and $n_{p_{obt}}$ are respectively the imposed pores number and the detected pores number for a given (t_f, n_s) couple.

The method M1 defines the error between the generated pores field and the detected pores field as a function of the pore ratios whereas the method M2 defines a more extensive error function as a function of both the pore ratios and the pores amounts (Eq.4 and 5). In the M2 formulation, a couple (α_1, α_2) is

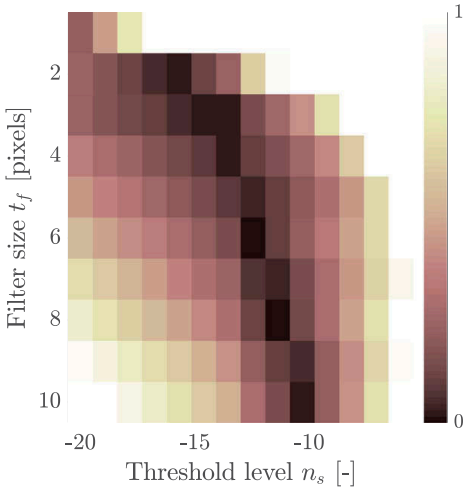
introduced so it is possible to assign different weights to each one of the two terms if need be. By default, these values are set to 0.5, so as to obtain an equivalent weight for each term in Eq.5. The optimisation loop is performed in a first stage for the M1 approach, and delivers a first set $(t_f, n_s)_{M1}$ identified as the parameters corresponding to the lowest error value ($t_{f_{M1}} = 3$ and $n_{s_{M1}} = -15$) easily pinpointed on the error map (Figure 11a). The loop is then repeated for the M2 approach, which delivers two error maps (Figure 11b and c) instead of one, as two terms are used to compute the error. By combining the minimum valleys obtained through the M2 method, it is possible to compute the global error for this approach (Figure 11d). Due to the removal of I_0 from the baseline signal (Figure 9c and Figure 9d), a negative value is obtained for n_s. It is therefore not a 8-bits grayscale level anymore, but a grayscale intensity.



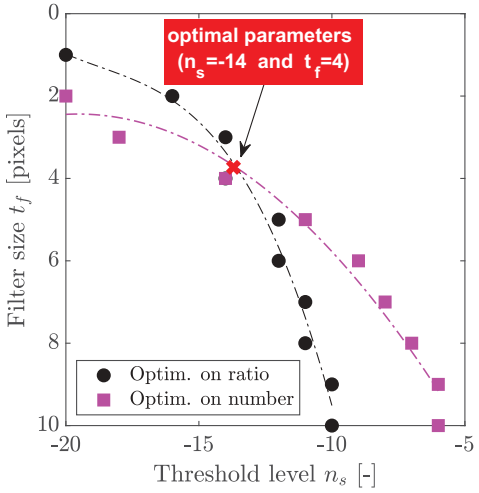
(a) Error map obtained for the M1 method as a function of t_f and n_s



(b) Error map relative to the number of pores for the M2 method as a function of t_f and n_s



(c) Error map relative to the pore ratio for the M2 method as a function of t_f and n_s

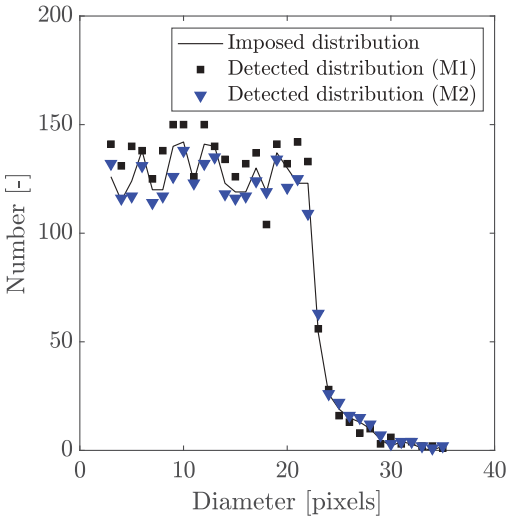


(d) Optimal parameters for the M2 method

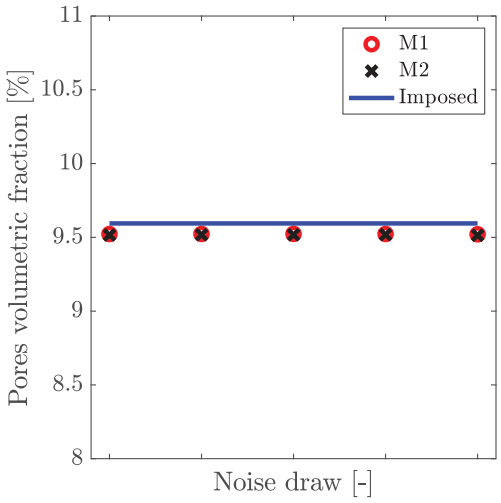
Figure 11. Identification of the $(n_s, t_f)_{M2}$ set.

From the intersection of these domains (Figure 11d), it is possible to extract a second parameters set $(t_f, n_s)_{M2}$, which outputs not only the correct pores volume fraction, but also the correct pores amount. From these observations, it can be concluded that the processing tool designed in this paper allows for a correct evaluation of the pore distribution in an adhesive layer, in terms of both spatial distribution and radius distribution.

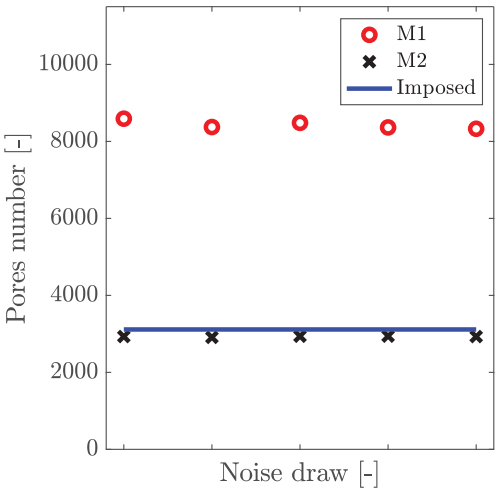
It is clear from Figure 12a that the M1 method is inefficient to accurately detect the correct number of pores, especially for the lowest diameters. This inefficiency tends to fade along with the increase of the equivalent diameters of the pores to be detected. The M2 method displays results of overall higher quality, and is less prone to be disturbed by very small pores. This method



(a) Comparison between methods M1 and M2 in terms of pore detection



(b) Effect of the noise on the pore ratio



(c) Effect of the noise on the number of pores

Figure 12. Comparison between the results delivered by the M1 and M2 approaches for 5 different noise draws.

allows the user to accurately detect the voids in the adhesive, with a fairly high accuracy in terms of both number and equivalent diameter.

The tool, successfully calibrated here, was used on a generic adhesive volume including a pores field whose diameters are randomly distributed in a given range representative of the actual configuration. To be perfectly in compliance with a real experimental case, these diameters should be normally distributed. However, this slight inadequacy is expected to be of negligible influence, as it seems from Figure 12a that the designed tool outputs the correct number of pores for nearly every equivalent diameter. The only difference between a normal and a random distribution being the number of entities for each equivalent diameter, one should expect that the processing tool would correctly estimate the voids field for a different distribution.

3.3. *Influence of measurement noise on pores detection*

Although it appears that the two approaches presented give similar results, they can be evaluated in a more extensive fashion by studying the influence of the picture noise level on the pore field detected. To perform this comparison, the two resulting tools are applied to five cases with five noise draws (Figure 12b and 12c).

From Figure 12b it is obvious that even though the two methods presented previously give similar results in terms of pores volume fractions (which is slightly underestimated due to the voxelisation of a continuous media), only the M2 approach is able to deliver a correct estimation of the pores amount (Figure 12c) in a given volume. It is then concluded that the M2 method should be used, for $t_f = 4$ and $n_s = -14$. The obtained results are summarised in Tables 3 and 4, where $\bar{i}$ and σ_i are respectively the mean value and the standard deviation of the quantity i

Table 3. M1 and M2 methods results compared to the theoretical pore ratio.

	p_{th} [%]	$\overline{p_{obt}}$ [%]	$\sigma_{p_{obt}}$ [%]
Theoretical	9.59	–	–
M1	–	9.522	$1.05.10^{-3}$
M2	–	9.516	$1.80.10^{-3}$

Table 4. M1 and M2 methods results compared to the theoretical number of pores.

	$n_{p_{th}}$ [-]	$\overline{n_{p_{obt}}}$ [-]	$\sigma_{n_{p_{obt}}}$ [-]
Theoretical	3114	–	–
M1	–	8427.2	107.7
M2	–	2930.1	12.7

Even though fairly similar results are obtained in terms of pore ratio p_{obt} with both methods (Table 3), it is clear from Table 4 that the M1 method is not able to accurately detect the correct number of pores in the artificial datasets. Quantitatively, the error on the dectected number of pores is above 170% using M1, whereas it is only of 6% using M2. This is explained by the fact that M1 tends to detect erroneous pores for small diameters (Figure 12a).

4. Results and discussion

Given the extensive use of X-ray tomography in materials science since the early 1990s, and due to the large amount of published works based on this method,[10] it is accepted that this experimental technique provides fairly good results. Consequently, the measurements performed using this technique are considered to be valid, and do not require any further characterisation.

4.1. *Evolution of the pores number and of the pore ratio with respect to the applied load*

From the observations made regarding the two methods presented above, it was chosen to use the M2 methodology, with an optimised $(t_f, n_s)_{M2}$ couple equal to $(4, -12)$.

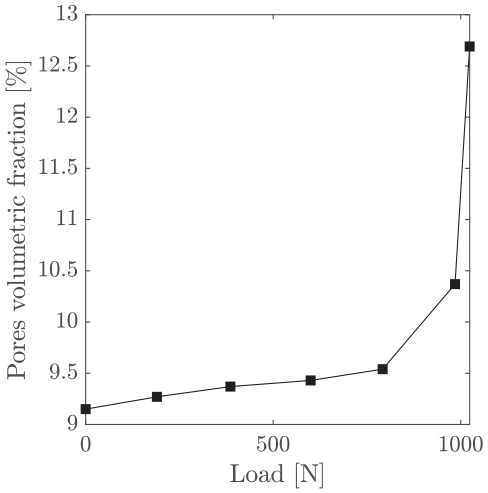
An immediate output of the processing tool presented in the previous section is the pores-to-adhesive volume ratio. It is then possible to track the evolution of this quantity along with the increase in the applied load (Figure 13a).

In addition, by means of the M2 method defined by the Eq.5, it is possible to obtain a fairly accurate estimation of the number of pores included in the adhesive layer, which may be plotted versus the increasing load as well (Figure 13b).

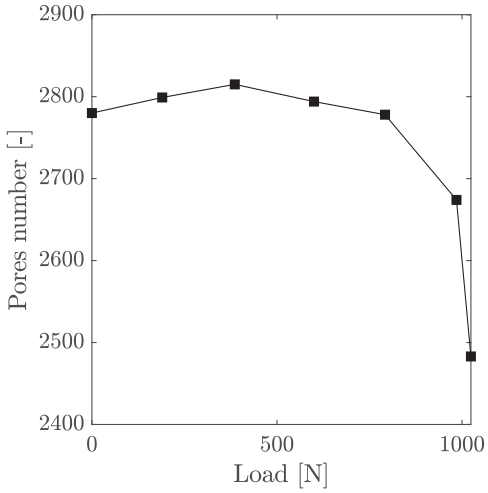
It appears from these data that the mechanical solicitation applied to the sample may lead to significant changes in the microstructural properties of the adhesive. Both these quantities seem to follow a trend defined by two distinct domains: $F \leq 800$ N, for which the evolution seems fairly linear with respect to the applied load; and $F \geq 800$ N, for which the evolution becomes non-linear as a function of the applied load, with a sudden increase in pore volume fraction, and with a sudden decrease in pores number.

It is possible to validate the results presented above by verifying that the developed method outputs the correct glass beads ratio, which is given by the manufacturer.

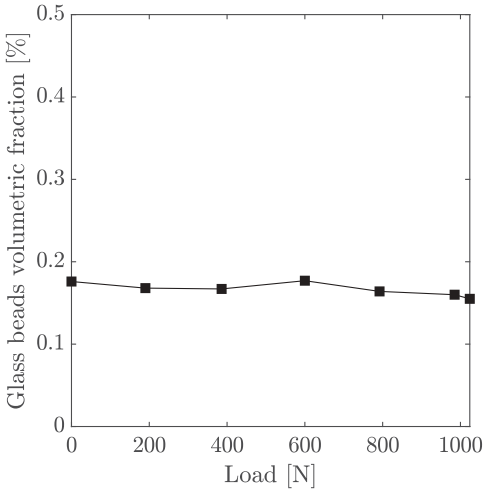
It appears from Figure 13c that this quantity remains almost constant, as it should be since there is obviously no external glass beads input. It is possible to compute the mean $\overline{p_{beads}}$ of these values, to be compared to the manufacturer data:



(a) Evolution of the pore volumetric fraction with respect to the applied load



(b) Evolution of the number of detected pores with respect to the applied load



(c) Glass beads ratio with respect to the applied load

Figure 13. Changes undergone by the internal microstructure of the adhesive joint along with the increasing load.

$$\overline{p_{beads}} = 0.167\%$$

These numerical values are fairly consistent with the numbers provided by the manufacturer regarding this adhesive, since the adhesive theoretically contains 0.16% of beads (in terms of volume).

Finally, the distribution of the diameters of the detected glass beads may be computed. This distribution is shown in Figure 14.

4.2. *Evolution of the diameters distribution with respect to the applied load*

Most of the pores are quasi-spherical, and thus may be characterised by their equivalent diameter. More specifically, it is possible to compute the

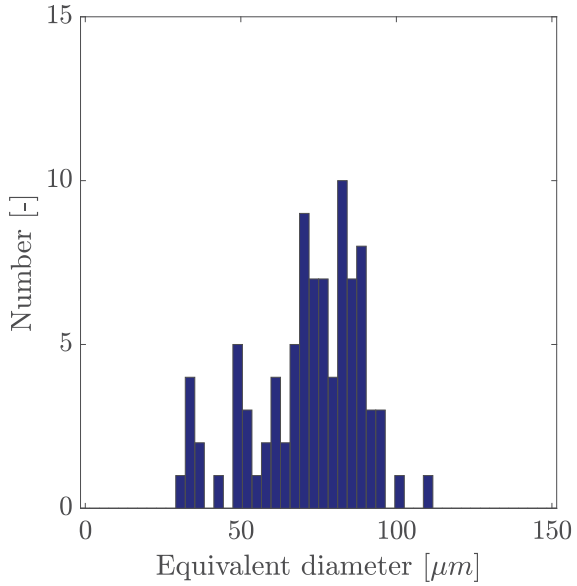


Figure 14. Distribution of the equivalent diameters of the glass beads.

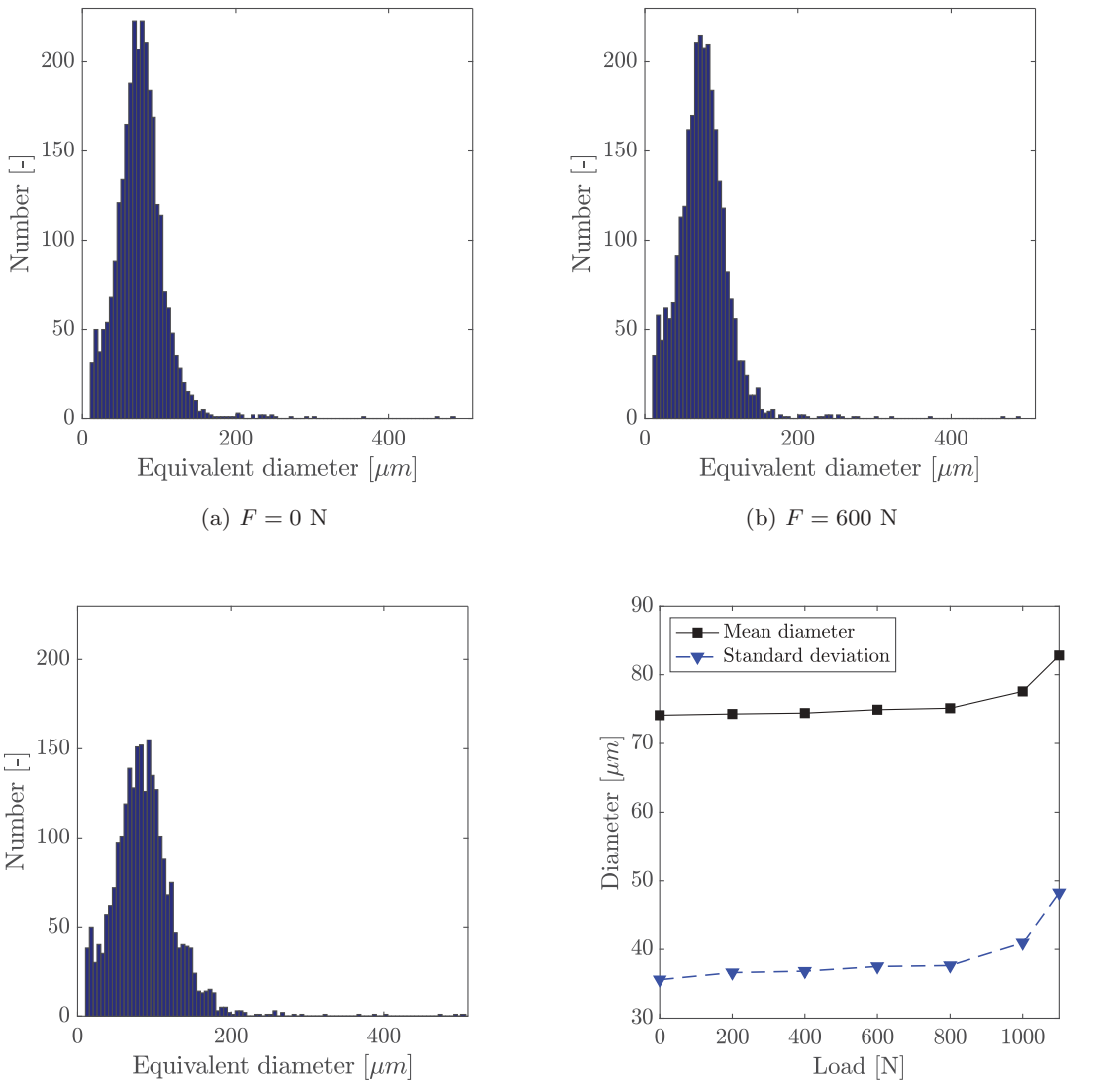
distribution of those equivalent diameters in the adhesive layer, and to track the evolution of this distribution along with the increase in the applied load.

It appears from Figure 15a–c that the equivalent diameters distribution variations are somehow negligible for a load below 800 N. Starting from this load state (Figure 15b–c), the evolution becomes much clearer, as the distribution, which roughly follows a Gaussian shape, tends to widen.

To better visualise this trend, it is possible, for each distribution displayed in Figure 15, to fit a Gaussian distribution function (Eq.6) to compute the mean equivalent diameter μ_d and the standard deviation σ_d.

$$f(x) = \frac{1}{\sigma_d\sqrt{2\pi}} \exp\left[-\left(\frac{x-\mu_d}{\sigma_d}\right)^2\right] \tag{6}$$

This approach results in the data presented in Figure 15d. A clearer trend can be seen in Figure 15d, which points out that even for the relatively low loads ($F < 800$ N), the microstructure of the adhesive undergoes slight, but nonetheless visible, transformations. Both the mean and the standard deviation of the distributions seem to follow the same trend. As it was expected from the data in Figure 13 and Figures 15a-c, from $F = 800$ N and higher, the distributions start to change significantly. The increase in size of the detected pores may be explained by two factors: (i) the increasing load tends to open and expand the pores (Figure 16d) and (ii) the increasing load may trigger coalescence phenomena, which cause neighboring pores to merge (Figure 16a–c). These hypotheses are directly linked with the observations formulated regarding Figure 13 and Figures 15a-c, as they seem to be the most plausible explanation for these phenomena.



(a) $F = 0$ N

(b) $F = 600$ N

(c) $F = 1100$ N

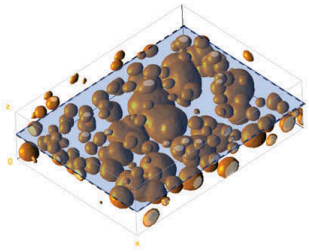
(d) Parameters of the Gaussian distribution of the pores diameters for every load investigated

Figure 15. Effect on an increasing mechanical load on the equivalent diameters distribution.

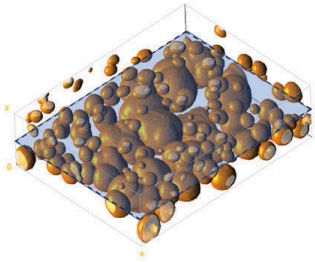
It is fairly easy to notice that some entities merged due to the application of the mechanical load, especially where the initial pores were already close to each other. This is perfectly supported by the diminishing number of pores detected by the processing tool, as it is shown in Figure 13b. Such merger phenomena were expected, as they have already been reported for other materials.[21,25]

The visualisation of these simultaneous phenomena may be performed on the reconstructed volume using *FiJi* software,[26] as presented in Figure 17.

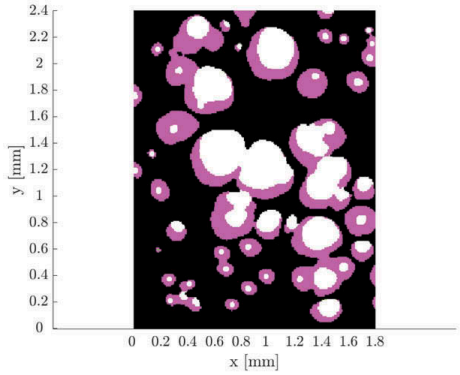
The global increase in volume of the pores in the adhesive is easy to visualise in Figure 17. This suggests that it is a phenomena which occur in the entierety of the joint, and not only in specific, predisposed locations. Moreover, it is possible to see in Figure 17 that there are a few locations where the pores seem to be more concentrated. The adhesive bond is therefore weaker in these spots, and one may hypothesise that such concentrations



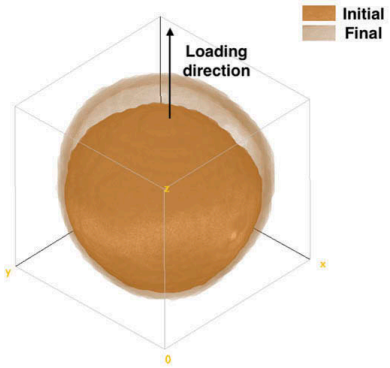
(a) Coalescence site, initial state (- - -: section plane)



(b) Coalescence site, final state (- - -: section plane)

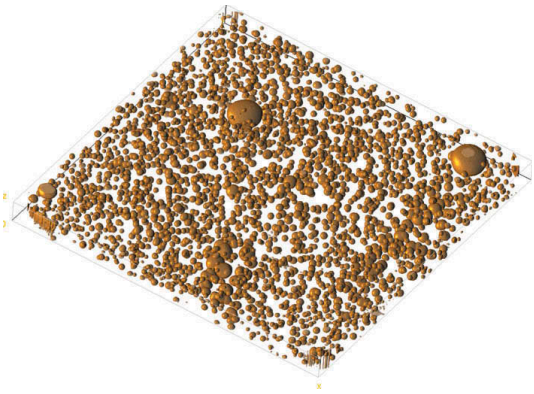


(c) Sliced view of coalescing pores (white: initial state / magenta: final state)

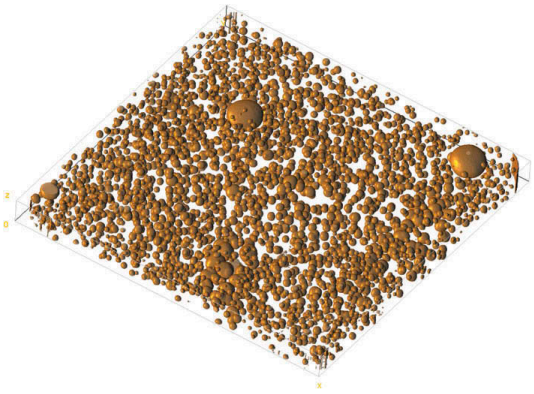


(d) Increase in volume ($F = 0$ N and $F = 1100$ N) for an arbitrarily chosen pore

Figure 16. Changes undergone by the pores along with the increasing load.



(a) Pores field - Initial state



(b) Pores field - Final state

Figure 17. 3D visualisation of the pores fields at initial and final states.

of pores could trigger mechanical failure mechanisms (microcracking, stress concentrations, localised plasticisation, *etc.*) when stressed, and lead to the premature ruin of the assembly. Finally, the pores in Figure 17 may be divided into two groups, depending on their size and incidence: (i) the most common pores are rather small (a few tens of micrometers in terms of equivalent diameter) and they are created during the mixing of the adhesive, (ii) and the less usual pores (in particular 2 specimens in Figure 17, easily identifiable), one order of magnitude bigger than the others

(a few hundreds of micrometers in terms equivalent diameter), which are created during the spreading of the adhesive with the spatula on the adherends. This last type of pores is the most critical threat to the mechanical strength of the joint, due to the size they feature. One might expect that if several of these large, but uncommon, pores are located within a certain sphere of influence of each other (still to be determined), this could lead to an important and localised decrease in mechanical properties of the joint and once again be the cause of the unexpected mechanical ruin of the assembly.

4.3. *Sphericity of the pores*

The pores detected by the tomography measurements display for the most part a sphere-like shape, therefore a description based on the sphericity seems to be the best approach to characterise the evolution of their general shape. The sphericity Ψ of an object is, as introduced by Wadell in 1935[27], defined by the expression in Eq.7:

$$\Psi = \frac{\pi^{\frac{1}{3}}\left(6V_p\right)^{\frac{2}{3}}}{A_p} \tag{7}$$

where V_p stands for the volume of the entity and A_p for its area.

It is obvious from Eq.7 that the sphericity varies theoretically between 0 (the studied entity being a plane) and 1 (the studied entity being a perfect sphere).

The volume and the areas of the pores being quantities easily accessible from the tomography data, the sphericity of each pore may be computed, for various load states. The resulting data are plotted in Figure 18.

The technique employed in this paper is then able to detect the variation of the shape of each pore, caused by the mechanical solicitation applied to the sample. It seems that the overall shape of the points clouds remains fairly the same, the most significant change in Figure 18 being the increase in equivalent diameters of the pores, which tends to shift these points clouds to the right. Most of the computed sphericities are located around 1, which corroborates the observation according to which most of the pores are quasi-spherical.

One can see in Figure 18 that some points are located above the theoretical limit of 1, especially for the lowest equivalent diameters. This may be due to the effect of the voxelisation during the measurements, as the voxel size is of 6 m. For very small objects, this may induce seemingly incorrect sphericity values, due to areas miscalculations.[28]

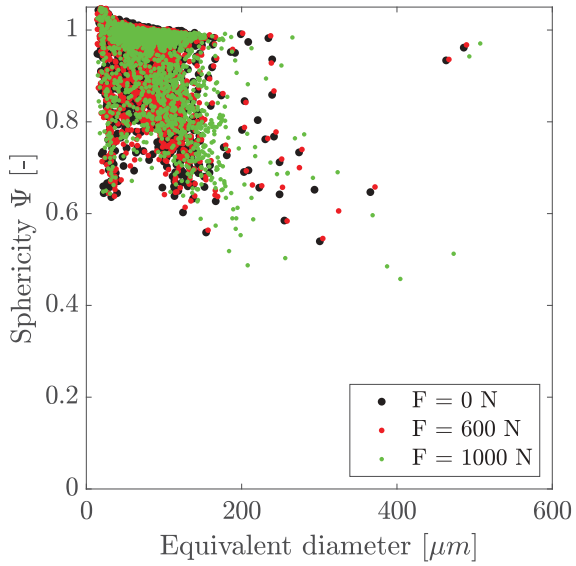


Figure 18. Sphericity of each detected pore, for different load levels.

5. Conclusion

Pores are commonplace defects in adhesive joints, formed during the mixing of the adhesive and during the bonding step. As such, adhesively bonded samples were made in order to investigate the pore state within the bulk of their joints. The influence of tensile loadings on this pore state was characterised using *in-situ* X-ray microtomography, until the mechanical failure of the samples.

In order to process the tomographic datasets, a processing tool was designed and calibrated on artificial datasets. This calibration was performed using optimisation algorithms to tune the parameters of this processing tool: the size of kernel of the median filter, and the grayscale threshold used to identify the pores in the reconstructed volumes. Two methods were proposed for this parameters optimisation, and their performances were discussed. It was found that the best approach was to optimise the parameters of the tool using both the pores number and the pore ratio.

Finally, it was experimentally proven that the application of a mechanical stress on the adhesive bonds has a significant influence on the pores located in the medium. Once a certain stress is reached, coalescence phenomena are triggered, resulting in an abrupt decrease in pores number. Moreover, due to the effect of the mechanical stress, the pores tend to expand, resulting in an increasing pore volumetric ratio. These changes in microstructure could be viewed as indicators that damage is occuring in the material. This is confirmed by the fact that the rate of growth significantly increase shortly before the fracture of the samples. Moreover, coalescence is occuring roughly for the

same stress levels, leading to the possible relationship between these observed phenomena and mechanical damage.

These results could give new ways of improvements for models developed to predict the damage and the failure of the adhesively bonded joints. Indeed, it seems that the damage is due to a cavitation proecess (increase in the size of existing pores or creation of new voids) and the failure is due to the coalescence of these pores/voids. Thus, the effects of the triaxiality should be included in the damage model instead of only the out-of-plane stresses as commonly considered.

ORCID

V. Dumont http://orcid.org/0000-0001-6214-3451

References

[1] Adams, R. D.;. *Adhesive Bonding Science, Technology and Applications*; Woodhead Publishing Ltd Elsevier, 2005.

[2] da Silva, L. F. M.;. *Modeling of Adhesively Bonded Joints*; Springer-Verlag Berlin Heidelberg, 2005.

[3] Mahnken, R.; Schlimmer, M. Simulation of Strength Difference in Elasto-plasticity for Adhesive Materials. *Int. J. Numer. Methods Eng.* 2005, *63*(10), 1461–1477. DOI: 10.1002/nme.1315.

[4] Cognard, J. Y.; Davies, P.; Sohier, L.; Créac'hcadec, R. A Study of the Non-linear Behaviour of Adhesively-bonded Composite Assemblies. *Compos. Struct.* 2006, *76*, 34–46. DOI: 10.1016/j.compstruct.2006.06.006.

[5] Cognard, J. Y.; Créac'hcadec, R.; Sohier, L.; Davies, P. Analysis of the Nonlinear Behavior of Adhesives in Bonded assemblies-Comparison of TAST and Arcan Tests. *Int. J. Adhes. Adhesives*. 2008, *28*, 393–404. DOI: 10.1016/j.ijadhadh.2008.04.006.

[6] Maurice, J. Characterization and Modelling of the 3D Elastic-plastic Behaviour of an Adhesively Bonded Joint under Monotonic tension/compression-shear Loads: Influence of Three Cure Cycles. *J. Adhes. Sci. Technol.* Jan, 2012, *27*, 1–17. DOI: 10.1080/01694243.2012.701528.

[7] Cognard, J. Y.; Créac'hcadec, R.; Maurice, J. Numerical Analysis of the Stress Distribution in Single-lap Shear Tests under Elastic assumptionApplication to the Optimisation of the Mechanical Behaviour. *Int. J. Adhes. Adhesives*. 2011, *31*(7), 715–724. DOI: 10.1016/j.ijadhadh.2011.07.001.

[8] Carrere, N.; Badulescu, C.; Cognard, J.-Y.; Leguillon, D. 3D Models of Specimens with a Scarf Joint to Test the Adhesive and Cohesive Multi-axial Behavior of Adhesives. *Int. J. Adhes. Adhesives*. 2015, *62*, 154–164. DOI: 10.1016/j.ijadhadh.2015.07.005.

[9] Badulescu, C.; Cognard, J. Y.; Créac'hcadec, R.; Vedrine, P. Analysis of the Low Temperature-dependent Behaviour of a Ductile Adhesive under Monotonic tensile/compressionshear Loads. *Int. J. Adhes. Adhesives*. 2012, *36*, 56–64. DOI: 10.1016/j.ijadhadh.2012.03.009.

[10] Buffiere, J. Y.; Maire, E.; Adrien, J.; Masse, J. P.; Boller, E. In Situ Experiments with X Ray Tomography: An Attractive Tool for Experimental Mechanics. *Exp. Mech.* Mar, 2010, *50*, 289–305. DOI: 10.1007/s11340-010-9333-7.

[11] Toda, H.; Maire, E.; Yamauchi, S.; Tsuruta, H.; Hiramatsu, T.; Kobayashi, M. In Situ Observation of Ductile Fracture Using X-ray Tomography Technique. *Acta Mater.* 2011, *59*(5), 1995–2008. DOI: 10.1016/j.actamat.2010.11.065.
[12] Bouterf, A. Identification of the Crushing Behavior of Brittle Foam: From Indentation to Oedometric Tests. *J. Mech. Phys. Solids*. 2017. DOI: 10.1016/j.jmps.2016.09.011.
[13] Roux, S.; Hild, F.; Viot, P.; Bernard, D. Three-dimensional Image Correlation from X-ray Computed Tomography of Solid Foam. *Compos. A*. 2008, *39*, 1253–1265. DOI: 10.1016/j.compositesa.2007.11.011.
[14] Morgeneyer, T. F.; Starink, M. J.; Sinclair, I. Evolution of Voids during Ductile Crack Propagation in an Aluminium Alloy Sheet Toughness Test Studied by Synchrotron Radiation Computed Tomography. *Acta Mater.* 2008, *56*(8), 1671–1679. DOI: 10.1016/j.actamat.2007.12.019.
[15] Bastani, A.; Adamopoulos, S.; Koddenberg, T.; Militz, H. Study of Adhesive Bondlines in Modified Wood with Fluorescence Microscopy and X-ray Micro-computed Tomography. *Int. J. Adhes. Adhesives*. 2016, *68*, 351–358. DOI: 10.1016/j.ijadhadh.2016.04.006.
[16] Evans, P. D.; Morrison, O.; Senden, T. J.; Vollmer, S.; Roberts, R. J.; Limaye, A.; Arns, C. H.; Averdunk, H.; Lowe, A.; Knackstedt, M. A. Visualization and Numerical Analysis of Adhesive Distribution in Particleboard Using X-ray Micro-computed Tomography. *Int. J. Adhes. Adhesives*. 2010, *30*(8), 754–762. DOI: 10.1016/j.ijadhadh.2010.08.001.
[17] Paris, J. L.; Kamke, F. A. Quantitative Woodadhesive Penetration with X-ray Computed Tomography. *Int. J. Adhes. Adhesives*. 2015, *61*, 71–80. DOI: 10.1016/j.ijadhadh.2015.05.006.
[18] Pollak, B.;. Experiences with Planography. *Chest*. 1953, *24*(6), 663–669. DOI: 10.1378/chest.24.6.663.
[19] Avinash, C. K.; Slaney, M. *Principles of Computerized Tomographic Imaging*; Society for Industrial and Applied Mathematics: Philadelphia, 2001.
[20] Feldkamp, L. A.; Davis, L. C.; Kress, J. W. Practical Cone-beam Algorithm. *Tech. Rep.* 1984, *6*.
[21] Pinzer, B. R.; Medebach, A.; Limbach, H. J.; Dubois, C.; Stampanoni, M.; Schneebeli, M. 3d-characterization of Three-phase Systems Using X-ray Tomography: Tracking the Microstructural Evolution in Ice Cream. *Soft Matter*. 2012, *8*(17), 4584. DOI: 10.1039/c2sm00034b.
[22] Ilioni, A.; Badulescu, C.; Carrere, N.; Davies, P.; Thévenet, D. A Viscoelastic-viscoplastic Model to Describe Creep and Strain Rate Effects on the Mechanical Behaviour of Adhesively-bonded Assemblies. *Int. J. Adhes. Adhesives*. 2018, *82*, 184–195. DOI: 10.1016/j.ijadhadh.2017.12.003.
[23] Lim, J. S. Two-dimensional Signal and Image Processing. In *Prentice Hall*. 469–476, 1990.
[24] Gallagher, N. C.; Wise, G. L. A Theoretical Analysis of the Properties of Median Filters. *IEEE Trans. Acoust. Speech Signal Process.* 1981, *29*(6), 1136–1141. DOI: 10.1109/TASSP.1981.1163708.
[25] Klocker, H.; Tvergaard, V. Void Growth and Coalescence in Metals Deformed at Elevated Temperature. *Int. J. Fract.* 2000, *106*(3), 259–276. DOI: 10.1023/A:1026509829181.
[26] Schindelin, J.; Arganda-Carreras, I.; Frise, E.; Kaynig, V.; Longair, M.; Pietzsch, T.; Preibisch, S.; Rueden, C.; Saalfeld, S.; Schmid, B. Fiji: An Open-source Platform for Biological-image Analysis. *Nat. Methods*. June 2012, *9*, 676 EP. DOI: 10.1038/nmeth.2019.
[27] Wadell, H.;. Volume, Shape, and Roundness of Quartz Particles. *J. Geol.* 1935, *43*(3), 250–280. DOI: 10.1086/624298.
[28] Lehmann, G.; Legland, D.; Génie, U. M. R. Efficient N-Dimensional Surface Estimation Using Crofton Formula and Run-length Encoding. *Insight J.* 2012, *2*, 1–11.

2.3 Contraintes résiduelles et contraintes thermiques

Une pratique courante sur les adhésifs époxy bi-composants consiste à appliquer un cycle thermique au matériau non polymérisé afin d'activer la réaction de polymérisation. Les cycles que l'on peut appliquer sont divers et variés, comme en témoignent les fiches techniques fournies par les fabricants de ces adhésifs. En particulier, les niveaux de température atteints au cours de ces cycles [85], [86] sont nombreux et peuvent avoir une importance significative sur la résistance mécanique globale des joints collés.

Les contraintes résiduelles peuvent avoir un effet négatif sur les propriétés de rupture d'un adhésif et par conséquent sur la durée de vie en fatigue des assemblages collés. L'intensité des contraintes résiduelles dépend principalement de quatre facteurs [12] :

- le changement de volume dû à la réaction de durcissement ;
- les propriétés mécaniques de l'adhésif et des adhérents ;
- les coefficients de dilatation thermique des matériaux impliqués ;
- la géométrie de la liaison et de l'assemblage.

Tout naturellement, en raison du décalage très important entre les propriétés thermo-mécaniques des adhérents métalliques et celles de la plupart des adhésifs, des contraintes résiduelles sont susceptibles d'apparaître lorsque les joints passent de la température de durcissement à la température ambiante. De même, un champ de contraintes supplémentaire peut être introduit par la variation de température de l'environnement. Ces contraintes résiduelles thermiques contribuent donc au champ de contraintes à l'intérieur du joint de colle, durant la sollicitation mécanique et peuvent entraîner des défaillances prématurées de l'assemblage [87], [88]. En outre, ces contraintes pourraient également avoir une incidence sur l'identification des paramètres d'une loi de comportement donnée, et principalement pour deux raisons. Premièrement, certaines hypothèses exprimées à des fins pratiques et de simplification et, bien que valables pour un état de contrainte initial nul, peuvent être remises en question si l'on tient compte des contraintes résiduelles et thermiques initiales. Dans le cas des travaux que j'ai supervisés, la pression hydrostatique a été supposée marginale pour les charges de cisaillement. Cette hypothèse s'est avérée particulièrement utile au cours du processus d'identification des paramètres, puisque tous les paramètres relatifs à la pression hydrostatique ont été considérés comme négligeables pendant les charges de cisaillement. Le champ de contraintes réelles $\sigma_m(x,y,z)$ dû à la charge mécanique appliquée n'est donc pas égal au champ de contraintes totales dans le joint $\sigma(x,y,z)$. On peut donc écrire la relation suivante :

$$\sigma(x,y,z) = \sigma_m(x,y,z) + \sigma_r(x,y,z) + \sigma_{th}(x,y,z)$$

avec $\sigma_r(x,y,z)$ le champ de contraintes résiduelles dues aux phénomènes liés au durcissement de l'adhésif et $\sigma_{th}(x,y,z)$ le champ de contraintes induites par le changement de température après la fin du durcissement. Il est donc légitime d'étudier l'influence

des termes $\sigma_r(x,y,z)$ et $\sigma_{th}(x,y,z)$ sur le comportement mécanique de l'assemblage collé. Cette étude nécessite deux étapes :

1. identifier les champs de contraintes induites ;
2. inclure ces champs de contraintes dans l'analyse par éléments finis réalisée lors de l'identification des paramètres du matériau, afin d'accéder à leurs valeurs réelles, correspondantes uniquement au comportement mécanique (c'est-à-dire à $\sigma_m(x,y,z)$).

Une pratique courante pour étudier les contraintes résiduelles dans les assemblages collés consiste à utiliser des méthodes de courbure de poutre bilame ou trilame [89], [90], [91]. Ces méthodes permettent de visualiser les déformations induites par les contraintes résiduelles créées pendant le durcissement de l'adhésif. Alors il est légitime de se pencher sur le développement des stratégies de détermination numérique des champs de contraintes thermiques dans les assemblages collés.

L'estimation des contraintes résiduelles créées pendant le cycle de durcissement nécessite une méthodologie numérique, basée sur une analyse par éléments finis. L'objectif est d'identifier la température libre de contraintes, c'est-à-dire la température qui, une fois appliquée à un modèle de type éléments finis de l'échantillon, conduit à la même courbure que celle obtenue expérimentalement.Alors, la notion de température libre de contraintes [92], [93] peut être considérée comme représentative du champ de contraintes résiduelles créé par le cycle de durcissement et ses mécanismes associés.

Publications jointes

- C. Badulescu, J.Y. Cognard, R. Créac'hcadec, P. Vedrine, **Analysis of the low temperature-dependent behaviour of a ductile adhesive under monotonic tensile/compression–shear loads**, *International Journal of Adhesion and Adhesives*, 36, 56-64,(2012), DOI : https ://doi.org/10.1016/j.ijadhadh.2012.03.009.
- J. Y. Cognard, C. Badulescu, J. Maurice, R. Créac'hcadec, N. Carrère, P. Vedrine, **On modelling the behaviour of a ductile adhesive under low temperatures**, *International Journal of Adhesion and Adhesives*, 47, 46-56,(2013), DOI : https ://doi.org/10.1016/j.ijadhadh.

Références associées : Bibliographie des publications

International Journal of Adhesion & Adhesives 36 (2012) 56–64

Contents lists available at SciVerse ScienceDirect

International Journal of Adhesion & Adhesives

journal homepage: www.elsevier.com/locate/ijadhadh

Analysis of the low temperature-dependent behaviour of a ductile adhesive under monotonic tensile/compression–shear loads

C. Badulescu [a], J.Y. Cognard [a,*], R. Créac'hcadec [a], P. Vedrine [b]

[a] Laboratoire Brestois de Mécanique et des Systèmes, ENSTA Bretagne/Université de Brest/ENIB/UEB, ENSTA Bretagne, 2 rue F. Verny, 29806 Brest Cedex 9, France
[b] CEA Saclay, DSM/Irfu/SACM, 91191 Gif sur Yvette, France

ARTICLE INFO

Article history:
Accepted 10 March 2012
Available online 5 April 2012

Keywords:
Thermal analysis
Finite element stress analysis
Mechanical properties of adhesive
Joint design

ABSTRACT

Various models exist to describe the non-linear behaviour of an adhesive in an assembly, taking into account the two stress invariants, hydrostatic stress and von Mises equivalent stress, which can be explained by the nature of the adhesive, i.e., a polymer. The identification of the material parameters of such pressure-dependent constitutive models requires a large experimental database taking into account various tensile–shear loadings. Under quasi-static loadings at low temperature, for a given strain rate range, viscous effects can be neglected, but only a few experimental results are available to model the behaviour of an adhesive in a bonded assembly accurately under realistic loadings. Moreover, edge effects often have a large influence on the mechanical response. This paper presents the possibility of combining the use of a modified Arcan device, which strongly limits the influence of the stress concentrations, with a usual thermal chamber. Experimental results, underlining the temperature-dependent non-linear responses of an adhesive, are presented in the case of various tensile/compression–shear monotonic loadings for a temperature range between 20 °C and −60 °C. The analysis of experimental results, obtained in the load-displacement diagram, focuses herein on the modelling of the initial temperature-dependent yield surface; but such results are also useful for the development of the flow rules in the case of pressure-dependent models.

© 2012 Elsevier Ltd. All rights reserved.

1. Introduction

Bonded assemblies are increasingly used in the design of mechanical structures due to major advantages of this technique, i.e., the weight reduction and the facility to join different materials and especially composites [1–3]. However, bonded assemblies are often characterised by large stress concentrations at the ends of the overlap length which are mainly associated with a high ratio of the mechanical properties between the adhesive and the adherends (mainly the Young's modulus), the low thickness of the adhesive in the assembly and the mechanical load [4,5]. Moreover, the use of bonded assemblies at different temperatures [6] can lead to an increase in the stress concentration associated with the thermal stresses [7,8]. Thus, specific studies are required as the mechanical behaviour of the adhesive and the stress concentrations in bonded assemblies can depend on the service temperature. For instance, the development of huge superconducting magnets requires a cooling system using a 4 K pressurised bath of Helium [9]. For such systems, the use of adhesively bonded assemblies is of great interest, especially to ensure the electrical insulation by using composites. Therefore, a precise analysis of the mechanical behaviour of the adhesive for very low or cryogenic temperatures is necessary, to allow an optimisation of the design of such superconducting magnets. Few experimental studies have been developed at low temperatures and therefore at cryogenic temperatures: bulk, lap-shear and pull-off tests under various temperatures are usually proposed [10,11]. Such experiments give information about the mechanical behaviour of the adhesive but the influence of defects and the influence of stress concentrations are often difficult to take into account. Moreover, in order to model the complex behaviour of adhesives in assemblies, non-associated pressure-dependent constitutive models have to be used [12–14], The identification of the material parameters of such models requires a large data base of experimental results under various compression/tensile–shear tests and a precise analysis of the non-linear behaviour of the adhesive; for instance, for such models, the initial yield surface is represented using the two stress invariants, hydrostatic stress and von Mises equivalent stress. Usual tests such as lap-shear and pull-off tests are often associated with stress concentrations. Some improvements can be proposed in order to increase the accuracy of the analysis of the mechanical behaviour without taking into account crack propagations (which is, itself, a complex problem). For instance, in the case of cryogenic analysis (at 4 K)

* Corresponding author. Tel.: +33 2 98 34 88 16; fax: +33 2 98 34 87 30.
E-mail address: jean-yves.cognard@ensta-bretagne.fr (J.Y. Cognard).

0143-7496/$ - see front matter © 2012 Elsevier Ltd. All rights reserved.
http://dx.doi.org/10.1016/j.ijadhadh.2012.03.009

[15], TAST type specimens (standard thick adherend shear test), using grooves, have been proposed; such geometries allow, at room temperature, a reduction in the stress concentrations [16,17]. In order to determine, at low temperatures, the behaviour of adhesives in an assembly under various tensile–shear loads, it is interesting to analyse the possibilities of the modified Arcan device developed to strongly limit the stress concentrations and used mainly at present time at room temperature [18]. The long term objective is to define a reliable strategy for analysing the mechanical behaviour of adhesive bonded joints at very low temperatures (cryogenic ones).

The objective of the paper is to characterize the temperature-dependent behaviour of a ductile adhesive under monotonic tensile/compression–shear loads at low temperature. The first part presents, starting from 2D numerical simulations, the influence of the service temperature on the stress concentrations in order to define the requirements of the bonded specimens analysed using the modified Arcan device. Second, experimental results are presented for a temperature range between 20 °C and −60 °C which is available using a usual thermal chamber. The last part analyses the influence of temperature on the so-called "initial elastic limit", and on the failure limit in stress and deformation at failure.

2. Experimental details

2.1. Modified Arcan device

A modified Arcan fixture, which enables compression or tension to be combined with shear load was previously developed. By the use of beaks, careful cleaning of the free edges of the adhesive, and by designing a special fixing system for the bonded specimen, the influence of edge effects can be significantly reduced, and pre-loading of the adhesive is avoided [5,18]. For a previous project associated with the analysis of the influence of the hydrostatic pressure on the mechanical behaviour of an adhesive, using a pressure vessel, a small Arcan fixture with an external diameter of 155 mm was developed [14]. Special fixing systems were used to fix the modified Arcan device in order to prevent parasitic loadings (Fig. 1). An advantage of this device, with respect to the old one, is the lower requested time in order to reach the prescribed temperature, as tests were realised with respect to temperatures between 20 °C (room temperature) and −60 °C.

2.2. Bonded assemblies

To ensure a precise adhesive thickness and a good relative positioning of the two substrates during the bonding process, spacers are manufactured during the machining process of the substrates (Fig. 2(a)). It can be noted in Fig. 2(b) that beaks are machined all around the substrates close to the bonded area and a cleaning of the free edges of the adhesive is performed before the curing process in order to limit stress concentrations [5,18]. Screws are used to ensure the relative positioning of the two substrates during the bonding process; moreover, a torque of 2.5 mN is applied with a screwdriver to limit the scatter in the adhesive thickness. After the curing process, the spacers are cut to obtain the bonded specimen to be used with the modified Arcan device. For such specimens, the area of the bonded section is 50 mm × 9 mm.

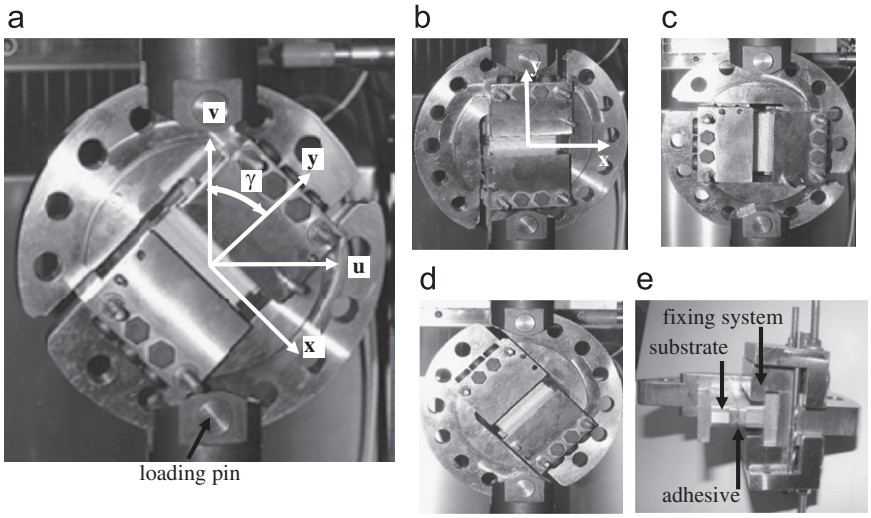


Fig. 1. Modified Arcan device. (a) **t**est under tensile–shear loading $\gamma=45°$, (b) tensile loading $\gamma=0°$, (c) shear loading $\gamma=90°$, (d) compression–shear loading $\gamma=90°$ and (e) fixing system.

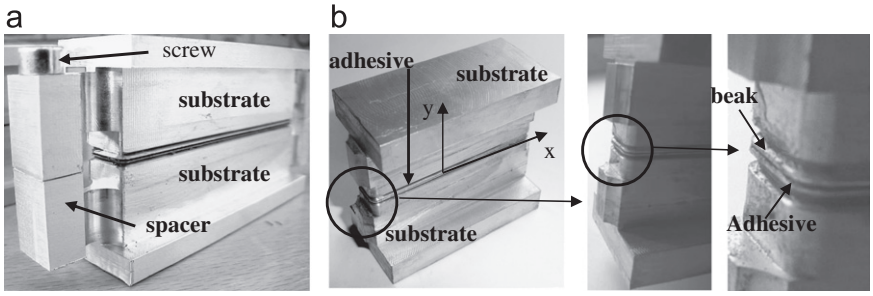


Fig. 2. Presentation of the bonded specimens. (a) bonding procedure, (b) geometry of the bonded specimens.

The different results presented in the following were obtained using the epoxy resin Huntsman™ Araldite® 420A/B with a joint thickness of 0.2 mm. The bonding procedure adopted starts with an immersion of the machined substrates in acetone for three hours to eliminate any presence of cooling oil used in the machining process, which will undoubtedly affect the bonding. After that, surfaces are prepared with sandpaper (grade of 180) to remove any impurities and oxide layer that can potentially exist; moreover, the associated roughness increases the adhesion. A degreasing and cleaning of the surface is accomplished to remove any particles that may remain after sanding. The curing process used is: 1 h at 110 °C.

2.3. Experimental environment

Tests were performed using a hydraulic tensile testing machine (Instron), with a maximum load of 100 kN and a thermal chamber (Servatin) available in the laboratory (Fig. 3). The thermal chamber has a view-glass which allows us to use an optical 3D measuring system by digital image correlation [19] in order to measure the relative displacement of the two substrates, and thus the deformation of the adhesive, in the *x* and *y* directions (Figs. 1 and 2). In the following, *DN* and *DT* denote the relative displacements of both ends of the adhesive in the normal (direction *y*, Fig. 1) and tangential directions (direction *x*, Fig. 1). It is important to notice that the displacement measurement through the view-glass of the thermal chamber requires specific adjustments in order to obtain images with a good quality. *FN* and *FT* represent the normal and tangential components of the applied load in the normal and tangential directions.

It should be noted that, the time required to stabilise the temperature of the sample, is more than 2 h for a temperature of −60 °C. This time has been determined using a specific bonded specimen with a thermocouple in the middle of the adhesive. Moreover, during the cooling phase a constant load of 0.6 kN is prescribed (a chosen preload) to prevent a possible increase in the stress in the adhesive and little movements of the modified Arcan system in relation to the tensile testing machine.

3. Influence of thermo-mechanical loads on the stress state in the adhesive

This section presents the influence of service temperature on the stress state in the adhesive in a bonded assembly in order to validate the proposed experimental approach.

3.1. Simplified mechanical model

Starting from 2D finite element simulations (Abaqus software [20]) under elastic assumption of the components, the influence of the local geometry close to the free edges of the adhesive is analysed with respect to the mechanical load and to the thermal

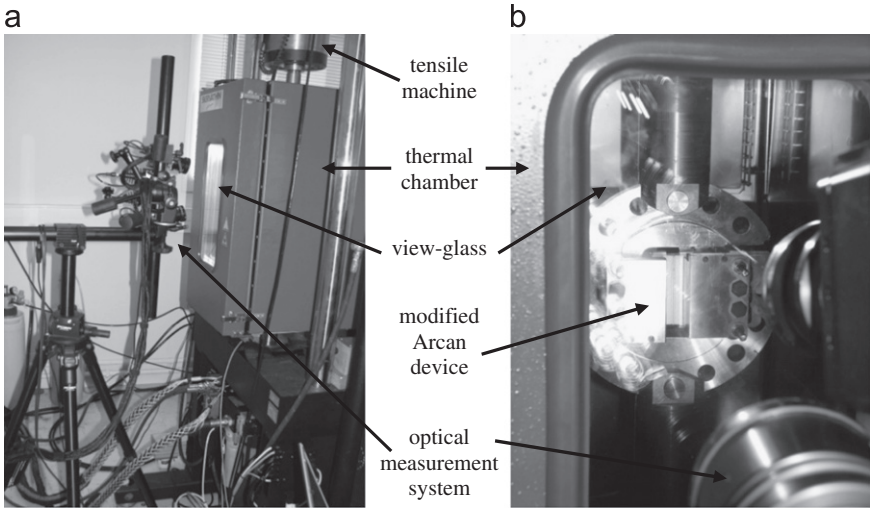


Fig. 3. Presentation of the experimental configuration (tensile testing machine, thermal chamber, modified Arcan device and optical measurement system). (a) global view (b) Arcan device in the thermal chamber.

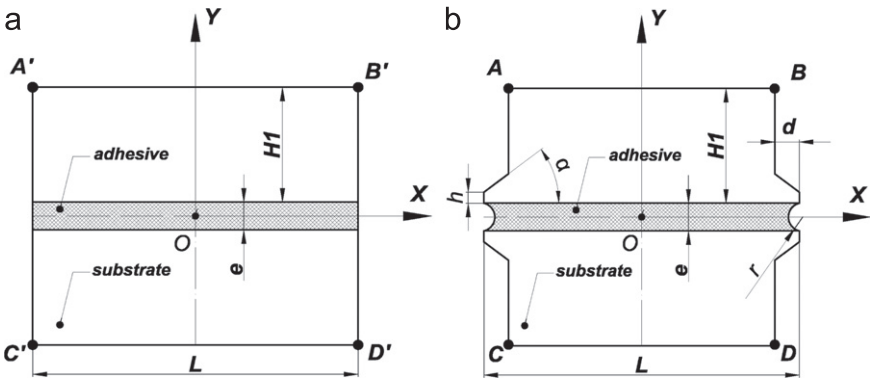


Fig. 4. Presentation of two geometries of the bonded assemblies (not to scale). (a) geometry *A*: specimen with straight edges (b) geometry *B*: specimen with beaks and cleaned edges.

stress state associated with a change in service temperature. For this analysis, one assumes that no residual stress exists at room temperature. Following previous works [5], results are presented for two geometries of the bonded specimens used with the modified Arcan device (Fig. 4). The first geometry is associated with straight substrates and straight edges of the free edges of the adhesive (Fig. 4(a)). The second geometry (Fig. 4(b)) represents the bonded specimens proposed for the experimental tests; they are characterised by the use of beaks on the substrates and a cleaning of the free edges of the adhesive in order to obtain a significant reduction in the stress concentrations in the adhesive under mechanical loads [5]. Geometries are defined with the following parameters: $L=50$ mm, $H1=20$ mm, $\alpha=30^{\circ}$, $h=0.1$ mm, $d=0.5$ mm, $r=0.1$ mm and $e=0.2$ mm.

The elastic properties of both materials are: $Ea=2$ GPa (Young's modulus), $va=0.3$ (Poisson's ratio) for the adhesive and $Es=75$ GPa, $vs=0.3$ for the substrates. The coefficient of thermal expansion used in this study is equal to $2.3\times10^{-5}\,^{\circ}C^{-1}$ for the substrate and $4.6\times10^{-5}\,^{\circ}C^{-1}$ for the adhesive (value obtained experimentally by analysing the deformation of a bulk specimen with respect to temperature). Computations were made under plane strain assumption using eight node rectangular elements. Refined meshes are used in order to obtain good numerical results, especially in the case of high stress concentrations which are required [5] (40 elements were used in the adhesive thickness of 0.2 mm). It can be noted that it is possible to analyse only half of the model using adequate boundary conditions.

3.2. Stress under thermo-mechanical loads

In order to analyse the stress concentrations, the evolution of the equivalent von Mises equivalent stress is plotted over half of the bonded overlap length ([Ox], Fig. 4). Under mechanical loads, the maximum value of the stress in the adhesive is obtained close to the substrate–adhesive interface for geometry A, and within the adhesive for geometry B [5]. Thus, in order to simplify the

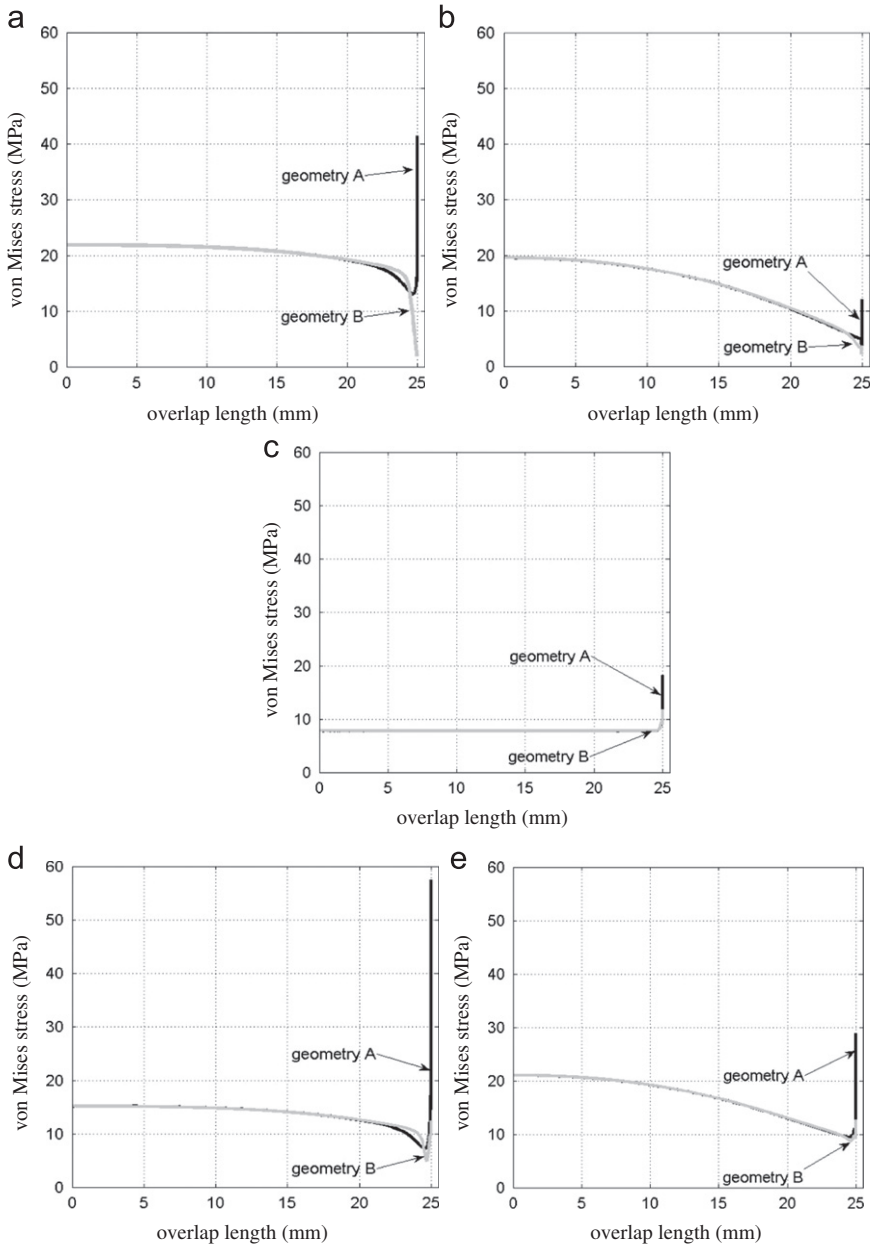


Fig. 5. Influence of the geometry of the substrates on the mechanical, thermal and thermo-mechanical stress distributions in the adhesive under tensile and shear loadings. (a) tensile loading, $d=0.02$ mm, (b) shear loading, $d=0.02$ mm, (c) thermal loading $\Delta T=-80\,^{\circ}C$, (d) tensile and thermal loadings and (e) shear and thermal loadings.

presentation, we have chosen to plot the maximum value of the von Mises equivalent stress through the adhesive thickness for a given point of the overlap length, with respect to the overlap length *x*.

For the mechanical load, displacements (in the *x* and *y* direction) are prescribed on the upper and lower lines of the model presented in Fig. 4. These boundary conditions can be justified by the fact that the Arcan support is nearly rigid with respect to the adhesive rigidity. Fig. 5(a) and (b) present the evolution of the maximum value of the equivalent von Mises stress with respect to the overlap for geometries *A* and *B*. *A* prescribed displacement of 0.02 mm is prescribed in the direction *y* and *x*, respectively in order to analyse results under tensile and shear loads. It can be noted that the stress states are different for the two loading conditions and that geometry *B* allows a large reduction in the stress concentrations close to the free edges of the adhesive [5].

For the thermal load, one assumes that only a variation in temperature is prescribed without mechanical constrains (the fixing system of the bonded specimen on the Arcan support has nearly no influence on the stress state under such loading). As the aim of this study is to analyse the influence of low temperature on the mechanical behaviour of an adhesive, a variation of $\Delta T = -80\ ^\circ C$ (test at $-60\ ^\circ C$) is prescribed (analysis between room temperature (20 °C) and $-60\ ^\circ C$). Fig. 5(c) underlines that such a loading leads to a quite low stress state in the adhesive, but for geometry *A*, larger stress concentrations can be noted than for geometry *B*.

For the thermo-mechanical loads, Fig. 5(d) and 5(e) present the stress state for a variation in temperature of $\Delta T = -80\ ^\circ C$ followed by a prescribed displacement of 0.02 mm. It represents a test at $-60\ ^\circ C$. The superposition of the thermal load to the mechanical load leads to an increase in the stress concentrations close to the free edges of the adhesive for geometry *A*. *A* complete analysis of this problem requires an increase in the mechanical load after applying the thermal load. Therefore, for geometry *B*, an increase in the mechanical load leads to a decrease in the stress state close to the free edges of the adhesive with respect to the stress state in the middle of the joint; thus it leads to a reduction in the stress concentrations associated with the initial thermal stress state. On the other hand, it has been shown that for tests with quite large stress concentration, cracks can appear quickly at the two edges of the joint, close to the adhesive–substrate interfaces [21,22], and thus can lead to an incorrect analysis of the behaviour of the adhesive. Therefore, for geometries characterised with large stress concentrations under mechanical loads (such as geometry *A*) a decrease in the temperature of the mechanical test is associated with an increase in the stress concentrations and thus to earlier crack initiation.

Moreover, for geometry *A*, associated with large stress concentrations, better precision of the numerical results can require more refined meshes. However, this point does not affect the conclusion of the study: a large reduction in the stress concentration, associated with the mechanical load is an important point in order to obtain accurate experimental results taking into account thermal loadings.

In this study, constant elastic properties of the adhesive (Young's modulus and Poisson's ratio) with respect to temperature is assumed. In fact, the decrease in the temperature can lead to a slight increase in the Young's modulus of the adhesive; thus, it can lead to only a little reduction in the stress concentrations. Therefore, in the case of the temperature range analysed, the numerical results presented previously give a good representation of the real behaviour.

4. Experimental results with respect to temperature

4.1. Behaviour under tensile/compression–shear loads

The different tests were made with a displacement rate of the crosshead of the tensile testing machine of 0.5 mm/min. Different loading paths were analysed using the modified Arcan device (Fig. 1): tensile ($\gamma = 0^\circ$), tensile–shear ($\gamma = 45^\circ$), shear ($\gamma = 90^\circ$) and compression–shear ($\gamma = 135^\circ$). Moreover, different temperatures were taken into account starting from room temperature: 20 °C, 0 °C, −20 °C, −40 °C and −60 °C. The experimental results are presented in the load-displacement diagrams in Fig. 6. The results present the mechanical load transmitted by the bonded assembly for a given temperature. A more precise analysis requires the stress state associated with the thermal loading to be taken into account; such a study is not presented herein.

For compression–shear loads ($\gamma = 135^\circ$), the failure load is not easy to determine. In fact, for such tests, in the non-linear phase of the adhesive behaviour, the change in the slope of the response in the load-deformation diagram can be associated with the failure of the joint. These points are represented using the following marks "x" in Fig. 6(f). After this inflexion point, the experimental results are not representative of the behaviour of the adhesive in an assembly (the load can be transmitted by friction after failure of the joint). For the analysis of the experimental results, these points are associated with failure under compression–shear loads ($\gamma = 135^\circ$). Moreover, for such compression–shear loads ($\gamma = 135^\circ$) the scatter in the experimental results is higher for the normal displacement (Fig. 6(e)), mainly associated with the view-glass of the thermal chamber; in fact for such loadings, the tangential displacement is much higher than the normal displacement (Fig. 6(e) and (f)).

Fig. 7 presents the failure modes for the different loadings in the case of a temperature of 20 °C. It can be seen that mainly mixed failure (cohesive and adhesive–substrate interface failures) is obtained for the different loadings, with the mechanical surface preparation and the curing process used. For compression–shear tests, the compression stress leads to adhesive–substrate interface failures. As mentioned previously the failure load is not easy to determine; in fact after the adhesive failure, an increase of the load can be noted which can lead to adhesive–substrate interface type failures. For the other temperature, nearly same failures modes are observed (a slight increase in adhesive–substrate interface failures can be noted).

4.2. Discussions

First, it can be noted that the scatter in the experimental results is quite low for the different temperatures. For instance, under tensile ($\gamma = 0^\circ$) and shear ($\gamma = 90^\circ$) loads results of two tests are presented for $T = 20\ ^\circ C$, $-20\ ^\circ C$ and $-60\ ^\circ C$ (Fig. 6(a) and (b); it can be noted that experimental responses in the load-displacement diagram are nearly identical. Similar low scatter in the results has been obtained with such a modified Arcan device designed to limit stress concentrations significantly [22].

Second, it can be noted that a decrease in the temperature, leads to:

- a low increase in the rigidity of the adhesive,
- a low reduction in the deformation at failure of the adhesive, especially under tensile, shear and compression–shear loads,
- a large increase in the elastic limit and in the failure stress of the adhesive for the different compression/tensile–shear loads.

The last property explains that for some tests, the failure has not been reached as the maximum transmitted load has been limited to 50 kN in order to prevent permanent deformation of the Arcan device and of the loading pins, as they have not been designed for such heavy loads.

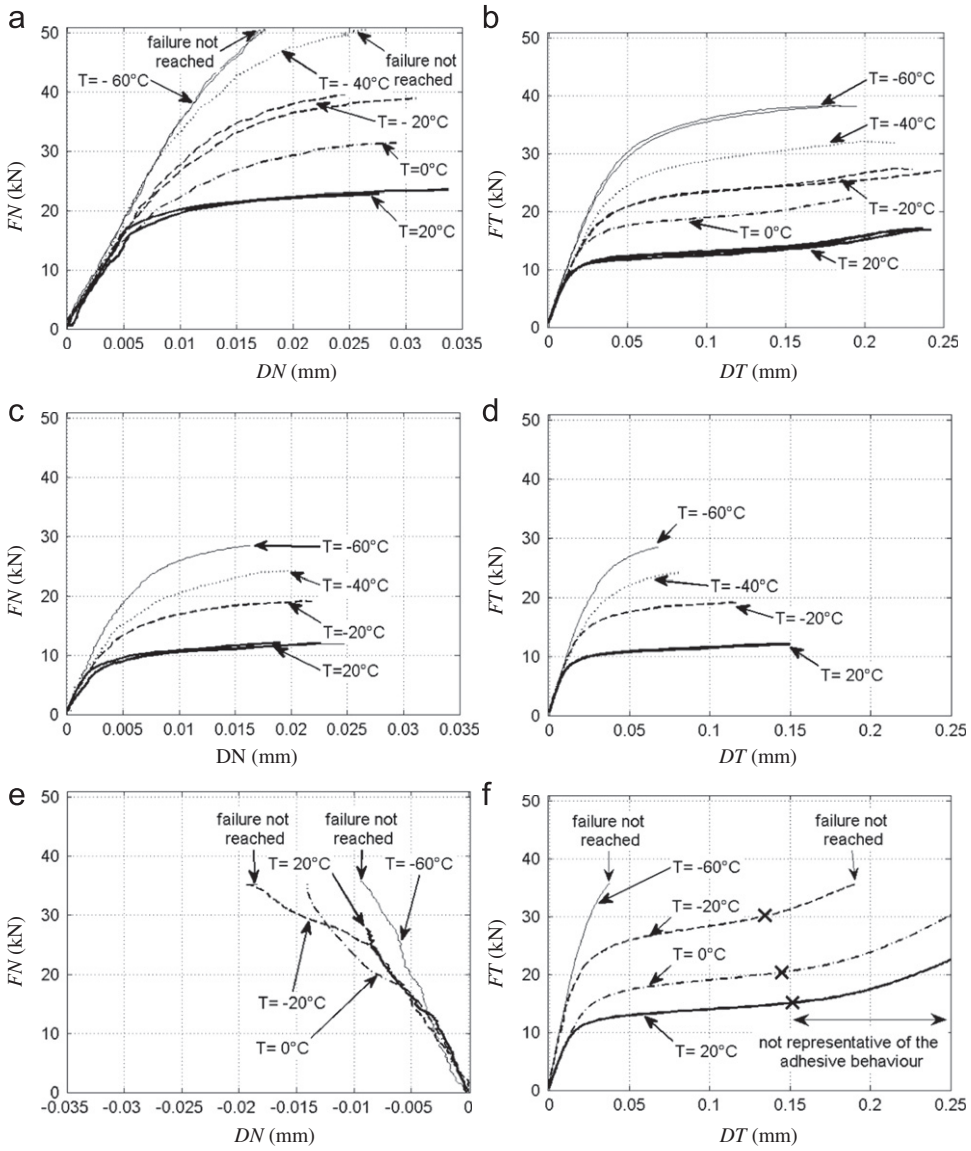


Fig. 6. Influence of the temperature on the mechanical behaviour of the adhesive in the load-relative displacement diagram for different monotonic radial loads. (a) tensile loading – $\gamma=0^\circ$ (b) shear loading – $\gamma=90^\circ$ (c) tensile–shear – $\gamma=45^\circ$ – normal direction (d) tensile–shear – $\gamma=45^\circ$ – tangential direction (e) compression–shear – $\gamma=135^\circ$ – normal direction (f) compression–shear – $\gamma135^\circ$ – tangential direction.

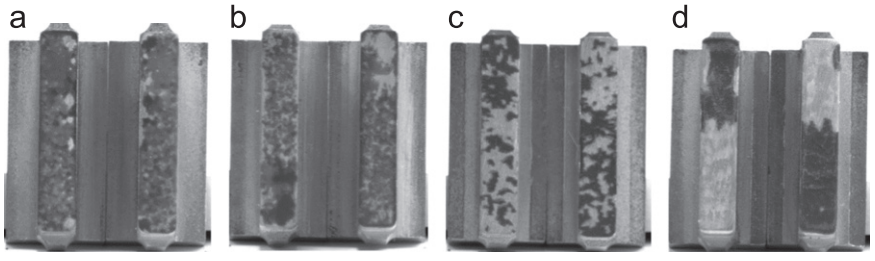


Fig. 7. Failure modes for different loadings for $T=20$ °C. (a) $\gamma=0^\circ$, (b) $\gamma=45^\circ$, (c) $\gamma=90^\circ$, (d) $\gamma=135^\circ$.

4.3. *Influence of the temperature on the elastic and failure envelopes*

This section provides precise analyses of the temperature evolution of the elastic and failure envelopes of the adhesive for the stresses and the deformations associated with the mechanical loads.

In the case of linear elastic behaviour, the stress distribution is not constant in the adhesive for the modified Arcan test, thus, inverse identification techniques have to be used in order to analyse the experimental results [22,23]. For ductile adhesives, such as the used adhesive, it has been shown that simplified approaches can be used to determine the so-called elastic limit of the adhesive and the maximal stress at failure [24]. The first important point is that under elastic assumptions, starting from 3D finite element results, the maximum values of the peel and shear components of the stress are obtained from the average

stress [14], based on the components of the loads measured during the experimental test, and the section of the adhesive (Sc):

$$\sigma_{max} = 1.12\sigma_{average} \text{ with } \sigma_{average} = FN/Sc \quad (1)$$

$$\tau_{max} = 1.29\tau_{average} \text{ with } \tau_{average} = FT/Sc \quad (2)$$

where σ and τ denote, respectively the normal and shear stresses.

The second important point is that close to failure, nearly a homogeneous stress state is obtained in the case of ductile adhesives.

Fig. 8 presents the influence of the temperature on the elastic and fracture envelopes in the shear stress-normal stress diagram, starting from the experimental results presented in Fig. 6. These results underline that compression stress increases the elastic and the rupture shear stress of the adhesive significantly, which is very important for industrial applications. Fig. 9 presents the elastic and fracture envelopes in the shear strain-normal strain diagram with respect to the temperature. The relative displacement of both ends of the adhesive (DN and DT) is normalised by the adhesive thickness (e), in order to propose a more intrinsic result for this adhesive; such results are acceptable for a given range of adhesive thicknesses [5]. This figure underlines the different level of deformation in the normal and tangential directions at failure; it is important to notice that for the failure envelope different scales are used in the two directions.

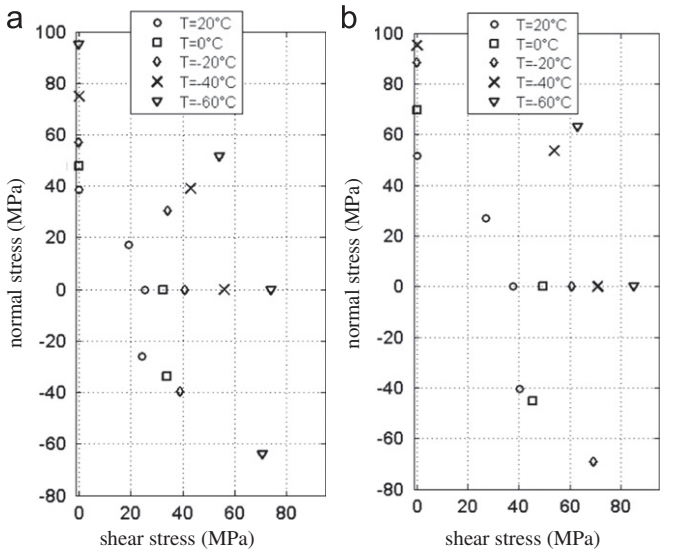


Fig. 8. Influence of the temperature on the elastic and fracture envelopes in the shear stress-normal stress diagram. (a) initial elastic envelope, (b) failure envelope.

4.4. Modelling of the temperature-dependent elastic limit of the adhesive

This section presents two simple models to represent the temperature dependent elastic limit of the adhesive.

In the case of 2D models, the yield surface can be defined using an elliptic function taking into account the differences between traction and compression:

$$\frac{\langle\sigma\rangle_+^2}{(R_+(T))^2} + \frac{\langle\sigma\rangle_-^2}{(R_-(T))^2} + \frac{\tau^2}{(S(T))^2} = 1 \quad (3)$$

where σ and τ denote, respectively the normal and shear stresses, $\langle x\rangle_+$ and $\langle x\rangle_-$ are, respectively the positive and negative parts of the real x; and R_+, R_- and S are material parameters [23]

The experimental results show a nearly linear evolution of various parameters of the elastic limit of the adhesive with respect to the temperature. Thus, in order to model the elastic limit, a global optimisation using the different experimental results (Fig. 8(a)) was proposed taking into account a linear evolution of the material parameters with respect to the temperature. The temperature evolution of the material parameters are such that:

$$R_+(T) = A_1 \cdot T + B_1$$
$$R_-(T) = A_2 \cdot T + B_2$$
$$S(T) = A_3 \cdot T + B_3 \quad (4)$$

The results of the identification are presented in Table 1. Fig. 10(a) presents a comparison between the experimental results

Table 1
Material parameters for the initial yield surface (2D model, shear stress-normal stress diagram).

A_1 (MPa/°C)	A_2 (MPa/°C)	A_3 (MPa/°C)	B_1 (MPa)	B_2 (MPa)	B_3 (MPa)
−0.65	−0.84	−0.56	48.6	147.3	33.3

Table 2
Material parameters for the initial yield surface (3D model, hydrostatic pressure-von mises stress diagram).

C_1(SI units)	C_2(/°C)	C_3(MPa/°C)	D_1(SI units)	D_2	D_3(MPa)
−1.65 E−6	9.43 E−4	−0.62	1.35 E−4	3.1	41.32

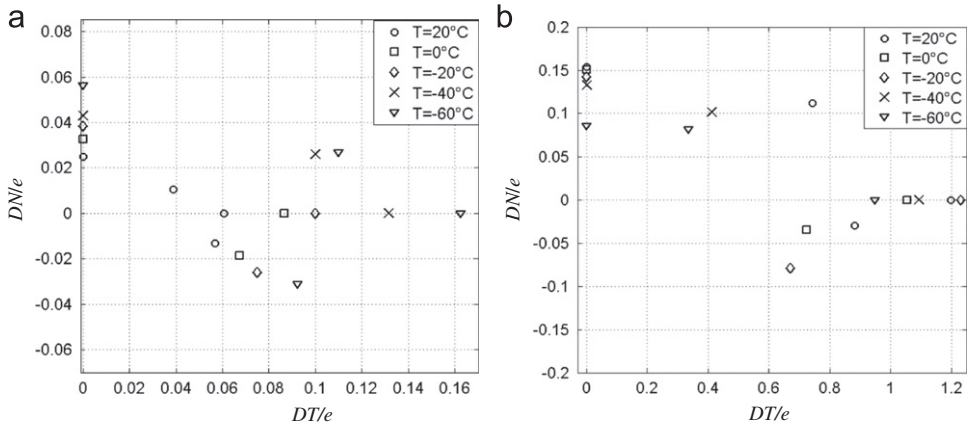


Fig. 9. Influence of the temperature on the elastic and fracture envelopes in the shear strain-normal strain diagram (average values). (a) initial elastic envelope, (b) failure envelope.

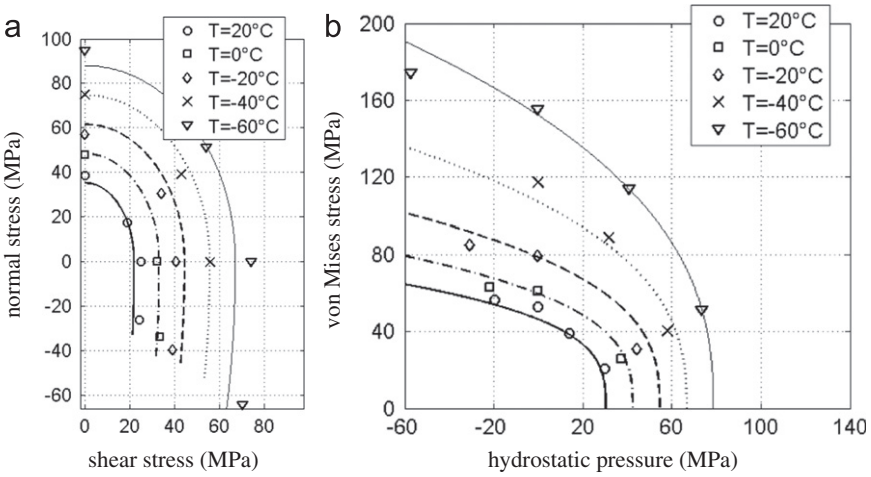


Fig. 10. Modelling of the temperature-dependent elastic limit of the adhesive. (a) shear stress-normal stress diagram, (b) hydrostatic pressure-von Mises stress diagram.

and the numerical model for the different studied temperatures in the shear stress-normal stress diagram; a good agreement is observed.

Various studies underline that an accurate representation of the elastic yield surface of an adhesive requires the use of a pressure-dependent constitutive model, i.e., a model taking into account the two stress invariants, hydrostatic stress and von Mises equivalent stress. For this study, only elastic behaviour of the adhesive is used. An exponential Drucker–Prager yield function allows a good representation of the experimental data for the so-called "initial elastic limit" [14]:

$$F_0 = a(T)\cdot(\sigma_{vm})^{b(T)} + P_h - P_{h0}(T) = 0 \quad (5)$$

where σ_{vm} is the equivalent von Mises stress and P_h is the hydrostatic stress. a, b and P_{h0} are material parameters.

A similar optimisation approach, as for the previous model, was developed taking into account a linear evolution of the material parameters with respect to the temperature. The temperature evolution of the material parameters are such that:

$$a(T) = C_1\cdot T + D_1$$
$$b(T) = C_2\cdot T + D_2$$
$$P_{h0}(T) = C_3\cdot T + D_3 \quad (6)$$

The results of the identification are presented in Table 2. Fig. 10(b) presents a comparison between the experimental results and the numerical model for the different studied temperatures in the hydrostatic pressure-von Mises stress diagram. A good representation of the experimental results is obtained using such type of model.

5. Conclusions

A modified Arcan device, which has been designed to strongly limit the influence of the stress concentrations, combined with a usual thermal chamber have been used to analyse the influence of temperature on the mechanical behaviour of an adhesive. Tests have been performed on bonded assemblies under various tensile/compression–shear monotonic loadings for a temperature range between 20 °C and −60 °C. The behaviour of a ductile adhesive under a given strain rate has been analysed. The experimental results underline that a diminution in the temperature leads, on the one hand to a low reduction in the deformation at failure of the adhesive, especially under tensile, shear and compression–shear loads; and on the hand, to a large increase in the elastic limit and of the failure stress of the adhesive for the different compression/tensile–shear loads. The analysis of the results has shown that an exponential Drucker–Prager yield function, using linear evolution of the material parameters with respect to temperature, allows a good representation of the experimental data for the initial elastic limit. Moreover, these results constitute a large experimental database, which is essential in order to define accurate models for the thermo-mechanical behaviour of an adhesive in an assembly using non-associated pressure-dependent constitutive laws.

As the stress state in an adhesive joint is quite complex, inverse identification techniques using 3D finite element models are necessary to analyse the experimental results accurately. Moreover, an optimisation of the geometry of the bonded joint can be done to improve the tests for a large range of temperature: the aim is to limit the stress concentrations close to the free edges of the joint taking into account the effects of the thermo-mechanical loads. Thus, the proposed experimental strategy can be interesting to analyse the temperature-dependent visco-plastic behaviour of an adhesive in an assembly under various thermo-mechanical loads.

Acknowledgements

The authors wish to thank Hervé Trébaol, Pierre Martinat and Bruno Mecucci from ENSTA Bretagne/CMA for their collaboration in designing and manufacturing the adaptation of the experimental mechanical device to the thermal chamber.

References

[1] Adams RD. Adhesive Bonding: Science, Technology and Applications. Bristol: Woodhead Publishing Ltd; 2005.
[2] da Silva LFM, Öchsner A. Modeling of Adhesive Bonded Joints. Berlin: Springer; 2008.
[3] da Silva LFM, Öchsner A, Adams RD. Handbook of Adhesion Technology. Heidelberg: Springer; 2011.
[4] Qian ZQ. On the evaluation of wedge stress intensity factor of bi-material joints with surface tractions. Comput. Struct. 2001;79:53–64.
[5] Cognard JY. Numerical analysis of edge effects in adhesively-bonded assemblies application to the determination of the adhesive behaviour. Comput. Struct. 2008;86:1704–17.
[6] Chiu WK, Chalkley PD, Jones R. Effects of temperature on the shear stress–strain behavior of structural adhesive. Comput. Struct. 1994;53:483–9.
[7] Apalak MK, Gunes R. On non-linear thermal stresses in an adhesively bonded single lap joint. Comput. Struct. 2002;80:85–98.
[8] da Silva LFM, Adams RD. Stress-free temperature in a mixed-adhesive joint. J. Adhes. Sci. Technol. 2006;20:1705–26 2006.
[9] Rey JM, Gallet B, Kircher F, Lottin JC. Epoxy resin developments for large superconducting magnet impregnation. Cryogenics 1998;38:19–23.

[10] da Silva LFM, Adams RD. Measurement of the mechanical properties of structural adhesives in tension and shear over a wide range of temperatures. J. Adhes. Sci. Technol. 2005;19:109–41.
[11] Lee CS, Chun MS, Kim MH, Lee JM. Debonding failure characteristics of multi-laminated bonding system under cryogenic temperature. Int. J. Adhes. Adhes. 2011;31:226–37.
[12] Raghava RS, Cadell RM. The macroscopic yield behaviour of polymers. J. Mater. Sci. 1973;8:225–32.
[13] Mahnken R, Schlimmer M. Simulation of strength difference in elasto-plasticity for adhesive materials. Int. J. Numer. Methods Eng. 2005; 63:1461–77.
[14] Cognard JY, Créac'hcadec R, da Silva LFM, Teixeira FG, Davies P, Peleau M. Experimental analysis of the influence of hydrostatic stress on the behaviour of an adhesive using a pressure vessel. J. Adhes. 2011;87:804–25.
[15] Levesy B, Kircher F, Rey JM, Reylier M, Rondeaux F, Desirelli A. Shear test of glas reinforced composite materials at 4.2 K. IEEE Trans. Appl. Supercond. 2000;10:1306–9.
[16] Sancaktar E, Simmons SR. Optimization of adhesively-bonded single lap joints by adherend notching. J. Adhes. Sci. Technol. 2000;14:1363–404.
[17] Cognard JY, Creac'hcadec R. Analysis of the non linear behaviour of an adhesive in bonded assemblies under shear loadings. Proposal of an improved TAST. J. Adhes. Sci. Technol. 2009;23:1333–55.
[18] Cognard JY, Davies P, Sohier L, Créac'hcadec R. A study of the non-linear behavior of adhesively-bonded composite assemblies. Compos. Struct. 2006;76:34–46.
[19] Gom documentation, 〈www.gom.com〉.
[20] Abaqus documentation, Version 6.6. Simulia, 2007.
[21] Dean G, Crocker L, Read B, Wright L. Prediction of deformation and failure of rubber-toughened adhesive joints. Int. J. Adhes. Adhes. 2004;24:295–306.
[22] Cognard JY, Créac'hcadec R, Sohier L, Davies P. Analysis of the non linear behaviour of adhesives in bonded assemblies. Comparison of TAST and ARCAN tests. Int. J. Adhes. Adhes. 2008;28:393–404.
[23] Créac'hcadec R, Cognard JY. 2D modeling of the behavior of an adhesive in an assembly using a non-associated elasto-visco-plastic model. J. Adhes. 2009;85:239–60.
[24] Créac'hcadec R, Cognard JY, Heuzé Th. On modelling the behaviour of thin adhesive films in bonded assemblies with interface elements. J. Adhes. Sci. Technol. 2008;22:1541–63.

Author's personal copy

International Journal of Adhesion & Adhesives 47 (2013) 46–56

Contents lists available at ScienceDirect

International Journal of Adhesion & Adhesives

journal homepage: www.elsevier.com/locate/ijadhadh

On modelling the behaviour of a ductile adhesive under low temperatures

J.Y. Cognard [a], C. Badulescu [a,*], J. Maurice [a], R. Créac'hcadec [a], N. Carrère [a], P. Vedrine [b]

[a] Laboratoire Brestois de Mécanique et des Systèmes, ENSTA Bretagne, Brest, France
[b] CEA Saclay, DSM/Irfu/SACM, 91191 Gif sur Yvette, France

ARTICLE INFO

Article history:
Accepted 30 June 2013
Available online 27 September 2013

Keywords:
Adhesively-bonded joint
Stress concentration
Thermo-mechanical loads
Finite element analysis
Joint design

ABSTRACT

The objective of the paper is to propose a strategy in order to develop accurate numerical models to describe the behaviour of a ductile adhesive in an assembly under mechanical proportional monotonic loads at different low temperatures. This study requires the use of precise 3D numerical analysis of the stress state within a bonded assembly in order to develop an inverse identification technique starting from the load–displacement curves obtained using a modified Arcan apparatus. First, the influence of the geometry of the bonded assembly close to the free edges of the adhesive on the stress state under a mechanical load at a given temperature is analysed with a 2D numerical analysis. These results allow us to propose some rules in order to define accurate experimental devices for such thermo-mechanical loads. The second part is associated with the estimation of the residual stresses within an adhesive in an assembly and the identification of the material parameters of a 3D elastic–plastic Mahnken–Schlimmer type model, for tensile/compression–shear proportional monotonic mechanical loads and for a temperature range between 20 °C and −60 °C.

© 2013 Elsevier Ltd. All rights reserved.

1. Introduction

Adhesive joints are widely used as a structural element in various applications (automotive, aerospace, naval…) [1,2]. Two of the main advantages of this joining technique are the weight reduction and the facilitation of joining different materials, especially composites; in fact, this technique does not require holes, as riveted or bolted joints do, which can lead to stress concentrations. However, adhesively bonded joints are also often characterised by significant edge effects associated with geometrical and material parameters. Various simplified approaches, using 1D or 2D models, have been proposed in order to describe the behaviour of some bonded joints [3,4], but often such models cannot describe the effect of stress concentrations which often have an influence on the maximum stress state in the bonded assemblies. Therefore, understanding the stress distribution in an adhesive can lead to improvements in adhesively-bonded assemblies; for instance, designing assemblies which strongly limit the edge effects can be very interesting as stress singularities can contribute to the initiation and propagation of cracks in the adhesive [5,6]. In order to optimise the design of high-tech applications, it is also necessary to take into account the complex, non-linear behaviour of the adhesive (influence of viscous effects, of hydrostatic pressure, complex anelastic flow rule, etc. [7–9]). Moreover, the curing process of adhesives and thermal loads can also induce stresses within the adhesive, especially for stiff substrates [10–12]. The curing process is complex as it involves phase transformations and chemical reactions with volume changes [13]. Moreover; associated with difference in thermal expansion of the adhesive and substrates, thermal stresses evolve during cool down from the curing temperature and during a variation in the service temperature [14]. It is important to notice that various applications are subjected to a wide range of temperatures (for instance between −40 °C and 80 °C for some automotive applications). Such stresses, in combination with the temperature-dependent mechanical behaviour of the adhesive [15] can have a significant influence on the service life of the bonded assemblies [16] and can also change the stress concentrations close to the free edges of the joint [17–19]. Various experimental techniques, often associated with strain measurement, exist to analyse the residual stresses in a bonded joint (neutron and X-ray diffraction techniques…). The analysis of the deformation of a bi-material beam is an easy experimental technique which is often used for the determination of the stress free temperature of the adhesive in an assembly [10,20,21]. However, the viscous mechanical behaviour of the adhesive can reduce the residual stresses [22]. The influence of aging during the service life of a bonded assembly is often associated with a modification in the mechanical properties of the adhesive and can also modify the stress distribution within the assembly [23,24]. It has been shown that the identification of the material parameters of representative models

* Correspondence to: ENSTA Bretagne, LBMS, 2 rue François Verny, 29806 Brest Cedex 9, France. Tel.: +33 2 98 34 89 77; fax: +33 2 98 34 87 30.
E-mail address: claudiu.badulescu@ensta-bretagne.fr (C. Badulescu).

0143-7496/$ - see front matter © 2013 Elsevier Ltd. All rights reserved.
http://dx.doi.org/10.1016/j.ijadhadh.2013.09.024

Author's personal copy

for adhesives requires a large data base of experimental results under various compression/tensile–shear tests [25]. Bulk, lap-shear and pull-off tests are usually proposed [15,26] to analyse the mechanical behaviour of the adhesive but the influence of defects and the influence of stress concentrations are often difficult to take into account with such specimens. Herein, experimental results obtained using modified Arcan apparatus, designed to strongly limit influences of edge effects under mechanical loads [27] have been used. In a previous study, results were determined under low temperature (from 20 °C to −60 °C) [19].

The objective of the paper is to develop an accurate numerical model to describe the influence of temperature on the non-linear mechanical behaviour of a ductile adhesive in an assembly under proportional monotonic mechanical loads, i.e. the definition of the temperature-dependent initial elastic limit of the adhesive and the definition of the temperature-dependent flow rules. This study requires the use of precise 3D numerical analysis of the stress state within a bonded assembly in order to develop an inverse identification technique starting from the load–displacement curves obtained using the modified Arcan apparatus results. First, the influence of the geometry of the bonded assembly close to the free edges of the adhesive on the stress state under a mechanical load at a given temperature is analysed in the case of shear and tensile loads. The aim is to underline the influence of stress concentrations under such thermo-mechanical loads in order to propose some rules to define accurate experimental devices. The second part is associated with the estimation of the residual stresses within an adhesive in an assembly and the identification of the material parameters of a 3D elastic–plastic Mahnken–Schlimmer type model, for tensile/compression–shear proportional monotonic loads and for a temperature range between 20 °C and −60 °C.

2. Description of the materials

In order to analyse the influence of the geometry of the specimens on stress concentrations under thermo-mechanical loads, a comparison of numerical results is firstly presented in the case of shear type loadings using the TAST (standard thick adherend shear test [28]) and modified Arcan apparatus [29]. In a second stage, the influence of the local geometry of a bonded specimen, close to the free edges of the adhesive is analysed using modified Arcan apparatus in the case of tensile loads which are often associated with large stress concentrations [27].

2.1. TAST specimen

The single lap joint is the most used test in order to analyse the behaviour of an adhesive in an assembly as the manufacturing of such specimens is quite easy, and they require only a classic tensile testing machine. However, such specimens are associated with complex loading of the adhesive i.e. non uniform shear stress along the overlap length, quite high peel stress at the two ends of the overlap and significant edge effects associated with geometrical and material parameters. TAST type specimens (Fig. 1) [28], and its variant proposed by Althof [30], were designed to simplify the stress distributions in the adhesive. Therefore, they can be seen as optimised simple lap shear configurations but edge effects still exist. Moreover, it has been shown that the use of grooves (Fig. 2) allows a reduction in the stress concentrations [31,32]; thus, such geometries are used herein.

2.2. Modified Arcan device

A modified Arcan fixture, which enables compression or tension to be combined with shear load was previously developed [29].

The use of substrates with thin beaks and clean free edges of the adhesive can significantly limit the peel stress state close to the free edges of the joint. Moreover, an optimisation of the fixing system for the bonded specimen can avoid the pre-loading of the adhesive. In order to prevent parasitic loadings special fixing systems were used to fix the modified Arcan device (Fig. 3). The external diameter of the modified Arcan apparatus used was of 155 mm [33]. To ensure a precise adhesive thickness and a good relative positioning of the two substrates during the bonding process, spacers were manufactured during the machining process of the substrates, in order for the surfaces of the spacers to be used as reference for the manufacture of the bonded surfaces (Fig. 3b). The relative positioning of the two substrates during the bonding process is ensured using screws. Before testing, with the modified Arcan device, the spacers were cut. For such specimens, the area of the bonded section was 50 mm × 9 mm.

Numerical results are presented for two geometries of the bonded specimens used with the modified Arcan device (Fig. 4). The first geometry is associated with straight substrates and straight edges of the free edges of the adhesive and the second represents the bonded specimens proposed for the experimental tests (use of beaks on the substrates and cleaning of the free edges of the adhesive). By clean free edges we mean the surfaces we obtain after eliminating the excess adhesive. The geometry of the clean free edges presents a curvature r shown in Fig. 4b. Geometries are defined with the following parameters: $L=50$ mm, $H1=20$ mm, $\alpha=30°$, $h=0.1$ mm, $d=0.5$ mm, $r=0.1$ mm and $e=0.2$ mm.

The different experimental results presented in the following were obtained using the epoxy resin Huntsman™ Araldite® 420 A/B with a joint thickness of 0.2 mm and a curing process of 1 h at 110 °C [19].

2.3. Parameters of the numerical simulations under elastic assumption

The elastic properties of both materials, at room temperature, are: $Ea=2$ GPa (Young's modulus), $\nu a=0.3$ (Poisson's ratio) for the

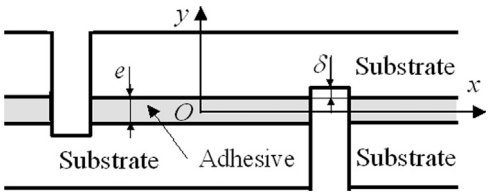


Fig. 2. Geometry of the TAST specimen with deep grooves (central part, not to scale).

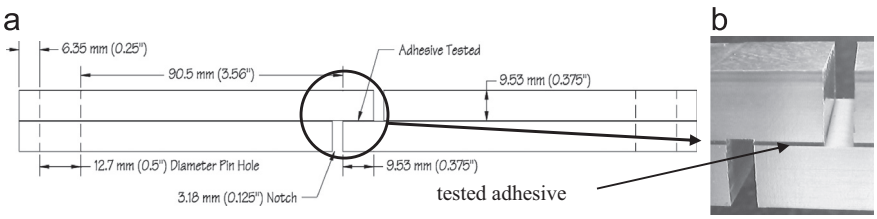


Fig. 1. Presentation of the TAST specimen (width: 25.4 mm) [6]. (a) Geometry and (b) useful zone.

Author's personal copy

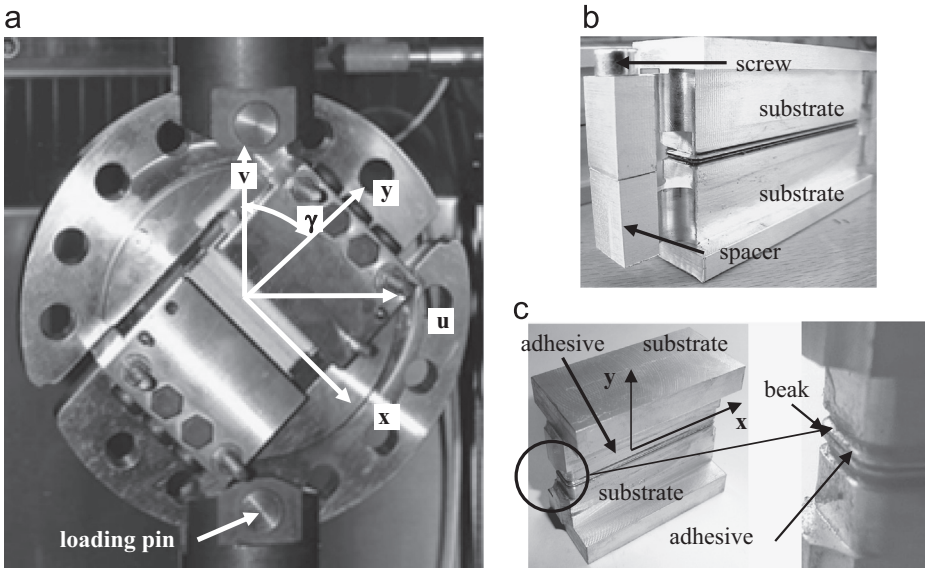


Fig. 3. Modified Arcan device. (a) Test under tensile–shear loading $\gamma=45$, (b) bonding procedure and (c) geometry of the bonded specimens.

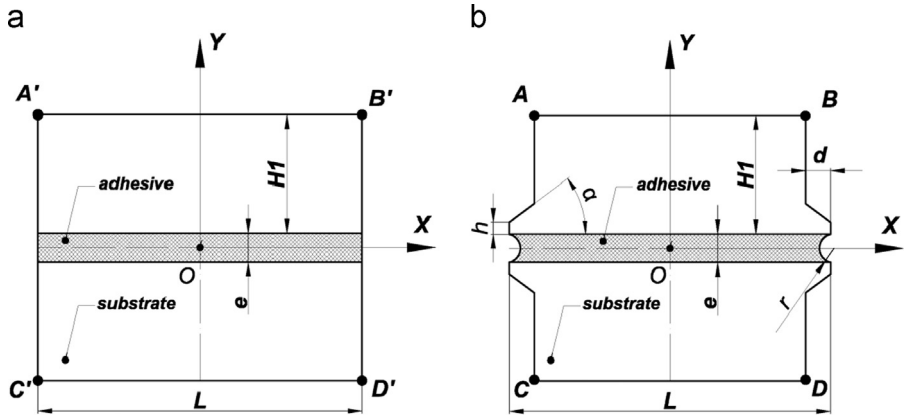


Fig. 4. Presentation of two geometries of the bonded assemblies (not to scale). (a) Geometry *A*: test under tensile-she specimen with straight edges and (b) geometry *B*: specimen with beaks and cleaned edges.

adhesive and $Es=70$ GPa, $\nu s=0.3$ for the substrates. The coefficient of thermal expansion used in this study is equal to 2.3 E-5 $°C^{-1}$ for the substrate and 8 E-5 $°C^{-1}$ for the adhesive [19]. Various simulations have shown that good numerical results are obtained using meshes with 20 linear rectangular elements for a 0.1 mm thickness of adhesive, especially when stress concentrations are not too large. By good numerical results we understand that, for the geometry shown in Fig. 4b, the convergence of the finite element model is attained. Moreover, it is important to notice that the aim of this study is to analyse specific geometries which significantly limit the influence of edge effects. Computations were made under plane strain assumption.

Various studies underline that an accurate representation of the elastic yield surface of an adhesive requires the use of a pressure-dependent constitutive model, i.e. a model taking into account the two stress invariants, hydrostatic stress and von Mises equivalent stress [9–25]. For the first numerical study, only elastic behaviour of the adhesive is used. An exponential Drucker–Prager yield function allows a good representation of the experimental data for the initial elastic limit [33]:

$$F_0 = a(\sigma_{vm})^b + P_h - P_{h0} = 0 \quad (1)$$

where σ_{vm} is the equivalent von Mises stress and P_h is the hydrostatic stress; a, b and P_{h0} are material parameters. A good representation of the experimental results is obtained using such a type of model. In this case the yield criteria was not part of the material model, but was only used for post-processing the results. The results of the identification [19] are presented in Table 1 for a temperature test of -60 °C; this initial elastic yield surface is used in this section as an example.

Table 1
Material parameters for the initial yield surface for a temperature test of -60 °C [19].

a (−)	b (−)	P_{h0} (MPa)
2.34E-04	3.10	41.32

3. Stress state in the adhesive under thermo-mechanical loadings

3.1. Behaviour under shear loadings

Fig. 5 presents the stress state within the adhesive for the TAST specimen (Fig. 1) with quite deep grooves ($\delta=e/2$, where e is the joint thickness, Fig. 2) and for the modified Arcan (Fig. 3) with

Author's personal copy

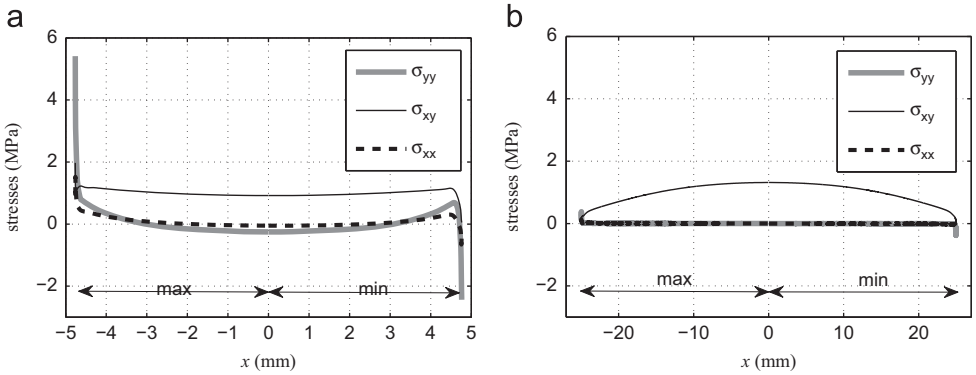


Fig. 5. Minimum and maximum values of the stress components throughout the thickness of the adhesive along the overlap length for a TAST specimen (Fig. 2) and for a modified Arcan specimen under shear load (Fig. 4b) in the case of an average shear stress of 1 MPa. (a) TAST specimen and (b) Arcan specimen under shear.

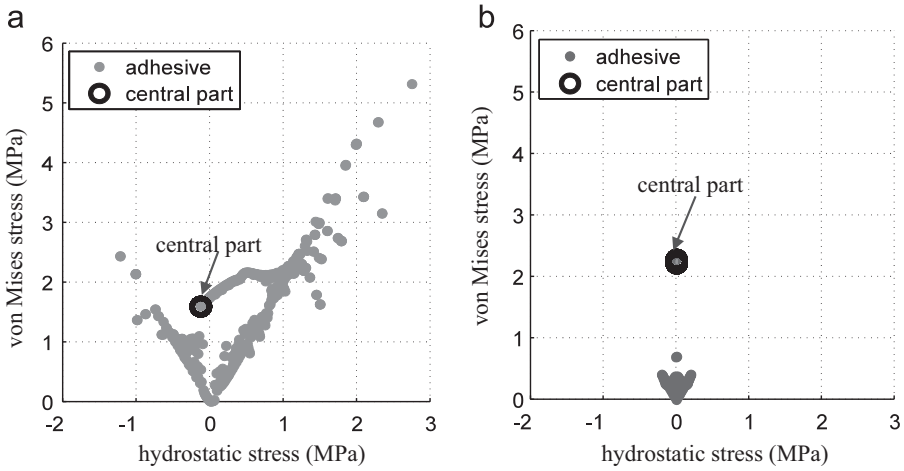


Fig. 6. Stress state in the adhesive in the hydrostatic stress–von Mises equivalent stress diagram for a TAST specimen (Fig. 2) and for a modified Arcan specimen under shear load (Fig. 4b) in the case of an average shear stress of 1 MPa. (a) TAST specimen with grooves and (b) modified Arcan specimen under shear load.

specimens with beaks and cleaned edges (geometry *B*, Fig. 4) under shear loads. Results are presented in the case of an average shear stress of 1 MPa as the overlap length is different for the two tests and as the analyses are developed under linear elasticity. In order to simplify the presentation, as the stress state is symmetrical with respect to point *O* (Fig. 4), only the maximum and minimum values of the stress components (σ_{xx}; σ_{yy}: peel stress and σ_{xy}: shear stress), are presented with respect to the overlap length. The maximum and minimum values of the stresses components are obtained in each point x throughout the adhesive thickness. The right-hand side of the graphs (overlap part associated with $x>0$) gives the maximum values and the left-hand side of the graphs (overlap part associated with $x<0$) presents the minimum values of the stress components in the thickness of the adhesive for a given point of the overlap length. It should be noted that, for the TAST specimen, the stress state is quite complex; in particular, high peel stresses are observed close to the free edges of the adhesive. The stress concentrations are mainly associated with the influence of the peel stress [27]. On the other hand, for the Arcan specimen, mainly a shear stress is observed, with a maximum value in the middle of the joint, and *only low stresses* are observed close to the free edges of the adhesive.

Fig. 6 presents the stress state within the adhesive in the hydrostatic stress–von Mises equivalent stress diagram for a mechanical shear load. The different points represent the stress states of the different integration points of the mesh in the adhesive; moreover, the stress state in the middle of the joint (the circles) is also presented in order to underline the stress distribution within the central part of the adhesive. This figure underlines the influence of the stress concentrations in the case of the TAST specimen. The stress state is not maximal in the central part of the joint as for the Arcan specimen under shear loads. Moreover, the stress states are not exactly identical in the middle of the joint for the two specimens as the stress state in the middle of the TAST specimen is not pure shear and results are presented in the case of an average shear stress of 1 MPa.

Fig. 7 presents the stress state in the adhesive for the maximum transmitted load under elastic behaviour for an experimental test at $-60\,^{\circ}$C (difference of temperature of $\Delta T=-80\,^{\circ}$C with respect to the room temperature) in the hydrostatic stress–von Mises equivalent stress diagram. The maximum transmitted load is the load at which yield would first be predicted to occur based on the FE modelling. This maximum transmitted load is obtained for an average shear stress (σ_{xy}) of 12.3 MPa for the TAST specimen and for an average shear stress of 83 MPa for the modified Arcan specimen. Moreover, in Fig. 7 the elastic limit of the adhesive for an experimental test at $-60\,^{\circ}$C is plotted. Only for the Arcan specimen, is the elastic limit first reached in the middle of the joint as this bonded joint has been designed to strongly reduce stress concentrations under mechanical loads. Moreover, the elastic limit is not reached for the same average shear stress for the two tests. Table 2 presents the values of the average shear stress in the adhesive for the maximum transmitted load by the two assemblies

Author's personal copy

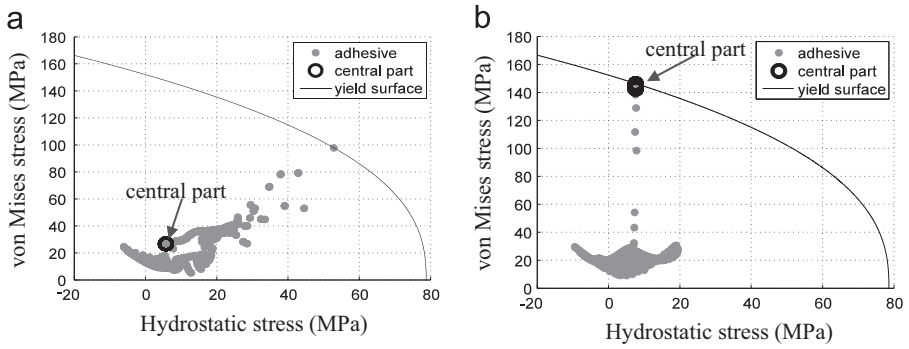


Fig. 7. Stress state in the adhesive for the maximum transmitted load under elastic behaviour for an experimental test at −60 °C in the hydrostatic stress–von Mises equivalent stress diagram. (a) TAST specimen with grooves (average shear stress of 12.3 MPa), (b) modified Arcan specimen (average shear stress of 83.0 MPa).

Table 2
Average shear stress in the adhesive for maximum transmitted load under elastic behaviour computed for tests at room temperature (20 °C) and at −60 °C.

	20 °C	−60 °C
TAST with deep grooves (MPa)	5.9	12.3
Modified Arcan under shear (MPa)	26.4	83.0

under elastic behaviour computed for tests at room temperature (20 °C) and at −60 °C.

These results underline the possible strong influence of edge effects in the case of thermo-mechanical loads. The stress concentrations can contribute to fracture initiation in adhesive joints and thus can lead to an incorrect analysis of the behaviour of the adhesive [5,6].

3.2. Behaviour under tensile loadings

It has been shown that, for a given specimen geometry using the modified Arcan apparatus, the maximum values of the stress concentrations are obtained under tensile loading [27]. Thus, it is interesting to analyse the influence of thermo-mechanical loads on the stress state throughout the adhesive thickness for such loadings.

Figs. 8 and 9 present the minimum and maximum values of the stress components throughout the thickness of the adhesive along the overlap length for a modified Arcan specimen with geometries *A* and *B* respectively under a tensile load in the case of an average peel stress of 1 MPa and under a thermal load associated with a test at −60 °C. It can be noted that geometry *B* is associated with lower stress concentrations with respect to geometry *A*. Under mechanical loads, stress concentrations are mainly observed for the peel stress (*yy* stress component). For the thermal load, stress concentrations exist for the two geometries, but they are lower for geometry *B*. For thermal loadings the stress state is mainly associated with the *xx* stress component in the case of the studied specimens.

Fig. 10 presents the stress state in the whole adhesive under a tensile loading associated with an average peel stress (σ_{yy}) of 34.3 MPa, and under thermal loading at −60 °C, for geometries *A* and *B*. Moreover, Fig. 10 also presents the elastic limit of the adhesive for an experimental test at −60 °C. The elastic limit is reached in adhesive close to the free edges for geometry *A*, for this thermo-mechanical load, with an average peel stress of 34.3 MPa. It is noticeable that the stress state in the middle part of the joint is identical for the two geometries for the same prescribed load. Once again, it can be noted that quite large stress concentrations can lead to a reduction in the transmitted load by the assembly.

Fig. 11 presents, the stress state in the adhesive for a test at −60 °C for geometry *B*. With only the thermal load (Fig. 11a) the stress state is not maximal in the central part of the joint. Fig. 11b shows the stress state in the adhesive for the maximum transmitted load under elasticity (average peel stress of 96 MPa); it can be noted that the elastic limit is reached in the central part of the adhesive. For geometry *B*, the superposition of the mechanical load to the thermal load leads to a reduction in the stress state close to the free edges of the adhesive with respect to the stress state in the central part of the joint. On the other hand, for geometry A associated with large stress concentrations in the case of mechanical loads, the superposition of the mechanical load to the thermal load leads to an increase in the stress concentrations close to the free edges of the adhesive.

3.3. Influence of thermal loads and of residual stresses

In the previous section, it has been shown that some stress concentrations can exist in the adhesive under thermal loads. Thus, it is interesting to use geometries of bonded assemblies which are associated with low stress states close to the free edges of the adhesive under mechanical loads to reach a maximum stress state in the central part of the joint in the case of an increasing mechanical load (such as for geometry *B* for the modified Arcan apparatus). An intermediate behaviour can be observed at the beginning of the prescribed mechanical load as a coupling between the components of the stresses of the two loads exists (associated with a non-proportional loading). In particular, for a prescribed monotonic mechanical load, a non-monotonic evolution of the stress state can be observed especially for the von Mises equivalent stress and for the hydrostatic stress. Therefore, it is interesting to determine, for a given geometry of the specimen and for a given proportional mechanical load, the value of the mechanical load required to obtain the maximum stress state in the middle part of the adhesive with respect to the level of the thermal load. Such properties should be determined in order to ensure the quality of the experimental tests. In the following, the minimum values of the average shear and tensile stresses are respectively denoted by σ_m and τ_m in order to respect such conditions. In fact, under such conditions, the influence of the mechanical load is preponderant with respect to the thermal load. For a given thermal load state, it is possible to apply a mechanical load in order for the first point that reaches the yield stress to be in the central part of the adhesive. This procedure is used to determine σ_m and τ_m by drawing the stress state in the hydrostatic stress–von Mises equivalent stress diagram.

If T_R represents the room temperature and T_T the temperature of the test, the thermal load is defined by the following difference in temperature:

$$\Delta T_{Th} = T_T - T_R \tag{2}$$

Assuming that the stress free temperature (T_{FS}) of the adhesive in an assembly is known [10,20,21], the residual stresses are

Author's personal copy

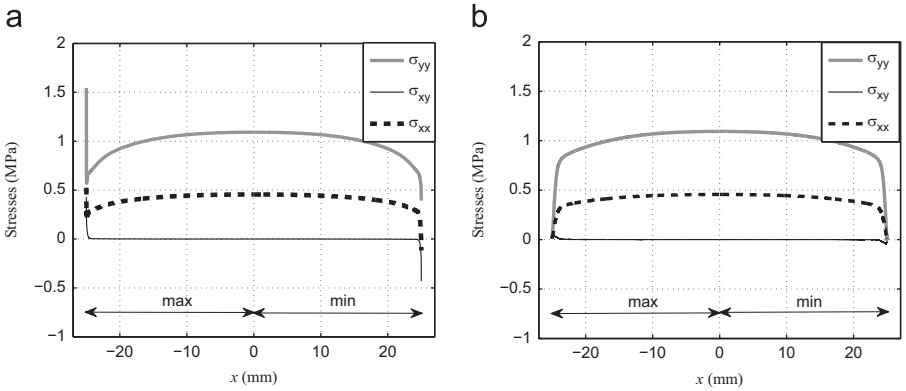


Fig. 8. Minimum and maximum values of the stress components throughout the thickness of the adhesive along the overlap length for a modified Arcan specimen (Fig. 4—geometries *A* and *B* respectively) under tensile load in the case of an average peel stress of 1 MPa. (a) Geometry *A* and (b) geometry *B*.

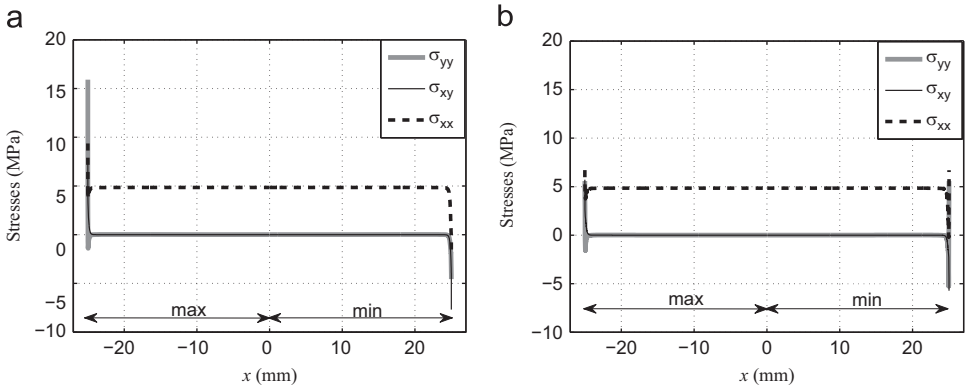


Fig. 9. Minimum and maximum values of the stress components throughout the thickness of the adhesive along the overlap length for a modified Arcan specimen (Fig. 4) under thermal load associated with a test at −60 °C. (a) Geometry *A* and (b) geometry *B*.

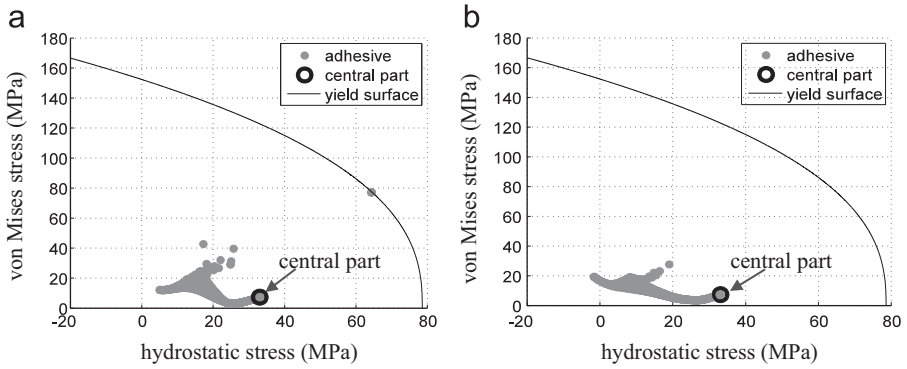


Fig. 10. Stress state in the adhesive for geometry *A* and *B* in the hydrostatic stress–von Mises equivalent stress diagram for a test at −60 °C under a tensile load with an average peel stress of 34.3 MPa (maximum transmitted load under elasticity for geometry *A*). (a) Geometry *A* and (b) geometry *B*.

associated with the following difference in temperature:

$$\Delta T_{RS} = T_R - T_{SF} \quad (3)$$

Fig. 12 presents for modified Arcan specimens with geometry *B*, in the case of a constant coefficient of thermal expansion and T_R=20 °C, the influence of the temperature test and of the value of ΔT_{RS} (associated with the residual stresses) on the values of the parameters σ_m and τ_m. It is important to notice that an increase in the residual stresses and a decrease in the test temperature lead to an increase in the value of the mechanical load required to reduce strongly the stress state close to the free edges of the joint, especially under tensile loading. Moreover, the values of σ_m and τ_m depend on the type of tensile–shear loading.

Thus, these results, which are only indicative, underline that the experimental characterisation of the mechanical behaviour of an adhesive in an assembly can be more difficult when the temperature test decreases, associated with stress concentrations, especially for brittle adhesives.

4. Modelling of the temperature-dependent non-linear behaviour

This section presents the results of the identification of the temperature-dependent behaviour of the non-linear behaviour of

Author's personal copy

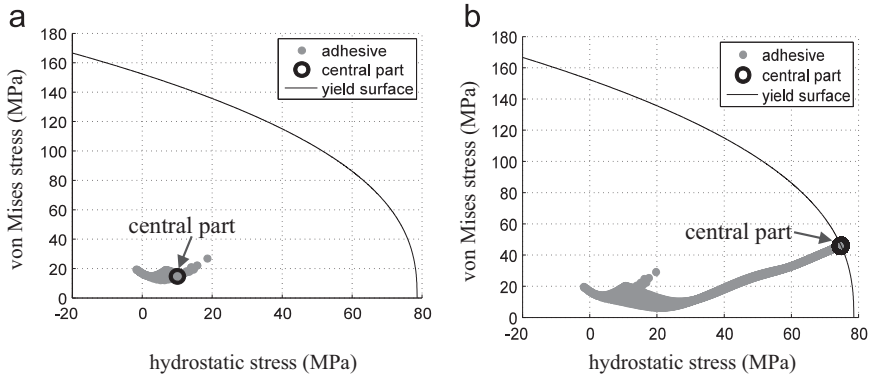


Fig. 11. Stress state in the adhesive for geometry *B* in the hydrostatic stress–von Mises equivalent stress diagram for a test at −60 °C without mechanical load and under a tensile load for the maximum transmitted load under elasticity. (a) No mechanical load (thermal loading for a test at −60 °C) and (b) maximum transmitted load (average tensile stress of 96 MPa).

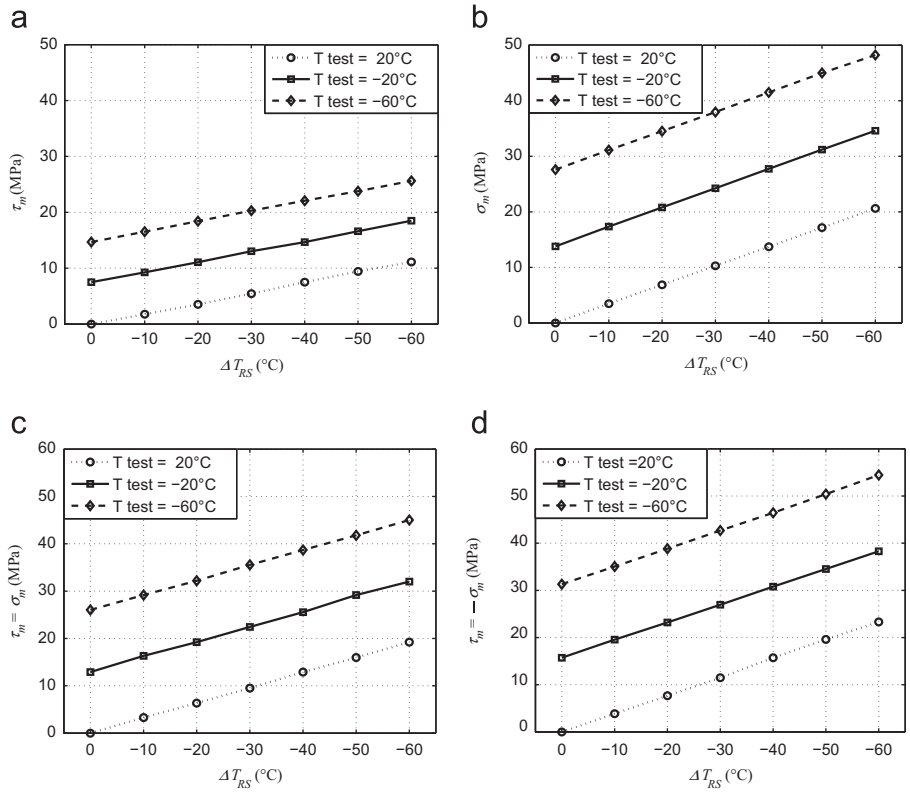


Fig. 12. Influence of the value of ΔT_{RS} (residual stresses) on the value of the minimal mechanical load associated with a maximum stress state in the middle of the joint for different temperature tests (T_T) for modified Arcan specimens with geometry *B*. (a) Shear load, (b) tensile load, (c) tensile–shear load and (d) compression–shear load.

the adhesive in an assembly taking into account an estimation of the residual stresses and the thermal stresses.

4.1. Stress free temperature of the bonded joint

An investigation of residual stresses in a bonded assembly is proposed using a bi-material beam. Such an approach is easy to develop and does not require specific measurement techniques [10,20,21]. The same materials (adherend and adhesive) and the same bonding procedure were used for manufacturing the bi-material beam as used for the experimental tests presented in [19]. Aluminium beams (160 mm × 9 mm), cut out from a 1.5 mm thick plate and an adhesive thickness of 1.5 mm were used. During the curing process, the bi-material was clamped above the beam using an aluminium plate. Fig. 13 presents the deformed shape of the beam, two weeks after the curing process, which was analysed using a high-resolution digital camera. Two samples were analysed and similar results were obtained.

A reduction in the curvature of the beam with respect to time for an exposure under room environment was observed. The displacement of the extremity of the beam was equal to about 3.2 mm just after curing, was equal to about 2.3 mm after two weeks and was equal to about 2 mm after a month. The reduction in the curvature of the beam can be associated to the viscous behaviour of the adhesive and to the influence of the environment [21]; but the geometry of the beam used is not exactly representative of a real bonded assembly (joint thickness, only one adherend and adhesive area exposed to environment conditions). 2D finite element simulations were used to estimate the stress free temperature of the adhesive, using a simplified model, i.e. constant material elastic properties with

Author's personal copy

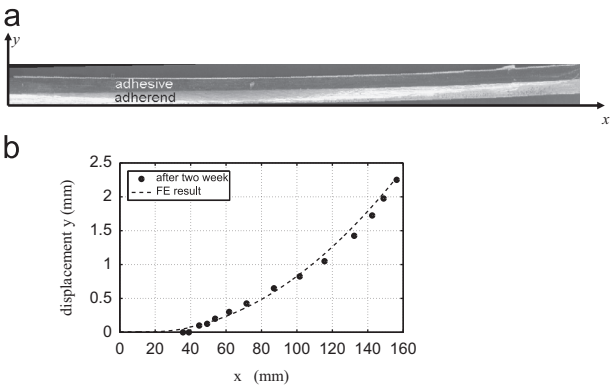


Fig. 13. Deformed shape of the bi-material beam two weeks after the curing process. (a) Image of the deformed shape of the beam just after curing, (b) measured displacement and numerical finite element results.

respect to temperature and assuming a constant coefficient of thermal expansion. Using such a model under plane strain assumption, a stress-free temperature of about $T_{SF}=40$ °C was obtained two weeks after the curing process (Fig. 13); this value was chosen for the following computations. The value of $T_{SF}=40$ C was chosen as being the most representative for the Arcan specimens because, if we consider the associated thermal model, we must add 20 °C (value identified with the bi-material beam) to the 20° room temperature in order to attain stress free temperature. A glass transition temperature of the adhesive of around $T_G=60$ °C was obtained using the Modulated Differential Scanning Calorimetry tests. Thus, the results obtained are in good agreement with literature results [10].

4.2. Non-associated elastoplastic pressure dependent model

The model proposed by Schlimmer was chosen following a previous study [25]. The yield surface, F^{MS}, is given by

$$F^{MS}=\sqrt{\sigma_{VM}^2+a_1Y_0p+a_2p^2}-Y \tag{4}$$

where σ_{VM} is the von Mises equivalent stress, p the hydrostatic stress component defined according to the decomposition of the stress tensor ($\underline{\underline{\sigma}}$) into a deviatoric ($\underline{\underline{S}}$) and a hydrostatic part:

$$\underline{\underline{\sigma}}=\underline{\underline{S}}+p\underline{\underline{I}}_d \qquad \sigma_{VM}=\sqrt{\frac{3}{2}\underline{\underline{S}}:\underline{\underline{S}}} \qquad p=\frac{1}{3}tr(\underline{\underline{\sigma}}) \tag{5}$$

a_1 and a_2 are two parameters defining the shape of the function in the von-Mises-hydrostatic pressure (Mises-p) plane, Y_0 the von Mises stress at the elastic–plastic limit in pure shear and $\underline{\underline{I}}_d$ the third order identity tensor. The hardening is defined by

$$Y=Y_0+q(1-e^{-be_v})+He_v \tag{6}$$

where q, b and H are the three parameters to be identified. The internal strain-like variable of model, e_v, is given by the relation:

$$\dot{e}_vY_0=\underline{\underline{\sigma}}:\underline{\underline{\dot{\varepsilon}}}^{pl} \tag{7}$$

$\underline{\underline{\dot{\varepsilon}}}^{pl}$ is the plastic strain tensor which is defined by a classical normal rule such as

$$d\underline{\underline{\dot{\varepsilon}}}^{pl}=d\lambda\frac{\partial G}{\partial\underline{\underline{\sigma}}} \tag{8}$$

where $d\lambda$ is the plastic multiplier and G the flow function:

$$G=\sqrt{\sigma_{VM}^2+a_2^*p^2}-Y \text{ when } p\geq 0 \tag{9.1}$$

$$G=\sqrt{\sigma_{VM}^2+a_3^*p^2}-Y \text{ when } p\leq 0 \tag{9.2}$$

This definition allows the representation of the differences between the responses under tensile–shear and compression–shear loadings [25]. Continuity of the flow direction $\frac{\partial G}{\partial\underline{\underline{\sigma}}}$ is assured by the horizontal tangent at the point of zero hydrostatic stress (p).

For such a model, a simplified inverse identification approach was developed for proportional loads using experimental results obtained using the modified Arcan apparatus [25]. Taking into account thermal stresses as initial state of specimen, it involves a sequential approach, using a minimum number of optimisation/FEA coupling steps:

- Identification of the initial yield surface (a_1, a_2 and Y_0), using mainly elastic simulations,
- Identification of the hardening function (q, b and H), using inverse identification and experimental results under shear loads,
- Identification of the flow rule parameters (a_2^* and a_3^*), using inverse identification and experimental results under tensile/compression–shear loads.

This technique of obtaining a_1, a_2, Y_0, q, b, H, a_2^* and a_3^* is explained in detail in reference [25].

4.3. Modelling of the temperature-dependent non-linear behaviour of the adhesive

Experimental tests were performed using a thermal chamber [25] with a view-glass allowing the use of an optical 3D measuring system by digital image correlation in order to measure the relative displacement of the two substrates, and thus the deformation of the adhesive, in the x and y directions (Fig. 3). In the following, *DN* and *DT* denote the relative displacements of adjacent sides of the adhesive in the normal (direction y, Fig. 3) and tangential directions (direction x, Fig. 3). It is important to notice that the displacement measurement through the view-glass of the thermal chamber requires specific adjustments in order to obtain images of sufficient quality. *FN* and *FT* represent the normal and tangential components of the applied load in the normal and tangential directions. The experimental results obtained using the

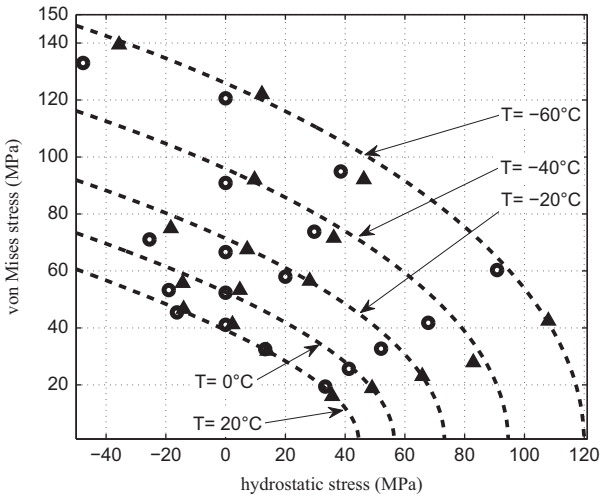


Fig. 14. Initial elastic limit with respect to the different temperatures studied ("●" taking into account only the mechanical load, "▲" taking into account the residual stresses, the thermal stresses and the mechanical load). The dashed curves represent the numerical modelling.

Author's personal copy

modified Arcan apparatus developed in the laboratory are characterised by a low scatter in the results [19]. Thus, the experimental results are presented in the load–displacement diagrams in Fig. 16 for only one test for each loading condition. Different loading paths were analysed (Fig. 3): tensile ($\gamma=0^\circ$), tensile–shear ($\gamma=45^\circ$), shear ($\gamma=90^\circ$) and compression–shear ($\gamma=135^\circ$). Moreover, different temperatures were taken into account starting from room temperature: 20 °C, 0 °C, −20 °C, −40 °C and −60 °C.

Starting from the experimental results the first stage is associated with the modelling of the initial yield surface for the different studied temperatures. The temperature evolution of Young's modulus was firstly identified; results are presented in Table 3. In Fig. 14,

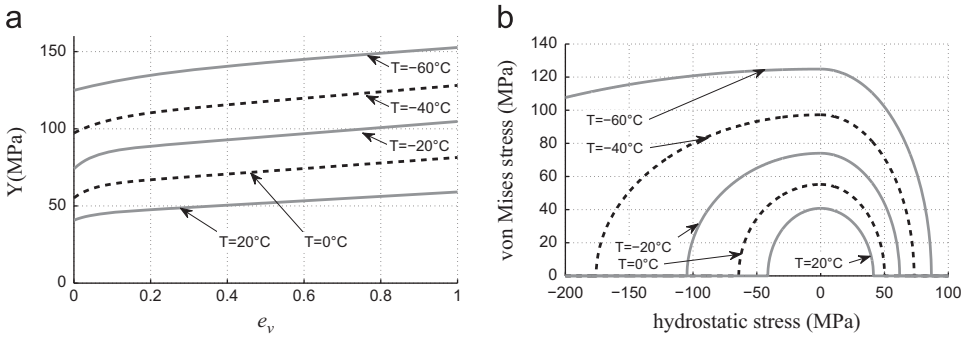


Fig. 15. Evolution of the hardening functions and of the flow functions with respect to temperature (20, −20 and −60 °C) (▬: identification at a given temperature; - - - - - -: temperature-dependent model). (a) Hardening functions and (b) initial flow functions.

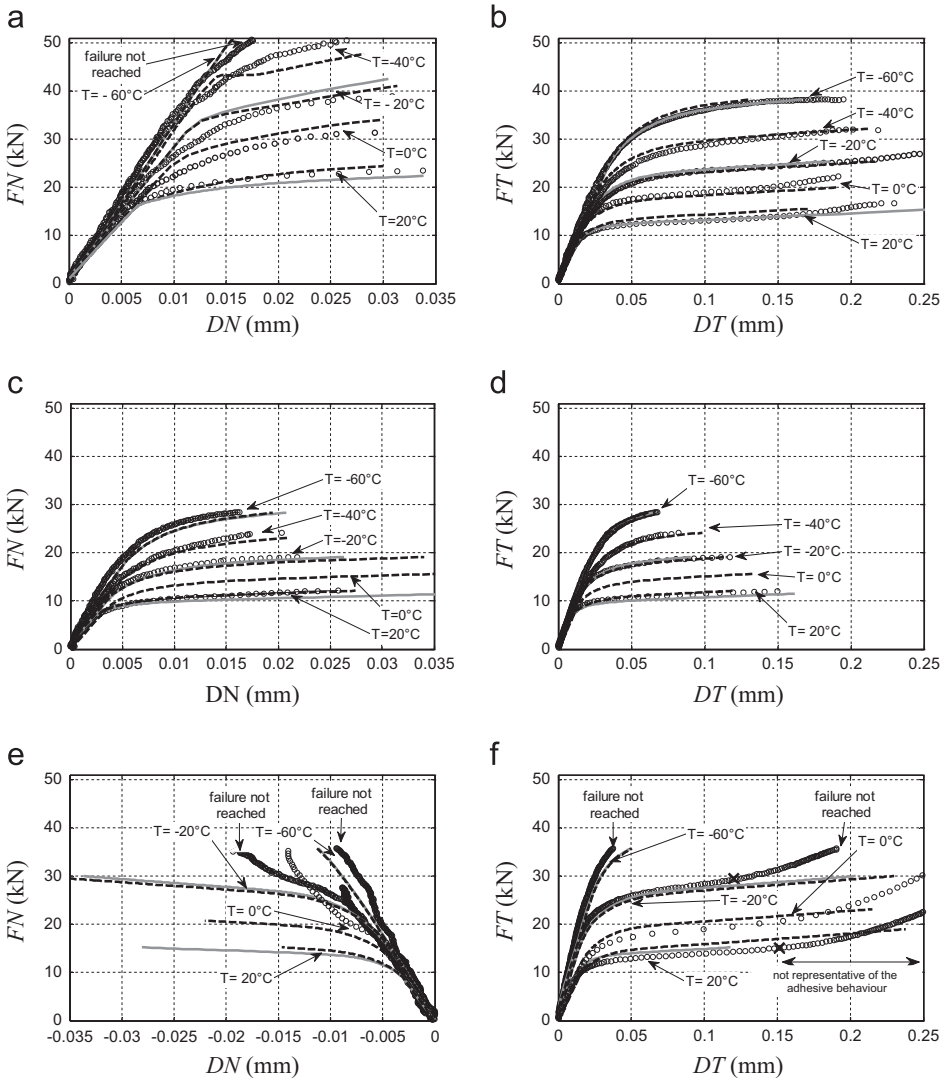


Fig. 16. Influence of the temperature on the mechanical behaviour of the adhesive in the load-relative displacement diagram for different monotonic radial loads (**o o o o**: experimental results; (▬) identification at a given temperature; - - - - - -: temperature-dependent model). (a) tensile loading—$\gamma=0^\circ$, (b) shear loading—$\gamma=90^\circ$, (c) tensile–shear—$\gamma=45^\circ$—normal direction, (d) tensile–shear—$\gamma=45^\circ$—tangential direction, (e) compression–shear—$\gamma=135^\circ$—normal direction, (f) compression–shear—$\gamma=135^\circ$—tangential direction.

Author's personal copy

the different points, of the temperature-dependent initial elastic limit are plotted in the von Mises equivalent stress—hydrostatic stress diagram. The points represented by the marks "o" are obtained using only the mechanical load and the marks "▲" are computed using the residual stresses, the thermal stresses and the mechanical load. The differences between the two results are quite large. Thus, for each temperature, it is possible to model the initial elastic limit using Eq. (4). The values of the material parameters (a_1, a_2 and Y_0) are presented in Table 3 for each temperature.

In order to obtain an accurate representation of the initial elastic limit at the different temperatures studied, the following time evolution of the material parameters was chosen:

$$a_1(T) = c_1 T + c_2$$
$$a_2(T) = c_3 T + c_4$$
$$Y_0(T) = c_5 T^2 + c_6 T + c_7 \quad (9)$$

The results of the identification are presented in Table 4. Fig. 14 presents a comparison between the experimental results (marks) and the numerical model (dashed lines) for the different temperatures studied in the hydrostatic pressure–von Mises stress diagram. A good representation of the experimental results is obtained using such a type of representation.

The simplified inverse identification approach developed for the hardening function [25] cannot be directly used under thermo-mechanical loads. In fact, the initial thermal load changes the stress state associated with a mechanical shear load: the hydrostatic stress is not equal to zero for such loading which leads to plastic deformations in the normal and tangential directions. In order to reduce the numerical cost of the material parameter identification, a first step is proposed using the simplified approach. In a second step, starting from the previous results, a global approach, for the hardening function and the flow rule parameters is taken. It can be noted that the results obtained in the first step are quite good.

The identification of the material parameters for the hardening function and the flow rule (parameters q, b, H, a_2^* and a_3^*) was accomplished for the following temperatures (20, −20 and −60 °C) and the results are presented in Table 5. A representation of the temperature dependence of the material parameters has been proposed as follows:

$$q(T) = d_1 T + d_2$$
$$b(T) = d_3 T + d_4$$
$$H(T) = d_5 T + d_6$$
$$a_2^*(T) = d_7 T + d_8$$
$$a_3^*(T) = d_9 T + d_{10}$$

The results of the identification are presented in Table 6.

Fig. 15 presents the evolution of the hardening functions and the flow functions with respect to temperature. This figure underlines, through the non-associated elastoplastic pressure dependent model used, the influence of the temperature on the non-linear behaviour of the adhesive. The shape of the initial flow rules close to pure shear loadings (hydrostatic stress equal to zero) underlines the feasibility of the first step of the proposed inverse identification technique, especially for the identification of the hardening functions.

In order to increase the precision of the identification of the model for compression–shear mechanical loads, we recommend a more precise measurement of the normal displacement for such tests to be performed. It is important to notice that the measurement of the displacement is made through the view-glass of the thermal chamber and the relative displacement of the two substrates is very low in the normal direction for such tests.

Fig. 16 presents in the load–displacement diagrams (in the normal and tangential directions) experimental results and numerical solutions obtained with the proposed non-associated elastoplastic pressure dependent model taking into account residual and thermal stresses. For the temperatures (20, −20 and −60 °C) the following loadings were used for the identification procedure (tensile–shear (γ=45°), shear (γ=90°) and compression–shear (γ=135°)). Results under tensile loading can be considered to be a validation test for the proposed numerical model.

The comparisons between experimental and numerically identified results (identification at a given temperature and temperature-dependent model) are presented in Fig. 16. In each case, the numerical results are in good agreement with the experimental results.

In order to complete this modelling study an analysis of the influence of the different material parameters on the response of the numerical model has to be performed. Moreover a global identification of the temperature-dependent material parameters of the 3D elastic–plastic Mahnken–Schlimmer type model taking into account the whole experimental results (for the different tensile/compression–shear loads and for the different temperatures) can also improve a little the prediction of the numerical

Table 3
Temperature evolution of the elastic parameters of the adhesive and of the material parameters for the initial yield surface.

T (°C)	Ea (MPa)	νa (−)	a_1 (−)	a_2 (−)	Y_0 (MPa)
20	2200	0.34	0.988	−0.024	40.72
0	2480	0.34	0.905	0.045	53.01
−20	2764	0.34	0.923	0.029	70.23
−40	2965	0.34	1.024	0.023	94.70
−60	3152	0.34	1.066	−0.067	123.22

Table 4
Material parameters for the modelling of the temperature-dependent initial yield surface.

c_1 (1/°C)	c_2 (−)	c_3 (1/°C)	c_4 (−)	c_5 (MPa/°C^2)	c_6 (MPa/°C)	c_7 (MPa)
0.0002989	0.9745	−0.008077	0.5171	0.00758	−0.7588	55.21

Table 5
Material parameters for the evolution laws for the following temperatures (20, −20 and −60 °C).

T (°C)	q (MPa)	b (−)	H (MPa)	a_2^* (−)	a_3^* (−)
20	4.0	21.0	14.28	0.97	0.97
−20	10.94	20.07	19.79	1.43	0.50
−60	9.71	5.03	18.17	2.07	0.10

Table 6
Material parameters for the modelling of the temperature-dependent flow rules.

d_1 (MPa/°C)	d_2 (MPa)	d_3 (1/°C)	d_4 (−)	d_5 (MPa/°C)	d_6 (MPa)	d_7 (1/°C)	d_8(−)	d_9 (1/°C)	d_{10} (−)
−0.04733	8.305	0.2546	20.69	−0.0684	17.9	−0.01375	1.215	0.0109	0.7408

Author's personal copy

model by giving nearly the same weight for the different experimental results.

5. Conclusions

The behaviour of adhesively-bonded joints under thermo-mechanical loadings has been analysed; especially, the influence of low temperatures has been studied for a ductile adhesive. It has been shown, using finite element simulations with refined meshes, that for bonded assemblies a coupling between the influences of edge effects under mechanical loads and under thermal loads can exist. Therefore, the results of experimental analysis can be greatly influenced by the stress concentrations at the ends of the overlap length. Numerical simulations, under elastic assumptions, have shown that the modified Arcan device, which was previously designed to strongly limit the influence of the edge effects under mechanical loads, is also suitable for the analysis of the influence of low temperatures on the mechanical behaviour of an adhesive in an assembly.

Starting from experimental results under various compression/tensile–shear tests and under low temperature (from 20 to 60 °C) it has been shown that a 3D elastic–plastic Mahnken–Schlimmer type model can accurately represent the temperature-dependent behaviour of a ductile adhesive under a wide range of proportional monotonic mechanical loads. The analysis of the results of experimental tests under thermal load followed by a mechanical load has to take into account the non-proportional properties of such loads. Moreover, such an analysis can also take into account the residual stresses in the adhesive in a bonded assembly associated with the curing process.

Accurate numerical models of adhesive behaviours for a wide range of thermo-mechanical loads are necessary to optimise the design of bonded assemblies for high-tech applications. Thus, it is interesting to extend this study for very low or cryogenic temperatures, for instance in order to analyse the behaviour of huge superconducting magnets using cooling system with a 4 K pressurised bath of Helium [34]. Moreover, it is interesting to extend this study to high temperatures. Such condition, require taking into account the influence of viscous effects of the adhesive and the possible increase in stress concentrations associated with the decrease in Young's modulus of the adhesive with respect to the increase in the temperature.

References

[1] da Silva LFM, Öchsner A. Modeling of adhesive bonded joints. Berlin: Springer; 2008.
[2] da Silva LFM, Öchsner A, Adams RD. Handbook of adhesion technology. Heidelberg: Springer; 2011.
[3] Volkersen O. Die Nietkraftverteilung in Zugbeanspruchten Nietverbindungen mit Konstanten Laschenquerschnitten. Luftfahrtforschung 1938;15:41–7.
[4] Lubkin JL, Reissner E. Stress distribution and design data for adhesive lap joints between circular tubes. Transactions of the ASME 1956;78:1213–21.
[5] Dean G, Crocker L, Read B, Wright L. Prediction of deformation and failure of rubber-toughened adhesive joints. International Journal of Adhesion and Adhesives 2004;24:295–306.
[6] Cognard JY, Créac'hcadec R, Sohier L, Davies P. Analysis of the non linear behaviour of adhesives in bonded assemblies. Comparison of TAST and ARCAN tests. International Journal of Adhesion and Adhesives 2008;28:393–404.
[7] Raghava RS, Cadell RM. The macroscopic yield behaviour of polymers. Journal of Materials Science 1973;8:225–32.
[8] Wang CH, Chalkley P. Plastic yielding of a film adhesive under multiaxial stresses. International Journal of Adhesion and Adhesives 2000;20:155–64.
[9] Mahnken R, Schlimmer M. Simulation of strength difference in elasto-plasticity for adhesive materials. International Journal for Numerical Methods in Engineering 2005;63:1461–77.
[10] da Silva LFM, Adams RD. Stress-free temperature in a mixed-adhesive joint. Journal of Adhesion Science and Technology 2006;20:1705–26.
[11] Yu Y, Ashcroft IA, Swallowe G. An experimental investigation of residual stresses in an epoxy–steel laminate. International Journal of Adhesion and Adhesives 2006;26:511–9.
[12] Jumbo FS, Ashcroft IA, Crocombe AD, Abdel Wahab MM. Thermal residual stress analysis of epoxy bi-material laminates and bonded joints. International Journal of Adhesion and Adhesives 2010;30:523–38.
[13] Li C, Potter K, Wisnom MR, Stringer G. In-situ measurement of chemical shrinkage of MY750 epoxy resin by a novel gravimetric method. Composites Science and Technology 2004;64:55–64.
[14] Wang X, Geng H, He S, Pokhyl YO, Koval KV. Effect of thermal expansion coefficient on the stress distribution in solar panel. International Journal of Adhesion and Adhesives 2007;27:288–97.
[15] da Silva LFM, Adams RD. Measurement of the mechanical properties of structural adhesives in tension and shear over a wide range of temperatures. Journal of Adhesion Science and Technology 2005;19:109–41.
[16] Kim MG, Kang SG, Kim CG, Kong CW. Tensile response of graphite/epoxy composites at low temperatures. Composite Structure 2007;79:84–9.
[17] Ioka S, Kubo S, Ohji K, Kishimoto J. Thermal residual stresses in bonded dissimilar materials and their singularities. JSME International Journal-Series A: Solid Mechanics and Material Engineering 1996;39:197–203.
[18] Apalak MK, Gunes R. On non-linear thermal stresses in an adhesively bonded single lap joint. Computers and Structures 2002;80:85–98.
[19] Badulescu C, Cognard JY, Créac'hcadec R, Vedrine P. Analysis of the temperature-dependent behaviour of a ductile adhesive under monotonic tensile/compression-shear loads. International Journal of Adhesion and Adhesives 2012;36:56–64.
[20] Wang HB, Yang WG, Yu HH, Sun WM. Assessment of residual stresses during cure and cooling of epoxy resins. Polymer Engineering and Science 1995;35:1895–8.
[21] Loh WK, Crocombe AD, Abdel Wahab MM, Ashcroft IA. Modelling anomalous moisture uptake, swelling and thermal characteristics of a rubber toughened epoxy adhesive. International Journal of Adhesion and Adhesives 2005;25:1–12.
[22] Liljedahl CDM, Crocombe AD, Wahab MA, Ashcroft IA. The effect of residual strains on the progressive damage modelling of environmentally degraded adhesive joints. Journal of Adhesion Science and Technology 2005;19:525–47.
[23] Humfeld GR, Dillard DA. Residual stress development in adhesive joints subjected to thermal cycling. Journal of Adhesion 1998;65:277–306.
[24] Bordes M, Davies P, Cognard JY, Sohier L, Sauvant-Moynot V, Galy J. Prediction of long term strength of adhesively bonded joints in sea water. International Journal of Adhesion and Adhesives 2009;29:595–608.
[25] Maurice J, Cognard JY, Créac'hcadec R, Davies P, Sohier L, Mahdi S. 3D modeling of the behavior of an adhesive in an assembly using a non-associated elasto-plastic pressure dependent model. Journal of Adhesion Science and Technology 2012:1–17, http://dx.doi.org/10.1080/01694243.2012.701528.
[26] Lee CS, Chun MS, Kim MH, Lee JM. Debonding failure characteristics of multi-laminated bonding system under cryogenic temperature. International Journal of Adhesion and Adhesives 2011;31:226–37.
[27] Cognard JY. Numerical analysis of edge effects in adhesively-bonded assemblies. Application to the determination of the adhesive behaviour. Computers and Structures 2008;86:1704–17.
[28] ASTM D5656-95. Standard test method for thick-adherend metal lap-shear joints for determination of the stress–strain behavior of adhesives in shear by tension loading. ASTM; 1995 www.astm.org.
[29] Cognard JY, Davies P, Sohier L, Creac'hcadec R. A study of the non-linear behaviour of adhesively-bonded composite assemblies. Composite Structures 2006;76:34–46.
[30] Althof WCreep. Recovery and relaxation of shear-loaded adhesive bondlines. Journal of Reinforced Plastics and Composites 1982;1:29–38.
[31] Sancaktar E, Simmons SR. Optimisation of adhesively-bonded single lap joints by adherend notching. Journal of Adhesion Science and Technology 2000;14:1363–404.
[32] Cognard JY, Creac'hcadec R. Analysis of the non linear behaviour of an adhesive in bonded assemblies under shear loadings. Proposal of an improved TAST. Journal of Adhesion Science and Technology 2009;23:1333–55.
[33] Cognard JY, Créac'hcadec R, da Silva LFM, Teixeira FG, Davies P, Peleau M. Experimental analysis of the influence of hydrostatic stress on the behaviour of an adhesive using a pressure vessel. Journal of Adhesion 2011;87:804–25.
[34] Rey JM, Gallet B, Kircher F, Lottin JC. Epoxy resin developments for large superconducting magnet impregnation. Cryogenics 1998;38:19–23.

2.4 Influence de l'environnement à différentes échelles

Les structures collées étudiées se retrouvent dans des secteurs industriels divers et variés comme l'aéronautique, le médical, le naval, l'automobile ou bien le spatial. La nature des adhésifs est principalement imposée par les spécifications de l'application visée, en étroite cohérence avec le cahier de charges. Pour les liaisons structurelles, les adhésifs thermodurcissables époxy bi-composants sont les plus adaptés. Néanmoins ces adhésifs sont avant tout, des matériaux de type polymère pour lesquels l'environnement pourrait avoir une influence significative sur la résistance mécanique du joint [94], [95], [96], et plus particulièrement sur son comportement thermo-mécanique. Deux facteurs majeurs sont susceptibles d'influencer de manière significative la tenue d'une telle liaison : *i)* la température [97], [98], [99] et *ii)* l'humidité [100], [101]. Alors ces influences doivent être prises en compte tant sur le comportement mécanique jusqu'à rupture que dans les stratégies de dimensionnement.

D'abord, l'influence de la température a été étudiée sur des adhésifs époxy pour un large spectre de températures (entre -60°C et 120°C). En collaboration avec le CEA de Saclay nous avons pu réaliser des essais Arcan modifié à 4°K dans des cryostats à hélium liquide. La difficulté ici est d'obtenir le comportement mécanique fiable dans ces conditions extrêmes, et qui sera ensuite la base pour la construction et l'identification des modèles de comportement mécanique. En conséquence, des approches expérimentales ont été développées et appliquées pour mettre en évidence l'effet de la température sur le comportement mécanique non linéaire tant de l'adhésif lui-même (échantillons massiques), que de l'assemblage. Sur la base de ces investigations, des modèles de comportement ont été proposés en modélisant les différentes briques élémentaires de comportement mécanique comme l'élasticité, la viscosité, la plasticité, etc., mais surtout l'influence de la température sur ces mécanismes élémentaires [12], [9]. De plus, ces connaissances expérimentales ont été intégrées dans les stratégies d'identification des paramètres de modèles afin de s'affranchir de différents biais qui pourraient altérer les différentes hypothèses. Pour rappel, que les contraintes thermiques et résiduelles sont systématiquement intégrées dans la procédure d'identification des paramètres matériels.

Ensuite, l'effet de l'humidité sur le comportement de l'adhésif a été examiné. Des échantillons massiques obtenus dans des conditions similaires à celles de l'assemblage ont été conditionnés de différentes manières (immersion dans de l'eau déionisée ou de mer ou maintien à différents taux d'humidité) jusqu'à saturation. Des essais mécaniques sur ces échantillons sont alors réalisés et finement dépouillés permettant ainsi de mettre en évidence l'effet de l'eau sur le comportement mécanique de l'adhésif. Toutefois, la question relative au temps de maintien dans l'environnement humide pour atteindre la saturation est encore ouverte, car très difficile de déterminer expérimentalement le front d'eau dans l'échantillon d'adhésif même si sa masse n'évolue quasiment plus. Il est légitime de se poser alors des questions sur la modélisation de l'évolution de la prise en eau. Des modèles phénoménologiques (Fick, dual Fick ou Langmir, etc.) sont disponibles, mais le choix judicieux entre l'un ou l'autre reste encore une question ouverte [102],

[103], [104]. Alors des analyses plus fines en utilisant la tomographie aux rayons X sont proposées. Cette technique a permis de mettre en évidence, dans un premier temps, la microstructure volumique du joint (matrice adhésive, défauts, charges, etc.) et par la suite le gonflement hydrique comme une conséquence directe de prise en eau [49]. Pour des adhésifs époxy bi-composants, les défauts de type pores sont clairement visibles. La variation de volume et la cinétique de remplissage des pores par l'eau ont été identifiées avec précision. L'étude du remplissage de ces pores au cours du temps de vieillissement a permis de choisir entre différents modèles de manière plus judicieuse. Ces choix de modèles de diffusion sont cruciaux dans une logique de prédiction du comportement local via des modèles numériques, notamment pour des assemblages complexes où le front d'eau est susceptible de présenter un gradient. Très récemment, des résultats obtenus dans la thèse d'Andrea TINTATU montrent une corrélation très encourageante entre les résultats expérimentaux et numériques.

Enfin, il a été également observé que le couplage entre la température et l'humidité [105] pourrait conduire à des évolutions de comportement mécanique inattendues. Ces évolutions pourraient être expliquées, en partie, par l'effet de remplissage des pores sur le comportement mécanique, mais également par des phénomènes complexes liés au vieillissement physique du polymère.

Publications jointes

- A. Ilioni, P.Y. Le Gac, C. Badulescu, D. Thévenet, P. Davies, **Prediction of Mechanical Behaviour of a Bulk Epoxy Adhesive in a Marine Environment**, *The Journal of Adhesion*, 95 :1, 64-84,(2019),
  DOI : 10.1080/00218464.2017.1377616
- A. Tintatu, C. Badulescu, P. Bidaud, P. Le Grognec, J. Adrien, E. Maire, H. Bindi, C. Coguenanff, **Understanding of water uptake mechanisms in an epoxy joint characterized by pore-type defects**, (2023), *The Journal of Adhesion*,
  DOI : 10.1080/00218464.2023.2187293

Références associées : Bibliographie des publications

THE JOURNAL OF ADHESION
2019, VOL. 95, NO. 1, 64–84
https://doi.org/10.1080/00218464.2017.1377616

Taylor & Francis
Taylor & Francis Group

Check for updates

Prediction of Mechanical Behaviour of a Bulk Epoxy Adhesive in a Marine Environment

Alin Ilioni[a,b], Pierre-Yves Le Gac [b], Claudiu Badulescu[a], David Thévenet[a], and Peter Davies[b]

[a]ENSTA Bretagne, Brest, France; [b]Marine Structures Laboratory, IFREMER, Plouzané, France

ABSTRACT

This article describes an approach to predict the behaviour of an epoxy adhesive in bulk form in a marine environment. First, the material, the experimental conditions and the predictive framework are described. Then the experimental results are presented, which indicate that the effects on yield stress of either a uniform water profile or elevated testing temperature can be shown to be equivalent when plotted versus T-Tg. Moreover, a discussion of these results shows how they can be used to predict changes in the mechanical properties of the adhesive. Prediction results for yield stress are in good agreement when they are compared with experimental results for the case of a water profile gradient, in order to evaluate the relevance and limitations of the model.

ARTICLE HISTORY
Received 17 July 2017
Revised 6 September 2017
Accepted 6 September 2017

KEYWORDS
Epoxide; water ageing; glass transition temperature; mechanical properties of adhesives; plasticisation

1. Introduction

Structural adhesives have a long history in marine applications, playing a key role in the assembly of pleasure boats and racing craft.[1] The interactions between water and polymers have been studied by many authors, and effects are usually classified as either reversible (plasticisation[2], swelling[3]) or irreversible (hydrolysis[4], oxidation). The influence of water on epoxy resins has received particular attention. *Zhou & Lucas* described how water bonds with epoxy resins[5], and how this reduces the glass transition temperature.[6] Various studies have shown that significant amounts of water can enter epoxies. For those with amine hardener water content is usually less than 5%. Much higher water content can be observed when the polarity of the polymer increases or when fillers are used. Epoxy based adhesive formulations are more complex, often containing small amounts of fillers and other additives to assist bonding operations. For some epoxy adhesives and exposure conditions the weight gain plots show Fickian behaviour, *e.g.*[7], in others more complex behaviour is observed. For example, *De Nève* and *Shanahan* showed an initial Fickian response followed by a second increase

CONTACT Alin Ilioni alin.ilioni@ensta-bretagne.org Institute de Recherche Dupuy de Lôme, 2 rue François Verny, 29806, Brest, Cedex 09, France.

Colour versions of one or more of the figures in the article can be found online at www.tandfonline.com/gadh.

© 2017 Taylor & Francis

in weight for an epoxy adhesive[8], while *Mubashar et al.*[9] proposed a dual Fickian model for water ingress into a rubber toughened 120°C cure one-part epoxy system.

This water can be quite detrimental to both adhesive properties and their assembled joints, and environmental effects are often cited as one of the main reasons for not using adhesive assembly more extensively.[10] For example, *Bordes et al.*[11] showed drops in adhesive tensile modulus and strength after saturation of up to 50% of initial unaged values.

In many cases, complete restoration of property losses has been noted after drying *e.g.*[12], suggesting that adhesive plasticisation is the dominant mechanism.

In assembled joints the adhesive/substrate interfaces must also be considered. For example, *Zanni-Deffarges & Shanahan* described diffusion of water in adhesives and bonded joints.[13] They found considerably higher diffusion coefficients for the bonded joint, and suggested that capillary diffusion exacerbates water ingress, but when focusing on water diffusion in bulk specimens, these considerations can be neglected. *Brewis et al.*[12] found a linear relationship between joint strength and the water content of metal/epoxy joints, but a strong dependency on the aluminium surface preparation, with strength either decreasing or increasing as water content increased. This is not the subject here but it is interesting to note that some authors have suggested that the presence of a critical amount of water at the interface leads to interface failure.[14] A reliable diffusion model is essential to predict the local water concentration. Finally, it should be noted that residual stresses may also have a significant influence on the environmental degradation of adhesive assemblies[15]

There are several useful reviews available concerning moisture effects on adhesive joints; *Bowditch* presented an overview of the influence of water on durability[16] and C*omyn* and colleagues have provided detailed reviews of environmental effects.[17–19]

This brief overview shows that there are a number of relevant test results in the published literature, and there is also considerable practical experience of the long-term reliability of adhesives in water. However, it is also clear that there is a range of behaviours which depend on adhesive formulation and environmental conditions, and there are few predictive tools available to the designer looking to develop bonded assemblies in new marine applications, such as renewable marine energy structures. There are some exceptions, in particular, the work of *Crocombe et al.*[20–22], who have developed an overall methodology and also specific approaches based on both damage mechanics-[23] and cohesive zone models[24] to account for the influence of moisture in a coupled approach.

Bordes et al.[11] also describe a partially coupled approach to predict long term behaviour during immersion, while other recent work includes that of

Arnaud et al.[25], who applied a *Mahnken–Schlimmer* model[26] with parameters identified on unaged and aged Arcan specimens. *Leger et al.*[27] *have* also studied coupling effects; they examined temperature/humidity equivalence in a highly filled adhesive and modelled the influence on mechanical behaviour. Moreover, *Viana et al* presented a review on the temperature and moisture degradation of adhesive joints[28] and correlated the glass transition temperature of a bulk epoxy adhesive with the water uptake to determine the evolution of its properties as a function of environmental temperature and moisture.[29]

The aim of the present article is to focus on how water ingress in a two-part epoxy adhesive, widely used in marine applications, affects its mechanical behaviour, in order to provide a physically based relationship for subsequent predictive modelling. First, results from a wet aging study are presented. Samples have then been characterised in tension; a first set was tested after conditioning to saturation for different humidity conditions, to produce uniform water profiles through the sample thickness; a second set was tested at different temperatures. A semi-coupled model is then applied, to predict the water profiles in immersed samples and predict their tensile behaviour. Finally, predictions of stress-strain plots are compared to test results from a third set of tensile samples immersed for different times.

2. Material and Methods

2.1. *Material*

Samples studied here were obtained using thin bulk samples made from the epoxy based Huntsman™ (Europe, B-Everberg) adhesive *Araldite 420 A/B*. This is an epoxy with a Bisphenol A diglycidyl ether prepolymer and a diamine hardener mixed in stoichiometric conditions. Table 1 summarises initial properties of the bulk adhesive.

2.2. *Samples Preparation*

The samples used for this study were obtained from a sheet of adhesive made by mixing 100 parts by weight of the resin A and 40 parts by weight of the hardener B using a *Speedmixer* at 2500 rpm for 5 minutes. The mixture was compressed between two aluminium plates and the final thickness was controlled using

Table 1. Main characteristics of the Araldite 420 studied here.

Property	Value
Density	1075 g/cm^3
Inorganic filler content	4 ± 1%
Tg	66°C ± 2°C
Young's Modulus	1850 ± 80 MPa
Yield Stress	36 ± 1 MPa

1mm thick spacers. Then the polymer was cured for 1h10 at 115°C. After curing, sheets were removed from the mould and thermally post treated for 1 hour at 80°C (i.e. above Tg) in order to remove any residual stresses. Samples were then cut out from the sheets using a water jet cutting system.

2.3. *Ageing*

Two kinds of ageing were considered here. The first is immersion in continuously renewed natural sea water taken directly from the Brest estuary, more details about Ifremer ageing tanks are available in.[30] The second is a humid ageing at three humidity level (33, 50 and 75%) carried out in a Memmert™ conditioning chamber, type HP110. All ageing was performed at 40 ± 1°C and all samples were dried prior to ageing at 40°C in a desiccator until mass stabilisation.

2.4. *Water Absorption*

The water diffusion was determined from the weight change of square samples (30x30mm^2). Mass gain was followed by periodic weighing on a Sartorius™ LA 310 S balance (precision 0.1 mg). Samples were removed from the ageing containers and wiped with article towels before weighing to dry the surfaces, three samples were tested per condition. The change in water content in each sample (M_t) with time is defined with respect to the initial mass of the sample (m_0) using Eq.1, where m(t) is the mass of a sample at a time t and m_0 the initial mass.

$$M_t = \frac{\mathrm{m(t)} - m_0}{m_0} \times 100 \qquad \text{(Eq.1)}$$

Given the dimensions of the samples, the water diffusion was considered unidirectional. The diffusion coefficient is determined on the initial linear part of the sorption curve, $\frac{M_t}{M_\infty} \leq 0.5$, M_∞ being the mass at complete saturation. Its value is calculated using Fick's 1D law (Eq.2):

$$D = \frac{\pi}{16}\frac{e^2}{t} \times \left(\frac{M_t}{M_\infty}\right)^2 \qquad \text{(Eq.2)}$$

where, e is the sample thickness in *mm* and *t* is the immersion time in s.

2.5. *Glass Transition Temperature (Tg) easurements*

Tg was measured using DSC analysis. The experimental device used for this measurement is a Q200 machine from TA Instruments™, with a temperature scan between 0°C and 100°C at a heating rate of 10°C/min.

2.6. Tensile Tests

Tensile tests were performed using at least three dog-bone samples per condition (type 3 in ISO 37[31]) and an Instron™ machine with a cross head speed of 0.5 mm/min. The load was measured using a 500N load cell and the strain using a digital image correlation system (DIC).

If not specified, the testing temperature was 21°C. When samples were tested at higher temperature the samples were held for 20 minutes in the thermal chamber, at the testing temperature, to homogenise the temperature in the thickness of the sample before testing.

Young's modulus is defined as the slope between 0 and 2% strain. An average and a standard deviation are then calculated using all the tested samples for each condition. The yield stress is considered to be the point where the first derivative of the stress-strain curve changes by more than 5% of the initial value. Poisson's coefficient is defined as the ratio between the average transverse and longitudinal strains measured by DIC.

2.7. Modelling of Mechanical Behaviour

The mechanical model used here to predict the changes in mechanical properties with water conditioning is a simplified version of a more complete viscoelastic-viscoplastic model developed to describe the mechanical behaviour of the adhesive in a bonded joint. The total strain (ε_{tot}) is supposed to be the sum of the elastic strain (ε_{el}), the viscoelastic strain (ε_{ve}) and the viscoplastic strain (ε_{vp}), as shown in Eq.3.

$$\varepsilon_{tot} = \varepsilon_{el} + \varepsilon_{ve} + \varepsilon_{vp} \quad \text{(Eq.3)}$$

The viscoelastic part (ε_{ve}) is described using a modified version of the viscoelastic spectral model developed by *Badulescu et al.*[32] and the parameters were identified using the presented method. The viscoplastic strain (ε_{vp}) is based on an approach developed by *Cognard et al.*[33] In the current version, it was used in an associated model where both the yield and flow functions are defined using the same function which has a linear dependency on the hydrostatic pressure.

The viscoelastic parameters and the hardening parameters were identified using initial state behaviour (no ageing) and were considered here not to be dependent on environmental conditions. The parameters used to model the evolution of the mechanical properties of the tensile behaviour as a function of water quantity are the Young's modulus, Poisson's ratio and the yield stress.

The mechanical model has been implemented in Abaqus™ software. In parallel a diffusion model was developed using the equivalence between the water diffusion and the heat transfer (Eq.4):

$$D = \frac{\lambda}{\rho C} \qquad \text{(Eq.4)}$$

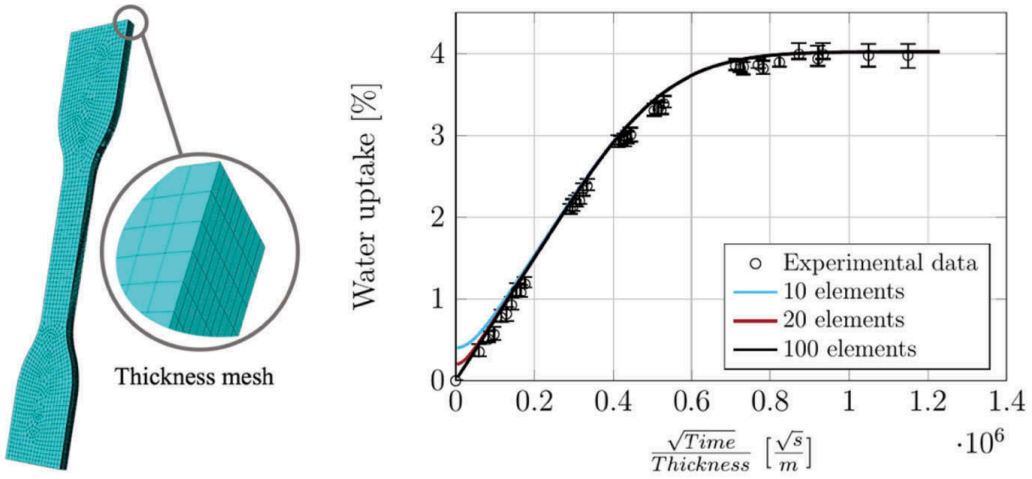
where D is the diffusion coefficient in the immersed condition, ρ the density of the material, C the heat capacity and, λ the thermal conductivity. Using this model, it is possible to establish the water profile in the thickness of a sample that was immersed in water for a defined period. For this approach, the diffusion was supposed to be unidirectional and the quantity of water diffused through the edges of the sample was considered negligible.

The Finite Elements (FE) mesh, more precisely, the number of elements in the thickness of the specimen (Figure 1a) is very important in order to obtain a good prediction of the water diffusion at the beginning of the process. Therefore, a convergence analysis has been performed. The results are shown in Figure 1b. It can be seen that 100 elements in the thickness of the sample are sufficient to obtain a good prediction of the mass change of the sample due to water absorption.

This diffusion model enables the water profiles through the thickness direction to be established. The changes in the mechanical properties are then related to the water content and integrated at each point of the specimen through the FE mesh.

3. Results

This section is devoted to the presentation of experimental results. First, we will focus on water absorption and then on the consequences of the presence of water on both tensile behaviour and Tg changes.



a) b)

Figure 1. FE model used for used for mechanical behaviour prediction (a), convergence study for water uptake prediction (b).

3.1. *Water Absorption*

The mass variation measured during exposure of the polymer to a wet environment at 40 °C is plotted in Figure 2. For each of the conditions considered herein, *i.e.* a relative humidity of 33%, 50% and 75% and immersion in sea water, Fickian behaviour is observed, with increasing weight gain during the first stage of ageing and then the appearance of a saturation plateau. Based on these results it is possible to consider two main characteristics for water diffusion: the water diffusivity and the amount of absorbed water.

The water diffusion coefficient is equal to $1.15\text{x}10^{-12}$ $m^2.s^{-1}$ at 40°C and independent of the relative humidity as shown in Figure 3a. This value is in accordance with existing results in the literature for epoxy material with an amine hardener.[3,34]

The water uptake in the epoxy adhesive at saturation when immersed in sea water at 40°C is 4% by mass, this amount of water is also similar to previous results obtained on epoxy with amine hardener; the presence of a polar group such as amine leads to this high-water absorption. Moreover, as expected, the amount of absorbed water at saturation depends on the water activity in the surrounding environment. The higher the water activity the higher the water content at saturation in the polymer as shown in Figure 3b. However, it also appears that water content at saturation is not directly proportional to the partial pressure of water indicating that Henry's law is not verified here. The water content in the epoxy adhesive has been described based on an existing relationship (Eq.5) developed elsewhere[35,36]:

$$W_{H_20} = H \times a + N \times a^m \tag{5}$$

where W_{H_20} is the water content in the polymer in %, a is the water activity in the surrounding environment and H, N and m are parameters identified experimentally.

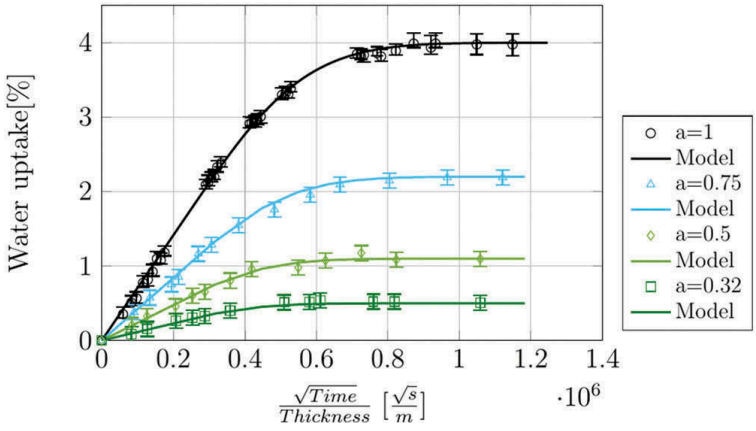


Figure 2. Water absorption in the polymer for ageing conditions considered here (symbols are experimental data and lines are modelling with Fickian behaviour).

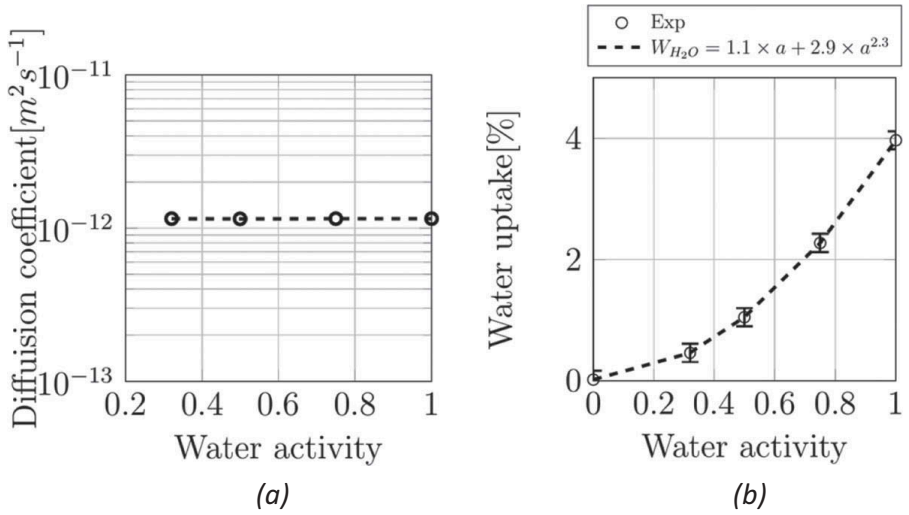


Figure 3. Influence of the water activity in the environment on water diffusion coefficient (a) and water content at saturation in the epoxy (b).

This behaviour is usually explained by a clustering phenomenon where the molecules can form microscopic droplets of water.[37,38] This will not be considered in detail in this study.

3.2. *Tensile Behaviour Changes with Water Content*

This section is focused on the effect of the presence of water in the polymer on its mechanical properties. It is worth nothing that all the results presented in this section were obtained on fully saturated samples but with different amounts of water, meaning that there is no water profile through the specimen thickness. Tensile behaviour for several water contents is plotted in Figure 4. The presence of water leads to large change in the mechanical behaviour of this epoxy with a large decrease in yield stress, modulus and an increase in strain at break. All these changes in properties are plotted in Figure 5 together with the Poisson's ratio.

3.3. *Decrease of Tg with the Water Content at Saturation*

Figure 6 shows the Tg values as a function of water content in samples. A large decrease from 66°C in the dry state to 40°C after saturation in sea water (*i.e.*, with 4% of water) is observed. The water solubility in polymers is not related to the state of the material meaning that the amount of water absorbed by a polymer (with no fillers) is not significantly affected when the polymer goes from the glassy to the rubbery state. This behaviour can be explained by the fact that the presence of water in the polymer leads to an increase of the macromolecular chains mobility and so a decrease in Tg. This

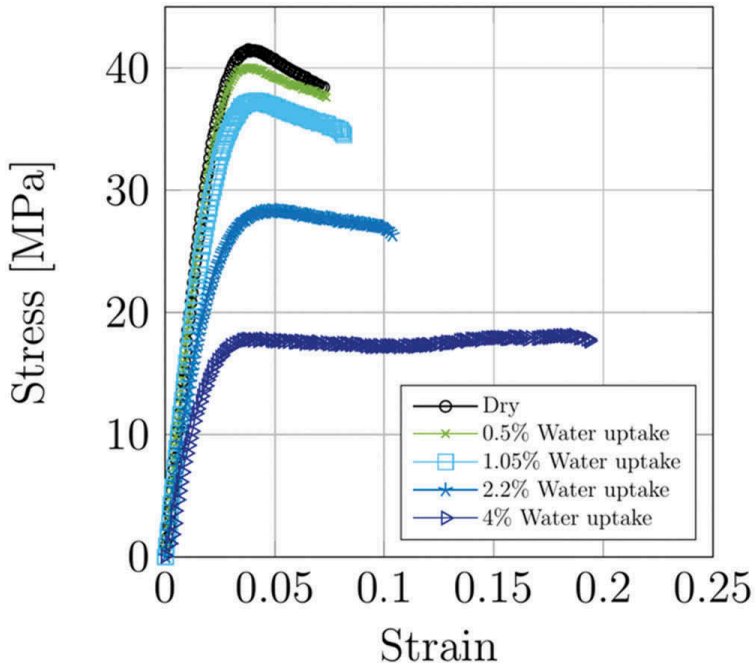


Figure 4. Tensile behaviour as a function of water content at saturation (i.e. without any water profile gradient through the thickness).

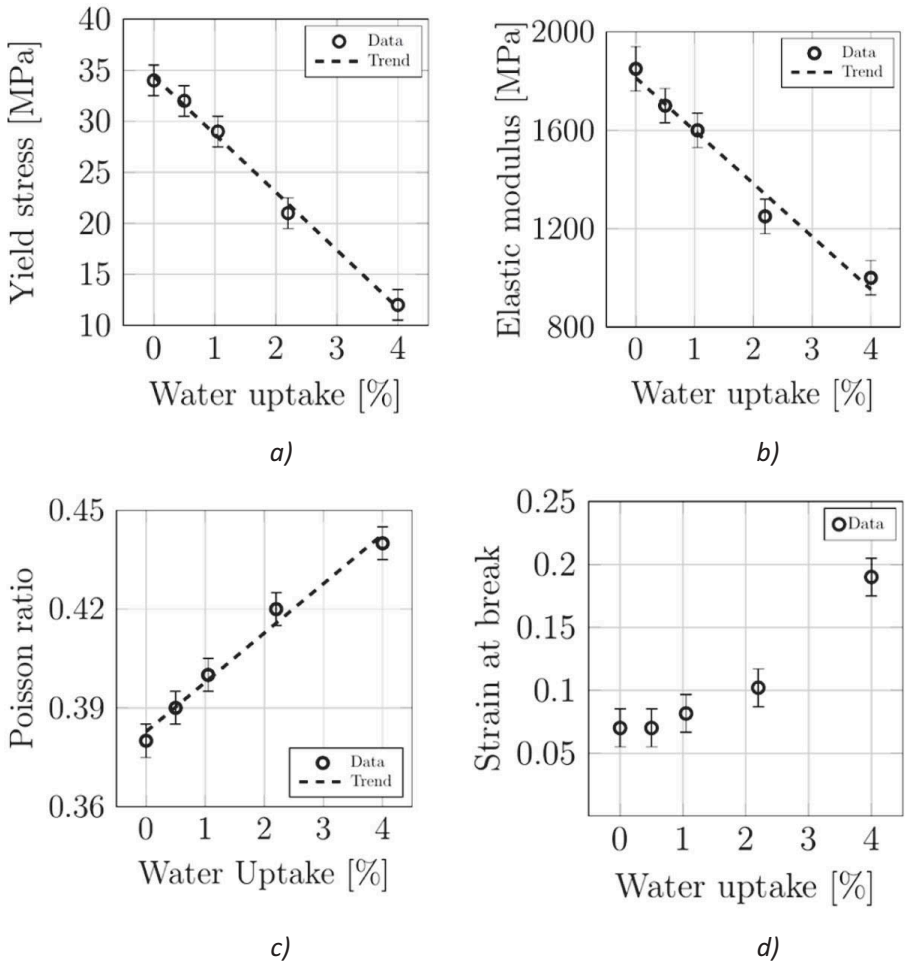


Figure 5. Change in yield stress (a), Young's modulus (b), Poisson's ratio (c), and Strain at break (d), as a function of water content in the polymer.

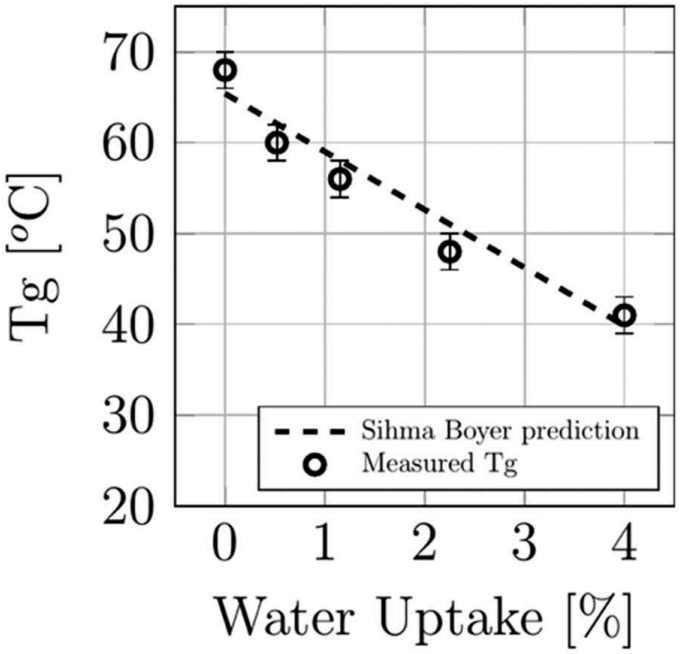


Figure 6. Decrease in Tg as a function of water content at saturation in the epoxy adhesive.

decrease in Tg with water content can be described by the Simha-Boyer equation[39]:

$$\frac{1}{T_g} = \frac{1}{T_{g\ polymer}} + A \times v_{H_2O} \ with\ A = \frac{1}{T_{g_{H_2O}}} - \frac{1}{T_{g\ polymer}} \qquad \text{(Eq.6)}$$

where Tg is the predicted glass transition temperature, $T_{g\ polymer}$ is the glass transition temperature of the polymer in the initial state, $T_{g_{H_2O}}$ is the Tg of the solvent (here water), taken equal to 100K (a value between the range of accepted values since the real Tg of water is difficult to measure[40]), and v_{H_2O} is the volume fraction of water in the sample.

3.4. *Tensile Tests at Different Temperatures*

Since the presence of water increases the mobility in the polymer it leads to large changes in mechanical behaviour. An alternative way to increase mobility was then investigated, by increasing the testing temperature with dried samples. Tensile results are plotted in Figure 7. Large changes in the tensile behaviour are induced by an increase of the testing temperature up to 50°C (*i.e.*, we are still in the glassy state). In fact, here again an increase of strain at break and Poisson's ratio are observed, as well as a decrease in the Young's modulus and the yield stress. All these properties are plotted in Figure 8.

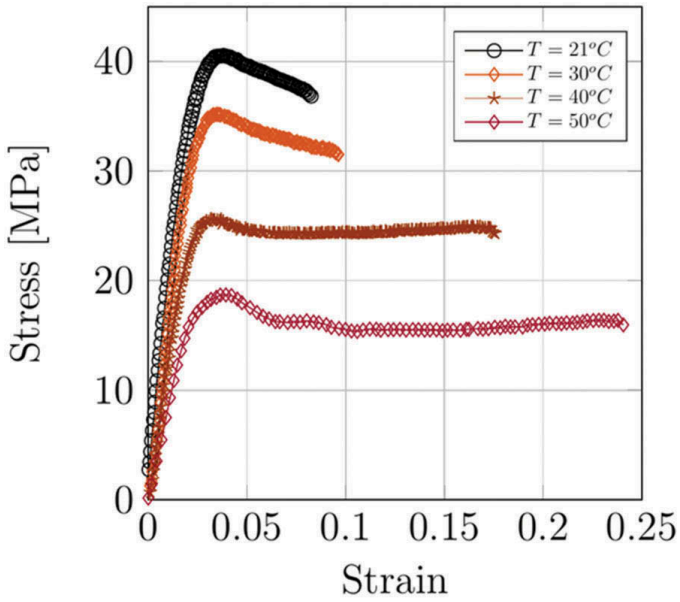


Figure 7. Tensile behaviour as a function of testing temperature on dry samples.

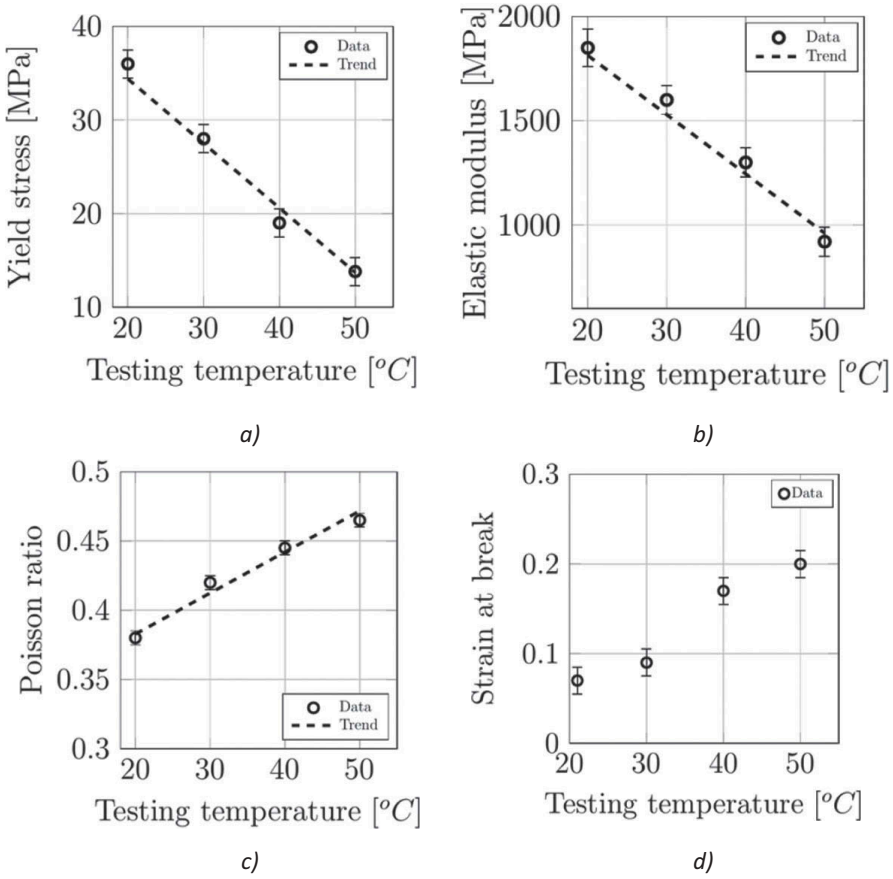


Figure 8. Change in yield stress (a), Young's modulus (b), Poisson's ratio (c), and Strain at break (d), as a function of testing temperature.

3.5. *Tensile Tests during Ageing in Sea Water*

The tensile behaviour of the bulk adhesive was also investigated after several immersion durations in sea water at 40°C before saturation of the sample, meaning that in this case there was a water profile gradient through the specimen thickness. A summary of the samples tested is presented in Table 2 and tensile behaviour is plotted in Figure 9. Here again the presence of water, even if there is a profile through the sample thickness, leads to a large decrease in modulus and yield stress. An increase of strain at break and Poisson's ratio is also observed; all these values are plotted as a function of immersion time in Figure 10.

Furthermore, samples aged at 40°C for 14 days in sea water have then been dried in a desiccator at 40°C at less than 1%RH to remove all the absorbed water. Tensile results before and after drying are plotted in Figure 11 and compared to those for unaged samples. A similar behaviour is observed, with the same modulus, yield stress and strain at break after drying, compared to unaged samples. It is interesting to note that there is a small strain softening effect

Table 2. Summary of ageing duration in sea water and corresponding amount of absorbed.

Ageing duration at 40°C in sea water (hours)	Amount of absorbed water (%)
6	1
24	1.8
55	2.8
336	4

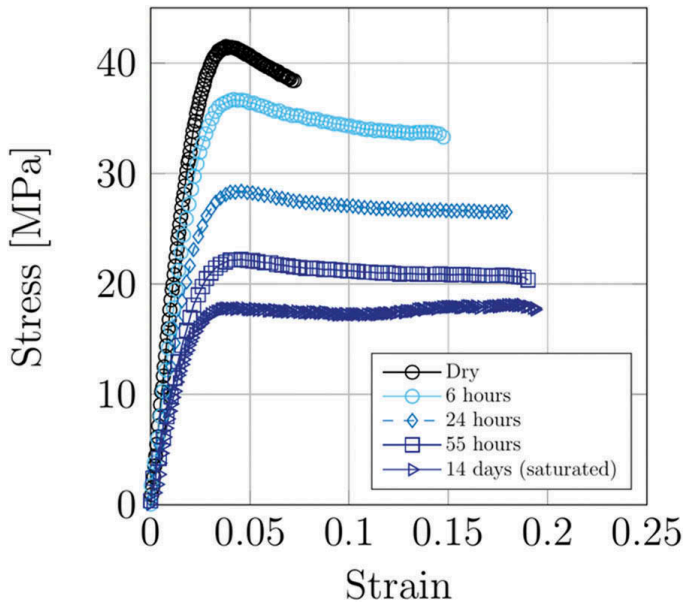


Figure 9. Tensile curves obtained for samples immersed in sea water at 40°C for several durations.

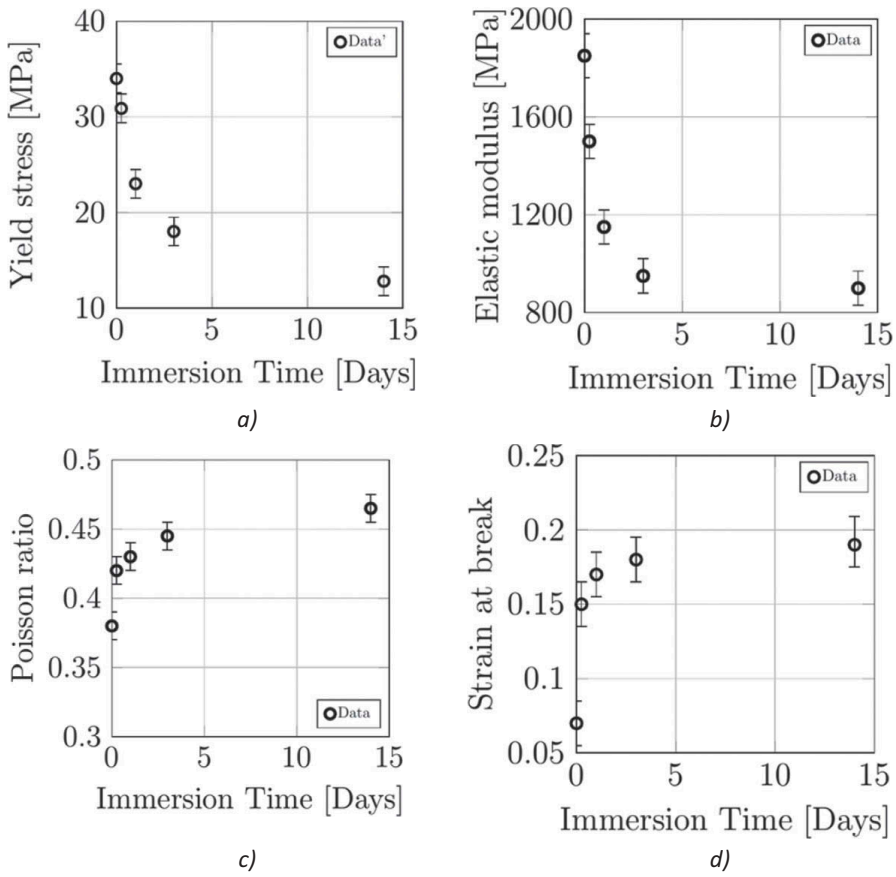


Figure 10. Change in yield stress (a), Young's modulus (b, and Poisson's ratio (c), Strain at break (d) as function of immersion time in sea water.

after yield for unaged specimens; the reasons for this are not clear and further work is underway to examine the parameters which affect post-yield behaviour.

4. Discussion and Prediction

This section is devoted to the discussion of results presented previously with the aim to be able to predict the tensile behaviour of the epoxy studied here as a function of ageing.

4.1. *Degradation Mechanism*

When exposed to humid environment, water diffuses into the polymer through a Fickian mechanism and the material absorbs up to 4% when immersed in sea water. The presence of water leads to an increase in mobility of the macromolecular chains and a decrease in Tg from 66°C to 41°C, this phenomenon is well known as plasticisation. Large changes in mechanical behaviour are induced by the plasticisation: a decrease in stiffness as well as yield stress and an increase in strain at break and Poisson's ratio. The increase in the Poisson's ratio can be explained by the fact that the polymer

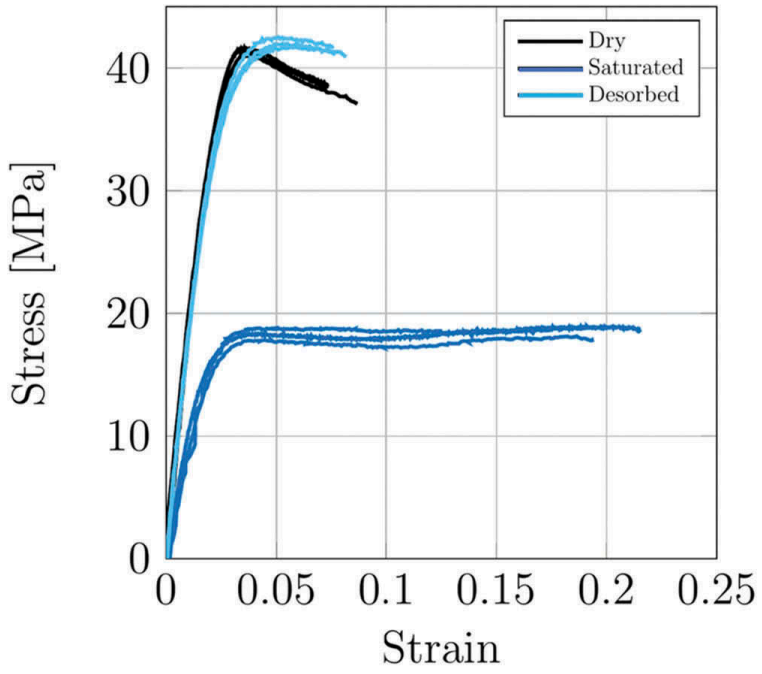


Figure 11. Tensile behaviour for unaged sample, fully saturated sample and sample dried after 14 days of ageing in sea water at 40°C.

tends towards its rubbery behaviour when Tg decreases. It is worth noting that the degradation observed here is fully reversible (Figure 11) meaning that plasticisation is the only mechanism involved (for the ageing conditions used in this study).

4.2. *Prediction Set Up*

A prediction of the mechanical behaviour of the bulk adhesive is now proposed using a multi-step process. First, the water diffusion is modelled using a numerical FE approach. Second, the decrease in yield stress is described, based on physical considerations. Then changes in Young's' modulus are considered, and finally we will focus on the increase in Poisson's ratio with water content.

4.3. *Prediction of Water Diffusion*

The prediction of water content through the thickness is the first step of the prediction and can be done using a typical Fickian behaviour coupled with the Eq.3. Water profiles are presented in Figure 12a for several immersion durations. Results obtained by modelling are then compared to experimental results in Figure 12b, and a good agreement is observed. This means that we are able to predict water content in the polymer as a function of thickness or external environment.

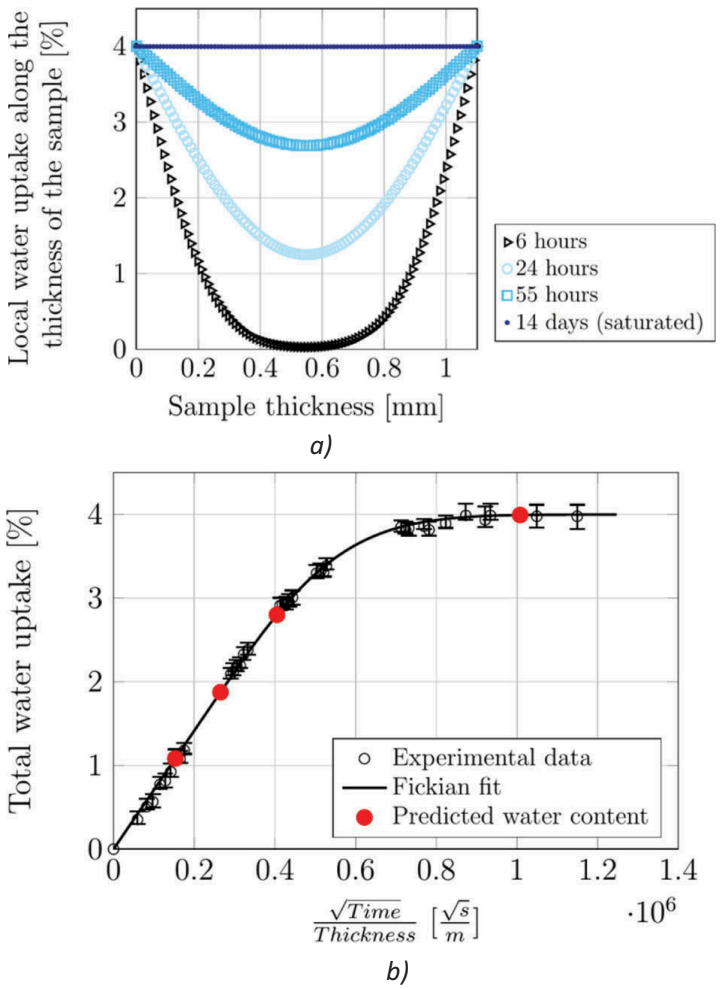


Figure 12. Modelling of water diffusion when epoxy adhesive is immersed in sea water at 40°C a) water profile through thickness b) comparison between modelled water content (red dots) and experimental data (blue).

4.4. *Prediction of Yield Stress with Water Content*

Prediction of the yield stress is possible based on physical considerations. In fact, it has been shown that the yield stress is strongly affected by the mobility in polymer molecules and moreover is directly proportional to the difference between the polymer Tg and the testing temperature. This relationship can be expressed by the following Eyring relationship (Eq.7) that has been checked experimentally for several polymers[41–43]:

$$\sigma_y = A.\left(T_g - T\right) + B \tag{7}$$

Here again, using both results on dry samples tested at different temperatures and samples saturated at several levels of water content (tested at 21°C), it is possible to show that the Eyring relationship is verified here (Figure 13) with A equal to 0.77 and B equal to 0.2. The correlation factor R^2 is equal to 0.96 based on experimental results.

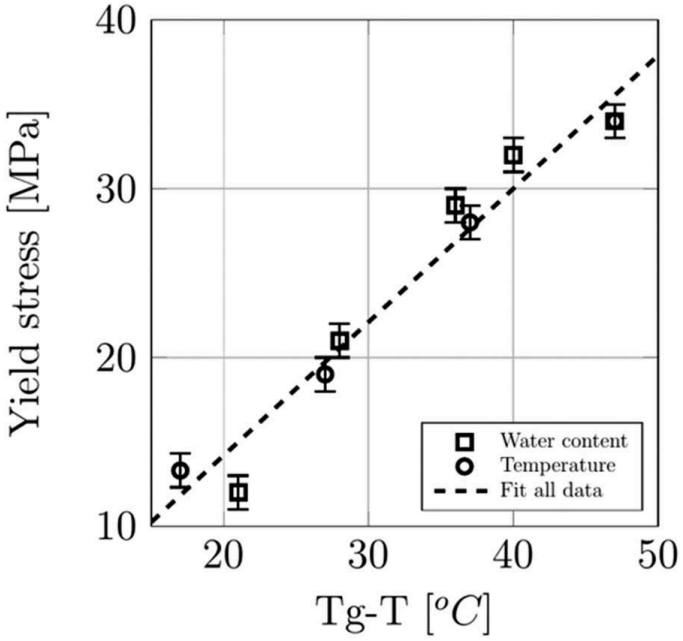


Figure 13. Relationship between yield stress and Tg-T obtained from tensile tests with several water contents at 21°C, and at several testing temperatures on dry specimens.

Because we are able to model the water diffusion in the epoxy through the thickness and the Tg is related to water content through the Simha-Boyer equation it is possible to predict the local value of Tg. Moreover, once the Tg is known it is possible to calculate the local value of Yield stress using the Eyring relationship.

4.5. *Description of Young's Modulus Decrease with Water Content*

The presence of water leads to a decrease in Young's modulus that can be explained by two main phenomena; the decrease in Tg and a decrease of the secondary transition. Unfortunately, due to the presence of these two mechanisms this behaviour cannot be described easily using physical considerations, thus an empirical relationship (Eq.8) was used to relate water content and the Young's' modulus value:

$$E = 1850 - 220 \times W_{H_20} \tag{8}$$

where E is the Young's modulus in MPa and W_{H20} is the water content in the polymer in %.

This basic relationship is plotted in Figure 5a and compared to experimental results. It appears that despite its simplicity, it is useful to describe the Young's modulus loss. However, it is important to note that this relationship is only valid for a given test temperature, here 21°C. It cannot be used to predict the evolution of properties at any other temperature.

4.6. Description of Poisson's Ratio Changes with Water Content

With the presence of water that leads to a decrease of Tg, the polymer tends to move from glassy to rubbery behaviour. This leads to an increase of the Poisson's ratio that becomes closer to 0.5, the value for a rubber. Here again this increase has been described using a linear empirical relationship:

$$\nu = 0.395 + 0.015 \times W_{H20} \tag{9}$$

Where Nu is the Poisson's ratio and W_{H20} is the water content in the polymer in %.

Figure 5c shows that (Eq.9) can describe the increase in Poisson's ratio with water content at 21°C, but again only for this temperature.

4.7. Validation of the Prediction

Using the parameters identified in the previous section it appears that a prediction of the tensile behaviour at 21°C can be made during humid ageing: we are able to predict the water content through the thickness using a Fickian behaviour model. Knowing the local water content, it is then possible to define values for Young's modulus and Poisson's ratio using empirical equations 5 and 6 respectively. In parallel, it is possible to relate the water content to the Tg of the polymer and hence to define local yield stress using the physically-based relationship (section 4.4). The validity of this approach can now be considered by comparing experimental results obtained for different immersion durations in sea water (with water profile gradients) with predictions obtained by the model proposed here. The material models have been integrated in ABAQUS FE software (section 2.7) and the tensile specimen has been modelled. From the water profile the mechanical behaviour was calculated for increasing loads, and the resulting stress-strain behaviour was determined after different immersion times.

Results are plotted in Figure 14. A good agreement is observed between the predicted tensile behaviour and experimental data.

4.8. Limits of the Prediction

As for all predictions of mechanical changes during ageing, the one that is proposed here has some limitations. First, this prediction is limited to a mechanical behaviour at 21°C (testing temperature) because the temperature effect on Young's modulus and Poisson's ratio have not been considered here. Moreover, the model used here is not able to predict the strain at break, which is strongly affected by the presence of water. And finally, the relationships that have been identified in this study depend on the nature of the polymer,

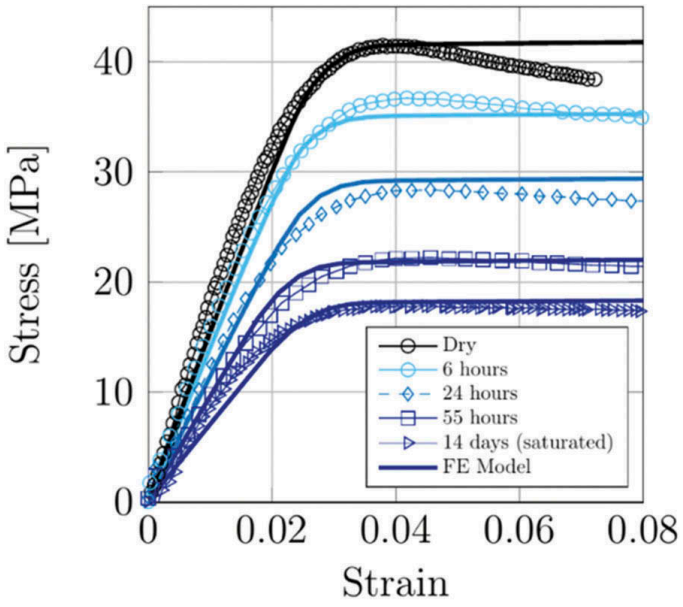


Figure 14. Comparison of predicted tensile behaviour (continuous lines) with experimental data (symbols) for different immersion times in sea water.

meaning that the approach developed here can be applied to other adhesives, but it is not possible to use directly the values identified from this study.

5. Conclusions

This article describes an approach to predict the influence of water on the tensile properties of an epoxy adhesive. It has been shown that for yield stress there is an equivalence between moisture content and test temperature, when these are expressed in terms of (T-Tg), while Young's modulus and Poisson's ratio can be expressed as a function of moisture content. Using these relationships and an FE model to predict water profiles the influence of aging conditions on the tensile stress-strain behaviour has been predicted. Results are in good agreement with tests for specimens with different water profile gradients.

Acknowledgments

The authors are grateful to colleagues at the IFREMER Centre in Brest for their help with the aging measurements, in particular to Nicolas Lacotte and Mickael Premel Cabic. The work was performed within the French ANR COSICO project.

ORCID

Pierre-Yves Le Gac http://orcid.org/0000-0003-3183-1715

References

[1] Davies, P.;. *Handbook of Adhesion Technology*; Berlin, Heidelberg: Springer: 2011. pp 1237–1262.

[2] Silva, L.; Tognana, S.; Salgueiro, W. Study of the Water Absorption and Its Influence on the Young's Modulus in a Commercial Polyamide. *Polym. Test.* 2013, **32**, 158–164. DOI: 10.1016/j.polymertesting.2012.10.003.

[3] Toscano, A.; Pitarresi, G.; Scafidi, M.; Di Filippo, M.; Spadaro, G.; Alessi, S. Water Diffusion and Swelling Stresses in Highly Crosslinked Epoxy Matrices. *Polym. Degrad. Stab.* 2016, **133**, 255–263. DOI: 10.1016/j.polymdegradstab.2016.09.004.

[4] De Oliveira, G. L.; Gomez, A. J. A.; Caire, M.; Vaz, M. A.; Da Costa, M. F. Characterization of Seawater and Weather Aged Polyurethane Elastomer for Bend Stiffeners. *Polym. Test.* 2017, **59**, 290–295. DOI: 10.1016/j.polymertesting.2017.02.012.

[5] Zhou, J.; Lucas, J. P. Hygrothermal Effects of Epoxy Resin. Part I: The Nature of Water in Epoxy. *Polymer*. 1999, **40**, 5505–5512. DOI: 10.1016/S0032-3861(98)00790-3.

[6] Zhou, J.; Lucas, J. P. Hygrothermal Effects of Epoxy Resin. Part II: Variations of Glass Transition Temperature. *Polymer*. 1999, **40**, 5513–5522. DOI: 10.1016/S0032-3861(98)00791-5.

[7] Brettle, J.; Brewis, D.; Comyn, J.; Cope, B.; Goosey, M.; Hurditch, R. The Interaction of Water with an Epoxide Adhesive Based on the Diglycidylether of bisphenol-A and Triethylene Tetramine. *Int. J. Adhes. Adh.* 1983, **3**, 189–192. DOI: 10.1016/0143-7496(83)90092-1.

[8] De Nève, B.; Shanahan, M. Effects of Humidity on an Epoxy Adhesive. *Int. J. Adhes. Adhesives*. 1992, **12**, 191–196. DOI: 10.1016/0143-7496(92)90053-X.

[9] Mubashar, A.; Ashcroft, I. A.; Critchlow, G. W.; Crocombe, A. Moisture Absorption–Desorption Effects in Adhesive Joints. *Int. J. Adhes. Adhesives*. 2009, **29**, 751–760. DOI: 10.1016/j.ijadhadh.2009.05.001.

[10] Cowling, M.;. A Review of Adhesive Bonding for Offshore Structures. Great Britain: *Health Saf. Executive*. 1997.

[11] Bordes, M.; Davies, P.; Cognard, J.-Y.; Sohier, L.; Sauvant-Moynot, V.; Galy, J. Prediction of Long Term Strength of Adhesively Bonded Steel/Epoxy Joints in Sea Water. *Int. J. Adhes. Adh.* 2009, **29**, 595–608. DOI: 10.1016/j.ijadhadh.2009.02.013.

[12] Brewis, D.; Comyn, J.; Tegg, J. The Durability of Some Epoxide Adhesive-Bonded Joints on Exposure to Moist Warm Air. *Int. J. Adhes. Adhesives*. 1980, **1**, 35–39. DOI: 10.1016/0143-7496(80)90032-9.

[13] Zanni-Deffarges, M.; Shanahan, M. Diffusion of Water into an Epoxy Adhesive: Comparison between Bulk Behaviour and Adhesive Joints. *Int. J. Adhes. Adhesives*. 1995, **15**, 137–142. DOI: 10.1016/0143-7496(95)91624-F.

[14] Gledhill, R.; Kinloch, A.; Shaw, S. A Model for Predicting Joint Durability. *J. Adhes.* 1980, **11**, 3–15. DOI: 10.1080/00218468008078901.

[15] Liljedahl, C.; Crocombe, A.; Wahab, M.; Ashcroft, I. Modelling the Environmental Degradation of Adhesively Bonded Aluminium and Composite Joints Using a CZM Approach. *Int. J. Adhes. Adhesives*. 2007, **27**, 505–518. DOI: 10.1016/j.ijadhadh.2006.09.015.

[16] Bowditch, M.;. The Durability of Adhesive Joints in the Presence of Water. *Int. J. Adhes. Adhesives*. 1996, **16**, 73–79. DOI: 10.1016/0143-7496(96)00001-2.

[17] Comyn, J.;. In Durability of Structural Adhesives, A J Kinloch (Ed), London: Applied Science Publishers, 1983, 85–131.

[18] Adams, R. D.;. *Adhesive Bonding: Science, Technology and Applications*; Boca Raton, USA: Elsevier: 2005.

[19] Ashcroft, I. A.; Comyn, J. *Handbook of Adhesion Technology*; Berlin, Heidelberg: Springer: 2011. pp 787–822.
[20] Crocombe, A.;. Durability Modelling Concepts and Tools for the Cohesive Environmental Degradation of Bonded Structures. *Int. J. Adhes. Adhesives*. 1997, **17**, 229–238. DOI: 10.1016/S0143-7496(97)00008-0.
[21] Wahab, M. A.; Crocombe, A.; Beevers, A.; Ebtehaj, K. Coupled Stress-Diffusion Analysis for Durability Study in Adhesively Bonded Joints. *Int. J. Adhes. Adhesives*. 2002, **22**, 61–73. DOI: 10.1016/S0143-7496(01)00037-9.
[22] Crocombe, A.; Hua, Y.; Loh, W.; Wahab, M.; Ashcroft, I. Predicting the Residual Strength for Environmentally Degraded Adhesive Lap Joints. *Int. J. Adhes.* 2006, **26**, 325–336. DOI: 10.1016/j.ijadhadh.2005.04.003.
[23] Hua, Y.; Crocombe, A.; Wahab, M.; Ashcroft, I. Continuum Damage Modelling of Environmental Degradation in Joints Bonded with EA9321 Epoxy Adhesive. *Int. J. Adhes. Adhesives*. 2008, **28**, 302–313. DOI: 10.1016/j.ijadhadh.2007.08.005.
[24] Katnam, K.; Sargent, J.; Crocombe, A.; Khoramishad, H.; Ashcroft, I. Characterisation of Moisture-Dependent Cohesive Zone Properties for Adhesively Bonded Joints. *Eng. Fract. Mech.* 2010, **77**, 3105–3119. DOI: 10.1016/j.engfracmech.2010.08.023.
[25] Arnaud, N.; Créac'hcadec, R.; Cognard, J.-Y.; Davies, P.; Le Gac, P.-Y. Analysis of the Moisture Effect on the Mechanical Behaviour of an Adhesively Bonded Joint under Proportional Multi-Axial Loads. *J. Adhes. Sci. Technol.* 2015, **29**, 2355–2380. DOI: 10.1080/01694243.2015.1067018.
[26] Mahnken, R.; Schlimmer, M. Simulation of Strength Difference in Elasto-Plasticity for Adhesive Materials. *Int. J. Numer. Methods Eng.* 2005, **63**, 1461–1477. DOI: 10.1002/(ISSN)1097-0207.
[27] Leger, R.; Roy, A.; Grandidier, J. A Study of the Impact of Humid Aging on the Strength of Industrial Adhesive Joints. *Int. J. Adhes. Adhesives*. 2013, **44**, 66–77. DOI: 10.1016/j.ijadhadh.2013.02.001.
[28] Viana, G.; Costa, M.; Banea, M.; Da Silva, L. Behaviour of Environmentally Degraded Epoxy Adhesives as a Function of Temperature. *J. Adhes.* 2017, **93**, 95–112. DOI: 10.1080/00218464.2016.1179118.
[29] Viana, G.; Costa, M.; Banea, M.; Da Silva, L. *Proc. Ins. Mech. Eng. Part. L*. 2017, **231**, 488–501.
[30] Le Gac, P.-Y.; Choqueuse, D.; Melot, D. Description and Modeling of Polyurethane Hydrolysis Used as Thermal Insulation in Oil Offshore Conditions. *Polym. Test.* 2013, **32**, 1588–1593. DOI: 10.1016/j.polymertesting.2013.10.009.
[31] ISO/TC 45/SC 2 Rubber. *Vulcanized or Thermoplastic – Determination of Tensile Stress-Strain Properties*: Switzerland; 2011.
[32] Badulescu, C.; Germain, C.; Cognard, J.-Y.; Carrere, N. Characterization and Modelling of the Viscous Behaviour of Adhesives Using the Modified Arcan Device. *J. Adhes. Sci. Technol.* 2015, **29**, 443–461. DOI: 10.1080/01694243.2014.991483.
[33] Cognard, J.-Y.; Badulescu, C.; Maurice, J.; Créac'hcadec, R.; Carrère, N.; V́ edrine, P. On Modelling the Behaviour of a Ductile Adhesive under Low Temperatures. *Int. J. Adhes. Adhesives*. 2013, **47**, 46–56. DOI: 10.1016/j.ijadhadh.2013.09.024.
[34] Park, G. S.; Crank, J. *Diffusion in Polymers*; London and New York: Academic Press: 1968.
[35] Broudin, M.; Le Saux, V.; Le Gac, P. Y.; Champy, C.; Robert, G.; Charrier, P.; Marco, Y. Moisture Sorption in Polyamide 6.6: Experimental Investigation and Comparison to Four Physical-Based Models. *Polym. Test.* 2015, **43**, 10–20. DOI: 10.1016/j.polymertesting.2015.02.004.

[36] Gaudichet-Maurin, E.; Thominette, F.; Verdu, J. Water Sorption Characteristics in Moderately Hydrophilic Polymers, Part 1: Effect of Polar Groups Concentration and Temperature in Water Sorption in Aromatic Polysulfones. *J. Appl. Polym. Sci.* 2008, **109**, 3279–3285. DOI: 10.1002/(ISSN)1097-4628.
[37] Le Gac, P. Y.; Roux, G.; Davies, P.; Fayolle, B.; Verdu, J. Water Clustering in Polychloroprene. *Polymer*. 2014, **55**, 2861–2866. DOI: 10.1016/j.polymer.2014.04.024.
[38] Fedors, R.;. Osmotic Effects in Water Absorption by Polymers. *Polymer*. 1980, **21**, 207–212. DOI: 10.1016/0032-3861(80)90062-2.
[39] Kelley, F. N.; Bueche, F. *J. Poly. Sci.* 1961, **50**, 549–556.
[40] Fayolle, B.; Verdu, J. Vieillissement Physique Des Matériaux Polymères. France: *Tech. Ing.* 2005.
[41] Kambour, R.;. *J. Poly. Sci.* 1973, **7**, 1–154.
[42] Cook, W. D.; Mayr, A. E.; Edward, G. H. Yielding Behaviour in Model Epoxy Thermosets — II. Temperature Dependence. *Polymer*. 1998, **39**, 3725–3733. DOI: 10.1016/S0032-3861(97)10335-4.
[43] Le Gac, P.-Y.; Arhant, M.; Le Gall, M.; Davies, P. Yield Stress Changes Induced by Water in Polyamide 6: Characterization and Modeling. *Polym. Degrad. Stab.* 2017, **137**, 272–280. DOI: 10.1016/j.polymdegradstab.2017.02.003.

THE JOURNAL OF ADHESION
https://doi.org/10.1080/00218464.2023.2187293

Taylor & Francis
Taylor & Francis Group

Check for updates

Understanding of water uptake mechanisms in an epoxy joint characterized by pore-type defects

Andreea Tintatu[a], Claudiu Badulescu[a], Pierre Bidaud[a], Philippe Le Grognec[a], Jérôme Adrien[b], Eric Maire[b], Hervé Bindi[c], and Corentin Coguenanff[c]

[a]ENSTA Bretagne, UMR CNRS 6027, IRDL, F-29200, Brest, France; [b]Univ. Lyon, INSA Lyon, UMR CNRS 5510, Laboratoire MATEIS, F-69621, Villeurbanne Cedex, France; [c]Thalès DMS France, F-06560, Valbonne, France

ABSTRACT

This work aims to characterize the water uptake mechanisms of a two-component epoxy adhesive joint immersed in deionized water. The pore-type defects in the bulk adhesive after the cure cycle are highlighted and characterized using X-ray µ-tomography. Two population patterns of defects are generated and analyzed, for two different thicknesses. The waterfront is not detectable by µ-tomography for this adhesive because the densities of the water and the adhesive remain relatively close to each other. Instead, the volume variation and kinetics of pore water filling have been accurately identified. This analysis was completed by optical observations and gravimetric measurements.

ARTICLE HISTORY
Received 24 January 2023
Accepted 23 February 2023

KEYWORDS
Structural bonding; water aging; X-ray µ-tomography; pores

1. Introduction

The complexity and efficiency of underwater systems including composite structures and multi-material watertight assemblies must be constantly increasing, showing long-range, real-time investigation capabilities. The constitution of such complex systems passes by a phase of assembly of various subsystems. Although most structures can be assembled by screws or riveting systems,[1] adhesive bonding is becoming an increasingly attractive alternative, due to its numerous advantages: (i) lightweight, (ii) more uniform load distribution, (iii) ease of implementation, and (iv) possibility of joining different materials (metal with composite).[2] The structural mechanical resistance as well as the durability of bonded structures are closely related to the degradation mechanisms to be integrated in the dimensioning stage. In structural assemblies, epoxy adhesives are most often used because they are characterized by a relatively high mechanical resistance to failure, allowing them to reach load levels close to those that the primary structure supports. Nevertheless, these adhesives require careful characterization of their thermo-mechanical behavior so as to correctly predict the long-term mechanical response of the

CONTACT Philippe Le Grognec philippe.le_grognec@ensta-bretagne.fr ENSTA Bretagne, 2 rue François Verny, 29806 Brest Cedex 9, France

© 2023 Taylor & Francis Group, LLC

assembly. Additional complexity is experienced if the mechanical behavior of the adhesive is influenced by the humidity of the water environment that diffuses into the material.

The influence of water on the mechanical behavior of adhesives is a widely studied topic.[3–5] The phenomenon of aging of an adhesive, when water diffuses into it, is manifested by a loss of its mechanical properties. Also, humidity could lead to a degradation of the assembly interface, an aspect that is not addressed in this paper. Generally, the studies investigating the effect of water on the mechanical behavior of an assembly may be very costly in terms of time and experimental means deployed. When possible, accelerated aging investigations are a good alternative, remedying to these difficulties. In the context of accelerated aging, bulk adhesive samples drastically reduce the time required to obtain a uniform humidity inside the material, due to the very large contact surface between the wet medium and the adhesive. Moreover, the increase of the temperature of the hydrous environment used to age the samples (immersion in water or humid atmosphere controlled at a certain percentage of RH) drastically decreases (from months to weeks) the time necessary for the samples to reach the water saturation. This accelerated aging strategy has already been successfully applied to several adhesives, confirming its relevance.[3] However, phenomena such as the physical aging of adhesives cannot be observed over short durations associated with rapid investigation strategies.

Many authors agree that the sorption of water by polymeric materials, such as epoxy adhesives, causes a weakening of the mechanical properties and also a swelling of the samples.[6] These swelling changes are relatively small and difficult to measure by conventional means. In previous works,[7,8] the authors proposed an experimental strategy to measure the moisture in an adhesive using a fiber optic sensor (Bragg or Fresnel). However, this method of investigation is intrusive and, considering the diameter of the fibers, this approach is not suitable for thin adhesive joints (with thicknesses less than 1 mm). Direct experimental measurements of the percentage of water in an adhesive are difficult to perform and, in the few cases where it is possible (using Neutron Radiography, for example), it is necessary to deploy very sophisticated means and methods of investigation.[9] A potential technique to determine the moisture gradient in a joint is represented by X-ray μ-tomography. This technique has been successfully used in several studies,[10,11] mainly for the detection of the advancement of the moisture front in concrete or other civil engineering structures. Recently, Dumont et al.[12] also used X-ray μ-tomography successfully to identify, at the micrometric scale, the pore-type defects present in an adhesive joint and their evolution depending on the mechanical loading.

The objective of this paper is to investigate by X-ray μ-tomography the mechanisms of water uptake within a structural bi-component epoxy adhesive.

More precisely, the aim is to understand the mechanisms of water linked to the water uptake during hydric aging, but also to study the influence of pore-type defects on global sorption. These investigations are completed by gravimetric measurements and optical observations in order to better understand the mechanisms that govern the absorption of water in such an adhesive. The paper is organized in two main sections. In Section 2, the adhesive material is described, and the different methods used to investigate its water uptake are presented. Section 3 displays then the results of the tomographic analyses performed directly after curing and at different aging times, so as to highlight the changes in the microstructure due to water uptake. These results are finally correlated with classical gravimetric measurements and confronted to microscopic observations.

2. Material and experimental methods

2.1. Sample preparation

The nature and characteristics of the samples used must be carefully selected, depending on the final application. The main objective of the overall project in hand is to understand, characterize and model the water uptake and its effect on the mechanical behavior of a bonded assembly (such as between a composite material and a polyurethane, but not only). The adhesive thickness within the assembly is supposed to vary between 300 µm and 500 µm. Such an assembly is designed to remain immersed in seawater for long periods of time. Owing to the low mechanical load that this adhesive joint must withstand, one will mainly focus on the degradation of the mechanical properties caused by water absorption.

The specimens used in this study are bulk samples made of an epoxy-based adhesive with a bisphenol A diglycidyl ether prepolymer and a diamine hardener mixed under stoichiometric conditions. Table 1 summarizes some main properties of this material.

The two components of the adhesive were mixed according to the manufacturer's specifications in the following proportions: 100 parts by weight of resin A and 40 parts by weight of hardener B, using a Speedmixer planetary mixer (FlackTek Inc., Landrum, USA). The mixing parameters correspond to a rotation speed of 2500 rpm during 4 minutes. With this type of adhesive, it has been observed that the mixing process was prone to generate porosities

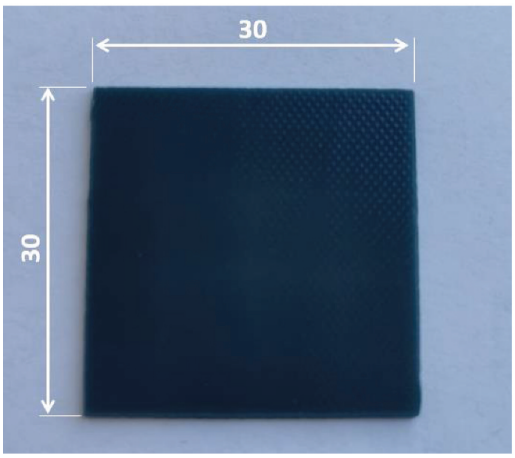
Table 1. Main characteristics of the considered adhesive.

Property	*Component* A	*Component* B	Mix
Density	1,2 g/cm^3	1,0 g/cm^3	~ 1,07 g/cm^3
Glass transition temperature (DSC)			~ 55°C
Young modulus			1700 MPa
Known fillers			Glass beads

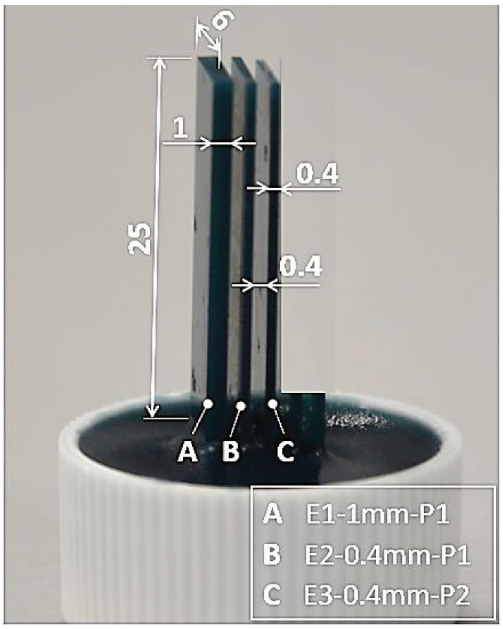
inside the material.[13] This mixture was then cast between two aluminum plates, each 300 × 300 × 30 mm^3 in size. These plates were wrapped in a Teflon film, in order to avoid the adhesion of the adhesive material once it has cured. The distance between these two plates is controlled with calibrated spacers, so as to obtain the desired adhesive thicknesses. Two adhesive plates were finally made with two different thicknesses, namely 0.4 mm and 1 mm. A third plate, with a thickness of 0.4 mm, was made by vacuuming the adhesive mixture during 5 minutes before pouring it in the apparatus, for further comparison purposes.

The curing cycle used for the three types of samples was set at 50°C for 12 hours. It was performed using a MEMERT UF110+ thermal chamber which allows the temperature to vary between 20°C and 310°C. The density of the adhesive was determined to be equal to 1087 kg/m^3. DSC analyses have shown that this curing process ensures a polymerization rate of 95%. Several samples were then taken from the three adhesive thin plates, respectively named E1–1 mm-P1, E2–0.4 mm-P1 and E3–0.4 mm-P2. In this paper, for clarity purposes, they will be referred to as E1, E2 and E3, respectively.

First, three samples of size 30 × 30 mm^2 for each of the three plates were cut as shown in Figure 1a, using a waterjet cutting machine. These dimensions are chosen following the recommendations proposed by previous studies,[3] in order to ensure unidirectional (through-the-thickness) patterns while minimizing edge effects, which could have a non-negligible influence for small sample sizes. These first specimens were used for gravimetric analyses.



a) Sample for classical gravimetry investigation (1 mm thickness)



b) Samples for X-ray tomography investigation

Figure 1. Geometry of the samples (dimensions in mm).

Thereafter, samples of size $25 \times 6\ mm^2$, taken from each sheet (A, B and C), were put together in a holder, as shown in Figure 1b. The interest in placing together these last three samples is to decrease the tomographic analysis time. In other words, with such a configuration, a single tomographic scan allows one to obtain the results for the three samples simultaneously.

Samples E1, E2 and E3 were obtained for a curing cycle (12 h @ 50°C) by varying two parameters: (i) thickness and (ii) porosity ratio, as presented above. For a better understanding of the effect of water uptake in the samples and the influence of thickness and porosity ratio, the study is focused on two investigations: classical water absorption by gravimetric measurements on immersed samples, and analysis by X-ray tomography. For efficiency reasons and coherence with the availability of experimental means, the temperature of aging was established at 22°C.

2.2. Optical microscopy

Experimental observations were performed using the KEYENCE VHX-7000 3D microscope. The corresponding samples, $30 \times 30 \times 0.4\ mm^3$ in size, were investigated using the through illumination system, with which the observation device is equipped. The aim here is to observe qualitatively the porosity distribution but also the time needed for the first water droplets to occur in the pores of the samples.

2.3. Global water uptake

The three samples of size $30 \times 30\ mm^2$ (collected from each plate) were first dried in order to remove residual moisture. The presence of moisture in the samples can be explained first by the absence of moisture control during the curing cycle, but also by the contact of the samples with water, during the cutting operation. This drying phase was carried out by placing the samples in a glass container with Silica gel at 35°C. Periodic measurements of mass decrease were performed to determine the necessary time for mass stabilization. Twenty-one days were needed to reach a quasi-dry state of the samples. These dried samples were then immersed in demineralized water for practical reasons (manufacturing and water control). Deroiné et al.[14] have also shown that water diffusion kinetics are slightly faster in demineralized water. The density of demineralized water is $1020\ kg/m^3$. The aging tanks containing the demineralized water, at a temperature of 22°C ±0.3°C, are equipped with a water circulation system, responsible for the homogenization of the temperature in the whole water mass. Weight measurements were periodically performed during 4 months. These measurements were carried out with a more important frequency at the beginning of the water uptake (every 12 hours for the first three days) and a less important one thereafter. Water

diffusion was determined from the change in weight of the square samples. Samples were removed from the aging tanks and wiped before weighing. The mass increase was followed by periodic weighing on a Kern AEJ 200-4 CM balance with an accuracy of 0.0001 g.

2.4. X-ray tomography

Since its first applications in the medical field,[15] X-ray tomography has been the subject of numerous studies from both a theoretical and applied point of view. A brief description is therefore given here to introduce the main concepts. A wide variety of experimental setups can be used to perform X-ray tomography, but the basic principles of the technique always remain the same (see Figure 2). Tomography measurements are based on the variation of the linear X-ray attenuation coefficient, denoted μ, through the volume of a material. For a material considered as homogeneous, the coefficient μ turns out to be constant with respect to the spatial coordinates (x, y, z). Conversely, in heterogeneous materials such as porous environments, μ is a function of these coordinates.

It is possible to obtain the spatial distribution of this coefficient μ by sending a beam of X-rays into the mass of the studied sample, under different angles, and by collecting the transmitted beam. In practice, the sample is mounted on a rotator included in the tomograph chamber, and for each angular step, an X-ray beam is emitted, attenuated by the internal structure of the sample, and

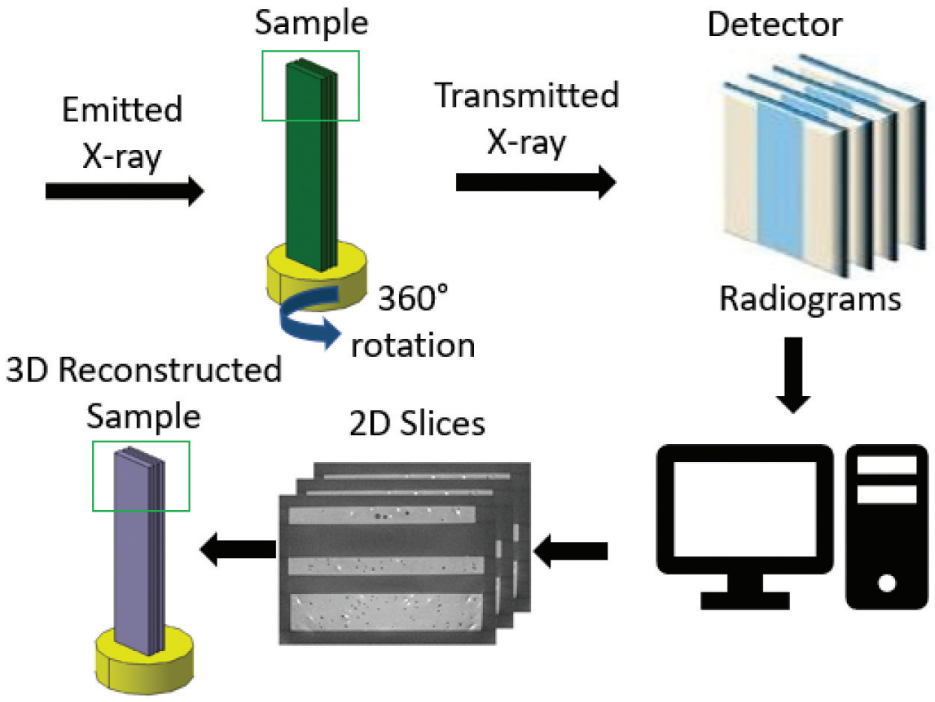


Figure 2. Principle of tomography measurements.

collected by a detector. The attenuation phenomenon in the $\vec{x}$ direction is described by a Beer-Lambert law depending on $\mu(x, y, z)$:

$$\frac{I}{I_0} = exp\left(\int_{x_0}^{x_{max}} \mu(x, y, z)dx\right) \quad (1)$$

where I_0 represents the initial intensity of the source (emitted), I is the detected intensity (transmitted and collected by the X-ray detector) and x represents the distance along the transmission path between x_0 and x_{max}.

A series of N radiographs is obtained by the complete acquisition process. A reconstruction algorithm is then used to generate the 3D internal structure of the sample (i.e. the spatial distribution of $\mu(x, y, z)$) from the series of radiographs. This algorithm can be based on two different approaches: the software can either solve a set of linear equations to compute $\mu(x, y, z)$ (algebraic approach) or use a back-projection of the detected intensity by a Fourier transformation (analytical approach). Although the analytical approach is faster to compute, it requires a complete data set with no missing pictures of the X-ray series.

The results presented in this paper were obtained using a filtered back-projection approach. The X-ray computed tomography equipment (model Phoenix vTomeX/X-ray, see Figure 3) that is used during this experimental study is located in the MATEIS laboratory (INSA Lyon, France). The tomograph is equipped with a *Varian Paxscan*™ flat-panel detector with a resolution of 1920 × 1536 pixels^2. This detector produces 14-bit coded grayscale pictures of the attenuation.

The acquisition was performed with a rotational movement of the sample in order to reconstitute all the investigated volume. A total of 1200 pictures were taken throughout the rotation, for a complete acquisition time of 15 min. The X-ray source was operated with a voltage of 60 kV and a current of 80 µA. These values are chosen so as to ensure the best compromise between

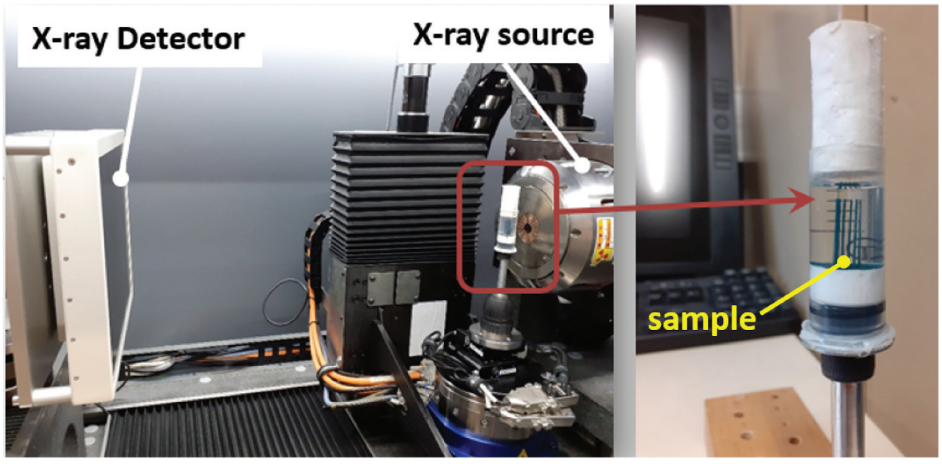


Figure 3. X-ray computed tomography equipment, model Phoenix vTomex (MATEIS/INSA Lyon).

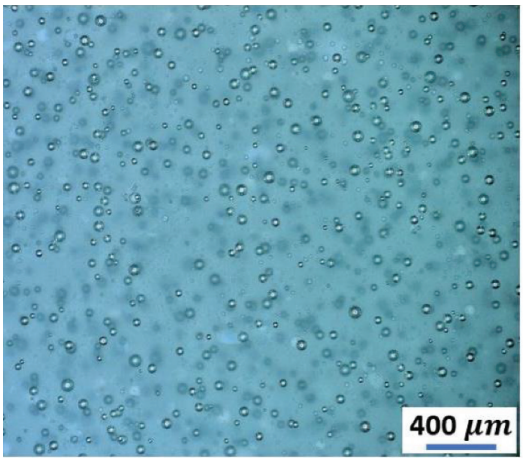
transmission and contrast. Concerning the current, the maximum value (before defocusing) is used in order to obtain the maximum photon flux without increasing the size of the source spot.

In parallel to the measurements of mass changes, measurements of X-ray μ-tomography were made periodically with a similar frequency to the previous tests. The samples used are shown in Figure 1b. Only the upper part of these samples is analyzed, namely a volume of $6 \times 6 \times 6\,mm^3$ as described in Figure 2. Under these conditions, a voxel of $4.5 \times 4.5 \times 4.5\,\mu m^3$ is obtained. The samples were placed in a cylindrical container made of transparent plastic material. This container, filled with demineralized water, ensures the immersion of the sample and significantly facilitates the execution of the tests. The samples are positioned centrally and then fixed to a metal rod as shown in Figure 3. The purpose of the rod is to ensure an almost identical positioning between the X-ray tube and the specimen, during the acquisition of the various radiograms, and thus to facilitate the setting up of the acquisition.

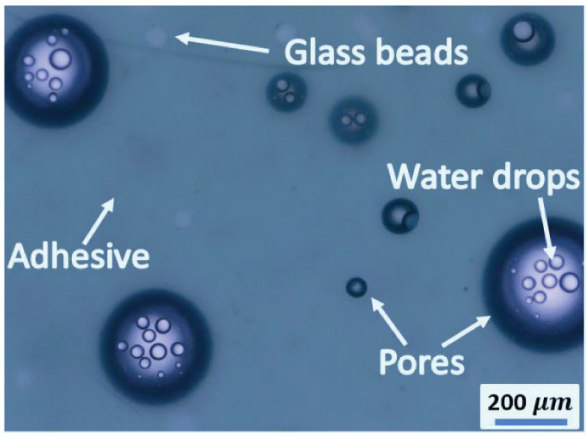
3. Results and discussions

3.1. Preliminary observation of the samples by optical microscopy

In Figure 4, two images of two samples E1 and E3, both with a thickness of 0.4 mm, are depicted. These images were obtained with the KEYENCE VHX-7000 microscope with an illumination of the sample by the bottom side. When the sample is semi-transparent and not too thick, this illumination serves to highlight the different phases within the samples. The presence of porosities after curing can be qualitatively observed in Figure 4a, in the form of dark small spheres, which are characterized by a relatively uniform distribution.



a) Sample E1 (0.4 mm thick) after curing



b) Sample E3 (0.4 mm thick) after 1 month in demineralized water

Figure 4. Different types of porosities observed by microscope within the samples obtained from the two mixtures.

Regular white dots are also detected, which represent glass beads. Figure 4b illustrates the microscopic image of a sample E3. In this case, the adhesive mixture has been put under vacuum during 5 minutes (before the process of curing) and then immersed into water during 30 days. The vacuum effect clearly appears through the absence of small porosities and the presence of very large ones (these large pores could have further a significant influence on the long-term mechanical strength of the adhesive). What is remarkable is that keeping the adhesive in a viscous state under vacuum cannot completely eliminate the presence of porosities. Moreover, from 21 days of immersion, the first water droplets appeared inside the largest porosities closest to the two faces of the sample. Water-filled porosities positioned in the vicinity of the adhesive-substrate interface in assemblies may also accelerate local degradation of the interface with significant consequences for the integrity of the structure.

Although these observations are only qualitative, they give an insight of the mechanisms of water absorption in the adhesive, e.g. the migration of water through the material to the pores so as to occupy the free volumes. The kinetics of such a mechanism will clearly be influenced by the distribution and size of the porosities.

As these preliminary observations remain qualitative, analyses by X-ray μ-tomography were carried out in order to understand more deeply these mechanisms in a quantitative and local way. The interest is to investigate whether it is possible to determine the concentration profile of water in the adhesive during aging. Mass change measurements were performed in parallel so as to complete these observations.

3.2. Global water uptake

The purpose of gravimetric tests is to determine the kinetics of water uptake in adhesive samples. These macroscopic measurements will complement tomographic investigations. The mass change measurements were performed on square-shaped samples, as presented in Section 2.1. Regarding the sample dimensions used, the assumption of a unidirectional diffusion is made. The temperature of water has been set to 22°C. Nine samples per condition were used with three measurements at each time. Specimens were dried with lint-free tissue before recording the final weight. The water uptake was determined by gravimetric measurements. The mass water content in the adhesive can be calculated from:

$$C(t) = \frac{m(t) - m_0}{m_0} \times 100 \tag{2}$$

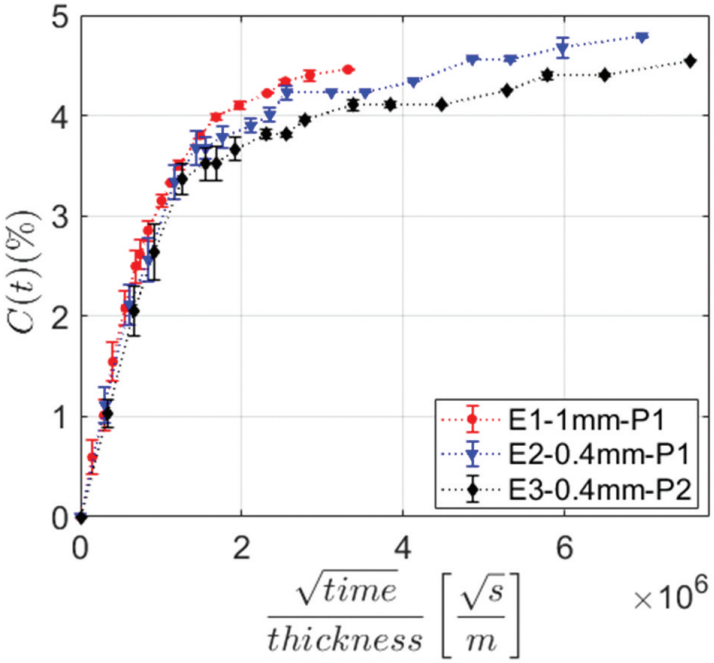


Figure 5. Water uptake of the three samples during immersion.

where $m(t)$ and m_0 represent the mass of the adhesive during immersion and the initial mass, respectively. The water uptake results for the three sample types are plotted in Figure 5.

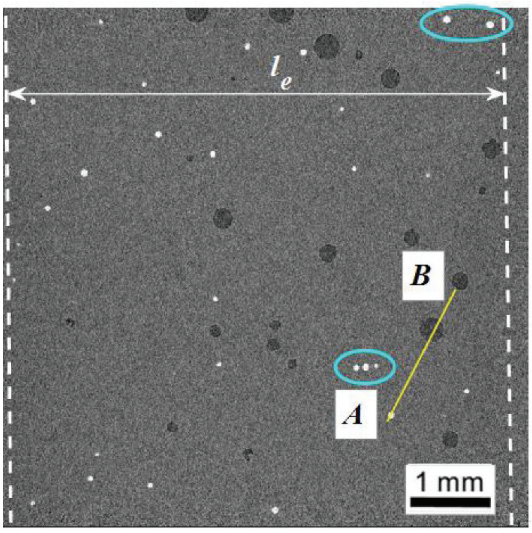
In the present case of unidirectional diffusion, the evolution of the mass water content $C(t)$ can be classically represented as a function of the square root of time. It allows one to identify a first linear part in the sorption kinetics. Furthermore, the linear growth in the second part instead of a plateau suggests a non-Fickian water uptake kinetics for the adhesive in hand. All the results were normalized with respect to the thickness, so as to be free from thickness effects, while considering sufficiently thin samples in such a way that water diffusion remains unidirectional.

3.3. X-ray tomography and image analysis

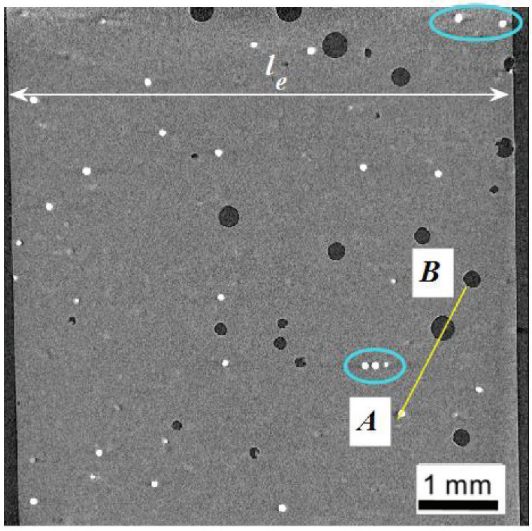
3.3.1. Configuration choice

The quality of the tomographic measurements is a key point for obtaining reliable results. For the scale being considered, three phases are supposed to be determined in the adhesive composition: the polymeric medium (adhesive phase), the glass beads and the pores, as shown in Figure 4. The measurement parameters of the tomograph have been selected in order to detect at best these three phases in a robust manner.

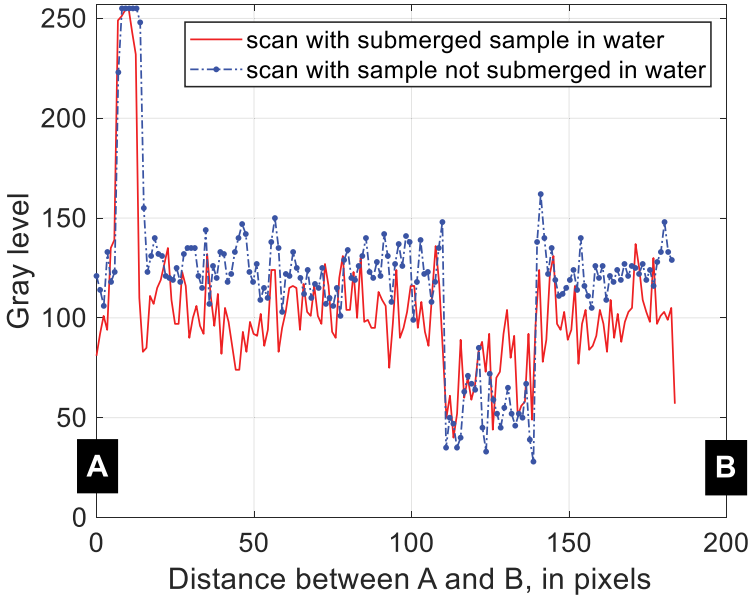
Regarding now the scanning investigations performed, two configurations were considered: (i) samples immersed in water and (ii) samples without water in the container. The first configuration avoids water desorption during the 15



a) Slice of sample E3 scanned when surrounded by water



b) Section in the middle of sample E3 scanned when not submerged in water (l_e represents the width of the sample equal to 6 mm at the initial state)



c) Gray level comparison between the two configurations on the same AB path

Figure 6. Two configurations of tomographic analyses.

minutes of scanning. It also eliminates some artifacts occurring at the interface between the glass beads and the adhesive phase, as shown in Figure 6b (see the blue ellipses). However, in this configuration, it is no longer possible to distinguish the edges of the sample, which further complicates the analysis of each volume. Also, the water that penetrates the pores cannot be separately identified. Moreover, the measurement noise is more important in this configuration. Conversely, the second configuration allows the separation of the ambient air surrounding the volumes and the measurement of their variation.

Gravimetric analyses were also performed so as to determine the loss of mass of the samples in configuration (ii). These measurements showed that about 0.15% of the mass is lost in 15 minutes if the sample is in ambient air at the temperature of 22°C and a humidity of 75% RH. This desorption phenomenon could therefore be considered as negligible, when compared to the long-term water uptake.

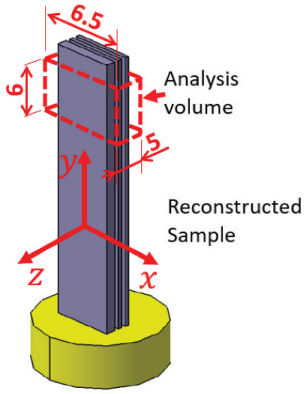
Figure 6c shows an overlay of the gray levels along the AB path (which is represented with a yellow line in Figure 6(a,b) for both configurations. It can be observed that the measurement noise decreases slightly for the configuration (ii). On top of that, the pore contrast increases, which facilitates the segmentation step of the different pores with fewer errors. Based on these preliminary investigations, it can then be justified that configuration (ii) provides more advantages than configuration (i). Nevertheless, it is important to note that a systematic loss of mass could explain some discrepancies in the comparison between the gravimetric measurements and the tomographic observations.

3.3.2. Image analysis

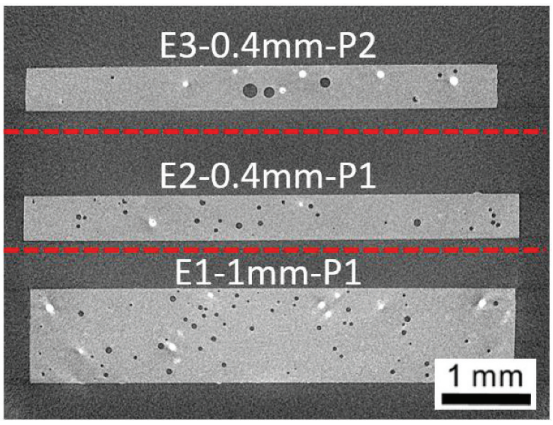
In order to make the best use of data arising from the reconstructed volumes, it is necessary to perform segmentation so as to isolate properly the different phases. This is a common concern in the field of image processing and computer vision, and it has been the subject of many studies, which have proposed a wide variety of methodologies.[16]

The simplest way to segment grayscale data with multiple phases is based on thresholding segmentation. Even if this method is rather basic, it generally provides satisfactory results, taking into account that the histogram of the data is adequate (i.e. the phases are easily distinguishable). The threshold can be chosen manually or calculated algorithmically; the latter being often preferred. The numerical determination of the threshold can be achieved in different ways: it can be based on the analysis of the histogram,[17] or by grouping the grayscale levels,[18] for example. More details concerning such methods are presented in Dumont et al.[19]

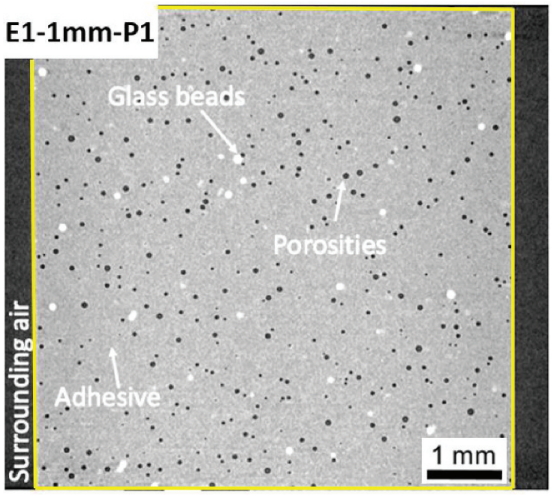
The processing strategy adopted in this study, dedicated to the segmentation of the three phases in hand, is described in the sequel. First, the reconstructed volume, represented by the red parallelepiped in Figure 7a, takes the following dimensions of $6.5 \times 6 \times 5\ \text{mm}^3$. This volume, initially coded on 14 bits, is converted to 8 bits in order to facilitate data exploitation on conventional computers. The coding depth degradation affects insignificantly the phase segmentation. The three volumes of each sample are then separated as shown in Figure 7b, using the Fiji software.[20] Some artifacts are visible around glass beads for sample E1. In Figure 7(c,d) a section in the *xy* plane at half thickness is shown for samples E1 and E3, respectively. In these two



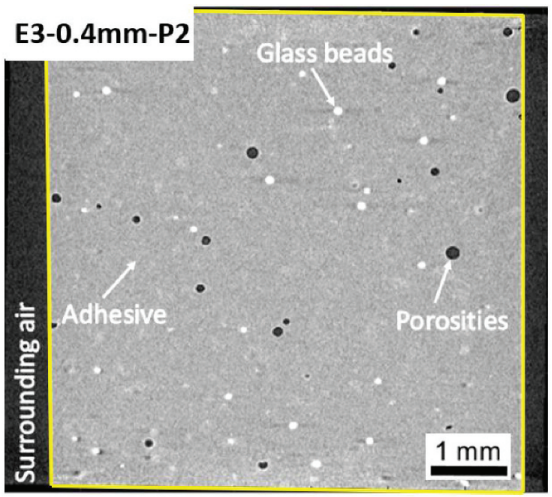
a) Samples and volume investigated by X-ray µ-tomography (dimensions in mm)



b) Section in the *xz* plane of the reconstructed volume of the three samples



c) Reconstituted CT-scan in *xy* plane (sample E1)



d) Reconstituted CT-scan in *x*y plane (sample E3)

Figure 7. Reconstituted volumes of the samples obtained from the CT scan.

figures, the porosities, the glass beads and the adhesive phase as well as their distribution are clearly visible.

The air surrounding each sample was removed by detecting the effective contour of the sample (marked in yellow in Figure 7(c,d)). This contour was identified for each image in the *xy* plane. Finally, the volume of sample E1 is composed of 227 images parallel to the *xy* plane, each image having a size of 1300×1400 pixels^2. As for samples E2 and E3, the corresponding volumes contain respectively 103 and 86 images parallel to the *xy* plane, with the same size of 1300×1400 pixels^2.

The identification of the sample contour in each image was obtained using the Random Walks algorithm proposed in Grady[21], which turns out to be very efficient in this case. Hence, the total volume occupied by the sample can be considered as the sum of all the pixels that are inside the contour of all the images. A mask can be then constructed for each image. In Figure 8b, the mask

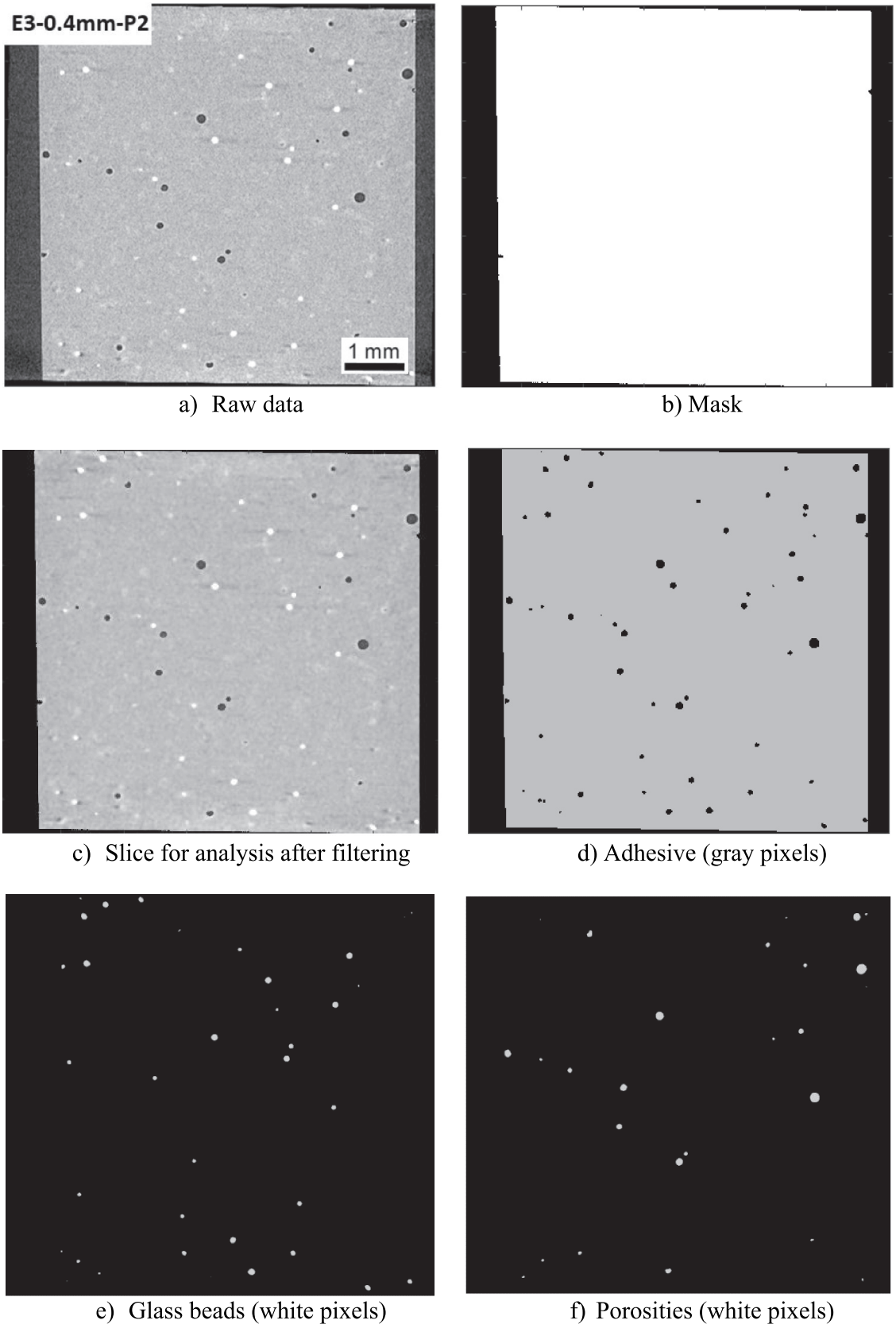


Figure 8. Results obtained from the segmentation of the phases in the adhesive.

associated with the image shown in Figure 8a is presented. White pixels represent the volume of the sample and black pixels represent the area surrounding the sample.

The thresholds that allow the segmentation of phases in the sample volume are automatically detected using the Otsu algorithm.[18] Thus, a multi-threshold process is used with $N_{thr} = 3$, aiming to discriminate the following phases: (i) pores, (ii) adhesive and (iii) glass beads. These multi-threshold values are obtained by maximizing the inter-class variance of grayscale levels for each class. To minimize the influence of the Charge-Coupled Device (CCD) sensor noise on the segmentation of each phase, a 3D median filter is applied to the complete raw volume. The filter size adopted here is of $3 \times 3 \times 3$ voxels^3. The effect of the filter can be seen in Figure 8c when compared to the raw image shown in Figure 8a. Measurement of noise effect on the detection of pores or glass beads has been analyzed in-depth in Dumont et al.[13], where the detection accuracy of pore volumes can go down to $1.8 \cdot 10^{-3}$%.

In Figure 8d, the adhesive phase is represented alone. The glass beads are shown in Figure 8e and the pores in Figure 8f. No pores or glass beads smaller than 3 voxels in diameter (13.5 μm) were considered in the analysis because the effect of CCD sensor noise on these features remains important despite the filtering used. At the end, all entities (pores or glass beads) for which the diameter is less than or equal to the size of the 3D median filter are excluded from the analysis.

3.3.3. Initial state of the adhesive

For an accurate understanding of the water absorption effect in adhesive materials, it is of great interest to know the microstructure, the distribution and the proportions of each phase at the initial state. The initial state can be referred to as the state of the adhesive immediately after curing. If the classical optical analysis with the KEYENCE VHX-7000 microscope was able to reveal the presence of each of these phases, the X-ray μ-tomography allowed us to determine quantitatively the different phases that compose the adhesive.

In Figure 9a, the spatial distribution of pores in sample E1 (with a thickness of 1 mm) is shown. A mostly homogeneous distribution is observed with some larger pores located close to the $\vec{y}$ axis. The origin of these pores could mostly be linked to the mixing process of component A and component B. In a direct manner, the process performed in atmospheric conditions could incorporate some air bubbles in the mix. Furthermore, the matrix contains glass beads, added by the manufacturer to ensure a minimum thickness during the bonding process in the case where the thickness of the adhesive is not imposed by specific elements. These glass beads could then be responsible for these larger porosities, as observed by Dumont et al.[19]

Figure 9c shows the pore distribution in sample E2. This distribution is mostly homogeneous and very similar to that of sample E1, despite the lower

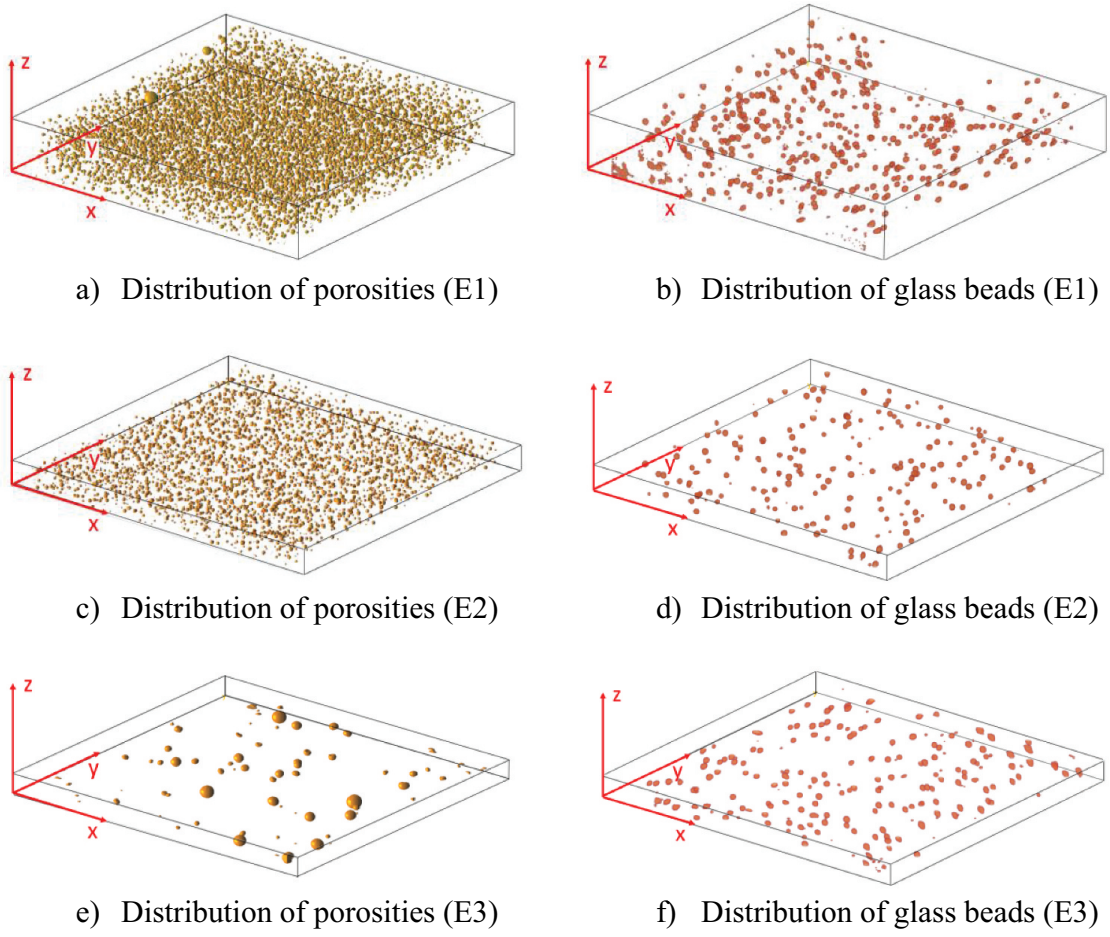
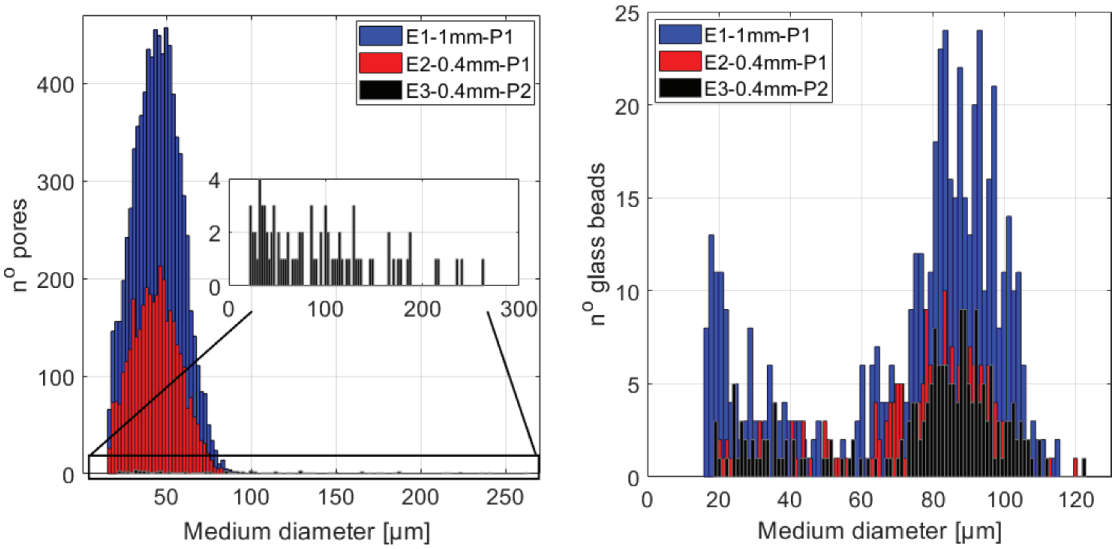


Figure 9. Distribution of the phases in the adhesive samples.

thickness of about 0.4 mm. Besides, the distribution of pores in sample E3 has been represented in Figure 9e. The effect of vacuum on pore size and distribution is clearly visible. Few pores are observed and characterized by very large diameters. The distribution of glass beads within the samples E1, E2 and E3 is shown in Figures 9(b,d,f) respectively. The glass beads have a rather spherical geometric shape. They are mostly solid, but hollow beads were also observed with a wall thickness between 20 µm and 30 µm.

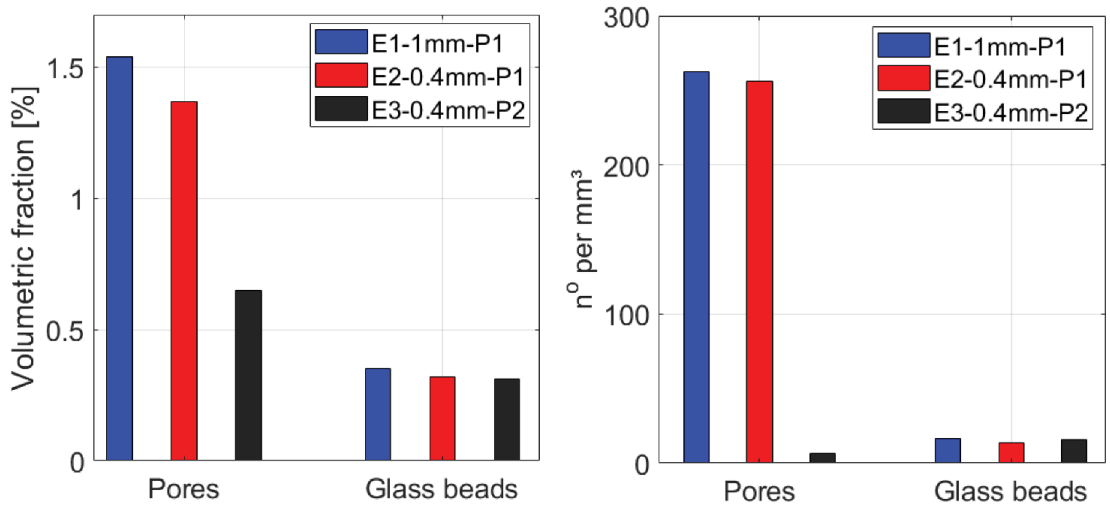
The distribution of pores is plotted in Figure 10a versus their equivalent diameter for the three samples. The distribution is rather Gaussian for E1 and E2, with equivalent diameters varying between 10 µm and 90 µm. More pores are detected for sample E1 than for E2, what was expected because of the larger thickness of sample E1, leading to a volume about 2.2 times greater.

Conversely, for sample E3, the distribution is mostly linear, with an equivalent diameter varying between 20 µm and 274 µm. The distribution of glass beads versus their equivalent diameter is shown in Figure 10b. The equivalent diameter of glass beads varies between 18 µm and 120 µm, with a similar trend for the three samples. More beads are detected in sample E1 again since its volume is larger.



a) Pores b) Glass beads

Figure 10. Number of pores and glass beads in the samples.



a) Pores/Glass beads volumetric fraction b) Pores/Glass beads number per mm^3

Figure 11. Volume fractions and numbers of pores and glass beads in the different samples.

In order to further understand the differences between the three samples, the volume fraction of each phase was represented in Figure 11a for each of them. The porosity rate differs for the three samples. In the present case, porosity fractions of 1.54% and 1.37% were found, respectively for sample E1 and E2. Therefore, the thickness variation seems to influence the volumetric fraction of porosities, in the sense that the pore volume fraction increases with the thickness. In the literature,[22–25] it has been shown that thicker joints had a lower breaking strength. This decrease in the maximum breaking strength could find an explanation in the presence of pores with a greater density in

thicker joints. In Figure 11a, it can also be seen that the effect of creating a vacuum on the adhesive, in the pasty state just after mixing, brings a significant improvement. The volume fraction of porosities is reduced from 1.37% for sample E2 (without vacuum) to 0.65% for sample E3 (with vacuum). Even though the overall porosity rate is much lower in sample E3, the presence of large pores can be very detrimental to the long-term mechanical strength of the adhesive joint. The volume fraction of glass beads is worth about 0.33% and is quasi-similar for the three samples. Furthermore, the numbers of pores and glass beads per unit volume are shown in Figure 11b. For sample E1, one finds 263 pores per mm^3 versus 255 pores per mm^3 for sample E2. In this way, the effect of thickness on the formation of pores can be hardly observed. In contrast, only 6 pores per mm^3 are found in sample E3. Besides, the density of glass beads is about 16 beads per mm^3, whatever the sample considered.

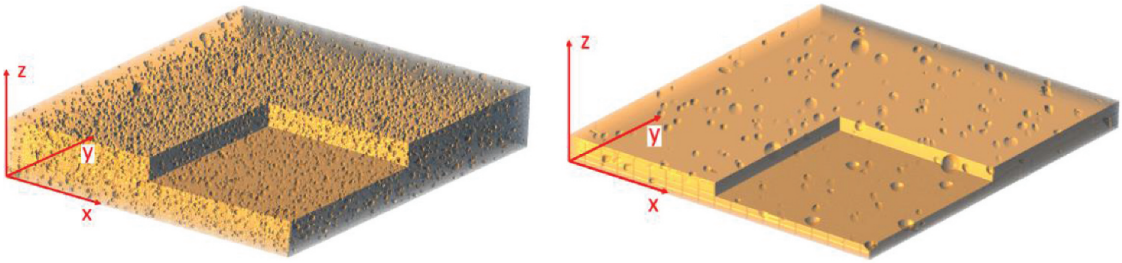
In Figure 12, the real architecture of the reconstructed volume containing adhesive has been represented by eliminating the pores and excluding 1/8 of the volume in order to better visualize the adhesive phase inside the volume. The change in the effective section is a semi-local indicator that could provide relevant information about the compactness of the adhesive.

Figure 13 shows the three relative effective sections, according to the three directions of the reference frame displayed in Figure 12. These relative effective sections are obtained by using the following expressions:

$$S_x = \frac{S_{ex}}{S_{tx}} \tag{3}$$

$$S_y = \frac{S_{ey}}{S_{ty}} \tag{4}$$

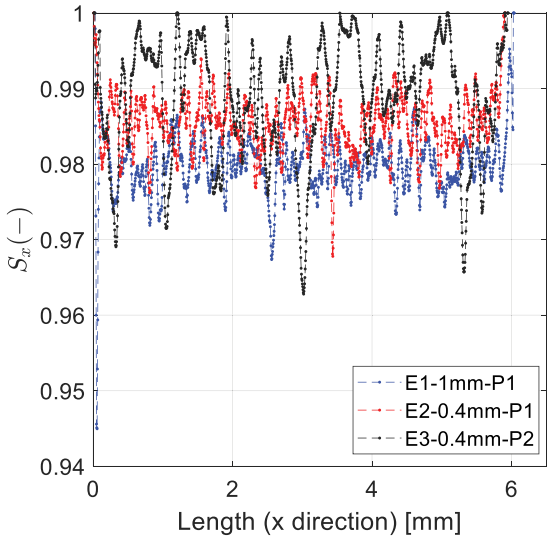
$$S_z = \frac{S_{ez}}{S_{tz}} \tag{5}$$



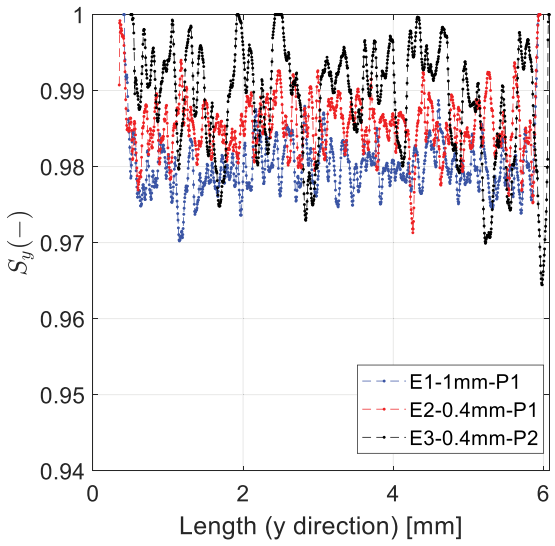
a) Effective volume of adhesive for sample E1

b) Effective volume of adhesive for sample E3

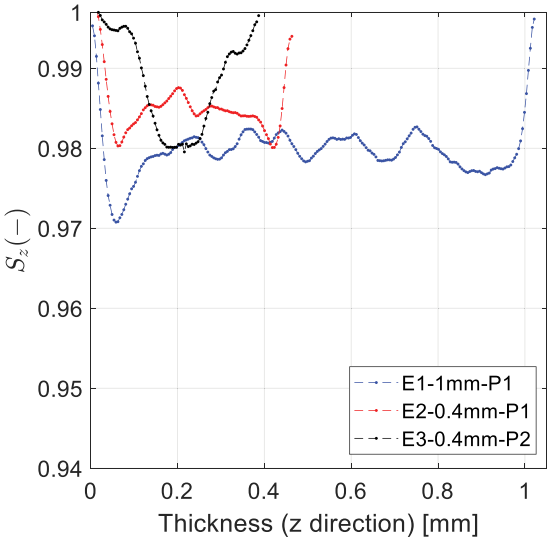
Figure 12. 3D representation of the effective volume of adhesive for samples E1 and E3.



a) Effective section S_x in $\vec{x}$ direction



b) Effective section S_y in $\vec{y}$ direction



c) Effective section S_z in $\vec{z}$ direction

Figure 13. Evolution of the effective sections for the three samples.

where S_{ex}, S_{ey} and S_{ez} represent the effective sections in the $\vec{x}$, $\vec{y}$ and $\vec{z}$ directions, respectively. To determine S_{ex}, for instance, a section is carried out in the adhesive at a given value of x, with a plane perpendicular to the $\vec{x}$ axis (such a section is similar to the one proposed in Figure 8d). S_{ex} is defined by the intersection of the plane with only the polymeric material (adhesive phase). S_{tx}, S_{ty} and S_{tz} represent the total section dimensions considered in the $\vec{x}$, $\vec{y}$ and $\vec{z}$ directions, respectively. To determine S_{tx}, a section is carried out in the adhesive as previously done, but all the phases are considered here in the determination of the intersection of the plane with the sample.

In Figure 13a, the evolution of the relative effective section S_x is plotted for the three samples. A rather homogeneous distribution in the $\vec{x}$ direction is observed for all three samples. The average value of each curve is very consistent with the associated porosity rate determined earlier. In samples E1 and E2, normal sections without any porosity (with $S_x = 1$) are not observed. The range of variation of S_x is wider for sample E3. This is due to the fact that, locally, there may be relatively large porosities that could reduce the section S_x by almost 4% and, by contrast, there are also several sections with no porosities at all. The evolution of the relative effective section S_y is shown in Figure 13b, which turns out to be very similar to the previous one in the $\vec{x}$ direction. This means that the pore-type defects are uniformly distributed in sections perpendicular to the xy plane. On the contrary, in Figure 13c, significantly different evolutions are observed for the relative effective section S_z. Considering first samples E1 and E2, there is a sharp decrease/increase in S_z on the top/bottom surfaces, which indicates a significant localization of pores far from these surfaces. The explanation could be that, close to the two aluminum plates used, there is enough surface energy to "attract" the polymeric material, and the pores would be "pushed" towards the center of the joint. A similar evolution is observed for sample E3 where the largest pores are positioned in the middle of the joint, leading to a decrease/increase of 2% of the effective section for a variation of the through-thickness position of about 100 µm, located here at mid-thickness.

In addition to the previous analysis, the shape of the pore-type defects was thoroughly characterized by calculating their sphericity, which represents the level of similarity between the shape of an object and a sphere. The formula used here to calculate the sphericity was initially proposed by Wadell[26] and writes:

$$\psi = \frac{\pi^{\frac{1}{3}}\left(6V_p\right)^{\frac{2}{3}}}{A_p} \tag{6}$$

where V_p and A_p represent the pore volume and surface area, respectively. The sphericity rate necessarily lies between 0 and 1. As an example, ψ is equal to 1 for a sphere, 0.806 for a cube, 0.874 for a cylinder and 0.671 for a tetrahedron.

In Figure 14, the sphericity distribution of the pores with respect to their equivalent diameter is plotted for the three different samples. It can be shown that most pores have a geometry close to a sphere. Only very few pores have a sphericity value below 0.6. These pores may result from the fusion of several pores and are characterized by a small equivalent diameter, often less than 20 µm, which gives rise to complex geometric shapes after voxelization.

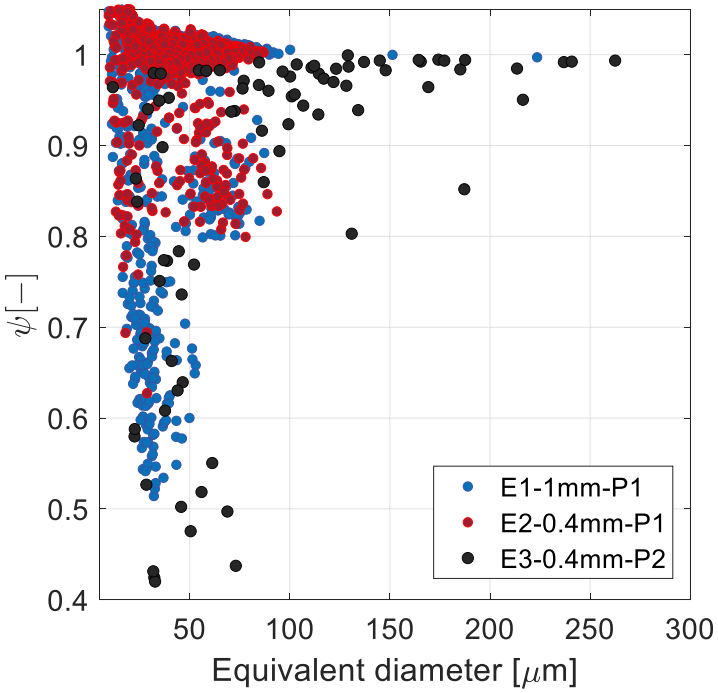


Figure 14. Sphericity of the pores.

3.3.4. Water effect on the adhesive

Visualization of the waterfront. Dealing with water diffusion, several authors have been interested in the detection of the waterfront, particularly in heterogeneous media such as concrete, for example.[11] During diffusion, the water penetrates the material and may change its density locally, allowing one to detect the presence of water by X-ray investigations.

In Figure 15, a cross-section of sample E3 is represented. This section is obtained by cutting the sample with a plane parallel to the *xz* plane at mid-distance between the edges (see Figure 7a). In order to get the visualization of the evolution of the water profile, this section is represented for eight successive aging times between the initial state (0 days) and a final state, 4 months later (120 days). Unfortunately, the waterfront within the sample, which should have been located through a variation of gray levels in the normal direction to the sample surface, is not detected here. Several reasons are likely to explain that.

First, the water is supposed to fill the free volume of the sample by capillarity. The free volume is the difference between the total macroscopic volume of the sample and that actually occupied by the molecules that constitute it. This free volume is localized between the chains of molecules[27] with a characteristic size lower than a micrometer and does not represent, in any case, the porosities. Hence, if this scenario occurs, the volume change should not be detected during the water uptake until this free volume is completely filled. That being said, it can be noticed in Figure 15 that the width of sample E3, denoted as l_0 at the initial state, slightly changes from 5 days of immersion,

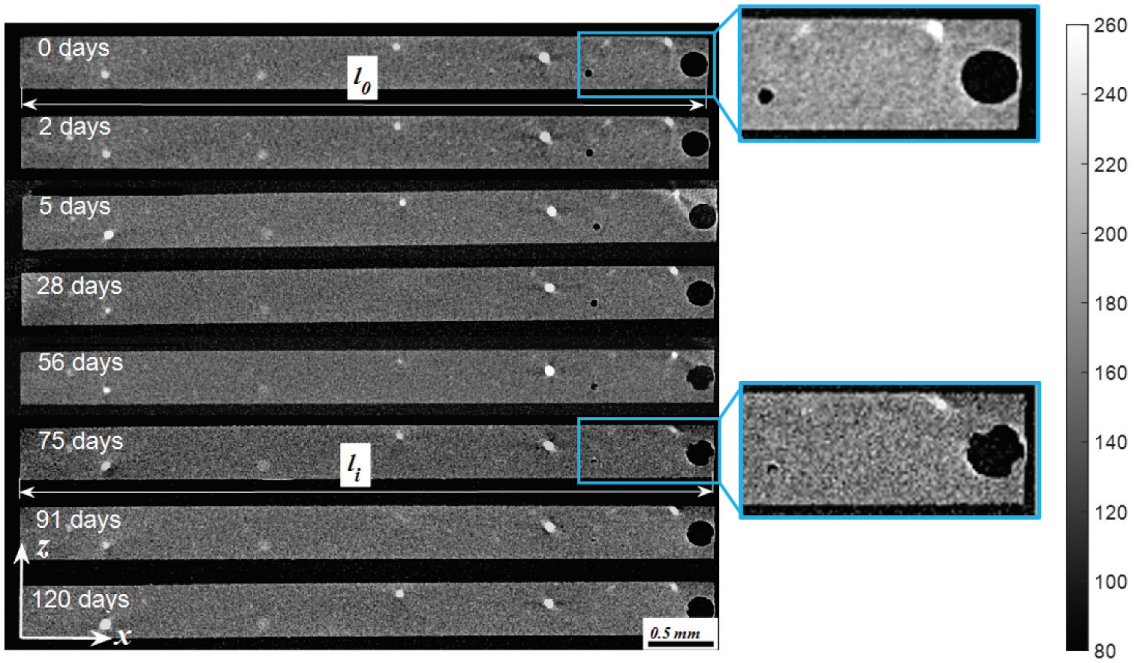


Figure 15. Gray levels in sample E3 versus aging time.

becoming then l_i. This variation in size is certainly due to hydric swelling. Most of all, if the pores end up filling with water (whereas the glass beads remain quasi-unchanged), the water occupying the pores displays a gray level almost identical to the one of the adhesive phase, due to the closeness of the respective densities of the demineralized water and the adhesive.

Figure 16 depicts the same observations performed on a section of sample E1 for similar aging times. Although this sample is 1 mm thick, no variation in gray level has been detected either, which could represent the water profile in the sample. However, the pore filling is more visible, especially in the vicinity of the faces normal to the $\vec{z}$ direction. As for the glass beads, they do not

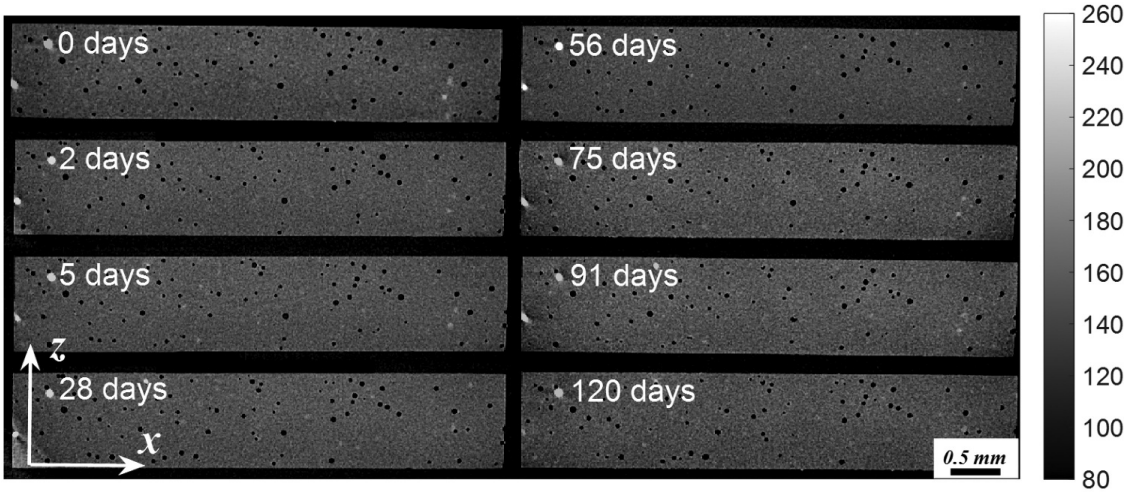


Figure 16. Gray levels in sample E1 versus aging time.

present a detectable evolution, keeping their diameters virtually constant. Some artifacts are also visible on the beads near the left edge.

In order to further analyze the pore filling, a section in the *xy* plane was performed at a distance of 54 µm from the surface of sample E2. Figure 17 shows the filling evolution at this section between the initial state (Figure 17a) and after 28 days (Figure 17b). The pores seem to shrink considerably and change their geometric shape due to the water that occupies their volumes.

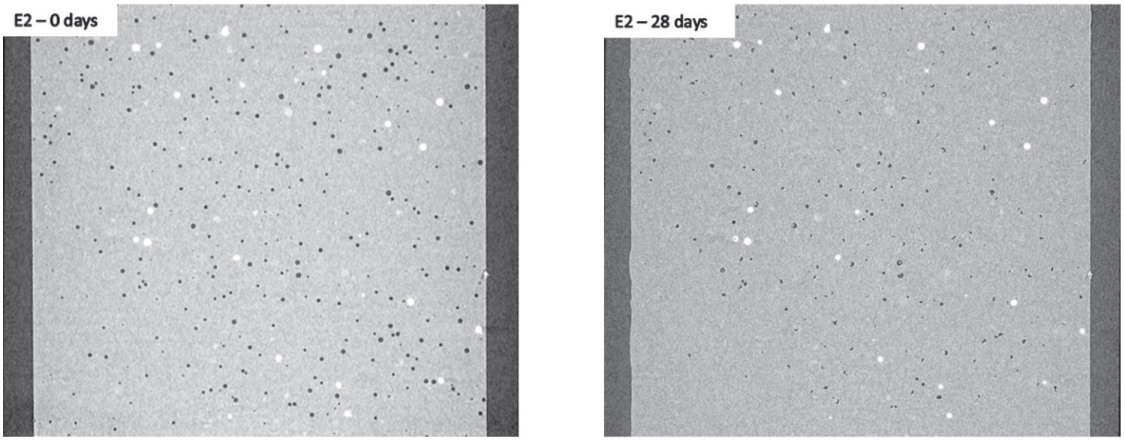
Evolution of volume ratios of adhesive, pores and glass beads. Despite the fact that one cannot detect the evolution of the waterfront in the samples, it is however possible to determine the evolution of each phase constituting the adhesive material in terms of volume ratio. First of all, the evolution with the aging time of the volume with a density (gray scale) close to that of the polymeric material or water is investigated. This volume change is calculated as follows:

$$\Delta V_a(\%) = \frac{V_{adh(t)} - V_{adh_0}}{V_{adh_0}} \times 100 \tag{7}$$

where $V_{adh(t)}$ represents the polymer and water volume for an aging time t, and V_{adh0} the polymer and water volume in the initial state. At each time t, the polymer and water volume $V_{adh(t)}$ is determined as the difference between the total volume of the sample $V_{total(t)}$ and both the volume of glass beads $V_{beads(t)}$ and the pore volume $V_{pores_{(t)}}$:

$$V_{adh(t)} = V_{total(t)} - V_{beads(t)} - V_{pores_{(t)}} \tag{8}$$

The volumetric fractions of pores and beads are determined using the following expressions:



a) Initial section located at 54 µm depth in the thickness ($\vec{z}$ direction)

b) Section after 28 days taken at 54 µm depth in the thickness ($\vec{z}$ direction)

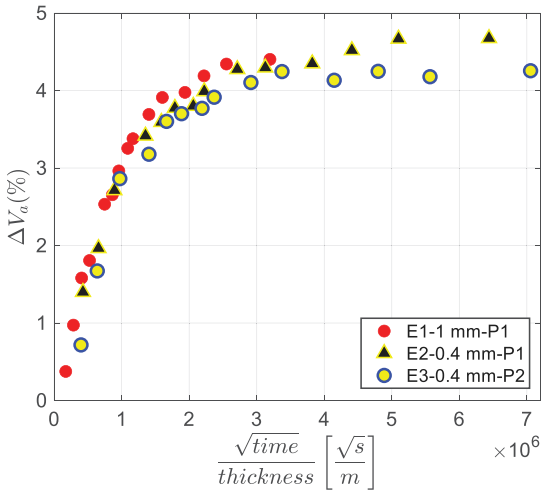
Figure 17. Sections in sample E2 illustrating the pore filling.

$$\Delta V_p(\%) = \frac{V_{pores_{(t)}} - V_{pores_0}}{V_{adh_0}} \times 100 \tag{9}$$

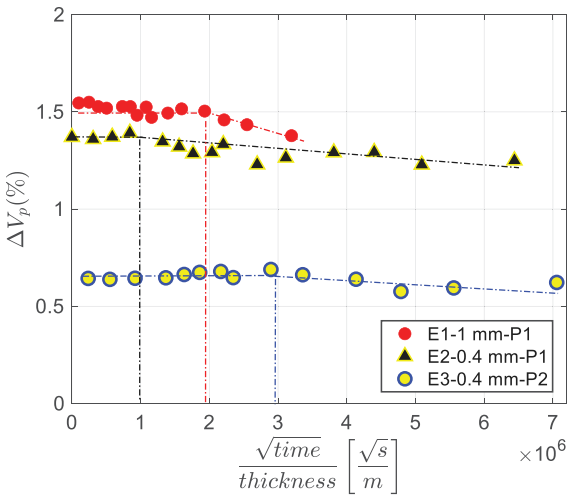
$$\Delta V_b(\%) = \frac{V_{beads(t)} - V_{beads_0}}{V_{adh_0}} \times 100 \tag{10}$$

where $V_{pores_{(t)}}$ and $V_{beads(t)}$ represent respectively the pore and bead volumes at an aging time t, and V_{pores_0} and V_{beads0} represent the same volumes at the initial state.

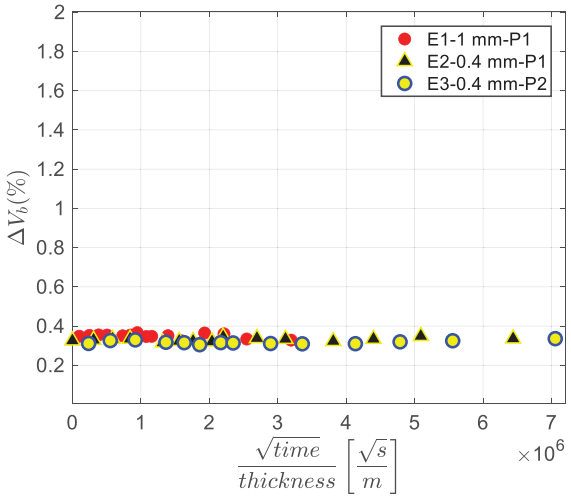
Figure 18a displays the relative evolution of the polymer and water volume ΔV_a for each sample as a function of the square root of time normalized by the



a) Evolution of polymer and water volume versus aging time



b) Evolution of the volumetric fraction of pores versus aging time



c) Evolution of the volumetric fraction of glass beads versus aging time

Figure 18. Evolution of the different phases of the adhesive material.

sample thickness. This representation is similar to the one depicted in Figure 5. This evolution in volume should be correlated with the variation of mass mentioned previously. However, a slight shift is observed between these two quantities, as will be discussed later.

In Figure 18b, the evolution of the porosity fraction ΔV_p is represented, again as a function of the square root of time divided by the sample thickness. For sample E1, a first regime is observed during which the global pore volume remains quasi-constant, followed by a slow decrease from $2 \times 10^6 \sqrt{s}$. This reduction may be attributed to the filling of pores with water, which starts in the pores closest to the sample free surfaces and gradually evolves towards the center of the sample. A similar behavior is observed with sample E2, for which the first regime ends around $1 \times 10^6 \sqrt{s}$ with a very slight decrease. In both cases of samples E1 and E2, the second regime allows one to determine the pore filling speed when the sample is immersed in water. For sample E3, the first regime ends at nearly $3 \times 10^6 \sqrt{s}$. This first regime seems to be influenced as much by the joint thickness as by the size and spatial distribution of pores. If the first regime ends so late, it is probably due to the quite significant average distance between the free surfaces of the sample (normal to $\vec{z}$) and the first closest pores. Owing to the relatively large size of pores in this sample, they are found to be located more at mid-thickness than close to the free surfaces. Moreover, the average distance between pores (still significant in sample E3) could also be a factor influencing the pore filling start time.

Figure 18c presents the evolution of the volumetric fraction of glass beads ΔV_b. The three samples show a quasi-constant volumetric fraction of glass beads during the entire measurement period, which suggests that water does not penetrate the beads, as naturally expected. By the way, these results enhance the robustness of the image processing method and enable one to ensure that the volumes investigated are representative with respect to the phases analyzed.

Further understanding of the correlation between the polymer and water volume change ΔV_a and the mass change C was achieved by plotting their relative dependence in Figure 19. It can be observed, at the initial stage of water absorption, that the mass of the samples increases without detecting a variation in volume. This phenomenon may be explained by the fact that water penetrates the sample in filling first some free volumes by capillarity. Once these free volumes are filled, a linear dependence between the mass of the samples and their volume is observed. This pattern is in perfect agreement with previous works in the literature (see Adamson[28], for instance).

Sphericity of the pores. The water which penetrates the pores modifies considerably their geometry. The relevant parameter to characterize the

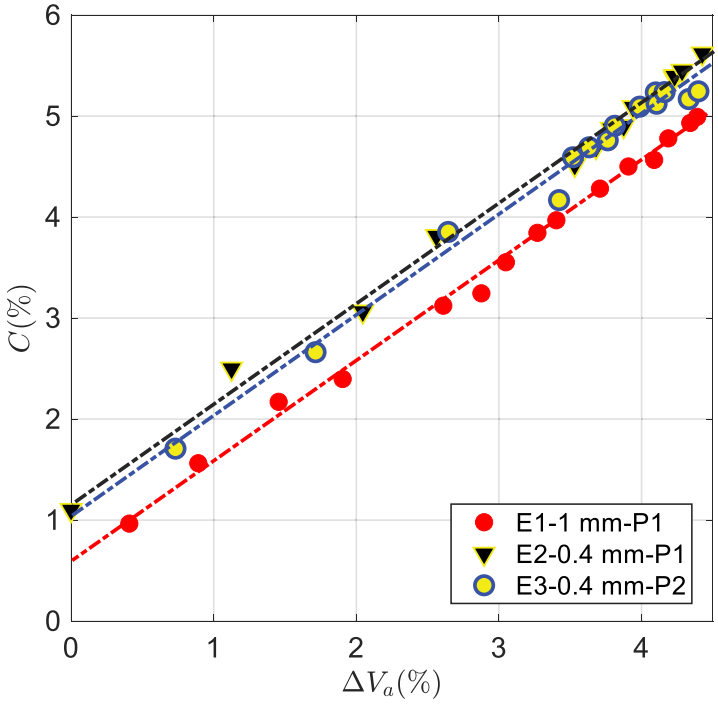
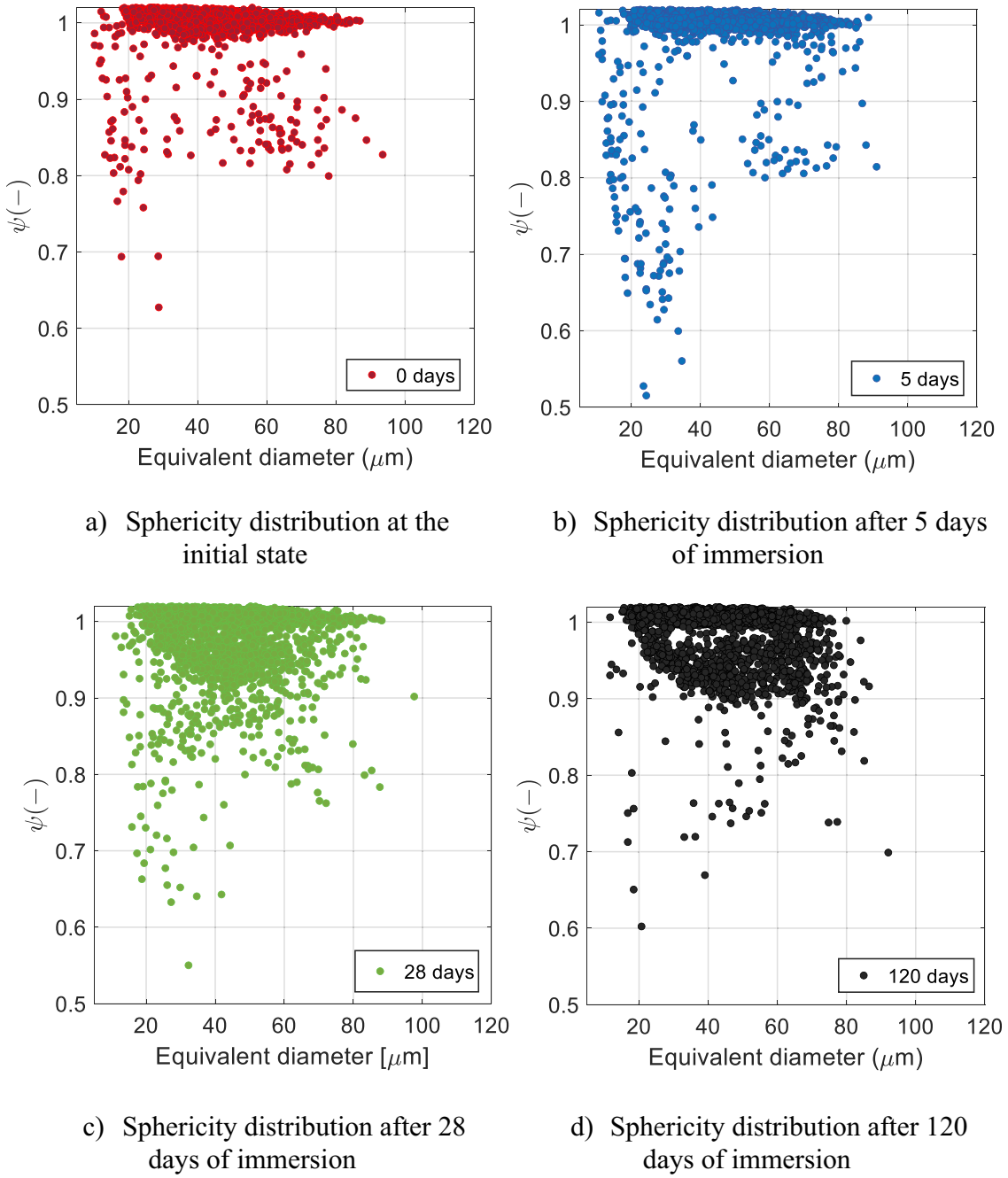


Figure 19. Mass change of the samples versus variation in the effective volume of the adhesive.

geometric shape of the pores during water aging is again the sphericity. In Figure 20, the sphericity distribution of pores in sample E2 is represented at four aging times (including the initial state) with respect to their equivalent diameter.

As formerly observed in Figure 14, most of the pores have initially a quite spherical shape, but with a large variety of diameters. Only few pores (whose diameter is around 20 μm) have a sphericity index lower than 0.8. Such pores are mainly close to the free surfaces of the sample and have been generated by the waterjet cutting, or these are small pores which must certainly have merged during the curing cycle. The sphericity of pores after 5 days of immersion is shown in Figure 20b. For most of them, there is no relevant change in the geometric shape, except for some characterized by an equivalent diameter between 20 μm and 30 μm. As said before, such pores of small diameter are generally located near the free surfaces and water naturally begins to penetrate them, leading thus to a decrease of their sphericity. Bigger pores also localized not far from the edges may also fill up with water. However, at this time, the amount of water brought into play is very small when compared to the size of the larger pores and it does not result in any significant change of their shape, unlike smaller ones. After 28 days of water aging, it is observed that the geometric shape of a considerable proportion of pores is affected. As previously noted, the lowest sphericity level is obtained with the smallest pores, reducing down to 0.55. However, water begins to modify significantly the sphericity of pores of intermediate diameters. At this aging time, an average decrease in sphericity from 1 to 0.92 is observed for pores between 30 μm and



a) Sphericity distribution at the initial state

b) Sphericity distribution after 5 days of immersion

c) Sphericity distribution after 28 days of immersion

d) Sphericity distribution after 120 days of immersion

Figure 20. Evolution of the sphericity distribution of pores with aging time for sample E2.

70 µm, with a maximum change for pores between 45 µm and 50 µm. This decrease in sphericity can be further visualized in Figure 20d, where it is obvious that the larger pores are also affected by water penetration. In Figure 20d, it is even possible to notice a separation between two regions, a first one where the pores are not yet affected by water (with a sphericity close to 1), and a second one where sphericity has dropped down to 0.9 at the minimum, due to the increasing amount of water in the material. The comparison between the initial and final states is also represented in Figure 21 in a different manner.

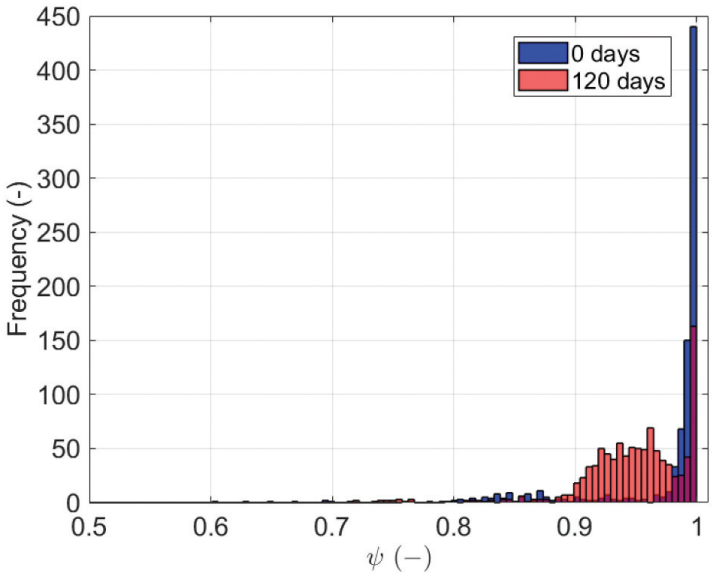


Figure 21. Evolution of the sphericity distribution of pores in terms of frequency.

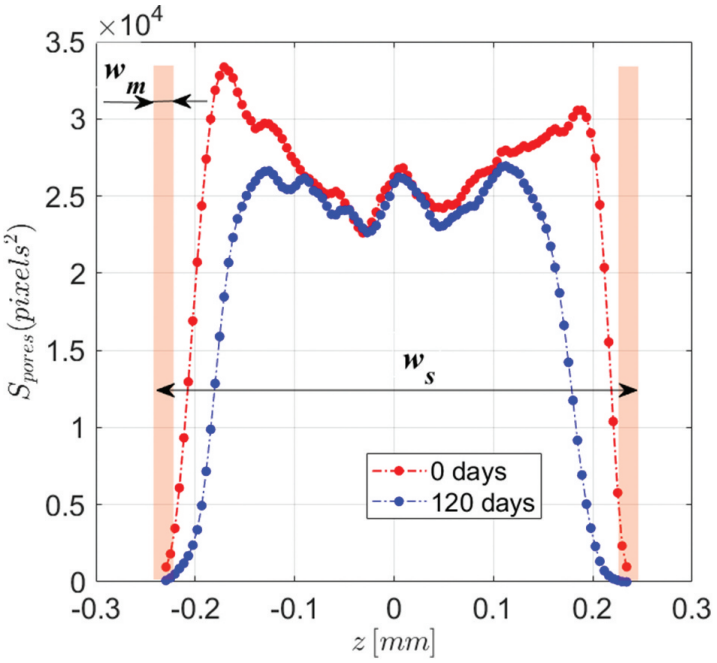


Figure 22. Evolution of the pore sections along the thickness direction in sample E2, at the initial state and after 120 days of aging.

Local distribution of water in the pores. A straightforward way to better understand the evolution of pore filling in a preferential direction (along the thickness of the samples, for example), when the sample is immersed in water, amounts to studying the evolution of the pore sections. Figure 22 depicts the global area S_{pores} occupied by the pores (in pixels^2), for several sections in the xy plane at different positions along the thickness. The parameter w_s represents the effective thickness of the sample. As formerly shown, between the free surfaces of the sample and the first pores, there is a slice of adhesive with

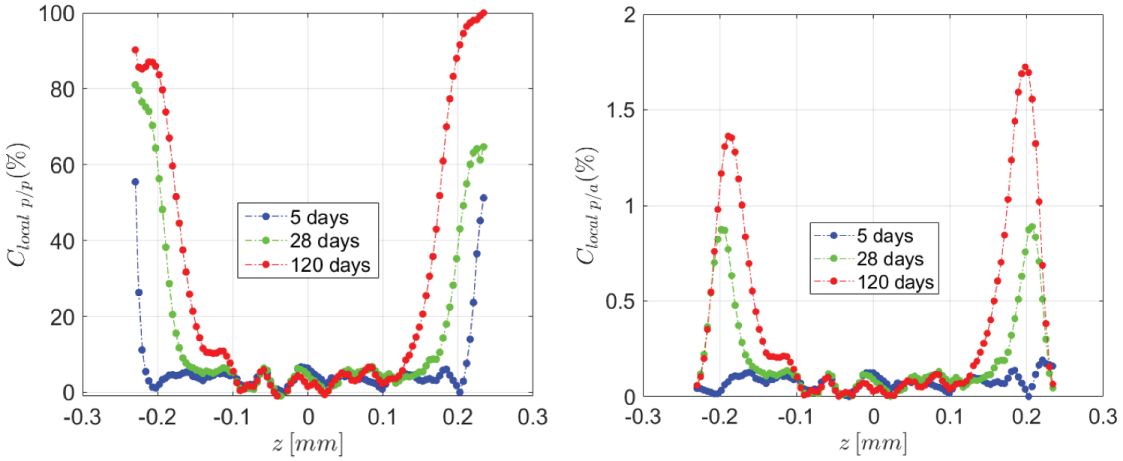
a thickness w_m varying between 12 µm and 25 µm (depending on the process and the sample), in which no pores are present.

At the initial state, the variation of the pore section along the thickness of the sample is quite consistent with the porosity profile according to the $\vec{z}$ direction represented in Figure 13c, with two peaks of pore concentration in the vicinity of the two free surfaces normal to the $\vec{z}$ axis. Then, the water effect on the evolution of these pore sections is clearly visible. A significant decrease is particularly observed around the free surfaces between the initial state and the final state after 120 days of immersion. Therefore, this evolution only concerns the areas with high pore concentration, i.e. for z varying between ±0.2 mm and ±0.1 mm. Conversely, almost no changes occur in the central part of the sample, i.e. for z in the interval [−0.1 mm, 0.1 mm].

The filling percentage of the initial pore sections, determined from the section evolution, is calculated with the following expression:

$$C_{localp/p}(\%) = \frac{S_{pores_{(0)}} - S_{pores_{(t)}}}{S_{pores_{(0)}}} \times 100 \tag{11}$$

This analysis is performed in each section at a whole and does not provide a filling value for each pore individually. This pore filling percentage $C_{localp/p}$ is plotted in Figure 23a. It is observed that, after only 5 days, the first sections tangent to the first pores are affected by the presence of water, even if it is not possible to clearly detect any water droplets at the local scale (probably because of the insignificant amount of water existing in the pores). After 28 days of immersion, the first pores closest to the free surfaces are filled to an average amount of 80%. At this time, it is also noticed that the first pores in which water is detected are found to lie at about 65 µm from the corresponding external surface. After 120 days, the pores closest to the free surfaces are



a) Percentage of water in pores related to the section area of pores

b) Percentage of water in pores related to the entire section area of adhesive

Figure 23. Evolution of water proportion in pores along the $\vec{z}$ direction in sample E2.

almost totally filled (with a percentage of water close to 100%) and the area along the $\vec{z}$ direction in which water is detected is about 130 µm thick.

Furthermore, the average percentage of water in the pores, related to the initial entire section area of the adhesive $S_{tz(0)}$, has been determined using the following expression, for each successive section in the $\vec{z}$ direction:

$$C_{localp/a}(\%) = \frac{S_{pores_{(0)}} - S_{pores_{(t)}}}{S_{tz(0)}} \times 100 \tag{12}$$

Figure 23b displays this water percentage $C_{localp/a}$ in the pores. It can be observed that the two areas where the pores are almost filled (after 120 days) show a global percentage of water equal to 1.4% at the maximum on the left side and 1.76% on the right side, respectively. This dissymmetry should naturally be correlated with the pore concentration which is slightly higher on the right side.

All these results show that a tomographic analysis allows one to characterize the water uptake inside an adhesive material with a very good accuracy. The evolution of the waterfronts shall be deduced from the evolution of the volumes of the pores within the adhesive. Then, these evolutions will provide relevant information on the kinetics of water uptake, allowing one to tend more judiciously towards an optimal diffusion model.

4. Conclusions and perspectives

This paper presents an investigation on the mechanisms of water uptake in a bi-component epoxy structural adhesive by using X-ray µ-tomography (a non-contact and therefore non-intrusive technique), by measuring weight variations, and by performing microscopic analyses. At the initial state, the adhesive joint is heterogeneous and also displays a population of pore-type defects. These porosities are mainly generated during the mixing process between the two components of the adhesive. The curing cycle may contribute additionally to the creation of pores, but it remains relatively inconsequential, due to the low cure temperature in the present study. The number of porosities highly increases with the thickness of the adhesive specimen, which weakens its effective section. Concerning the initial state, it has been finally shown that no pores appear near the free surfaces of the samples (at the interface with the substrates in the bonded assembly) with a minimal distance between these surfaces and the first pores varying between 15 µm and 20 µm.

Dealing now with water uptake, attempts were made to measure the waterfront and thus the filling speed throughout the adhesive material. Unfortunately, water could not be identified separately from the adhesive material, due to the proximity between the polymer and water densities. Weight and volume measurements allowed one, however, to rule on the course of events. The water that penetrates

the adhesive fills in first the free volume of the material by capillarity and then, the absorbed quantity of water is found almost entirely in the volume of pores. The dependence relationship between the mass and volume of samples is quasi-linear, with a shift upon the beginning of aging corresponding to the filling of the free volume. The occurrence of water in the shape of droplets inside the pores has then been detected, first qualitatively by microscopic observations, and then quantitatively by tomographic investigations. Finally, the evolution of the pore filling front may alternatively contribute to a judicious choice of a water diffusion model.

This work opens up a number of perspectives. Primarily, the proportionality between the change in mass and the change in volume of the adhesive is probably related to the affinity of water with the adhesive. This aspect associates the diffusion of water within the polymer with the presence of polar chemical groups. These groups have the capacity to create hydrogen bonds with the water molecules, which increases the global volume of the material. Hydroxyl or amine groups, found in most epoxy resins or epoxy adhesives, are highly hydrophilic. The dependence between mass and volume could also enable the determination of a swelling coefficient. Next, the definition and prediction of swell is interesting with the idea of estimating its effect on the distribution of mechanical stresses within the adhesive during water aging. Subsequently, all these tomographic observations, when performed during sorption/desorption cycles, may show the irreversibility and the damage that an adhesive joint could suffer during the cycling of water aging.

Acknowledgments

The authors are indebted to the DGA (Direction Générale de l'Armement) for its financial support.

Disclosure statement

The authors declare that they have no known competing financial interests or personal relationships that could have appeared to influence the work reported in this paper.

Funding

The work was supported by the Direction Générale de l'Armement .

ORCID

Jérôme Adrien http://orcid.org/0000-0003-0341-3559

References

[1] Leconte, N., Bourel, B., Lauro, F., Badulescu, C., Markiewicz, E. Strength and Failure of an Aluminum/PA66 Self-Piercing Riveted Assembly at Low and Moderate Loading Rates: Experiments and Modeling. *Int. J. Impact Eng.* 2020, *142*, 103587. DOI: 10.1016/j.ijimpeng.2020.103587.

[2] Badulescu, C., Cognard, J. Y., Créac'hcadec, R., Vedrine, P. Analysis of the Low Temperature-Dependent Behaviour of a Ductile Adhesive Under Monotonic Tensile/compression-Shear Loads. *Int. J. Adhes. Adhes.* 2012, *36*, 56–64. DOI: 10.1016/j.ijadhadh.2012.03.009.

[3] Ilioni, A., Le Gac, P. Y., Badulescu, C., Thevenet, D., Davies, P. Prediction of Mechanical Behaviour of a Bulk Epoxy Adhesive in a Marine Environment. *J. Adhes.* 2018, *95*, 1–21. DOI: 10.1080/00218464.2017.1377616.

[4] Ilioni, A., Badulescu, C., Carrere, N., Davies, P., Thévenet, D. A Viscoelastic-Viscoplastic Model to Describe Creep and Strain Rate Effects on the Mechanical Behaviour of Adhesively-Bonded Assemblies. *Int. J. Adhes. Adhes.* 2018, *82*(2017), 184–195. DOI: 10.1016/j.ijadhadh.2017.12.003.

[5] Toscano, A., Pitarresi, G., Scafidi, M., Di Filippo, M., Spadaro, G., Alessi, S. Water Diffusion and Swelling Stresses in Highly Crosslinked Epoxy Matrices. *Polym. Degrad. Stab.* 2016, *133*, 255–263. DOI: 10.1016/j.polymdegradstab.2016.09.004.

[6] Selakjani, P. P., Dorieh, A., Pizzi, A., Shahavi, M. H., Hasankhah, A., Shekarsaraee, S., Ashouri, M., Movahed, S. G., Abatari, M. N. Reducing Free Formaldehyde Emission, Improvement of Thickness Swelling and Increasing Storage Stability of Novel Medium Density Fiberboard by Urea-Formaldehyde Adhesive Modified by Phenol Derivatives. *Int. J. Adhes. Adhes.* 2021, *111*, 102962. DOI: 10.1016/j.ijadhadh.2021.102962.

[7] Oliveira, R., Bilro, L., Marques, T. H. R., Cordeiro, C. M. B., Nogueira, R. Simultaneous Detection of Humidity and Temperature Through an Adhesive Based Fabry–Pérot Cavity Combined with Polymer Fiber Bragg Grating. *Opt. Lasers Eng.* 2019, *114*, 37–43. DOI: 10.1016/j.optlaseng.2018.10.007.

[8] Grangeat, R., Girard, M., Lupi, C., Leduc, D., Jacquemin, F. Measurement of the Local Water Content of an Epoxy Adhesive by Fiber Optic Sensor Based on Fresnel Reflection. *Mech. Syst. Signal Process.* 2020, *141*, 106439. DOI: 10.1016/j.ymssp.2019.106439.

[9] Bridarolli, A., Odlyha, M., Burca, G., Duncan, J. C., Akeroyd, F. A., Church, A., Bozec, L. Controlled Environment Neutron Radiography of Moisture Sorption/Desorption in Nanocellulose-Treated Cotton Painting Canvases. *ACS Appl. Polym. Mater.* 2021, *3*(2), 777–788. DOI: 10.1021/acsapm.0c01073.

[10] Dewanckele, J., De Kock, T., Fronteau, G., Derluyn, H., Vontobel, P., Dierick, M., Van Hoorebeke, L., Jacobs, P., Cnudde, V. Neutron Radiography and X-Ray Computed Tomography for Quantifying Weathering and Water Uptake Processes Inside Porous Limestone Used as Building Material. *Mater. Charact.* 2014, *88*, 86–99. DOI: 10.1016/j.matchar.2013.12.007.

[11] Van Belleghem, B., Montoya, R., Dewanckele, J., Van den Steen, N., De Graeve, I., Deconinck, J., Cnudde, V., Van Tittelboom, K., De Belie, N. Capillary Water Absorption in Cracked and Uncracked Mortar – a Comparison Between Experimental Study and Finite Element Analysis. *Constr. Build. Mater.* 2016, *110*, 154–162. DOI: 10.1016/j.conbuildmat.2016.02.027.

[12] Dumont, V., Badulescu, C., Stamoulis, G., Adrien, J., Maire, E., Lefèvre, A., Thévenet, D. On the Influence of Mechanical Loadings on the Porosities of Structural Epoxy Adhesives Joints by Means of in-Situ X-Ray Microtomography. *Int. J. Adhes. Adhes.* 2020, *99*, 1025681–10256814. DOI: 10.1016/j.ijadhadh.2020.102568.

[13] Dumont, V., Badulescu, C., Adrien, J., Carrere, N., Thévenet, D., Maire, E. Experimental Investigation of Porosities Evolution in a Bonded Assembly by Means of X-Ray Tomography. *J. Adhes.* 2021, *97*(6), 528–552. DOI: 10.1080/00218464.2019.1685984.
[14] Deroiné, M., Le Duigou, A., Corre, Y. M., Le Gac, P. Y., Davies, P., César, G., Bruzaud, S. Accelerated Ageing of Polylactide in Aqueous Environments: Comparative Study Between Distilled Water and Seawater. *Polym. Degrad. Stab.* 2014, *108*, 319–329. DOI: 10.1016/j.polymdegradstab.2014.01.020.
[15] Pollak, B., "Experiences with Planography from the Fort William Sanatorium, Fort William, Ontario, Canada" *Dis. Chest*, vol. *24*, no. 6, pp. 663–669, 1953, doi: 10.1378/chest.24.6.663. Dis. Chest
[16] Sezgin, M. Survey Over Image Thresholding Techniques and Quantitative Performance Evaluation. *J. Electron. Imaging.* 2004, *13*(1), 146–165. DOI: 10.1117/1.1631315.
[17] Rosenfeld, A., La Torre, P. D. Histogram Concavity Analysis as an Aid in Threshold Selection. *IEEE Trans. Syst. Man. Cybern.* 1983, *13*(2), 231–235. DOI: 10.1109/TSMC.1983.6313118.
[18] Otsu, N. A Threshold Selection Method from Gray-Level Histograms. *IEEE Trans. Syst. Man. Cybern.* 1979, *9*(1), 62–66. DOI: 10.1109/tsmc.1979.4310076.
[19] Dumont, V., Badulescu, C., Stamoulis, G., Adrien, J., Maire, E., Lefèvre, A., Thévenet, D. On the Effect of the Curing Cycle on the Creation of Pores in Structural Adhesive Joints by Means of X-Ray Microtomography. *J. Adhes.* 2021, *97*(12), 1073–1106. DOI: 10.1080/00218464.2020.1728257.
[20] Schindelin, J., Arganda-Carreras, I., Frise, E., Kaynig, V., Longair, M., Pietzsch, T., Preibisch, S., Rueden, C., Saalfeld, S., Schmid, B., et al. Fiji: An Open-Source Platform for Biological-Image Analysis. *Nat. Methods.* 2012, *9*(7), 676–682.
[21] Grady, L. Random Walks for Image Segmentation. *IEEE Trans. Pattern Anal. Mach. Intell.* 2006, *28*(11), 1768–1783. DOI: 10.1109/TPAMI.2006.233.
[22] Gleich, D. M., Van Tooren, M. J. L., Beukers, A. Analysis and Evaluation of Bondline Thickness Effects on Failure Load in Adhesively Bonded Structures. *J. Adhes. Sci. Technol.* 2001, *15*(9), 1091–1101. DOI: 10.1163/156856101317035503.
[23] da Silva, L. F. M., Rodrigues, T. N. S. S., Figueiredo, M. A. V., de Moura, M. F. S. F., Chousal, J. A. G. Effect of Adhesive Type and Thickness on the Lap Shear Strength. *J. Adhes.* 2006, *82*(11), 1091–1115. DOI: 10.1080/00218460600948511.
[24] Chai, H. The Effects of Bond Thickness, Rate and Temperature on the Deformation and Fracture of Structural Adhesives Under Shear Loading. *Int. J. Fract.* 2004, *130*(1), 497–515. DOI: 10.1023/B:FRAC.0000049504.51847.2a.
[25] Carbas, R. J. C., Dantas, M. A., Marques, E. A. S., da Silva, L. F. M. Effect of the Adhesive Thickness on Butt Adhesive Joints Under Torsional Loads. *J. Adv. Join. Process.* 2021, *3*, 100061. DOI: 10.1016/j.jajp.2021.100061.
[26] Wadell, H., Volume, Shape, and Roundness of Quartz Particles, *J. Geol*, vol. *43*, pp. 250–280, May 1935, doi: 10.1086/624298.
[27] Chen, C.; Han, B., Li, J., Shang, T., Zou, J., Jiang, W., A New Model on the Diffusion of Small Molecule Penetrants in Dense Polymer Membranes, *J. Memb. Sci*, vol. *187*, no. 1, pp. 109–118, 2001, doi: 10.1016/S0376-7388(00)00689-X.
[28] Adamson, M. J. Thermal Expansion and Swelling of Cured Epoxy Resin Used in Graphite/Epoxy Composite Materials. *J. Mater. Sci.* 1980, *15*(7), 1736–1745. DOI: 10.1007/BF00550593.

2.5 Origine de défauts et mécanismes d'endommagement

La qualité des collages dépend de divers facteurs : taux de polymérisation, qualité du mélange des constituants de la colle ou bien les défauts de collage comme la variation de l'épaisseur ou les défauts à l'intérieur du joint. Ceux-ci peuvent prendre la forme de pores, de géométries et de tailles différentes, et constituent une menace potentielle pour la résistance mécanique des joints [106], surtout lorsqu'on évalue l'intégrité de la liaison à long voire très long terme. Plus précisément, ces pores peuvent favoriser des concentrations de contraintes de très forte intensité et sont susceptibles d'affaiblir localement le joint d'adhésif. Comme ils sont créés au cours du processus de collage [56], l'hypothèse selon laquelle les conditions de collage et de cuisson devraient influencer leurs propriétés est bien fondée. Afin de valider cette affirmation, des échantillons collés ont été réalisés, pour différents adhésifs et différents cycles de durcissement. En particulier, l'influence de la température maximale atteinte pendant le cycle de durcissement a été étudiée. Les pores des joints ont ensuite été observés et étudiés à l'aide de la µ-tomographie aux rayons X.

En fonction de leurs caractéristiques, ces pores sont susceptibles d'influencer le comportement mécanique des joints collés, car ils induisent un affaiblissement local dans la liaison collée et peuvent également créer des concentrations de contraintes, par endroit très intense. On peut également constater que les caractéristiques des pores à l'intérieur d'un joint adhésif peuvent varier lorsque les assemblages sont sollicités mécaniquement par des charges externes différentes. Afin d'étudier en profondeur ces changements dans la microstructure de l'adhésif, des échantillons collés ont été fabriqués, à l'aide de deux adhésifs structurels époxydiques bi-composants différents.

Il a été constaté qu'une température de polymérisation plus élevée peut induire des phénomènes notables de croissance des pores (principalement la dilatation et la coalescence). En particulier, cette croissance semble être prédominante à mi-épaisseur des joints, ce qui entraîne une diminution détectable de la section effective.

Des mesures in situ par tomographie aux rayons X ont été effectuées simultanément à l'application d'une charge de traction sur les échantillons. Il a ainsi été possible de caractériser l'état de la porosité de chaque échantillon sous charge mécanique et de calculer diverses grandeurs (rapport volumétrique de la porosité, nombre de pores, distribution des diamètres équivalents, etc). Il a été constaté que les pores dans les joints sont affectés par l'augmentation de la contrainte mécanique, ce qui entraîne la nucléation, la croissance et la coalescence des pores. En outre, des analyses plus poussées montrent que ce comportement microstructural ne peut pas être généralisé [12], car des adhésifs différents peuvent présenter des propriétés différentes.

Publications jointes

- V. Dumont, C. Badulescu, G. Stamoulis, J. Adrien, E. Maire, A. Lefèvre, D. Thévenet, **On the effect of the curing cycle on the creation of pores in structural adhesive joints by means of X-ray microtomography**, *The Journal of Adhesion*, 97 :12, 1073-1106,(2021) DOI : 10.1080/00218464.2020.1728257
- V. Dumont, C. Badulescu, G. Stamoulis, J. Adrien, E. Maire, A. Lefèvre, D. Thévenet, **On the influence of mechanical loadings on the porosities of structural epoxy adhesives joints by means of in-situ X-ray microtomography**, 99, 102568, (2020), *International Journal of Adhesion and Adhesives*, https ://doi.org/10.1016/j.ijadhadh.2020.102568.

Références associées : Bibliographie des publications

THE JOURNAL OF ADHESION
2021, VOL. 97, NO. 12, 1073–1106
https://doi.org/10.1080/00218464.2020.1728257

Taylor & Francis
Taylor & Francis Group

Check for updates

On the effect of the curing cycle on the creation of pores in structural adhesive joints by means of X-ray microtomography

V. Dumont [a,b], C. Badulescu[a], G. Stamoulis[c], J. Adrien[d], E. Maire[d], A. Lefèvre[b], and D. Thévenet[a]

[a]ENSTA Bretagne, UMR CNRS 6027, IRDL, Brest, France; [b]Safran Reosc - Engineering & Integration Department, Saint-Pierre-du-Perray, France; [c]UMR CNRS 6027, IRDL, University Bretagne Occidentale, Brest, France; [d]UMR CNRS 5510, Laboratoire MATEIS, University Lyon, INSA Lyon, Villeurbanne, France

ABSTRACT

Adhesive bonding is increasingly used in numerous industrial branches (aeronautics, space, *etc.*) for the many advantages this technique features. The quality of the adhesive bonds depends on diversified factors, and bonding defects within the joints are common. These defects may take the shape of pores, of various sizes, which are a possible threat to the good mechanical strength of the joints. These pores may create unwanted stress concentrations, and they are susceptible to locally weaken the adhesive joints. As they are created during the bonding process, the hypothesis that the bonding and curing conditions should influence their properties is well-founded. In order to validate this assertion, adhesively bonded samples were made, for different adhesives and different curing cycles. In particular, the influence of the peak temperature reached during the curing cycle was studied. The pores in the joints were then observed and studied using X-ray microtomography. The performances of the segmentation technique developed for the data processing were studied beforehand on synthetic data, in order to identify the limitations of the suggested methodology and to quantify the uncertainty on the computed quantities. It was found that a higher curing temperature may induce noticeable pore growth phenomena (mainly dilation and coalescence). In particular, this growth seems to be predominant halfway-through the thickness of the joints, resulting in an observable decrease in the effective section.

ARTICLE HISTORY
Received 4 November 2019
Accepted 7 February 2020

KEYWORDS
Structural bonding; X-ray microtomography; pores; curing cycle; image processing

1. Introduction

Structural bonding has known a surge in use and popularity in the past two decades, for several reasons: (i) this technique allows engineers to design lighter and more energy-saving structures, (ii) it is well-suited to multimaterials assemblies, (iii) it paved the road to mechanical assemblies using materials incompatible with traditional techniques (welding, bolting, riveting, *etc.*), and (iv) bonded structures feature fairly interesting stress distribution properties. Therefore,

CONTACT V. Dumont vincent.dumont@ensta-bretagne.org ENSTA Bretagne, UMR CNRS 6027, IRDL, Brest 29200, France

© 2020 Taylor & Francis Group, LLC

more and more industrial fields started to include this technique in their processes and in their designs, as in aeronautics, space, medical, *etc.* However, these advantages come with some drawbacks: the quality of the adhesive bond is sensitive to the bonding process,[1] the mechanical behaviour of adhesives is highly non-linear,[2,3] and the strength of the adhesive joint depends on a multitude of factors, related to both adhesion and cohesion phenomena. Due to the numerous elements impacting the quality of the joint, bonded structures are highly sensitive to defects which may occur during the bonding process. Among these commonplace defects that cannot be avoided in standard bonding conditions, one may reference the creation of pores throughout the mixing, bonding, and curing steps. These pores could possibly be a significant disturbance to the good mechanical resistance of the bond, as (i) they decrease the cross-section of the joint, (ii) the continuum and the stability of the adhesive are challenged and put at risk, (iii) they may induce unwanted stress concentrations, and (iv) they may lead to predisposed crack propagation paths within the material. As these voids within the material are created during the bonding and the curing of the adhesive, it is fair to hypothesise that the bonding conditions and the curing conditions should have an influence on their characteristics (mainly number, volume fraction, and size).

Unfortunately, as they are located inside the material, they are not easily detected and visualised. It is nonetheless possible to do so, using advanced imaging technologies such as X-ray microtomography. This technique has multiple advantages: (i) it is a non-destructive technology, (ii) it provides information from the bulk of opaque materials, (iii) the resolution can reach 1 μm (or even below) and (iv) the gathered data are three-dimensional. In the scope of materials science, it was at first used mainly on metallic alloys as in the work of Liu and Bathias[4] on the influence of defects on both tensile and fatigue properties of an aluminium alloy reinforced composite. They showed that the presence of pores and misorientation of fibres had a significant influence on the decrease in terms of fatigue life, and therefore the authors bring to attention the importance of a carefully controlled manufacturing process regarding these aspects. Composite materials were also the subject of such measurements. It is also worth referencing the works of Hirano *et al.* who performed damage characterisation and assessment in 1995 using *in-situ* tomography measurements on aluminium alloy matrix composites with SiC fibre reinforcements.[5]

X-ray microtomography is nowadays widely used in materials science papers, for the many advantages it features. These studies use tomography measurements mainly for two purposes: the characterisation of the processing conditions for given materials,[6] and damage characterisation. Regarding this aspect, the possibility to perform *in-situ* X-ray tomography measurements, while a mechanical load is applied, is a definitive edge. In particular, the teams of Maire *et al.*, and Adrien *et al.* took advantage of this tool to investigate the creation of damage in metals under tensile loading[7] and in polymeric syntactic foams under compressive stress.[8] In the 2007 study of Maire,[7] it is notably

shown that data from acoustic emission measurements and X-ray tomography measurements lead to similar conclusions in terms of crack and void detection, which validates the use of X-ray tomography for such purposes. It is also an interesting tool to build accurate finite element models, as it was done by Maire *et al.*[9] in the case of metallic foams. It was then possible to reconstruct their structure down to the cellular level and to use this geometry in finite element softwares.

Regarding the study of polymers specifically, a few studies may be found in the literature. A topic often encountered is the fabrication of polymeric structures *via* additive manufacturing techniques, as they are prone to generate voids in the material. For instance, a 2016 paper by Pavan *et al.* characterised the porosity of laser-sintered polyamide structures, of various sizes.[10] It was found that the size of the structure influenced the properties of the pores created during the process. More recently, Wang *et al.* proposed a micromechanical model in order to characterise the mechanical behaviour of 3D-printed polymers.[11] Nonetheless, few studies may be found specifically on adhesives, and even more so regarding adhesively bonded assemblies. This is probably explained by the *a priori* low risk of pores creation for these materials when compared to additive manufactured polymers.

As far as the field of structural bonding is concerned, X-ray tomography has been used on bonded wooden structures in order to characterise the bonding process and the adhesive penetration in the wood by McKinley *et al.*[12] Still in the context of wooden structures, Schwarzkopf[13] coupled tomography observations with numerical simulations to describe the micromechanical strains in the joints and in the substrates, where the adhesive tends to diffuse due to the fibrous nature of wood. This results in a fairly accurate description of the kinematics of the interfaces, even though the authors highlight a few limitations, such as the commonplace reconstruction artefacts. No particular attention has been given so far to the microstructural characterisation of adhesive joints through this technique, and the use of X-ray microtomography is hence fairly new in the field of structural bonding for this type of subject, as opposed to other materials: minerals,[14] food,[15] composites,[16,17] *etc.* Nonetheless, a 2019 paper by Dumont *et al.* investigated the evolution of the microstructural characteristics of adhesive joints under mechanical stress by means of *in-situ* X-ray microtomography.

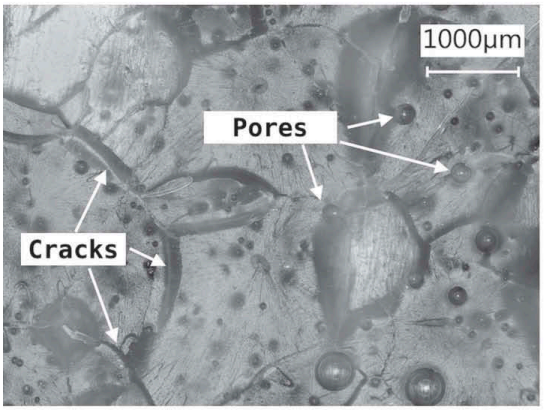
In the following study, the authors investigate the effects the curing process may have on the pores within adhesive joints. This study is performed using two different bicomponent epoxy adhesives, for two curing cycles, with means of X-ray microtomography. First, the samples and their preparation are detailed. Then, the experimental procedure for X-ray microtomography measurements is presented. The authors also describe the tomographic data segmentation tool which was developed and discuss its performances and abilities using synthetic

data, before its use on experimental data. Lastly, the experimental results are outlined, along with a discussion on the observed phenomena.

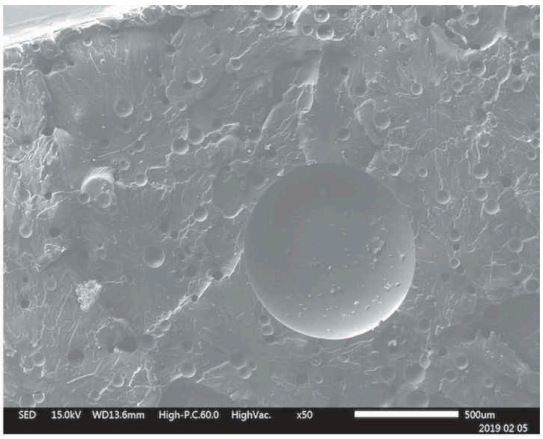
2. Motivation

The observation of failure profiles of ruined samples after tensile tests through an optical microscope (Figure 1a) and a scanning electron microscope (Figure 1(b,d)) highlights the presence of pores in the material. Moreover, these pores seem to play a part in the failure of the samples, as it is illustrated in detail by Figure 1(a,c and d) where cracks can be spotted in the neighbourhood of pores.

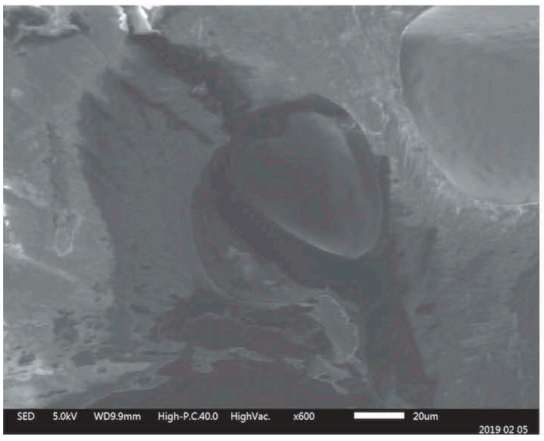
Even if any characterisation is impossible this way due to the lack of provided information, it is fairly easy to visualise the creation and the growth of pores within an adhesive using a mere optical microscope. In a first stage, a layer of bicomponent epoxy adhesive (*Araldite 420 A/B* from the German manufacturer *Huntsman* ^{TM}) is spread between two sets of glass sheets, to be



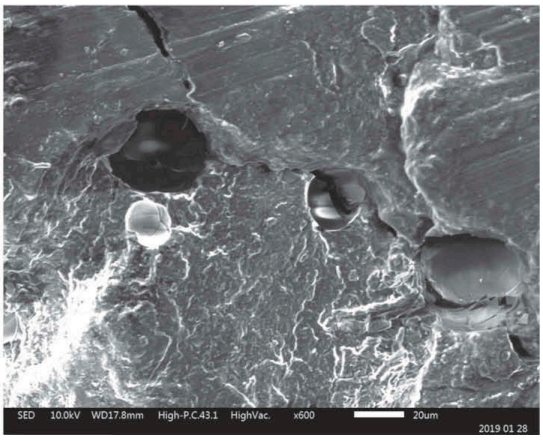
(a) Optical microscope view



(b) Scanning Electron Microscopy (SEM - secondary electrons) view



(c) Cracked pore (SEM - secondary electrons)



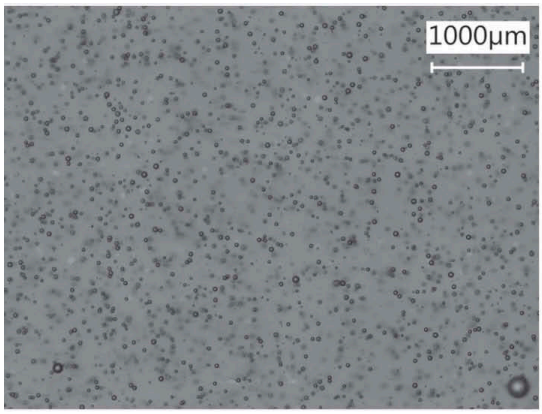
(d) Crack propagation through pores (SEM - secondary electrons)

Figure 1. Microscopic observations of failure profiles of adhesively bonded samples (adhesive B – tensile tests).

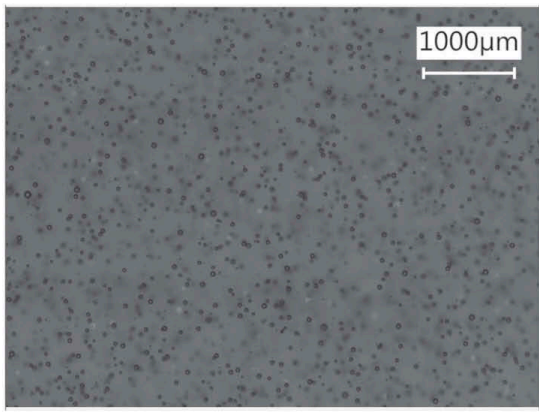
observed using a *Keyence*^{TM} *VHX* electronic optical microscope. The components of this adhesive were mixed together using a planetary mixer, so as to obtain a homogeneous material. One of these glass-adhesive-glass assembly was then left at ambient temperature for 12 hours, and the other one was polymerised at high temperature for a short period of time (1h10 at 110°C). They were then put back under the microscope. The picture of these samples can be found in Figure 2.

It is then quite obvious that the high curing temperature used for the material in Figure 2(a,c) had a significant influence on the pores inside the adhesive: they greatly increased in volume, and decreased in number, meaning that coalescence phenomena were very likely to happen during the polymerisation. Also, it is possible to detect these pores even in the initial state (Figure 2a), meaning that they are created as soon as the joint is formed (and possibly as soon as the components of the adhesive are mixed).

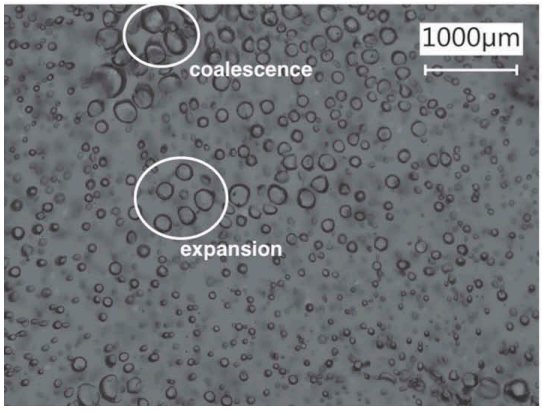
Moreover, it is possible to detect lighter, circular areas on these pictures: these denote the presence of glass beads in the adhesive, as it is common for



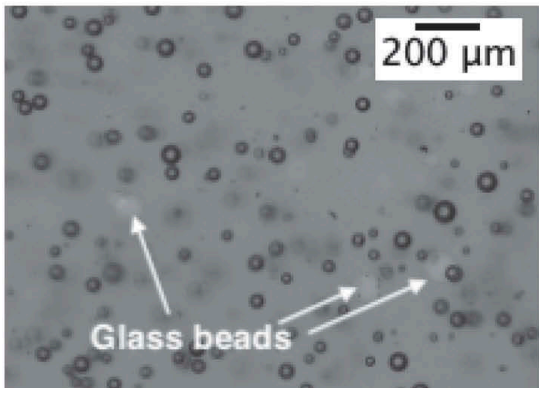
(a) Pores created within an adhesive joint before curing



(b) Pores within an adhesive joint after 12h at ambient temperature



(c) Pores within an adhesive joint after 1h10 at 110°C



(d) Glass beads spotted on microscopy pictures (extracted from Fig.2a)

Figure 2. Highlighting the presence of pores in the adhesive as soon as the joint is shaped using an optical microscope.

various reasons (mainly, to guarantee a minimal thickness for adhesive joints). Such beads are shown in Figure 2d, as an example. The adhesive used here is also used in the following microtomography measurements and is referred to adhesive B.

As stated in preamble, these microscopy techniques only allow for visualisation, and they are not suitable for characterisation. X-ray tomography is a fairly interesting answer to this defect, as it features high-resolution data acquisition, three-dimensional visualisation and measurements-oriented capabilities. These pores being structural defects, the assumption that they have an influence on the mechanical properties of the material seems reasonable, as expressed in[18] for composite materials. The conditions about this influence (in terms of pores size, number, volumetric ratio, *etc.*) are however not investigated in this study.

3. Preparation of the specimen

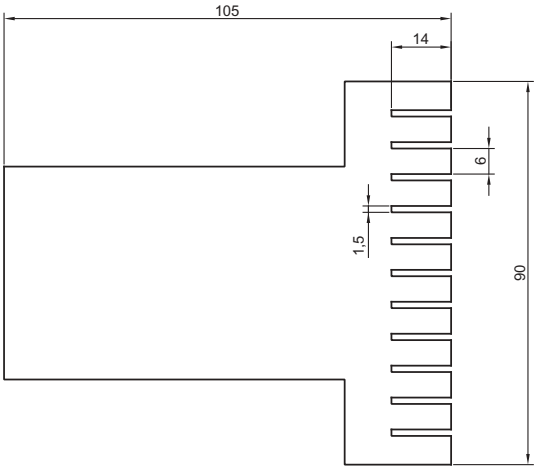
3.1. *Samples geometry*

The geometry of the samples must meet two criteria, to remain in the scope of this study: (i) they must be bonded assemblies (as opposed to bulk samples), and (ii) their dimensions must be adequate to the resolution of the X-ray microtomography measurements to be performed. Bonded samples are required as this study on the effect of curing is part of a more complete and extensive tests campaign performed on bonded assemblies. In order to check these requirements, mini-Scarf samples (Figure 3c) will be used. These samples are made out of traditional aluminium 2017A Scarf samples, where a rake-like shape is machined using water-jet cutting (Figure 3a). They are to be bonded using two different bicomponent epoxy adhesives, whose general characteristics are presented in Table 1). The adhesives are spread on each bonding surface of this pattern, and the Scarf samples (Figure 3a) are then assembled for the curing (Figure 3b). After the curing of the adhesive, each individual is then water-jet cut from the main structure to form the mini-Scarf samples, whose dimensions are presented in Figure 3c.

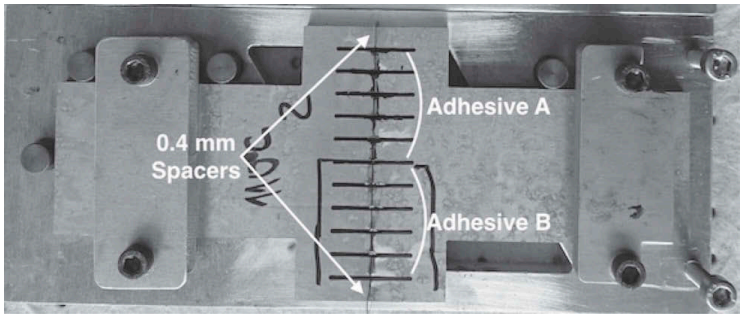
Moreover, in order to install the samples in a device for subsequent X-ray tomography *in-situ* tensile tests, threaded holes are accommodated at each end of the samples (Figure 3c). In the following study, no mechanical loading will be applied, but the aforementioned tensile machine is used as a mounting setup.

3.2. *Bonding and curing*

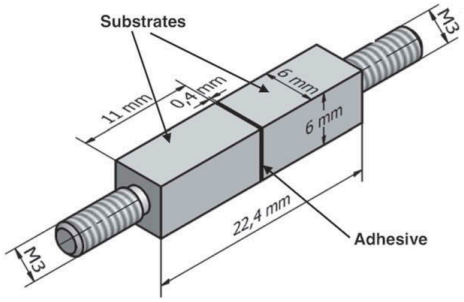
The substrates are prepared so as to remove any potential impurities, oily components, dirt, and oxides: (i) they are first degreased with acetone, (ii) a mechanical treatment (grade 180 sandpaper) is then applied, and (iii) another acetone cleaning is performed.



(a) Mini-Scarf samples layout (dimensions in mm)



(b) Bonded modified SCARF samples



(c) *In-situ* microtomography tensile samples geometry

Figure 3. Modification of SCARF geometries for *in-situ* tomography applications.

As it has been evoked in introduction, two different adhesives will be tested in this study; hereafter they will be referred to as adhesive A and adhesive B (namely, *Huntsman Araldite 420 A/B*). The commercial reference of the adhesive A will not be expressed in this paper for confidentiality reasons. Both are bicomponent epoxy adhesives. Some general properties about these materials may be found in Table 1, as provided by the suppliers. The glass transition temperatures in Table 1 were measured using Differential Scanning Calorimetry (DSC).

Table 1. A few properties for the considered adhesives.

Property	Adhesive A	Adhesive B
Texture	paste-like	honey-like
Known fillers	–	Glass beads
Glass transition temperature (DSC)	~ 90°C	~ 60°C
Young's modulus [MPa]	1400	2000
Poisson ratio [-]	0.33	0.41
Coefficient of Thermal Expansion [ppm.°C^{-1}]	83	78

The components of the considered adhesives are mixed according to the guidelines provided by the manufacturers. The mixing is performed using a planetary mixing device, at 1500 rpm for 7 minutes. These parameters are arbitrary, but chosen for the resulting product to be homogeneous (*i.e.* the hardener and the resin are visually indissociable).

In spite of the variation in terms of texture (Table 1), the application on the substrates follows the same pattern no matter the adhesive: a layer of adhesive is spread using a stainless steel spatula on both the substrates constituting a sample, which are then assembled (Figure 3b). The excess of adhesive dripping from the joint is cautiously cleaned. The alignment of the substrates and the thickness of the joints (set to 0.4 mm) are controlled using a specially designed setup (Figure 3b).

Two curing cycles are performed, in order to investigate the effects of this factor on the resulting pores in the adhesives. Their characteristics may be found in Table 2.

The curing is done with a *Memmert UF110+* ^{TM} thermal chamber. It should be noted that these cycles yield a satisfyingly polymerised material for both adhesives, even though they are different in durations and temperatures. This was checked with DSC measurements, by comparing the cross-linking enthalpies of the uncured and cured material. It should be noted that, even though it is advised to cure such adhesives above their maximal glass transition temperatures,[19] the low-temperature cycle has been designed to meet other additional requirements whose details are out of the scope of this study. Nonetheless, even if the high temperature configuration features a slightly higher curing degree, the low temperature curing configuration displays curing degree higher than 95%, leading to the assumption that both cycles yield rather similar materials.

Once the curing cycle completed, the samples were water-jet cut from their Scarf base, to create microtomography individual samples such as presented in Figure 3c. For the present study, one sample is considered per case. It should be

Table 2. Curing cycles steps and temperatures.

Cycle	Step 1	Step 2
Low temperature	23°C for 24h	80°C for 2h
High temperature	110°C for 1h10	–

noted that two other specimens were examined for the following configurations: adhesive A cured at low temperature, and adhesive B cured at high temperature. A very low scattering was found in terms of porosity and number of pores. Consequently, it was decided to keep the number of investigated samples to one for each test case, in order to reduce the CPU usage on the computing cluster used to process the tomographic results.

4. Experimental procedure

4.1. *X-ray tomography principle*

Microtomography is an imaging technique which offers the possibility to reconstruct the internal structure of an object without causing any damage. This non-destructive characteristic is a significant advantage in materials science, in the case of *in-situ* acquisition for instance, as extensively presented by Buffière.[20] Moreover, it is superior to many other imaging techniques such as any microscope-based methods, as it provides three-dimensional data, with a resolution down to 1 μm,[20] and even below, depending on the X-ray source used in the tomograph.

Tomography is based upon the variation of the linear X-ray attenuation coefficient (μ) within a material. For anisotropic materials, such as composites or foams, μ depends on the spatial coordinates (x, y, z). Hence, building the three-dimensional map of $\mu(x, y, z)$ is equivalent to reconstruct the internal microstructure of the observed sample. More detailed information may be found concerning the theoretical background of tomography imaging.[21] The sample to be studied is mounted on a rotary platform (Figure 4), which incrementally performs a 360° rotational movement in order to perform the data acquisition on a variety of organised propagation paths for the X-ray beams. The reconstruction of the volume is then performed using a Fourier transform-based algorithm. Extensive details on the theory of the reconstruction techniques may be found in the reference work of Kak.[21]

4.2. *Test procedure*

The samples are placed in the chamber of a *Phoenix VtomeX* laboratory tomograph, which contains a *Varian Paxscan* X-ray detector featuring a resolution of 1920 × 1536 pixels. This detector outputs a 14-bits coded greyscale pictures (or radiograms, see Figure 4) of the attenuation. The tensile machine in the chamber of the tomograph (Figure 5) is used as a mounting setup for the samples.

The voxel size obtained using this experimental set-up is 4.5 μm x 4.5 μm x 4.5 μm, which suits the typical size of the pores that are expected. Moreover, the glass beads included in the adhesive B feature a diameter above 60 μm according to SEM observations, meaning that they will not be difficult to detect.

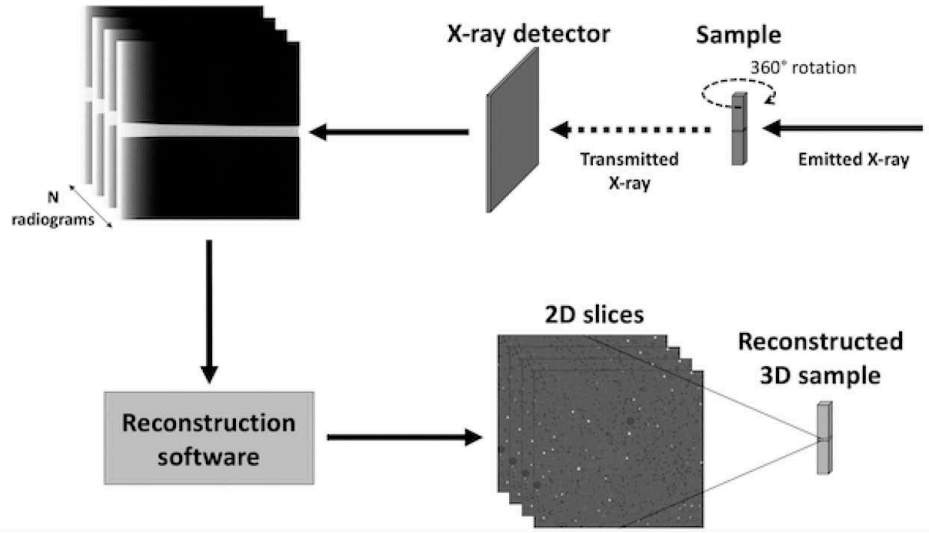


Figure 4. Tomography measurements principle.[22]

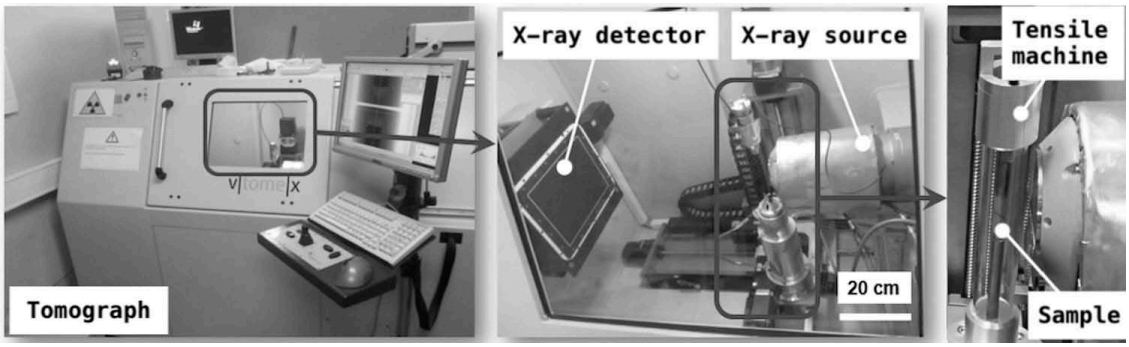


Figure 5. Experimental setup.[22]

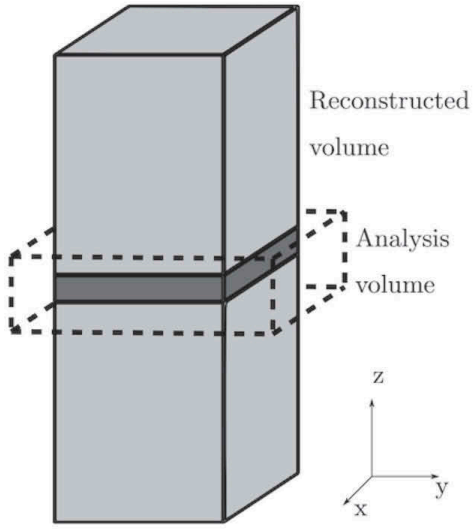
The acquisition is performed for 1200 angular positions (Figure 4), for a total duration of approximately 10 minutes, with an exposure time of 500 ms for each projection, and an X-ray source operated with a voltage of 80 kV and a current of 280 µA. The size of the reconstructed volume is 1500x1500x500 voxels. Examples of tomographic slices may be found in Figure 6.

5. Analysis technique

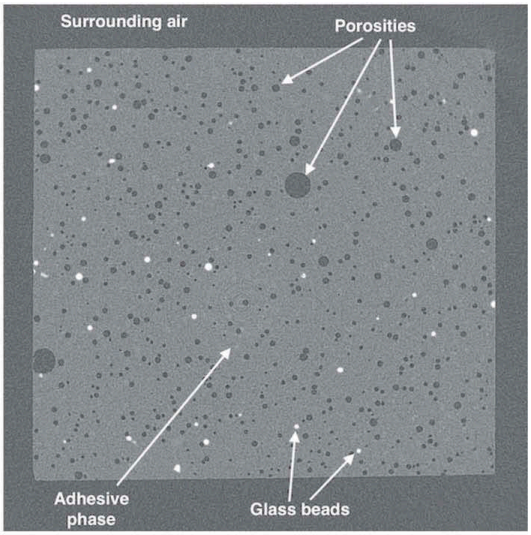
5.1. *Preliminary discussion*

In order to exploit the data from the reconstructed volumes, it is necessary to perform a segmentation, in order to isolate the different phases. It is a common concern in the image processing and computer vision fields, and it has been the object of many studies, which suggested a large variety of methodologies to answer this issue.[23]

The easiest way to segment biphasic greyscale data is to use a threshold: a greyscale level (*i.e.* the threshold) is chosen, and the pixels of the image are



(a) Region of interest of the mini-Scarf samples



(b) CT-scan after reconstruction (adhesive B, XY plane)

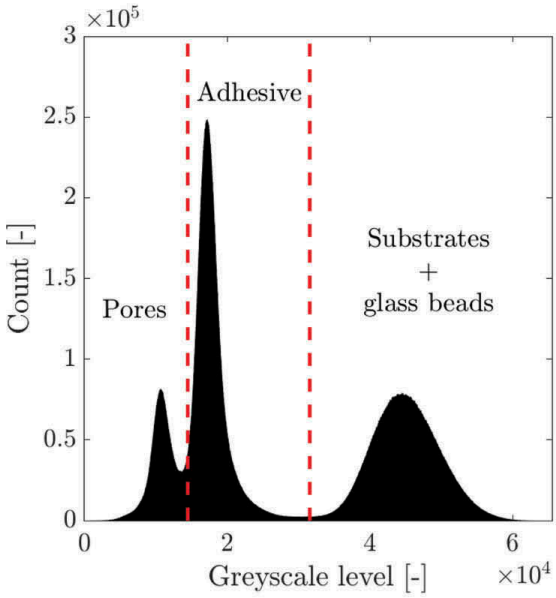


(c) CT-scan after reconstruction (adhesive A, XZ plane)

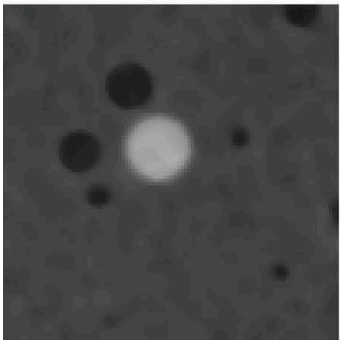
Figure 6. Reconstructed data after filtering and cropping.

separated whether they are brighter or darker than this value. Even though this method is fairly basic, it usually gives satisfactory results, given the fact that the data histogram is adequate (*i.e.* that the phases are easily distinguishable). The threshold can be manually chosen or algorithmically computed, the latter being preferable. The numerical determination of the threshold can be performed in various ways: one may base the calculation upon the analysis of the histogram,[24] or by clustering the greyscale levels,[25] for instance. The thoroughly documented paper of Sezguin *et al.*[23] compiles an extensive list of methodologies and should be consulted for advanced details. Other methods, not necessarily based on thresholding, are available, but they will not be discussed here, as it is out of the scope of this paper.

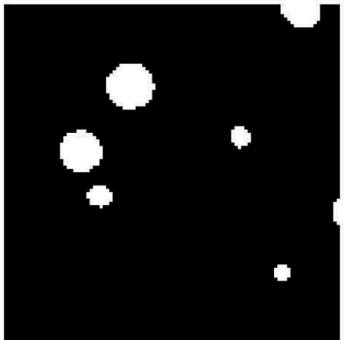
Due to the shape of the histogram in Figure 7a, an Otsu thresholding[25] is used. In this paper, Otsu demonstrates that it is possible to compute an optimal threshold to segment bimodal data by maximising the interclass variance of the greyscale levels in each class. It is though necessary to generalise this approach to a thresholds number N_{thr} greater than 1, as Figure 7a displays a trimodal histogram. Otsu suggests that it is easily performed, by definition of the discriminant criterion chosen to optimise the thresholds values,[25] upon which there is no constraint regarding N_{thr}. In this study, a multithresholding process is used for $N_{thr} = 2$, in order to discriminate the following phases: (i) the pores and the surrounding air in the tomograph chamber, (ii) the adhesive matrix, and (iii) the substrates (added to the glass beads, depending on the adhesive). It should



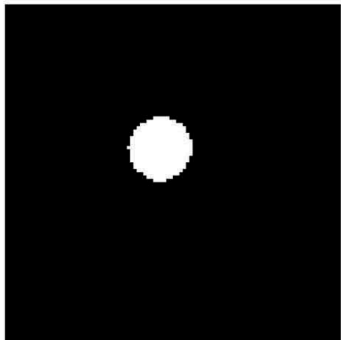
(a) Histogram of a reconstructed volume and thresholds computed using Otsu's method



(b) Example of raw volume data



(c) Pixels below the first threshold (*i.e.* pores,)



(d) Pixels above the second threshold (*i.e.* glass beads,)

Figure 7. Segmentation principle.

also be noted that no significant change in illumination for the same phase has been experienced, which could have prevented us from using such a method.

It is then obvious that the weak spot of the chosen methodology is the sensitivity to the noise in the experimental data. In order to minimise the influence of this measurement noise, it is then advised to filter the data in order to increase as much as possible the signal-to-noise ratio. It is however paramount not to damage the data, and especially the contours of the objects that must be segmented (*i.e.* the pores). A great number of filters (two-dimensional or three-dimensional) are available.[26] Among all these possibilities, the median filter and its derivates stand out with their edges preservation properties, as it was proven by Gallagher *et al.*[27] The filter used for the works presented in this paper is a three-dimensional median filter, whose kernel size will be discussed further.

5.2. *Preprocessing*

As mentioned previously, the reconstructed data need to be filtered, using a 3D median filter. The size of the kernel of the median filter will determine the minimal size of the segmented entities to consider. The filtering is performed with *Matlab*. A kernel size of 5 voxels is chosen, to remain relatively small when compared to the majority of the pores. As a consequence, any segmented pore whose volume is lesser than 125 voxels (*i.e.* the volume of the kernel) will be considered as too uncertain, and therefore will be discarded. The chosen filter is three-dimensional to prevent as much as possible the loss of information during the filtering.

The shape of the reconstructed volumes is a $(1500, 1500, 500)$ matrix. They are cropped to keep only the region of interest (the adhesive joint and a small part of the substrates, Figure 6a).

5.3. *Segmentation*

As stated in preamble, the segmentation is performed using Otsu algorithm[25] to compute the required thresholds. The greyscale values of these thresholds are hence unsupervisedly computed, using the histogram of the data and the statistics of the greyscale levels. Such data display well-defined peaks and valleys in-between (in Figure 7a, from left to right, pores, adhesive, and substrates and beads which show roughly the same attenuation coefficient), enabling an histogram-based segmentation method. The computed thresholds may be visualised on the histogram in Figure 7a, which is provided as an example. One may notice that the lowest threshold does not exactly fit the minimum between the two corresponding peaks in Figure 7a, which is rather counter-intuitive. This is due to the slight asymmetry in terms of measurement noise, as it will be addressed later in the study.

Using these thresholds, it is then possible to build volumes containing only the identified phases so far: pores + surrounding air, adhesive, and substrates + beads.

These volumes need to be filtered either to remove unwanted objects (the air surrounding the sample in the tomograph chamber, the measurements artefacts which may occur near the interfaces and the objects whose size is too small to be taken into account) or to separate different objects that were placed in the same phase (typically, the glass beads if the adhesive contains some and the aluminium substrates). This step is easily completed by considering the sizes of all these items, to identify those that should be discarded. For instance, the air surrounding the sample features a volume significantly larger than any other pore in the adhesive joint, and thus may be easily labelled in the segmented volume to be erased. The same method may also be used to classify the objects contained in the *(substrates + glass beads)* phase since the substrates volumes are several orders of magnitude greater than the volume of a glass bead.

Before being used on the experimental data, this tool needs to be characterised on synthetic representative data, in order to validate its architecture and to investigate its limitations.

6. Characterisation of the analysis tool

6.1. *Creation of synthetic volumes*

In order to validate the methodology proposed in this paper, it was important to verify the segmentation performances of the tool on synthetic data. These artificial datasets should be representative of the experimental data in terms of (i) greyscale levels, (ii) noise, and (iii) pores sizes. The diameters of the pores are assumed to be following a Gaussian distribution, whose parameters will be discussed later. Their centroids are assumed to be randomly distributed within the adhesive joint. This hypothesis is validated further in this paper.

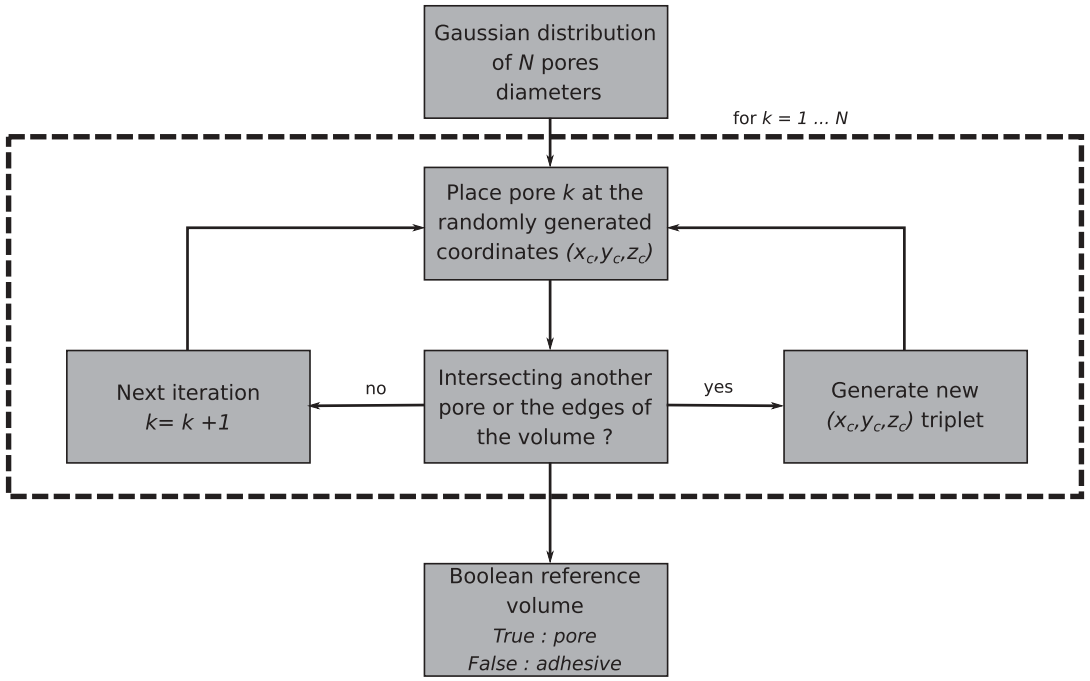
The creation of such a volume is divided into four steps. Firstly, a reference boolean volume is created, where *true* values denote the presence of pores pixels, and *false* values denote the absence of pores. Secondly, this boolean volume is turned into a 16-bits greyscale volume, where the pores display a unique greyscale level, and where the adhesive displays another, distinct, greyscale level. Then, padding is added (*i.e.* the air surrounding the sample and the substrates), since it influences the shape of the histogram of the data. Lastly, Gaussian noise is added to the synthetic volume, and a slight blurring of the contours is applied in order to best resemble the experimental data. The process adopted to create these synthetic volumes is summarised in Figure 8(a,b).

6.1.1. *On the boolean reference generation*

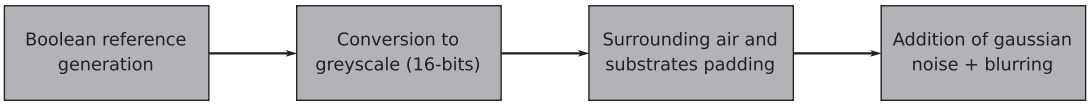
A representative volume of $[300, 300, 100]$ voxels for the adhesive joint is used in the following considerations. The complete synthetic volume will be slightly larger, due to the padding operated in the following steps, as presented in Figure 8b. The pores diameters follow a Gaussian distribution whose mean and standard deviation are, respectively, μ_d and σ_d. The study is done for 200 pores randomly located in the adhesive joint. The boolean reference is under the shape of a matrix $[300, 300, 100]$ M^{ref}, whose elements (i, j, k) are defined by Eq.1.

$$\begin{cases} M^{ref}_{ijk} = 1, \text{ if} \sqrt{(i - x_c)^2 + (j - y_c)^2 + (k - z_c)^2} \leq r_{por} \\ M^{ref}_{ijk} = 0 \text{ else} \end{cases} \tag{1}$$

where r_{por} is the radius of the considered pore, and (x_c, y_c, z_c) the coordinates of the centre of this pore. As a side note, the properties of the pores are not constrained to be integers (*i.e.* the quadruplet $(x_c, y_c, z_c, r_{por}) \in \mathbb{R}^4$).



(a) Creation of a boolean reference volume, to be used as a template for a synthetic greyscale volume



(b) Process adopted to create synthetic microtomographic reconstructed data from a boolean reference

Figure 8. Generation of synthetic data to characterise the performances of the proposed analysis tool.

The process mathematically expressed in Eq.1 also simulates the voxelisation which occurs during the microtomography measurements, with the discretisation of continuous quantities (*i.e.* the material) by the X-ray detector.

It is conspicuous that the parameters chosen for the diameters Gaussian distribution will play an important part on the segmentation performances of the designed tool: the smaller the generated pores, the poorer the tool will compare to the reference. The values of these $[\mu_d, \sigma_d]$ parameters will be discussed later in the study.

6.1.2. *On the greyscale levels of the different phases*

The determination of the greyscale values to be used for each phase is straight-forward, as the histograms of the reconstructed volumes are provided. The nominal greyscale value for each synthetic phase is the peak value evaluated on the histograms of the experimental data (see Figure 7a for example). The greyscale values (before the addition of the Gaussian noise, see in Figure 8b) are summarised in Table 3.

Table 3. 16-bits nominal greyscale values for each phase in the investigated adhesives.

Phase	Adhesive A	Adhesive B
Pores + ambient air	10407	10563
Adhesive material	18250	17220
Substrates (+ glass beads if needed)	44980	44700

6.1.3. *On measurement noise*

The measurement noise is estimated by acquiring data for the same volume twice, and by subtracting one of the resulting reconstructed volumes to the other. The remaining greyscale values correspond to the measurement noise caused by the X-ray detector. A significantly higher noise for the substrates and the glass beads is expected due to their higher X-ray linear attenuation coefficient μ. The noise values for each phase are listed in Table 4.

A light Gaussian filter ($\sigma = 0.4$ voxel) is applied in order to slightly blur the edges of the pores to replicate the experimental data. The comparison between the histograms of the simulated data and of the experimental data should provide a good indicator of the quality of the synthetic volumes, and of their representativeness of the actual microtomographic data (Figure 9). The data represented in Figure 9 have been normalised with respect to the total numbers of pixels in each case (synthetic data and experimental data), and therefore they are expressed in terms of frequencies.

A few remarks should be made at this point of the study: (i) one can see a slight mismatch in terms of frequencies for each peak, certainly due to the padding added during the creation of the synthetic volume; (ii) the in-between zone for the pores and adhesives peaks is seemingly representative of the real data; (iii) the brightest pixels for the synthetic adhesive (greyscale levels between 20000 and 30000, Figure 9) are lacking a few occurrences to match the experimental frequencies. Due to the large difference between the peak values for the adhesive pixels and for the substrates pixels, this particular mismatch should not impact too much the computation of the corresponding threshold. Moreover, the pixels of the substrates in this in-between zone are mostly located within the bulk of the aluminium (visible in Figure 6c), meaning that segmentation errors potentially occurring in these area can easily be fixed by morphological operations if need be (*i.e.* opening, closing, filling, *etc.*). Alternatively, this mismatch (due to the fact that each phase does not follow a perfectly symmetrical Gaussian distribution) could be corrected by stretching the greyscale levels in this interval

Table 4. 16-bits noise greyscale values for each phase in the investigated adhesives.

Phase	Adhesive A	Adhesive B
Pores + surrounding air	2281	2254
Adhesive material	2554	2462
Substrates (+ glass beads if needed)	6586	6681

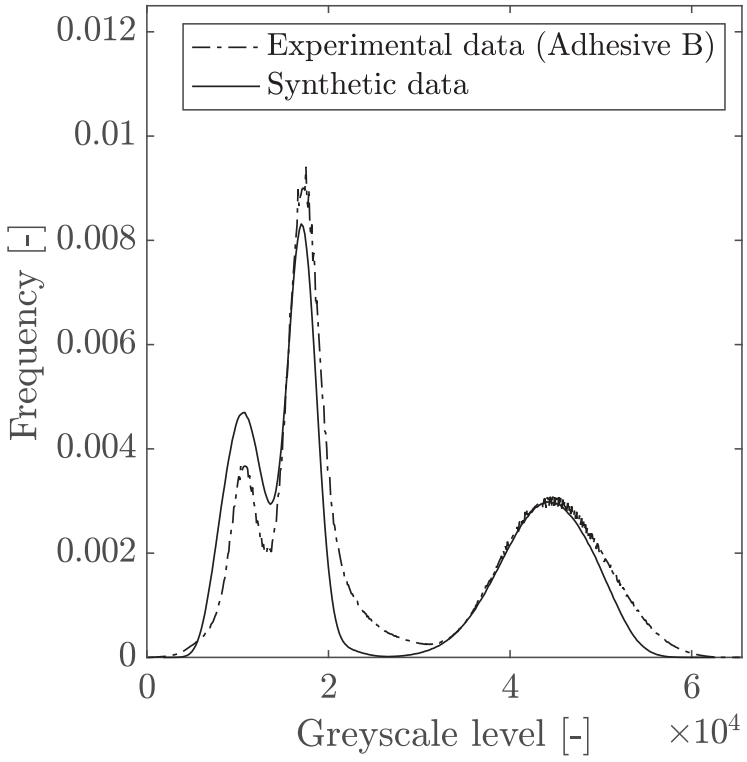


Figure 9. Comparing the histogram of synthetic data with the histogram of experimental data (adhesive B).

by a multiplicative factor until the synthetic histogram matches the experimental histogram. It is however not performed in this study as it is assumed to be a second-order factor on the segmentation abilities of the developed tool. Another indicator of the representativeness of the simulated volume is the similarity between the thresholds computed for the synthetic data and the ones computed for the experimental volumes, which were used as a reference pattern to build the artificial data. A comparison is made for the two adhesives studied in this paper in Table 5, where the first (pores/adhesive) and second (adhesive/substrates) thresholds values are provided.

6.2. *Segmentation abilities*

The segmentation tool is then applied to these synthetic volumes, in order to compare the segmented data with the reference pores patterns (Figure 8a). As it has been evoked earlier in this paper, significant variations are expected in terms of performances depending on the size of the pores to be segmented. Various diameters distributions are therefore considered, included in several simulated volumes as detailed previously. In practice, the parameters of the diameters Gaussian distribution ($[\mu_d, \sigma_d]$) will be incrementally increased in two intervals, in order to sweep a matrix of values for this couple. The mean value μ_d will be varied from 8 to 20 voxels, and the standard deviation σ_d will be varied from 1 to 5 voxels. Due to the similarity in terms of greyscale levels between the adhesive

Table 5. Comparison between the experimental and synthetic 16-bits greyscale thresholds for adhesive A and B.

Thresholds	Adhesive A	Adhesive B
First threshold (exp.)	15009	14035
First threshold (synth.)	14151	13781
Second threshold (exp.)	32192	31531
Second threshold (synth.)	31085	30466

A and the adhesive B (see Tables 3, 4 and 5), the study will be carried out only for one adhesive (adhesive B). For each couple $[\mu_d, \sigma_d]$, a relative error ε for the pores number and the pores ratio with respect to the references values will be calculated, as shown in Eqs.2 and 3. It should be noted that these errors are expressed as percentages, due to the normalisation with respect to N_{por}^{ref} and η_{por}^{ref} in Eqs.2 and 3.

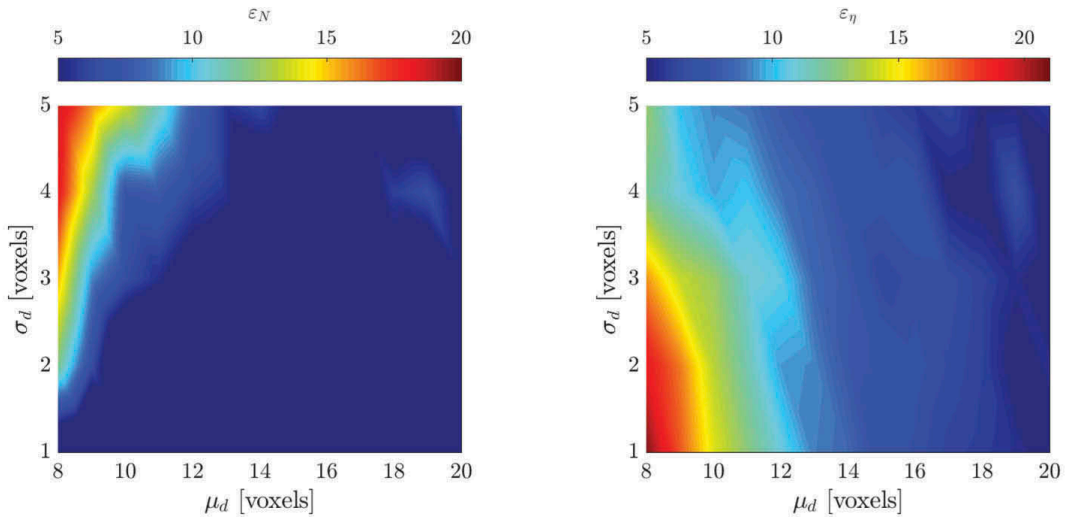
$$\varepsilon_N = 100 * \frac{\sqrt{\left(N_{por}^{det} - N_{por}^{ref}\right)^2}}{N_{por}^{ref}} \tag{2}$$

$$\varepsilon_\eta = 100 * \frac{\sqrt{\left(\eta_{por}^{det} - \eta_{por}^{ref}\right)^2}}{\eta_{por}^{ref}}, \text{with } \eta_{por} = \frac{V_{por}}{V_{joint}} \tag{3}$$

where N_{por}^{det} and N_{por}^{ref} are, respectively, the numbers of pores detected and of reference, η_{por}^{det} and η_{por}^{ref} are, respectively, the detected and reference pores volumetric ratio, and V_{por} and V_{joint} are, respectively, the volumes of the pores and of the joint. In order to reduce the influence of the greyscale noise on the results, 5 computations will be carried out for each couple $[\mu_d, \sigma_d]$ for different Gaussian noise draws (the standard deviation of this noise being tuned using the data displayed in Table 4). The results of this parametric study are displayed in Figure 10, where the mean values for ε_N and ε_η are presented.

Apart from the extreme cases of small pores distributions, satisfactory results are obtained (typically, for $\mu_d \leq$ 10 voxels), as the relative errors ε remain *circa* 5% or below. The major part of the segmentation errors are expected to happen near the edges of the pores, due to the slight blurring occurring at these locations.

These results on synthetic volumes ensure us that once applied on the experimental data, our method should yield fairly satisfying results, to be pondered with the size of the segmented pores, which was labelled as an important factor in terms of results accuracy.



(a) Mean value of the relative error on the detected pores number ε_N

(b) Mean value of the relative error on the detected pores volume ratio ε_η

Figure 10. Segmentation performances on the pores numbers and volume ratio as functions of $[\mu_d, \sigma_d]$.

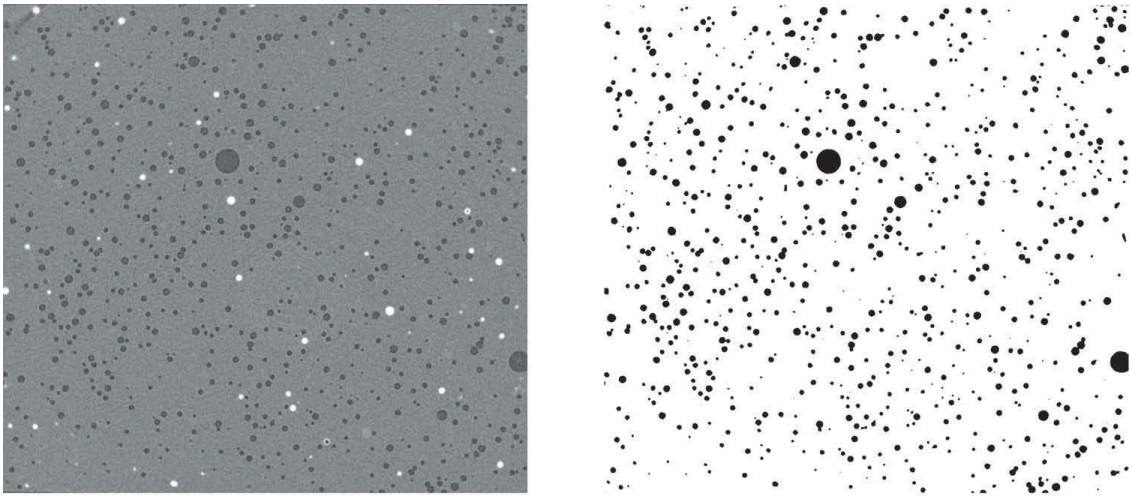
7. Results

Data similar to Figure 11(b,d) are obtained once the segmentation process is completed. It is then possible to carry out various considerations on these datasets, whether geometrical (volume, shape, equivalent diameter, *etc.*) or microstructural (pore-to-joint volumetric ratio, pores number, *etc.*).

A 3D view of a reconstructed sample computed with *FiJi* software[28] can be seen in Figure 12. The Cartesian coordinate system defined in this figure is used in the following sections to express the location of the pores. As one may notice, the surfaces of the substrates are not perfectly parallel to one another. This is most certainly caused by the machining of the substrates, the mechanical treatment applied to the bonding surfaces and more generally an imperfect bonding process. This misalignment, however, does not disturb the observations made in this study.

7.1. *Pores numbers, volumetric fractions, and diameters distributions*

The X-ray microtomography measurements data are segmented (see Figure 13 for 3D viewing) using the previously detailed methodology in their initial state. Two different curing cycles are then to be investigated, for two different adhesives. As a reminder, the studied curing cycles are the following: (i) 110°C for 1h10, hereafter referred to as "high temperature" and (ii) 23°C for 24h + 80°C for 2h, hereafter referred to "low temperature". For each case, it is possible to compute the number of pores included in the adhesive joint, and the volumetric fraction of these pores with respect to the whole joint. These results are shown in Figure 14(c,d). The uncertainty on the considered quantities (*cf.* the error bars in



(a) Raw data (b) Adhesive (white pixels)

(c) Pores (white pixels) (d) Glass beads (white pixels)

Figure 11. Segmentation step results (adhesive B, slice in the middle of the adhesive joint).

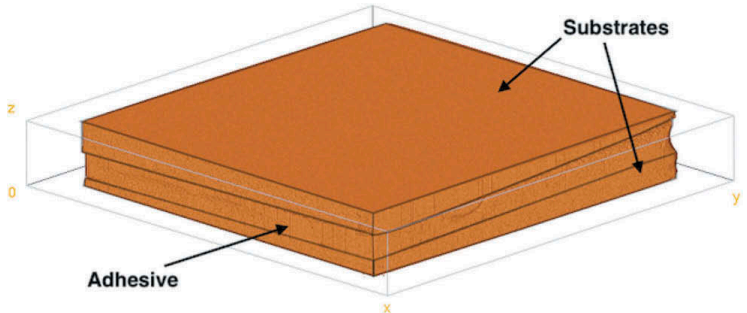
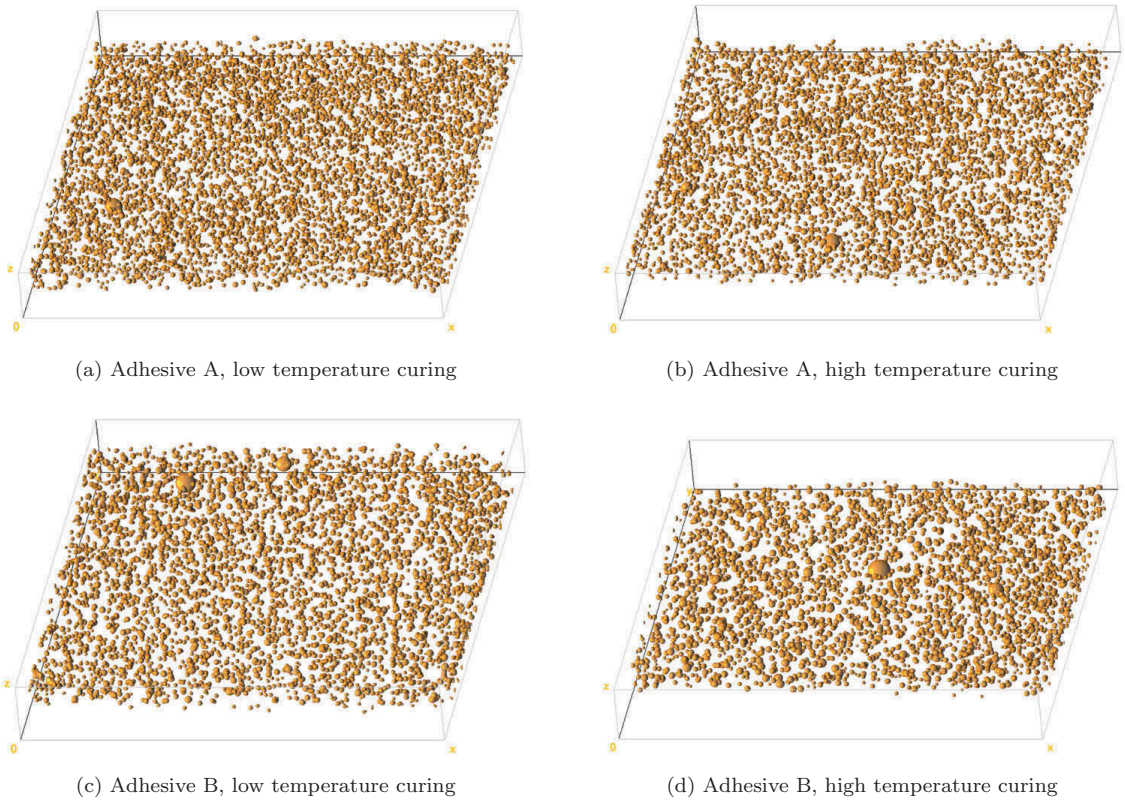


Figure 12. 3D view of a reconstructed sample (outlined contours for better visualisation).

Figure 14(c.d)) was estimated by cross-referencing the data in Table 7 and in Figure 10. It is also possible to compute the distributions of the equivalent diameters of the pores for each case, as it is done in Figure 14(a,b). The pores count in each bin in these histograms is normalised with respect to the total



(a) Adhesive A, low temperature curing

(b) Adhesive A, high temperature curing

(c) Adhesive B, low temperature curing

(d) Adhesive B, high temperature curing

Figure 13. 3D views of segmented pores in adhesive joints.

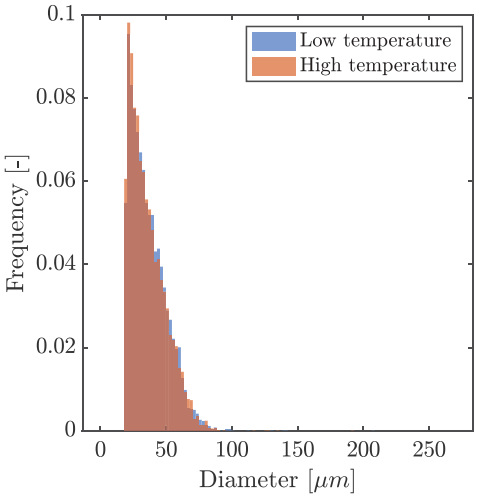
number of pores, in order to obtain frequencies histograms, in order to easily compare the different samples, each one containing a different number of pores.

From the data displayed in Figure 14, it appears that the two adhesives investigated in this paper feature different sensitivities to the curing conditions, at least for the considered thermal cycles examined in the present study.

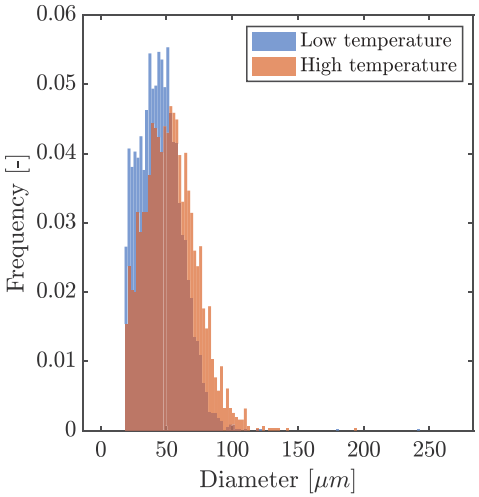
On one hand, the adhesive A seems rather unresponsive to the curing temperature: very little changes can be identified between high temperature curing and low temperature curing, in terms of pores number (Figure 14c), porosity volume ratio (Figure 14d) and diameters distribution (Figure 14a). Detailed numerical values may be found in Table 6.

On the other hand, the adhesive B is far more impacted by an increased curing temperature, as it may be seen in Figure 14(b,d). From these data, one may notice that a higher polymerisation temperature for the adhesive B translates into a slightly higher average pore diameter (from 43 μm to 50 μm, Table 7).

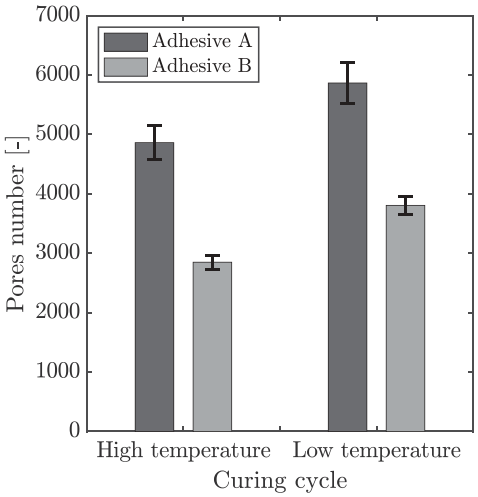
A possible conclusion to these findings could be that the high temperature cycle tends to trigger void growth phenomena, either relying on material expansion, or on coalescence mechanisms possibly activated by the thermal environment.[15] Another finding of these initial state measurements is that, no matter the curing cycle, the microstructural properties of the adhesive A and those of the adhesive B are extremely different (see Figures 14a and 14a), even though they are similar materials: both are bicomponent epoxy



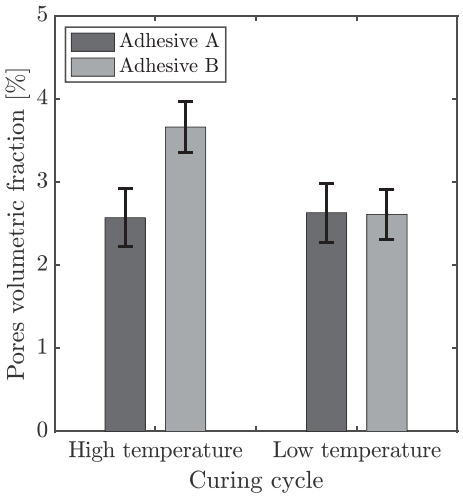
(a) Influence of the curing cycle on the pores diameters, adhesive A



(b) Influence of the curing cycle on the pores diameters, adhesive B



(c) Influence of the curing cycle on the pores number



(d) Influence of the curing cycle on the pores volumetric fraction

Figure 14. Comparisons of the pores diameters, numbers, and volumetric fractions for high and low temperatures curing cycles.

Table 6. Characteristics of the created pores in the adhesives A and B for different curing cycles.

Adhesive	Curing	Pores [-]	Pores ratio [%]
A	Low temperature	5866	2.63
A	High temperature	4862	2.57
B	Low temperature	3806	2.61
B	High temperature	2849	3.67

structural adhesives, with similar mechanical properties. The major differences between the two considered materials (aside from their chemical compositions, as they are not available) are shown in Table 1.

Table 7. Pores diameters statistics for all the considered cases.

Adhesive	Curing	Mean diameter [µm]	Standard deviation [µm]
A	Low temperature	43.1	12.0
A	High temperature	42.9	11.9
B	Low temperature	49.5	14.1
B	High temperature	56.3	18.2

As a reminder, it was evoked earlier in this paper that two additional specimens were studied for the following cases: adhesive A cured at low temperature and adhesive B cured at high temperature. Given for informative purposes only regarding the experimental scattering, these samples displayed the following properties, respectively: 2.63% pores ratio with 5828 pores, and 3.87% pores ratio with 3108 pores.

7.2. *Pores shape*

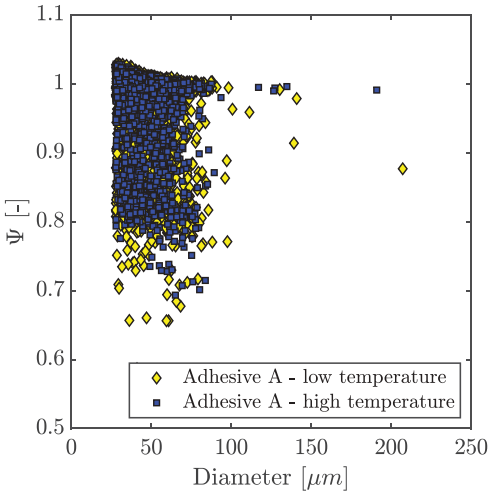
From the gathered data (Figure 2a,d, 6b, 6c and 11, for example), the pores in the adhesives are assumed to be rather spherical. It is however possible to quantify their roundness and their resemblance to a sphere. A quantity useful for such considerations is the sphericity, defined by Wadell in 1935.[29] The sphericity Ψ of a particle of volume V_p and of area A_p is defined according to Eq.4.

$$\Psi = \frac{\pi^{\frac{1}{3}}\left(6V_p\right)^{\frac{2}{3}}}{A_p} \tag{4}$$

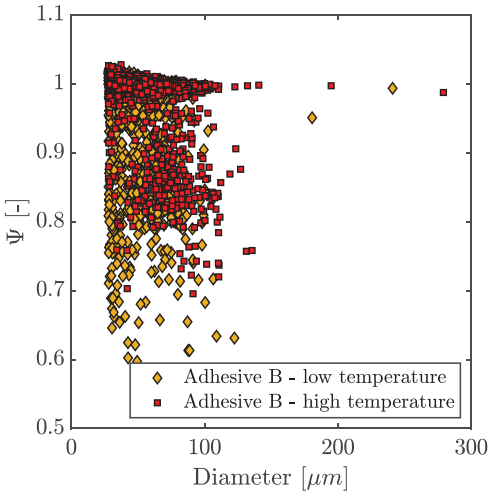
In the case of a perfect sphere, $\Psi = 1$. Thus, the closer to 1 is the sphericity, the more spherical the considered object is. Using connected components analysis on the segmented pores volumes, it is possible to extract, for each pore, its volume and its surface, and to use the expression in Eq.4 to compute its sphericity. The data plotted in Figure 15 represent these sphericities with respect to the equivalent diameters of the pores for all the considered cases.

It is fairly obvious from Figure 15(a,b) that the majority of the detected pores are almost perfectly spherical, since for both the adhesives and for both the curing cycles, there are clusters of point located near $\Psi = 1$. This assertion is confirmed by the data in Figure 15(c,d), where the distributions of the sphericities values are presented. These distributions are normalised with respect to the total number of pores, yielding frequencies instead of counts for each interval in the histograms. One may clearly see that the vast majority of these values are close to $\Psi = 1$.

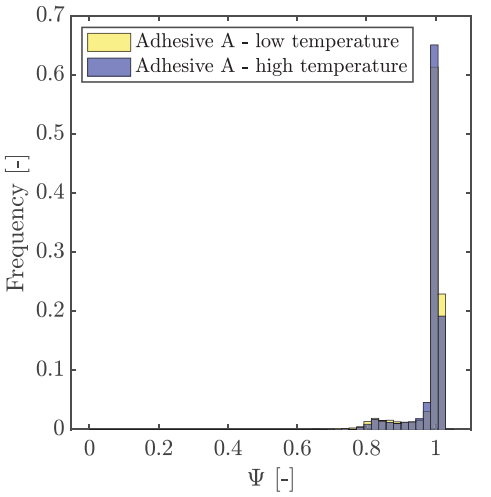
The definition of the sphericity introduced by Wadell[29] assumes that $\Psi = 1$ is a theoretical limit for Ψ. However, values slightly greater than 1 may be noticed in Figure (15a,d). The fact that these paradoxical values occur for small diameters tends to suggest that it may be an effect of the voxelisation,



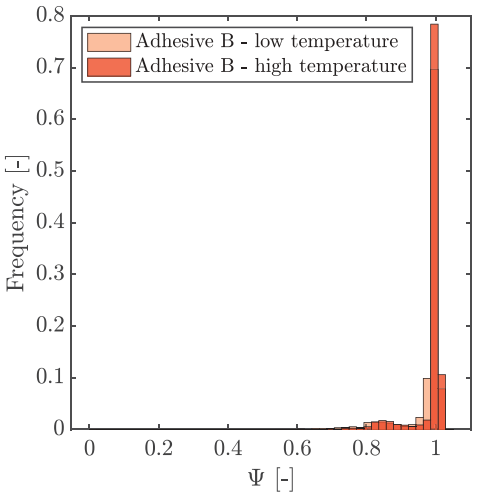
(a) Sphericitiy of the pores in adhesive A plotted with respect to their diameter



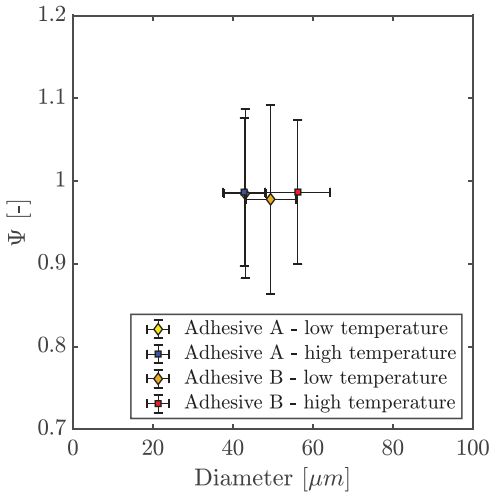
(b) Sphericity of the pores in adhesive B plotted with respect to their diameter



(c) Sphericity values distribution for the adhesive A



(d) Sphericity values distribution for the adhesive B



(e) Average sphericities for all the considered cases

Figure 15. Sphericities of the created pores.

leading to slightly erroneous areas or volumes calculations. It is easy to understand that the smaller the size of the pore, the greater the effect of voxelisation, and therefore the greater the potential error on the sphericity.

One may also notice a few sphericity values rather small when compared to the trend on each graph (see in Figure 15(a,d)), lesser than 0.7. These points may be due to coalescing pores or to segmentation errors for pores very close to one another (and mistakenly identified as one unique entity). Examples of these punctual values can be found in Figure 16, where pores with $\Psi < 0.75$ are displayed. It is, however, arduous to determine whether these values are segmentation errors or whether they are due to actual coalescence phenomena occurring during the curing of the adhesive. For this reason, it was chosen not to disconnect them, even though several algorithms such as the watershed transform exist to answer similar issues.

No noticeable difference between the adhesives and between the curing cycles can be highlighted in terms of shape of the pores, though, as the points clouds displayed in Figure 15(a,b) feature highly similar shapes. This is put into perspective in Figure 15e, where the average points of each point clouds presented in Figure 15(a,b) are plotted together. The error bars are computed using the standard deviations of the equivalent diameters and of the sphericities ($\pm 2\sigma$). Almost no gap between the adhesive A data can be spotted, which suggests that this particular adhesive is rather insensitive to the polymerisation conditions, at least with respect to the adhesive B. This conclusion should nonetheless be pondered by the fact that phenomena similar to the adhesive B may be happening in the adhesive A, but at a lower scale, undetectable with the measurements performed in this configuration. A slight shift is however detectable for the adhesive B (Figure 15e), both in terms of diameter (which was expected, see the data in Table 7, for example) and in terms of sphericity. Several factors could explain this difference between these samples: (i) it could simply be due to the experimental discrepancy from one adhesive joint to another and therefore be unrelated to the curing conditions, or (ii) the dilation happening throughout the curing cycle due to the increase in temperature could counter the effect of the slight mechanical load applied to the Scarf samples in their bonding apparatus (visible in Figure 3b) in order to control the joint thickness. More advanced and extensive measurements are needed in order to validate this hypothesis or to develop another possible explanation of this phenomenon.

7.3. *Effective section of the adhesive joint*

One of the most critical effects of the presence of pores within an adhesive joint is the decrease in effective section. The effective section is defined in Eq.5 as the ratio between the surface of adhesive S_{adh} and the surface of joint (*i.e.* the sum of the surfaces of adhesive S_{adh}, of pores S_{por} and of glass beads S_{beads}).

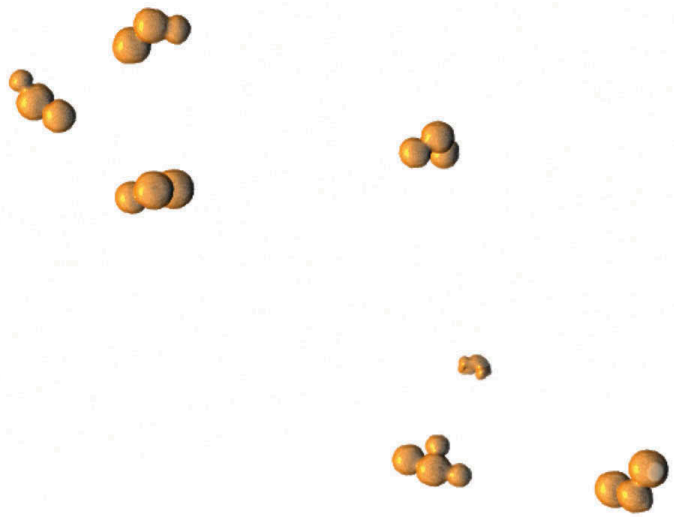
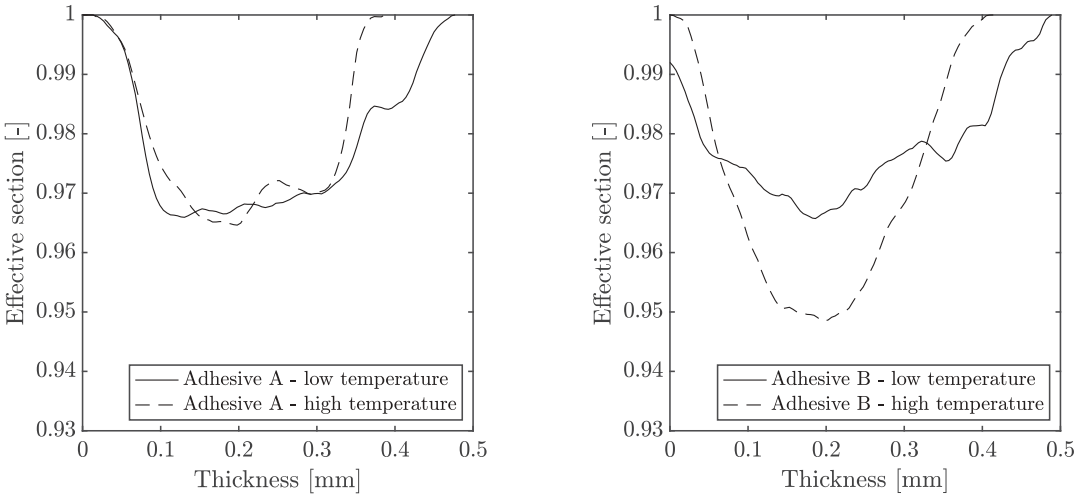


Figure 16. Merged pores inducing low sphericities (adhesive B, high temperature curing).

$$\Sigma = \frac{S_{adh}}{S_{adh} + S_{por} + S_{beads}} \tag{5}$$

This Σ ratio (somehow similar to a surface ratio, by analogy with the volumetric ratio used earlier in our study) can then be computed for each slice of reconstructed volume containing adhesive (*i.e.* the slices where there is only aluminium are excluded). As the investigated bonded assemblies are designed for tensile loadings, the section planes are defined to be parallel to (xy) in Figures 6a and 12. It is then possible to compute Σ with respect to the distance along $\vec{z}$ (defined in Figure 6a). It is assumed that $z = 0$ for the first slice where adhesive is segmented.

Once again, the differences for the adhesive A are small for the two curing cycles studied in this paper. It should, however, be noticed that the pores seem to be concentrated at the center of the joint ($\sim z = 0.2$ mm) for both cycles, with a sharper trend in the case of a high temperature curing. This remark is also to be made for the adhesive B, for which the differences between curing temperatures are once again more pronounced. If the rate of change of Σ with respect to z seems to be rather equivalent for both curves in Figure 17b in the first and last quarters of the joint ($z \leq 0.08$ mm and $z \geq 0.3$ mm, roughly), it is however not the case in the middle: there is a sudden gap between low and high temperature curing, which could be explained by void growth patterns thermally activated during the polymerisation of the material. Such coalescence phenomena have been widely observed and studied for porous materials. The works of Pinzer[15] in particular show that coalescence mechanisms can be thermally activated, which could explain the differences experienced between low temperature and high temperature curing for the adhesive B. This phenomenon is seemingly localised in the middle of the thickness of the joint, where the pores are more numerous. Additional work focused on the creation of the pores during the



(a) Effective sections throughout the thickness of the adhesive joint (adhesive A)

(b) Effective sections throughout the thickness of the adhesive joint (adhesive B)

Figure 17. Effective sections evolutions along the thickness of adhesive joints.

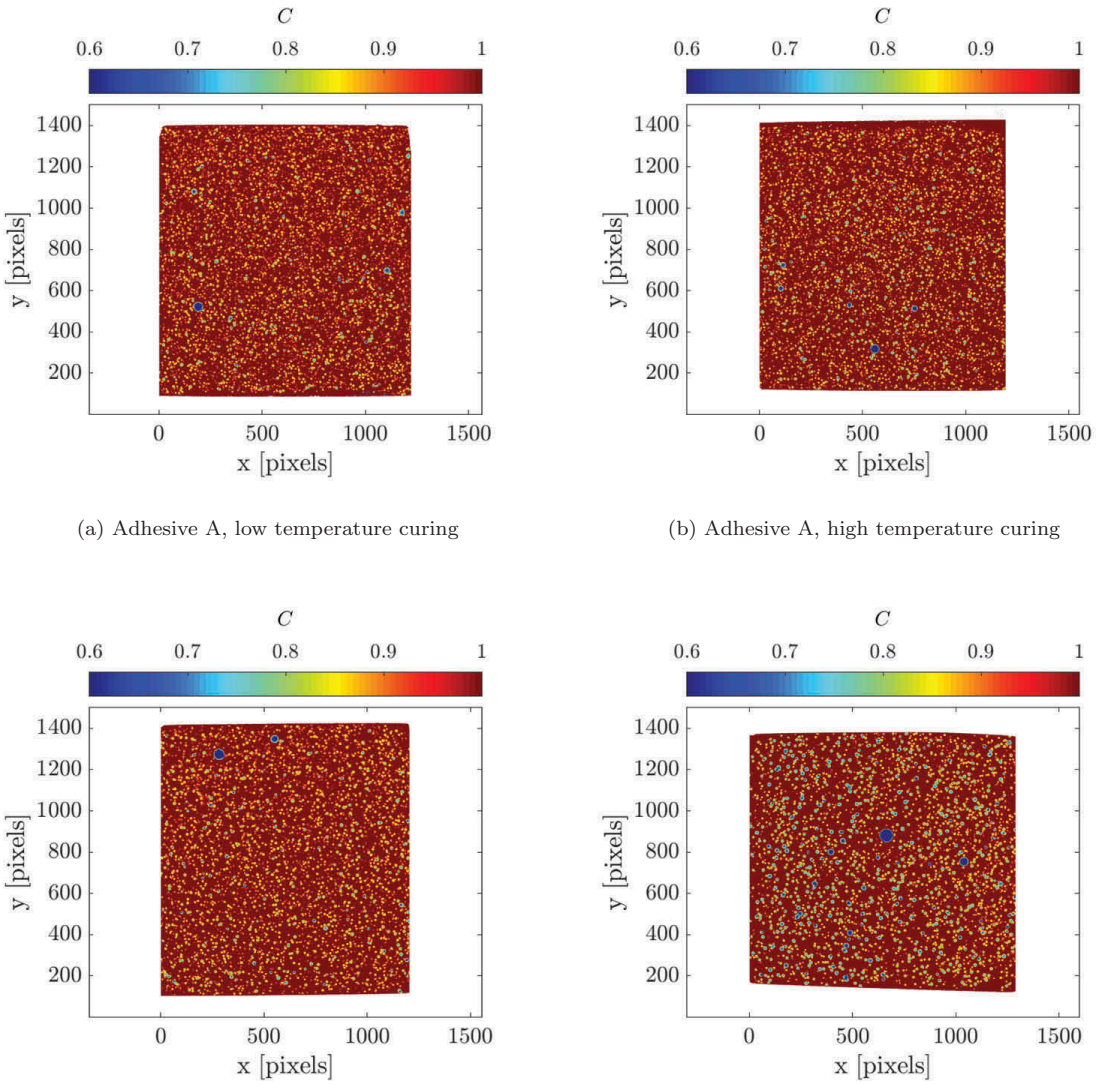
fabrication and the curing of the joint could bring elements to understand the mechanisms leading to the trends seen in Figure 17.

7.4. *Compactness*

Similar considerations can be pursued to investigate the existence of concentration zones for pores in the plane of the adhesive joint (as opposed to the data provided in Figure 17, where concentration zones along the direction normal to the adhesive joint were investigated). To do so, a similar approach is used, and define a compactness quantity C computed along the $\vec{z}$ axis (see Figure 6a for axis definition). Therefore, this C quantity will take the shape of a $[m, n]$ matrix for a given segmented adhesive phase and a given joint (adhesive+pores+beads) represented, respectively, by $[m, n, p]$ boolean matrices M_{adh} and M_{joint}, as it is expressed in Eq.6. The value of C is an indicator of the effective thickness, by analogy with Figure 17 and its corresponding discussion.

$$C(i,j) = \frac{\sum_{k=1}^{p} M_{adh}(i,j,k)}{\sum_{k=1}^{p} M_{joint}(i,j,k)} \tag{6}$$

The resulting maps of the compactness C for all our experimental cases can be found in Figure 18. From these data, it seems that there are no noticeable zones for which the compactness of the adhesive joint is lower. In other words, there is no part of the joint where pores are more abundant or bigger in the (xy) plane. As such, this would imply that the shift in curing temperature does not induce any major changes in terms of planar distribution of the centroids of the created pores and that the concentration mechanisms which appear to exist are occurring along the thickness of the joint, as demonstrated by Figure 17.



(a) Adhesive A, low temperature curing

(b) Adhesive A, high temperature curing

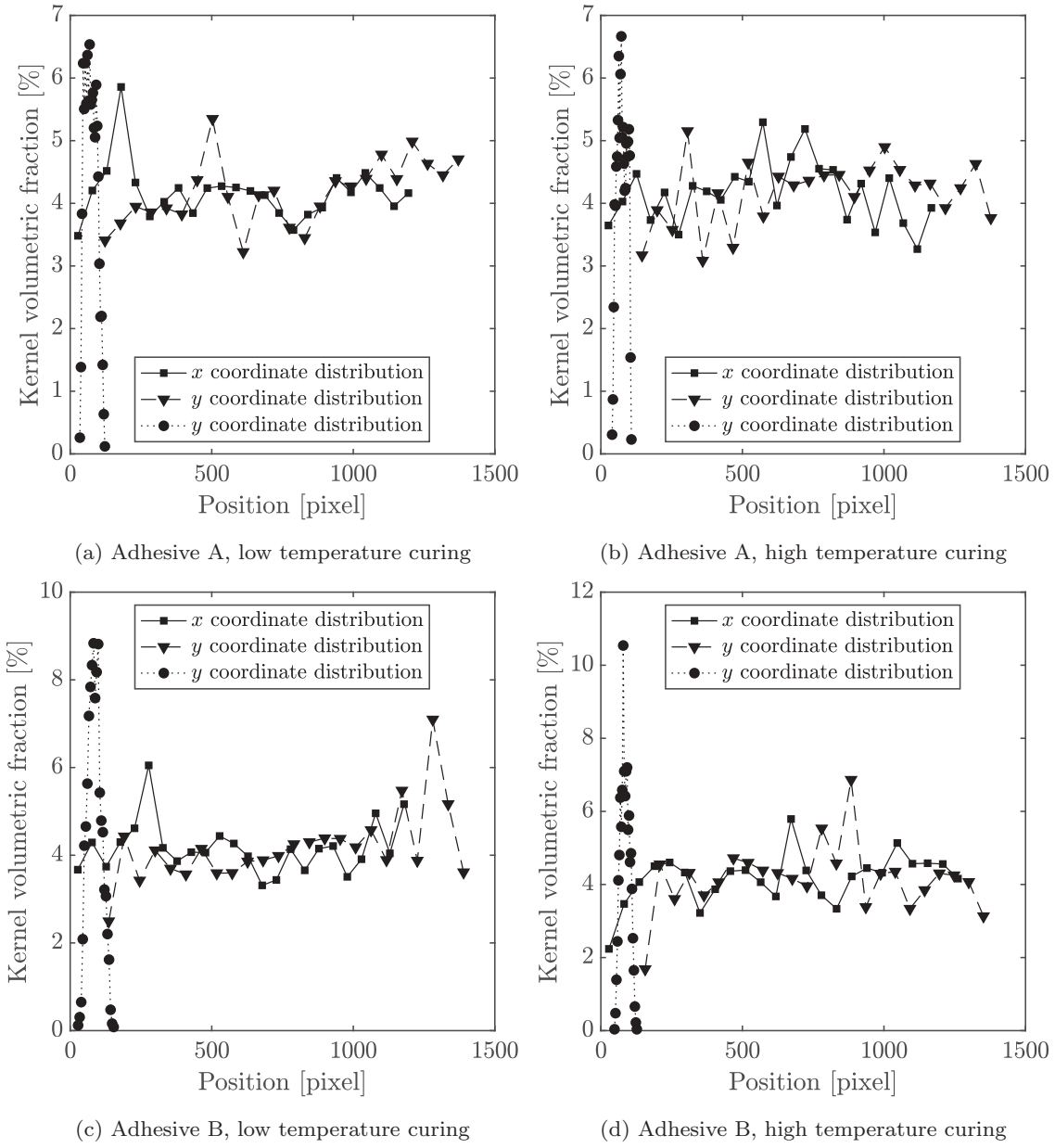
(c) Adhesive B, low temperature curing

(d) Adhesive B, high temperature curing

Figure 18. Compactness maps computed for all the adhesive joints under investigation.

This can be confirmed by analysing the distributions of the coordinates of the pores for each segmented volume, as it is done in Figure 19. In these graphs, each one of the three plotted lines shows the distribution of the coordinates x, y and z respectively. The distribution of a given coordinate component (x, for instance) is evaluated disregarding the values of the two others (*i.e.* y and z). Moreover, these distributions are not evaluated in terms of numbers of individuals in each kernel, but in terms of volumetric fraction of each kernel with respect to the complete volume of pores. It should be noted that the count of each interval used to compute these distributions has been normalised with respect to the total number of individuals to obtain frequencies.

As it may be easily seen in Figure 19(a,d), there are no prevalent coordinates for the pores centroids along the $\vec{x}$ and $\vec{y}$ which corroborates the



(a) Adhesive A, low temperature curing

(b) Adhesive A, high temperature curing

(c) Adhesive B, low temperature curing

(d) Adhesive B, high temperature curing

Figure 19. Pores coordinates distributions within the adhesive joint.

observations done in Figure 18. In addition, the concentration of the pores in the middle of the joint following $\vec{z}$ can be quite clearly visualised, as expressed earlier in this paper (Figure 17).

7.5. *Local pores volumetric fraction*

The data displayed in Figure 19(a,d) provide with knowledge about the number of pores as a function of the coordinates, but any volumetric ratio consideration is left aside in this approach. In order to obtain such information, the computation of a local porosity ratio is suggested, hereafter referred to as η_{loc}, in a sliding window sweeping the complete volume. The dimensions of said window can be selected

arbitrarily, but it was chosen to use the sizes of the pores as a basis for their calculation. The window used to compute these local ratios needs to be sufficiently large to not be outweighed by large pores (*i.e.* not to yield cases where there are only pore-related pixels in the window), but at the same time it needs to be small enough to remain local. As such, a window size Δ defined with respect to the statistics computed on the diameters distributions is used for each studied case, as expressed in Eq.7. The resulting kernel sizes vary between 20 and 29 pixels. The size of the window along $\vec{z}$ is set equal to the joint thickness. Therefore, η_{loc} will be computed in $[\Delta, \Delta, p]$ subvolumes within the complete adhesive joint.

$$\Delta = \lfloor \mu_d + 4\sigma_d \rfloor \tag{7}$$

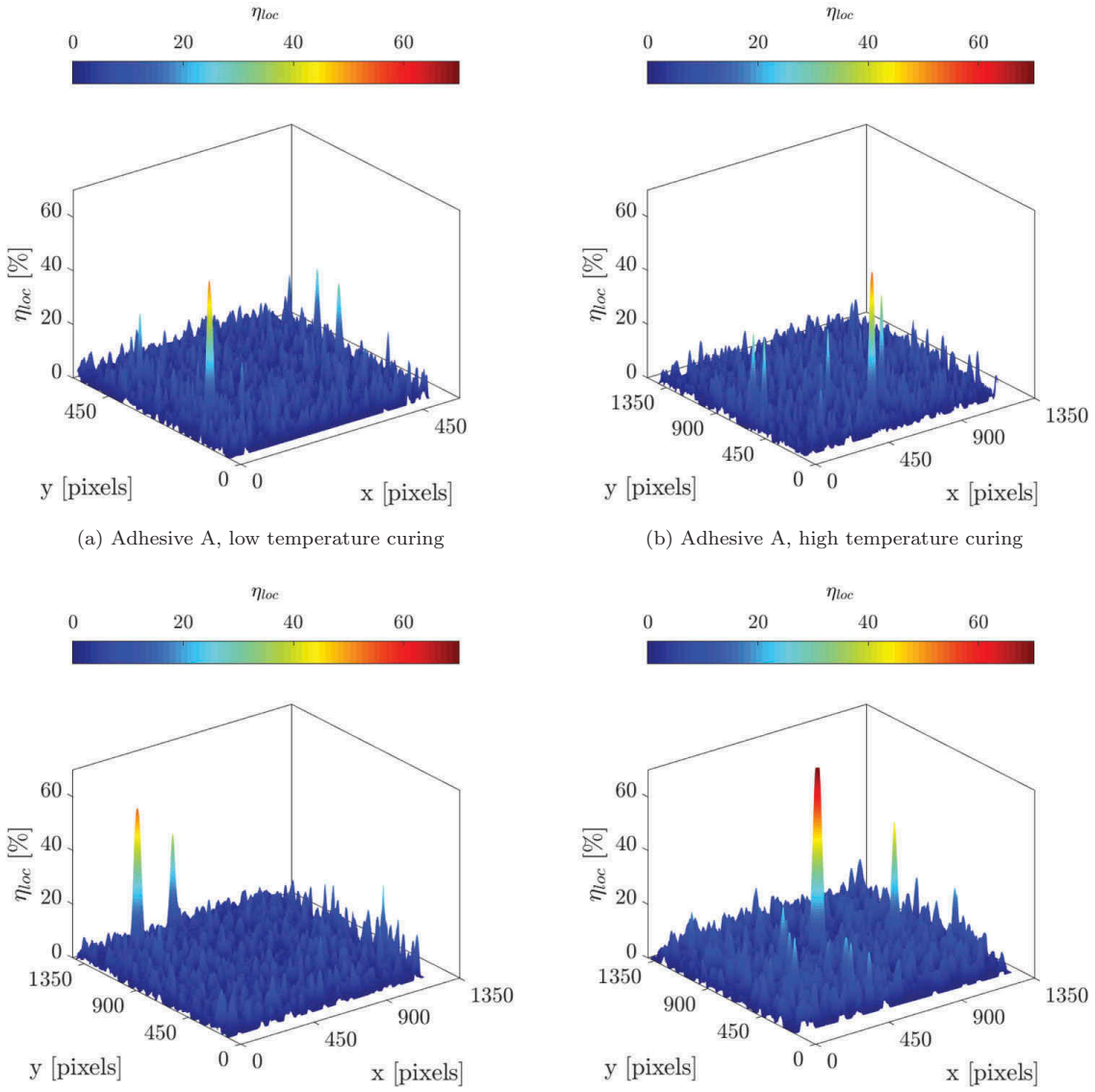
where μ_d and σ_d are the average diameter and the diameters standard deviation for a given pores dataset.

The value maps for η_{loc} can be found in Figure 20. These maps are to be linked with the data presented in Figure 18(a,d), as they give similar but complementary information. Several conclusions may be extracted from these figures: (i) a higher curing temperature does not induce local increase of porosity ratio, (ii) the physico-chemical properties of the investigated adhesives do not impact this quantity for the studied cases, and (iii) the only concentration zones are linked to high diameters pores. These larger pores are hopefully the most uncommon as well (as demonstrated by the diameters distributions displayed in Figure 14) and usually created while spreading the adhesive on the bonding surfaces. There does not seem to be a general trend once these peculiar values put aside, leading the authors to conclude that there are no favoured sites for pores concentrations in the place of the joint, may it be in terms of number or in terms of volumetric fraction.

Very high values for η_{loc} are reached in all the studied cases (up to 75% for the adhesive B cured at 110°C), comforting the hypothesis that pores within an adhesive joint are, to some extent, a threat to the mechanical strength of the bonded structure.

8. Conclusion

Adhesively bonded samples were made for two different curing cycles and two different bicomponent epoxy adhesives. These samples were placed in the chamber of an X-ray tomograph, in order to characterise the microstructure of the adhesive joints. The goal of these measurements was to detect the pores created during the bonding and during the curing inside the adhesive joints, and to investigate the potential change of their properties depending on the adhesive formulation and on the polymerisation cycle used to cure the materials. A segmentation-oriented image processing tool was then developed, so as to process the resulting CT-scans. This tool has been tried on artificial datasets to ensure its performances and to check its limitations. There are multiple findings for this study.



(a) Adhesive A, low temperature curing

(b) Adhesive A, high temperature curing

(c) Adhesive B, low temperature curing

(d) Adhesive B, high temperature curing

Figure 20. Local pores volumetric fractions.

First, it has been shown that the curing cycle and the adhesive formulation could have significant influences on the pores created during the manufacturing of the joint. These differences could be explained by the disparities between the adhesives in terms of texture and chemical compositions, but no tangible answer can be provided at this stage of the study regarding these aspects. However, among the two adhesives tested, one seemed to be relatively insensitive to the curing conditions (adhesive A), as little to no difference was experienced for the curing cycles used in this study. This implies that different adhesives may have different sensitivities to the bonding and curing conditions, but the factors driving this sensitivity remain unknown so far. Further information could be obtained through *in-situ* X-ray microtomography observations during the curing of the materials. Particularly, such experiments would provide interesting data regarding the effect of the viscosity changes which happen during the curing, due to the increase in

temperature and to the cross-linking reaction. Directly related to the curing reaction, the effects of the chemical shrinkage and of the residual stresses should also be investigated, in spite of their relative difficulty to be quantified.

It was also shown that pores are likely to be concentrated halfway through the thickness of the adhesive joint. Depending on the porosity volume fraction, this could be a factor to take into account in mechanical dimensioning computations, as the cross-section of the joint could be decreased by a noticeable and easily detectable amount, and the proximity of several large pores could also create preferred crack propagation paths since the adhesive bond would be locally weaker. Therefore, it would make sense, for mechanical strength reasons, to decrease as much as possible their creation during the bonding and the curing of the adhesives, especially for critical industrial fields such as aeronautics or space industry. Depending on the sensitivity of the material to the curing temperature, this decrease in pores number and volumetric ratio could be achieved by optimising the curing cycle so as to be as complete as possible in terms of polymerisation rate of the adhesive, and at the same time to be as low-temperature as possible. It is common for adhesives manufacturer to provide advised curing cycles in their datasheets, some of them being high-temperature cycles. This study shows that even if these advised cycles result in a fully polymerised material, the induced microstructure could trigger premature failure mechanisms, not necessarily for basic loadings such as monotonic or even creep, but perhaps for cyclic and fatigue loadings, or any long-term loading from a general standpoint. Working on the curing cycles is however not the only solution, as it is conceivable to mix the adhesive components in a vacuum environment, for example, which could decrease the pores created during the mixing.

ORCID

V. Dumont http://orcid.org/0000-0001-6214-3451

References

[1] Moussa, O.; Vassilopoulos, A. P.; Keller, T. Effects of Low-temperature Curing on Physical Behavior of Cold-curing Epoxy Adhesives in Bridge Construction. *Int. J. Adhes. Adhesives*. 2012, *32*, 15–22. DOI: 10.1016/j.ijadhadh.2011.09.001.

[2] Adams, R. D. *Adhesive Bonding Science, Technology and Applications*; Woodhead Publishing Ltd Elsevier, 2005.

[3] Da Silva, L. F. M. *Modeling of Adhesively Bonded Joints*; Springer-Verlag Berlin Heidelberg, 2008.

[4] Liu, X.; Bathias, C. Defects in Squeeze-cast Al2O3/Al Alloy Composites and Their Effects on Mechanical Properties. *Compos. Sci. Technol.* 1993, *46*, 245–252. DOI: 10.1016/0266-3538(93)90158-D.

[5] Hirano, T.; Usami, K.; Tanaka, Y.; Masuda, C. *In Situ* X-ray CT under Tensile Loading Using Synchrotron Radiation. *J. Mater. Res.* 1995, *10*, 381386. DOI: 10.1557/JMR.1995.0381.

[6] Cottrino, S.; Jorand, Y.; Maire, E.; Adrien, J. Characterization by X-ray Tomography of Granulated Alumina Powder during in Situ Die Compaction. *Mater. Charact.* 2013, *81*, 111–123. DOI: 10.1016/j.matchar.2013.04.004.
[7] Maire, E.; Carmona, V.; Courbon, J.; Ludwig, W. Fast X-ray Tomography and Acoustic Emission Study of Damage in Metals during Continuous Tensile Tests. *Acta Mater.* 2007, *55*, 6806–6815. DOI: 10.1016/j.actamat.2007.08.043.
[8] Adrien, J.; Maire, E.; Gimenez, N.; Sauvant-Moynot, V. Experimental Study of the Compression Behaviour of Syntactic Foams by in Situ X-ray Tomography. *Acta Mater.* 2007, *55*, 1667–1679. DOI: 10.1016/j.actamat.2006.10.027.
[9] Maire, E.; Fazekas, A.; Salvo, L.; Dendievel, R.; Youssef, S.; Cloetens, P.; Letang, J. M. X-ray Tomography Applied to the Characterization of Cellular Materials. Related Finite Element Modeling Problems. *Compos. Sci. Technol.* 2003, *63*, 2431–2443. DOI: 10.1016/S0266-3538(03)00276-8.
[10] Pavan, M.; Craeghs, T.; Verhelst, R.; Ducatteeuw, O.; Kruth, J. P.; Dewulf, W. CT-based Quality Control of Laser Sintering of Polymers. *Case Stud. Non- Destruct. Test. Eval.* 2016, *6*, 62–68. DOI: 10.1016/j.csndt.2016.04.004.
[11] Wang, X.; Zhao, L.; Fuh, J. Y. H.; Lee, H. P. Effect of Porosity on Mechanical Properties of 3D Printed Polymers: Experiments and Micromechanical Modeling Based on X-ray Computed Tomography Analysis. *Polymers*. 2019, *11*. DOI: 10.3390/polym11071154.
[12] McKinley, P.; Ching, D.; Kamke, F.; Zauner, M.; Xiao, X. Micro X-ray Computed Tomography of Adhesive Bonds in Wood. *Wood Fiber Sci.* 2016, *48*, 2–16.
[13] Schwarzkopf, M.; Muszynski, L. Strain Distribution and Load Transfer in the Polymer-wood Particle Bond in Wood Plastic Composites. *Holzforschung*. 2015, *69*, 53–60. DOI: 10.1515/hf-2013-0243.
[14] Taud, H.; Martinez-Angeles, R.; Parrot, J. F.; Hernandez-Escobedo, L. Porosity Estimation Method by X-ray Computed Tomography. *J. Petrol. Sci. Eng.* 2005, *47*, 209–217. DOI: 10.1016/j.petrol.2005.03.009.
[15] Pinzer, B. R.; Medebach, A.; Limbach, H. J.; Dubois, C.; Stampanoni, M.; Schneebeli, M. 3D-characterization of Three-phase Systems Using X-ray Tomography: Tracking the Microstructural Evolution in Ice Cream. *Soft Matter*. 2012, *8*, 4584. DOI: 10.1039/c2sm00034b.
[16] Little, J. E.; Yuan, X.; Jones, M. I. Characterisation of Voids in Fibre Reinforced Composite Materials. *NDT E Int.* 2011, *46*, 122–127. DOI: 10.1016/j.ndteint.2011.11.011.
[17] Alonso-Sierra, S.; Velázquez-Castillo, R.; Millán-Malo, B.; Nava, R.; Bucio, L.; Manzano-Ramírez, A.; Cid-Luna, H.; Rivera-Mun˜oz, E. M. Interconnected Porosity Analysis by 3D X-Ray Microtomography and Mechanical Behavior of Biomimetic Organic-Inorganic Composite Materials. *Mater. Sci. Eng. C*. 2017. DOI: 10.1016/j.msec.2017.05.106.
[18] Plank, B.; Mayr, G.; Reh, A.; Kiefel, D.; Stoessel, R.; Kastner, J. *Evaluation and Visualisation of Shape Factors in Dependence of the Void Content within CFRP by Means of X-ray Computed Tomography*. tech. rep.; 2014.
[19] Enns, J. B.; Gillham, J. K. Time–Temperature–Transformation (TTT) Cure Diagram: Modeling the Cure Behavior of Thermosets. *J. Appl. Polym. Sci.* 1983, *28*, 2567–2591. DOI: 10.1002/app.1983.070280810.
[20] Buffiere, J.-Y.; Maire, E.; Adrien, J.; Masse, J.-P.; Boller, E. In Situ Experiments with X Ray Tomography: An Attractive Tool for Experimental Mechanics. *Exp. Mech.* 2010, *50*, 289–305. DOI: 10.1007/s11340-010-9333-7.
[21] Kak, A. C.; Slaney, M. *Principles of Computerized Tomographic Imaging*; Society for Industrial and Applied Mathematics: Philadelphia, 2001.

[22] Dumont, V.; Badulescu, C.; Adrien, J.; Carrere, N.; Thévenet, D.; Maire, E. Experimental Investigation of Porosities Evolution in a Bonded Assembly by Means of X-Ray Tomography. *J. Adhes.* 2019. DOI: 10.1080/00218464.2019.1685984.
[23] Sezgin, M. Survey over Image Thresholding Techniques and Quantitative Performance Evaluation. *J. Electron. Imaging*. 2004, *13*, 146–165. DOI: 10.1117/1.1631315.
[24] Rosenfeld, A.; De La Torre, P. Histogram Concavity Analysis as an Aid in Threshold Selection. *IEEE Trans. Syst. Man Cybern.* 1983, *13*, 231–235. DOI: 10.1109/TSMC.1983.6313118.
[25] Otsu, N.;. A Threshold Selection Method from Gray-Level Histograms. *IEEE Trans. Syst. Man Cybern.* 1979, *9*, 62–66. DOI: 10.1109/TSMC.1979.4310076.
[26] Lim, J. S. *Two-dimensional Signal and Image Processing*; Hall, P. Ed., 1990; pp. 469–476. Upper Saddle River, NJ: Prentice-Hall, Inc.
[27] Gallagher, N. C.; Wise, G. L. A Theoretical Analysis of the Properties of Median Filters. *IEEE Trans. Acoust. Speech Signal Process*. 1981, *29*, 1136–1141. DOI: 10.1109/TASSP.1981.1163708.
[28] Schindelin, J.; Arganda-Carreras, I.; Frise, E.; Kaynig, V.; Longair, M.; Pietzsch, T.; Preibisch, S.; Rueden, C.; Saalfeld, S.; Schmid, B. Fiji: An Open-source Platform for Biological-image Analysis. *Nat. Methods*. 2012, *9*, 676 EP. DOI: 10.1038/nmeth.2019.
[29] Wadell, H. Volume, Shape, and Roundness of Quartz Particles. *J. Geol.* 1935, *43*, 250–280. DOI: 10.1086/624298.

International Journal of Adhesion & Adhesives 99 (2020) 102568

Contents lists available at ScienceDirect

International Journal of Adhesion and Adhesives

journal homepage: http://www.elsevier.com/locate/ijadhadh

On the influence of mechanical loadings on the porosities of structural epoxy adhesives joints by means of *in-situ* X-ray microtomography

V. Dumont [a,d,*], C. Badulescu [a], G. Stamoulis [c], J. Adrien [b], E. Maire [b], A. Lefèvre [d], D. Thévenet [a]

[a] ENSTA Bretagne, UMR CNRS 6027, IRDL, F-29200, Brest, France
[b] Univ. Lyon, INSA Lyon, UMR CNRS 5510, Laboratoire MATEIS, F-69621, Villeurbanne Cedex, France
[c] Univ. Bretagne Occidentale, UMR CNRS 6027, IRDL, F-29200, Brest, France
[d] Safran Reosc, Engineering & Integration Department, 91280 St, Pierre-du-Perray, France

ARTICLE INFO

Keywords:
Structural bonding
X-ray microtomography
Pores
Image processing

ABSTRACT

Structural bonding is a beneficial technique extensively used in numerous industrial fields. This technique is however prone to structural defects such as pores, which are created during the mixing of the adhesive and during the shaping of the joint. Depending on their characteristics, these pores are likely to influence the mechanical behaviour of adhesively bonded joints, as they induce local decreases in the cross-section of the bonds and they may also create threatening stress concentrations. It is also fair to assume that the characteristics of the pores within an adhesive joint are subject to changes when the assemblies are submitted to external loads. In order to investigate these changes, adhesively bonded samples were made using two different bicomponent epoxy structural adhesives. These samples were placed inside an X-ray tomograph, containing a tensile machine. *In-situ* X-ray tomography measurements were made simultaneously with the application of a tensile load on the samples. It was therefore possible to characterise the porosity states of each sample under mechanical loading, and to compute various quantities (porosity volumetric ratio, the pores number, equivalent diameters distributions, *etc.*). It was found that the pores in the joints are impacted by the increasing mechanical stress, resulting in pore nucleation, pore growth and coalescence. Moreover, the present study shows that this microstructural behaviour cannot be generalised, as different adhesives may display different properties.

1. Introduction

A wide range of industrial fields nowadays use structural bonding for their applications, such as aeronautics, automotive or renewable energies. This extensive use is explained by the many advantages adhesive bonding features as opposed to bolting or riveting: multimaterials assembly capabilities, decrease in weight, preserved structure integrity, *etc.* Unfortunately, this technique also has disadvantages [1]: the quality of the bond highly depends on the bonding process (surface treatment, curing, *etc.*) [2], the mechanical behaviour of structural adhesives is non-linear and difficult to model accurately, and bonding defects are very likely to happen during the shaping of the joint. These imperfections, often unavoidable, include the presence of pores within the material. These pores, created during the mixing of the adhesive components and during the shaping of the adhesive joint, can be a threat to the good mechanical strength of the bond: they damage the integrity of the material, they decrease the cross-section of the joint, and they can induce unwanted stress concentrations. These pores being structural defects inside the adhesive joint, it is fair to hypothesise that they could have an influence on the mechanical properties of a bonded assembly. To validate this assertion, it is however essential to be able to detect these pores inside an adhesive joint.

X-ray microtomography is a fairly popular solution to detect and visualise such entities located in a bulk of a medium. This technique is increasingly used in materials science due to its various advantages as it is detailed by Buffière et al. [3]: it is non-destructive, the measurements are three-dimensional, it allows the visualisation of the internal structure of non-transparent media, *etc.* Moreover, depending on the tomograph, the resolution of the measurements can be lesser than 1 μm, which is a quite attractive feature for damage and defects detection. That is why this tool has been used in the past on a variety of materials for similar purposes such as alloyed metals and composite materials. For instance, Liu and Bathias studied the effects of the presence of pores in a Aluminium alloy reinforced composite in terms of tensile and fatigue

* Corresponding author. ENSTA Bretagne, UMR CNRS 6027, IRDL, F-29200, Brest, France.
E-mail address: vincent.dumont@ensta-bretagne.org (V. Dumont).

https://doi.org/10.1016/j.ijadhadh.2020.102568

Available online 12 February 2020
0143-7496/© 2020 Elsevier Ltd. All rights reserved.

properties [4]. In a similar fashion, Breunig et al. managed to detect fibre fracture and interface debonding in a SiC/Al MMC material under wedge and 3-points bending loadings using X-ray tomography [5]. Polymeric materials were also studied using such a technique: in particular Garcea et al. succeeded in visualising cracks in a polymer composite [6], in spite of the many experimental issues specific to X-ray measurements performed on these materials. Notably, the authors used the reconstructed volumes to build a Finite Element Model, so as to be able to predict both damage initiation and propagation in the material. As far as damage characterisation is concerned, *in-situ* microtomography measurements are particularly useful, as they enable the tracking of both the appearance and the evolution of damage-related phenomena under mechanical stress (crack propagation, pores coalescence, delamination, *etc.*), as shown in numerous studies carried on by the teams of Maire, Adrien and Buffière [7–11]. Most of these reference works take advantage of *in-situ* X-ray tomography to characterise materials under various types of loadings: metals under tensile loading [10], polymeric syntactic foams under compression [11], metal matrix composites loaded in tension [8], *etc.*

On the subject of polymers, a few studies may be found in the literature. A commonly found topic is the fabrication of polymeric structures by means of additive manufacturing processes. These techniques tend to generate voids in the resulting materials, which are easily studied using X-ray microtomography. For instance, a paper released by Pavan et al. in 2016 characterised the porous network of laser-sintered polyamide structures, for different sizes [12]. It was found that the size of the structure had a significant influence the characteristics of the voids created during the process. More recently, Wang et al. proposed a micromechanical model in order to characterise the mechanical behaviour of 3D-printed polymers [13]. Nonetheless, few studies may be found specifically on adhesives, and even more so regarding adhesively bonded assemblies. This is probably explained by the *a priori* low risk of pore creation for these materials when compared to additive manufactured polymers. X-ray tomography has been fairly recently applied to the field of structural bonding, but mainly to characterise the interfaces between adhesives and adherend. For example, Schwarzkopf [14] used tomography measurements coupled with simulations to build a micromechanical model of adhesive-wood interfaces. McKinley et al. [15] took advantage of this experimental technique to characterise the bonding process and the penetration of the adhesive in the fibrous structure of wooden pieces. Virtually no attention has been given to the precise study of the microstructure of adhesive joints, whereas it may be an important factor to describe macroscopic phenomena, such as crack propagation. It should however be reminded that microtomography is not the only experimental technique able to quantify the porous state of polymers, or materials in general. For instance, one can use gas sorption and Hg injection, as it has been done by Rohr et al. [16] for porous resins derived from acrylate monomers. Such techniques are able to provide valuable data for extremely small pores, which cannot be visualised through X-ray tomography. However, it should be noted that less extensive knowledge regarding the geometry of the pores is obtained using these techniques, and they may not be suited to the study of bonded assemblies for *in-situ* testings, for example.

In this paper, the authors characterise the effect of an out-of-plane tension stress on the detectable pores included in adhesives joints using *in-situ* X-ray microtomography measurements. This is achieved on bonded assemblies, using two bicomponent epoxy adhesives. This characterisation is performed for various values of the applied load, in order to track diverse porosity-related quantities, such as the number, the volume fraction, the diameters distribution *etc.* A discussion on the results is finally proposed, so as to explain the highlighted phenomena. It should be reminded that this aim of this study is not the absolute characterisation of the porous network of these materials, but the detection of phenomena achievable with state-of-the-art laboratory tomography on adhesively bonded assemblies.

2. Preparation of the samples

2.1. Design

The samples used in this study are butt-joint samples, bonded using a structural bicomponent epoxy adhesive. The dimensions of the samples are kept relatively small, in order to fit in the tomograph used for the tests campaign. As such, they are designed to feature a 6×6 mm^2 bonded surface (Fig. 1a). These samples are waterjet cut from aluminium 2017A Scarf samples to form a rake-shaped pattern as shown in Fig. 1b. Each specimen is then to be cut from its Scarf base after the curing (Fig. 1c), as it is detailed further.

A standard surface treatment procedure is applied to the samples to obtain good adhesion conditions. This treatment sequentially includes acetone degreasing, grinding with grade 180 sandpaper, and a final acetone cleaning. These steps ensure the removal of any oily impurities and oxide layers which could have been formed during the machining, the storage and the handling of the substrates.

As it has been stated in the introduction section, the study is performed on two different bicomponent epoxy adhesives (adhesive A and adhesive B). Adhesive B is commercially known as the *Huntsman^{TM} Araldite 420* adhesive. The trade name of adhesive A cannot be communicated for reasons of confidentiality. A few general properties are given in Table 1. These adhesives have similar curing properties in terms of duration and temperature, according to the datasheets provided by the manufacturers and to Differential Scanning Calorimetry (DSC) measurements. The mixing of the components is performed with a planetary mixing device (1500 rpm for 7 min) in order to guarantee homogeneity.

The *Huntsman^{TM} Araldite 420* is an epoxy-based adhesive with a bisphenol A diglycidyl-ether prepolymer and a diamine hardener mixed in stoichiometric conditions. The adhesive A is also an epoxy-based adhesive, with a bisphenol A epichlorohydrin prepolymer, and a titanium dioxide charged propylamine hardener.

The adhesives were spread on the bonded surfaces using a stainless steel spatula, and the two Scarf substrates are then assembled together (Fig. 1c) with a specially designed setup. The role of this setup is to control both the alignment of the substrates and the thickness of the adhesive joint. In this work, the thickness is set to 0.4 mm, using calibrated spacers (Fig. 1c).

The Scarf assemblies are then put inside a *Memmert UF110+^{TM}* thermal chamber to be cured (1h10 at 110 °C). DSC tests were performed on the adhesives thusly cured, to check that the polymerisation rates were above 95% (*i.e.* that the adhesives can be considered to be fully polymerised).

Finally, the microtomography samples (Fig. 1a) were waterjet cut from their Scarf base (Fig. 1b), and threaded holes are machined at each end so as to apply a mechanical load.

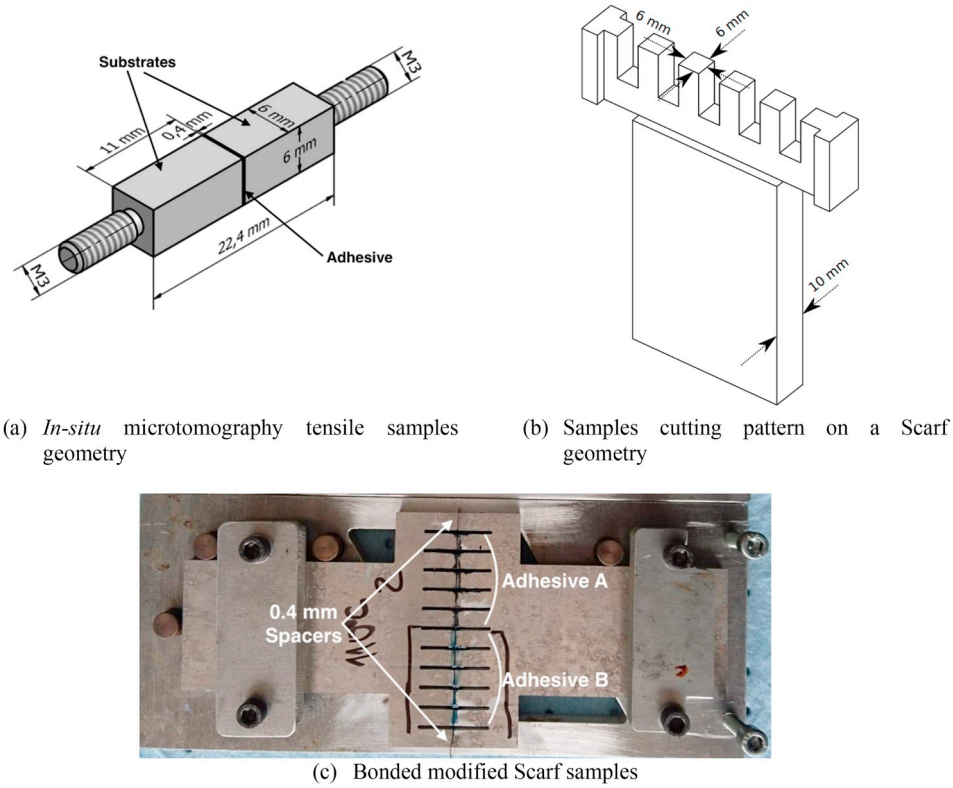
3. Experimental method

3.1. X-ray tomography principle

The interested reader may find detailed information on this particular matter in Ref. [17].

Microtomography is a non-destructive, three-dimensional imaging technology originally developed and used for medical applications [3, 18]. As such, it quickly became of interest for materials science, as it allows researchers to access data from the bulk of a non-transparent material. Moreover, these data are three-dimensional, with a resolution down to 1 μm per pixel [3].

The technique relies upon the variation of the X-ray attenuation phenomenon within an inhomogeneous material, when crossed by X-ray beams. This variation, closely linked to the internal structure of the medium, can be used to reconstruct the complete volume of the observed sample. To do so, the investigated volume is exposed to X-rays



(a) *In-situ* microtomography tensile samples geometry

(b) Samples cutting pattern on a Scarf geometry

(c) Bonded modified Scarf samples

Fig. 1. Modification of SCARF geometries for in-situ tomography applications2.2. Bonding and curing.

Table 1
A few properties for the considered adhesives.

Property	Adhesive A	Adhesive B
Texture	paste-like	paste-like
Known fillers		glass beads
Glass transition temperature (DSC)	~90 °C	~60 °C
Young's modulus [MPa]	1400	2000
Poisson ratio [−]	0.33	0.41

along various propagation paths using different angular positions (Fig. 2). The gathered data from the X-ray detector (Fig. 2) for each of these paths allow for the reconstruction of the complete volume by means of a reconstruction algorithm, provided by the manufacturer of the tomograph. More information about the possible reconstruction techniques may be found in Ref. [17]. The reconstruction step allows for the visualisation of the map of the linear attenuation coefficient $\mu(x,y,z)$, which results from the X-ray attenuation phenomenon within the material. This coefficient being inherently linked to the medium structure, the spatial map of $\mu(x,y,z)$ is equivalent to the spatial reconstruction of the medium microstructure.

In the following paper, it is assumed that this technique is reliable enough to give an accurate description of the microstructure of the investigated joints. This is moreover validated by comparing the dimensions of substrates measured by an optical microscope on one hand and by the tomograph on the other hand. A gap lesser than 0.15% was

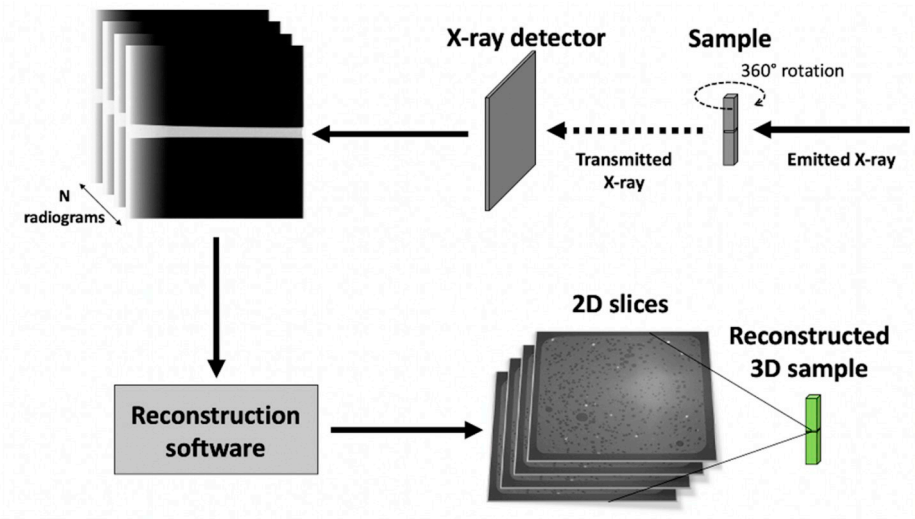


Fig. 2. Tomography measurements principle.

found.

3.2. Test procedure

The tomograph used in the following study is a *Phoenix*^{TM} *VtomeX* equipped with a 1920x1536 pixels *Varian Paxscan*^{TM} X-ray detector. The chamber of this tomograph includes a 3 kN electromechanical tensile machine to perform *in-situ* measurements as shown in Fig. 3. The radiograms (Fig. 2) delivered by the detector are 16-bits greyscale pictures, to be used by the reconstruction software to build the 3D volume of the investigated sample. The measurements are performed with a voxel size of 4.5 µm × 4.5 µm x 4.5 µm, which is the best achievable resolution with respect to the dimensions of the samples. As it is shown in Fig. 2, attenuation data for several propagation paths (*i.e.* several angular positions of the sample with respect to the X-ray beam) are needed. For these measurements, 1200 radiographs were recorded during the 360° rotation (Fig. 2) with an exposure time of 500 ms each, resulting in an acquisition time of roughly 10 min. The X-ray source was operated with a voltage of 80 kV and a current of 280 µA.

This was performed for various tensile loads in order to investigate the influence of the application of a mechanical stress to the detected pores in the adhesive joints. During the acquisition time, the displacement of the moving part of the tensile machine was stopped (Fig. 4). The displacement was then increased to proceed to the next step, with a rate of 0.4 mm min^{-1}. This process was continued until the failure of the sample. The resulting load on the samples is shown in Fig. 5. It is clear that the load is evolving for each step, especially for the higher levels, due to stress relaxation mechanisms. In order to reduce the influence of this phenomenon on the measurements, a stabilisation time is kept before launching the acquisition.

3.3. Tomographic data processing

The main challenge is to isolate the different phases in the reconstructed volumes: the air in the pores, the adhesive, and the aluminium substrates. If the adhesive contains glass beads or other mineral charges, such as the adhesive B, they are included in the substrates phase, for they appear at similar greyscale levels. This step, known as segmentation, is very common in image processing and a large number of methodologies has been suggested to segment greyscale or colour data.

An easy approach is to use one or several thresholds depending on the number of phases to be segmented. These thresholds divide the pixels in the data depending on their greyscale level, to form the desired phases. The value of the thresholds can be chosen, or preferably computed by means of various algorithms [19].

Other methodologies, which do not rely on thresholds, also exist. Among these, the watershed algorithm [20] was successfully applied to image segmentation [21]. Another popular approach is to use region growing algorithms [22], adapted from the random walker probabilistic model [23]. Due to the shape of the histogram of the reconstructed volumes (Fig. 6), a threshold-based method is chosen: the three phases within the material are well-defined (see the peaks on the histogram in Fig. 6).

The thresholds are calculated using Otsu's method [24]. This method optimises the thresholds values so as to obtain maximal inter-phase variance in terms of pixels greyscale levels. Firstly introduced for the calculation of one threshold to segment bimodal data, it may also be generalised to a greater number of thresholds [24]. In the scope of this study, two thresholds are needed (*i.e.* multithresholding), in order to segment trimodal data (Fig. 6). Thresholding is however sensitive to measurement noise; that is why a contour-preserving [25] three-dimensional median filter is previously applied to reduce this disturbance. The kernel size of this filter is set to 5 voxels. As a result, all the segmented objects whose size is lesser than that of the kernel of this filter were removed (which roughly corresponds to a 22 µm pore diameter, since too high of an uncertainty impacts their segmentation).

The volumes are then segmented using the computed thresholds, resulting in the data shown in slices to Fig. 7.

The segmented volumes are then screened to remove segmentation errors or unwanted objects (*i.e.* pores whose volumes are lower than the median filter kernel size, for instance). Finally, connected components analysis can be performed on these screened volumes to obtain various geometrical and statistical quantities.

In order to investigate the influence of the measurement noise on the segmentation, artificial tomographic results were generated, in such a way they resemble the experimental volumes as well as it is possible at this stage of the study, in terms of greyscale levels, noise, and pores sizes. In particular, the experimental noise was estimated by subtracting two microtomographic acquisitions of the same volume. The standard deviation of the resulting greyscale levels was then used to generate an artificial Gaussian noise, to be applied on the synthetic volumes. The tool was then applied to these artificial datasets, and the detected pores numbers and pores volumetric ratios were compared to the values imposed during the creation of the artificial data. The results are presented in Fig. 8.

From these data, one may notice that the error committed during the segmentation can be divided into two separate parts: a systematic error (*i.e.* a global offset from the reference values) and a punctual error, resulting in fluctuations around a mean value (Fig. 8c and d).

The systematic error is expected to be a consequence of the processing method itself. Since the pores from one load step to another are subjected to minor changes, this component of the error should lead to an offset between the actual experimental values and the detected experimental values, fairly independent of the applied load. On the other hand, the measurement noise varies from one load step to the next, and therefore may have a quantifiable influence on the results, mostly in terms of uncertainty on the detected quantities. This influence may be estimated using the standard deviation of the detected data in Fig. 8a and b. More precisely, it is possible to compute a relative error for each noise draw in Fig. 8a and b, and to extrapolate these error values and their statistics to the experimental data, so as to estimate the uncertainty on the detected results.

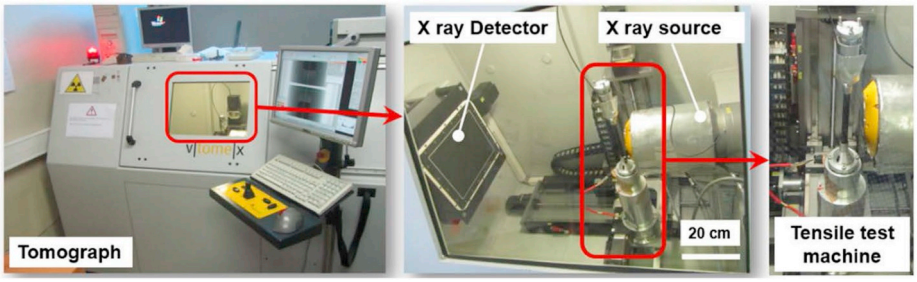


Fig. 3. Experimental set-up.

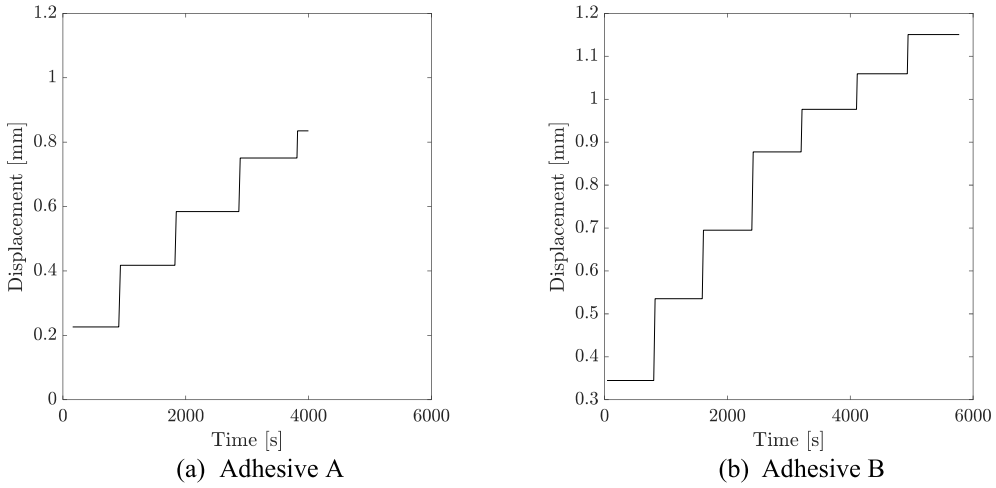


Fig. 4. Displacement steps applied to the samples.

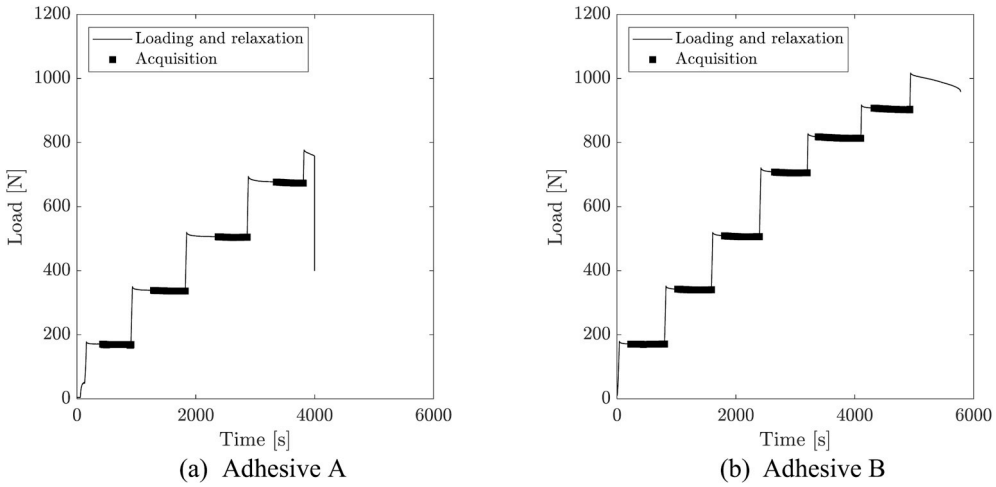


Fig. 5. Resulting load on the samples.

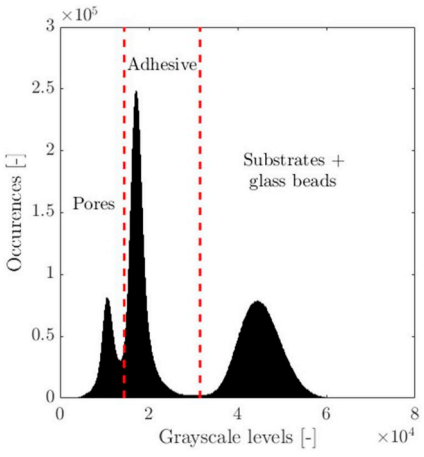


Fig. 6. Histogram of a reconstructed volume and thresholds computed using Otsu's method.

4. Results

4.1. Porosity volumetric ratio and number of pores

As these tomographic measurements were performed for various loads applied to the samples, it is possible to apply the analysis technique presented above to each dataset, in order to track the evolution of some characteristics that may be extracted from the segmented volumes. In a first stage, the following quantities shall be investigated: the porosity ratio η (Equation (1)), and the number of pores in the adhesive joints.

$$\eta = 100^{*}\frac{V_{por}}{\sum_{i \in phases} V_i} \tag{1}$$

where V_{por} is the volume of the pores and V_i is the volume of the phase i.

Three-dimensional views of the detected pores in each adhesive joint (in their initial state) can be found in Fig. 9. An immediate observation that can be made is that the pores properties depend on the adhesive, since the segmentation yields very different results between adhesives A and B.

These quantities are computed for each load step, and the results are given in Fig. 10 and Fig. 11. It should be noted that the porosity presented in Equation (1) is expressed as percentages in Fig. 11. The data in Figs. 10 and 11 feature error bars estimating the uncertainty caused by

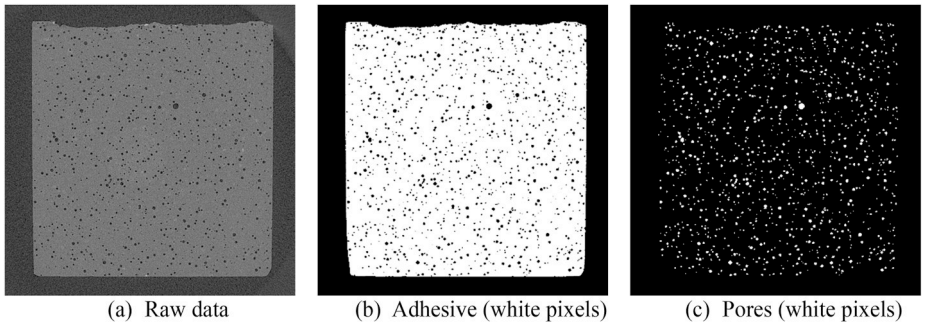


Fig. 7. Data segmentation output (Adhesive A, initial state, sliced halfway through the joint thickness).

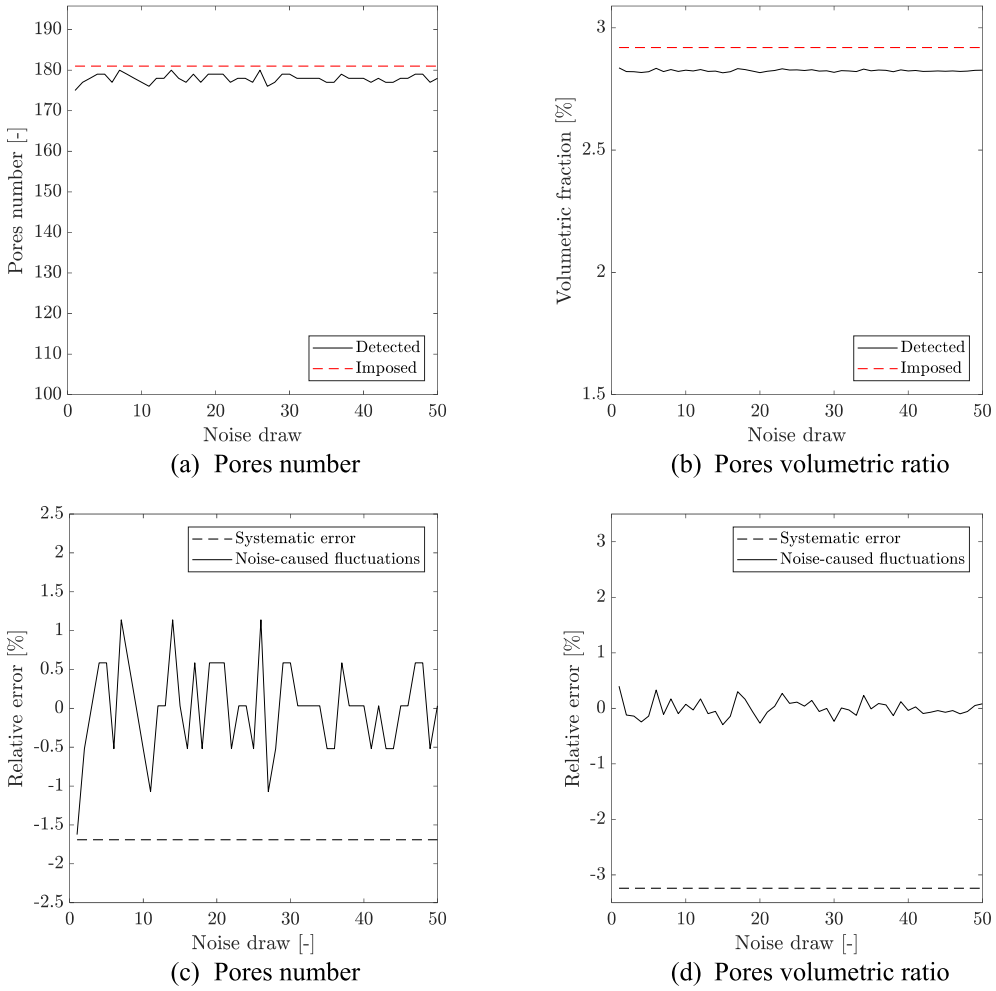


Fig. 8. Comparison between imposed and detected properties for various noise draws in a synthetic dataset.

the experimental noise. These error bars were computed using the relative errors displayed in Fig. 8c and d. It should also be noted that the error bars in Fig. 11b are plotted but almost undistinguishable from the data.

It appears from Fig. 10 that the two adhesives exhibit very different behaviours when the joint is mechanically stressed. The adhesive A shows an ever-increasing number of pores, which tends to suggest that voids nucleate all along the experiment. On the contrary, the behaviour of the adhesive B may be divided into two successive regimes. At first, the number of detected pores slowly increases, similarly to the behaviour of the adhesive A, until a critical load value F_{cr} (approximately 700 N). Once this critical value is reached, there is an abrupt decrease in the number of pores from this F_{cr} value to the failure of the sample, which is typical of pores coalescence. Those two domains seem to be linear with respect to the applied load, as is the behaviour shown by the adhesive A. One may also notice that the adhesive A contains significantly more air voids than the adhesive B (Fig. 10, roughly between 2.8 to 3 more pores in the adhesive A than in the adhesive B).

This piecewise definition is also valid for the porosity ratio in the adhesive B when it is plotted versus the applied load (Fig. 11). The transition between the first and the second regime for the porosity ratio occurs at the same F_{cr} as for the pores number. However, contrary to what could be expected from the data presented in Fig. 10, the second regime for the porosity ratio consists of a steeper increase of this

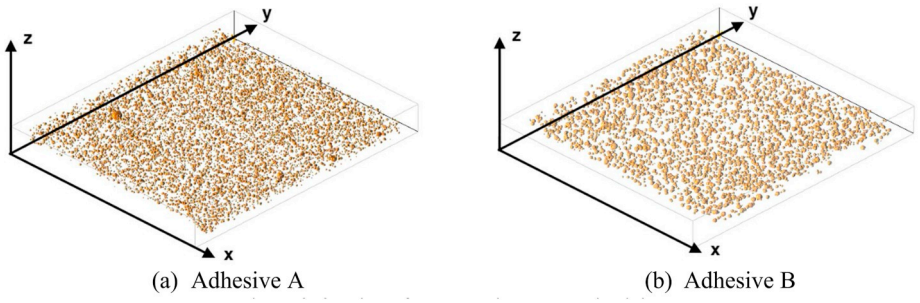


Fig. 9. 3D view of the pores in the adhesive joints.

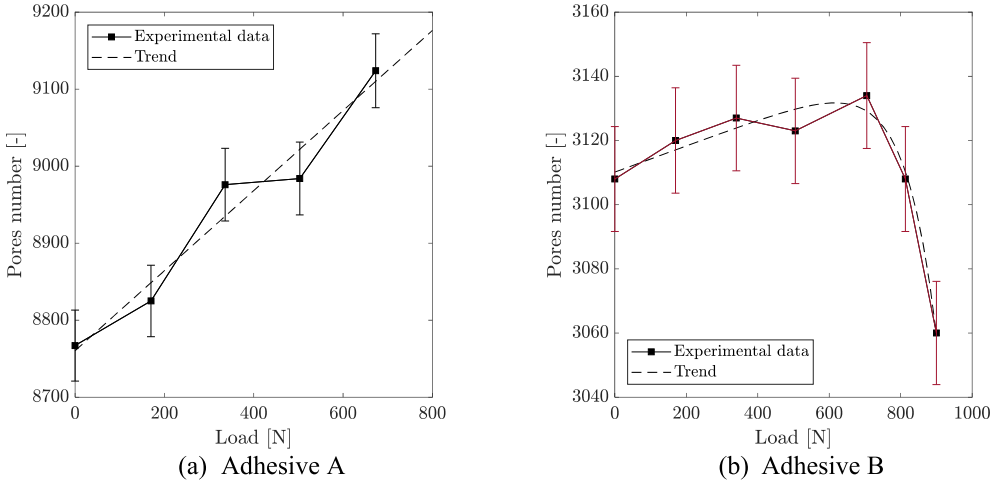


Fig. 10. Number of pores detected in the adhesive A and the adhesive B versus the applied load.

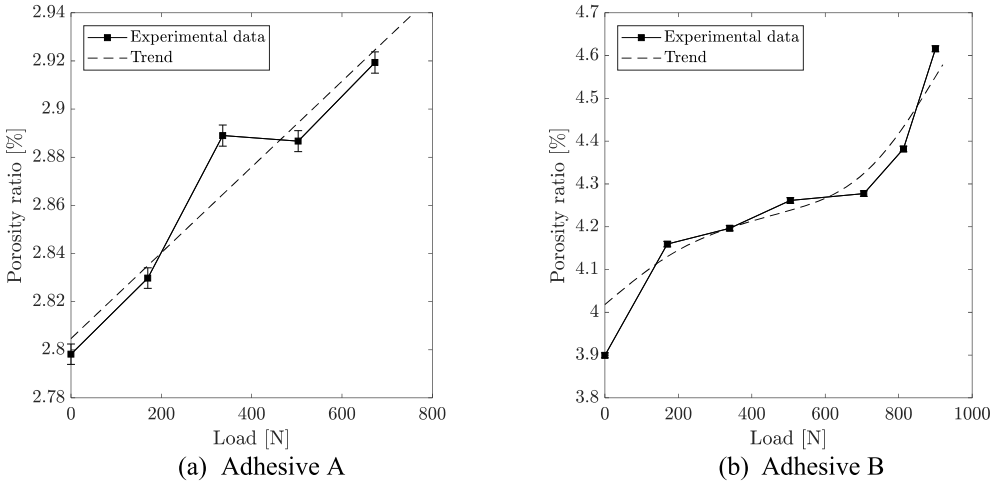
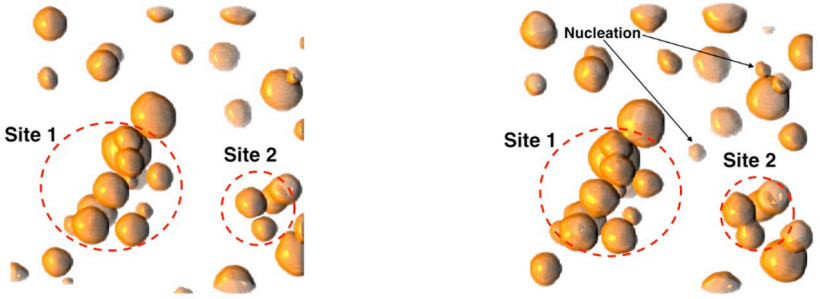


Fig. 11. Porosity ratios in the adhesive A and the adhesive B versus the applied load.

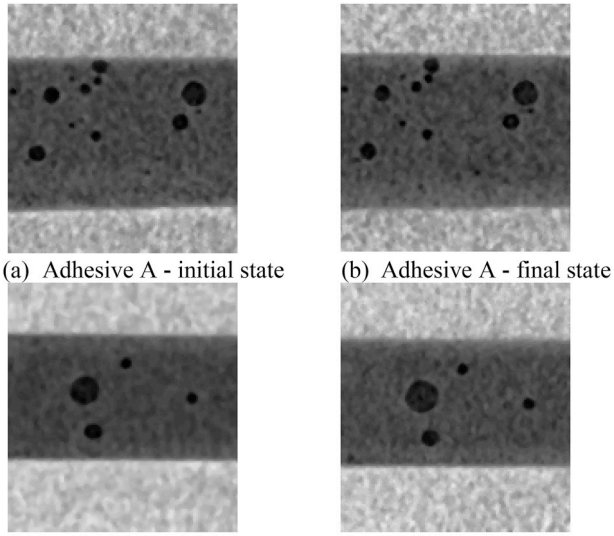
quantity. Even though this observation may seem paradoxical in a first stage, it could also be the appearance of a coalescence phenomenon, meaning that the pores are merging, rather than disappearing. This coalescence phenomenon has been widely observed and studied for various materials [26–28]. One may visualise this phenomenon, coupled with pore growth, on the CT-scans images, located in various sites. Once the segmentation is performed, it is possible to build the 3D geometry of the pores from the binary segmented volumes, and one may clearly see that the coalescence of the relevant pores has been correctly detected. One can also notice in Fig. 12a and b that in addition to the merging of the voids, the pores undergo an increase in volume and tend to expand. New pores also opened, through nucleation phenomena (Fig. 12b).

Even though an influence of the applied load is detected using the segmentation tool, little to no changes can be pinpointed visually on the reconstructed volumes, as it is shown in Fig. 13. This is due to the fact the changes undergone by the material from the initial to the final state of the experiments are very tenuous. For most cases, these changes correspond to differences of a few pixels, which makes them difficult to visualise.



(a) Coalescence sites, adhesive B, 0 N (b) Coalescence sites, adhesive B, 900 N

Fig. 12. Coalescence sites visualised for two different load levels, adhesive B.



(a) Adhesive A - initial state (b) Adhesive A - final state

(c) Adhesive B - initial state (d) Adhesive B - final state

Fig. 13. Reconstructed volumes sliced in the middle of the bonded surface.

4.2. Equivalent diameters distributions

The apparent absence of coalescence for the adhesive A could be explained by the very different characteristics of the corresponding detected pores field. This difference may be highlighted by the comparison of the distribution of the equivalent diameters of the voids, as already suggested for the comparisons in the initial state (see Fig. 14a and b). The equivalent diameter of an object is defined as the diameter of the sphere featuring the same volume.

It is obvious from Fig. 14a that the large majority of the pores in the adhesive A are rather small (the average diameter being of approximately 36 μm), while the average diameter for the adhesive B is roughly 1.6 times greater (˜57 μm, Fig. 14c and d). Due to the limitations in terms of measurement resolution, and given the shape of the distribution presented in Fig. 14a, one could possibly conclude that there are some data and phenomena related to adhesive A that cannot be detected in this test configuration. The shape of the diameters distribution given in Fig. 14a suggests that there is a fair number of pores whose diameters are lesser than 20 μm going undetected.

It is worth noticing that the fluctuations of the statistics of the distribution for the adhesive A are one order of magnitude lower than those for the adhesive B (Fig. 14c and d), and therefore should be pondered with respect to the resolution of the measurements. One possible conclusion would be that very few changes of the microstructure are occurring for the adhesive A. This could be confirmed by Fig. 14e, which shows seemingly identical distributions, contrary to Fig. 14f, for which a slight offset towards the increasing diameters is observed. This corresponds to the increase of the average diameter shown in Fig. 14d and visible in Fig. 12.

4.3. Pores shape

The extracted pores seem to be spherical in all the investigated cases, as it is suggested by Fig. 12. It is possible to quantify this roundness, for each individual, by computing its sphericity Ψ as shown by Wadell [29]. This quantity, defined by Equation (2), is useful to characterise the similarity between a particle of volume V_p and of area A_p, and a sphere.

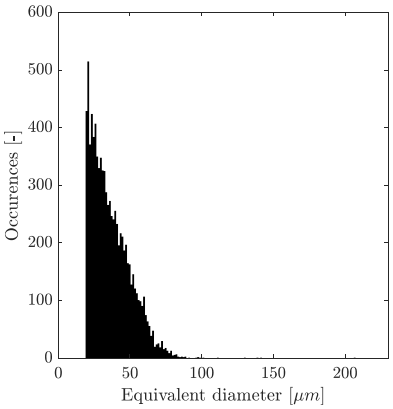
$$\Psi = \frac{\pi^{\frac{1}{3}}(6V_p)^{\frac{2}{3}}}{A_p} \tag{2}$$

Thanks to connected components analysis, it is easy, for each segmented pore, to access its volume and its area, and therefore to compute Ψ. This allows to track the possible variations in shape that may occur during the application of a mechanical load. The corresponding data is displayed in Fig. 15.

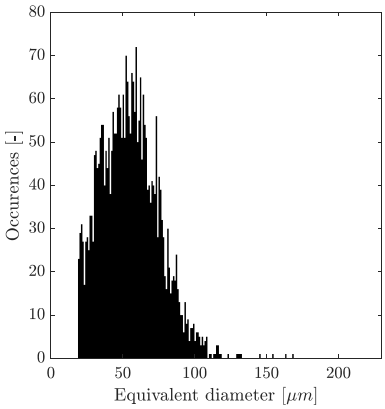
From the data in Fig. 15a and b, it is clear, as it was assumed, that the large majority of the pores, are quasi-spherical for both adhesives. One may also spot a few values greater than 1, especially for small equivalent diameters, which is seemingly paradoxical. This is due to the effect of voxelisation which can lead to slightly erroneous areas calculations, as it is explained in Ref. [30].

Even if the data provided in Fig. 15a and b are very exhaustive and give a good visualisation of the pores shapes for a given load state, due to the large amount of points it is difficult to extract a trend from one point cloud to another. In order to do so, it was chosen to compute the average point for each point cloud, as shown in Fig. 15c and d. These average points are simply located at the coordinates (μ_d, μ_Ψ), μ_d being the mean of the equivalent diameters and μ_Ψ being the mean of the sphericity values. The error bars on these figures are calculated using the standard deviations of the equivalent diameters and the sphericities respectively. These graphs highlight the shift occurring towards the decreasing sphericities, especially in the case of the adhesive B (Fig. 15d). This result seems consistent with the application of a mechanical load, as the initially spherical pores (due to the surface tension) are slightly deformed into ovoids due to the normal stress applied to the adhesive joints.

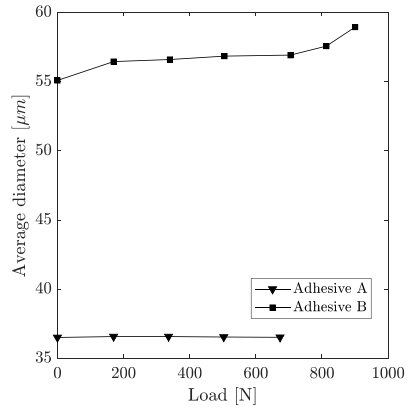
This leads to the conclusion that the geometrical transformations undergone by the pores within an adhesive joint under mechanical loading are strongly influenced by the nature of the adhesive (*i.e.* mechanical properties, chemical formulations, fillers, *etc.*): even though both adhesives A and B are bicomponent epoxy adhesives, the pores in the adhesive B are more prone to changes that those in adhesive A. These changes being mainly growth and coalescence, it is plausible that they may contribute to premature failure mechanisms.



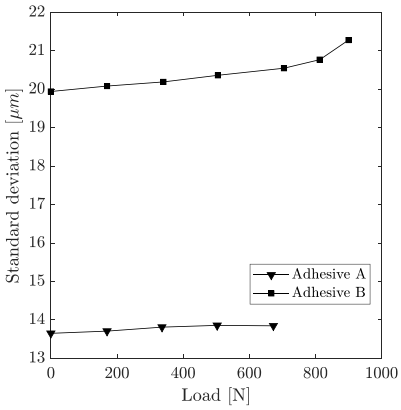
(a) Diameters distribution for the adhesive A, 0 N



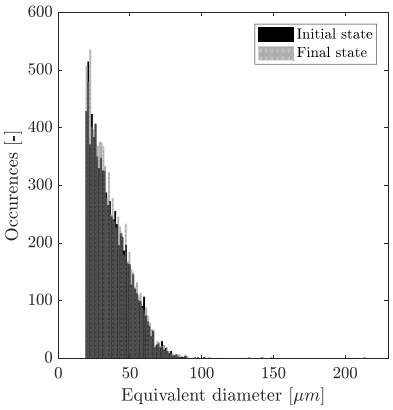
(b) Diameters distribution for the adhesive A, 0 N



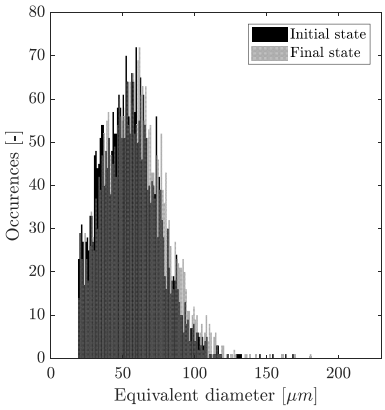
(c) Evolution of the average diameter with the applied load



(d) Evolution of the standard deviation with the applied load



(e) Initial and final diameters distributions, adhesive A



(f) Initial and final diameters distributions, adhesive B

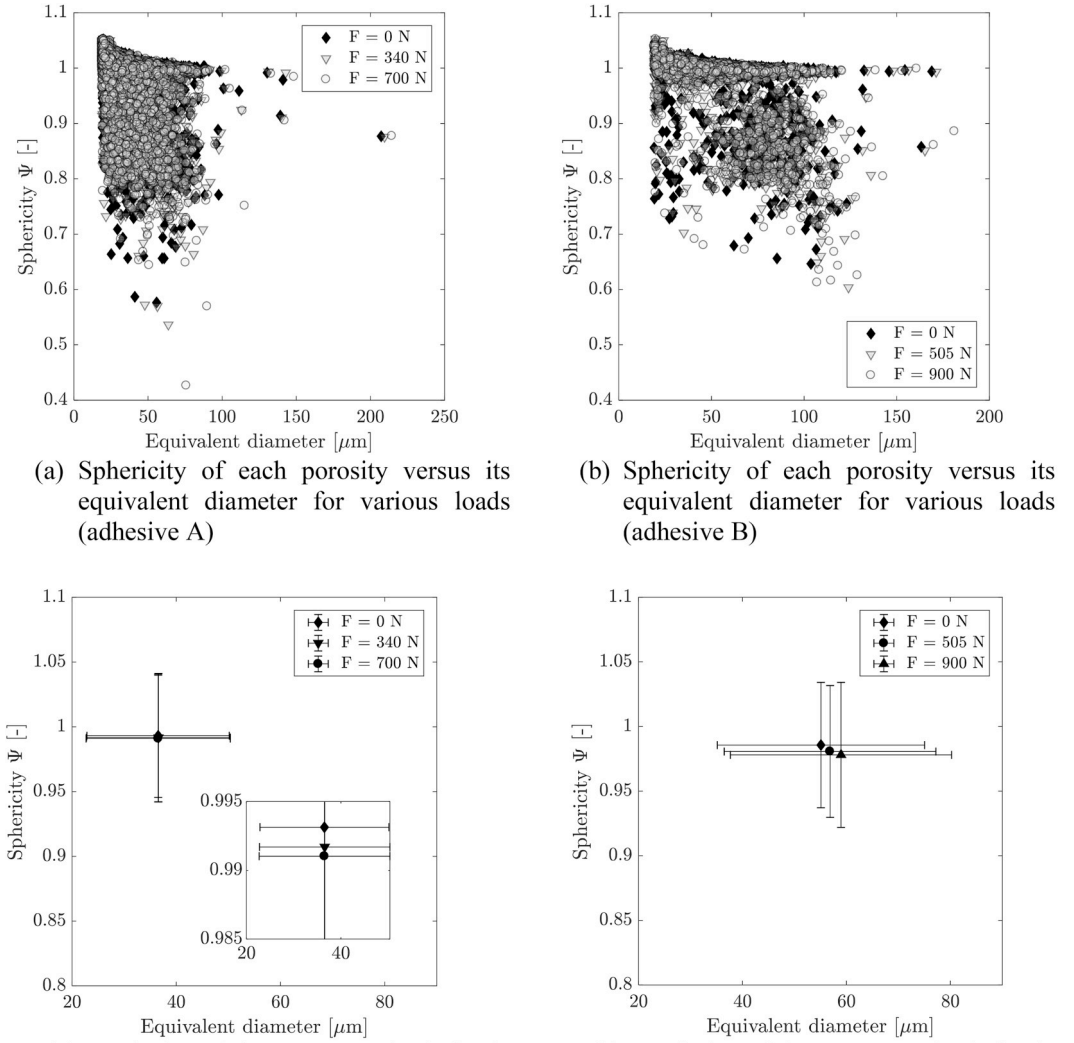
Fig. 14. Comparison of the diameters distributions and evolution of their statistics.

It is also important to investigate the influence of the spatial localisation of the pores on their sphericity. In a first stage, the influence of the position in the (xy) plane is studied (see in Fig. 12 for the plane definition), as presented in Fig. 16. Only the data for the initial state ($F = 0\,N$) are displayed, since they are sufficient to analyse the influence of this factor.

No significant influence of the coordinates along $\vec{x}$ and $\vec{y}$ can be evidenced so far, regardless the adhesive. In particular, it seems that the proximity of the edges of the substrates does not impact the roundness of the pores. However, due to the significant decrease in sphericity caused by merged pores, it is rather difficult to extract a trend for the variation of Ψ with respect to the localisation in the plane of the adhesive joint. This trend is expected to be undetectable on the sphericity maps in Fig. 16. Another convenient way to study this effect is to consider the radial distance of the pores with respect to the central axis of the adhesive joint (collinear with the $\vec{z}$ axis, Fig. 12). This radial distance is computed using Equation (3).

$$\rho = \sqrt{(x - x_c)^2 + (y - y_c)^2} \tag{3}$$

where x and y are the coordinates of the centre of a given pore, and x_c and y_c are the coordinates of the centre of the joint.



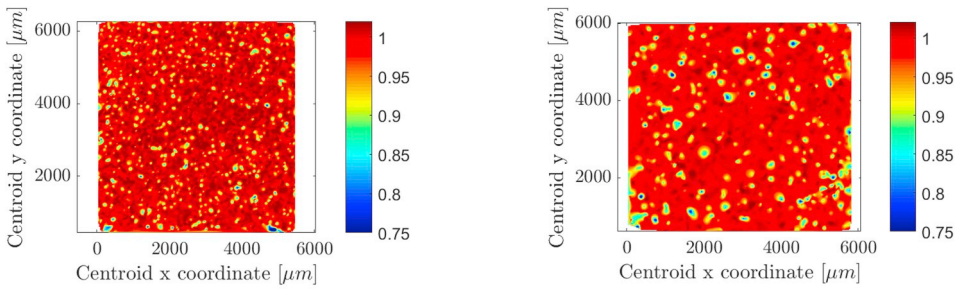
(a) Sphericity of each porosity versus its equivalent diameter for various loads (adhesive A)

(b) Sphericity of each porosity versus its equivalent diameter for various loads (adhesive B)

(c) Evolution of the average point (adhesive A)

(d) Evolution of the average point (adhesive B)

Fig. 15. Influence of a mechanical load on the sphericities of the pores.



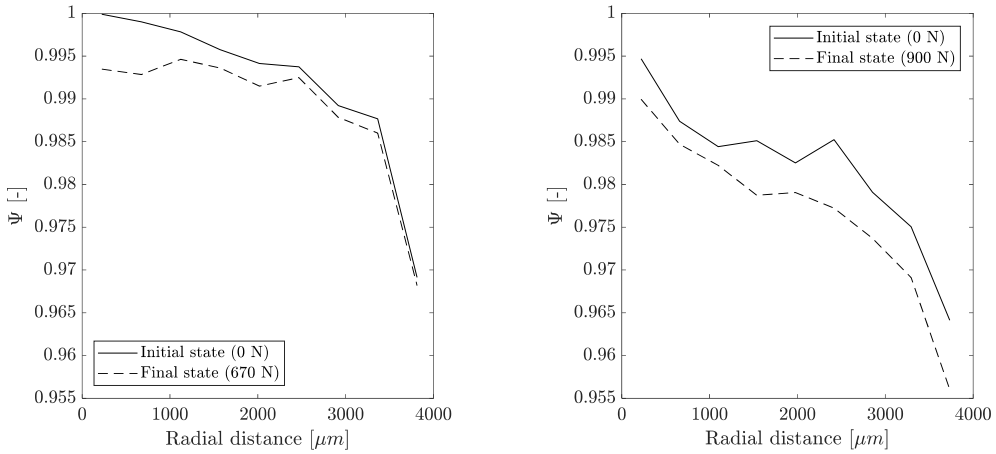
(a) Adhesive A

(b) Adhesive B

Fig. 16. Sphericity maps with respect to the coordinates along $\vec{x}$ and $\vec{y}$.

Such an approach allows for a better visualisation of the effect of the pore localisation on its shape, even though it is downgraded to a 1D quantity where Fig. 16 featured a 2D mapping. The corresponding results are plotted in Fig. 17, for the initial load and the final load.

The data in Fig. 17a and b show a fairly interesting trend, which was somehow overlooked in the sphericity maps in Fig. 16. For both the studied adhesives, it seems that the roundness of the pores decreases with the radial distance to the centre of the joint. This could be explained by an effect of the surrounding material being different depending on the position within the joint (*i.e.* a confinement effect more homogeneous for a pore near the centre than for a pore close to the edges). Moreover, the decrease in sphericity caused by the application of a mechanical stress can also be seen in these curves, similarly to Fig. 15c and d. Nonetheless, an additional aspect is brought to light in Fig. 17: the



(a) Adhesive A (b) Adhesive B

Fig. 17. Effect of the radial distance on the sphericity of the pores.

decrease seems to be more localised in the centre of the joint for the adhesive A, while it is more homogeneously distributed for the adhesive B. One may even notice a seemingly more intense decrease near the edges (radial distance above 2500 μm, Fig. 17b). One may argue that it is a manifestation of the transversal strains caused by the tensile stress on the adhesive. This explanation could be supported by the fact that the Poisson ratios of the two adhesives are different (Table 1), that of the adhesive B being greater than that of the adhesive A. Therefore, the subsequent transversal strains being greater, the Poisson effect would explain the difference in behaviour for the considered adhesives.

Similar considerations can be made for the position of the pores centroids along $\vec{z}$, displayed in Fig. 18.

The pores featuring the lowest sphericities tend to be located near the middle of the adhesive joint following $\vec{z}$, for both the adhesive A and the adhesive B. This could be explained by the fact that they are larger and more numerous in these parts, as shown later in this study. These characteristics are prone to induce segmentation errors for agglutinated pores, which are sometimes incorrectly merged into one unique binarised connected component during the segmentation. An example of such defects may be found in Fig. 19. It is also possible to encounter actually merged pores, which probably coalesced during the curing. It is also clear that these coalescence phenomena are more likely to happen in the areas where the pores are bigger and more plentiful.

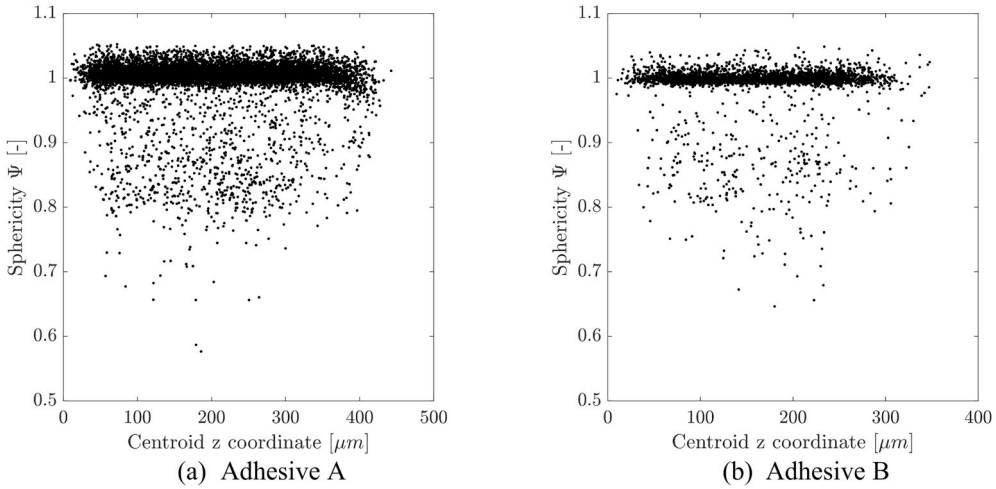
4.4. Effective section

The effective section is defined in Equation (4) as the ratio between the surface of adhesive $S_{adh}^{F_k}$ and the surface of joint ($\sum_{i \in phases} S_i^{F_k}$). Each quantity in Equation (4) exists for all the applied loads F_k, resulting in the following expression for the effective section $\Sigma_{eff}^{F_k}$.

$$\Sigma_{eff}^{F_k} = \frac{S_{adh}^{F_k}}{\sum_{i \in phases} S_i^{F_k}} \tag{4}$$

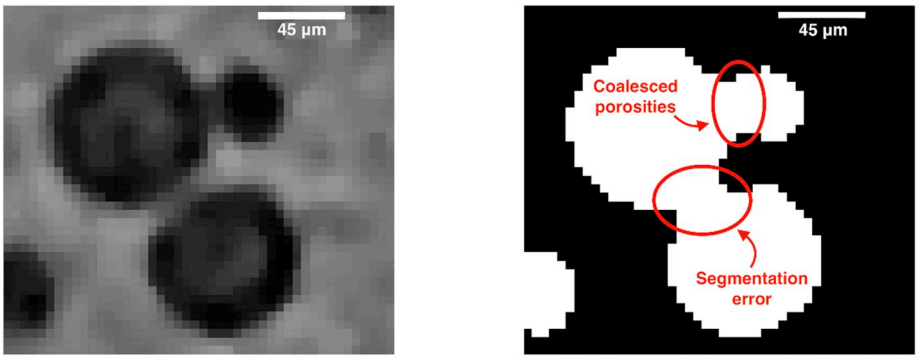
This quantity can be computed for each reconstructed slice along the $\vec{z}$ axis (see Fig. 12 for the $\vec{z}$ axis definition). It provides information about the concentration zones of pores along this axis, which is also the loading direction. Moreover, by computing Σ_{eff} for various mechanical loads, it is possible to monitor the evolution of these concentration zones within the thickness of the adhesive joint. Fig. 20 displays these evolutions for both adhesives A and B.

Both of the investigated adhesives feature lower effective sections approximately halfway through the thickness of the joint. This is explained by the fact that the largest pores tend to be located in the middle of the joint, as demonstrated by Fig. 21. The pores tend also to be more numerous in this region (Fig. 22). Furthermore, the application of a tensile loading accentuates this trend (dashed curves in Fig. 20a and



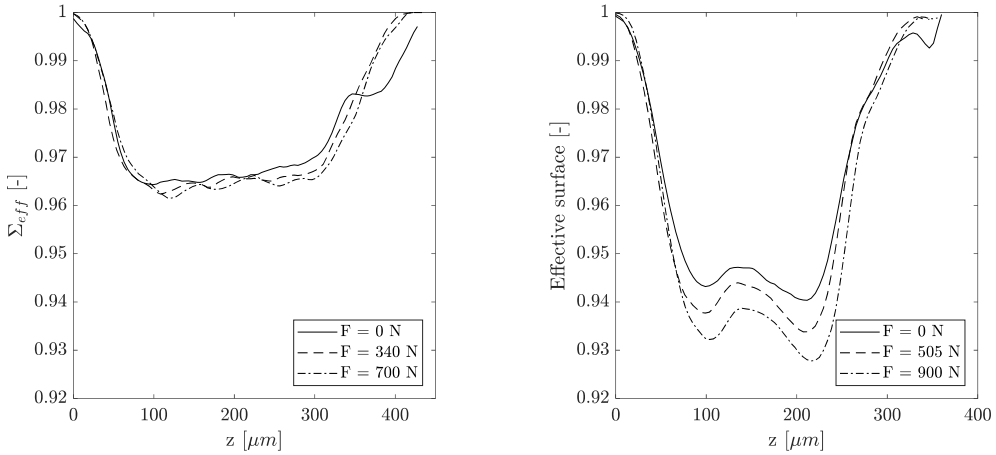
(a) Adhesive A (b) Adhesive B

Fig. 18. Sphericity fluctuations along $\vec{z}$.



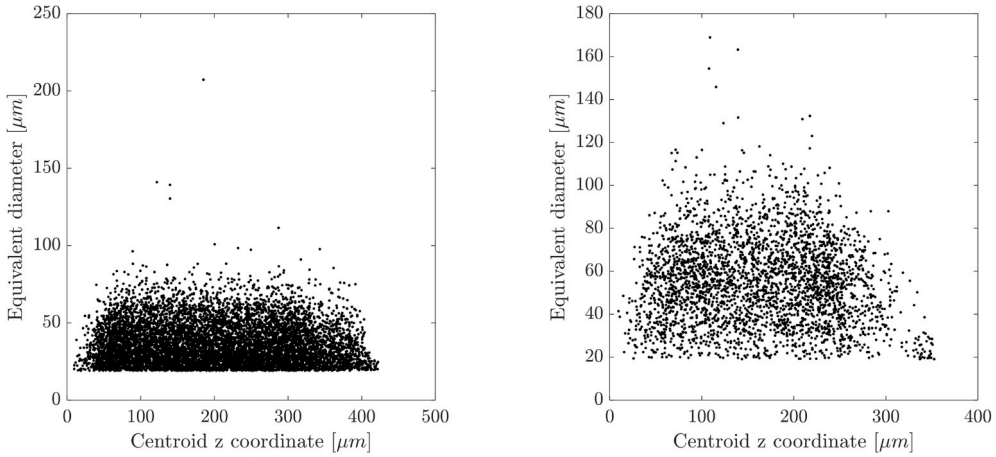
(a) Raw tomography data (b) Segmented pores (white pixels)

Fig. 19. Segmentation defects and coalescence inducing low sphericity values (adhesive B, halfway through the joint thickness).



(a) Adhesive A (b) Adhesive B

Fig. 20. Evolution of the effective sections Σ_{eff} of adhesive joints under tensile mechanical loadings.



(a) Adhesive A (b) Adhesive B

Fig. 21. Equivalent diameters of the pores plotted versus their location along $\vec{z}$ (initial states only).

b).

Several possible explanations of this phenomenon can be expressed. Due to the applied tensile loading, the Poisson effect along the $\vec{x}$ and $\vec{y}$, coupled with the expansion of the pores along $\vec{z}$ (suggested by the modification of their sphericities, Fig. 15), could contribute to the reduction of the effective section.

Moreover, as shown in Figs. 10 and 11, the application of the tensile load tends to nucleate new pores (which may or may not coalesce afterwards), resulting in an increasing porosity ratio. It is therefore a similar observation that is made in Fig. 20, except that instead of being volumetric quantities (such as the porosity ratio, see Equation (1)), it is merely planar (surfaces in Equation (4)).

One may notice that rather low values of Σ_{eff} are reached in the case of the adhesive B (Σ_{eff}~0.93 in the worst case). An impact on the

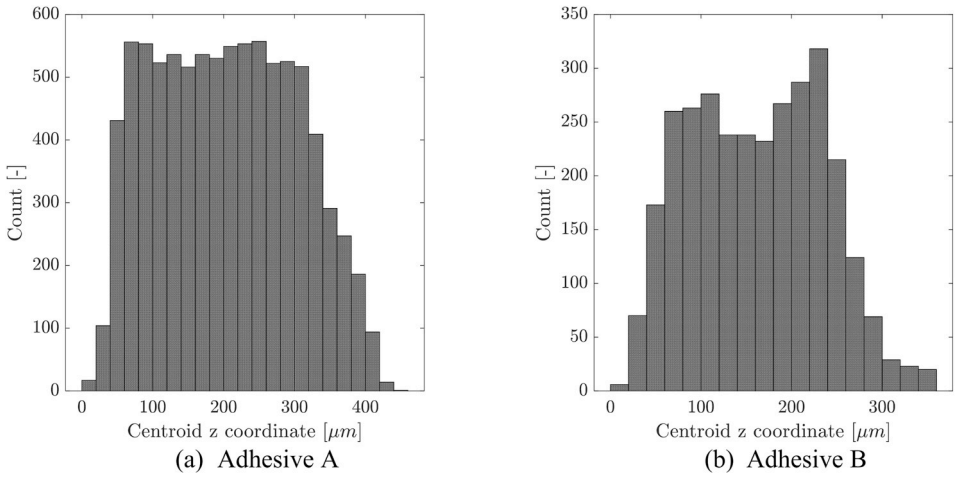


Fig. 22. Distributions of the pores centroids $\vec{z}$ coordinates.

mechanical strength of the assembly could be expected from these low Σ_{eff}, especially due to the fact that the higher the load, the more Σ_{eff} decreases. Even in the scope of an approximate dimensioning, based on average stresses in the adhesive joint, the effect of such a decrease in the effective section is easily evidenced. In the case of the adhesive B, the application of a 900 N load on a 36 mm^2 bonded surface results in an average stress of $\sigma = 25$ MPa. However, by taking into account this reduction in terms of effective surface, the average stress rises to $\sigma = 27$ MPa, *i.e.* an 8% increase. In addition to this point, the stress concentrations induced by the presence of pores suggests that, depending on their characteristics (size, relative spacing, *etc.*), their impact on the mechanical behaviour (in the context of both the strength of materials theory and the fracture mechanics theory) could be significant, such as premature failures due to unexpected stress concentrations in a low effective section zone of the bond.

5. Conclusion

Samples were bonded using structural epoxy adhesives in order to perform *in-situ* microtomography measurements under mechanical loads. Two adhesives were studied under out-of-plane tensile loadings, to investigate the influence of the applied load on the pores inside the joint. Using a specially designed segmentation tool, the tomography reconstructed volumes were segmented into their different constitutive phases. The isolated pores were firstly characterised using global quantities over the whole joint, such as their number and their volumetric fraction. It was shown that, depending on the adhesive, the evidenced phenomena were different: in both cases the tensile load induce the nucleation of new pores, but coalescence was experienced for only one of the materials. At this stage of the study, no particular explanation of this variation in behaviour can be brought into light.

The geometrical properties of the created pores were also studied. The distributions of their equivalent diameters showed different characteristics from one adhesive to another, and the impact of the tensile loading on these distributions was also quantified. Moreover, the computation of their sphericity demonstrated that the pores tend to deform from quasi-spherical into ellipsoidal entities.

Finally, the effective sections of the adhesive joints were calculated in all the investigated cases, resulting into two main conclusions. Firstly, the pores tend to be larger and more numerous halfway through the thickness of the adhesive bond, resulting in a fairly low effective section in this region of the joint. Secondly, this tendency is intensified by the application of a mechanical load, leading to even lower effective sections. This is an indicator of the threat that can be induced by the creation of pores in these materials. It can be easily understood that such structural defects can lead to stresses higher than expected, either due to precisely this decrease in effective section, or due to stress concentrations; and therefor trigger the premature mechanical failure of the assembly.

Another lead for future research worth to be mentioned is the possibility to perform a finer characterisation of the microstructure of such materials, either through X-ray microtomography with a higher resolution, or using other experimental techniques, such as N_2 sorption and Hg injection. Such experiments would provide interesting information regarding the minimal size of pores encountered in these materials, but significant difficulties are expected for them to be employed on assemblies. Therefore, at a first stage, a study on bulk samples would likely yield better results on this aspect.

References

[1] Adams RD. Adhesive bonding: science, technology and applications. Elsevier; 2005.
[2] Moussa O, Vassilopoulos AP, Keller T. Effects of low-temperature curing on physical behavior of cold-curing epoxy adhesives in bridge construction. Int J Adhesion Adhes 2012;32:15–22. https://doi.org/10.1016/j.ijadhadh.2011.09.001.
[3] Buffiere J-Y, et al. In situ experiments with X ray tomography: an attractive tool for experimental mechanics. Exp Mech 2010;50:289–305. https://doi.org/10.1007/s11340-010-9333-7.
[4] Liu X, Bathias C. Defects in squeeze-cast Al2O3/Al alloy composites and their effects on mechanical properties. Compos Sci Technol Jan. 1993;46(3):245–52. https://doi.org/10.1016/0266-3538(93)90158-D.
[5] Breunig TM, Stock SR, Guvenilir A, Elliott JC, Anderson P, Davis GR. Damage in aligned-fibre SiC/Al quantified using a laboratory X-ray tomographic microscope. Composites Jan. 1993;24(3):209–13. https://doi.org/10.1016/0010-4361(93)90165-5.
[6] Garcea SC, Wang Y, Withers PJ. X-ray computed tomography of polymer composites. Compos Sci Technol 2018;156:305–19. https://doi.org/10.1016/j.compscitech.2017.10.023.
[7] Buffiere J-Y, et al. Damage assessment in an Al/SiC composite during monotonic tensile tests using synchrotron X-ray microtomography. Mater Sci Eng, A Aug. 1997;234(236):633–5. https://doi.org/10.1016/S0921-5093(97)00302-X.
[8] Buffiere J-Y, et al. Characterization of internal damage in a MMC-p using X-ray synchrotron phase contrast microtomography. Acta Mater 1999;47(5):1613–25.
[9] Maire E, et al. X-ray tomography applied to the characterization of cellular materials. Related finite element modeling problems. Compos Sci Technol Dec. 2003;63(16):2431–43. https://doi.org/10.1016/S0266-3538(03)00276-8.
[10] Maire E, Carmona V, Courbon J, Ludwig W. Fast X-ray tomography and acoustic emission study of damage in metals during continuous tensile tests. Acta Mater Dec. 2007;55(20):6806–15. https://doi.org/10.1016/j.actamat.2007.08.043.
[11] Adrien J, Maire E, Gimenez N, Sauvant-Moynot V. Experimental study of the compression behaviour of syntactic foams by in situ X-ray tomography. Acta Mater Mar. 2007;55(5):1667–79. https://doi.org/10.1016/j.actamat.2006.10.027.
[12] Pavan M, Craeghs T, Verhelst R, Ducatteeuw O, Kruth JP, Dewulf W. CT-based quality control of laser sintering of polymers. Case Stud Nondestruct Test Eval Nov. 2016;6:62–8. https://doi.org/10.1016/j.csndt.2016.04.004.
[13] Wang X, Zhao L, Fuh JYH, Lee HP. Effect of porosity on mechanical properties of 3D printed polymers: experiments and micromechanical modeling based on X-ray computed tomography analysis. Polymers 2019;11(7). https://doi.org/10.3390/polym11071154.

226

[14] Schwarzkopf M, Muszynski L. Strain distribution and load transfer in the polymer-wood particle bond in wood plastic composites. Holzforschung 2015;69(1):53–60. https://doi.org/10.1515/hf-2013-0243.
[15] McKinley PE, Ching DJ, Kamke FA, Zauner M, Xiao X. Micro X-ray computed tomography of adhesive bonds in wood. Wood Fiber Sci 2016;48(May):2–16.
[16] Rohr T, Knaus S, Gruber H, Sherrington DC. Preparation and porosity characterization of highly cross-linked polymer resins derived from multifunctional (Meth)acrylate monomers. Macromolecules 2002. https://doi.org/10.1021/ma0110958.
Kak AC, Slaney M. Principles of Computerized Tomographic Imaging, Society of Industrial and Applied Mathematic. IEEE Press; 2001.
[18] Pollak B. Experiences with planography from the Fort William Sanatorium, fort William, Ontario, Canada. Dis Chest 1953;24(6):663–9.
[19] Sezgin M. Survey over image thresholding techniques and quantitative performance evaluation. J Electron Imag 2004;13(1):146–65. https://doi.org/10.1117/1.1631316.
[20] Beucher S, Meyer F. Mathematical morphology in image processing. Marcel Dek; 1993.
[21] Lin CL, Videla AR, Yu Q, Miller JD. Characterization and analysis of Porous, Brittle solid structures by X-ray micro computed tomography. J Occup Med 2010;62(12):86–9.
[22] Grady L. Random Walks for image segmentation. IEEE Trans Pattern Anal Mach Intell 2006;28(11):1768–83.
[23] Spitzer F. Principles of the random walk. Princeton University Press; 1964.
[24] Otsu N. A threshold Selection method from gray-level histograms. IEEE Trans Syst Man Cybern 1979;9(1):62–6. https://doi.org/10.1109/TSMC.1979.4310076.
[25] Gallagher NC, Wise GL. A theoretical analysis of the properties of median filters. IEEE Trans Acoust 1981;29(6):1136–41. https://doi.org/10.1109/TASSP.1981.1163708.
[26] Koplik J, Needleman A. Void growth and coalescence in porous plastic solid. Int J Solid Struct 1988;24(8):835–53. https://doi.org/10.1016/0020-7683(88)90051-0.
[27] Pinzer BR, Medebach A, Limbach HJ, Dubois C, Stampanoni M, Schneebeli M. 3D-characterization of three-phase systems using X-ray tomography: tracking the microstructural evolution in ice cream. Soft Matter 2012;8(17):4584. https://doi.org/10.1039/c2sm00034b.
[28] Landron C, Bouaziz O, Maire E, Adrien J. Experimental investigation of void coalescence in a dual phase steel using X-ray tomography. Acta Mater Oct. 2013;61(18):6821–9. https://doi.org/10.1016/j.actamat.2013.07.058.
[29] Wadell H. Volume, shape and roundness of quartz particles. J Geol 1935;43(3):250–80.
[30] Lehmann G, Legland D, Génie UMR. Efficient N-Dimensional surface estimation using Crofton formula and run-length encoding. Insight J 2012;2:1–11.

2.6 Modèles de comportement thermomécanique

Comme annoncé en introduction, l'un des objectifs de ces études est la mise en place de stratégies de modélisation de ces assemblages collés, de manière à mieux prédire le comportement mécanique, soumis à des chargements multiaxiaux complexes, en s'appuyant sur des caractérisations expérimentales adaptées aux modèles proposés. Bien que ces adhésifs soient essentiellement des polymères avec un comportement visqueux [107], [108] plus ou moins prononcé, le transfert de charge entre les composants du joint collé est généralement lié à leurs propriétés pseudo-élastiques instantanées [109]. Cependant, le comportement visqueux représente une caractéristique majeure des matériaux adhésifs polymères. Par conséquent, la compréhension de ces phénomènes est importante pour prédire avec précision la défaillance ainsi que la durée de vie des structures collées. Plusieurs modèles ont été développés au fur et à mesure de différents projets. Certains adhésifs peuvent être modélisés très simplement, en se limitant uniquement aux mécanismes de déformation élastiques ou viscoélastiques [107]. De manière plus générale, il a été montré qu'un modèle élasto-plastique [110], [72] pouvait être parfaitement adapté pour prédire le comportement de ce type d'adhésif en intégrant la dépendance du comportement mécanique à la pression hydrostatique. La nécessité d'une meilleure prédiction du comportement mécanique à long terme étant une de mes préoccupations, nous avons alors proposé et intégré une dépendance du comportement mécanique de la colle aux vitesses de déformation. Cela a permis d'enrichir et de développer des modèles plus complets de type viscoélastique linéaire et/ou non linéaire pour la prédiction du comportement des adhésifs.

Pour certains adhésifs, malgré les mécanismes de viscoélasticité introduits, la réponse macroscopique de ces modèles ne conviendrait pas. En conséquence, nous avons opté pour le développement de stratégies de modélisation plus sophistiquées qui s'appuient sur un modèle élasto-viscoélastique-viscoplastique pour la description du comportement mécanique d'adhésifs structuraux. L'idée principale est de disposer d'un modèle capable de décrire de manière quasi exhaustive l'ensemble des mécanismes pouvant apparaître au cours de la durée de vie de de tels matériaux, en considérant une grande variété de chargements mécaniques et en s'intéressant au comportement jusqu'à rupture. La loi de comportement développée à ce stade est alors basée sur deux modèles distincts permettant tous les deux de rendre compte de l'influence de la pression hydrostatique : un modèle spectral viscoélastique introduit dans les travaux de Maire [111] et un modèle viscoplastique dérivé du modèle élastoplastique de Mahnken et Schlimmer [72]. Ces deux modèles sont associés conformément à la décomposition additive suivante de la déformation en trois composantes : élastique, viscoélastique et viscoplastique. Ce type de modèle a été utilisé en particulier par Ilioni [46], [112] et dans les travaux de Dumont [12] pour modéliser le comportement à long terme d'assemblages collés en intégrant la dépendance des paramètres à l'hygrométrie ou à la température.

Publications jointes

- C. Badulescu, C. Germain, J.Y. Cognard, N. Carrère, **Characterization and modelling of the viscous behaviour of adhesives using the modified Arcan device**, *Journal of Adhesion Science and Technology*, 29 :5, 443-461,(2015), DOI : 10.1080/01694243.2014.991483
- A. Ilioni, C. Badulescu, N. Carrère, P. Davies, D. Thévenet, **A viscoelastic-viscoplastic model to describe creep and strain rate effects on the mechanical behaviour of adhesively-bonded assemblies**, *International Journal of Adhesion and Adhesives*, 82,184-195,(2018), https ://doi.org/10.1016/j.ijadhadh.2017.12.003.

Références associées : Bibliographie des publications

Journal of Adhesion Science and Technology, 2014
http://dx.doi.org/10.1080/01694243.2014.991483

Taylor & Francis
Taylor & Francis Group

Characterization and modelling of the viscous behaviour of adhesives using the modified Arcan device

Claudiu Badulescu, Celia Germain, Jean-Yves Cognard and Nicolas Carrere*

LBMS, ENSTA Bretagne, Université de Brest, Brest, France

(*Received 19 March 2014; final version received 6 November 2014; accepted 20 November 2014*)

The non-linear behaviour of an epoxy adhesive has been studied thanks to the use of a modified Arcan test device. Multilevel creep tests have been performed in order to characterize the time-dependent behaviour. A visco-elastic model has been chosen to describe the behaviour of the adhesive. This model is based on the decomposition of the visco-elastic strain into elementary viscous mechanisms. The non-linear behaviour of the visco-elasticity is taken into account thanks to a non-linear function which depends on the stress. A specific identification procedure based on a single test has been proposed. Finally, the model has been validated using tests that have not been used for the identification. The model proposed in this paper enables the time-dependent non-linear behaviour of adhesives to be reproduced in a correct manner.

Keywords: time-dependent behaviour; Arcan tests; visco-elasticity; temperature; inverse identification

Downloaded by [Ensta Bretagne], [Nicolas Carrere] at 00:27 23 December 2014

1. Introduction

Adhesively bonded joints present many advantages when assembling a range of diverse materials. As compared with mechanical joints (bolts or fasteners), adhesively bonded joints permit weight saving or the reduction of stress concentrations near the hole of the mechanical joints that could be catastrophic for the strength of composite structures.[1] However, the load capability transfer of such joints is associated to the instantaneous elastic properties of the adhesive.[2] Indeed, it has been shown that adhesive could exhibit time-dependent behaviour like classical polymers. This non-linear behaviour has been revealed in the literature thanks to different tests, with different loading rates, using bulk specimens [3,4] or shear tests with thick adherent [5,6] specimens. A review of the different tests used in the literature to characterize the behaviour of adhesives, can be found in Da Silva et al. [7]. The time-dependent behaviour could also be characterized using creep/recovery tests. While the tensile or shear tests at different strain rates permit the study of the instantaneous non-linear mechanisms, the creep and recovery tests permit the characterization of the long-term behaviour of materials. Different experimental devices have been proposed in the literature to assess the long-term behaviour of adhesives. Some authors perform creep tests thanks to the same kind of device as the ones used for the monotonic tests i.e. bulk specimens or single (or double) lap joint specimens.[8,9] However, these tests can be difficult to perform. For instance, the use of bulk tests requires significant expertise in order to manufacture

*Corresponding author. Email: nicolas.carrere@ensta-bretagne.fr

© 2014 Taylor & Francis

specimens without any defects.[10] Single or double lap joint specimens are more representative of the adhesive inside a joint, but they present high-stress singularities near the edges.[11] These edge effects could lead to the initiation of fracture at the interface between the adhesive and the substrate and thus, could lead to a premature failure of the specimen.[12] In order to overcome this problem, Cognard and his coworkers have developed a modified Arcan device. This device permits (i) the adhesive to be subjected to proportional multiaxial loadings and (ii) the edge effects to be strongly reduced thanks to a specific geometry of the substrate.[13] It has been shown that using this device, it is possible to characterize the non-linear behaviour of adhesives [14] without premature failure as compared with classical specimens.[12] In the present paper, this device will be used to characterise the time-dependent behaviour of an adhesive using monotonic tests at different loading rates and creep tests.

The non-linear behaviour of adhesives is often described in the literature by (visco) plastic,[15–18] which is characterized by a permanent strain and an elastic limit. Some authors proposed using visco-elastic models. In this case, the visco-elastic strain is created from the beginning of the loading. Moreover, theoretically, the visco-elastic strain can be totally recovered. Many models can be found in the literature to describe the visco-elastic behaviour. The simplest ones are based on rheological models (for instance the Maxwell or the Kelvin–Voigt models). These models are characterized by a single relaxation time which is sufficient. This is why some authors have proposed to take into account more than one relaxation time.[19] However, these models are not able to describe the non-linear evolution of the visco-elastic strain as a function of the applied stress. In order to attain this goal, non-linear visco-elastic models have been proposed.[20–22] These models permit the experimental results to be described in a correct manner, but are difficult to identify and to implement in a 3D general finite element (FE) code. However, it is obvious that for large strains, the behaviour is a combination of visco-elastic strains and permanent strains. Some authors have proposed visco-elastic and visco-plastic models to describe the behaviour of polymer-based materials [23,24] or adhesives.[25] However, this kind of model is difficult to implement and to identify.

The aim of this article is to propose a model able to describe the non-linear behaviour of adhesives under various kinds of loading conditions (monotonic with different loading rates, creep with different applied loads) using a non-linear visco-elastic model that only necessitates a few tests to be identified. In order to attain this goal, it is first necessary to obtain new experimental results that permit to show that a non-linear visco-elastic model is adequate to describe the behaviour of adhesives subjected to monotonic tests. The experimental procedure based on a modified Arcan test device is described in Section 2 of this article. In this section, the model used to describe the behaviour of the adhesive is also presented. The experimental results are presented in Section 3. The identification procedure of the model that necessitates only two creep tests (one for the normal behaviour and one for the shear behaviour) is also shown in this section. Finally, the last section is devoted to the discussion of the effect of the viscous behaviour on the stress distribution in the Arcan specimen and to the validation of the identification.

2. Methodology

2.1. Experimental procedure

In the present work, we have used the crash-optimized single-component epoxy adhesive SikaPower®-498 (made of a rigid epoxy matrix containing soft, tough polymer

Downloaded by [Ensta Bretagne], [Nicolas Carrere] at 00:27 23 December 2014

Downloaded by [Ensta Bretagne], [Nicolas Carrere] at 00:27 23 December 2014

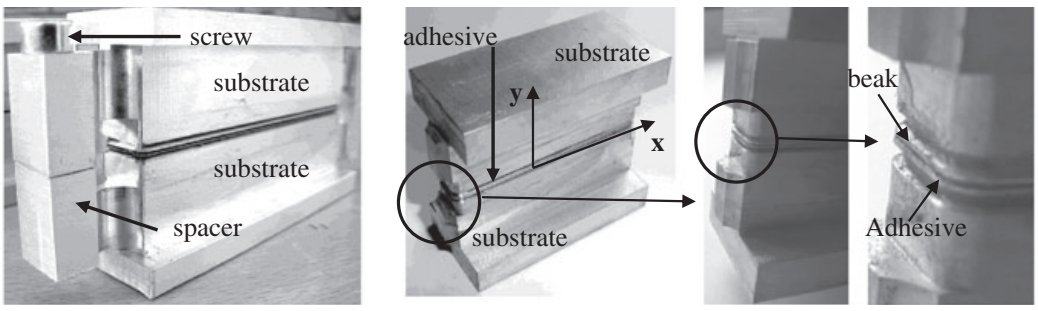
inclusions that provide additional ductility to the adhesive layer). The cure cycle provided by the manufacturer has been followed (1 h in a 180 °C pre-heated furnace) to obtain a fully cured adhesive.

The bonding procedure is divided into the following steps:

- First, the surfaces that will be bonded are cleaned with sandpaper of granulation 180, in order to remove the layers of oxides or other impurities that can be deposited on these surfaces.
- The next step is to degrease the surface using acetone, followed by cold air current drying.
- The adhesive is applied on the two surfaces. The thickness of the adhesive is controlled thanks to spacers that are removed before the test. The substrates are maintained in this position during the curing process by two screws (see Figure 1 (a)) screwed with a torque screwdriver set to a torque of 2.5 Nm.
- The adhesive is cured following the curing cycle proposed by the manufacturer.

To generate different loading states, a previously developed [26] modified Arcan apparatus is used (see Figure 2(a)). It enables tension or compression to be combined with shear load, changing the orientation of the Arcan apparatus as compared with the axis of the tensile loading system. For example, a pure shear loading in the adhesive can be generated by positioning the Arcan apparatus as shown in Figure 2(b) ($\gamma = 90°$). In order to apply a tensile shear loading, the Arcan apparatus must be positioned as shown in Figure 2(a). Special fixing systems have been designed to fix the modified Arcan device in order to prevent parasitic loadings (see Figure 2(c)). It has already been shown in previous study that the use of this experimental device permits to obtain very reproducible results.[27]

The relative displacement between the two substrates is measured thanks to a Digital Image Correlation System.[28] This is a system based on 3D digital image correlation, which has two CDD synchronized cameras that can capture 1040×1600 pixel^2 images. The focus of the images is ensured by two objectives with a focal length of 50 mm. The objectives are also equipped with polarizing filters. The contrast of the images taken is ensured by a polarized light system with LEDs and polarizing filters. The image acquisition frequency varies during the test. At the beginning of the tests (elastic part), the frequency is one image per second; the frequency of the acquisition increases (three images per second) when the pseudo-elastic limit is exceeded. The value of the force is registered for each image acquired. In the following, DT



(a) bonding procedure (b) geometry of the bonded specimens

Figure 1. Presentation of the bonded specimens.

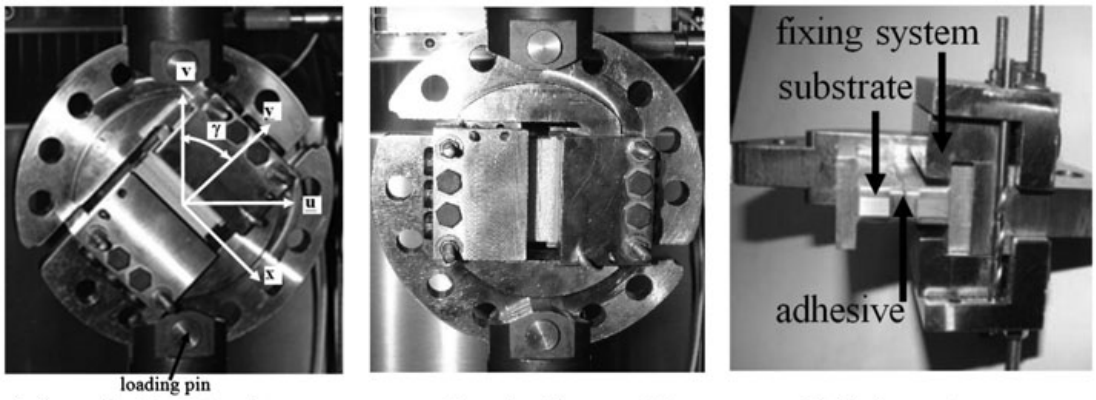


Figure 2. Modified Arcan apparatus.

(respectively DN) denotes the relative displacements of both ends of the adhesive in the tangential direction x (respectively the normal direction y). FT (respectively FN) represents the tangential component of the applied load (respectively the normal component of the applied load).

Tests were performed using a hydraulic tensile testing machine (Instron Model 1342), with a maximum load of 100 kN and a thermal chamber (Servatin) available in the laboratory (Figure 3(a)). The thermal chamber allows temperature variation between −70 and 200 °C and humidity variation for temperatures between 0 and 100 °C, which enables a wide range of test conditions. In addition, the thermal chamber has a view glass, which allows us to use the optical 3D measuring system (Figure 3(b)). The time required to stabilize the temperature inside the adhesive for a temperature range from 20 to 50 °C is 40 min. This time has been determined using a specific bonded specimen with a thermocouple in the middle of the adhesive.

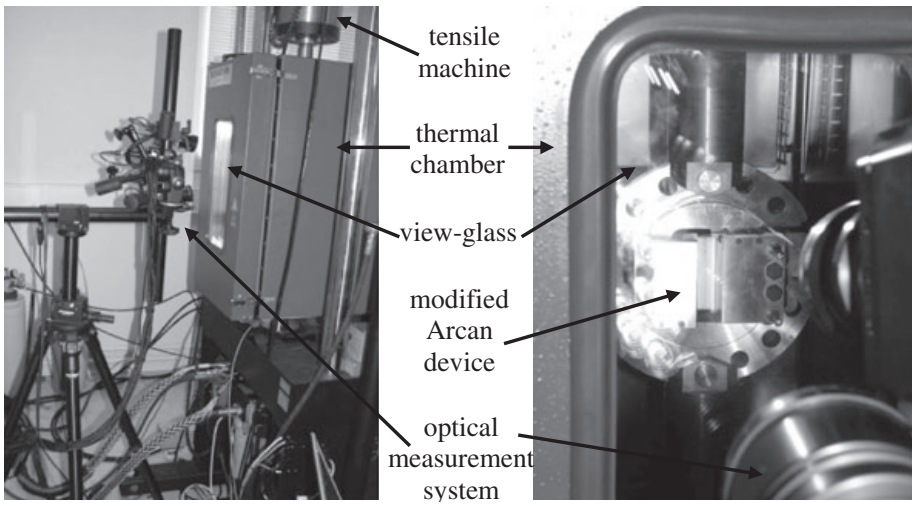


Figure 3. Presentation of the experimental configuration (tensile testing machine, thermal chamber, modified Arcan device and optical measurement system Gom).

Downloaded by [Ensta Bretagne], [Nicolas Carrere] at 00:27 23 December 2014

Downloaded by [Ensta Bretagne], [Nicolas Carrere] at 00:27 23 December 2014

2.2. Numerical procedure

The stress state being non-uniform in the adhesive, the analysis of the behaviour of a bonded assembly using the modified Arcan device necessitates a numerical analysis.[26] The aims of this numerical analysis are: first, to generate a numerical model that allows us an easy integration in inverse identification procedure of the parameters of the visco-elastic spectral model; and second, to analyse the influence of temperature on the visco-elastic behaviour of the adhesive.

A 2D numerical model, under the assumption of plane strain, was achieved with a dual purpose: first, to reduce computation time because the number of elements is much lower in a 2D FE model and second, to highlight the beaks near the free edge, which provide significant reduction in stress concentration near the free edge.

The geometry of the FE model is defined using the following parameters (see Figure 4(a)): $L = 50$ mm, $H1 = 20$ mm. $\alpha = 30°$, $h = 0.1$ mm, $d = 0.5$ mm, $r = 0.1$ mm and $e = 0.4$ mm, where r is the radius of curvature of the free surface, which in reality results from cleaning the adhesive and e represents the thickness of the adhesive which in this case is equal to 0.4 mm.

The boundary conditions imposed are the following:

- the line CD of the inferior substrate (Figure 4(a)) is blocked,
- the load is applied on a reference point to which the line AB is attached. The mesh is progressively refined near the edges (see Figure 4(b)). A study has been performed in order to determine the number of elements necessary to obtain a correct result (see the end of this section).

The mechanical behaviour of the two substrates is assumed to be linear elastic isotropic, characterized by Young's modulus $E = 70$ GPa and Poisson ratio equal to 0.34. The adhesive is modelled using a spectral thermo-visco-elastic model. This model has first been proposed to describe the non-linear behaviour of polymer matrix composite especially under shear loadings [29,30] and polymer materials taking into account

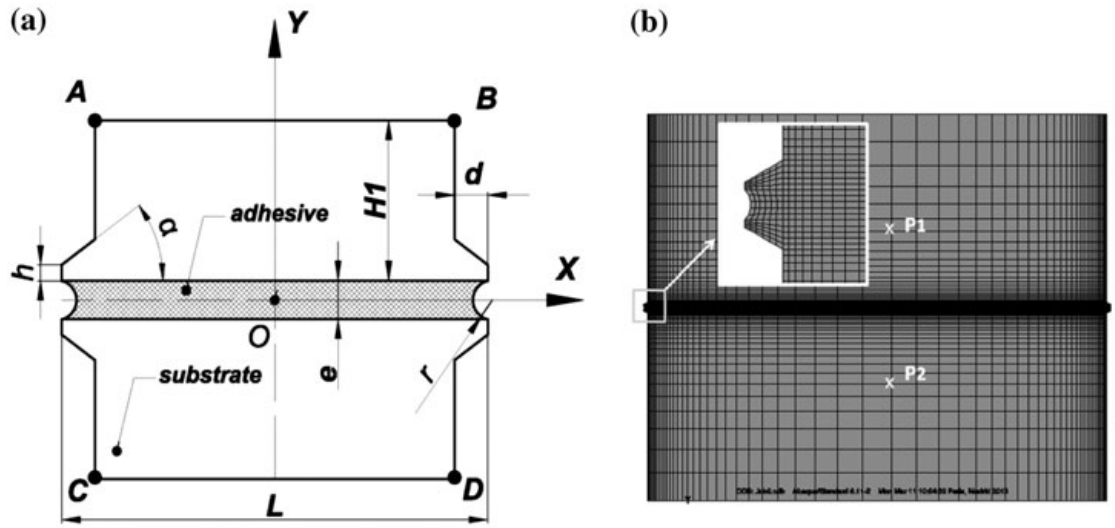


Figure 4. Presentation of the geometries of the FE model of the bonded assembly: (a) specimen with beaks and cleaned edges (not to scale) and (b) the mesh of the FE model. P_1 and P_2 are used to define the relative displacement between the two substrates.

the effect of hydrostatic pressure.[31] The behaviour of the adhesive is described as follows

$$\underline{\sigma} = \underline{\underline{C}}(\underline{\varepsilon} - \underline{\varepsilon}^{th} - \underline{\varepsilon}^{ve}) \tag{1}$$

where $\underline{\sigma}$ is the stress, $\underline{\underline{C}}$ the elastic stiffness, $\underline{\varepsilon}$ the total strain, $\underline{\varepsilon}^{th}$ the thermal strain and $\underline{\varepsilon}^{ve}$ the visco-elastic strain. The thermal strain $\underline{\varepsilon}^{th}$ is introduced in order to take into account the residual stresses due to the manufacturing process, which have an influence on the initial state of the adhesive as shown in [32]

$$\underline{\varepsilon}^{th} = \underline{\alpha}(T - T_0) \text{ with } \underline{\alpha} = \alpha \underline{I} \tag{2}$$

where α is the thermal dilatation coefficient and $\underline{I}$ the second-order unit tensor.

The visco-elastic strain $\underline{\varepsilon}^{ve}$ is decomposed into a series of n_t elementary viscous mechanisms

$$\dot{\underline{\varepsilon}}^{ve} = g(\underline{\sigma}) \sum_{i=1}^{n_t} \dot{\underline{\xi}}_i \text{ with } \dot{\underline{\xi}}^i = \frac{1}{\tau_i}\left(\mu_i g(\underline{\sigma}) \underline{\underline{S}}^R : \underline{\sigma} - \underline{\xi}_i\right) \tag{3}$$

The function $g(\underline{\sigma})$ which depends only on stress permits the possible non-linear nature of the viscosity to be described. The fourth-order tensor $\underline{\underline{S}}^R$ is the visco-elastic compliance. It is worth mentioning that $g(\underline{\sigma})$ and $\underline{\underline{S}}^R$ are the same for all the elementary viscous mechanisms, and these mechanisms only differ by their relaxation times τ_i and their weights μ_i. The function $g(\underline{\sigma})$ is divided into a linear part and a non-linear part

$$g(\underline{\sigma}) = 1 + w(\underline{\sigma}) \text{ with } w(\underline{\sigma}) = K\left(\underline{\sigma} : \underline{\underline{S}}^R : \underline{\sigma}\right)^{p/2} \tag{4}$$

where K and p are material parameters that must be identified.

The parameters τ_i and μ_i introduced in Equation (3) are, respectively, the relaxation time and the weight associated to the ith elementary viscous strain $\underline{\xi}_i$. These two quantities defined the spectrum of the relaxation time (which gave its name to the model) that is supposed in the present article to have a Gaussian form.

$$\tau_i = \exp(n_i) \text{ and } \overline{\mu}_i = \frac{1}{n_0\sqrt{\pi}} \exp\left(-\left(\frac{n_i - n_0}{n_c}\right)^2\right) \mu_i = \frac{\overline{\mu}_i}{\sum_{i=1}^{n_t} \overline{\mu}_i} \tag{5}$$

where n_0 and n_c are two material parameters that must be identified. n_i is comprised between two limits n_1 and n_2 that permit to eliminate the too low or too high relaxation times. To illustrate this point, the relaxation times and the associated weights are shown in Figure 5 for $n_t = 30$ elementary viscous mechanisms, $n_1 = -20$, $n_2 = 30$, $n_0 = 5$ and $n_c = 10$.

The visco-elastic compliance $\underline{\underline{S}}^R$ has the same symmetry as the elastic ones. It is, thus, defined by two parameters, for instance, the visco-elastic Young's modulus E_r and the visco-elastic Poisson ratio ν_r.

This model has been implemented in Abaqus via a UMAT subroutine.[33]

Only two tests are necessary to identify this model: a multiple stress level creep test under shear loading and another under tensile loading. The inverse identification procedure is explained in Section 3.2.

A parametric study has been performed in order to highlight the influence of the number of elements in the thickness of adhesive, on the macroscopic curve relative displacement of the substrates. Two models were analysed: the first model, named model

Downloaded by [Ensta Bretagne], [Nicolas Carrere] at 00:27 23 December 2014

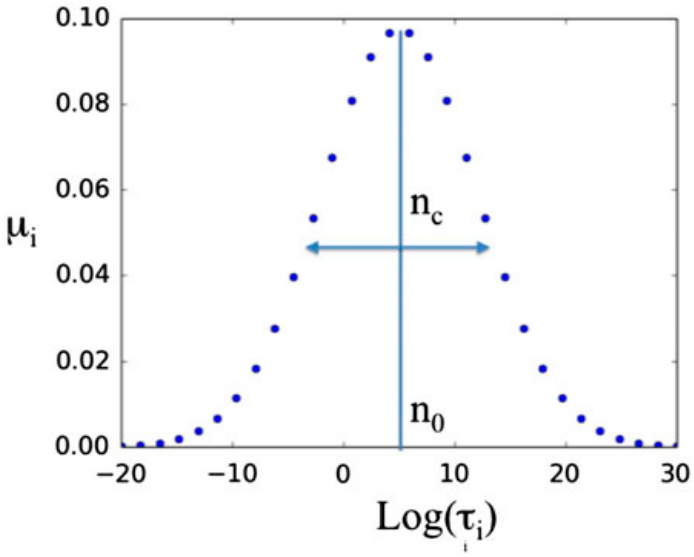


Figure 5. Definition of the spectrum (relaxation time τ_i and weight μ_i) for, $n_1 = -20$, $n_2 = 30$, $n_0 = 5$ and $n_c = 10$. Each point represents one of the 30 elementary viscous mechanism.

a (see Figure 6), that includes five elements in the thickness of the adhesive, and the second model, named b, that includes 80 elements in the thickness. The parameters of the visco-elastic model have been chosen to be representative of a classical non-linear behaviour of a polymer. The load imposed on the two models corresponds to a multiple stress creep/recovery test (see Figure 6). It was observed that for the two models, the macroscopic curve force vs. relative displacement remains closed. Therefore, in the following, model a has been chosen, because the computation time decreases from 75 min for model b to 4 min for model a.

3. Results

3.1. Experimental results

In this paper, we have focussed on the shear behaviour (using the modified Arcan device with $\gamma = 90°$), because the non-linear behaviour is greater for this kind of loading as compared with the tensile loadings ($\gamma = 0°$ with the Arcan test device). Two kinds of tests have been performed: monotonic tests in order to determine the general behaviour of the adhesive and multiple creep tests at different stress levels (to identify the visco-elastic behaviour). These tests have been performed at two different temperatures: 20 °C (room temperature) and 50 °C temperature, inferior to the glass transition temperature of the adhesive studied here.

The results of the two monotonic shear tests performed with a displacement rate of the tensile testing machine crosshead of 0.5 mm/min, for the two different temperatures mentioned above, are plotted in Figure 7. DT stands for relative displacement in the tangential direction of the joint between the two adherents, and FT stands for the load applied.

These tests allowed us to have a general view of the behaviour of the bonded assembly for the two temperatures. It can be observed from Figure 7 that the fracture load is about 25% smaller for a temperature of 50 °C than for a temperature of 20 °C (while the fracture strain is slightly bigger at 50 °C temperature). The slope of the

Downloaded by [Ensta Bretagne], [Nicolas Carrere] at 00:27 23 December 2014

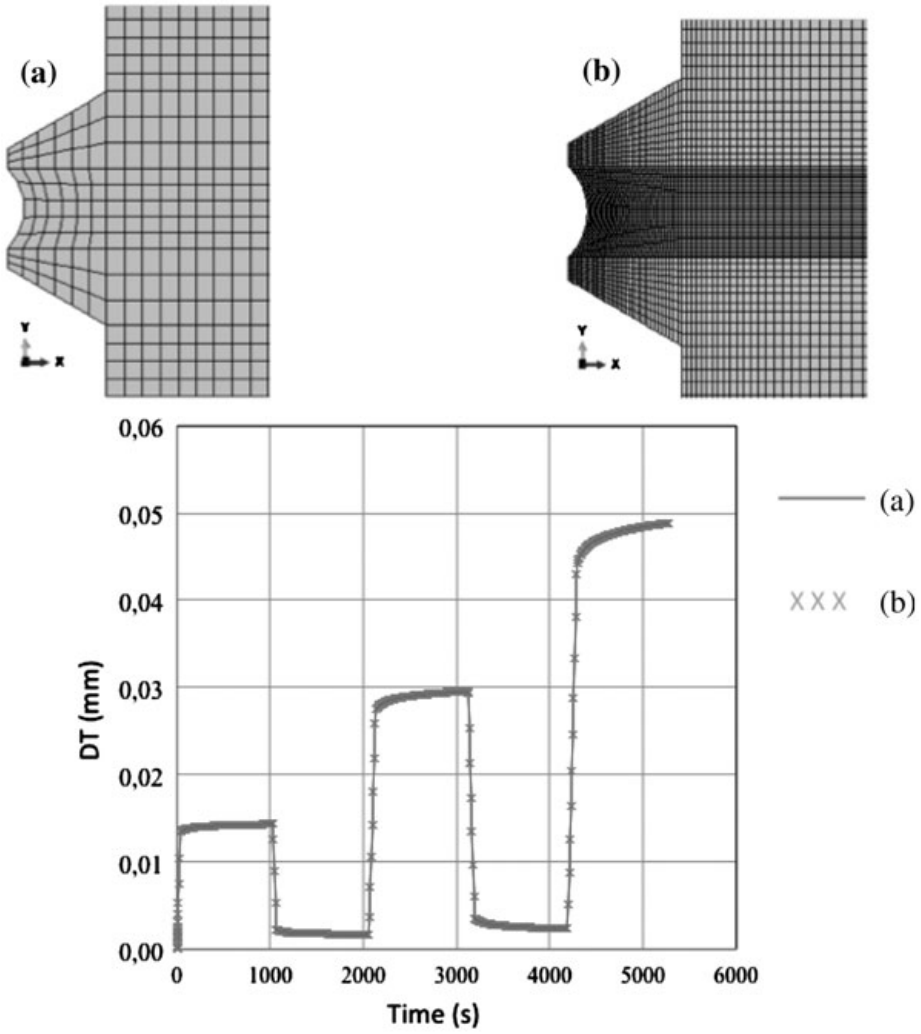


Figure 6. Tangential displacement as a function of time for the two different meshes for a multilevel creep/recovery test (3.5, 7 and 10 kN).

force/displacement curve is a combination of the instantaneous part (Young's modulus E in Equation (1)) and of the visco-elastic strain (which increased as a function of the applied load following Equation (3)). For very low loadings (lower than 2 kN), the two curves are very close, but their slopes tend to differ when the stress increases (it means that the visco-elastic strain increases). Above a threshold (around 11 kN at 20 °C and 7 kN at 50 °C), the behaviour becomes highly non-linear.

Two other tensile tests have been performed at 50 °C with displacement rates of the tensile testing machine crosshead equal to 0.05 and 5 mm/min. The displacement–load curves are given in Figure 8. For very low loadings (lower than 2 kN), the force/displacement are very close. This part of the curves is related to the instantaneous elastic part (Young modulus E in Equation (1)). The curve tends to differ as the stress increases (due to the increase of the visco-elastic strain). However, the curve is closer to the instantaneous elastic behaviour on a larger range, when the loading rate increases. The threshold at which the behaviour becomes highly non-linear is also a function of the loading rate (form 8 kN at 0.05 mm/min to 13 kN at 5 mm/min – see Figure 8).

Downloaded by [Ensta Bretagne], [Nicolas Carrere] at 00:27 23 December 2014

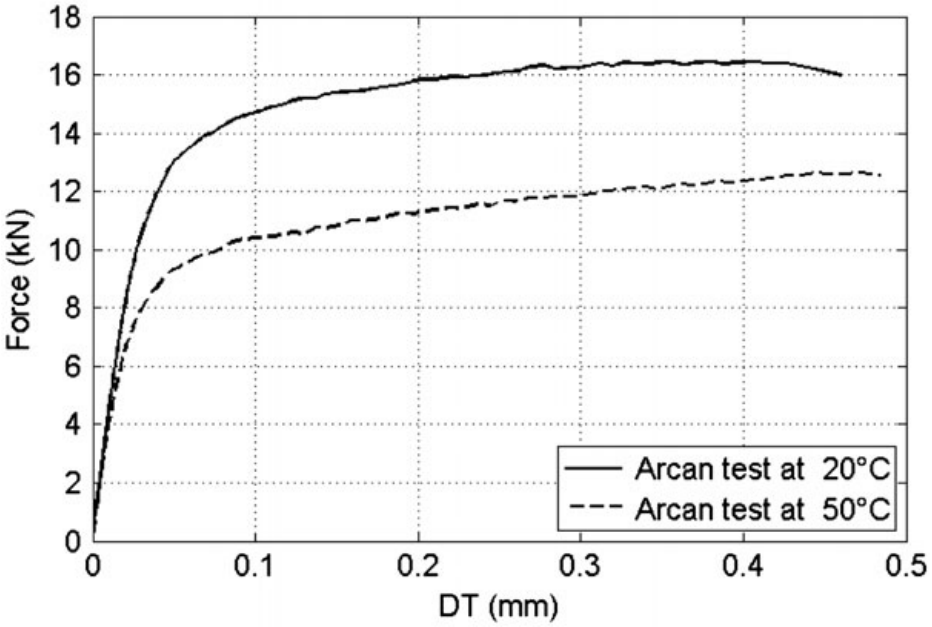


Figure 7. Macroscopic response of a monotonic test at 20 and 50 °C test for a displacement rate of the tensile testing machine crosshead of 0.5 mm/min.

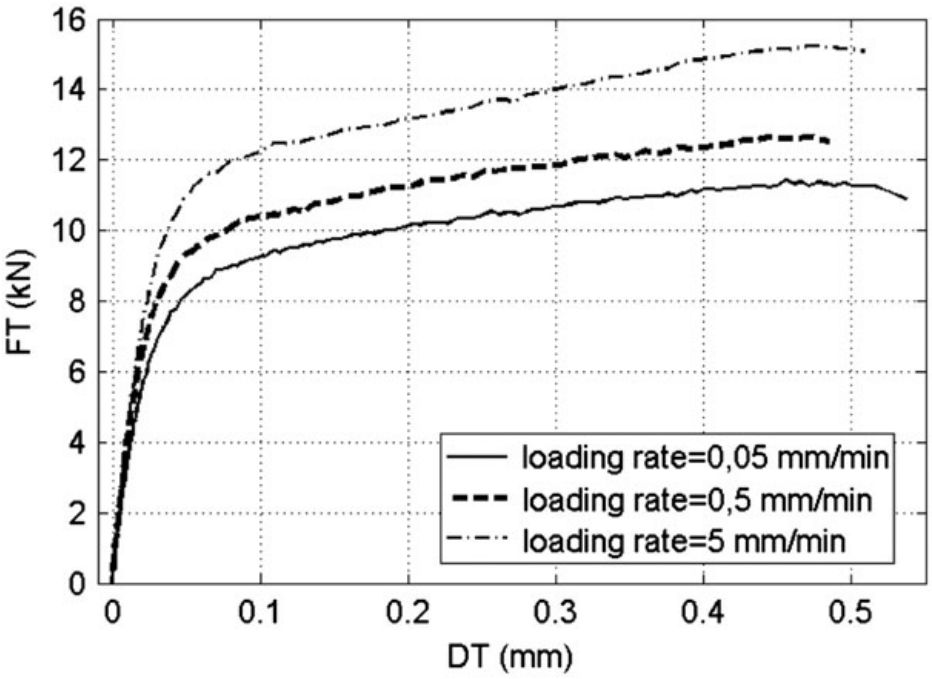


Figure 8. Macroscopic response of a monotonic test for a displacement rate of the tensile testing machine crosshead of 0.5, 0.05 and 5 mm/min at 50 °C.

The second type of tests represents a multiple creep test at five levels, the load at each level representing 20, 40, 60, 80 and 100% of the fracture load. The period where the force is maintained constant is 1000 s for each level test and the passage from one level test to another is made with a load speed of 0.1 kN/s for the two temperatures. The purpose of these tests is to characterise and model the time-dependent behaviour of this type of adhesive with respect to temperature.

Downloaded by [Ensta Bretagne], [Nicolas Carrere] at 00:27 23 December 2014

The load applied to the sample, with respect to time is plotted in Figure 9 for the two different temperatures. Immediately below this figure, we can see the macroscopic response of the sample under this share test, represented by the relative tangential displacement. These experimental results will be used in order to identify the parameters of the spectral visco-elastic model (E_r, ν_r, p and K).

The viscous part of the displacement (defined as the differences between the displacement at the end and at the beginning of the different levels of creep) and the elastic part of the displacement (defined as the difference between the total displacement at the end of the different levels of creep and the viscous part $DT^e = DT - DT^v$) for each step of the multilevel creep test are given in Figure 10. For room temperature (20 °C), the elastic part is greater than the viscous part, but this is no longer true for higher temperature (50 °C).

Figure 10 presents the evolution of the viscous displacements (defined as the difference between the total displacement and the elastic displacement at the end of the different levels of creep) as a function of the applied load. This evolution is clearly non-linear which means that the viscous behaviour is non-linear as a function of the stress.

It is apparent that even for an applied load lower than the threshold revealed during the monotonic test (around 11 kN at 20 °C and 7 kN at 50 °C), a viscous strain takes place. It means that the non-linear behaviour could not be easily described by a classical elasto-visco-plastic (even if slow creep could occur below the elastic limit in visco-plastic material). In our point of view, a visco-elastic model seems more suitable. Moreover, the viscous behaviour is non-linear as a function of the applied load. This is the reason why a non-linear visco-elastic model (presented in the next section) has

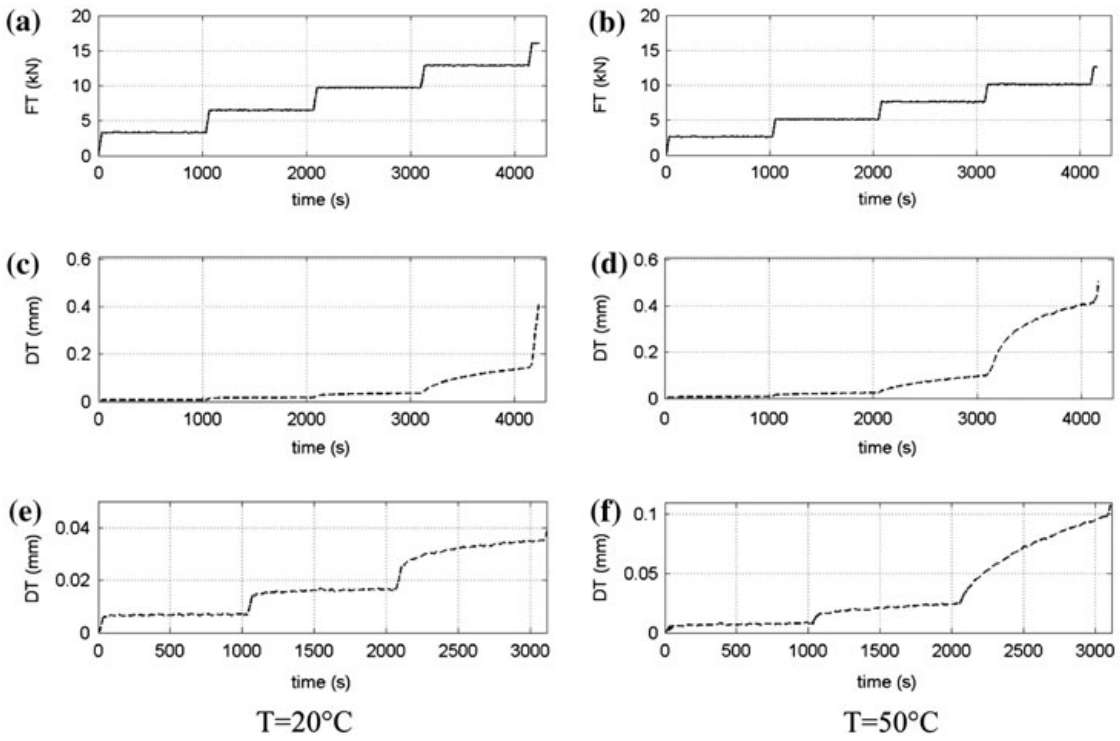


Figure 9. Macroscopic response of the multiple stress creep test. (a) and (b) the imposed shear load at 20 and 50 °C; (c) the response of the adhesive under shear loading at 20 and 50 °C; (d) the response of the adhesive under shear loading at 50 °C; (e) zoom at the beginning of curve (c); (f) zoom at the beginning of curve (d).

Downloaded by [Ensta Bretagne], [Nicolas Carrere] at 00:27 23 December 2014

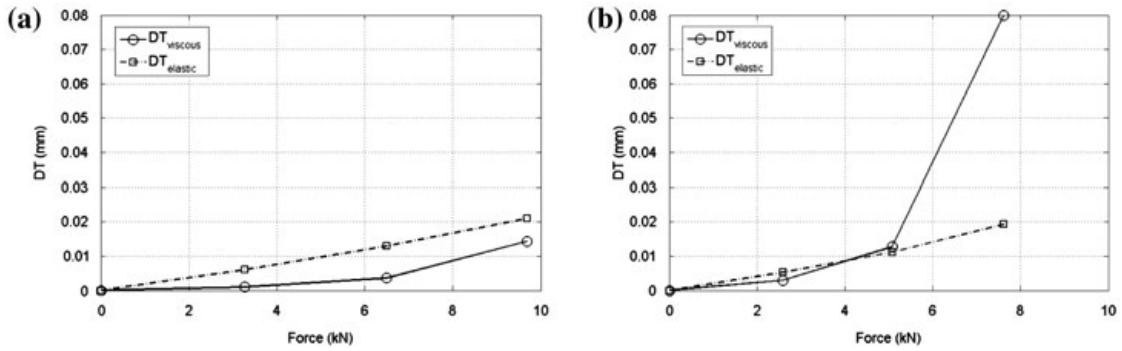


Figure 10. Evolution of the elastic part and the viscous part of the displacement at the end of each step of the creep tests at 20 °C (a) and 50 °C (b).

been chosen. It could be easily implemented in a FE code, is valid under various kinds of loading conditions (the domain of validity is discussed in Section 4) and necessitates only few tests to be identified (see next section).

3.2. *Identification of the visco-elastic model parameters*

As explained previously, the stress state being non-uniform in the adhesive, it is necessary to use an inverse identification procedure to identify the parameters of the model. A FE calculation is performed and the results in terms of displacements (DT and DN) are compared with the experimental results.

The spectral visco-elastic model is defined by 10 parameters that must be identified. These parameters could be classified into three groups: parameters related to the initial elastic behaviour, parameters that define the viscous spectrum of the model (i.e. the shape of a creep curve) and parameters that characterize the viscous behaviour of the adhesive. This classification makes the identification of the parameters easier, by decoupling these parameters. In order to identify the parameters of this model which are related to the behaviour of the adhesive, only two types of tests are required. The first type refers to monotonic tests, such as the tests represented in Figure 7, and allows the identification of the elastic parameters of the model, E and ν, respectively. The second type are the tests represented in Figure 9 and they allow the identification of the other parameters of the model. The identification of the parameters is made in the following steps.

3.2.1. *The identification of the elastic parameters (Young's modulus E and Poisson ratio ν)*

The instantaneous elastic properties are identified using the loading part of the first level of the multilevel creep tests. The Young's modulus and the shear modulus are identified using an Arcan test, respectively, at $\gamma = 0°$ and $\gamma = 90°$ (the adhesive being isotropic $G = E/2(1 + \nu)$.

The elastic properties of the adhesive are given in Table 1.

3.2.2. *The identification of the parameters that define the spectra of the model (n_0, n_c, n_1 and n_2)*

The n_1 and n_2 parameters have been set at $n_1 = -20$ and $n_2 = 30$, which are classical values used for epoxy resins to which Sikapower belongs. The number of elementary

Downloaded by [Ensta Bretagne], [Nicolas Carrere] at 00:27 23 December 2014

Table 1. Elastic properties of the adhesive SikaPower 498 at 20 and 50 °C.

E (MPa)	ν
8000	0.34

viscous mechanisms n_t has been chosen equal to 30 (it has already been shown [29] that 30 elementary viscous mechanisms permits to describe in a correct manner the spectrum with a reasonable computational cost). The identification of the n_0 and n_c parameters uses the isochronism principle of the spectral visco-elastic model. The isochronism principle used the normalized DT vs. time curves for each level of creep (each creep level must have the same duration). The normalization is defined as follows

$$\begin{cases} \mathrm{DT}^{\mathrm{norm}} = \frac{\mathrm{DT}(t)-\mathrm{DT}(t^{\mathrm{began}})}{\mathrm{DT}(t^{\mathrm{end}})-\mathrm{DT}(t^{\mathrm{began}})} \\ t^{\mathrm{norm}} = \frac{t-t^{\mathrm{began}}}{t^{\mathrm{end}}-t^{\mathrm{began}}} \end{cases} \tag{6}$$

where t^{began} is the time corresponding to the beginning of the creep level and t^{end} is the time corresponding to the end of the creep level. Figure 11 shows the normalized DT vs. time curves for the first three levels of creep at 20 and 50 °C (defined in Figure 9(a) and (b)). If all the curves fit to a master curve (that is the case in Figure 11) it means that the spectral description of the relaxation time is adapted. In this case, the spectrum of the relaxation time is having an influence only on the shape of the curve, the normalized curves permit to identify this spectrum (parameters n_0, n_c, n_1 and n_2). If this principle is not verified experimentally, the identification of the parameters, as well as the use of this model is not suited to the behaviour of the adhesive.

Figure 11 shows that the response of the adhesive under a multiple level creep test respects the isochronism principle for the first three levels for 20 °C temperature, as well as for 50 °C temperature. The results presented in Figure 11 also show that the normalized creep curves are the same for both temperatures. It means that temperature has no effect on the global shape of the creep curves.

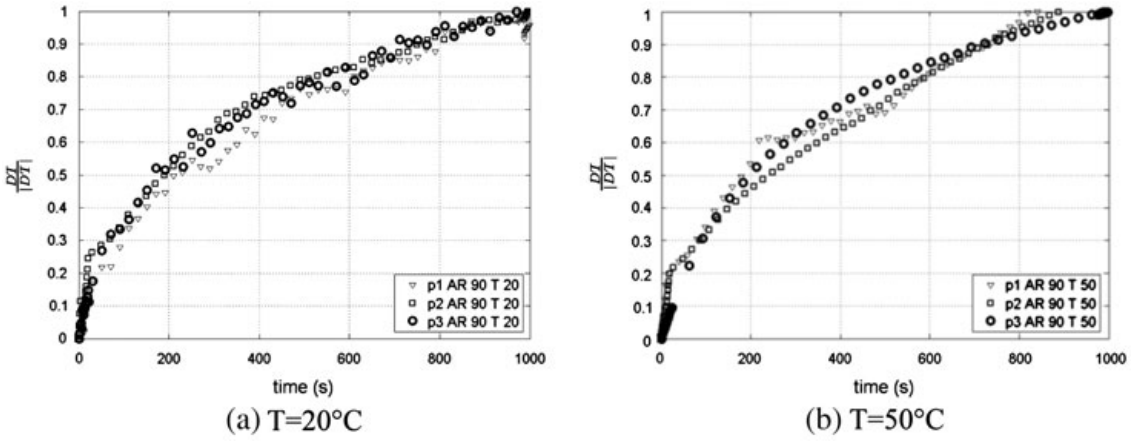


Figure 11. Normalized displacement vs. time for each loading level at two different temperatures (a) $T = 20$ °C and (b) $T = 50$ °C. All the curves fitting a master curve, the description of the relaxation time by a spectrum is adapted.

Downloaded by [Ensta Bretagne], [Nicolas Carrere] at 00:27 23 December 2014

Downloaded by [Ensta Bretagne], [Nicolas Carrere] at 00:27 23 December 2014

A parametric study using the FE model presented in Section 3.1 has been carried out with the purpose of identifying the two parameters (n_0 and n_c each of them varying between 1 and 20 with an increment of 1). The values of the other parameters of the model E_r, v_r, p and K, respectively, are chosen arbitrarily, as they do not influence the shape of the normalized curves. The loads applied to the FE model are the first three levels of the curves in Figure 9(a) and (b), for a period that varies from 0 to 3120 s. The relative displacements obtained as a result of FE simulation are expressed as the difference between points P_1 and P_2 (see Figure 4), found in the centre of the substrate area.

A quality factor (QF) used to compare the numerical and the experimental curves is defined as follows

$$\text{Quality Factor} = 1 - \sum_{i=1}^{n} \left(\left| \left| \text{DT}_{\text{norm}}^{\text{exp}} - \text{DT}_{\text{norm}}^{\text{FE}} \right| \right|_i \right) \tag{7}$$

where n is the number of points of the curve $\text{DT}_{\text{norm}}^{\text{exp}}$ and $\text{DT}_{\text{norm}}^{\text{FE}}$ are, respectively, the experimental and the numerical normalized displacements. The QF values obtained for all the (n_0, n_c) pairs are plotted in Figure 12. If the QF value is very close to 1, then the pair can be considered as acceptable.

In addition, we can observe that there are many acceptable pairs (the grey ridge in Figure 12). However, from all these acceptable values, we shall choose the value that is closest to 1 (the black circle in Figure 12), which, for us, corresponds to $n_0 = 7$ and $n_c = 18$. Indeed, it has been shown in a previous study on composite materials that choosing one pair randomly from all the best pairs has a low influence on the final result.[34]

3.2.3. *The identification of the parameters Er, vr, p and K*

The parameters E_r and v_r define the visco-elastic compliance (which is considered to be isotropic) and the parameters p and K define the non-linear character of the visco-elasticity (function g see Equation (4)).

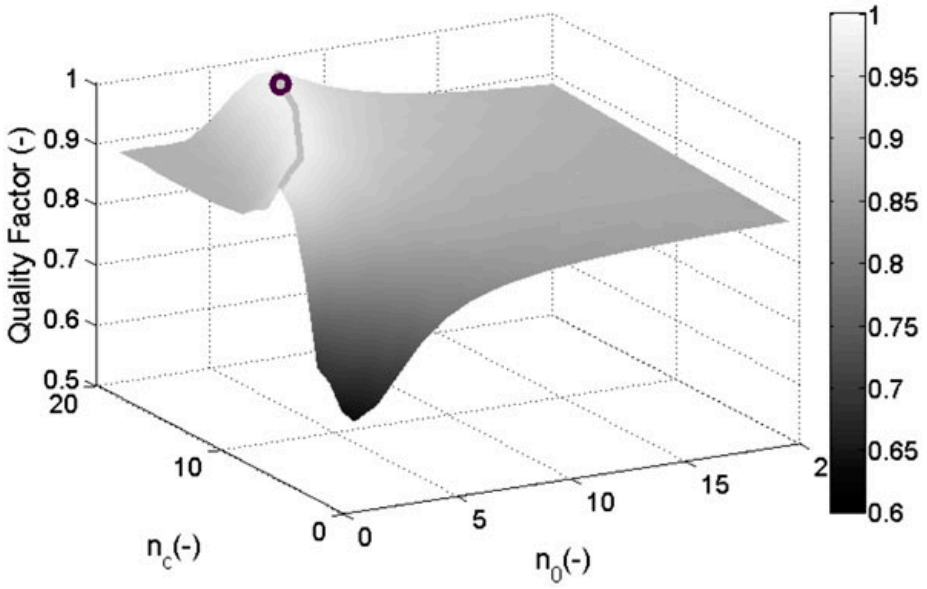


Figure 12. Evolution of the QF as a function of the n_c and n_0. The black circle represents the best solution.

The basic principle used in this stage is to minimize the error function (*Ef*) defined by relation (8) related to the four parameters of the model E_r, v_r, p and K

$$Ef(E_r, v_r p, K) = \sum_{j=1}^{n} \left(\mathrm{DT}^{\mathrm{exp}}_{\mathrm{norm}} - \mathrm{DT}^{\mathrm{FE}}_{\mathrm{norm}}(E_r, v_r p, K)\right)_j^2 \tag{8}$$

where n is the number of point if the DT/time curve. The comparison between the model and experimental results is performed using the curve DT vs. time. For this purpose, a coupling between the finite element software Abaqus© and the Matlab© software has been performed. Using the *fminsearch* function in Matlab© permits the error function in relation with the four parameters to be minimized. The algorithm used by the *fminsearch* function is a 'the Nelder–Mead Simplex Method' descent algorithm, described in detail in [35].

The communication between the software is based on the following principle: Matlab software, using the *fminsearch* function, generates a set of values for the four parameters. Abaqus software will automatically detect that those parameters have been generated and will start the FE task. Finally, FE results are post processed, and then the values of the $\mathrm{DT}^{\mathrm{FE}}$ vs. *time* curves are generated. Matlab software computes the value of the *Ef*, using the curve obtained previously, as a result of the FE task. The *fminsearch* function reads this value and generates a new set of parameters. The optimization is finished when the difference in value of the error function for two successive iterations is less than the imposed tolerance.

In this case, 18 iterations have been necessary to find the value of the parameters that can represent the results of the experiment very well.

The comparison at the end of the identification procedure is shown in Figure 13. It is important to note that only the first three steps of the multilevel creep tests have been used.

The values of the parameters are given in Table 2. It is interesting to note that, contrary to the other part of the model (elastic compliance and visco-elastic spectrum), the visco-elastic compliance and the non-linear visco-elastic function (g) are very sensitive to temperature.

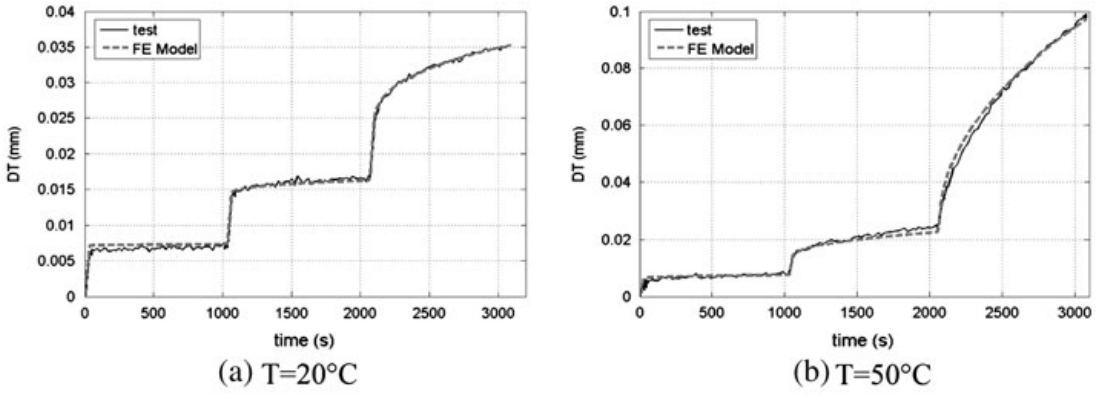


Figure 13. Comparison between the FE results and the experimental results for two different temperatures (a) $T = 20$ °C and (b) $T = 50$ °C.

Downloaded by [Ensta Bretagne], [Nicolas Carrere] at 00:27 23 December 2014

Table 2. Evolution of the visco-elastic modulus and of the parameters of the non-linear function g as a function of the temperature.

	E_r (MPa)	v_r	p	K
20 °C	2062	0.4	4.43	14.8
50 °C	492	0.4	4.19	2.76

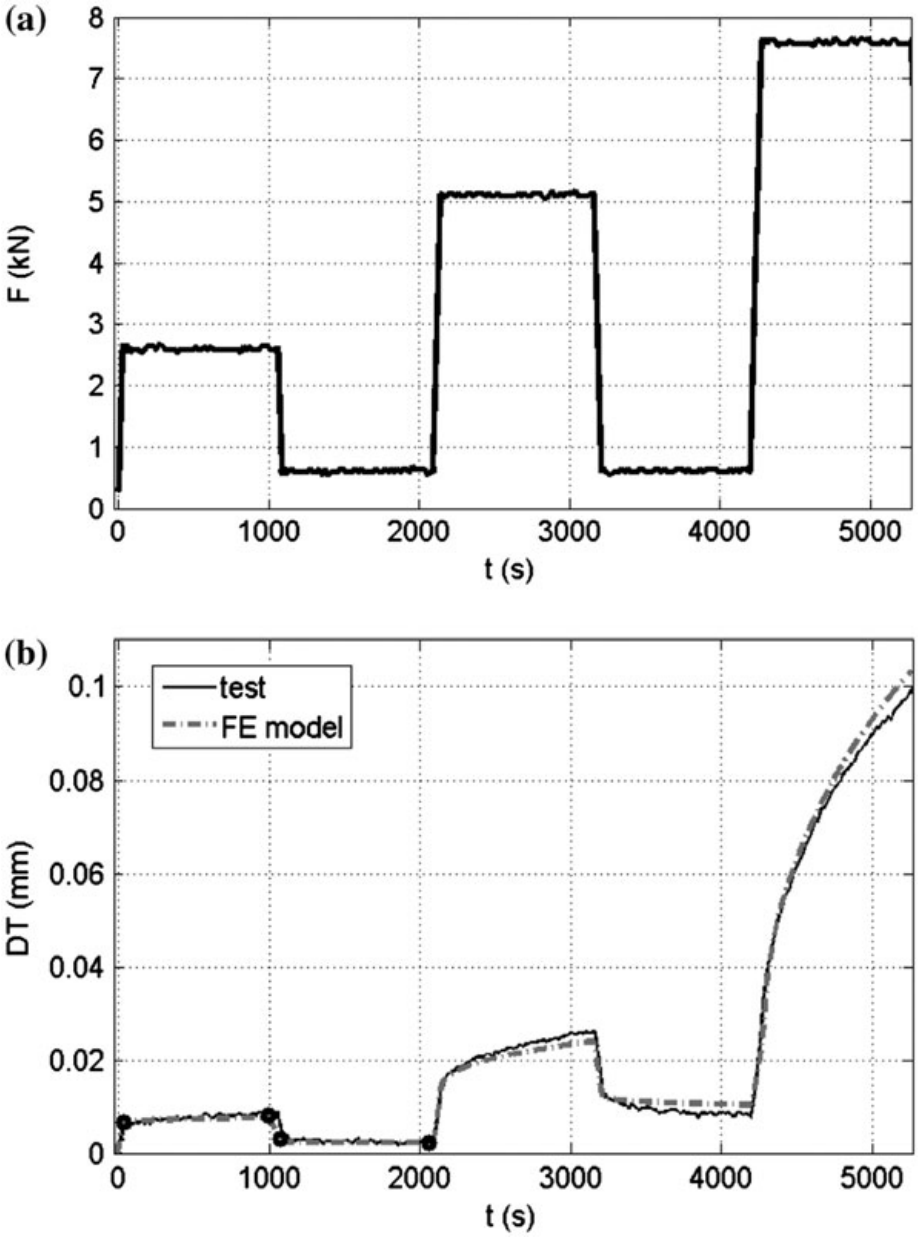


Figure 14. Validation of the model for a creep relaxation test at the temperature of 50 °C. The three dots represent the first level of creep (the end of the loading: 33 s; at the end of the creep phase: 992 s; at the end of the unloading: 1085 s and the end of the recovery: 2085 s).

4. Discussion and validation of the model

In order to validate the model, comparison between numerical prediction and experimental results has been performed thanks to other tests not used during the identification.

Downloaded by [Ensta Bretagne], [Nicolas Carrere] at 00:27 23 December 2014

Downloaded by [Ensta Bretagne], [Nicolas Carrere] at 00:27 23 December 2014

The first test is also a multilevel creep test, but with unloading and relaxation between each level of the creep test. The first step of this test could be compared with the one presented in Figure 13b that allows highlighting the reproducibility of the Arcan tests as it was pointed out in Section 2.1. The comparison between the numerical prediction and the experimental results is given in Figure 14(b). The model permits the unloading and the relaxation to be described very accurately, even if such a type of loading had not been used during the identification procedure. It is worth mentioning that the visco-elastic strain is not totally recovered, even for very long relaxation times. However, the slope of the DT vs. time curve is low but not null, which tends to indicate that the relaxation is not total. It could be seen that the relaxation predicted by the model is lower than that obtained experimentally. This difference will be discussed in the conclusion. In an experimental point of view, it will be interesting to increase the duration of the recovery steps in order to determine if a complete relaxation could be attain (as predict by the visco-elastic model for long time of relaxation) or if a permanent strain could be observed.

The evolution of the shear stress and the shear visco-elastic strain during the first level of the multilevel creep test (defined in Figure 14) is presented in Figure 15 (at the end of the loading: 33 s; at the end of the creep phase: 992 s; at the end of the unloading: 1085 s; and the end of the recovery: 2085 s). At the end of the loading step, the stress field in the adhesive presents a parabolic shape close to the one obtained with a pure elastic model.[26] During the creep phase (constant loading), the visco-elastic shear strain increases and the stress field in the adhesive becomes latter. At the end of the unloading phase, the stress field is no longer parabolic and is greater near the edge (however, it is worth mentioning that the stress is still equal to 0, which means there is no edge effect). The stress evolves a little during the recovery phase and tends to become flatter. The shape of visco-elastic strain is still the same (more or less parabolic), only its intensity increases as a function of the applied stress or of the time during creep tests.

The other tests used to validate the model are monotonic shear tests at different loading rates (displacement rates of the crosshead of the tensile testing machine equal to 0.05, 0.5 and 5 mm/min). The experimental and numerical displacement-load curves are given in Figure 16. It should be noted that the model permits the reproduction of the main characteristics revealed by the experiments: the apparent elastic modulus is constant as a function of the loading rate and the pseudo-elastic limit increases as a function of the

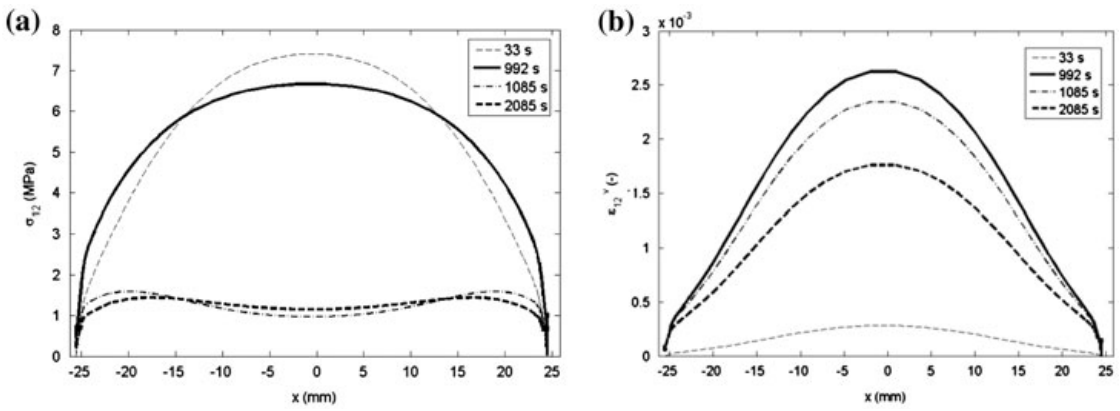


Figure 15. Stress (a) and strain (b) distribution in the middle of the adhesive for a different stage of the multilevel creep test (t = 33, 1085 and 2085 s correspond to the end of the loading steps representing 20, 40 and 60%; t = 1026, 2056 and 3081 s correspond to the end of the creep tests for each level of stress).

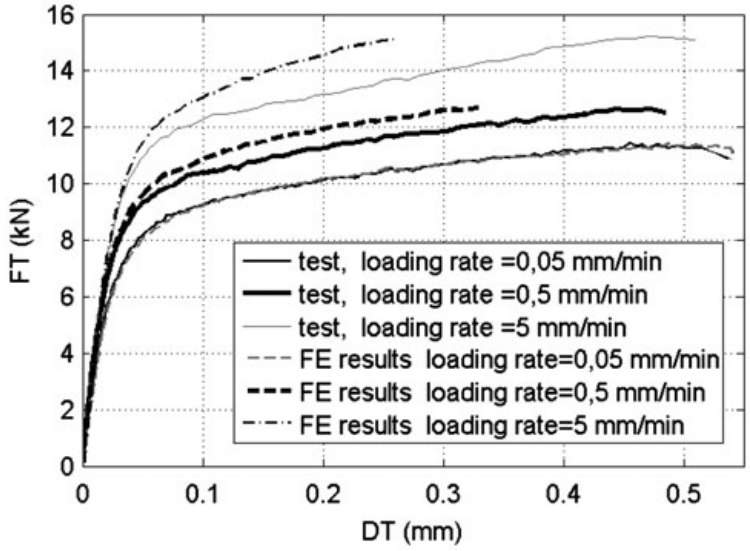


Figure 16. Validation of the influence of the loading rate on the visco-elastic behaviour at a temperature of 50 °C.

loading rate. The difference between the numerical prediction and the experimental results in the non-linear part of the curves increases when the loading rate increases. This result could be explained by the fact that only low characteristic times are activated during creep tests. Thus, the model gives better results at low loading rates. In order to overcome this problem, one solution should be to increase drastically the loading rate used during the loading part of the creep tests (then high characteristic times are activated during the loading part and low characteristic times during the creep part).

5. Conclusions

The non-linear behaviour of an epoxy adhesive has been studied thanks to the use of a modified Arcan test device. We have focused on shear loadings, the non-linear behaviour being greater in this direction. First, monotonic tests at different loading rates have been performed. It has been shown that the stress corresponding to the non-linear plateau and the stress at failure increase as a function of the loading rate. Multilevel creep tests have also been performed in order to characterize the time-dependent behaviour. It has been shown that the creep occurs even for loadings which were considerably lower than the pseudo-elastic limit. Moreover, the evolution of the non-linear displacement is non-linear as a function of the applied load.

Thanks to these experimental results, a visco-elastic model has been chosen to describe the behaviour of the adhesive. This model is based on the decomposition of the visco-elastic strain into elementary viscous mechanisms. The non-linear behaviour of the visco-elasticity is taken into account thanks to a non-linear function which depends on the stress.

The identification of this model necessitates only one multilevel creep test for each direction of loading (i.e. 0° and 90°). The identification procedure is divided into three groups: the instantaneous elastic behaviour, the spectrum (i.e. the shape of a creep curve) and the viscous behaviour of the adhesive. In the present study, we have focused on the shear behaviour, because the non-linear behaviour is more significant for this loading for two different temperatures: 20 and 50 °C. It has been shown that the instantaneous elastic properties and the spectrum are not a function of the temperature.

Downloaded by [Ensta Bretagne], [Nicolas Carrere] at 00:27 23 December 2014

On the other hand, the viscous behaviour (visco-elastic modulus and the non-linear function g) is very sensitive to the temperature.

Finally, the model and the identification have been validated using tests that have not been used for the identification. The validation case is a multilevel creep test with unloading and recovering. The second validation concerns the prediction of the effect of the loading rate during a monotonic shear test. The present model is essentially validated for monotonic loadings (tensile loads, creep and recovering). In order to describe in a correct manner cyclic loadings and the high-cyclic fatigue behaviour, the non-linear function must be modified to improve the description of the hysteresis loops. Moreover, in order to improve the long-term behaviour prediction, it should be necessary to improve the identification procedure, for instance, using less level of stress in the multilevel creep tests, but by increasing the duration of each creep steps. Finally, as explained in Section 4, an increase in the loading rate during the loading steps of the creep tests could also improve the prediction of the loading rate effects.

The visco-elastic spectral behaviour has been used to model the behaviour of an adhesive subjected to unidirectional loadings. It is well known that there is a large difference between the behaviour in shear and in tension. In order to reproduce this phenomenon, the model will be modified in order to take into account the effect of the Von-Mises stress σ^{VM} and the hydrostatic stress σ^{H} as proposed in [31]. Further work will be also done in order to introduce the progressive damage in order to model failure of adhesively bonded structures.

Acknowledgements

N. Carrere would like to thank the UIMM (Union des Industriels des Métiers de la Métallurgie) and 'La Région Bretagne' for the financial support that he has been granted.

References

[1] Irisarri F-X, Laurin F, Carrere N, Maire J-F. Progressive damage and failure of mechanically fastened joints in CFRP laminates – Part I: refined finite element modelling of single-fastener joints. Compos. Struct. 2012;94:2269–2277.
[2] Da Silva LFM, Öchsner A, editors. Modeling of adhesively bonded joints. Springer; 2008. ISBN: 978-3-540-79055-6 (Print) 978-3-540-79056-3 (Online).
[3] Yu XX, Crocombe AD, Richardson G. Material modelling for rate-dependent adhesives. Int. J. Adhes. Adhes. 2001;21:197–210.
[4] Iwamoto T, Nagai T, Sawa T. Experimental and computational investigations on strain rate sensitivity and deformation behavior of bulk materials made of epoxy resin structural adhesive. Int. J. Solids Struct. 2010;47:175–185.
[5] Chalkley PD, Chiu WK. An improved method for testing the shear stress/strain behaviour of adhesives. Int. J. Adhes. Adhes. 1993;13:236–242.
[6] Cognard J-Y, Créac'hcadec R. Analysis of the non-linear behavior of an adhesive in bonded assemblies under shear loadings. Proposal of an improved TAST. J. Adhes. Sci. Technol. 2009;23:1333–1355.
[7] Da Silva LFM, Öchsner A, Adams RD, editors. Handbook of adhesion technology. Vol. 1. Springer; 2011, XXIV, 1543 p. ISBN 978-3-642-01168-9.
[8] Geiss PL, Vogt D. Assessment and prediction of long-term mechanical properties of adhesives with high plasticity. J. Adhes. Sci. Technol. 2005;19:1291–1303.
[9] Choi K-K, Reda Taha MM. Rheological modeling and finite element simulation of epoxy adhesive creep in FRP-strengthened RC beams. J. Adhes. Sci. Technol. 2013;27:523–535.
[10] da Silva LFM, Adams RD, Gibbs M. Manufacture of adhesive joints and bulk specimens with high-temperature adhesives. Int. J. Adhes. Adhes. 2004;24:69–83.
[11] Cognard J-Y. Numerical analysis of edge effects in adhesively-bonded assemblies application to the determination of the adhesive behaviour. Comput. Struct. 2008;86:1704–1717.

Downloaded by [Ensta Bretagne], [Nicolas Carrere] at 00:27 23 December 2014

Downloaded by [Ensta Bretagne], [Nicolas Carrere] at 00:27 23 December 2014

[12] Cognard JY, Créac'hcadec R, Sohier L, Davies P. Analysis of the nonlinear behavior of adhesives in bonded assemblies—Comparison of TAST and Arcan tests. Int. J. Adhes. Adhes. 2008;28:393–404.
[13] Cognard JY, Davies P, Gineste B, Sohier L. Development of an improved adhesive test method for composite assembly design. Compos. Sci. Technol. 2005;65:359–368.
[14] Maurice J, Cognard J-Y, Creac'hcadec R, Davies P, Sohier L, Mahdi S. Characterization and modelling of the 3D elastic–plastic behaviour of an adhesively bonded joint under monotonic tension/compression-shear loads: influence of three cure cycles. J. Adhes. Sci. Technol. 2013;27:165–181.
[15] Mahnken R, Schlimmer M. Simulation of strength difference in elasto-plasticity for adhesive materials. Int. J. Numer. Methods Eng. 2005;63:1461–1477.
[16] Jousset P, Rachik M. Implementation, identification and validation of an elasto-plastic-damage model for the finite element simulation of structural bonded joints. Int. J. Adhes. Adhes. 2014;50:107–118.
[17] Zgoul M, Crocombe AD. Numerical modelling of lap joints bonded with a rate-dependent adhesive. Int. J. Adhes. Adhes. 2004;24:355–366.
[18] Pandey PC, Shankaragouda H, Singh A. Kr. Nonlinear analysis of adhesively bonded lap joints considering viscoplasticity in adhesives. Comput. Struct. 1999;70:387–413.
[19] Dean G. Modelling non-linear creep behaviour of an epoxy adhesive. Int. J. Adhes. Adhes. 2007;27:636–646.
[20] Majda P, Skrodzewicz J. A modified creep model of epoxy adhesive at ambient temperature. Int. J. Adhes. Adhes. 2009;29:396–404.
[21] Crocombe AD. Modelling and predicting the effects of test speed on the strength of joints made with FM73 adhesive. Int. J. Adhes. Adhes. 1995;15:21–27.
[22] Chiu WK, Jones R. Unified constitutive model for thermoset adhesive FM73. Int. J. Adhes. Adhes. 1995;15:131–136.
[23] Frank GJ, Brockman RA. A viscoelastic–viscoplastic constitutive model for glassy polymers. Int. J. Solids Struct. 2001;38:5149–5164.
[24] Boubakar ML, Vang L, Trivaudey F, Perreux D. A meso–macro finite element modelling of laminate structures Part II: time-dependent behaviour. Compos. Struct. 2003;60:275–305.
[25] Groth HL. Viscoelastic and viscoplastic stress analysis of adhesive joints. Int. J. Adhes. Adhes. 1990;10:207–213.
[26] Cognard JY, Sohier L, Davies P. A modified Arcan test to analyze the behavior of composites and their assemblies under out-of-plane loadings. Composites Part A. 2011;42:111–121.
[27] Cognard J-Y, Bourgeois M, Créac'hcadec R, Sohier L. Comparative study of the results of various experimental tests used for the analysis of the mechanical behaviour of an adhesive in a bonded joint. J. Adhes. Sci. Technol. 2011; 5:2857–2879.
[28] Gom Aramis, Handbook, 2014.
[29] Maire J-F. Etude théorique et expérimentale du comportement de matériaux composites en contraintes planes [Theoritical and experimental study of the behaviour of composite material under plane stresses assumptions]. PhD thesis, Besançon: Université de Franche-comté; 1992.
[30] Laurin F, Carrère N, Maire J-F. A multiscale progressive failure approach for composite laminates based on thermodynamical viscoelastic and damage models. Composites Part A. 2007;38:198–209.
[31] Carrere N, Laurin F, Maire J-F. Micromechanical-based hybrid mesoscopic 3D approach for non-linear progressive failure analysis of composite structures. J. Compos. Mater. 2012;46:2389–2415.
[32] Cognard J-Y, Badulescu C, Maurice J, Créac'hcadec R, Carrère N, Vedrine P. On modelling the behaviour of a ductile adhesive under low temperatures. Int. J. Adhes. Adhes. 2014;48:119–129.
[33] Abaqus, *User Manual*, 2014
[34] Laurin F. Approche multiéchelle des mécanismes de ruine progressive des matériaux stratifiés et analyse de la tenue de structures composites [Multiscale analysis of the progressive failure mechanisms of laminated composites and analyse of the strength of composite structures] PhD thesis, Besançon: Université de Franche-comté; 2005.
[35] Lagarias JC, Reeds JA, Wright MH, Wright PE. Convergence properties of the Nelder–Mead simplex method in low dimensions. SIAM J. Optim. 1998;9:112–147.

International Journal of Adhesion and Adhesives 82 (2018) 184–195

Contents lists available at ScienceDirect

International Journal of Adhesion and Adhesives

journal homepage: www.elsevier.com/locate/ijadhadh

A viscoelastic-viscoplastic model to describe creep and strain rate effects on the mechanical behaviour of adhesively-bonded assemblies

A. Ilioni[a,b,*], C. Badulescu[a], N. Carrere[c], P. Davies[b], D. Thévenet[a]

[a] ENSTA Bretagne, IRDL, FRE CNRS 3744, F-29200 Brest, France
[b] IFREMER, Marine Structure Laboratory, 29280 Plouzané, France
[c] SAFRAN Tech-Composites, 33 Avenue de la Gare, 91760 Itteville, France

ARTICLE INFO

Keywords:
A. Epoxides
D. Mechanical properties of adhesives
D. Creep / mechanical relaxation

ABSTRACT

Most of the adhesives used in the marine industry are polymers with a mechanical behaviour which is strongly influenced by the strain rate. Therefore, it is important to predict with accuracy their viscous behaviour. To describe their mechanical behaviour in a bonded joint, a viscoelastic-viscoplastic constitutive law is proposed here. The viscous effects on the elastic behaviour are described using a spectral distribution, which divides the viscous strain as the sum of the strains of several viscous mechanisms, each of them with a different characteristic time and weight. The viscoplastic component of the model permits a better description of the strong non-linear behaviour of the adhesives. The parameters of the constitutive law are obtained using an inverse identification procedure coupled with a finite element model. Two creep tests, in two loading directions, are needed in order to identify the viscoelastic part. The viscoplastic part is identified using monotonic tests. In order to validate the behaviour law and the identification procedure, the adhesive *Huntsman™Araldite* 420 *A/B* has been investigated and modelled. All the experimental tests have been conducted using the modified Arcan device.

1. Introduction

Composite materials have found many applications in naval and other marine structures over the past 50 years. In order to join the composite to other parts of the structure, adhesives represent an interesting solution. They can reduce the weight (avoiding bolts and fasteners) and decrease the stress concentrations that can be catastrophic for the strength of the structures [1].

Different tests can be used to characterize the adhesive directly in the bonded joint as shown by Adams et al. [2]. Single or double lap joints are an interesting solution to this problem [3], but due to the geometries of the substrates, they may present high stress singularities near the edges that can cause a premature failure of the joint [4]. Cognard et al. proposed the modified Arcan device in order to characterize the mechanical behaviour of adhesives in bonded joints up to failure. This can be achieved using substrates with special geometries [5] that can reduce the stress concentrations near the edges. This device has been used in this paper in order to characterize the behaviour of the studied adhesive.

Characterizing the mechanical behaviour of the adhesive used in bonded joints is a very important step in order to be able to describe the failure of this kind of structure. Even though these adhesives are essentially polymers with a viscous behaviour, the load transfer between the components of the bonded joint is usually linked to their instantaneous elastic properties [6]. However, the viscous behaviour represents a major characteristic of polymeric adhesive materials. Therefore, the understanding of these phenomena is important in order to accurately predict the failure and the lifetime of bonded structures. The experimental tests performed on bulk specimens show a non-linear behaviour of adhesives that is very sensitive to the strain rate [7,8]. The viscous response of different structural adhesives was also highlighted under impact loadings in previous studies [9]. All these tests require homogeneous bulk specimens, without any defects, that may be difficult to obtain [10].

Different models have been proposed in the literature in order to predict the mechanical behaviour of epoxy adhesives. In some cases, viscoelastic models [11–14] can be perfectly adapted to characterize the time-dependent behaviour and to predict the influence of the strain rate. Other authors have proposed elastoplastic models [15,16] or viscoplastic models [17–19] which are characterized by a threshold and a permanent strain. While various models of adhesive behaviour have been presented, the originality of the present approach is that the

* Corresponding author.
E-mail address: alin.ilioni@ensta-bretagne.org (A. Ilioni).

https://doi.org/10.1016/j.ijadhadh.2017.12.003
Accepted 15 November 2017
Available online 14 December 2017
0143-7496/ © 2017 Published by Elsevier Ltd.

viscoelastic response is treated in two separate parts, hydrostatic and deviatoric. This has allowed different viscoelastic behaviour to be attributed to shear and tensile loading components. In addition, an original identification method for the viscoelastic parameters is presented. A viscoplastic contribution is also modeled, derived from the Mahnken-Schlimmer model, but again simplifications have been made to reduce the number of parameters.

The article presents a viscoelastic-viscoplastic model that is able to describe the nonlinear behaviour of adhesives over a wide range of strain. The proposed viscoelastic part of the model is able to describe the adhesive behaviour in tensile and shear loading conditions. The viscoelastic strain is decomposed into a number of viscous mechanisms, each of them with a specific relaxation time. The viscous compliance is modelled in a manner that takes into account the effect of the hydrostatic pressure and its evolution to describe the non-linear behaviour as a function of the loading. This approach allows an accurate characterization of time-dependent behaviour. The viscoplastic part of the model is able to take into account the dependency of the elastic threshold as a function of the strain rate. The paper presents the development of the model and its identification procedure based on multi-level creep tests for the normal behaviour and for the shear behaviour using a modified Arcan device. The validation of the model by comparison with experimental results with different ratios of peel/shear stress is then presented.

2. Characterization tests and experimental results

2.1. Experimental procedure

2.1.1. Modified Arcan device

A bonded joint is an assembly that is very sensitive to testing conditions. There are several important details that should be taken into account in order to be able to perform a valid test. The tests presented have used the modified Arcan device. This device enables different types of loadings to be applied to bonded joint. The positioning angle on the tensile machine defines the state of load that is applied to the adhesive(Fig. 1a). Using a uniaxial tensile machine, it is possible to apply shear (Fig. 1b) or tensile (Fig. 1c) loads on a bonded joint. It is also possible to combine tensile or compression with shear loading (Fig. 1d,e). All these loadings can be applied because of the design of this experimental device.

An important aspect to be considered when performing this test is the complex stress. state for different loading conditions. Much detailed information concerning this subject can be found in literature [20,21].

2.1.2. Specimens

The substrates (Fig. 2a) used in the tests are made from aluminium alloy, *AW*2017.

Their geometry was developed and optimized previously as described in the literature [21]. They are provided with spacers (Fig. 2a) that are directly machined from a single block of aluminium alloy. These have an important role in order to obtain a correct alignment and keep a constant thickness when bonding a specimen. The results presented in this paper are obtained using a thickness of the bonded joint that is equal to $400 \pm 10\ \mu m$. During the curing cycle the substrates are kept in the final position by screws (Fig. 2b).

A constant torque of 2.5 *Nm* is applied to the screws.

Before starting the process of bonding, the bonded surfaces of the specimen ($S_0 = 50 \times 9.5\ mm^2$) are subjected to a mechanical treatment that involves a sanding process with different tapes of emery cloth (220 − 180 grit cloth) in order to ensure a clean surface. The next step is to degrease it using acetone. To ensure an homogeneous joint, the adhesive is applied on the surface of each substrate that will form the specimen. The excess adhesive after the bonding process is cleaned with a spatula.

The final bonded specimen can be seen in Fig. 2c. After the curing process, the spacers are removed. An important characteristic of the specimens is the beaks (Fig. 2d). They allow the edge effects to be reduced, as shown by Cognard et al. [22] and could lead to a cohesive failure of the assembly.

2.1.3. Equipment

To perform the experimental tests, the Arcan device was inserted in a hydraulic tensile testing machine (*Instron 1342*). The temperature in the testing room is controlled at about $23^{\circ}C$. The load cell can measure a maximum load of 100 *kN*.

The relative displacement of the substrates was measured using a DIC (digital image correlation) system (Fig. 3a) and no other independent measuring system was used in the present study. The specimen is speckled on one face before installing it in the Arcan device (Fig. 3b) and the shaded zone represents the area of interest for calculating the displacements. This relative displacement is correlated with the load measured by the tensile machine load cell.

The relative displacement between the two substrates during a test is decomposed into a *normal displacement*, (ND) and a *tangential displacement* (TD), (Fig. 3c).

2.2. Experimental results

The following results were obtained using the Huntsman *Araldite 420A/B* adhesive.

This is a bi-component epoxy. The two components are mixed using a *Speedmixer* at 2500 *rpm* for 5 min. After the bonding process the specimens are cured for 1 *h*15 at 115 ^{o}C.

Two types of tests have been performed to characterize the behaviour of this adhesive: monotonic tests in order to characterize the general behaviour of the adhesive up to failure and multi-level creep tests at different loading levels. The latter were performed to highlight the viscoelastic behaviour of the adhesive and to identify the constitutive law that will be presented later in this paper.

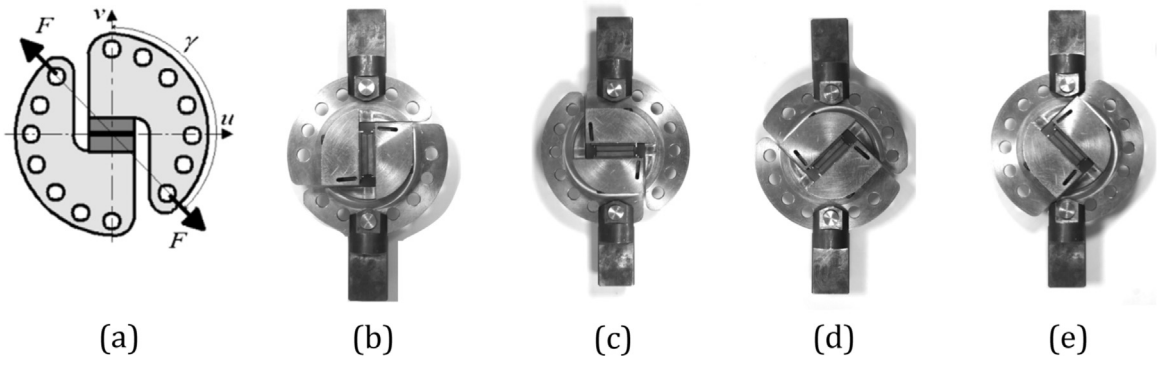


Fig. 1. Different types of Arcan device loading - (a) positioning angle (b) Shear $\gamma = 90°$ (c) tensile $\gamma = 0°$ (d) tensile/shear $\gamma = 45°$ (e) compression/shear $\gamma = 135°$.

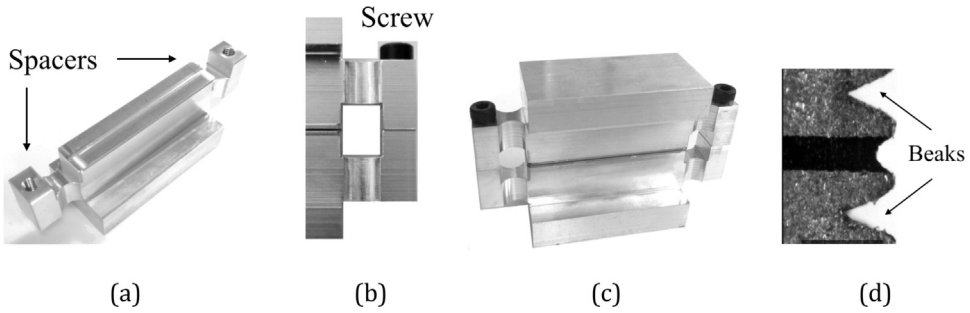


Fig. 2. Modified Arcan specimen – (a) substrate (b) screw (c) specimen (d) beaks.

It should be noted that in the two cases, tensile and shear loading, a cohesive failure is obtained in most of the tests (Fig. 4a,b). For each type of load, between two and three specimens were tested since low scatter could be observed, particularly in shear loading (Fig. 5b). It is also important to note that the relationship between the elastic limits is statistically equivalent for the different loading rates.

2.2.1. Stress-strain curves representation

In order to make possible the correlation of the adhesive behaviour with other published results, a stress-strain representation of the force-displacement curves is proposed. Hence, a mean stress σ was defined as the applied load*"F"* divided by the bonded are S_0 (Eq. 1):

$$\overline{\sigma} = \frac{F}{S_0} \tag{1}$$

Moreover, the normal and shear strains (), ε are defined as in Eq. (2):

$$\overline{\varepsilon_N} = \frac{DN}{e} \quad \overline{\varepsilon_T} = \frac{DT}{e} \tag{2}$$

where *DN* and *DT* represent the normal and tangential measured displacements and *e* the thickness of the adhesive layer.

2.2.2. Monotonic tensile tests

Using the Arcan, device it was possible to characterize the monotonic behaviour of this adhesive in tensile ($\gamma = 0^o$) and shear load ($\gamma = 90^o$). For each condition, two loading rates have been used: 0.4 *MPa/s* and 4 *MPa/s*. It is clear for the two cases (tensile and shear), this adhesive has a mechanical behaviour that is influenced by the loading rate, Fig. 5a, b.

In tensile tests (Fig. 5a), the apparent elastic threshold is increased about 12% from 28 *MPa* to 34 *MPa* when the applied loading rate is multiplied by ten. The failure load is also influenced by the loading rate. The same happens in the shear test. This time it can be seen that the apparent elastic threshold is increasing by about 15% when the loading rate is increased. Some additional combined tensile/shear tests ($\gamma = 45^o$) have also been carried out. These tests were used for validation and they will be presented in Section 3.4.

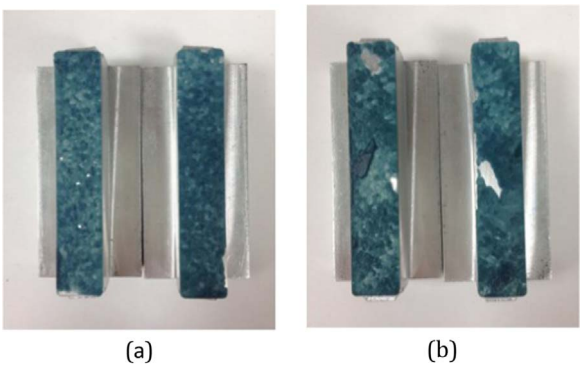


Fig. 4. Cohesive failure in (a) tensile and (b) shear loading.

2.2.3. Multi-level creep tests

In order to be able to characterize the viscous behaviour of this adhesive, multi-level creep tests have been performed. Only two tests will be used to identify the constitutive law that will be presented next in this paper. The aim was also to highlight any differences between the viscous behaviour under tensile and shear loading conditions.

In tension (Fig. 6a), three load levels have been applied for a period of 2000 s. These values correspond to 25%, 50%, and 80% of the apparent elastic limit at 0.4 *MPa/s* loading rate. This loading rate was used to make the passage from one level to another.

Under shear load, (Fig. 6b), four load levels have been applied. These levels represent 20%, 40%, 60%, 80% of the apparent elastic threshold observed in monotonic shear tests for a loading rate of 0.4 *MPa/s*. Four levels of load have been applied (and not three as in tensile loading) since in shear loading condition, a more significant creep response was observed.

The constitutive law was developed by analysing these two results. Based on the work of Badulescu et al. [11] the observed strains ($\overline{\varepsilon_N}^i_{total}$, $\overline{\varepsilon_T}^i_{total}$) at the end of each creep level were divided into two parts, as in Eqs. (3) and (4), where $\overline{\varepsilon_N}^i_{elastic}$, $\overline{\varepsilon_T}^i_{elastic}$ represent the strains generated by the applied load at the beginning of each creep level and $\overline{\varepsilon_N}^i_{viscous}$, $\overline{\varepsilon_T}^i_{viscous}$ are the strains measured at the end of the creep levels:

$$\overline{\varepsilon_N}^i_{total} = \overline{\varepsilon_N}^i_{elastic} + \overline{\varepsilon_N}^i_{viscous} \quad i = 1:3 \tag{3}$$

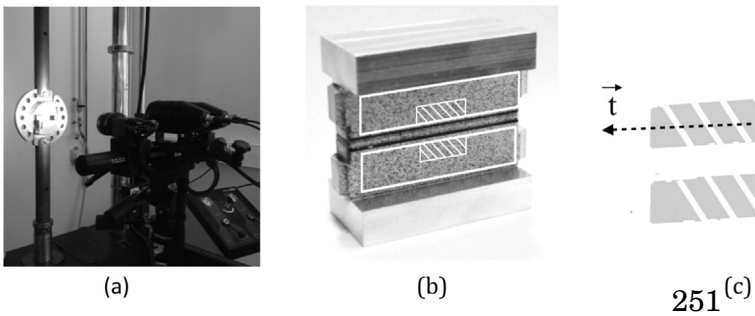


Fig. 3. Measurement of substrates displacements – (a) GOM system (b) speckled specimen ready for test (c) digital image correlation.

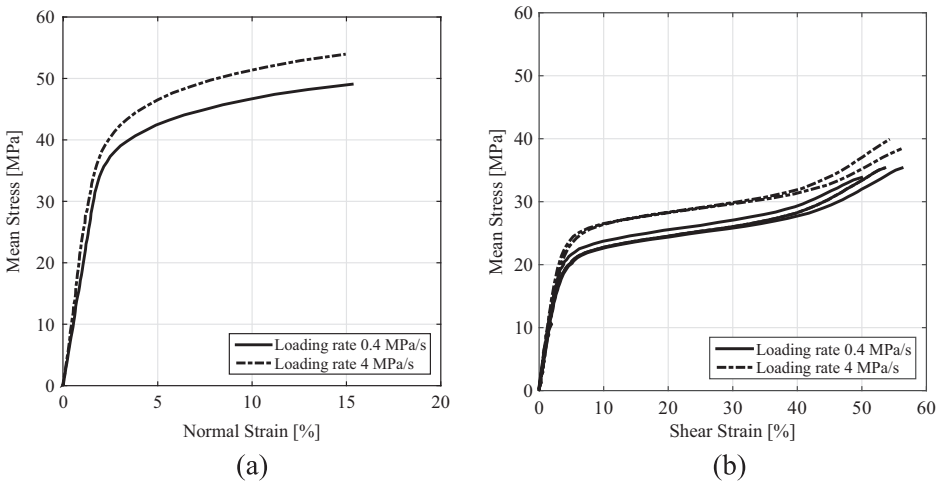


Fig. 5. Monotonic tests: tensile (a) and shear (b).

$$\overline{\varepsilon_T}^{i}_{total} = \overline{\varepsilon_T}^{i}_{elastic} + \overline{\varepsilon_T}^{i}_{viscous} \quad i = 1:4 \tag{4}$$

By analysing the results obtained in Fig. 7a and b it is possible to note that even though the applied load is below the apparent elastic threshold, viscous strains are taking place in both cases: tensile and shear. Another important aspect is that the viscous behaviour is not linear and it depends on the applied load. Moreover, viscous strain observed in shear behaviour is more important than the viscous displacement measured in tensile.

Due to these observations, the non-linear viscoelastic model developed by Badulescu et al. [11] was adopted and modified to describe the creep behaviour. The changes made in the model will be presented in the next section.

3. Modelling the mechanical behaviour of an epoxy adhesive in a bonded joint

3.1. Numerical procedure

In order to describe the mechanical behaviour of the adhesive in the bonded joint it is necessary to develop a realistic FEM model. The model has been developed to be implemented in 3D models that are subjected to complex 3D stress states. In this case, a 2D plane stress analysis would have been sufficient but we were constrained to use a model with one element in the width direction to have all the components of the stress and strain tensors. This approach implies an important reduction in terms of computation time. As has been shown in other studies by Cognard et al. [21], the stress state in the adhesive is not uniform, therefore an inverse identification method will be used in order to identify the parameters of the constitutive law.

Because of the geometry of the sample, only half of the sample has been modelled. An anti-symmetry boundary condition has been applied in the middle of the bonded joint. The load is computed in the loading point ”A” (Fig. 8a) and the relative displacements are calculated at the point located in the same zone as that the one used for the experimental characterization. Depending on the direction of the applied force, it is possible to obtain the expected stress state (tensile or shear).

The geometry used for the beaks (Fig. 8b) allows the reduction of the stress concentration near the free edge. As can be observed in Fig. 8a, the dimensions of the mesh have been decreased near the beaks. A convergence study has been performed in order to determine the right number of elements. The mechanical behaviour of the substrates is assumed to be linear elastic with a Young's modulus equal to 70 *GPa* and a Poisson's ratio of 0.34. These are the mechanical characteristics of the aluminium alloy used for the substrates.

The bonded joint has a thickness of 0.4 *mm*. Eight elements have been used to model half of the joint thickness because of the symmetry of the sample. This number has been chosen after a convergence study in order to obtain good results in terms of time and precision. The mechanical behaviour of the adhesives is described using the constitutive law presented in the next section of this paper.

3.2. Constitutive law

The final constitutive law used to describe the mechanical behaviour of the adhesive in the bonded joint is based on a viscoelastic-

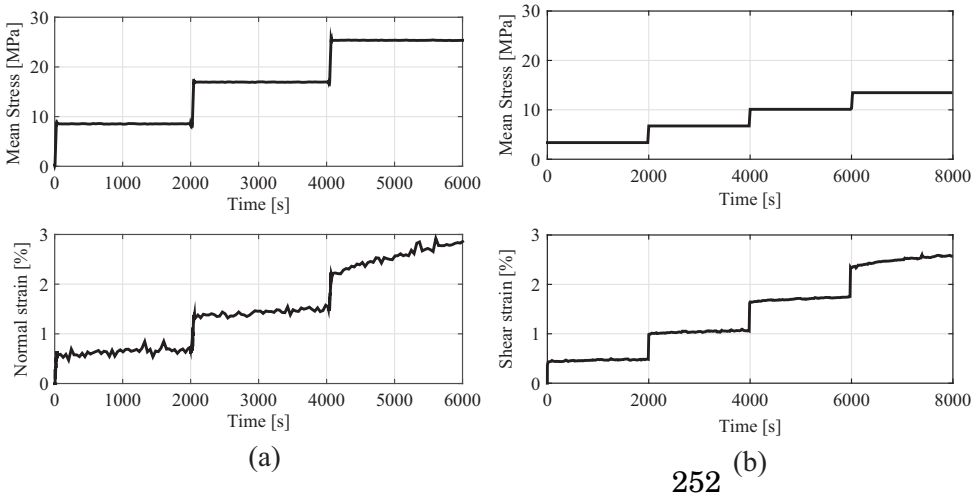


Fig. 6. Multi-level creep tests: tensile (a) and shear (b).

252

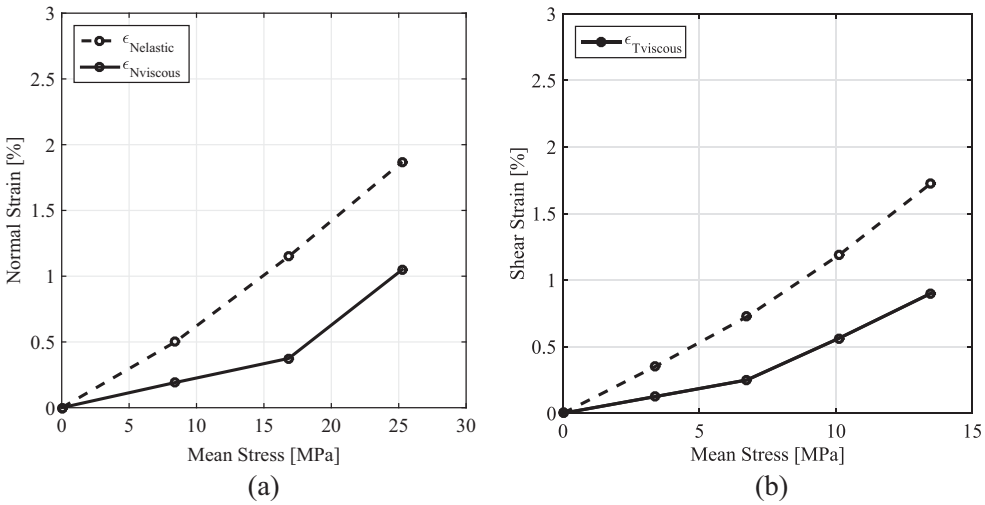


Fig. 7. Evolution of the viscous and elastic displacements at the end of each creep level: (a) tensile and (b) shear.

viscoplastic model. As will be shown in the next subsections, the viscoelastic part of the model was not sufficient to describe accurately the mechanical behaviour of the adhesive.

The development of the behaviour law will be presented step by step, starting with a method of identification for the elastic parameters. The viscoelastic part is then described and all the parameters presented. Finally, the viscoplastic part is added to the model in order to obtain the constitutive law.

It is important to note that in each case, the total strain $\underline{\varepsilon}$ is written as the sum of the different strains: elastic strain $\underline{\varepsilon_{el}}$, viscoelastic strain $\underline{\varepsilon_{ve}}$, and viscoplastic $\underline{\varepsilon_{vp}}$ (*Eq.* 5).

The stress tensor $\underline{\sigma}$ will then be written as in *Eq.* (6), where $\overline{\overline{C}}$ represents the instantaneous elastic stiffness.

$$\underline{\varepsilon} = \underline{\varepsilon_{el}} + \underline{\varepsilon_{ve}} + \underline{\varepsilon_{vp}} \tag{5}$$

$$\underline{\sigma} = \underline{\underline{C}} : (\underline{\varepsilon} - \underline{\varepsilon_{ve}} - \underline{\varepsilon_{vp}}) \tag{6}$$

3.2.1. Identification of the elastic parameters

The elastic parameters of the model (*Young's modulus E* and *Poisson's ratio* ν) are the first parameters that have to be identified. It is important to note that in this step the viscoelasticity and the viscoplasticity have no influence on the mechanical response of the model. The experimental curves (load vs displacement), obtained in monotonic tensile and shear Arcan tests, are used to determine an experimental elastic stiffness (*Eqs.* 7 and 8) using the measured load (F) and displacements (ND and TD).

$$K_N = \frac{F}{ND} \tag{7}$$

$$K_T = \frac{F}{TD} \tag{8}$$

In parallel, using the finite element model, a series of simulations are made using different couples of (E, ν). The range of *Young's Modulus* is chosen between 500 *MPa* and 6000 *MPa* (with a step of 100 *MPa*), and the Poisson's ratio between 0.2 and 0.45 (with a step of 0.01). These are classical values that can be found in the literature for this kind of adhesive. The numerical stiffness values obtained for each couple in both cases (tensile and shear) are compared with the experimental ones.

At the end of each simulation an error is calculated between the numerical and the experimental stiffness. This error is represented in Fig. 9*a* for the tensile loading and in Fig. 9*b* for the shear loading case. The shadowed zone in those figures represents the couples (E, ν) that have a minimum error compared to the experimental results. In Fig. 9*c* the couples with the minimal error are superposed in order to find the best couples that fit in both cases (tensile and shear loading). In Table 1 can be found the obtained values for the elastic parameters.

3.2.2. Modified viscoelastic spectral model

In a first step, the viscoelastic spectral model has been chosen to model the viscous behaviour of the adhesive. This model has been developed by Maire et al. [23] to describe the non-linear behaviour of polymer matrix composites.

In this model, the total strain $\underline{\varepsilon}$ is equal to the sum of the elastic strain $\underline{\varepsilon_{el}}$ and the viscous strain $\underline{\varepsilon_{ve}}$, *Eq.* (9). The mechanical behaviour of

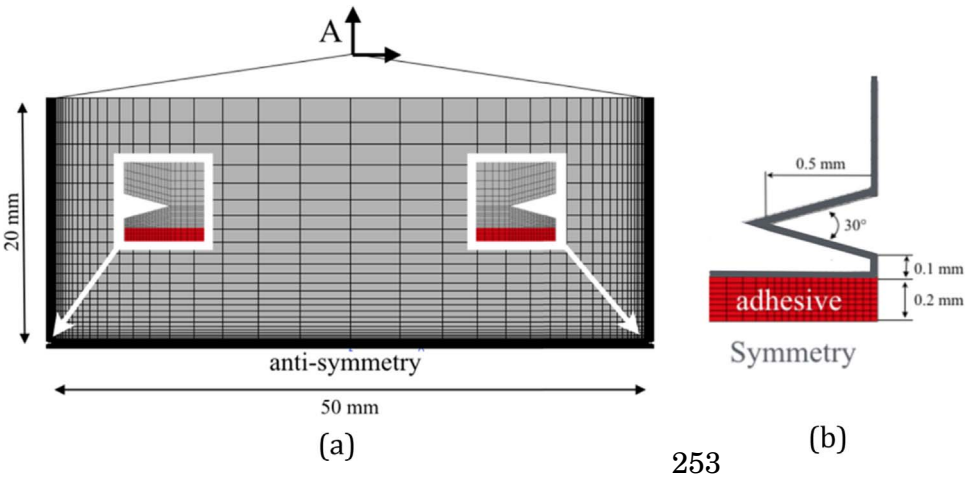


Fig. 8. Finite element model (FEM) of the assembly: (a) the geometry used to model the substrate and the bonded joint, (b) geometry of the beaks.

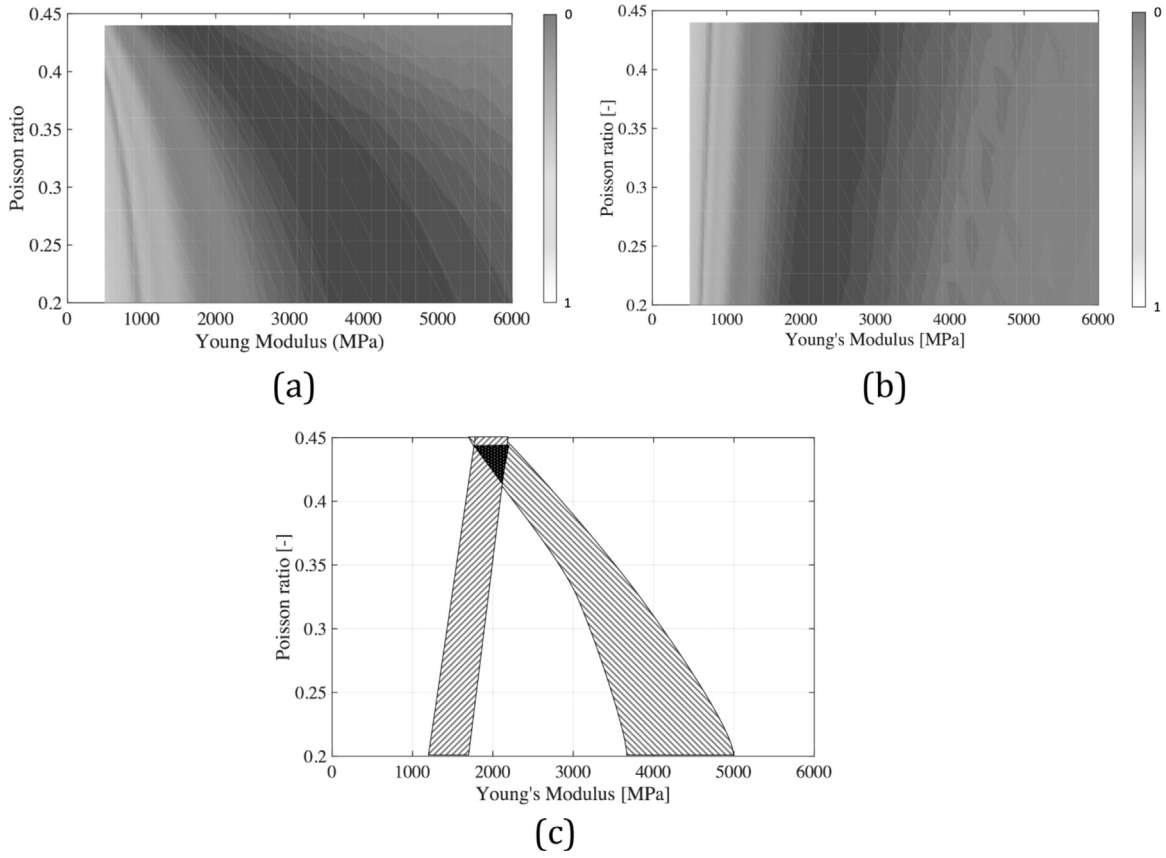


Fig. 9. Calculated error obtained for different couples of (E, ν) in (a) tensile and (b) shear behaviour. (c) Intersection of the best couples (E, ν).

Table 1
Elastic parameters.

Parameters:	E	ν
Units	MPa	[-]
Value	2000 ± 50	0.41 ± 0.01

the adhesive written in the referential of the bonded joint is the following: *Eq.* (10); where $\underline{\sigma}$ is the stress tensor, $\underline{\underline{C}}$ is the elastic stiffness.

$$\underline{\varepsilon} = \underline{\varepsilon_{el}} + \underline{\varepsilon_{ve}} \tag{9}$$

$$\underline{\sigma} = \underline{\underline{C}} : (\underline{\varepsilon} - \underline{\varepsilon_{ve}}) \tag{10}$$

The spectral viscoelastic model describes the viscoelastic strain $\underline{\varepsilon_{ve}}$ as the sum of the strains of a fixed number n_t of viscous mechanisms $\underline{\xi_i}$. The presented results are obtained with a number of $n_t = 20$ mechanisms. Each of these mechanisms is defined by a relaxation time τ_i, a weight μ_i in the total viscous strain and the viscoelastic compliance $\underline{\underline{S_R}}$, see *Eq.* (11).

$$\dot{\varepsilon}_{ve} = \sum_i^{n_t} \dot{\underline{\xi}}_i \quad \dot{\underline{\xi}}_i = \frac{1}{\tau_i}(\mu_i \, \underline{\underline{S_R}} : \sigma - \underline{\xi}_i) \tag{11}$$

The relaxation times are defined as in *Eq.* (12) where $n_i \in [n_1, n_2]$ is a value situated between two limits that depend on the material. In the case of an epoxy material, $n_1 = -20$ and $n_2 = 30$. This means that the characteristic times are situated between $10^{-9}\,s$ and $10^{13}\,s$. The mechanisms with high relaxation times have low weight in this case and they are not activated. By decreasing the upper limit and keeping the same number of viscous mechanism, it would be possible to increase the accuracy of the model but it wouldn't be possible to predict the creep behaviour for very long periods of time.

$$\tau_i = exp\,(n_i) \tag{12}$$

$$\overline{\mu_i} = \frac{1}{n_0\sqrt{\pi}}\, exp\left(-\left(\frac{n_i - n_c}{n_0}\right)^2\right) \quad \text{with} \quad \mu_i = \frac{\overline{\mu_i}}{\sum_i^{n_t} \overline{\mu_i}} \tag{13}$$

The weight of each elementary viscous strain depends on two parameters, n_0 and n_c which are introduced in *Eq.* (13). They have to be identified using the creep tests.

These two quantities, the relaxation time and the weight, define the so called spectrum of the model. The form of this spectrum is defined by two parameters n_0 and n_c. Each of the points in Fig. 10 represents the relaxation time and the weight of a viscous elementary mechanism.

The term S_R in *Eq.* (11) represents the viscoelastic compliance. This is a fourth order tensor that has been modified from the previous version of the viscoelastic spectral model [11]. Observing the results obtained in Fig. 7, it is possible to note that the adhesive mechanical

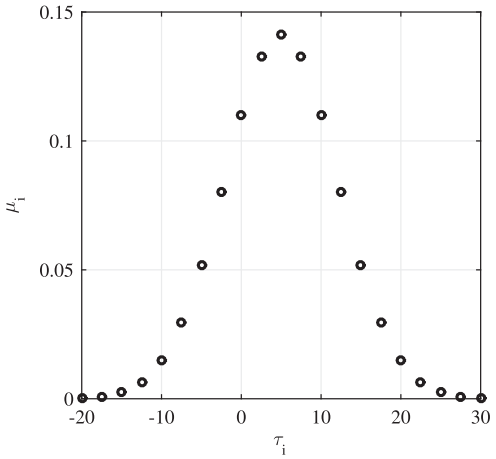


Fig. 10. Spectrum definition.

behaviour depends on the loading conditions. In shear loading, the viscous displacements are more important than in tensile loading. Moreover, a non-linear evolution of the viscous behaviour can be seen in the two cases. These observations led to the next equation representing the viscoelastic compliance (*Eq.* 14).

$$\underline{\underline{S_R}} = \frac{1}{(1-d_H)a_H}\underline{\underline{H_H}} + \frac{1}{(1-d_D)a_D}\underline{\underline{H_D}} \tag{14}$$

The $S_{\underline{R}}$ tensor is divided into two parts by the tensors H_H and H_D which allow the hydrostatic and the deviatoric mechanical behaviour to be defined. The I and I are the 2nd and 4th degree identity tensors respectively.

$$\underline{\underline{H_H}} = \frac{1}{3}\underline{I} \otimes \underline{I} \quad \underline{\underline{H_D}} = \underline{\underline{I}} - \underline{\underline{H_H}} \tag{15}$$

Also, the terms a_H and a_D in *Eq.* (14) define the viscosity in the hydrostatic and deviatoric directions. These two parameters need to be identified. The non-linearity is introduced using the variables d_H and d_D *Eq.* (16) which depend, each of them, on three parameters that need to be identified. The terms y_D° and y_H° are the threshold of the non-linear behaviour of the viscosity and y_D^{c} and y_H^{c} define the kinetics.

$$d_H = d_H^{max}\left(1 - exp\left(\frac{-\langle y_H - y_H^0\rangle}{y_H^C}\right)\right) \quad d_D = d_D^{max}\left(1 - exp\left(\frac{-\langle y_D - y_D^0\rangle}{y_D^C}\right)\right) \tag{16}$$

The internal forces of the model are y_H and y_D, *Eq.* (17). These depend on the hydrostatic and deviatoric stress tensors.

$$y_H = \frac{1}{2a_H}(\underline{\sigma} : \underline{\underline{H_H}} : \underline{\sigma}) \quad y_D = \frac{1}{2a_D}(\underline{\sigma} : \underline{\underline{H_D}} : \underline{\sigma}) \tag{17}$$

This modified viscoelastic spectral model has a total of 10 parameters that need to be identified (Table 2).

3.2.3. Identification of viscoelastic parameters

The viscoelastic parameters of the model only need two experimental multi-level creep tests in order to identify them (in two loading directions: tensile and shear). The hydrostatic parameters are identified using the tensile multi-level creep test shown in Fig. 6a. In the case of the deviatoric parameters, the results obtained in Fig. 6b will be used for identification. Because the method of identification is the same in both cases, in the next section, it will be applied only for the deviatoric parameters (shear loading).

3.2.3.1. Identification of the spectrum's parameters: n_0, n_c. The two parameters that define the spectrum are identified using the viscous displacements measured for each creep level. For this, the isochronism principle of the spectral viscoelastic model is used. In order to apply this principle, each creep level should have the same duration. The viscous displacements are normalized using *Eq.* (18), where j represents the number of the creep level, $j \in \{1,2,3,4\}$ because of the four shear creep levels (Fig. 6b). In the same equation, t_{begin}^{j} is the time at the beginning of the j^{th} level and t_{end}^{j} is the time at the end of the same level. It is also important to mention that the normalized creep curves are not a function of the applied load.

$$TD^{j}_{viscous_{normalized}} = \frac{DT^{j}_{viscous}(t) - DT^{j}_{viscous}(t^{j}_{begin})}{DT^{j}_{viscous}(t^{j}_{end}) - DT^{j}_{viscous}(t^{j}_{begin})} \tag{18}$$

In Fig. 11b, the normalized viscous displacement can be observed for the four creep levels in Fig. 11a. The normalized time for each creep level has been calculated using *Eq.* (19).

$$T^{j}_{norm} = \frac{t - t^{j}_{begin}}{t^{j}_{end} - t^{j}_{begin}} \tag{19}$$

It can be observed in Fig. 11b that the isochronism principle is respected for the four creep levels. In this case, these curves can be superposed to a master curve that is a function of the spectrum. The spectrum is then defined by only two parameters that need to be identified: n_0 and n_c.

Using the finite element model presented in Section 3.1, it is possible to apply an inverse identification to fit the obtained master curve. For this, a numerical simulation of the first creep level is made. The elastic parameters applied to the model are those identified using the monotonic tests.

$$Error = \sum_{1}^{m=200}\left(DT^{FE}_{viscous_{normalized}} - DT^{EXP}_{viscous_{normalized}}\right) \tag{20}$$

Couples of parameters (n_0, n_c) have been generated using *Matlab* software: $n_c \in [1:10]$ and $n_0 \in [1:20]$ - a total number of 200 combinations. For each couple, a numerical simulation is made. After normalizing the time and the viscous displacements obtained, the results are compared with the master curve created from the experimental curves (Fig. 12a). In this stage of the identification process, by normalising the time and the viscous displacement the influence of the rest of the parameters is not taken into account. This process is made automatically using a Python routine.

For each couple an error is calculated using *Eq.* (20). The couple with the closest error to zero is then used. The results are then normalized and they can be represented in an error map, as in Fig. 12b. The best couples are those that minimize this error and they have a low influence on the final results.

3.2.3.2. Identification of the linear viscoelastic parameters: a_H, a_D. Once the spectrum is defined, it is now possible to identify the parameters that correspond to the linear viscosity: a_H, a_D. These parameters are identified on the first creep level (corresponding to the linear viscoelastic behaviour) of the creep tests performed in tensile (a_H) and in shear (a_D), using the inverse identification method and the numerical model. It is important to note that in this step of the identification, the non linear part of the model is not considered. A very high value is fixed to the y_H and y_D parameters. The results are shown in Fig. 13a,b (curve corresponding to the visco-linear behaviour).

The identification has been made for the two cases of loading (tensile and shear) using the experimental results obtained in the multi-level creep tests.

3.2.3.3. Identification of the non-linear viscoelastic parameters: d_D^{max}, y_D°, y_D^{c}, y_H°, y_H^{c}, d_H^{max}. Examining Fig. 13b, it can be noted that a linear viscoelastic model is not sufficient to describe correctly the behaviour of the adhesive in the multi-level creep tests. Therefore, the variables d_H and d_D were introduced in the definition of the compliance tensor.

The threshold between the linear and non-linear viscosity is, in this

Table 2
Identified viscoelastic parameters.

	Spectrum		Hydrostatic				Deviatoric			
Parameters	n_0	n_c	a_H	d_H^{max}	y_H^0	y_H^C	a_D	d_D^{max}	y_D^0	y_D^C
Unit	–	–	MPa^{-1}	–	–	–	MPa^{-1}	–	–	–
Value	5	10	4000	0.9	0.03	0.015	1500	0.6	0.01	0.02

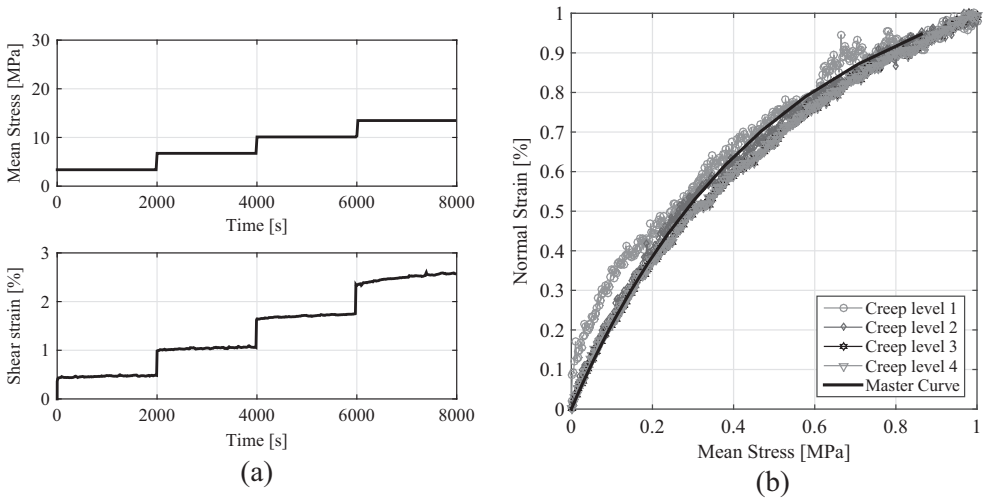


Fig. 11. (a) Multi-level shear creep test ($\gamma = 90^o$) used to identify the deviatoric parameters of the viscoelastic model, (b) Isochronism principle.

case, at the end of the second creep level (Fig. 13b). Using the FE model, it is possible to evaluate the internal force y_D in the middle of the bonded joint where its value is maximal. This value will correspond to the threshold y_D^c. The same approach is applied to find this variable in the case of a tensile creep test.

The last parameters of the model y_D^c and d_D^{max} and the hydrostatic equivalents are identified using the last two creep levels. These influence the kinetics of the displacements for the last creep levels. It can be seen in Fig. 13b that using the non-linear viscosity it is possible to have a good fit between the experimental curve and the numerical results.

Once the model is validated using the creep tests, it is now possible to evaluate if the model is able to predict the monotonic behaviour.

Fig. 14 represents the response of the identified viscoelastic model when simulating a monotonic shear or tensile test with the identified parameters (Table 2). These results are showing that even though the model is describing accurately the creep behaviour, it is not sufficient to predict the mechanical behaviour in monotonic loading. A solution to solve this problem would be to use an elasto-viscoplastic model. But the use of this kind of model would involve setting the elastic limit to a very low value to be able to model the creep behaviour for low loading levels. Thus, in order to predict the mechanical behaviour at high loading-levels, a viscoplastic part has been added in the present constitutive law.

3.3. Viscoelastic-viscoplastic behaviour

In the last section, it has been shown that the viscoelastic model is not sufficient to describe correctly the mechanical behaviour of this adhesive. In order to be able to predict the monotonic behaviour, a viscoplastic part has been added to the model. In this case, the total strain $\underline{\varepsilon}$ will be composed of the elastic strain $\underline{\varepsilon_{el}}$, the viscoelastic strain $\underline{\varepsilon_{ve}}$ and the viscoplastic strain ε_{vp}, as was shown in *Eq.* (5).

The viscoplastic part of the model is inspired by the model proposed by *Mahnken*-Schlimmer et al. [15]. In this case, the yield surface is described using a linear relation (*Eq.* 22), between *von Mises* and *hydrostatic* stresses. Other forms of this model could be found in literature [24,25]. This is a simple model that has a few parameters to be identified as it will be shown in the next section.

3.3.1. Constitutive law for viscoplastic behaviour

The stress tensor $\underline{\sigma}$ is decomposed into a deviatoric part $\underline{\sigma}^D$ and a hydrostatic part $\sigma^H\underline{I}$. The *von Mises* stress (σ^M) is then calculated using the *Eq.* (21).

$$\sigma^M = \sqrt{\frac{3}{2}\underline{\sigma}^D : \underline{\sigma}^D} \quad \text{where} \quad \underline{\sigma}^D = \underline{\sigma} - \underline{\sigma}^H\,\underline{I} \text{ and } \underline{\sigma}^H = \frac{1}{3}trace\,(\underline{\sigma}) \tag{21}$$

The yield surface of the viscoplastic behaviour is determined using the *Eq.* (22), where.

σ^M represents the *von Mises* stress tensor, σ_H is the hydrostatic component and R is the hardening parameter. a_1 is a parameter that defines the shape of the yield function (the slope) in the *von Mises* - *hydrostatic pressure plane*.

$$f = \sigma^M + a_1\sigma^H - R \tag{22}$$

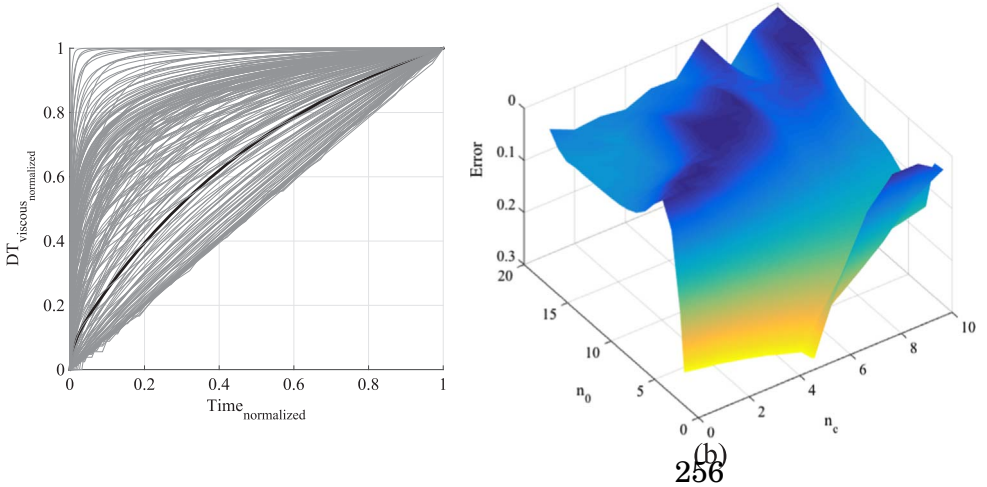


Fig. 12. (a) Normalized viscous displacement for different couples(n_0,n_c) (b) Error calculated for different couples (n_0,n_c).

256

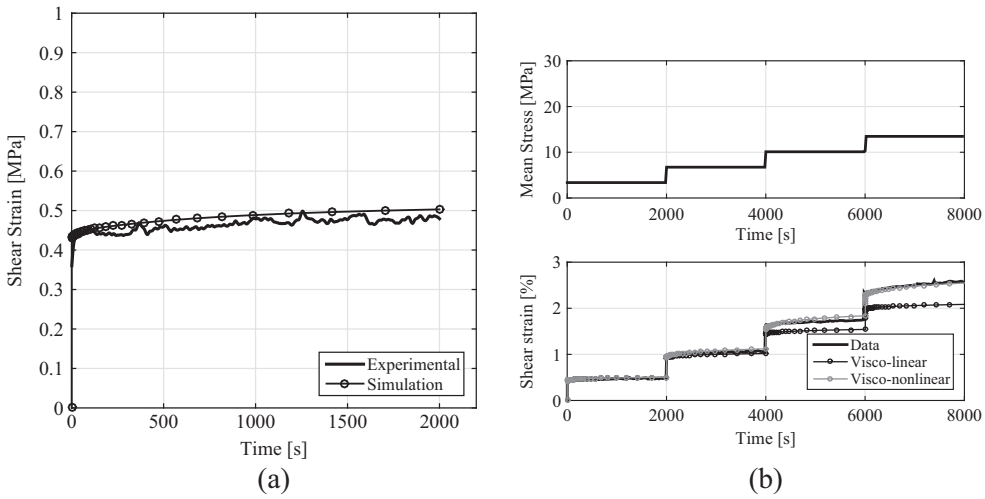


Fig. 13. (a) First level of the shear creep test (b) Identification of the viscoelastic model.

The *Eq.* (23) represents the evolution of the hardening parameter R. The parameters H, Q, b influence the monotonic non-linear behaviour of the adhesive and are identified from a pure shear test using the inverse identification method. It is important to note that when those parameters are identified, the viscoelastic part of the model is activated. R_0 is the elastic threshold.

$$R = R_0 + He_{vcum} + Q(1 - exp(-be_{vcum})) \tag{23}$$

The hardening is driven by the internal strain variable e_{vcum} defined in *Eq.* (24). The parameters K and n are identified after all the other parameters of the model are fixed. Because they depend on the strain rate, their identification needs a shear test at a different strain rate.

$$\dot{e}_{vcum} = \frac{3}{2}\left(\frac{\langle f \rangle}{K}\right)^n \tag{24}$$

The viscoplastic strain rate can finally be written as in *Eq.* (25). In this particular case, in order to reduce the number of parameters, an associative model has been developed, which means that the flow rule is described using the same function as the yield surface.
[15].

$$\underline{\dot{\varepsilon}}_{vp} = \dot{e}_{vcum}\frac{\partial f}{\partial \underline{\sigma}} \tag{25}$$

3.3.2. Identification of viscoplastic parameters using monotonic tests

The viscoplastic parameters of the model are also determined using an inverse identification method. It is important to note that the viscoelastic part is enabled during this operation.

3.3.2.1. Identification of the elastic limit: R_0, a_1. The elastic threshold R_0 is calculated at the end of the linear part of the mechanical behaviour. Because of the definition of the yield surface (Eq. 22), only two monotonic tests, performed in tensile ($\gamma = 0^o$) and shear ($\gamma = 90^o$) loading, are needed to obtain the experimental yield surface (see the points in Fig. 15a). These values of the elastic threshold are then used to perform a numerical simulation of the two loading conditions. For each case, the stress tensor in the middle of the adhesive joint, is plotted in a von Mises *vs* hydrostatic pressure plane [24]. It is clear that for $\gamma = 90^o$, no hydrostatic pressure is obtained in the middle of the joint. However, for tensile behaviour, due to the complex state of the stress in the bonded joint, the same point, in the middle of the joint is characterised by a hydrostatic and a deviatoric stress. The yield function is then analytically identified. The slope of this function allows the determination of the a_1 parameter (Fig. 15a).

3.3.2.2. Identification of the hardening: H, Q, b. The hardening parameters are also identified using the inverse identification method. The $0.2kN/s$ monotonic shear test (Fig. 15b) is used for the parameters identification. An optimization between the experimental curve and the numerical response of the finite element model has been performed in order to minimize the error between the two behaviours.

It is important to notice that since the model is not able to predict

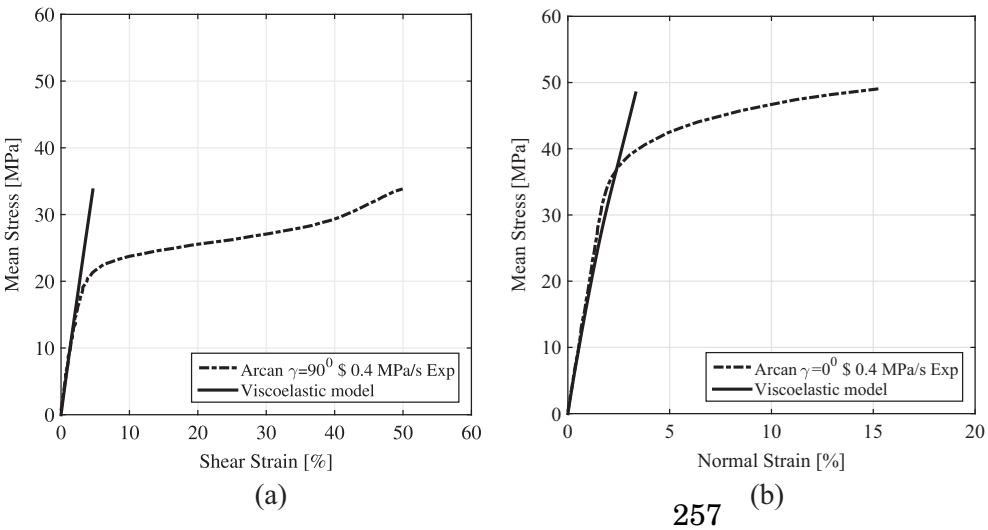


Fig. 14. Viscoelastic model prediction in monotonic (a) shear and (b) tensile tests.

257

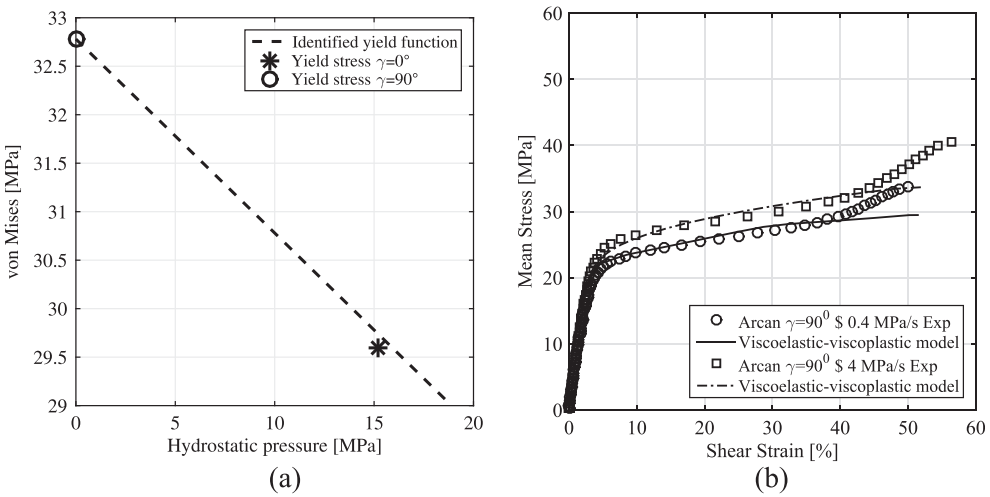


Fig. 15. (a) Experimental and numerical yield function (b) Identification of the viscoplastic parameters.

Table 3
Identified viscoplastic parameters.

Parameters	R_0	a_1	H	Q	b	n	K
Unit	MPa	–	MPa	MPa	–	–	–
Value	32	0.2	2	2.5	45	3.5	10

the hardening observed at the end, the last part of the curves was not considered during the identification process. This complex phenomenon can be explained by the presence of porosities or charges and to be able to model it, other components should be added to the present version of the model.

3.3.2.3. Identification of the viscous parameters: K, n. Once the hardening parameters have been determined, the couple (*K*, *n*) is identified. Because they depend on the strain rate, a second monotonic shear test (2 *kN/s*) is used for the identification (Fig. 15b).

It is important to note that in order to identify the viscoplastic behaviour, two monotonic shear tests have been entirely used. The yield surface has been determined using the elastic parts of tensile and combined tensile/shear tests. These tests can be used to validate the non-linear behaviour. The identified parameters can be found in Table 3.

3.4. Validation of the viscoelastic-viscoplastic model

The model validation is based on the comparison between experimental results and numerical predictions. In order to do this, experimental data that have not been used in the identification procedure are analysed.

The first test used to validate the model is a combined tensile/shear monotonic test. The positioning of the Arcan device can be observed in Fig. 1a, where $\gamma = 45°$. The load and the displacements are decomposed into a normal component and a tangential one.

The prediction of the model and the experimental curves are compared in Fig. 16a,b. As it can be observed, the obtained results are very satisfying. Moreover, this test was also used to validate the yield function. The elastic threshold for this type of test was calculated as it has been presented in Section 3.3.2.a). The representation of the yield stress for the combined tensile/shear test ($\gamma = 45^o$) in Fig. 17a indicates that the yield function is correctly predicting the evolution of the yield stress.

The prediction of the strain rate effects was validated using a monotonic tensile test at 2*kN/s* (Fig. 17b). The elastic modulus does not depend on the loading rate for this type of adhesive, instead, the failure load is increasing. It can be observed that by multiplying the loading rate by ten, the failure load is increased by about ten percent. This change in the mechanical behaviour of the adhesive can be predicted by the presented model.

For both tensile and shear creep behaviour, multi-level recovery

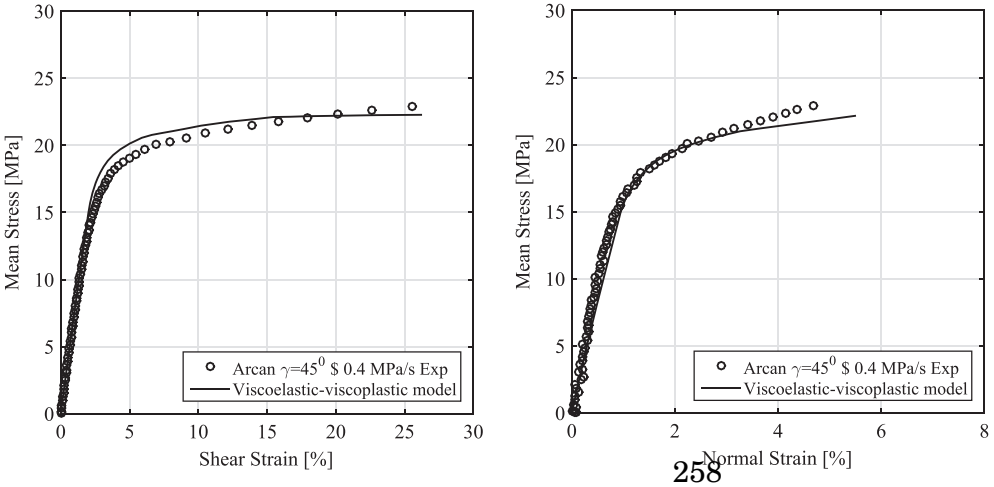


Fig. 16. Viscoelastic-viscoplastic model validation in combined tensile/shear test.

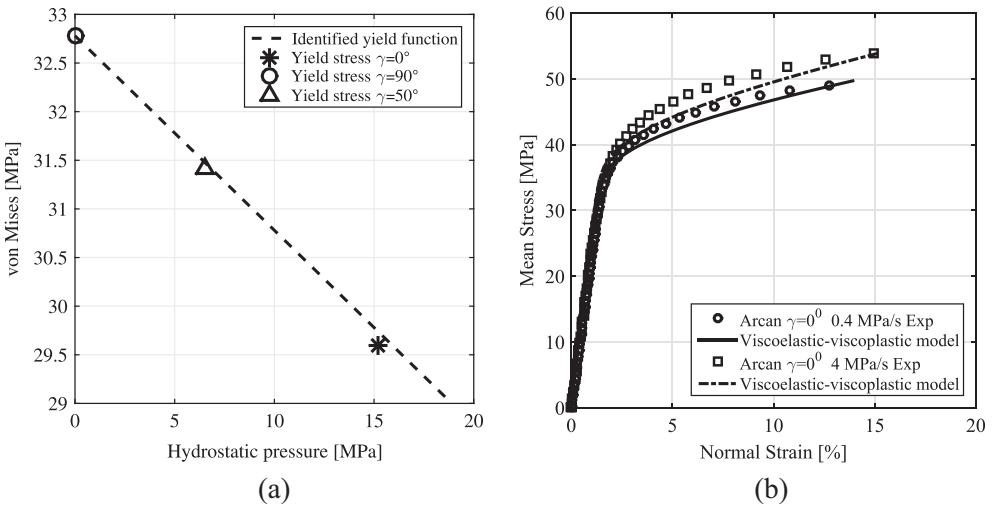


Fig. 17. (a) Validation of the yield function; (b) Strain rate effect validation in monotonic tensile tests.

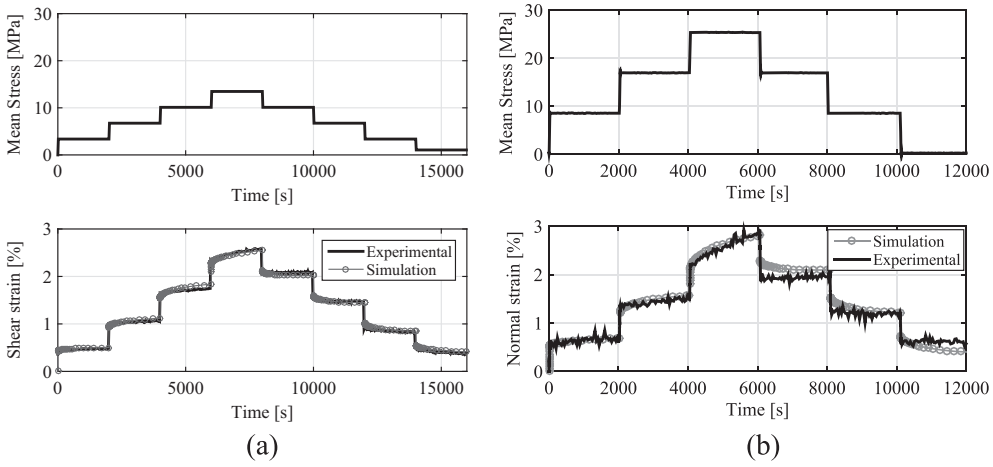


Fig. 18. Model validation in multi-level creep/relaxation (a) shear and (b) tensile tests.

tests were also used to validate the model. As it can be observed in Fig. 18, in the two cases, even though the model has been identified on the creep levels it can predict the behaviour of the recovery levels. An interesting point that should be mentioned is that looking at the last recovery level in shear(Fig. 18a) the viscoelastic strain is not totally recovered when completely unloading the bonded joint. The prediction of this recovery level is still very accurate. Regarding the tensile recovery levels(Fig. 18b), the model is a little bit less accurate but this can be explained by the very small displacements that are measured.

4. Conclusion and perspectives

This paper presents an original development of a viscoelastic-viscoplastic model capable of describing the mechanical behaviour of an adhesive in a bonded joint. As it can be seen in literature, the mechanical behaviour of some types of adhesives can be modeled only by using a viscoelastic constitutive law. In the case studied here, viscoelasticity was not sufficient to describe the important non-linearity in the behaviour of the studied adhesive. Moreover, the viscoelastic spectral model, initially developed to describe the composites matrix mechanical behaviour and then adapted by Badulescu et al. [11] for adhesives, has been modified in order to take into account the effect of the von Mises and the hydrostatic stress as proposed by Carrere et al. [26].

For identification and validation of the viscoelastic part of the model, only one multilevel creep recovery test is needed in two directions (tensile and shear). The loading of each level should be below the elastic threshold. For a better understanding of the timedependent behaviour, long creep levels are recommended. The creep levels are only used for identification of the model parameters. The validation of the model is made afterwards using the recovery levels of the same sample.

Once the viscoelastic part of the model is defined, the viscoplastic part of the model can be identified. The pseudo yield surface is determined using monotonic tests in three directions ($\gamma = 0°$, $\gamma = 45^0$, $\gamma = 90^0$). For the identification of the loading rate dependent parameters K and n, a second monotonic shear test ($\gamma = 90^0$), performed at another loading rate was needed.

Even though the proposed model has an important number of parameters (10 for the viscoelastic part and 7 for viscoplasticity), only two creep tests and three monotonic tests are needed to identify all these parameters. It is also important to highlight the method of identification which is simple to implement. Each parameter is determined step by step using the inverse identification method.

For further investigations, the sensitivity of each parameter of the model can be studied. In order to quantify it, first, the relevant tests should be defined for each type of parameters (viscoelastic or viscoplastic). In a second phase, an approach should be developed to calculate an error with respect to the global mechanical response after changing a specific parameter with a certain ratio.

As from a qualitative point of view, it can be confirmed that the viscoelastic parameters (a_i, d_i^{max} ,y_i^0, y_i^C where $i = \{H,D\}$) have a great influence in creep behaviour but they don't seem to influence that much the global mechanical response in monotonic tests. The spectrum parameters (n_0, n_c) characterize the form of the creep behaviour but

they will not impact the predicted strains. Viscoplastic parameters have great influence in both shear and tensile monotonic behaviour but they will not influence the creep behaviour as long as the applied load is be below the elastic limit.

Results show that a good agreement with the experimental curves is obtained. To test its capability, it would be interesting to test the prediction of the model in more realistic joints such as single lap joints. In further investigations, the model can be used to predict the cyclic mechanical behaviour, which is very important when considering fatigue lifetime prediction. Another aspect is to identify the evolution of the model parameters as a function of water ageing of the material, in order to predict the influence of water on the mechanical behaviour.

References

[1] Irisarri FX, Laurin F, Carrere N, Maire J-F. Progressive damage and failure of mechanically fastened joints in CFRP laminates – part i: refined finite element modelling of single-fastener joints. Compos Struct 2012;94(8):2269–77.

[2] Ochsner A, da Silva LFM, Adams RD. Handbook of adhesion technology. Springer; 2011.

[3] Papanicolaou GC, Charitidis P, Mouzakis DE, Karachalios E, Jiga G, Portan DV. Experimental and numerical investigation of balanced boron/epoxy single lap joints subjected to salt spray aging. Int J Adhes Adhes 2016;68:9–18.

[4] Cognard J-Y, Cr´eac'hcadec R, Sohier L, Davies P. Analysis of the nonlinear behaviour of adhesives in bonded assemblies—comparison of TAST and arcan tests. Int J Adhes Adhes 2008;28(8):393–404.

[5] Cognard JY, Davies P, Gineste B, Sohier L. Development of an improved adhesive test method for composite assembly design. Compos Sci Technol 2005;65(3):359–68.

[6] da Silva LFM, Ochsner A. Modeling of adhesively bonded joints. Springer; 2008.

[7] Iwamoto T, Nagai T, Sawa T. Experimental and computational investigations on strain rate sensitivity and deformation behaviour of bulk materials made of epoxy resin structural adhesive. Int J. Solids Struct 2010;47(2):175–85.

[8] Yu XX, Crocombe AD, Richardson G. Material modelling for rate-dependent adhesives. Int J Adhes Adhes 2001;21(3):197–210.

[9] Harris JA, Adams RD. An assessment of the impact performance of bonded joints for use in high energy absorbing structures. Proc Inst Mech Eng, Part C: J Mech Eng Sci 1985;199(2):121–31.

[10] da Silva LFM, Adams RD, Gibbs M. Manufacture of adhesive joints and bulk specimens with high-temperature adhesives. Int J Adhes Adhes 2004;24(1):69–83.

[11] Badulescu C, Germain C, Cognard J-Y, Carrere N. Characterization and modelling of the viscous behaviour of adhesives using the modified arcan device. J Adhes Sci Technol 2015;29(5):443–61.

[12] Crocombe AD. Modelling and predicting the effects of test speed on the strength of joints made with FM73 adhesive. Int J Adhes Adhes 1995;15(1):21–7.

[13] Majda P, Skrodzewicz J. A modified creep model of epoxy adhesive at ambient temperature. Int J Adhes Adhes 2009;29(4):396–404.

[14] Dean GD, McCartney LN, Mera R, Urquhart JM. Modeling nonlinear viscoelasticity in polymers for design using finite element analysis. Polym Eng Sci 2011;51(11):2210–9.

[15] Mahnken R, Schlimmer M. Simulation of strength difference in elasto-plasticity for adhesive materials. Int J Numer Methods Eng 2005;63(10):1461–77.

[16] Jousset P, Rachik M. Implementation, identification and validation of an elasto-plastic-damage model for the finite element simulation of structural bonded joints. Int J Adhes Adhes 2014;50:107–18.

[17] Chiu WK, Jones R. Unified constitutive model for thermoset adhesive, FM73. Int J Adhes Adhes 1995;15(3):131–6.

[18] Pandey PC, Shankaragouda H, Singh Arbind Kr. Nonlinear analysis of adhesively bonded lap joints considering viscoplasticity in adhesives. Comput Struct 1999;70(4):387–413.

[19] Zgoul M, Crocombe AD. Numerical modelling of lap joints bonded with a rate-dependent adhesive. Int J Adhes Adhes 2004;24(4):355–66.

[20] Badulescu Claudiu, Cognard Jean-Yves, Cr´eac'hcadec Romain, Vedrine P. Analysis of the low temperature-dependent behaviour of a ductile adhesive under monotonic tensile/compression–shear loads. Int J Adhes Adhes 2012;36:56–64.

[21] Cognard J-Y, Sohier L, Davies P. A modified arcan test to analyze the behaviour of composites and their assemblies under out-of-plane loadings. Compos Part A: Appl Sci Manuf 2011;42(1):111–21.

[22] Cognard J-Y. Numerical analysis of edge effects in adhesively-bonded assemblies application to the determination of the adhesive behaviour. Comput Struct 2008;86(17):1704–17.

[23] Laurin F, Carrere N, Maire J-F. A multiscale progressive failure approach for composite laminates based on thermodynamical viscoelastic and damage models. Compos Part A: Appl Sci Manuf 2007;38(1):198–209.

[24] Maurice J, Cognard J-Y, Creac'hcadec R, Davies P, Sohier L, Mahdi S. Characterization and modelling of the 3d elastic–plastic behaviour of an adhesively bonded joint under monotonic tension/compression-shear loads: influence of three cure cycles. J Adhes Sci Technol 2013;27(2):165–81.

[25] Cognard J-Y, Cr´eac'Hcadec R, Maurice J, Davies P, Peleau M, Silva LFM Da. Analysis of the influence of hydrostatic stress on the behaviour of an adhesive in a bonded assembly. J Adhes Sci Technol 2010;24(11):1977–94.

[26] Carrere N, Laurin F, Maire J-F. Micromechanical-based hybrid mesoscopic 3d approach for non-linear progressive failure analysis of composite structures. J Compos Mater 2012;46(19-20):2389–415.

2.7 Etudes en cours et perspectives

Le premier axe porte sur les travaux dédiés à **l'étude des assemblages collés, en particulier l'analyse fine de la génération des défauts et leur influence sur la tenue mécanique du joint**. Il a été démontré à travers plusieurs publications que les premiers pores qui apparaissent dans l'adhésif sont souvent générés pendant de la phase de préparation de la colle (mélange de la résine et du durcisseur). Plus précisément, la résine utilisée pour produire la colle contient des charges (billes de verre, par exemple) qui lors de la phase de mélange peuvent générer de petites bulles. Il a été également démontré que le cycle de polymérisation de l'adhésif peut aussi contribuer à la création de pores augmentant ainsi la fraction volumique globale. Si le cycle de polymérisation est caractérisé par des valeurs élevées de température durant la première rampe (phase de cuisson), on a pu observer que cela engendre d'une part, le grossissement des pores générés par l'opération de mélange, mais également l'apparition d'autres pores. Cette deuxième population est engendrée par l'emprisonnement du gaz dégagé durant la phase de cuisson et qui n'a pas la possibilité de se dissiper, car *i)* soit la viscosité de la colle diminue avec l'augmentation du taux de polymérisation, soit ii) les joints, d'une épaisseur de quelques centaines de µm, sont souvent confinés entre des substrats. Ces deux populations peuvent par ailleurs interagir, au moins en début de polymérisation, donnant naissance à des pores ou des régions poreuses très hétérogènes et caractérisées par une compacité du joint très faible. Il est alors question de comprendre de manière fine ce qui se passe au cours de cette phase de polymérisation. On rappelle également que si la température de polymérisation est élevée, le taux de réticulation peut atteindre des valeurs proches de 100 % assurant ainsi une résistance mécanique élevée. Il semblerait qu'il existe, en fait, une compétition entre le taux de réticulation et le taux de pores. Pour faire simple, une faible température de cuisson conduit à des taux de réticulation réduits et une résistance mécanique moindre avec, en conséquence, un faible taux de pores, et inversement. Une analyse fine de ces aspects méritera d'être menée afin de trouver un cycle de polymérisation qui maximise la résistance mécanique (taux de polymérisation maximale et taux de porosité minimale) tant pour des sollicitations monotones que pour des sollicitations cycliques. De plus, nous avons pu observer que les taux de pores augmentent avec l'épaisseur, du moins pour les adhésifs époxy bi-composantes investigués. Cet aspect mériterait également d'être abordé, notamment pour analyser la nature de la dépendance entre l'épaisseur, le taux de pores et la température de polymérisation.

Un autre point qui mériterait d'être abordé porte sur la mise en place d'une procédure de mesure de champ de déplacement volumique. Cela dit, on peut considérer les pores ou les différents constituants de l'adhésif comme des marqueurs qui serviront à mesurer le champ de déplacement volumique. Évidemment, on peut utiliser la corrélation d'images volumiques, mais cette méthode reste peu adaptée et très lourde en termes de temps de calcul. Ainsi, pour avoir une précision et une résolution plus rapide, on s'appuie sur des méthodes de suivi de marqueurs pouvant être utilisées du moment où leur volume reste quasi constant. Si leur volume ou leur forme géométrique varie dans le temps, des erreurs plus importantes que les quantités induites par le phénomène étudié pourront

apparaître. On prend ici comme exemple le cas d'adhésifs qui sont vieillis par immersion dans de l'eau déionisée. Dans ce cas précis, les pores n'évoluent pas beaucoup au début, mais au fur et à mesure de l'immersion, on peut constater que les pores les plus petits vont se remplir progressivement d'eau, en commençant par celles qui sont les plus proches de la surface de contact entre l'adhésif et l'eau. Ces pores sont susceptibles de ne plus être détectés une fois leur remplissage complète. Dans ce cas, on préfère s'appuyer sur des marqueurs qui n'évoluent pas ou du moins leur modification reste très faible. Les marqueurs qui respectent ce critère dans ce cas de vieillissement sont les billes de verre présentes dans la résine de l'adhésif Araldite 420 A/B. La finalité de l'obtention d'un tel champ de déplacement et par dérivation, le champ de déformation, pourrait alimenter grandement l'investigation du phénomène de gonflement hydrique.

Un deuxième axe d'investigation de mes travaux de recherche porte actuellement sur l'effet du vieillissement à des échelles micrométriques. C'est principalement un travail expérimental qui consiste à mieux appréhender ce qui se passe à l'échelle micrométrique quand l'eau pénètre dans l'adhésif. Nous avons pu constater récemment (thèse d'Andreea TINTATU) que le front d'eau reste difficilement identifiable, ou du moins n'est pas identifiable directement en analysant le niveau de gris des images tomographiques. Toutefois, nous avons pu démontrer que le remplissage de pores peut aider de manière indirecte à la compréhension de l'évolution du front de prise en eau. Si ces éléments ont grandement contribué aux choix des modèles de diffusion adaptés à l'identification de la quantité d'eau qui rentre dans les pores, ce phénomène physique reste pour l'instant indétectable, du moins par la tomographie aux rayons X. Nous avons tout de même identifié une piste d'avancement, en cours d'exploration, pour lever ce verrou scientifique en nous appuyant sur l'évolution du gonflement dans l'adhésif.

L'étude du phénomène de gonflement par des analyses expérimentales représente une autre préoccupation en cours d'investigation, avec l'objectif de pouvoir exprimer de manière quantitative, la dépendance entre la quantité d'eau et la variation du volume produite. À terme, nous souhaitons modéliser finement ce phénomène pour pouvoir ensuite remonter aux contraintes induites dans l'assemblage, dans un premier temps sur une configuration homogène puis sur une configuration plus réaliste intégrant la distribution de défauts et la présence de différentes phases (charges minérales, par exemple). Des modèles à différentes échelles seront nécessaires afin de mieux comprendre l'effet du gonflement sur l'assemblage, de même que l'impact qu'auraient ces contraintes sur le dimensionnement de ces structures sous différentes natures de sollicitation : monotone ou cyclique.

L'absorption et la désorption d'eau, de manière cyclique et en présence ou non d'un chargement mécanique, pourraient apporter des changements significatifs dans la microstructure de l'adhésif (gonflement et rétrécissement périodique) induisant potentiellement un endommagement à long terme de celui-ci. Ces aspects pourront influencer de manière non négligeable la tenue mécanique de l'assemblage. Ces points mériteraient d'être examinés par des analyses tomographiques en se focalisant sur la détection du champ de déformation volumique. Enfin, toutes ces observations évoquées précédemment peuvent grandement aider à l'enrichissement des lois de comportement utilisées dans nos modélisations de l'assemblage, en intégrant dans un premier temps la fraction

globale de pores dans ces adhésifs. Ces modélisations pourront être mieux adaptées dans certains cas (pour les forts taux de porosité en milieu humide par exemple) afin de prédire fidèlement le comportement mécanique de l'adhésif et de l'assemblage. Plus précisément, il serait intéressant de voir comment le taux de remplissage en eau des pores pourrait affecter le comportement mécanique de l'adhésif. Il a également été observé à l'échelle mésoscopique que la présence de pores s'accompagne d'une variation de volume. Si les pores sont remplis d'eau, alors ce comportement sera modifié, avec des conséquences sur l'état de contraintes ainsi obtenu.

Un troisième axe qui est actuellement abordé porte sur la caractérisation des mécanismes d'endommagement dans les joints collés. Toutes les analyses qui sont en cours, traitent principalement des mécanismes associés aux ruptures cohésives et non celles adhésives. Compte tenu de la complexité de la microstructure des adhésifs époxy bi-composants, il m'a paru important d'identifier et de comprendre les scénarios d'endommagement qui apparaissent dans l'adhésif lorsque celui-ci est sollicité dans son domaine de comportement non linéaire. Dans ce contexte d'étude, je m'appuie à nouveau sur des essais tomographiques interrompus afin de pouvoir comprendre, par exemple, comment les pores vont évoluer et ce qui se passe lorsque les pores se déforment de façon excessive. Jusqu'à présent, nous avons pu examiner de manière globale l'évolution du nombre de pores ainsi que la fraction volumique en fonction du niveau de chargement. L'idée et de mieux comprendre comment un tel adhésif s'endommage sous différents états de sollicitation et quels sont les mécanismes qui s'y retrouvent à l'initiation des microfissures. Pour faciliter la compréhension de ces mécanismes, nous avons déjà réalisé plusieurs études. D'abord ces études s'appuient sur l'analyse expérimentale des échantillons massiques sollicités en traction et couplée avec l'analyse tomographique. Nous avons pu observer que les pores s'allongent dans la direction de sollicitation avec des déformations maximales dans les zones les plus éloignées de la direction de sollicitation locale. Nous avons également pu constater que pour ces zones où les déformations sont les plus importantes, des fissures se sont amorcées et se sont propagées dans la direction perpendiculaire à la direction de sollicitation. De plus il a également été observé que des amorçages de microfissures se produisent également à l'interface entre les charges et la matrice adhésive. La dégradation de l'adhésif semblerait être influencée par trois mécanismes : *i)* des déformations excessives au voisinage des pores, *ii)* de l'amorçage de microfissures dans les zones fortement déformées et *iii)* des microfissures à l'interface entre la matrice adhésive et les billes de verres. Enfin, la détection de l'apparition de ces mécanismes de dégradation, sur des assemblages collés industriels, reste difficilement détectable en temps réel par des techniques d'imagerie comme la tomographie aux rayons X. Une potentielle solution à ce problème permettant de suivre l'intégrité et la santé d'un tel assemblage, s'appuie sur l'utilisation de l'émission acoustique. Cette technique pourrait apporter des informations très intéressantes sur l'apparition d'un des mécanismes d'endommagement, sur des périodes de monitoring très longues, si, au préalable, les signatures acoustiques des différents mécanismes d'endommagement sont clairement identifiées. Cette étape de corrélation entre les signaux acoustiques et les mécanismes de dégradation de l'adhésif peut se faire en couplant la tomographie aux rayons X avec l'émission acoustique sur des essais in situ interrompus, portant sur des

échantillons modèles avec des défauts maîtrisés.

CHAPITRE

3 Caractérisation des assemblages soudés par friction malaxage

Sommaire

3.1 Introduction 265
3.2 Estimation des paramètres optimaux du procédé de soudage FSW par des stratégies numériques 267
3.3 Identifications des défauts et de leur effet sur les joints FSW 285
3.4 Etudes en cours et perspectives 306

3.1 Introduction

Le soudage par friction-malaxage (FSW) est une technique de soudage proposée par le Welding Institute en 1991 [113] et qui permet d'assembler des alliages (tels que le cuivre, l'aluminium, le titane ou des combinaisons hybrides : aluminium et cuivre par exemple) difficiles à souder avec les techniques d'assemblage conventionnelles. Depuis qu'il a été inventé, ce procédé suscite un intérêt croissant, car il permet de surmonter les problèmes courants associés aux procédés classiques de soudage par fusion, tels que : les grandes distorsions, les fissures de solidification, l'oxydation ou la décoloration de la surface, la formation d'intermétalliques fragiles entre des matériaux dissimilaires, une large zone affectée thermiquement (HAZ), les structures dendritiques grossières, une consommation d'énergie élevée, la pollution de l'environnement [114], [115], etc. En outre, la possibilité de contrôler la microstructure et d'en obtenir d'autres difficiles à générer par d'autres techniques d'assemblage signifie qu'il est essentiel de comprendre la relation entre les conditions de soudage et la microstructure obtenue. afin de mieux adapter les propriétés de la soudure. En conséquence, le soudage par friction-malaxage est exploité dans un large spectre d'applications industrielles telles : l'aéronautique, le navale, l'automobile, le ferroviaire, etc.

Durant le procédé de soudage FSW, le matériau dans la zone de soudure subit de fortes déformations thermomécaniques qui entraînent des processus de recristallisation [116]. La rotation de l'outil entraîne un brassage et un mélange du matériau autour du pion rotatif par écoulement plastique, tandis que le frottement entre l'outil et les tôles à assembler contribue principalement à la production de chaleur. Une grande partie (entre 70% et 80%) du travail lié à l'écoulement plastique est dissipée sous forme de chaleur [117], ce qui donne lieu à un échauffement local. Par conséquent, les champs imposés (thermique, déformation ainsi que leur variation) sont fortement non uniformes, et varient en fonction de la distance par rapport au pion et à l'épaulement en rotation. Par ailleurs, ces champs sont influencés par la force axiale de l'épaulement de l'outil sur la pièce, sa forme, ses vitesses de rotation et de déplacement, l'inclinaison du pion [118], [119] et les propriétés des matériaux soudés, telles que la conductivité thermique, la contrainte d'écoulement en fonction de la température, etc. De manière plus macroscopique, la qualité du cordon de soudure ainsi obtenue dépend principalement de la présence ou non des défauts (pores, défauts de types tunnel, couches d'oxydes, etc.) et dans une moindre mesure de la microstructure obtenue [120], [121]. Tout d'abord, la minimisation de la quantité de défauts de type pores est étroitement liée à la valeur absolue de l'écart entre la température effective de soudage et celle dite optimale [122], [123] au voisinage de la matière qui forme le cordon. Cette température optimale est une fonction qui dépend de plusieurs paramètres, dont les plus importants sont *i)* les paramètres du procédé (exemple : vitesse de rotation et vitesse d'avancement dans le cas d'un soudage par friction malaxage linéaire) et *ii)* les comportements thermomécaniques des matériaux à souder. Cette température dite optimale pourrait être déterminée à travers d'une étude expérimentale paramétrique sur des configurations simples [124], [125]. Il est beaucoup plus difficile d'identifier cette température pour des configurations complexes, surtout lorsqu'elles sont composées de matériaux dissimilaires. Ainsi, une des préoccupations majeures de l'industrie est de pouvoir estimer, avec un coût minimal, ces paramètres optimaux du procédé de soudage associés à une configuration donnée. La modélisation et la simulation numérique représentent une alternative déjà utilisée pour apporter des réponses satisfaisantes. La manière la plus simple pour estimer le champ de température et son évolution durant la formation du joint s'appuie principalement sur des modèles analytiques [126], [127]. Ces modèles sont toutefois associés à des configurations simples (position des pièces à assembler et géométrie du pion). Elles peuvent devenir moins performantes pour des cas où les conditions aux limites changent au cours du procédé et/ou lorsqu'on veut enrichir les phénomènes physiques accompagnant le processus de soudage. Les modèles semi-analytiques [128] ou numériques de type éléments finis [129], représentent un moyen très efficace pour estimer les paramètres optimaux, à condition que les phénomènes physiques représentatifs y soient intégrés. Des travaux scientifiques récents montrent clairement la pertinence d'une telle stratégie [130], mais pour des configurations simples. Néanmoins la mise en place de ces modèles multiphysiques fait appel à des connaissances très spécifiques afin d'aboutir à des résultats exploitables [131]. On rappelle au passage que le temps nécessaire pour ces simulations pourrait devenir vite incompatible avec les approches paramétriques pour lesquelles l'optimisation nécessite la mise en place de techniques de diminution de temps

de simulation en s'appuyant sur des stratégies de type *« mass scaling »* ou *« time scaling »*. Même si ces outils numériques ne peuvent toujours pas répondre de façon satisfaisante à tout type de problème, ils aident toutefois à restreindre le domaine d'investigation et proposer des solutions pour des paramètres de soudage initiaux pertinents. Ces derniers aident à trouver expérimentalement, plus facilement et plus rapidement, les valeurs des paramètres du procédé qui permettent de générer une température proche de l'optimale et, par conséquent, une diminution de la quantité de défauts dans le joint. L'homogénéisation de la microstructure, fortement hétérogène après le soudage FSW, pourrait améliorer la tenue mécanique du joint, et plus particulièrement son comportement en fatigue [132], [133]. Nous nous appuyons sur un large spectre de traitements spécifiques (thermique, thermique + mécanique, etc), permettant ainsi d'arriver à une résistance mécanique du joint avoisinant celle du matériau de base [116], [134].

La détection des défauts dans le joint soudé et à différentes échelles pourra être réalisée de différentes manières : visuellement, pour des défauts de taille importante et proche de la surface extérieure, par des observations destructives en prélevant des échantillons dans des zones d'intérêt, ou alors par analyse avec des moyens d'observations optiques à différentes échelles. Plus récemment la tomographie aux rayons X, basée sur le principe d'atténuation des rayons X à travers le matériau, conduit à l'obtention d'images en niveaux de gris en lien avec les intensités transmises. Cette technique est donc particulièrement employée dans la détection de porosités et de fissures internes au sein de matériaux [135], [136]. Appliquée aux joints soudés par FSW, elle permet de mettre en évidence les différentes phases constituant le joint [137], la distribution des défauts, la caractérisation, la distribution et le réarrangement des matériaux à l'interface, etc.

3.2 Estimation des paramètres optimaux du procédé de soudage FSW par des stratégies numériques

La détermination des paramètres optimaux du procédé de soudage par friction-malaxage (FSW), et qui conviennent à une configuration de joint donné, reste un grand défi et est souvent réalisée au moyen d'études expérimentales extrêmement longues et coûteuses [138], [139]. Ces paramètres optimaux qui sont recherchés doivent permettre l'obtention d'une part d'un joint qui minimise le nombre de défauts et d'autre part d'une microstructure semblable à celle du matériau de base. L'approche adoptée ici s'appuie sur l'existence d'une température optimale dans la matière qui forme le joint, pour laquelle le malaxage se fait de manière optimale.

Cette stratégie d'identification des paramètres optimaux a été développée pour un joint soudé de type bout-à-bout constitué de plaques de cuivre quasi pur de 3 mm d'épaisseur. Elle est basée sur des simulations en utilisant des modèles basés sur la méthode des éléments finis et la température optimale du procédé supposée connue.

La modélisation du procédé FSW est une tâche difficile, car elle doit traiter d'un problème multi-physique caractérisé par des déformations plastiques, des distorsions im-

portantes et une température élevée. Alors, des modèles ***C**oupled **E**ulerian-**L**agrangian* (CEL) ont été mis au point pour simuler les déformations plastiques importantes. Les modèles de type CEL, qui à l'origine étaient utilisés pour décrire la réponse thermomécanique (forces et distribution de la température), permettent maintenant de prédire les défauts (de type tunnel, cavités et formation d'excès de flash) [140], [141] qui peuvent se produire. Le schéma d'intégration directe a été adopté et la résolution a été explicite. Ce schéma d'intégration est bien adapté aux problèmes qui comprennent de nombreuses non-linéarités, des phénomènes dynamiques et des effets thermiques. Il a été constaté qu'un coefficient de frottement dépendant de la température, améliorait la qualité du champ de température [142], [143]. En conséquence, dans cette stratégie de modélisation, le coefficient de frottement utilisé est supposé dépendant de la température, et identifié de manière indirecte. Afin d'améliorer le temps de calcul et permettre l'utilisation d'un tel modèle dans une approche d'optimisation ou une étude paramétrique, une stratégie de type *« mass scaling »* a été implémentée. Cette stratégie a permis de réduire le temps de calcul d'environ 20 fois avec une erreur qui ne dépasse pas 10%. Pour améliorer la qualité des champs de température obtenue par simulation, le comportement thermomécanique du joint soudé bout-à-bout a été modélisé à l'aide d'un modèle de plasticité Johnson-Cook et a été identifié sur le matériau de base au moyen d'essais en laboratoire, à différentes températures et vitesses de déformation. Des résultats d'une étude paramétrique a permis de tracer la surface de réponse en température, à l'aide de laquelle, les paramètres optimaux du procédé (la vitesse d'avancement $v_a[mm/min]$ et de rotation $v_r[rot/min]$) sont déterminés. Ces paramètres optimaux, estimés numériquement, basés sur la surface de réponse en température, ont été validés par une bonne concordance avec les résultats expérimentaux. En outre, des études expérimentales couplant la radiographie aux rayons X ,la méthode de corrélation d'images numériques et des faciès de rupture ont permis de mieux caractériser les joints soudés par friction - malaxage.

Publication jointe

- M.D. Iordache, C. Badulescu, M. Diakhaté, M. A. Constantin, E. Nitu, Y. Demmouche, M. Dhondt, D. Negrea, **A numerical strategy to identify the FSW process optimal parameters of a butt-welded joint of quasi-pure copper plates : modeling and experimental validation**. *The International Journal of Advanced Manufacturing Technology*, 115, 2505–2520 (2021), https ://doi.org/10.1007/s00170-021-07296-9

Références associées : Bibliographie des publications

The International Journal of Advanced Manufacturing Technology (2021) 115:2505–2520
https://doi.org/10.1007/s00170-021-07296-9

ORIGINAL ARTICLE

A numerical strategy to identify the FSW process optimal parameters of a butt-welded joint of quasi-pure copper plates: modeling and experimental validation

Monica Daniela Iordache[1] · Claudiu Badulescu[2] · Malick Diakhate[3] · Marius Adrian Constantin[1] · Eduard Laurentiu Nitu[1] · Younes Demmouche[2] · Matthieu Dhondt[2] · Denis Negrea[4]

Received: 19 February 2021 / Accepted: 17 May 2021 / Published online: 26 May 2021
© The Author(s), under exclusive licence to Springer-Verlag London Ltd., part of Springer Nature 2021

Abstract
Determining the optimal parameters of the friction stir welding (FSW) process, which are suitable for a given joint configuration, remains a great challenge and is often achieved through extremely time-consuming and costly experimental investigations. The present paper aims to propose a strategy for the identification of the optimal parameters for a butt-welded joint of 3-mm thick quasi-pure copper plates. This strategy is based on FEM (finite element method) simulations and the optimal temperature that is supposedly known. A robust and efficient finite element model that is based on the Coupled Eulerian-Lagrangian (CEL) approach has been adopted and a temperature-dependent friction coefficient has been used. Besides, the mass scaling technique has been used to significantly reduce the simulation time. The thermo-mechanical behavior of the butt-welded joint was modeled using a Johnson-Cook plasticity model that was identified through lab tests at different temperatures. The results of the parametric study help to define the numerical surface response, and based on this latter one can find the optimal parameters, advancing (v_a) and rotational (v_r) speeds, of the FSW process. This numerical surface response has been validated with good agreement between the numerical prediction of the model and the experimental results. Furthermore, experimental investigations involving x-ray radiography, digital image correlation method, and fracture surface analysis have helped a better understanding of the effects of FSW parameters on the welded joint quality.

Keywords Friction stir welding · Optimal process parameters · Cu-DHP copper · Finite element method · Mass scaling · Digital image correlation

1 Introduction

Copper and its alloys are widely used in many engineering applications since they have particular properties such as electrical and thermal conductivity, ductility, mechanical strength, and corrosion resistance. However, these materials are difficult to weld using conventional welding processes (fusion melting) because of the high thermal conductivity and the higher oxidation rate at temperature values close to fusion one [1]. Thus, an alternative and promising solution is friction stir welding (FSW). This joining process, environmentally friendly since it releases no toxic gas or radiations, is solid-state welding based on the generation of heat due to both the friction of the pin (rotating element) at the interface of the two plates to be joined and the plastic deformation of the material being welded. FSW is a metal-working process commonly characterized by a flow progressing through preheating, initial deformation, extrusion, forging, and cool-down processing zones. The rotating FSW pin plunges into the junction of two rigidly clamped plates until the shoulder touches the surface of the materials being welded before traversing along the weld line under the applied normal force [2, 3].

✉ Claudiu Badulescu
claudiu.badulescu@ensta-bretagne.fr

[1] Manufacturing and Industrial Management Department, University of Pitesti, Pitesti, Romania

[2] ENSTA Bretagne, IRDL-UMR CNRS 6027, F-29200 Brest, France

[3] University of Bretagne Occidentale, IRDL-UMR CNRS 6027, F-29600 Morlaix, France

[4] Regional Center of Research & Development for Materials, Processes and Innovative Products Dedicated to the Automotive Industry (CRC&D-Auto), University of Pitesti, Pitesti, Romania

Many research studies have focused on the use of FSW to joint aluminum-based alloys, such as [4–7], while limited literature on dissimilar FSW of copper is available. The limited research on FSW, and consequently its industrial application, is due to both the high melting point and the good thermal conductivity of the cooper as they lead to increasing the heat input during the welding process to obtain a joint without defects. This also results in higher requirements of materials and design of the welding tools. The effects of pin rotational speed on the microstructure, the mechanical properties, and the fracture localization of copper butt joints have been investigated [7]. The effects of both the shoulder cavity and the welding parameters on the applied torque, the formation of weld defects, and the mechanical properties of deoxidized copper (thin films) butt joints have been studied [8]. From the industrial point of view, the major challenge today is to able to predict the optimal welding parameters (advancing and rotational speeds of the pin), and many researchers have experimentally investigated this challenge [9, 10]. Most recently, some studies [11] have shown an optimal welding temperature at which the joint is free from defects, the homogeneity of the grain size within the joint is close to that of the base material, and the mechanical properties of the joint are optimum. This optimal temperature, which is associated with a welding configuration (material and geometry of the pin, the relative positioning of the parts to be welded), is often experimentally evaluated, thus leading to costly and long tests campaign. Furthermore, this optimal welding temperature seems to be an intrinsic parameter of the material, and the torque, the geometry of the pin, and the kinematics of the process help to achieve this temperature. Another recent study [12] used, for the first time, a fuzzy logic model to investigate and optimize the effect of FSW parameters on the tensile properties of the copper joints, such as ultimate tensile strength (UTS) and elongation. The microstructure of the optimum joint was characterized using different microscopy techniques to elucidate the origin of its behavior.

Several researchers have investigated the relationship between the microstructure of the welded assembly and the resulting mechanical properties. Findings from these studies show that the microstructural evolution of pure copper joint during the FSW process is mainly influenced by welding temperature. At temperature values lower than around 0.5 times Tf (Tf being the material fusion temperature), the microstructure is mainly governed by continuous recrystallization. The grain structure development at welding temperature values greater than around 0.5 times Tf is mainly dominated by discontinuous recrystallization, thus resulting in a relatively coarse grain structure in the stir zone [13]. Dynamic and static changes of grain size and texture of copper during the FSW process have been studied by Xu et al. [13]. They have shown that during the plastic deformation stage, the initial coarse grains in the base metal were subdivided with the increase in strain and temperature, and the stir zone exhibits ultrafine grains with a large number of low angle boundaries and a symmetrical simple shear texture. The effect of stacking fault energy on the restoration mechanisms and the mechanical properties of joints has been studied by Heidarzadeh et al. [14]. Authors have shown that in pure copper, the continuous dynamic recrystallization was the only restoration mechanism that leads to new grain formation. Moreover, the effect of restoration mechanisms on both the yield strength and the strain hardening of joints has been studied. For a deeper understanding, one can read the review paper recently published [15] which highlights the latest progress made in the microstructure analysis during the FSW process.

Based on the literature review [9, 10], one can identify the optimal parameters of the process through numerical simulations, thus leading to a drastic reduction of the experimental campaign. This finding highlights the importance of developing modeling strategies as well as efficient and robust numerical simulations. Today, the modeling of heat generation and material flow during the FSW process are addressed using different modeling techniques such as computational solid mechanics (CSM) and computational fluid dynamics (CFD) methods. The current literature proposes some approaches useful to tackle the mesh distortion. With this in mind, Al-Badour et al. [16] proposed the coupled Eulerian-Lagrangian (CEL) model. In this method, the plates being welded, governing the equations, are discretized using the Eulerian formulation whereas the welding tool is modeled as a Lagrangian body. These methods are based on explicit integration schemes which imply an extremely reduced step time, a high number of increments, and a high computational time. This is why most of the FSW numerical simulations are restricted to short computational times (penetration phase of the pin).

However, there are very few studies that propose robust numerical strategies and help to estimate the optimal process parameters without having to conduct extremely time-consuming and costly experimental parametric studies.

The current work aims to develop an efficient strategy to determine the welding process parameters based on numerical simulations with the finite element method and the optimal temperature that is supposedly known for all materials that will be welded. The numerical model developed in this work should be able to simulate within a reasonable computational time (1 to 2 days) an FSW process characterized by a welding time of about a few tens of seconds and a traversing length of the pin of about 100 mm. The mass scaling technique is used to minimize the computational time. Also, the numerical model has enabled us to take into account the thermo-mechanical boundary conditions (heat exchange with the ambient air), and the heat dissipation from plastic deformation, and that from the friction between the pin and the materials being welded.

The friction coefficient was supposed as a function of the temperature.

This strategy has been used to simulate the butt-welded joint of 3-mm-thick quasi-pure copper and has been validated by comparison with experimental results (identification of defects using x-ray technique, local mechanical behavior of the joint analyzed using digital images correlation, and fracture surface analysis through fractography technique).

2 Finite element model description

2.1 Finite element approach

Numerical simulations have been conducted to assess the effect of different FSW process parameters on the quality of the FSW joints. Modeling the FSW process is a challenging task since it needs to address a multi-physical problem that is characterized by large plastic deformation and high temperature. The more difficult to suitably model is the material flow in the vicinity of the pin. Nowadays, several numerical simulation strategies are proposed to model the FSW process. In the non-flow-based models, excessive deformations appear and thus leads to early termination of the computation. The ALE formulation is often used to ensure a better mesh quality during the simulation [17]. However, because of extremely large deformations, this strategy cannot eliminate the mesh distortion and consequently leads to prohibitive computation time [18]. Recently, Coupled Eulerian-Lagrangian (CEL) models have been developed to simulate severe plastic deformations [19]. CEL models, which were originally used to describe the thermo-mechanical response (forces and temperature distribution), now allow predicting defects (tunnel defects, cavities, and excess flash formation) that may occur [19].

In this work, a 3D thermomechanical finite element model based on the CEL formulation has been developed using ABAQUS software. The direct integration scheme was adopted, and the resolution was explicit. This integration scheme is well suited for problems that include numerous nonlinearities, dynamic phenomena, and thermal effects. The finite element model is described below.

2.2 Geometry of the model and applied boundary conditions

The two workpieces to be welded are 100 mm in length, 40 mm in width, and 3 mm in thickness. As shown in Fig. 1a, these workpieces are positioned into the Eulerian domain. This latter has a thickness of 3.5 mm. The geometry of the tool has a conical shape with diameters of 4 mm at its base and 3 mm at its upper part and a length of 2.8 mm (Fig. 1a). The tool is considered to be rigid and the workpieces deformable. All the lateral and bottom faces of the Eulerian domain are embedded. The tool is characterized by three movements. The first one is the rotation at a constant speed (v_r) coupled with a penetration speed (v_p) of about 2.8 mm/s for all the simulations. Once the penetration step is completed, the tool will begin the actual welding phase over a distance of 90 mm in the x-direction (Fig. 1a). During this latter, the tool keeps its rotational speed constant while at the same time it is subjected to an advancing speed. Several sets of parameters, which are characterized by different pairs of welding speed (v_r, v_a) values, are simulated. To save computational time, the tool retraction phase was not modeled. A constant ambient temperature field (22 °C) is applied to the whole Eulerian domain and at the beginning of the simulation. The heat exchange during the welding process has been taken into account by using a convection model that is characterized by a convection coefficient (h_f) of 30 W/m^2. ° C [20]. The heat exchange through the tool is not taken into account firstly to limit the size of the numerical model and secondly because of the low heat exchange that should be simulated since the thermal conduction coefficient of the copper remains relatively greater than the one of the tool. This step allows defining the boundary conditions at the surface to be welded.

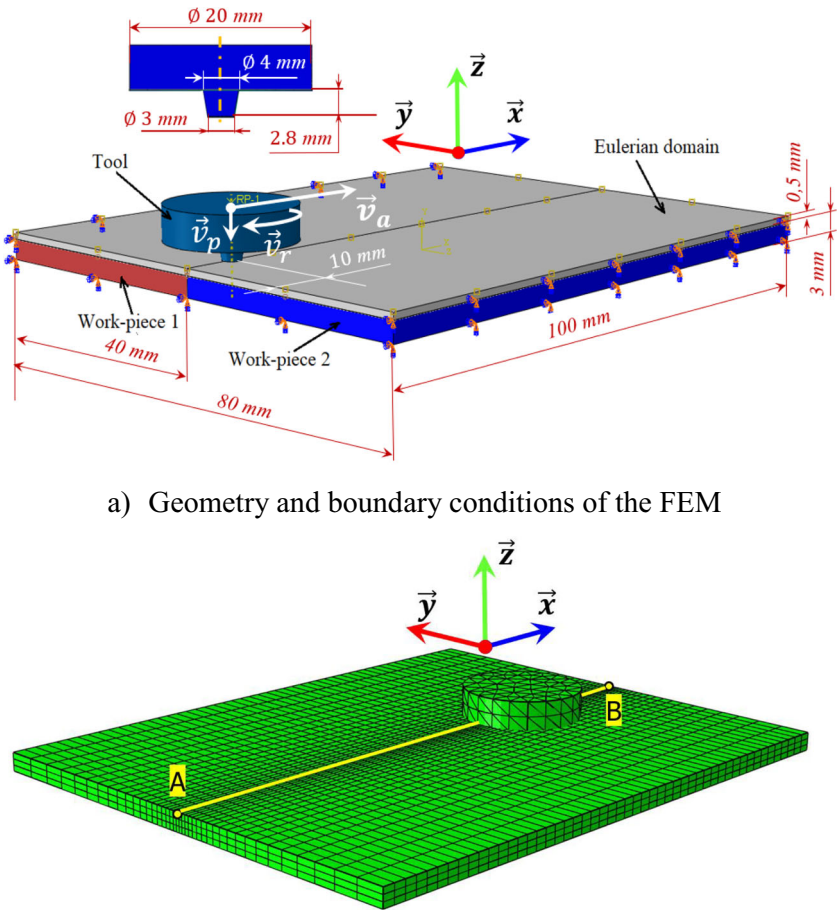
2.3 Mesh

The Eulerian domain mesh comprises 6785 thermally coupled 8-node Eulerian elements (EC3D8RT) and 8364 nodes as shown in Fig. 1b. The mesh was progressively performed by increasing the element width from the joint line to the edge. The tool is a Lagrangian rigid body and was meshed using 785 quadratic tetrahedral elements. The mesh has been adapted based on the following two main reasons. The first one is to ensure that each part of the tool which comes into contact with the plates being welded has the same contact surface by ensuring a relatively homogeneous of both friction and local distribution of the contact pressure, with effects on the temperature field distribution. The second main reason is to ease the modeling of complex geometries such as the tool's one. The number of elements has been chosen in the view of obtaining a good compromise between the computation time and the convergence of the field temperature.

2.4 Thermomechanical behavior of the material

In this work, the material being welded is phosphorus deoxidized copper (DHP-Copper) with 99.9% pure copper. This material is commonly used in industry due to its good corrosion resistance, high thermal conductivity, and electrical conductivity [21]. The linear thermo-elastic behavior of the used material is described using the following constitutive equation [21] :

$$\sigma = 2\mu\varepsilon_e + \lambda[tr(\varepsilon_e) - \alpha(T - T_0)]\boldsymbol{I} \quad (1)$$



a) Geometry and boundary conditions of the FEM

b) Central line mesh of the FEM

Fig. 1 Geometrical model, boundary conditions, and mesh of the FEM. **a** Geometry and boundary conditions of the FEM. **b** Central line mesh of the FEM

where $\boldsymbol{\sigma}$ is the stress tensor; ε_e is the linear-elastic strain tensor; λ and μ are the Lamé coefficients; T is the real temperature; $\boldsymbol{T}_0$ is the reference temperature; α is the thermal expansion coefficient, and $\boldsymbol{I}$ is the identity matrix.

The thermal field equation is expressed as follows [22]:

$$-k\nabla^2 T = \alpha\lambda T_0 tr\left(\dot{\varepsilon}_e\right) + \rho c_e \dot{T} \tag{2}$$

where k is the thermal conductivity, ρ is the density, and c_e is the specific heat.

The first term on the right-hand side of the previous equation (Eq. 2) describes the strain rate effect on the temperature field. The mechanical behavior is formulated using Navier's equations for thermoelectricity and is given hereafter [22]:

$$\mu\nabla^2 u + (\lambda+\mu)\nabla tr(\varepsilon_e) - \alpha\lambda\nabla T = \rho\frac{\partial^2 u}{\partial t^2} \tag{3}$$

where $\mathbf{u}$ is the displacement vector and $\mathbf{t}$ is the time.

The physical properties of the DHP copper at room temperature are given in Table 1.

In this study, the Johnson-Cook's model is used to describe the material flow. The model uncouples the plastic, viscous, and thermal behaviors and describes each of them through three independents terms [24].

$$\sigma = \left[A + B\cdot\left(\varepsilon_p\right)^n\right] \times \left[1 + C\cdot\ln\left(\frac{\dot{\varepsilon}_{pl}}{\dot{\varepsilon}_0}\right)\right]\left[1-\left(\frac{T-T_{ref}}{T_{melt}-T_{ref}}\right)^m\right] \tag{4}$$

where $\overline{\sigma}$ is the flow stress; $\overline{\varepsilon_p}$ is the effective plastic strain; $\dot{\varepsilon}_{pl}$ is the effective plastic strain rate; $\dot{\varepsilon}_0$ is the normalizing strain rate; A, B, C, n, T_{melt}, and m are material constants; T_{ref} is the room temperature (22°C in this study).

In the previous equation (Eq. 4), the parameter n takes into consideration the hardening of the material, whereas m depends on its fusion. C is influenced by the strain rate.

The material's constants were determined based on the experimental results from tensile tests that were carried out at different speeds (3 mm·min^{-1} and 30 mm·min^{-1}), which are equivalent to strain rates of 1.67×10^{-2}s^{-1} and 1.67×10^{-3}s^{-1} and temperatures (22 °C, 300 °C, and 500 °C). During the FSW process, the applied strain rate can sometimes,

Table 1 Physical properties of the DHP copper [23]

Material	Elastic modulus (GPa)	Poisson's ratio	Density (kg/m^3)	Thermal conductivity (W/m°C)	Specific heat (J/Kg°C)	Thermal expansion coefficient (10^{-6}/°C)
Cu-DHP	117.2	0.33	8913	388	385	16.8

depending on the welding configuration to perform, reach 1600 s^{-1} [25, 26]. Nevertheless, such high-performance equipment is not available in our research entities. The inverse identification method was used. A hydraulic testing machine (INSTRON 1342) equipped with a load cell (±100 kN capacity) was used to apply the loading rate and a climatic test chamber (CERHEC 1400), which can generate a controlled temperature for up to 1500 °C, helps regulate the testing temperature. For the sake of clarity, only results from tests at 22 °C and 500 °C are presented in Fig. 2.

The identified values of the constants of Johnson-Cook's model for DHP copper are obtained by fitting the equation (Eq. 4) with the experimental results and are shown in Table 2.

2.5 Friction model

A critical aspect of the FSW process simulation is the contact condition modeling between the tool and the plates being welded since the Eulerian domain interacts with the Lagrangian one. Many studies have focused on the development of contact models suitable for the FSW process. Most of them have opted for a friction coefficient that is kept constant during the simulation [27, 28]. However, the friction coefficient depends on speed, temperature, and deformation rate. Recently, Kareem et al. [29] have used the Coulomb friction model with a non-linear coefficient that is dependent on both the local temperature of the melted material and the deformation rate. This evolution of the coefficient has been previously proposed by Meyghani et al. [30] through a highly original work that integrates the shear stress of the contact interface (dependent on the temperature), the partial sliding/sticking condition, and the geometry of the tool.

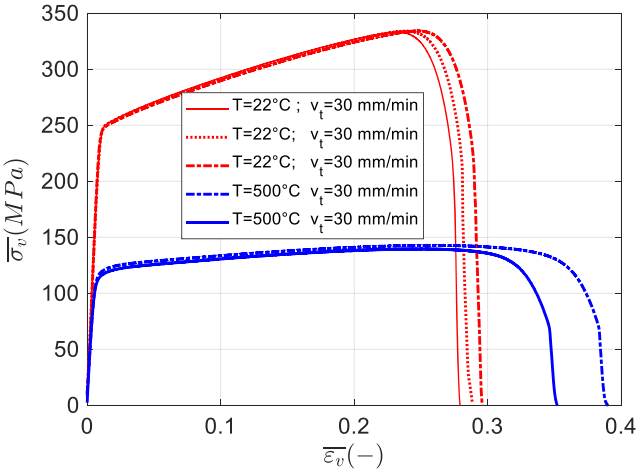


Fig. 2 Macroscopic behavior of base material as a function of temperature, where $\overline{\varepsilon}_v$ is the logarithmic strain and $\overline{\sigma}_v$ is the true stress

Very promising results from experimental tests [30], which were carried out using various FSW parameter sets, have validated this evolution of the friction coefficient as a function of temperature. Thus, this methodology was used in this work to describe the relationship between the friction coefficient evolution and the temperature (Fig. 3). At ambient temperature, $\mu_0 = 0.22$ (evaluated by using the inverse identification method).

2.6 Mass scaling strategy

In the FEM model, an explicit integration scheme was used for the resolution. One of the major criticisms of this integration scheme is the extremely long computational time that is associated with it, so it is mainly used for dynamic simulations (simulation time relatively short). If the time increment is less than a critical value Δt_{crit}, the integration scheme is considered conditionally stable. The critical time increment Δt_{crit} is computed from the mass and stiffness characteristics of the model and is expressed as follows [31]:

$$\Delta t_{crit} = min\left(\frac{L_{c\,i}}{C_d}\right) \tag{5}$$

where $C_d = \sqrt{\frac{E}{\rho}}$ is the wave propagation velocity within the material and $L_{c\,i}$ is the characteristic length of each element "i" of the mesh.

Mass scaling is a way of reducing the computational time, and it increases artificially the masses of the elements and can be applied even though there is rate dependency. The mass (Eq. 3) is scaled by replacing the density term ρ with the fictitious density $\rho^* = \kappa_m \cdot \rho$, with $\kappa_m > 0$ [22]. The mass scaling factor κ_m has to be chosen in such a way that the inertial forces, the right-hand side of the equation (Eq. 3), remain small. The substitution of the density ρ for a fictitious density

Table 2 Constants of Johnson-Cook's model for DHP copper

Material	T_{melt} (°C)	T_{ref} (°C)	A (MPa)	B (MPa)	C	n	m
DHP-Cu	1083	22	250	250.4	0.0137	0.81	0.73

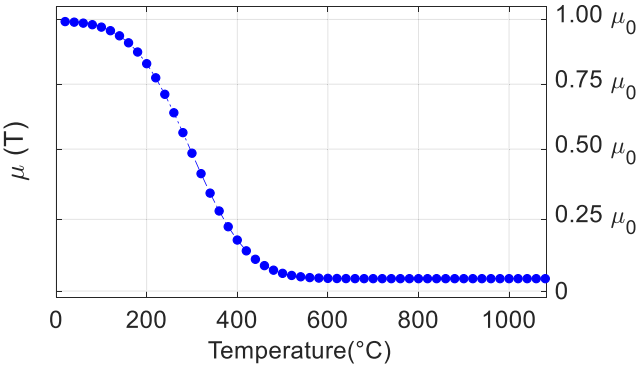


Fig. 3 Evolution of the friction coefficient as a function of temperature

ρ^* leads to a change in the thermal time constant (Eq. 2). This effect can be compensated by introducing the fictitious specific heat $c_e^* = c_e \kappa_m^{-1}$. Thus, we obtained the two following scaled thermo-elastic equations (Eq. 6 and Eq. 7). Mass inertia effects can be seen explicitly on the right-hand side of the equation (Eq. 6) [22].

$$-k\nabla^2 T = \alpha\lambda T_0 tr\left(\dot{\varepsilon_e}\right) + \rho^* c_e^* \dot{T} \tag{6}$$

$$\mu\nabla^2 \boldsymbol{u} + (\lambda+\mu)\nabla tr(\varepsilon_e) - \alpha\lambda\nabla T = \rho^* \frac{\partial^2 \boldsymbol{u}}{\partial t^2} \tag{7}$$

To achieve a reasonable accuracy of simulation results, the ratio of kinetic energy to internal one must be less than 2% of the simulated model. According to [20], a value of m= 1000 was chosen. Thus, the temperature error is less than 10% and the computational time is reduced by 25 times. As a consequence, the use of the mass scaling method combined with a reasonable computational time leads to a significant reduction in the increment number as well as the inherent numerical errors.

3 Validation of the finite element model

To allow validation of the FEM, two DHP copper plates with dimensions of 100 mm (length) × 100 mm (width) × 3 mm (thickness) have been welded with two sets of welding parameters. The assembly process is performed by using a welding machine FSW-4-10 that is characterized by a rotating speed in the range of 300 to 1450 rpm and an advancing speed between 10 and 480 mm/min. Throughout the welding process, this machine also allows both controlling the displacement and recording the force in the $\vec{z}$ direction (Fig. 1b). The temperature has been measured using an infrared camera (FLIR A40M) with an accuracy of ±2 °C, and at the interface between the tool and the plates being welded (precisely at 1 mm behind the tool and pointing to the weld bead). The infrared camera moves with the tool.

The first welded assembly, which is labeled W-90-800, was obtained with an advancing speed of 90 mm/min and a rotating speed of 800 rpm. The second welded assembly, which is labeled W-90-1000, was obtained with an advancing speed of 90 mm/min and a rotating speed of 1000 rpm. The rotational speed value of the tool was modified while the advancing one was kept constant. This choice was motivated by the fact that the welding temperature increase is mainly influenced by the rotational speed than the advancing one and this temperature value could be less affected by measurement errors.

The evolution of maximal welding temperature is plotted against the position of the tool during the welding of W-90-1000 (Fig. 4). This first result helps to evaluate the initial value of the friction coefficient μ_0 (Fig. 3) by minimizing the difference between values that are predicted by the model and those obtained from the experimental measurements.

Once the value of μ_0 identified, the validity of the numerical model can be evaluated by comparing the temperature distribution measured within the second welded assembly during the tool advance with the one predicted by the finite element model (Fig. 5). Moreover, the numerical axial force is compared with the experimental one (Fig. 5b). These findings indicate that the experimental results are in good agreement with those obtained from the numerical simulation; the force axial error is less than 6%.

4 Parametric study

It has been proven [1] that it is crucial to reach the optimal welding temperature for obtaining a welded joint of high quality characterized by a mechanical strength close to that of the base material. This temperature can be experimentally evaluated and is about 0.4 to 0.5 times T_{melt} for quasi-pure copper materials [1]. The optimal welding temperature of DHP copper materials [1, 32] is about 550 °C. At this temperature, the base material is in a pasty state, so this allows a homogeneous melting while avoiding defect formation. If this temperature is exceeded and approaching that of melting, the material

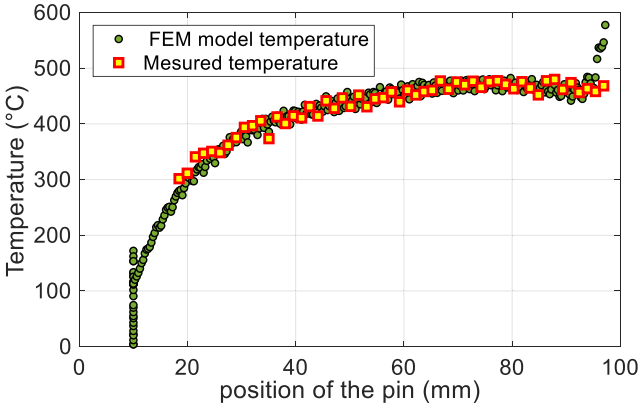
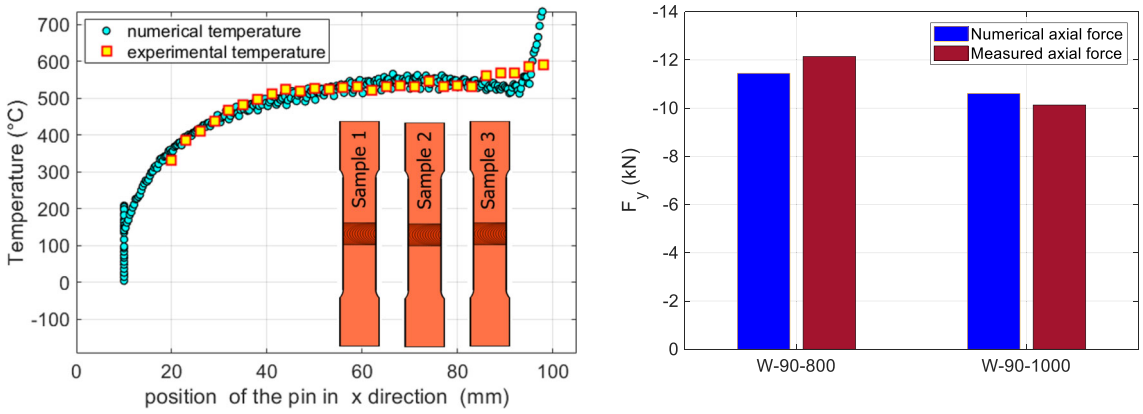


Fig. 4 Predicted versus measured temperatures against the position of the pin, in the $\vec{x}$ direction



a) Comparison between numerical and experimental temperature distributions for W-90-1000 sample

b) Comparison between numerical and experimental forces F_z, for W-90-800 and W-90-1000 samples

Fig. 5 Validation of the finite element method. **a** Comparison between numerical and experimental temperature distributions for W-90-1000 sample. **b** Comparison between numerical and experimental forces F_z, for W-90-800 and W-90-1000 samples

becomes too fluid, which will result in both void formation within the joint and inhomogeneous melting. This latter also leads to excessive burr of the weld bead and, under tensile loading, fracture at the welded joint.

This parametric study aims at carrying out numerous simulations which subsequently will help to identify the optimal welding parameters. Twelve simulations are carried out using the welding parameters specified in Table 3. Each simulation is individually labeled, indicating the speeds of both advancing and rotating.

For instance, Fig. 6a shows the computation field temperature obtained during the simulation of the welding configuration S-90-1000 and precisely when the tool position is at 85 mm from point A. As shown in Fig. 5a, both experimentally and numerically, the welding temperature takes time to reach its optimal value. In these welded areas where the temperature is not stabilized, defects likely have appeared. Consequently, for each numerical simulation, the temperature is recorded at a tool position greater than 85 mm from point A. These temperature values are shown in Fig. 6b by the red points. For a clear presentation of these temperature results, a polynomial surface interpolation was performed. This highlights the effects of the FSW process parameters on the stabilized welding temperature. This finding is in good agreement with experimental observations [33]. At a given advancing speed v_a, the stabilized temperature increases with the rotating speed v_r. However, when this latter is fixed, a decrease in the advancing speed leads to an increase in the stabilized process temperature.

Table 3 Simulation labels and speeds selected in the parametric study

v_a (mm/min)	60	90	120	150
v_r (rpm)				
1200	S-60-1200	S-90-1200	S-120-1200	S-150-1200
1000	S-60-1000	S-90-1000	S-120-1000	S-150-1000
800	S-60-800	S-90-800	S-120-800	S-150-800

5 Simulation results

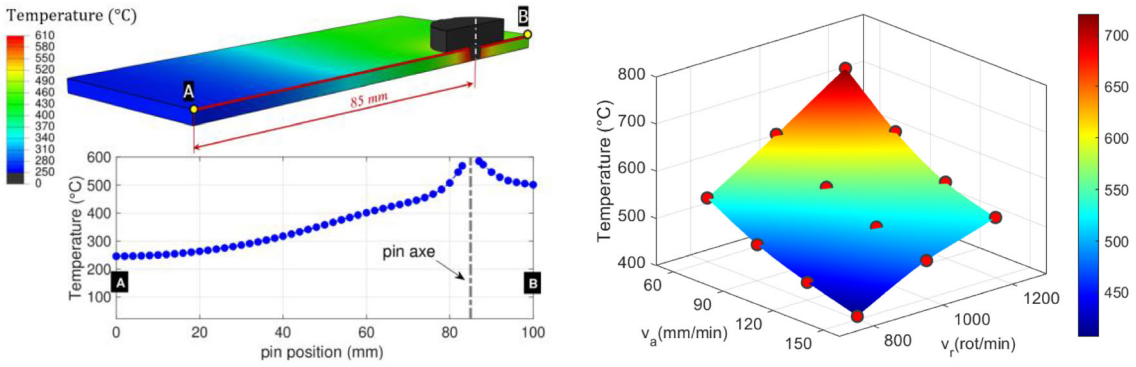
From the obtained results, one can compute a thermal efficiency surface indicator ($\boldsymbol{T_E}$) that is defined in the following formula (Eq. 8):

$$\boldsymbol{T_E}(v_a, v_r) = \left[1 - \frac{abs[\boldsymbol{T_S}(v_a, v_r) - \boldsymbol{T_O}]}{\boldsymbol{T_O}}\right] \times 100 \quad (8)$$

where $\boldsymbol{T_S}(v_a, v_r)$ represents the stabilized temperature obtained from the simulation with the speeds v_a and v_r, and T_O represents the optimal welding temperature identified from the literature [1, 32]. The maximal value of the indicator T_E might give a valuable indication of the optimal area of the welding process.

The thermal efficiency surface (T_E) mapping is shown in Fig. 7.

This mapping clearly shows an area, the one colored in red, that is characterized by values of T_E close to 100%, in other words, by stabilized temperature values close to the temperature T_O. This result means that, inside that particular area, one can identify FSW process parameters that help to obtain welded joints with mechanical strengths close to that of the base material. Ideally, it is recommended to perform the welding at relatively high speeds (v_a = 120mm/min and v_r = 1150 rpm) to avoid heat loss in the weld bead, but also to increase productivity. It should be noticed that these values



a) distribution of the temperature from the S-90-1200 simulation

b) stabilized surface temperature

Fig. 6 surface temperature from numerical simulation. **a** Distribution of the temperature from the S-90-1200 simulation. **b** Stabilized surface temperature

could be limited due to both the kinematics and rigidity of the welding machine. Conversely, selecting low optimal values leads to the use of both moderate kinematics and less effective welding machines, on the condition that the heat losses did not become too high. In this parametric study, only the heat exchange with the ambient air is integrated into the model. However, evaluating the effects of more realistic thermal boundary conditions remains possible.

From Fig. 7, the optimal dependency between the rotating speed and the advancing one might be expressed as follows (Eq. 9).

$$v_r = k_T \times v_a + k_r \tag{9}$$

with $k_T = 5.52$ rot/mm and $k_r = 483$ rot/min. These two constants depend on both the tool geometry and the material being welded. Their values are identified from the equation of the black-colored line plotted in Fig. 7.

The equation (Eq. 8) allows evaluating the optimal value of the tool rotating speed based on an imposed advancing speed value. Some experimental tests are then needed to both validate this strategy and evaluate the difference between the stabilized temperature and the optimal one (T_O), as well as the joint strength.

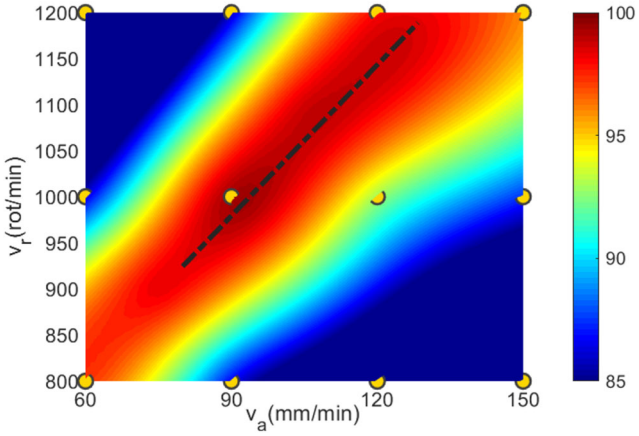


Fig. 7 Thermal efficiency surface, $T_E(v_a, v_r)$

6 Experimental validation

6.1 Experimental setup

In addition to two welding configurations (labeled W-90-800 and W-90-1000) that were used for both identification and validation of the finite element model, five other FSW assemblies have been manufactured using the same material (Cu-DHP) and geometry (length, width, and thickness). The labels (process parameters) of the five other welding configurations are specified in Table 4. The non-destructive testing using penetrating radiation (X-ray radiography) was performed on ANDREX X-ray Equipment model CMA357 using high contrast, very fine grain KODAK INDUSTREX T200 Film. The focal distance was 50 cm, current intensity 2 mA, working voltage 120 kW, and the exposure time 1 min and was performed on four specimens (labeled W-90-1200, W-150-1200, W-90-800, and W-150-800). This investigation aims at qualitatively evaluating the presence or absence of defects having a dimension greater than 300 μm within the joint. For each FSW specimen, the investigated volume size is graphically represented by the blue-colored parallelepiped shown in Fig. 8b. The x-rays pass through the

Table 4 Welding configurations tested investigated during the experimental study

v_a (mm/min)	90	120	150
v_r (rpm)			
1200	W-90-1200		W-150-1200
1000	W-90-1000	W-120-1000	W-150-1000
800	W-90-800		W-150-800

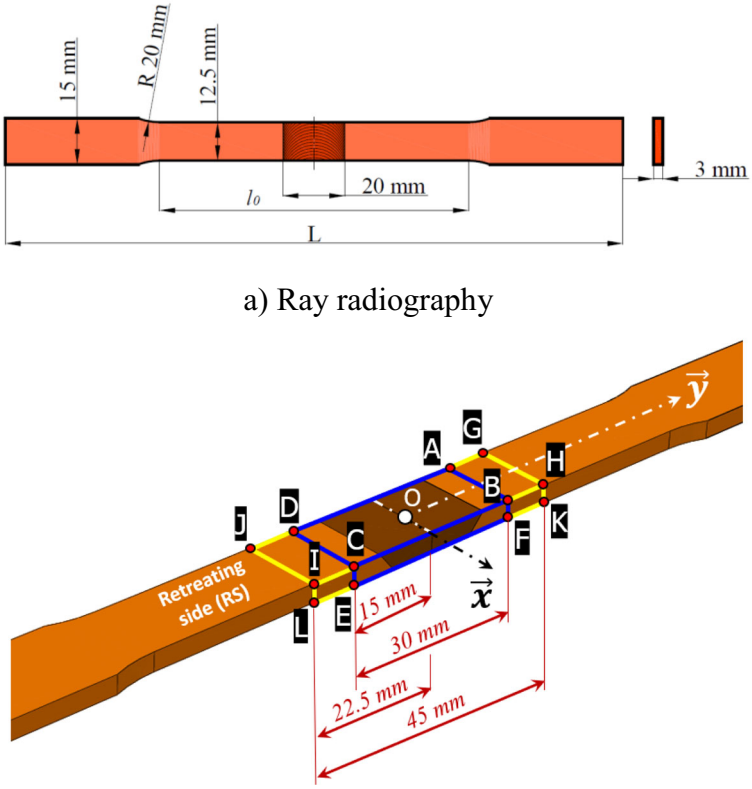


Fig. 8 Geometry and monitored faces of the sample. **a** Sample dimensions. **b** Position of the X-ray radiography and DIC investigated areas

specimen, and two of its faces (Fig. 8b) are projected for the defects analysis: the frontal one bounded by points A, B, C, and D, and the lateral one bounded by points B, F, E, and C.

For each welding configuration to be investigated through monotonic tensile tests, three specimens have been extracted from the welded stabilized area and at the following positions (from point A, Fig. 5a): 55 mm, 70 mm, and 85 mm respectively. The geometry of the extracted specimens is shown in Fig. 8a. Additional details about the specimen geometry are $l_0 = 100$ mm and $L = 200$ mm.

During tensile tests, the digital images correlation (DIC) method was used to monitor the local strain field ε_{yy} simultaneously on both the frontal face (area bounded by points G, H, I, and J in Fig. 8b) and lateral face (area bounded by points H, K, L, and I in Fig. 8b).

The experimental setup used to measure the displacement field on the abovementioned faces is shown in Fig. 9.

The testing machine used to investigate the mechanical behavior of the welded joint is the same as that for the thermo-mechanical characterization of the base material, namely INSTRON 1342. Monotonic tensile tests were performed at a loading rate of 3 mm/min. The displacement field measurement on the two perpendicular faces (frontal and lateral) of the sample was performed by simultaneously using two CCD cameras that are fully synchronized with the INSTRON machine: an Aramis-GOM system equipped with a 2448 × 2050 pixels CCD sensor and a Retiga 6000 equipped with a 2758 × 2208 pixels CCD sensor. The resulting strain field is computed by deriving the displacement field.

Before installing the specimen in the testing machine, its two perpendicular faces were speckled and on an area of interest which is 45 mm long and centered on the welded joint (Fig. 8b). This length has been selected so that a wide area around the welded joint can be monitored and recorded up to failure. A polarized lighting device was also set up for recording images with high contrast at a frequency of 1 Hz.

The mechanical loading is applied along the $\vec{y}$ -direction (Fig. 8). For image analysis, the spatial resolution is set to 19 pixels, and the standard deviation of the displacement field to ±0.5 μm.

To complete this experimental investigation, a digital microscope (KEYENCE VHX) was used to analyze the fracture surfaces of three specimens (labeled W-90-1000, W-120-1000, and W-150-1000) at ×100 magnification to highlight the failure scenario through different zones of FSW joints.

6.2 Results from X-ray analysis

The results from the X-ray analysis of the four specimens are shown in Fig. 10.

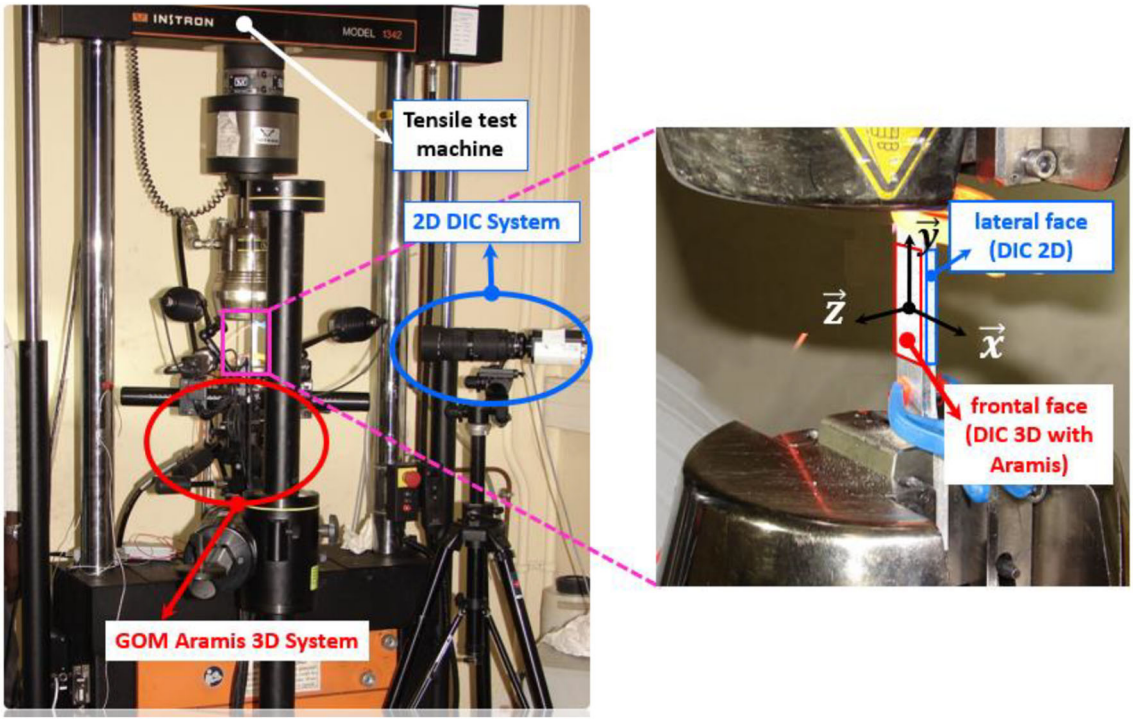


Fig. 9 Tensile test setup to investigate the mechanical behavior of the FSW joint

As shown in Fig. 10, false-color images of the abovementioned faces (frontal and lateral) allow detection of the defects along both the axis (y-direction) and width (z-direction) of the joint.

From image analysis, it can be noticed that there is no detectable defect within the specimen labeled W-90-1000 (Fig. 10a). Consequently, this FSW specimen should exhibit higher mechanical properties (maximum values of stress and strain at failure). The defects detected within the specimen labeled W-150-1000 (Fig. 10b) seem to be a tunnel type defect, are characterized by a variation in its width along the welding direction, and are located in the root of the weld (retreating side). The defects within the two other specimens labeled W-80-800 and W-150-800 (Fig. 10c and d, respectively) have a size bigger than that of those detected within the specimen labeled W-90-1000, extend over the whole width of the specimen, are located in the root of the weld (retreating side), and are characterized by a 1 mm in depth. These specimens are likely to exhibit low mechanical strength.

6.3 Results from monotonic tensile tests

The macroscopic mechanical responses of the welding configurations that were tested under tensile load (Table 4) are

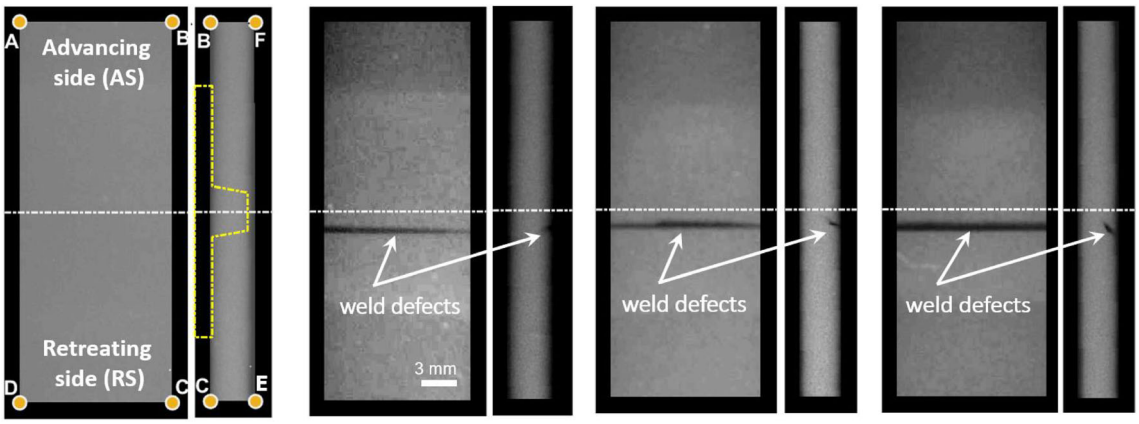


Fig. 10 Defects identification from X-ray radiography. **a** W-90-1000. **b** W-150-1000. **c** W-90-800. **d** W-150-800

shown in Fig. 11. In this figure, the true stress ($\overline{\sigma_v}$) is plotted as a function of the logarithmic strain ($\overline{\varepsilon_v}$).

Results from tensile tests (Fig. 11) highlight the effects of the welding parameters on the macroscopic mechanical behavior of the welded joint. For some process parameters, the values of both the logarithmic strain and true stress at the specimen failure are close to the ultimate strength of the base material. For a suitable analysis of the results, the mechanical efficiency E_M of the joint is computed by using the following formula:

$$E_M(v_a, v_r) = \frac{\overline{\sigma}_{v\ max} FSW\ (v_a, v_r)}{\overline{\sigma}_{v\ max}\ BM} \times 100 \qquad (10)$$

where $\overline{\sigma}_{v\ max} FSW$ represents the maximum value of the true stress resulting from the tensile test on an assembly welded at the speeds (v_a, v_r), and $\overline{\sigma}_{v\ max}\ BM$ represents the maximum value of the true stress of the base material. Based on the results shown in Figs. 11 and 2, E_M values are plotted on Fig. 12a as a function of the two welding speeds (v_a, v_r). This result (Fig. 12a) highlights an area, around the white-colored line, within which the selected welding speeds lead to a joint characterized by a mechanical efficiency value close to 90%. It is also clear from Fig. 12a that one can notice a very good correlation between the mapping of the E_M values and that of the thermal efficiency surface (T_E) values. Moreover, Fig. 12b shows a good agreement between the welding speeds (v_a, v_r) selected from the mapping of the T_E values and the resulting strain value at specimen failure ($\overline{\varepsilon}_{v\ max}\ FSW$). These findings validate the strategy for identifying the optimal process parameters.

The maximum strain ($\overline{\varepsilon}_{v\ max}\ FSW$) value is around 0.3 when the welding is performed at the optimal process speeds, and that strain value is close to the one obtained when the base material fails. The key parameter for manufacturing a joint of high quality is mainly governed by the welding temperature obtained in the vicinity of the tool. Optimizing this welding temperature prevents the generation of both tunnel and kissing bond defects.

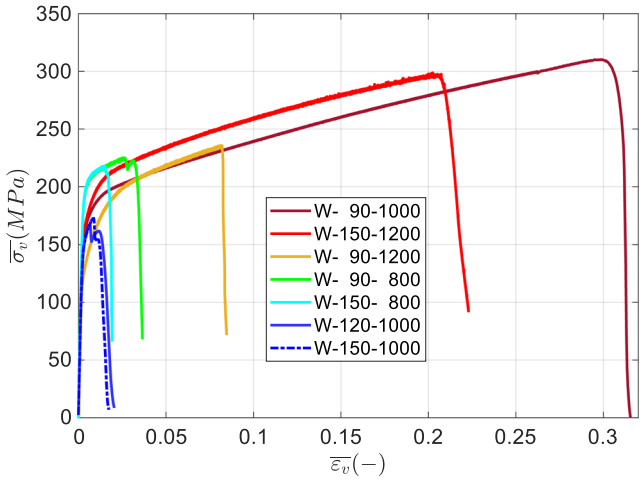


Fig. 11 Effects of process parameters: macroscopic behavior of the welded joint plotted in the plane true strain ($\overline{\varepsilon_v}$) versus true stress $\overline{\sigma_v}$ (MPa)

6.4 Strain map results

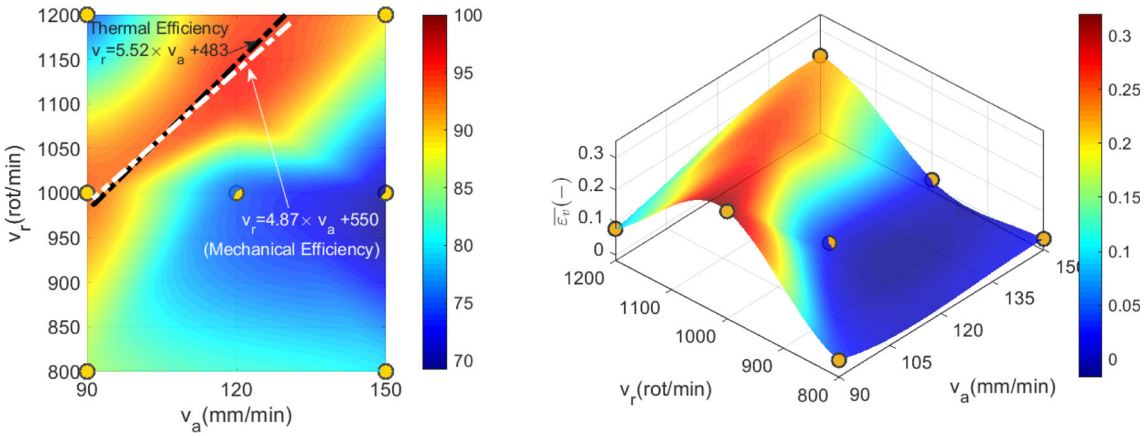
Differences between the macroscopic behavior of FSW joints (Fig. 11) could be better explained by analyzing the local behavior of the different zones of the joint. For this purpose, the strain fields (ε_{yy}) obtained on both faces (frontal and lateral) of the specimens W-90-1000 and W-150-1000 are shown in Fig. 13. Local strain maps (in the loading direction) resulting from seven different values of macroscopic stress (Fig. 13a) are compared. As stated previously, the analysis of X-ray results allows concluding that the defects detected within the specimen W-150-1000 are of tunnel type. This explains why the yield strength of that specimen is lower than that of the specimen labeled W-90-1000. From Fig. 13b, one can see on the strain maps of the lateral face (W-150-1000) that the defect starts appearing at a stress value of around 130 MPa (from point C, Fig. 13a). This localization reflects the tunnel defect propagation from the root of the joint to the welded area.

This propagation scenario is highlighted on strain maps labeled d and e. The sudden decrease in the macroscopic stress value of the specimen W-150-1000 is because of the sudden propagation of the defect to the opposite face.

When analyzing the strain field on each frontal face of the two specimens, one can see that the defect starts being detected from the stress level labeled d. These localizations are undoubtedly associated with defect propagation. From these strain maps, one can also notice that defects are located on the retreating side and their appearance leads to high strain values in their vicinity. Under the same loading rate level, the highest strain value is about 0.2 for the specimen W-150-1000 and 0.02 for the specimen W-90-1000.

To better understand the mechanisms that govern the fracture of joints, fracture surface analysis was performed on three specimens (labeled W-90-1000, W-120-1000, and W-150-1000) using a high-resolution digital microscope. The results are shown in Fig. 14.

From Fig. 14, one can notice a cross-section reduction of about 67.5%, 30.6%, and 15.9% for the specimen W-90-1000, W-120-1000, and W-150-1000 respectively. The specimen W-90-1000 exhibits a ductile fracture. Periodic striations are observed on the fracture surface of specimens W-120-1000 and W-150-1000. Similar striations have already been observed [34] on the fracture surface of an aluminum AA5083-H112 alloy FSW joint. Zettler et al. [35] have observed machining grooves that can be associated with the tool advancing along both the cross-section and welding direction of an aluminum AA6063-T6 alloy FSW joint.

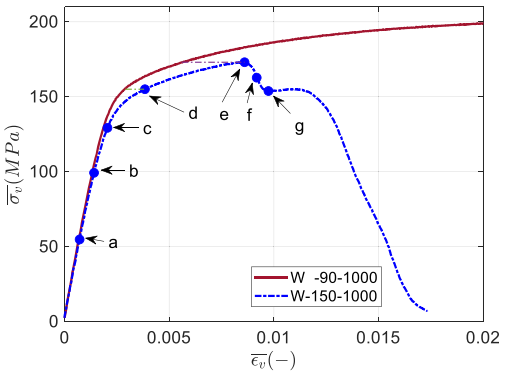


a) Mechanical efficiency (E_M) compared with the thermal one (T_E)

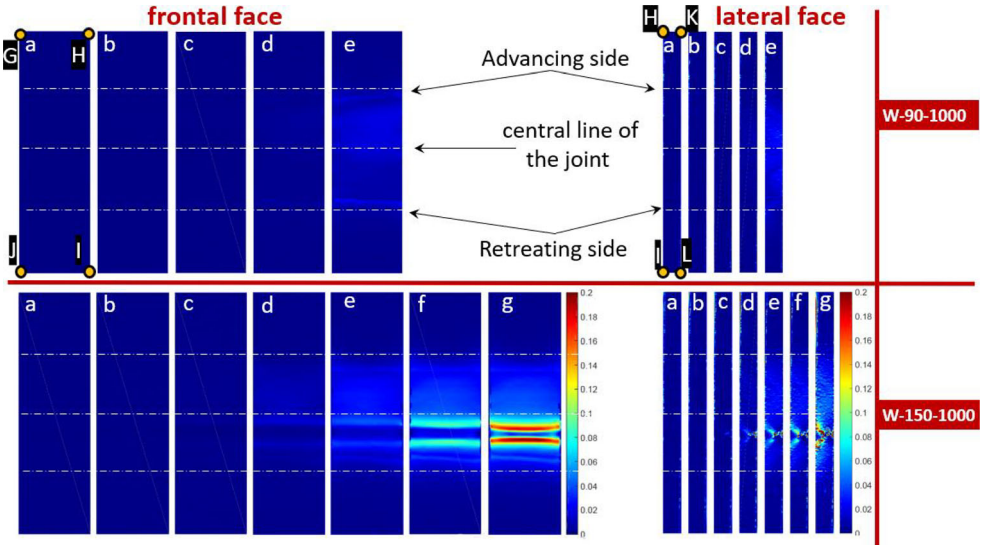
b) Maximum strain ($\bar{\varepsilon}_{v\ max}\ FSW$) as a function of the welding speeds (v_a, v_r)

Fig. 12 Correlation between the optimal welding speeds and the resulting maximum strain of the FSW assembly. **a** Mechanical efficiency (E_M) compared with the thermal one (T_E). **b** Maximum strain ($\bar{\varepsilon}_{v\ max}\ FSW$) as a function of the welding speeds (v_a, v_r)

Fig. 13 Strain maps comparison between W-90-1000 and W-150-1000 samples. **a** Macroscopic mechanical behavior of two specimens. **b** Local strain maps in the loading direction of two specimens



a) Macroscopic mechanical behavior of two specimens



b) Local strain maps in the loading direction of two specimens

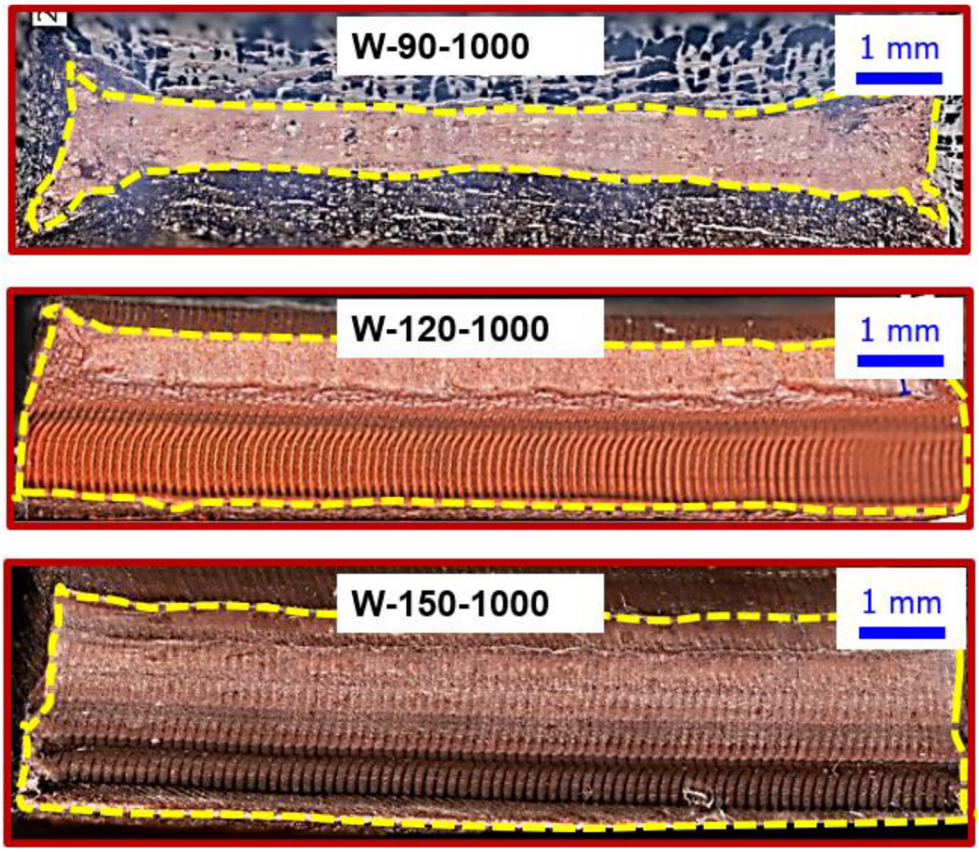


Fig. 14 Fracture surface analysis of three welded joints

In the present study, the striations at the fracture surface of W-120-1000 are localized in its lower side of the FSW joint and at a periodic interval. The localization of these striations in the lower half of the cross-section highlights the fact that the insufficient temperature at the root of the weld does not ensure melt quality, thus leading to the appearance of kissing bond defects. By comparing the specimens W-120-1000 and W-150-1000 (having the same rotating speed but different advancing speed), one can observe striations over the entire cross-section of the specimen W-150-1000 and are distributed at low density compared to the specimen W-120-1000. This pattern was more pronounced at the root of the weld.

6.5 Microstructure, microhardness, and fracture surfaces

Microstructure and microhardness of joints have been analyzed and compared to those from specimens obtained under extreme welding conditions, i.e., based on thermal and mechanical efficiency surface indicators T_E and E_M. Thus, the configuration W-90-1000 was obtained with the best indicators and the configuration W-150-1000 with the worst one (Fig. 16). The microstructures of both the base material and the weld nugget were analyzed for the two abovementioned welding configurations. For each of these, the specimen dedicated to the microstructure analysis was the one located in the vicinity of the specimen mechanically tested. The lateral face of the specimen was first polished to a depth of 3 mm using 600 to 1200 grit papers before it received a diamond polishing (3-μm granularity) to achieve a smooth and even surface. Then, a chemical attack, which was formulated with 50% of distilled water and 50% of HNO_3, was performed for 30 s and followed by rinsing with ethanol. One can see that the microstructure of the base material (Fig. 16a) is quite uniform and polyhedral, and is composed of grains having an average size of about 35 μm. The microstructure of the weld nugget of the specimen W-90-1000 (Fig. 16b) is less uniform and is composed of grains having a smaller average size (21 μm) and strongly deformed with diffuse edges compared to those of the base material. In Fig. 16d, one can see that the weld nugget of the specimen W-150-1000 is composed of grains having an even smaller average size (about 15 μm) than those of the weld nugget of W-90-1000. The welding temperature determines the dynamic recrystallization of the material in both configurations. However, the lower welding temperature of the configuration W-150-1000 led to the appearance of grains having an average size smaller than the one of grains from W-90-1000. This has also influenced the microhardness of both configurations (Fig. 16c). The microhardness of

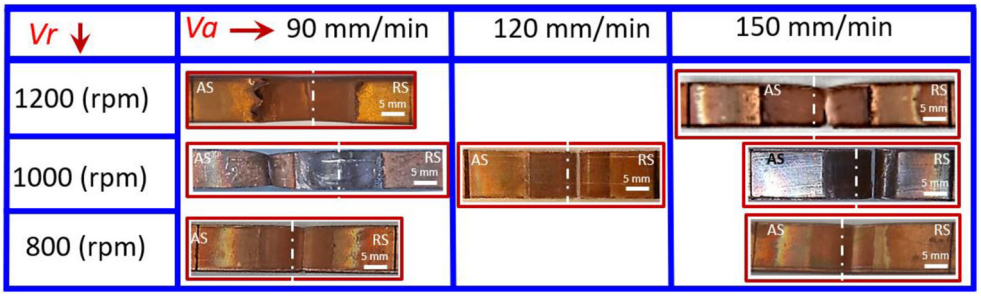
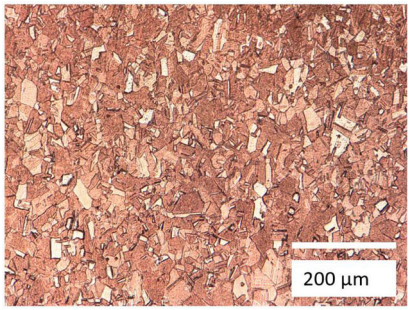


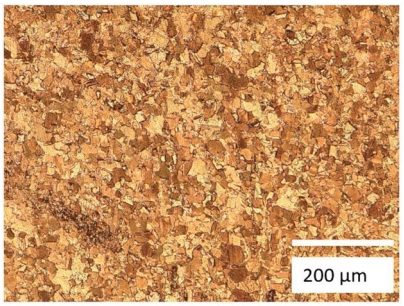
Fig. 15 Fracture path localization

W-150-1000 is higher than the one of W-90-1000. However, the insufficient heat induced by the welding of W-150-1000 did not allow the material to be in its optimal plastic state, thus generating weld defects of type "kissing bond" (Fig. 16f). This type of defect has not been detected in the configuration W-90-1000 (Fig. 16e).

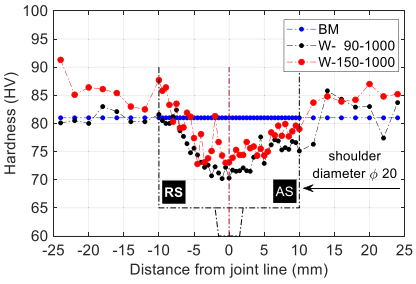
One last result is about the failure localization referring to the joint axis. Figure 15 shows the observations from each welding configuration tested. It can be seen that among the seven tested specimens, only the welding configuration W-90-1000 exhibits a fracture path localized outside the welded joint. This indicates



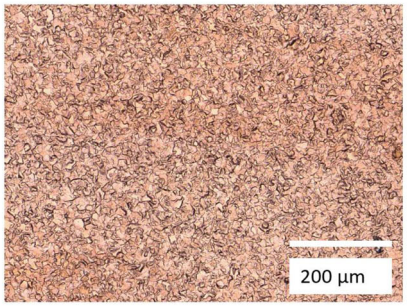
a) microstructure of the base material



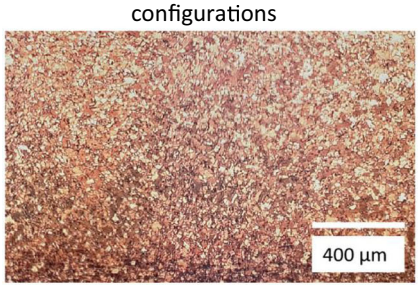
b) microstructure of the weld nugget (configuration W-90-1000)



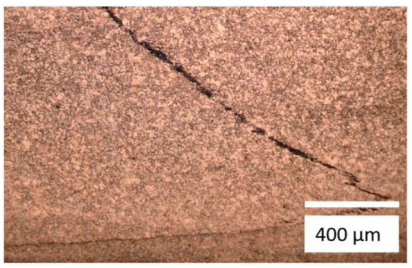
c) welding joints microhardness for W-90-1000 and W-150-1000 configurations



d) microstructure of the weld nugget (configuration W-150-1000)



e) microstructure of the root of the weld bead (configuration W-90-1000)



f) microstructure of the root of the weld bead (configuration W-150-1000)

Fig. 16 Microstructure and microhardness of the welds for different process parameters. **a** Microstructure of the base material. **b** Microstructure of the weld nugget (configuration W-90-1000). **c** Welding joints microhardness for W-90-1000 and W-150-1000 configurations. **d** Microstructure of the weld nugget (configuration W-150-1000). **e** Microstructure of the root of the weld bead (configuration W-90-1000). **f** Microstructure of the root of the weld bead (configuration W-150-1000)

that for this specimen, the process parameters (welding speeds) are optimal (Fig. 16).

Moreover, one can notice that for each of the other FSW configurations, the resulting fracture path is localized within the weld bead and always at the retreating side (RS). These findings are in good agreement with the prediction of the optimum parameters.

7 Conclusion

This work has enabled us to study the friction stir welding process applied on a quasi-pure copper material. A robust and efficient numerical strategy is proposed and aims at predicting the optimal welding parameters for which a butt joint welding of 3-mm-thick quasi-pure copper exhibits the maximum values of both mechanical strength and strain to fracture.

The simulation tool, which is based on the CEL (Coupled Eulerian-Lagrangian) model, takes into account some key aspects that make it robust and efficient: firstly, a friction coefficient that depends on the temperature has been used and its initial value was computed based on the ambient temperature and using the inverse identification method; secondly, the computational time has been reasonably optimized (2 days for the welding configurations simulated in this work) thanks to the use of the mass scaling technique, which has a low impact of the accuracy of the results since the temperature field is lowly overestimated (less than 10%); thirdly, the values of the constants of Johnson Cook's law were determined experimentally.

The key parameter of this simulation strategy lies in evaluating the optimum value of the welding temperature, which is intrinsic to both the welding configuration and material. This optimum value of welding temperature can be often found in the literature. However, for welding configuration that has never been studied, this optimum welding temperature could be identified through extremely long and costly experimental investigation. Thus, the simulation model developed in this work allows identifying the best combinations of welding speeds (v_a, v_r). An extensive testing campaign involving tensile test, X-ray technique, analysis of local strain fields, and analysis of fracture surfaces highlights the robustness of the simulation strategy proposed in this work. The experimental results were in good agreement with the FE simulations and then have enabled us to determine the suitable set of FSW parameters for the studied material.

Acknowledgements This work was supported by a grant of the Romanian Ministry of Research and Innovation, CCCDI-UEFISCDI, project number PN-III-P3-3.1-PM-RO-FR-2019-0048/01.07.2019 and Campus FRANCE, France

Availability of data and material Not applicable

Code availability Not applicable

Author contribution *Monica Daniela IORDACHE* - conceived of the presented idea and supervised the project
Claudiu BADULESCU - developed the theory and performed the computations
Malick DIAKHATE - wrote the manuscript in consultation with Claudiu BADULESCU
Marius Adrian CONSTANTIN - designed and performed the experiments
Eduard Laurentiu NITU - involved in planning and supervised the work, the analysis of the results, and the writing of the manuscript
Younes DEMMOUCHE - aided in interpreting the results and worked on the manuscript
Matthieu DHONDT - aided in interpreting the results and worked on the manuscript
Denis NEGREA - performed the x-ray radiography measurements
All authors discussed the results and commented on the manuscript

Funding The research reported was founded partially by "Romanian Ministry of Research and Innovation, CCCDI-UEFISCDI, project number PN-III-P3-3.1-PM-RO-FR-2019-0048/01.07.2019" and "Campus FRANCE," France.

Declarations

Ethical approval Not applicable

Consent to Participate Not applicable

Consent to publish Not applicable

Competing interests The authors declare no competing interests.

References

1. Hwang YM, Fan PL, Lin CH (2010) Experimental study on friction stir welding of copper metals. J Mater Process Technol 210(12): 1667–1672. https://doi.org/10.1016/j.jmatprotec.2010.05.019
2. Thomas WM, Nicholas ED, Needham JC, et al. (1991) Inventors: The Welding Institute, TWI, International Patent Application No. PCT/GB92/02203 and GB Patent Application No. 9125978.8, Dec 1991
3. Galvão I, Loureiro A, Rodrigues DM (2016) Critical review on friction stir welding of aluminium to copper. Sci Technol Weld Join 21(7):523–546. https://doi.org/10.1080/13621718.2015.1118813
4. Cole EG, Fehrenbacher A, Duffie NA, Zinn MR, Pfefferkorn FE, Ferrier NJ (2014) Weld temperature effects during friction stir welding of dissimilar aluminum alloys 6061-t6 and 7075-t6. Int J Adv Manuf Technol 71:643–652. https://doi.org/10.1007/s00170-013-5485-9
5. Dourandish S, Mousavizade SM, Ezatpour HR et al (2018) Microstructure, mechanical properties and failure behaviour of protrusion friction stir spot welded 2024 aluminium alloy sheets. Sci Technol Weld Join 23(4):295–307. https://doi.org/10.1080/13621718.2017.1386759

6. Jacquin D, Guillemot G (2021) A review of microstructural changes occurring during FSW in aluminium alloys and their modelling. J Mater Process Technol 288, yyy-yyy. https://doi.org/10.1016/j.jmatprotec.2020.116706
7. Zhou L, Zhang RX, Hu XY, Guo N, Zhao HH, Huang YX (2019) Effects of rotation speed of assisted shoulder on microstructure and mechanical properties of 6061-T6 aluminum alloy by dual-rotation friction stir welding. Int J Adv Manuf Technol 100:199–208. https://doi.org/10.1007/s00170-018-2570-0
8. Leal RM, Sakharova N, Vilaça P, Rodrigues DM, Loureiro A (2011) Effect of shoulder cavity and welding parameters on friction stir welding of thin copper sheets. Sci Technol Weld Join 16(2): 146–152. https://doi.org/10.1179/1362171810Y.0000000005
9. Ramachandran KK, Murugan N, Shashi Kumar S (2016) Performance analysis of dissimilar friction stir welded aluminium alloy AA5052 and HSLA steel butt joints using response surface method. Int J Adv Manuf Technol 86:2373–2392. https://doi.org/10.1007/s00170-016-8337-6
10. Shashi Kumar S, Murugan N, Ramachandran KK (2019) Identifying the optimal FSW process parameters for maximizing the tensile strength of friction stir welded AISI 316 L butt joints. Measurement 137:257–271. https://doi.org/10.1016/j.measurement.2019.01.023
11. Zhang W, Liu H, Ding H et al (2020) The optimal temperature for enhanced low-temperature superplasticity in fine-grained Ti–15V–3Cr–3Sn–3Al alloy fabricated by friction stir processing. J Alloys Compd 832 yyy-yyy. https://doi.org/10.1016/j.jallcom.2020.154917
12. Heidarzadeh A, Testik ÖM, Güleryüz G, Barenji RV (2020) Development of a fuzzy logic based model to elucidate the effect of FSW parameters on the ultimate tensile strength and elongation of pure copper joints. J Manuf Process 53:250–259. https://doi.org/10.1016/j.jmapro.2020.02.020
13. Xu N, Ueji R, Fujii H (2016) Dynamic and static change of grain size and texture of copper during friction stir welding. J Mater Process Technol 232:90–99. https://doi.org/10.1016/j.jmatprotec.2016.01.021
14. Heidarzadeh A, Saeid T, Klemm V, Chabok A, Pei Y (2019) Effect of stacking fault energy on the restoration mechanisms and mechanical properties of friction stir welded copper alloys. Mater Des 162: 185–197. https://doi.org/10.1016/j.matdes.2018.11.050
15. Heidarzadeh A, Mironov S, Kaibyshev R, Çam G, Simar A, Gerlich A, Khodabakhshi F, Mostafaei A, Field DP, Robson JD, Deschamps A, Withers PJ (2021) Friction stir welding/processing of metals and alloys: a comprehensive review on microstructural evolution. Prog Mater Sci 117:100752. https://doi.org/10.1016/j.pmatsci.2020.100752
16. Al-Badour F, Merah N, Shuaib A et al (2013) Coupled Eulerian Lagrangian finite element modeling of friction stir welding processes. J Mater Process Technol 213:1433–1439. https://doi.org/10.1016/j.jmatprotec.2013.02.014
17. Bussetta P, Dialami N, Boman R, Chiumenti M, Agelet de Saracibar C, Cervera M, Ponthot JP (2014) Comparison of a fluid and a solid approach for the numerical simulation of friction stir welding with a non-cylindrical pin. Steel Res Int 85(6):968–979
18. Dialami N, Chiumenti M, Cervera M, Agelet de Saracibar C, Ponthot JP (2015) Material flow visualization in friction stir welding via particle tracing. Int J Mater Form 8:167–181. https://doi.org/10.1007/s12289-013-1157-4
19. Chauhan P, Jain R, Pal SK, Singh SB (2018) Modeling of defects in friction stir welding using coupled Eulerian and Lagrangian method. J Manuf Process A 34:158–166. https://doi.org/10.1016/j.jmapro.2018.05.022
20. Constantin MA, Iordache MD, Nitu EL, Diakhaté M, Demmouche Y, Dhondt M, Bădulescu C (n.d.), ModTech International Conference - Modern Technologies in Industrial Engineering VIII. 2020, June 23-27, Iasi, Romania) An efficient strategy for 3D numerical simulation of friction stir welding process of pure copper plates. *IOP Conf Ser: Mater Sci Eng* 916:012021. https://doi.org/10.1088/1757-899X/916/1/012021
21. Gih-Keong Lau FL (2008) Johannes Goosen, Fred van Keulen, Thermo-elastic behavior of a polymeric layer bonded between rigid interfaces. Int J Solids Struct 45(18–19):5152–5164. https://doi.org/10.1016/j.ijsolstr.2008.05.016
22. Hammelmüller F, Zehetner C (2015) Increasing numerical efficiency in coupled eulerian-lagrangian metal forming simulations, XIII International Conference on Computational Plasticity. Fundamentals and Applications - COMPLAS XIII, (Barcelona, Spain)
23. Physical and mechanical properties of pure copper (2019) http://www-ferp.ucsd.edu/LIB/PROPS /PANOS/cu.html (accessed on 25.02.2019).
24. Johnson GR, Cook WH (1983) A constitutive model and data for metals subjected to large strains, high strain rates and high temperatures. Proceedings 7th International Symposium on Ballistics. The Hague, Netherlands, pp 541–547
25. Arora A, Zhang Z, De A et al (2009) Strains and strain rates during friction stir welding. Scr Mater 61(9):863–866. https://doi.org/10.1016/j.scriptamat.2009.07.015
26. Andrade DG, Leitão C, Dialami N, Chiumenti M, Rodrigues DM (2021) Analysis of contact conditions and its influence on strain rate and temperature in friction stir welding. Int J Mech Sci 191:106095. https://doi.org/10.1016/j.ijmecsci.2020.106095
27. Chiumenti M, Cervera M, Agelet de Saracibar M et al (2013) Numerical modeling of friction stir welding processes. Comput Methods Appl Mech Eng 254:353–369. https://doi.org/10.1016/j.cma.2012.09.013
28. Chao YJ, Qi X, Tang W (2003) Heat transfer in friction stir welding - experimental and numerical studies. J Manuf Sci Eng 125(1):138–145. https://doi.org/10.1115/1.1537741
29. Salloomi K (2019) Fully coupled thermomechanical simulation of friction stir welding of aluminum 6061-T6 alloy T-joint. J Manuf Process 45:746–754. https://doi.org/10.1016/j.jmapro.2019.06.030
30. Meyghani B, Awang M, Emamian S (2017) Developing a finite element model for thermal analysis of friction stir welding by calculating temperature dependent friction coefficient. In: Awang M (ed) 2nd International Conference on Mechanical, Manufacturing and Process Plant Engineering. Lecture Notes in Mechanical Engineering. Springer, Singapore. https://doi.org/10.1007/978-981-10-4232-4_9
31. Ducobu F, Rivière-Lorphèvre E, Filippi E (2015) On the introduction of adaptive mass scaling in a finite element model of Ti6Al4V orthogonal cutting. Simul Model Pract Theory 53:1–14. https://doi.org/10.1016/j.simpat.2015.02.003
32. Constantin MA, Boşneag A, Nitu E et al (2017) Experimental investigations of tungsten inert gas assisted friction stir welding of pure copper plates. IOP Conf Ser: Mater Sci Eng 252(1):012038. https://doi.org/10.1088/1757-899X/252/1/012038
33. Padhy GK, Wu CS, Gao S (2018) Friction stir based welding and processing technologies - processes, parameters, microstructures and applications: a review. J Mater Sci Technol 34(1):1–38. https://doi.org/10.1016/j.jmst.2017.11.029
34. Zhou N, Song D, Qi W, Li X, Zou J, Attallah MM (2018) Influence of the kissing bond on the mechanical properties and fracture behaviour of AA5083-H112 friction stir welds. Mater Sci Eng A 719: 12–20. https://doi.org/10.1016/j.msea.2018.02.011
35. Zettler R (2010) Material deformation and joint formation in friction stir welding, friction stir welding. Woodhead Publishing, Elsevier, Cambridge, UK, pp 42–72. https://doi.org/10.1533/9781845697716.1.42

Publisher's note Springer Nature remains neutral with regard to jurisdictional claims in published maps and institutional affiliations.

3.3 Identifications des défauts et de leur effet sur les joints FSW

Si la quantité de défauts ainsi que leur taille pourraient être réduits à travers l'utilisation des paramètres de soudage qui génèrent un champ de température autour du pion, avoisinant la valeur optimale, il n'en est pas de même pour les configurations complexes, comme par exemple avec trois tôles d'alliage d'aluminium superposées. Dans un premier temps, il est nécessaire de définir l'ordre de superposition par rapport à l'épaulement du pion. En conséquence, j'ai trouvé intéressant, à ce stade d'identifier la température optimale pour chacun des alliages utilisés et tenter de disposer les tôles d'aluminium par ordre décroissant de température optimale. Il est question ici, d'une analyse des défauts ainsi obtenus et de leur effet sur la résistance du joint constitué de trois couches en utilisant une stratégie d'investigation multi-instrumentation combinant : la micro-tomographie aux rayons X, la mesure des champs de déformation par l'analyse spectrale localisée et l'émission acoustique (EA) afin de détecter l'initiation des mécanismes d'endommagement au sein d'un joint FSW et de suivre son évolution au cours d'un essai mécanique. L'échantillon a été fabriqué en superposant et en soudant ensemble trois feuilles d'alliage d'aluminium de nuances AA6061, AA7075 et AA2024. Les défauts de la structure interne du joint ont été identifiés à l'aide de la micro-tomographie aux rayons X, avant sollicitation. L'échantillon a ensuite été soumis à un essai de traction. L'évolution des défauts en fonction de la contrainte de traction a été suivie en utilisant l'émission acoustique (EA) [144] couplée à des mesures de champs de déformation sans contact, simultanément sur deux faces perpendiculaires de l'échantillon. Les résultats mettent en évidence une bonne corrélation entre les zones de concentration de déformation et celles caractérisées par une forte densité de défauts de soudure, , tels qu'identifiés à partir de l'analyse des résultats de la micro-tomographie. La comparaison entre les résultats de l'EA et ceux obtenus à partir de l'analyse de la micro-tomographie a permis d'affirmer que les premières sources de fissuration ont été causées par les zones dites *de faiblesse*, où la densité de pores est maximale, et détectées dans l'état initial du joint soudé. Les résultats d'une classification non supervisée de l'activité EA, montrent que trois principaux mécanismes ont régi l'évolution de l'endommagement du joint FSW étudié. Une analyse approfondie des résultats expérimentaux met en évidence une bonne corrélation entre les résultats de l'EA et ceux de l'analyse des champs de déformations.

Publication jointe

- E.L. Nitu, M. Diakhaté, C. Bădulescu, M. Grédiac, B. Blaysat, D.M. Iordache, A. Bosneag, J. Adrien, E. Maire, M. Dhondt, Y. Demmouche, **Analyzing defects and their effects on the strength of a three-layer FSW joint by using X-ray micro-tomography, localized spectrum analysis, and acoustic emission**, *Materials Characterization*,190, 112069, 2022, https ://doi.org/10.1016/j.matchar.2022.112069.

Références associées : Bibliographie des publications

Materials Characterization 190 (2022) 112069

Contents lists available at ScienceDirect

Materials Characterization

journal homepage: www.elsevier.com/locate/matchar

Analyzing defects and their effects on the strength of a three-layer FSW joint by using X-ray microtomography, localized spectrum analysis, and acoustic emission

E.L. Nitu [a], M. Diakhaté [b], C. Bădulescu [c,*], M. Grédiac [d], B. Blaysat [d], D.M. Iordache [a], A. Bosneag [a], J. Adrien [e], E. Maire [e], M. Dhondt [c], Y. Demmouche [c]

[a] Manufacturing and Industrial Management Department, University of Pitesti, Pitesti, Romania
[b] IRDL-UMR CNRS 6027, Univ. Bretagne Occidentale, F-29600 Morlaix, France
[c] IRDL-UMR CNRS 6027, ENSTA Bretagne, F-29200 Brest, France
[d] Institut Pascal, UMR 6602, Université Clermont Auvergne, CNRS, SIGMA Clermont Institut Pascal, Clermont-Ferrand, France
[e] UMR CNRS 5510, Laboratoire MATEIS, University Lyon, INSA Lyon, Villeurbanne, France

ARTICLE INFO

Keywords:
Friction stir welding
X-ray micro-computed tomography
Localized spectrum analysis
Acoustic emission
Aluminum alloy

ABSTRACT

The present work aims at proposing an experimental strategy involving three measurement techniques, namely X-ray micro-computed tomography, Localized Spectrum Analysis, and Acoustic Emission (AE) in order to detect the initiation of damage mechanisms within an FSW joint and to track its evolution during a mechanical test. The specimen was manufactured by superimposing and welding together three aluminum alloy sheets named AA6061, AA7075, and AA2024. First, the defects within the internal structure of the joint were identified by using X-ray micro-computed tomography. The joint was then subjected to a tensile test. The evolution of the defects as a function of the tensile stress was monitored by using acoustic emission coupled with non-contact strain fields measurements on two perpendicular faces of the specimen. The findings highlight a good correlation between the strain-concentration zones and those characterized by a high density of weld defects, as identified from the analysis of the microtomography results. The comparison between AE results with those obtained from the computed microtomography analysis enabled us to state that the first crack sources were caused by the weakness zones detected within the initial state of the welded joint. The findings from an unsupervised classification of the AE activity are that three main mechanisms governed the damage evolution of the studied FSW joint. The acoustic signature of each cracking mechanism is defined by a pair of values (peak frequency, amplitude), each within a specific range. A deep analysis of the experimental results highlights a good correlation between the AE results with those from the strain analysis.

1. Introduction

The major challenge today mainly focuses on the reduction of energy consumption in different economic sectors. The conversion of energy significantly affects our environment and leads to high levels of air pollution. As an example, transport is the activity that contributes to most of the greenhouse gas emissions in France since it was estimated in 2019 at around 31% of the whole emissions [1]. Based on this observation, the design of mechanical structures in the transport industry should lead to a high strength/weight ratio [2]. Indeed, the use of these structures is an effective way to reduce the total weight of future vehicles, thus improving energy efficiency while reducing fuel consumption [3]. These structures are obtained by assembling different materials which are characterized by both a lightweight and a high mechanical strength. Such materials are generally difficult to weld and thus are conventionally joined by riveting, bolting, or screwing. One disadvantage of these joining processes is that they increase the weight of the assembly. An alternative to these assembling processes is the friction stir welding (FSW) technique. The latter was invented and patented by The Welding Institute (TWI) [4]. This is solid-state welding characterized by a low heat generation and a welding temperature lower than the fusion one of the materials involved in the joint. Because of the insignificant thermal distortions generated by the FSW process [5], the latter is suited for welding dissimilar materials. Many studies showed that the FSW

* Corresponding author.
E-mail address: claudiu.badulescu@ensta-bretagne.fr (C. Bădulescu).

https://doi.org/10.1016/j.matchar.2022.112069
Received 30 December 2021; Received in revised form 17 May 2022; Accepted 16 June 2022
Available online 22 June 2022
1044-5803/© 2022 Elsevier Inc. All rights reserved.

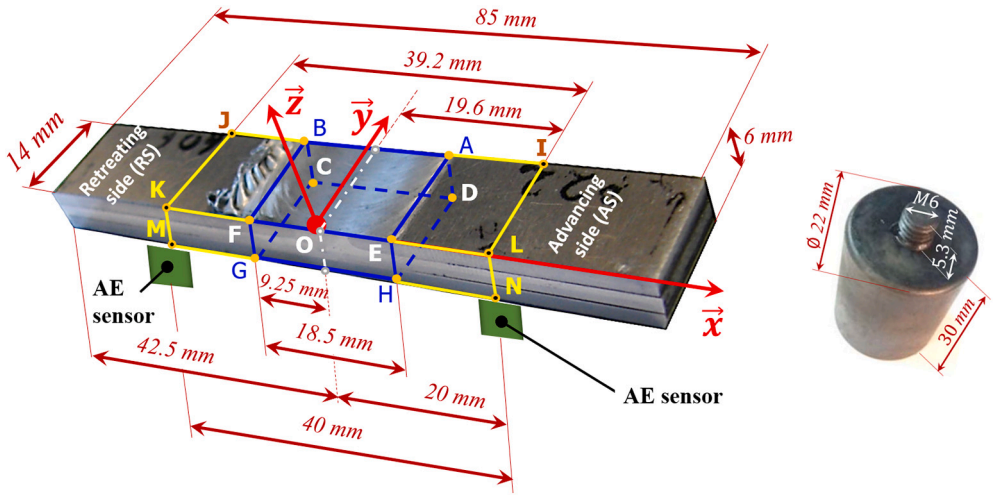


Fig. 1. Geometry of the FSW specimen with details of the investigated areas and the tool.

technique is well suited for assembling similar or dissimilar materials [6] by using either the lap joint [7] or the butt-joint method. Some recent studies have addressed welded joints made up of two superimposed sheets using the FSW process by performing several welding passes [8,9] and by varying the depth value of the welding tool. Welding defects were observed from the result analysis. However, their number, as well as their distribution, were not quantitatively evaluated. These defects could be of tunneling and kissing bond types [10] or pore types [11] that are specific to welding configurations of superimposed sheets.

The appearance of defects within this welding configuration is one of the most important issues because the heat generated by the friction between the shoulder of the pin and the alloy sheet is not always homogeneously spread at the interlayer between sheets. Another reason is that the values of both the mechanical and the thermal properties of the sheets being welded are generally different. Considering these experimental conditions involves choosing the joining parameters (advancing speed and rotational speed) in such a way that an optimal welding temperature is obtained in the stir zone [12]. This also ensures the strongest interface between the welded sheets and minimizes the creation of defects in the joint.

Compared to the studies mentioned above in which two superimposed and welded sheets were investigated, an FSW joint made of three superimposed steel sheets was investigated in [13] to understand the effect of the direction of the tool rotation on the joint quality, especially in terms of the formation of hooking defects [14]. Three ultra-thin aluminum alloy sheets, each having a thickness of 0.254 mm [15], were superimposed and welded by using micro friction stir welding before being experimentally tested. The authors were able to demonstrate that the shape of the tool highly affects the joint strength and that the creation of defects during the welding process can be minimized by selecting appropriate welding parameters. Nevertheless, few studies focus on quantifying these defects as well as their effect on the in-service life of FSW joints obtained by superimposing metal sheets. Recently, some authors [11,16] have successfully detected defects within FSW joints by using non-destructive testing such as X-ray micro-computed tomography (CT). Moreover, the authors have highlighted the dependency between the welding process parameters and the resulting number of defects. As a general conclusion of this brief bibliography, there is a need for coupling several experimental techniques to better understand the evolution of the defects in FSW joints as well as their effect on the in-service life of the joints when subjected to mechanical loading.

While the heterogeneity in the vicinity of the welded zone can be analyzed through strain fields measurements on the specimen surfaces [17,18], it is more difficult to investigate the internal structure of the joint, particularly when focusing on the identification of the damage mechanisms [19]. For this purpose, the acoustic emission [20,21] is a suitable technique for monitoring the creation of defects within the welded joint but also for identifying the acoustic signatures that could be associated with each of the damage mechanisms.

The present work aims at proposing an experimental strategy involving three different complementary measurement techniques (X-ray micro-computed tomography, Localized Spectrum Analysis, and Acoustic Emission), the main objective being to detect both the initiation and the evolution of damage mechanisms within an FSW joint. These three techniques were chosen because of their non-destructive and non-contact nature (except the acoustic emission). They also provide full-field measurements, which leads to a wealth of data. This turns out to be useful to understand the mechanisms that govern the mechanical behavior of the joint. Moreover, the synchronization of these three techniques enabled us to correlate the results that they provided. First, the defects within the internal structure of the joint were identified by using X-ray micro-computed tomography before subjecting the joint to tensile loading. The evolution of these defects as a function of the applied tensile stress was monitored by using acoustic emission coupled with non-contact strain fields measurements on two perpendicular faces of the specimen. These faces were marked with periodic patterns such as checkerboards to ensure a high quality of the displacement and strain fields measurement. This technique also aimed at detecting very early the appearance of strain concentrations on the two investigated surfaces of the specimen. The originality of this work is mainly the fact that the three experimental techniques which were used provided complementary information. This enabled us to investigate in detail a complex welding configuration. This would not have been the case if they had been employed separately.

2. Materials and experimental methods

2.1. Specimen preparation

Fig. 1 provides an overview of the studied specimen as well as the size of the zones under investigation. In this experimental study, (as shown in Fig. 3) three aluminum alloy sheets designated AA6061, AA7075, and AA2024 were superimposed in this order and welded together by using the FSW process. The initial size of each alloy sheet is 250 mm in length, 140 mm in width, and 2 mm thick. Once the sheets were welded, the specimen to be tested was cut by machining from a region where the FSW process could be considered as stabilized (i.e. roughly 70 mm away from the edge of the initial sheets), the measured welding temperature remaining constant and being no longer influenced

Table 1
Mechanical properties of the aluminum alloy sheets at the initial state before FSW joining.

Aluminum alloy	Melting temperature [°C]	Tensile strength R_m [MPa]	Yield strength at 0,2% plastic deformation $R_{p0.2}$ [MPa]	Elongation at break A_t [%]
AA 6061	585	120	65	22
AA7075	635	590	524	12
AA2024	500	465	340	17

by the welding tool (pin) advance.

The mechanical properties as well as the melting temperature of each of the three aluminum alloy sheets [22,23] are given in Table 1.

The chemical composition and the density of each aluminum alloy sheet [22] are provided in Table 2. The welding tool (pin) that was used to assemble the three alloy sheets (see Fig. 1) is made from highly alloyed steel, as required by the DIN 1.2312 standard for tools that are categorized P20 + S (40 CrMnMoS 8–6). The pin is an M6-thread and its length of 5.3 mm covers 85% of the specimen thickness to be welded.

The tool shoulder diameter of 22 mm sheets (see Fig. 1) was sufficient to generate the required heat for assembling the three sheets together by using an FSW machine (4–10 model). This machine allows selecting the rotational speeds v_r, within the range of 300 to 1450 rpm, and advancing speed v_a from 10 to 480 mm/min. This machine also allows monitoring the plunging depth of the pin along the z-direction (Fig. 1) while recording the corresponding force value all along the welding process. The temperature was measured using an infrared camera (FLIR A40M featuring a temperature resolution of ±2 °C) at the interface between the tool and the plates being welded (precisely 1 mm behind the tool and pointing to the weld bead). The kinematics parameters used in this study are as follows: v_r= 1400 rpm et v_a= 70 mm/min.

2.2. X-ray tomography

Computed microtomography (μCT) is an imaging technique that helps to have an overview of the internal structure of a test specimen without causing any damage. The non-destructive ability of this technique is a significant advantage in material science, particularly when performing in situ acquisition, as successfully experienced by Buffière et al. [24]. Moreover, this inspection technique is by far more efficient than numerous imaging methods such as microscopy-based ones since it provides 3D data with a resolution of up to 1 μm [24] and even lower, depending on the X-ray source used in the tomography equipment [25]. The X-ray computed tomography equipment (model Phoenix vTomeX / X-ray, see Fig. 2) that was used during this experimental study is located in the MATEIS laboratory (INSA de Lyon, France).

The analysis of the FSW specimen required the use of incident X-rays that were characterized by a voltage of 80 kV and an intensity of 280 μA without any filtering. The voltage of 80 kV was chosen to obtain the best compromise between transmission and contrast. Concerning the current, the maximum value (before defocusing) was used to obtain the maximum photon flux without increasing the source spot size.

Under these conditions, the source spot size was about 2–3 μm. The Varian Paxscan X-ray detector used in this study has an active surface of 200 mm × 250 mm along with a matrix of 1920 × 1536 pixels^2. This detector records radiograms that are encoded in greyscale, with a gray depth equal to 14 bits. The size of the reconstructed volume is 1500 × 1000 × 500 voxels^3 and the size of a voxel after reconstruction is equal to 18 × 18 × 18 μm^3. The data acquisition was performed by using the following procedure: 912 projections of X-rays were considered during the 360-degree rotation of the specimen and the exposure time for each angular position was equal to 333 ms. The resulting 3D images were reconstructed by using a filtered back-projection algorithm [26] which is implemented in the software provided with the tomograph. Information on the theory and the techniques used to reconstruct 3D images can be found in [27].

2.3. Localized spectrum analysis

The purpose here is to measure the strain fields that occur on both the front and the lateral faces of the specimen and to observe whether some coupling exists between the pattern of these strain fields and the internal structure of the solder characterized by tomography, or between these patterns and AE events. The constitutive material being strongly heterogeneous in this zone, strain fields are also expected to be heterogeneous. The technique to be used should therefore ideally be able to distinguish close features in the strain maps, and these maps should be as little as possible impacted by noise and systematic errors.

Table 2
Chemical composition and density of each aluminum alloy sheet.

Aluminum alloy	Chemical composition (in percent by weight)									Density (kg/m^3)
	Si	Fe	Cu	Mn	Mg	Cr	Zn	Ti	Ti + Zr	
AA6061	0,74	0.40	0.22	0.14	0,90	0.18	0.09	0.05	–	2700
AA7075	0.05	0.10	1.60	0.05	2.70	0.19	5,80	0.05	0.06	2810
AA2024	0.10	0.11	4,40	0.47	1.50	0.01	0.14	0.04	0.05	2773

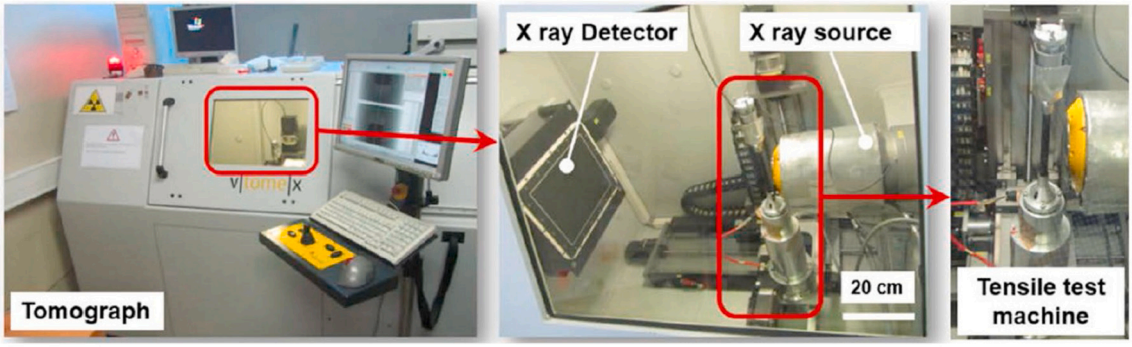


Fig. 2. X-ray computed tomography equipment, model Phoenix vTomeX (MATEIS/ INSA de Lyon).

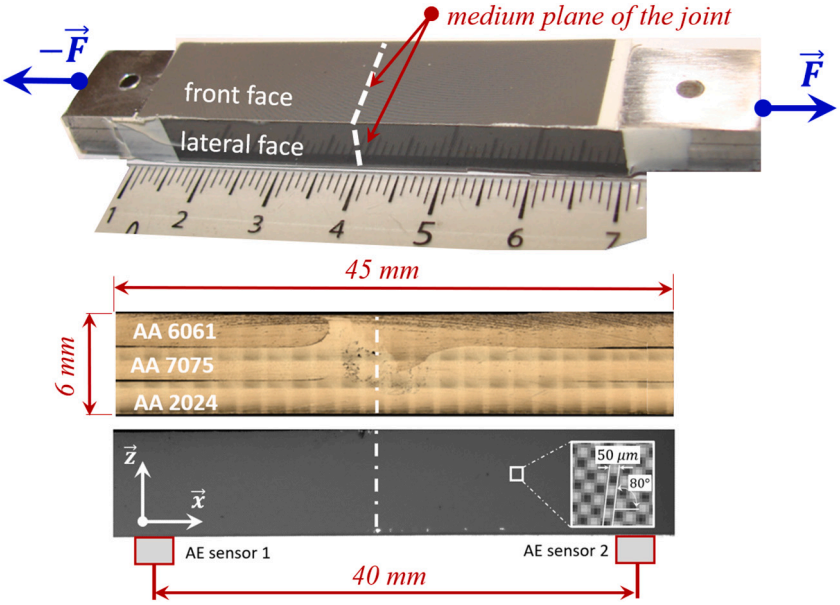


Fig. 3. LSA checkerboard patterns and AE sensors.

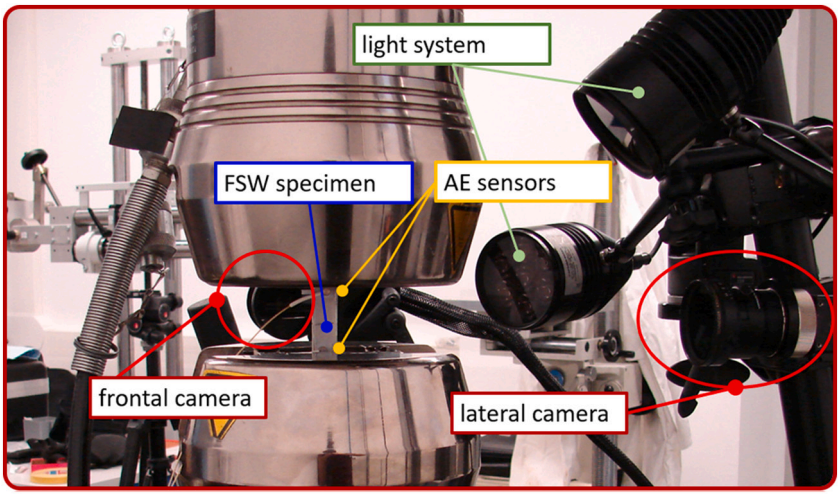
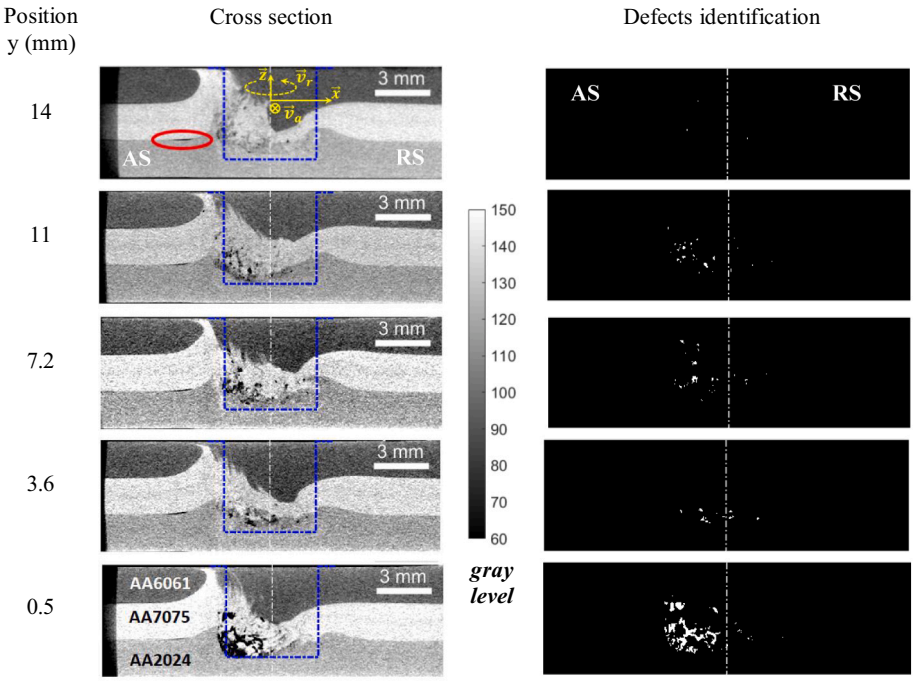


Fig. 4. General overview of the laboratory experimental setup

Digital Image Correlation is the most popular full-field measurement technique [28]. It consists of retrieving displacement and strain fields from images of speckled surfaces taken before and after deformation. However, it has been recently shown in [29] that considering periodic patterns like checkerboards instead of random speckles, and processing the corresponding images with a suitable spectral technique named Localized Spectrum Analysis (LSA) led to much better metrological performance, especially in terms of noise level, ability to distinguish close features in strain maps and systematic errors. The present specimen was therefore marked with such checkerboard patterns by using the transfer technique described in [30]. The period of the checkerboard was 0.1 mm, and the size of the squares forming the checkerboard was 50 µm. Fig. 3 shows a close-up view of such a pattern. It can be seen that the natural symmetry axes of the checkerboard are inclined by an angle of 10 degrees with respect to the borders of the image. This enables us to avoid the presence of possible parasitic fringes in the strain maps due to aliasing, as explained in [31] in the case of periodic grid patterns. The LSA technique as described in [32] was finally used to process the checkerboard images to extract the displacement and strain fields.

2.4. Acoustic emission (AE) monitoring

The purpose of AE monitoring is to analyze the mechanical vibrations emitted by the specimen after a sudden modification of the internal structure of the welded joint during the test. These vibrations can be due to damage, cracking, or plastic deformation for instance. Thus, under mechanical loading, the rapid release of energy from localized cracks within the welded joint generates transient elastic waves, referred to in this paper as AE waveforms. The latter propagate from the crack throughout the specimen before being detected by AE sensors. Thus, in addition to the displacement field measurement, a four-channel AE system equipped with Physical Acoustics' PCI-8 AE boards and preamplifiers was used to record the AE waveforms during the test. Due to the small dimensions of the specimen (see Fig. 1), two lightweight miniature piezoelectric sensors with an optimum operating frequency range of 200–750 kHz were bonded on the specimen with a double-face adhesive tape. They were used to perform a linear localization of AE sources (also termed AE events). The propagation velocity of AE waveforms was set at 4000 m/s following the pencil lead-breaking tests. The AE signal acquisition threshold was set at 50 dB, which is slightly



a) - several cross-sections from the reconstructed volume. The welding tool geometry is superimposed over each picture and represented by the blue dotted line.

b) - porosities detected within several cross-sections

Fig. 5. Reconstructed data after filtering and pores identification.

above the surrounding noise.

2.5. Tensile test set-up

The main dimensions of the specimen subjected to monotonic tensile loading are reported in Fig. 1. An INSTRON servo-hydraulic testing machine (model 1342) equipped with a +/− 100 kN cell force was used to perform the tensile tests at a controlled crosshead speed of 0.5 mm/min.

The displacement and strain fields occurring on two perpendicular faces of the FSW specimen (the front and the lateral ones) were measured by simultaneously using two cameras (Aramis-GOM system), as shown in Fig. 4. Their CCD sensor size is 2448 × 2050 pixels^2. The two cameras were synchronized with each other and with the INSTRON testing machine. Hence the tensile force corresponding to every couple of images was recorded. The checkerboard patterns were transferred to both the front and the lateral faces. These latter are represented in Fig. 1 as the IJKL and LKMN rectangles that are centered over the welded joint. Their length was equal to 40 mm to allow recording the images of the whole faces until specimen failure. A polarized lighting device was also set up for recording images with high contrast at a frequency of 1 Hz. The mechanical loading was applied along the x-direction (Fig. 1), which corresponds to the longitudinal direction of the specimen. For strain analysis, the spatial resolution was equal to 36 pixels with a standard deviation of about 200 $\mu\varepsilon$.

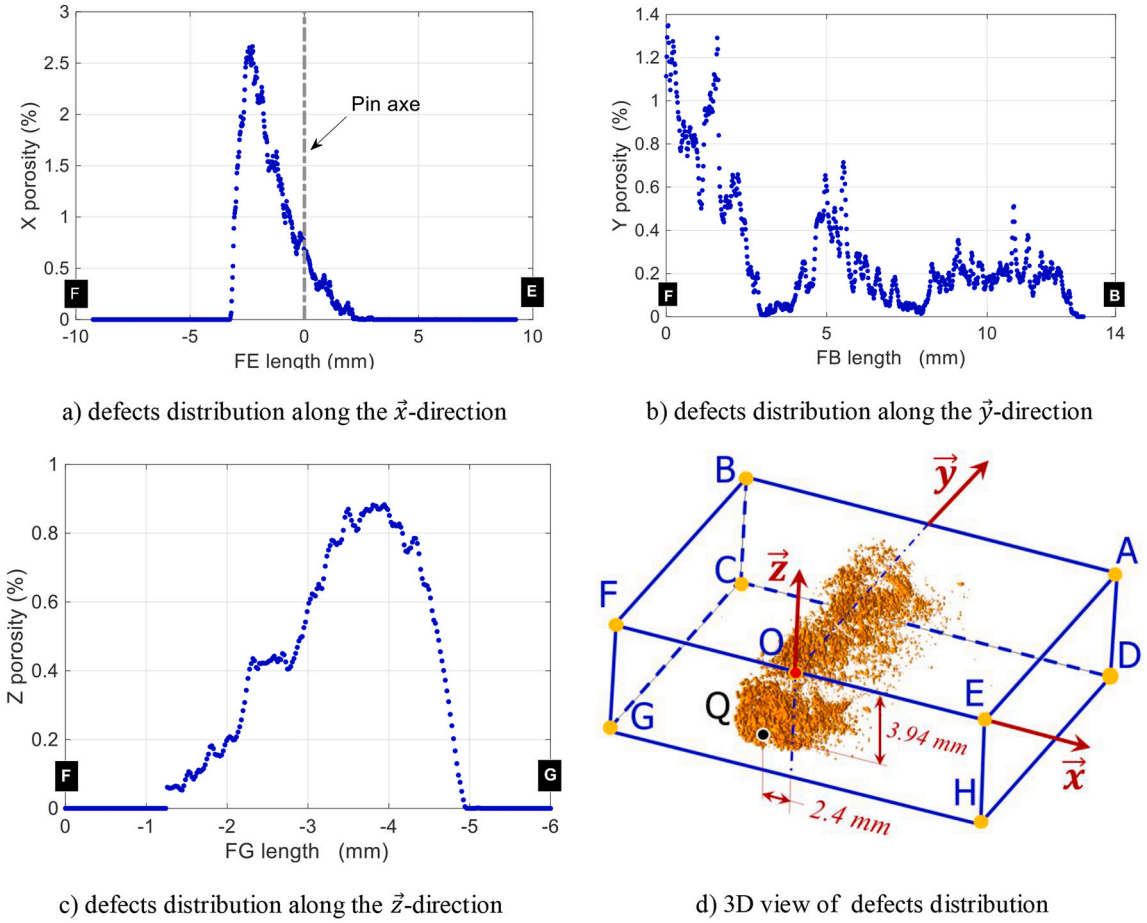
The AE sensors were placed on the specimen, symmetrically on both sides of the welded joint. They were spaced 40 mm apart. The monitoring of AE activity from the specimen was synchronized with both the image acquisition system and the testing machine.

3. Results and discussions

3.1. Thresholding and segmentation

The specimen volume investigated by using X-ray computed microtomography is shown in Fig. 1. It is represented by the blue parallelepiped (ABCDEFGH) centered over the median plane (see dotted lines) of the welded joint. The size of this volume was chosen to identify relatively small size defects (voxel size in reconstruction = 18 μm) but also the morphology of the melted alloys mixture. As mentioned in Section "2.2 X-Ray Tomography" above, the initial state of the internal structure of the specimen has been analyzed using the ImageJ software [33]. This is an open-source software dedicated to image processing and analysis. It can be extended with plugins and macros. The data processing steps described below were applied to the reconstructed volume. First, the quality of this latter was improved through the use of a 3D median filter of size 3 × 3 × 3 voxels^3. This allows reducing the noise level that could affect the different steps of both the thresholding and segmentation steps. Then, to analyze the whole volume and not be dependent on the random-access memory, the encoding of the volume was reduced from 14 to 8 bits. Loss of information following this re-encoding had almost no effect on the qualities of detected phases. To illustrate this, Fig. 5-a shows five sections that are parallel to the FEHG face (Fig. 1) for different values of y. The average gray level for a 8 bit gray depth is 99.5, 136.1, and 120.7, for the AA6061, AA7075, and AA2024 alloys, respectively. This difference is in good agreement with the density variation of each alloy, as shown in Table 2. Indeed, the density is slightly different for each alloy being welded. This is a great advantage to fully understand the mixing of these three materials.

For efficient analysis of data from the studied volume, it is necessary to perform segmentation to separate the different phases: the air surrounding the specimen, the pores, or the spatial distribution of the



a) defects distribution along the $\vec{x}$-direction

b) defects distribution along the $\vec{y}$-direction

c) defects distribution along the $\vec{z}$-direction

d) 3D view of defects distribution

Fig. 6. Internal defects distribution within the welded joint.

different welded aluminum alloys. The simplest way to segment data into polyphasic gray levels consists of using thresholds [34,35]. The latter can be manually selected or preferably computed algorithmically. Because of the form of the volume histogram, a so-called Otsu threshold [36] was applied. In his paper, Otsu demonstrates that a threshold can be computed to segment bimodal data by maximizing the inter-class variance of the gray levels in each class. Yet, it is necessary to generalize this approach to some thresholds greater than one. The idea here is not to separate each alloy sheet, even if the reconstructed data allow it, but also and particularly to automatically block out the air surrounding the specimen before identifying the porosity. Both components were detected by using the same thresholding level. In this case, the differentiation between the air surrounding the specimen and the porosities generated during the FSW process lies in the volume of the characteristic size associated with each phase as it is quite obvious that the air surrounding the specimen is characterized by a volume greater than that of the biggest identified porosity. Then, the thresholding step (grayscale level lower than 30) was applied again over the specimen volume without its surrounding air to separate the pore-type defects within the join. The pores distribution is shown in Fig. 5-b. All pores having a size lower or equal to that of the 3D median filter (pores with sizes lower than 60 μm) are not considered representative, the noise effect on their detection being too high. One can also notice by superimposing the pin over the different cross-sections shown in Fig. 5-a that the highest volume fraction of pores is located on the advancing side at the edge of the pin, and at the interface between the AA7075 and AA2024 aluminum alloy sheets.

3.2. Defects measurement by X-Ray μtomography

3.2.1. Distribution of the pores in the joint

Computed microtomography is a highly efficient tool for the analysis of a structure consisting of several phases characterized by various densities [37]. This experimental technique provides relevant details on the investigated welded joint, as shown in Fig. 5. These pictures allow an in-depth understanding of the effects of the welding parameters on joint quality. It helps predict different failure mechanisms (initiation and propagation of cracks) which occur when the joint is subjected to mechanical loading. First, one can observe the spatial distribution of the three alloys in the vicinity of the pin. This visualization was made possible because of the difference in the density values of the tested alloys (see Table 2). One can see that the AA6061 and AA7075 alloys are well mixed. Few pore-type defects are visible at the interface between the two alloys. These defects are located in the welding direction. In Fig. 5-a (at y = 14 mm), hooking defects are also observed. This leads to a lift of the interface between two sheets. These hooking defects are generated by the translation of the material in its pasty state. This translmation is caused by the threaded welding tool. The formation of the hooks as well as their contribution to the mechanical behavior of the welded joints have been studied in [14] for instance. Different hook sizes and shapes were observed in this reference. These features depend on the welding parameters (welding speed, rotational speed, and advancing speed). By coupling digital image correlation (DIC) and tomographic analysis during tensile-shear tests, it was found that the hook characteristics govern the fracture behaviors and, consequently, the mechanical properties of the whole welded joints.

We focus here mainly on the characterization of the pores and their distribution within the joint. The spatial distribution of the detected

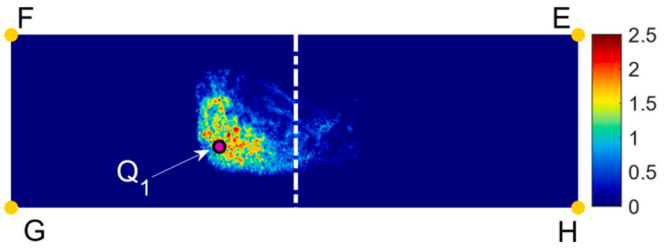


Fig. 7. Compacity of the joint in the $\vec{y}$-direction.

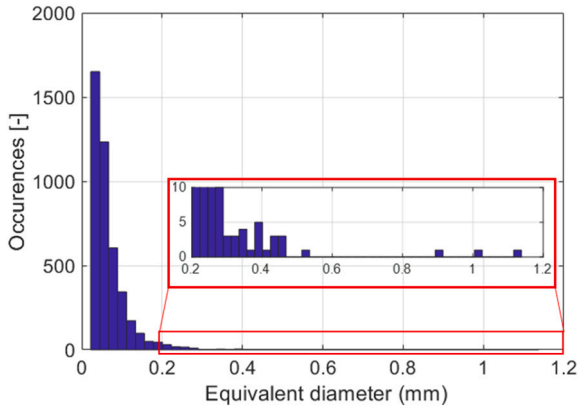


Fig. 8. Number of defects as a function of their equivalent diameter.

pores is visualized in three dimensions (Fig. 6-d). The porosity is evaluated along each of the three directions of the specimen volume in order to identify the areas that are highly affected by the defects. The formula used to calculate these porosity values are as follows:

$$X\ porosity\ (x) = \frac{S_{pores}(x)}{S_{0x}} \times 100 \tag{1}$$

$$Y\ porosity\ (y) = \frac{S_{pores}(y)}{S_{0y}} \times 100 \tag{2}$$

$$Z\ porosity\ (z) = \frac{S_{pores}(z)}{S_{0z}} \times 100 \tag{3}$$

Where S_{0x} is the FBCG cross-section (see Fig. 1) along the $\vec{x}$-direction and between points G and H within the reconstructed volume. The cross-section is considered as constant over the calibrated area of the specimen. S_{0y} represents the FEGH cross-section (see Fig. 1) along the $\vec{y}$-direction and over the whole width of the specimen. S_{0z} is the ABFE cross-section (see Fig. 1) along the $\vec{z}$-direction and over the thickness of the specimen. $S_{pores}(x)$ represents the cross-section of the pores. It is perpendicular to the $\vec{x}$ axis and computed between points G and H, within the reconstructed volume. $S_{pores}(y)$ is the cross-section of the pores on areas that are parallel to FEHG (see Fig. 1) along the $\vec{y}$-direction. $S_{pores}(z)$ represents the cross-section of the pores on zones which are parallel to ABFE along the $\vec{z}$-direction (see Fig. 1). Fig. 6-a shows the evolution of *X porosity* (x). Monitoring this porosity provides some information that are useful for understanding the evolution of the real cross-section of the joint. First, one can note that the pores are mainly located along a segment that is nearly centered (±3 mm) around the location of the welding tool axis along a zone, which is greater than the pin diameter. The zone, which is the most affected by the pores is located within the advancing side and at −3 mm from the pin axis. At this position, the cross-section of the specimen is reduced by slightly more than 2.5%. This is likely the zone where the very first cracks would be initiated. One can also point out a rapid and gradual decrease in the number of pores towards point E since the value of the cross-section at this position is nominal. Fig. 6-b shows the evolution of *Y porosity* (y). This characterizes the distribution evolution of the pores along the specimen width, in other words in the welding direction. Based on the analysis of this evolution, one can conclude that the welding process is locally not completely stabilized. This is probably due to a discontinuous interfacial contact during the welding phase and to the fact that the fusion temperature of the AA7075 alloy is higher than those of the AA6061 and AA2024 alloys. It is worth noting that this evolution should lead to heterogeneous stress distribution during a tensile test. Consequently, the strain distribution should also be heterogeneous over the whole width of the specimen. Finally, the pore distribution along the $\vec{z}$-direction is analyzed through the parameter *Z porosity* (z). This quantity is plotted in Fig. 6-c. 60% of the specimen width is affected by the pores, with a high concentration at the interface between the AA7075 and AA2024 alloys. This zone featuring high pore concentration is located at about 4 mm below the contact surface between the pin shoulder and the AA6061alloy sheet. This is, firstly, because the heat, which is generated mainly from friction between the pin shoulder and the AA6061alloy sheet, is not continuously spread out due to some discontinuities such as the thin air layers, which are visible in Fig. 5-a. They appear between the alloy sheets to be welded and in the vicinity of the pin, and as a consequence the appearance of a strong temperature gradient in the joint thickness and a reduction in the effective welding temperature of the AA7075 and AA2024 sheets. A significant difference between the effective welding temperature and the optimal one (supposed to be equal to [0.7 to 0.8] times T_f(°C) [38], this latter being the melting temperature) can result in pores appearance. The volume fraction of these pores is proportional to the difference between the effective welding temperature and the optimal one.

Given the foregoing, it can be argued that the zone where the fraction of pores is maximal is represented by point "Q" in Fig. 6-d. The coordinates of this point are the following: x = −2.4 mm, y = 0 mm, and z = 3.94 mm.

3.2.2. Local porosity fraction

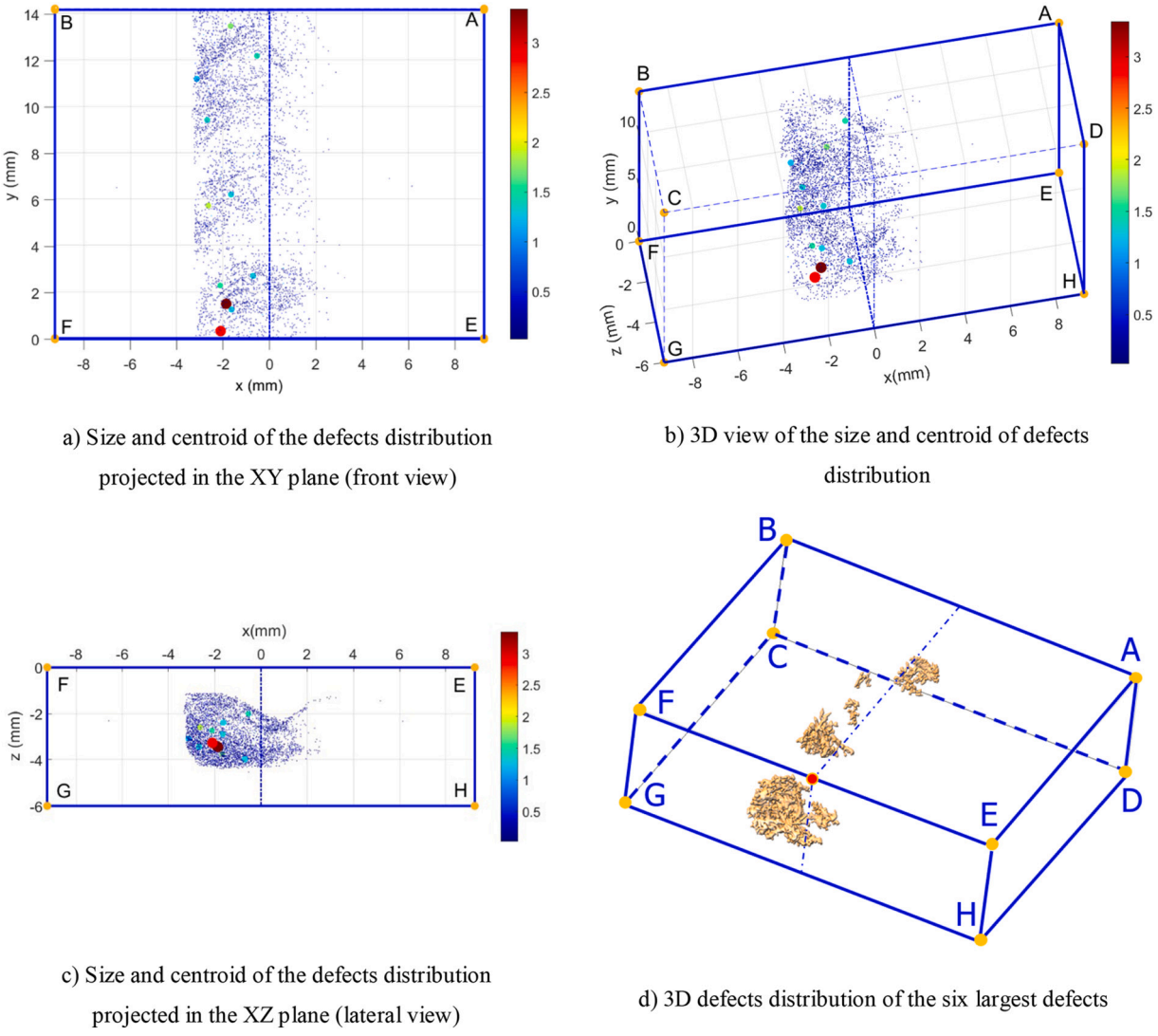
Similar strategies can be applied to identify in the $\vec{x}O\vec{z}$ plane and along the $\vec{y}$-direction (see Fig. 1) the zones that are characterized by a high volume fraction of pores. To this end, a similar approach has been applied thus allowing to calculate the compacity parameter η_{loc}, defined in Eq. 4. This parameter, referred to as the local porosity volume fraction, takes the form of either a matrix $M_{pores} = [m,p]$ for the segmented pore phase or a Boolean matrix $M_{joint} = [m,n,p]$ for the whole joint. These matrices are computed as follows:

$$\eta_{loc}(i,k) = \frac{\sum_{j=1}^{n} M_{pores}(i,j,k)}{\sum_{j=1}^{n} M_{joint}(i,j,k)} \times 100 \tag{4}$$

The map, shown in Fig. 7, allows one to point out that the zone which exhibits the highest pore volume fraction is located within the AA7075 alloy sheet and on the advancing side. In this area, the maximal value of η_{loc} is 2.5% (shown by point Q_1in Fig. 7). There is a good agreement between the η_{loc} map and the details observed on the lateral face of the specimen shown in Fig. 3. However, the most affected zone, in other words, the one characterized by a value of η_{loc} greater than 1.5%, is mainly located within the AA7075 alloy sheet and along the whole width of the specimen ($\vec{y}$-direction).

3.2.3. Equivalent diameter, maximal length of the major axes, and shape of defects

Another method could be used to analyze the defect distribution within the joint. It consists of evaluating both the size and the center of gravity of each defect along the welding line. The distribution of the diameter of 4275 pores is plotted in Fig. 8. Once again, only the pores having a diameter greater than 60 μm are considered in this histogram. Significant fluctuations of the equivalent diameter of the defects can be



a) Size and centroid of the defects distribution projected in the XY plane (front view)

b) 3D view of the size and centroid of defects distribution

c) Size and centroid of the defects distribution projected in the XZ plane (lateral view)

d) 3D defects distribution of the six largest defects

Fig. 9. Centroid, maximal length of the major axes, and shape of defects. The color scale represents the size (the major axes) of defects in mm.

observed. This diameter lies between 0.06 mm and 1.2 mm, with a high concentration between 0.06 and 0.3 mm.

The equivalent diameter is well suited to characterize spherical-shaped defects. Thus, one can see in the present study (see Fig. 5) that the shape of larger defects is far different from a sphere. To better understand the defect distribution within the joint and to have a more realistic picture of the effective size of the defect, we focused on the longest major axis of the defect. This axis represents the major axis of the ellipsoid that has the same normalized second central moments as the defects under investigation [39].

Fig. 9-b shows the spatial distribution of the defects as a function of their center of gravity as well as the size (color level) of the longest major axis. It should be noted that the defects under 0.5 mm in size are asymmetrically distributed (78% of them are located on the advancing side) with respect to the welding line. It is very clear from Fig. 9-a that the defects characterized by a maximal length of the major axes greater than 1 mm are all located on the advancing side, with a downward trend for positive values along the y-axis. It should also be noted that the defects are spread out over three main zones that are defined by their position along the y-axis. This result is in very good agreement with the Y porosity evolution shown in Fig. 6-b.

Fig. 9-c shows that these defects are mainly located within the melted area of the three alloys. A high density of defects was also observed in the initial position of the AA7075 alloy sheet. As a complement to the above analysis, we plotted the six largest defects in Fig. 9-d. In this figure, it is clear that the shape of the defects is complex since it looks like a network of interconnected defects, as previously observed in [11]. It's worth noting that the largest defect is characterized by a maximal half-axis of length 3 mm. It is located close to the EFGH plane. These complex shapes that spread out over a few millimeters should probably negatively affect the strength of the assembly because they should be activated first when the joint is subjected to mechanical loading.

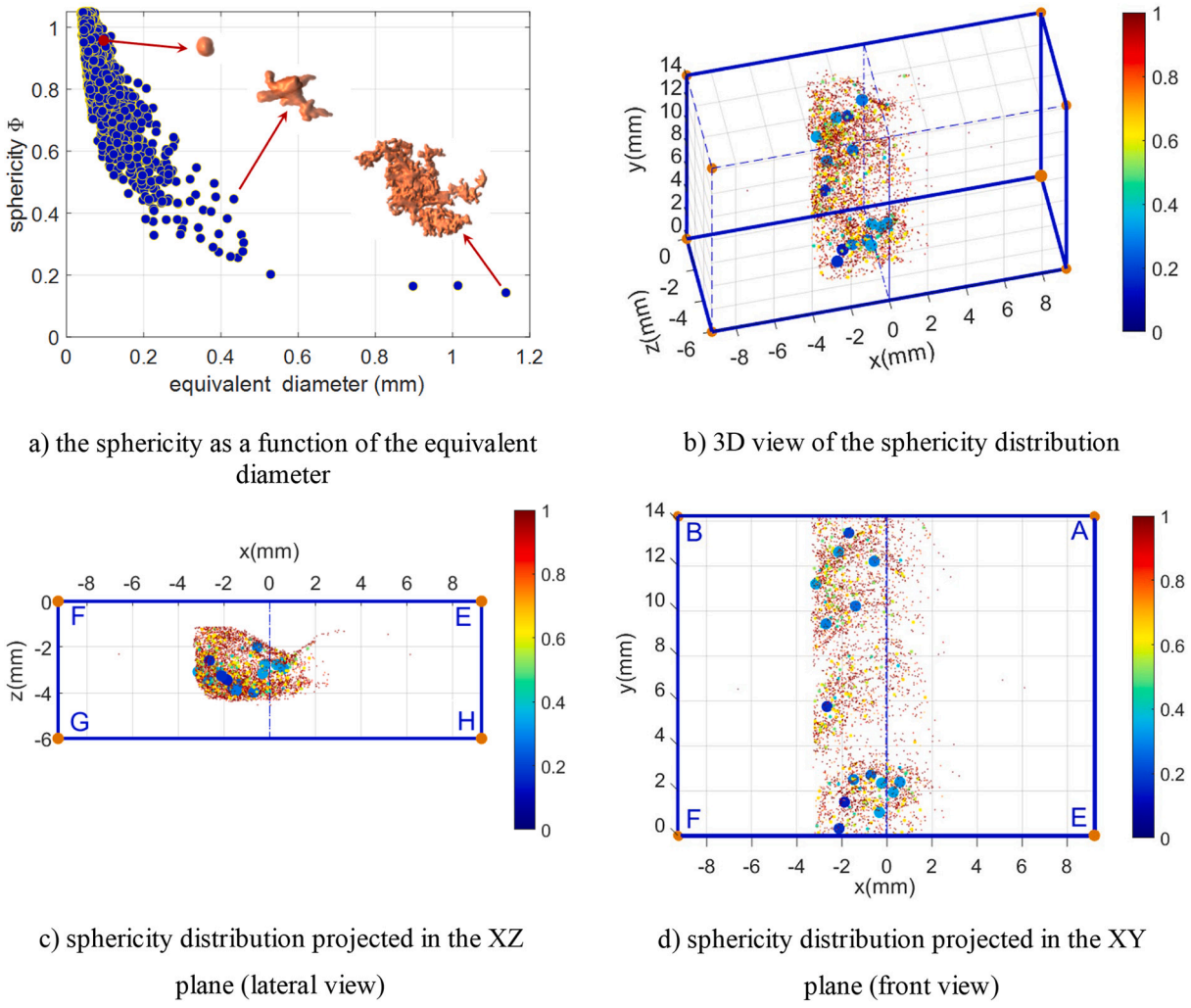
3.2.4. *Sphericity of the defects*

As a complement to the above analysis, the shape of defects has been thoroughly characterized by computing its sphericity denoted by ψ. The latter represents the similarity level between the shape of an object and a sphere. The rate of sphericity ranges between 0 and 1. For example, it equals 1 for a sphere, 0.806 for a cube, 0.874 for a cylinder, and 0.671 for a tetrahedron.

The formula used to compute the sphericity is the one proposed by Wadell in 1935 [40]. It is given in Eq. 5. In this formula, V_p and A_p represent respectively the volume and the surface of the defect.

$$\psi = \frac{\pi^{\frac{1}{3}}(6V_p)^{\frac{2}{3}}}{A_p} \tag{5}$$

The evolution of the sphericity as a function of the equivalent



a) the sphericity as a function of the equivalent diameter

b) 3D view of the sphericity distribution

c) sphericity distribution projected in the XZ plane (lateral view)

d) sphericity distribution projected in the XY plane (front view)

Fig. 10. Defects distribution as a function of their sphericity. The color scale represents the sphericity of defects.

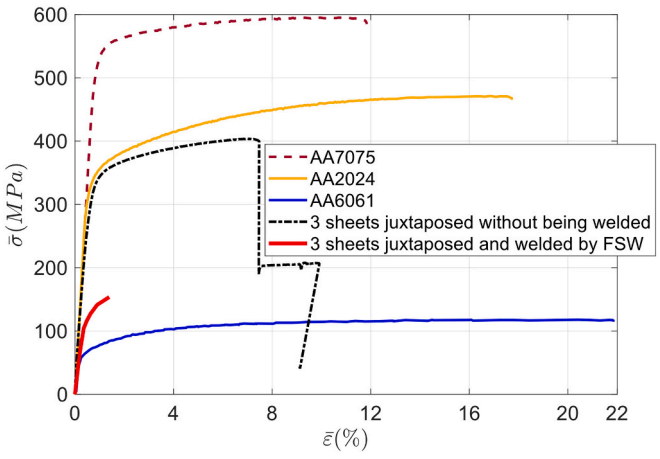


Fig. 11. Macroscopic mechanical behaviors of a specimen made of the studied alloy sheets, a specimen made of non-welded superimposed alloy sheets, and the FSW specimen under study.

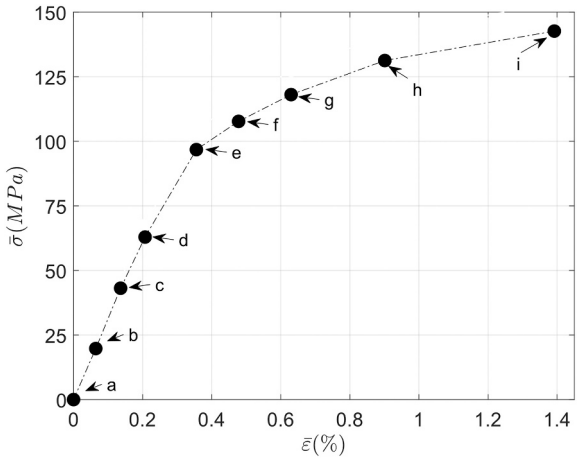


Fig. 12. Macroscopic behavior of the FSW specimen.

diameter is plotted in Fig. 10-a. It can be seen that most of the defects, particularly those under 0.1 mm in diameter, exhibit a shape close to a sphere whereas the largest defects are characterized by sphericity slightly lower than 0.2, which means highly complex shapes. To illustrate this, we superimposed on the same figure the shape (not to scale) of different types of defects that are characterized by sphericity of 0.96, 0.45, and 0.16. One can also see from this figure that for some defects, the sphericity is greater than the theoretical limit of 1, particularly for those with the smallest equivalent diameters. This can be due to the voxelization effect during data acquisition since the size of the

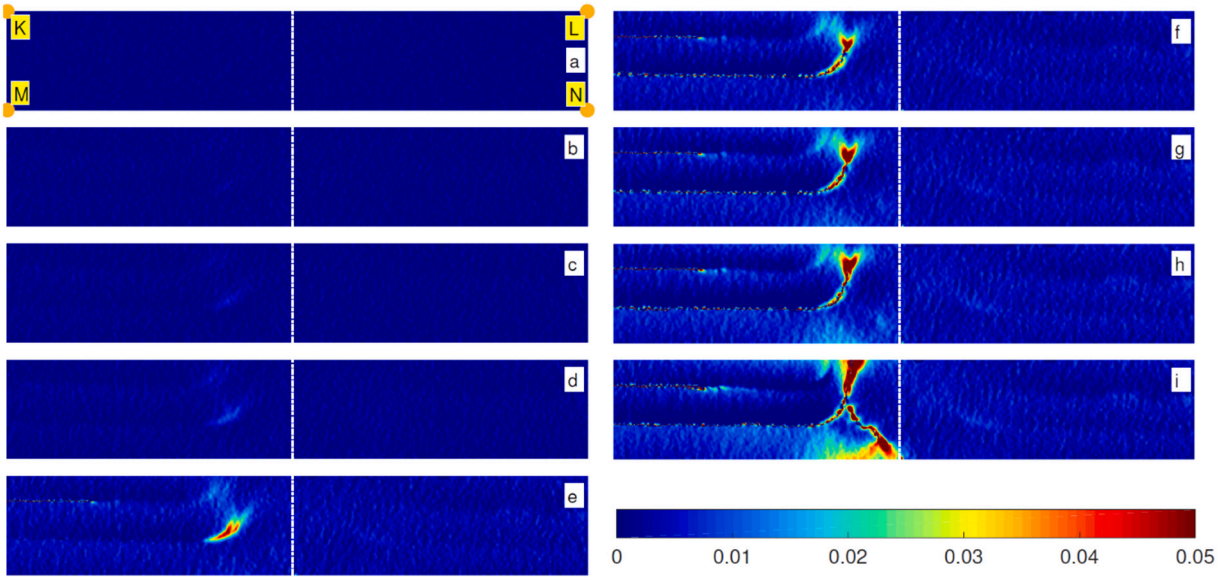


Fig. 13. Local strain field (ε_{xx} [in ***μdef***]) maps on the joint lateral face.

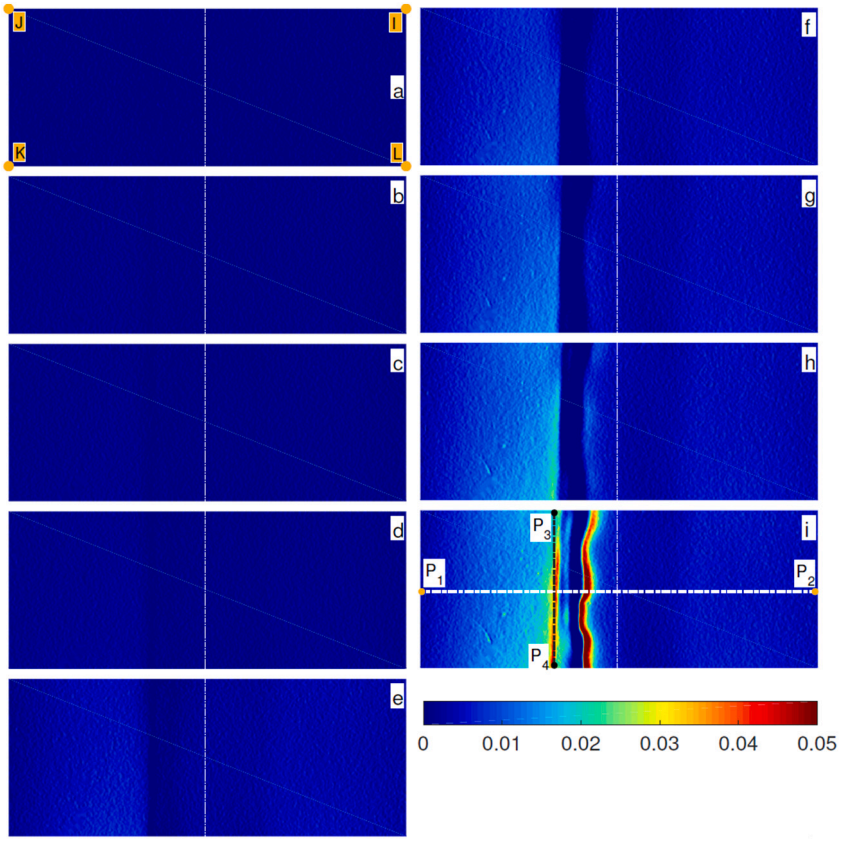
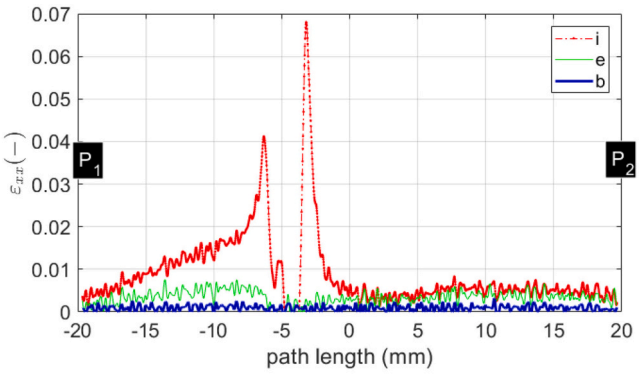


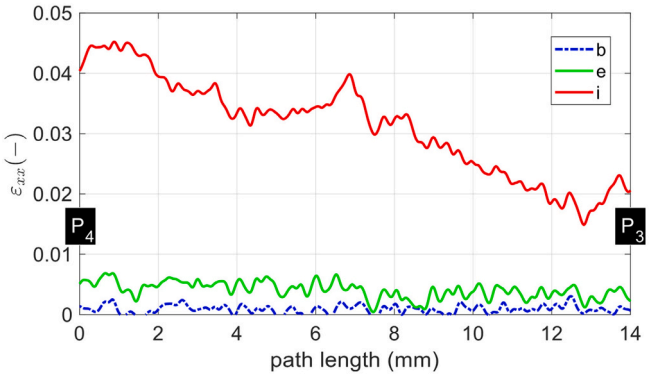
Fig. 14. Local strain field (ε_{xx} [in ***μdef***]) maps of the joint front face.

voxel is 18 μm. For very small objects, this can lead to aberrant rates of sphericity because of miscalculations of the volume [40].

It is also interesting to plot the sphericity as a function of the initial position of each defect. This position is represented by the coordinates of the center of gravity. Fig. 10-b shows the spatial distribution of the defects. The color scale is correlated with the rate of sphericity. The red dots have a rate of sphericity close to one while the blue ones indicate a value close to zero. It is clear that defects with a low rate of sphericity, in other words, characterized by a high equivalent diameter, are located on the advancing side of the joint. Based on another graphical presentation (Fig. 10-d) it can be seen that the defects characterized by a sphericity lower than 0.4 are spread out over three main zones. The first one located between y = 0 and y = 4 is the most affected (presence of 8 defects characterized by an equivalent diameter greater than 0.4). This leads to a weakening of the strength of the joint because its effective cross-section is reduced in this zone. The appearance of these zones is



a) ε_{xx} of the front face: mean values projected along the $\vec{x}$-direction



b) ε_{xx} of the front face: mean values projected along the $\vec{y}$-direction

Fig. 15. Mean values of ε_{xx} projected along two directions.

undoubtedly due to the inhomogeneity of the mixing during the welding process associated with a local change in both the welding temperature and the force applied by the welding tool.

Fig. 10-c shows the distribution of defects over the thickness of the joint. It should be noted that the most irregular defects, which are characterized by a complex shape, are located in the AA7075 alloy sheet and at the interface between this sheet and the other two alloy sheets.

3.3. Macroscopic and local behavior

The macroscopic mechanical behavior (nominal stress $\bar{\sigma}(MPa)$ versus nominal strain $\bar{\varepsilon}(\%)$) of the three alloy sheets subjected each to monotonic tensile loading is shown in Fig. 11. A loading rate of 1 mm/min (crosshead speed) was applied in each case. Three tests were carried out with a very good repeatability in terms of elongation and maximum stress at failure. For each configuration, good reproducibility of the tensile tests is observed. However, only one curve by tested configuration has been plotted for the sake of clarity. These results show that the welded configuration leads to a tensile strength lower than those of the other specimens except the AA6061 alloy sheet. The presence of a significant density of defects within the joint is undoubtedly the cause of the early cracking of the assembly and thus the low strength of the weld. This strength is 37% lower than that of the non-welded configuration obtained by only superimposing the three aluminum alloy sheets. As a consequence, the macroscopic nominal strain at specimen failure is equal to 1.4%, which is also low compared to its counterpart obtained with a specimen made up of three superimposed but non-welded alloy sheets. The latter configuration leads to a nominal strain at failure of about 7.75%, see Fig. 11.

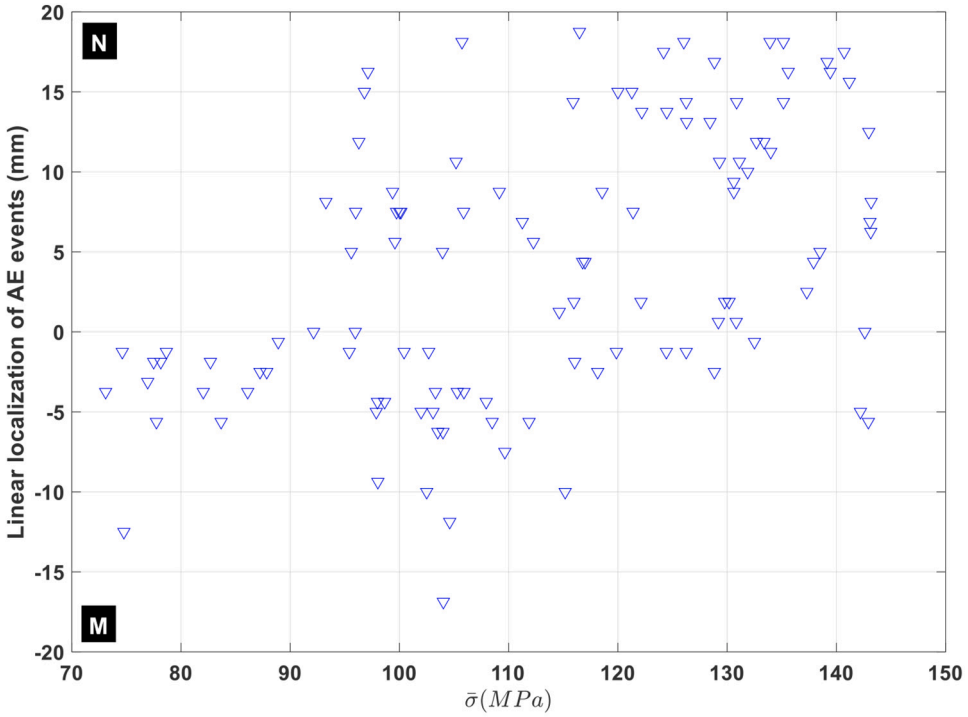
Based on the microtomographic analysis presented above, one can state that this FSW welding configuration is characterized by a very heterogeneous defect distribution. This distribution leads to the appearance of stress concentrations which are added to the residual stresses resulting from the welding process. To better understand the effect of the defects on the joint behavior, we investigated the strain local fields along the loading direction. Fig. 12 shows the macroscopic strain of the FSW specimen. The nine black dots represent the moments at which the strain field (ε_{xx}) evolution was finely analyzed along the loading direction, on the front and lateral faces (IJKL and LKMN, respectively), see Fig. 1. The first four dots, labeled a, b, c, and d, lie in the quasi-linear elastic portion of the macroscopic response whereas the last five, labeled e, f, g, h, and i, are located in the non-linear portion of the response.

Fig. 13 shows with a good spatial resolution the strain field (ε_{xx}) measured on the front face of the joint. Thanks to the LSA technique that is powerful to get small strains values over small regions, it can be seen that small strain peaks are detected early (dot labeled b), namely for macroscopic stress levels lower than 20 MPa. These strain peaks are located at the interface between the AA7075 and AA2024 alloy sheets and on the advancing side. There is a very good agreement between the deformed zone and the one characterized by a high density of defects, as identified from the microtomography results analysis. In addition, the location of the deformed zone is very close to that of the point Q represented in Fig. 6-d above. It should be noted that this deformed area is progressively widening when the nominal stress reaches the values represented by the dots c and d (Fig. 12), leading to an increase in the local deformation of nearly 2% for a corresponding macroscopic strain ten times lower. The transition between the elastic-linear portion and the non-linear one, which is materialized by the dot labeled e, highlights a significant growth of the value of the local strain field, which clearly means a crack initiation. This crack propagates when the stress level reaches that of dots f, g, and h, successively. The crack propagation path is easily visible from the strain maps (see Fig. 13). The form of the crack path shown on these maps only makes sense for the lateral face of the specimen under investigation. This crack path may have a three-dimensional shape within the volume of the welded joint but this is not detectable by this 2D strain measurement technique.

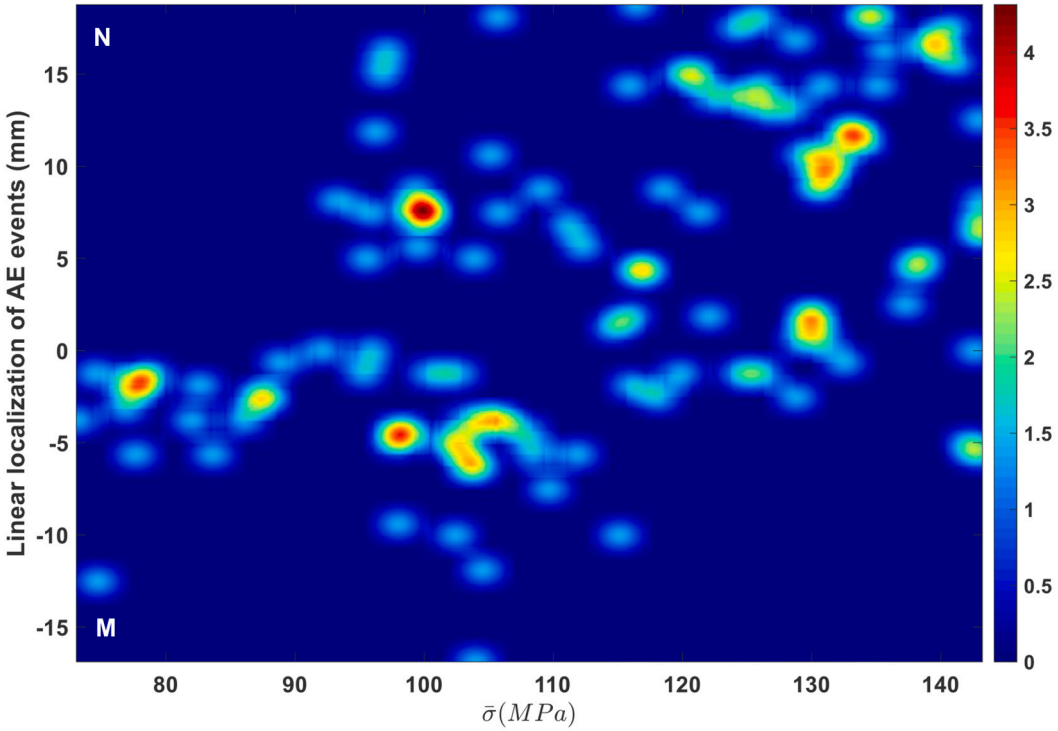
The strain field map associated with the testing moment labeled i (Fig. 13) exhibits a crack bifurcation when the specimen fails, thus enabling monitoring of the crack propagation through each alloy sheet.

The strain maps measured on the front face (see Fig. 14) provide additional information. These maps computed at the first four testing moments (dots: a, b, c, and d) do not put in evidence notable deformation zones. Strain values observed on these maps are in good agreement with both the deformation measured on the front face (on the AA6061 alloy sheet) and the macroscopic nominal strain. Similarly, one can see on these maps a 2 mm-wide strip where the local strain value is close to zero. This strip is still visible in the non-linear portion of the macroscopic behavior (dots labeled e to i). It represents the area where the specimen, particularly the front face, fails. To understand why the strain value is low within this strip, it is necessary to correlate the strain maps with the different results obtained from the microtomography analysis and presented in Fig. 5. One can see from this figure that the AA7075 alloy sheet moves and penetrates in the AA6061 alloy sheet. Fig. 11 shows a significant difference in the yield strength values of the alloy sheets. This suggests that when the FSW specimen is subjected to mechanical loading, the AA6061 alloy sheet deforms, which is not the case for the strip of AA7075. Moreover, the welded area, which is composed of an AA7075 portion melted with AA6061, exhibits a low strength. Indeed, this is where the crack initiates, as shown on the maps corresponding to points f, g, h, and i (Fig. 14). One last analysis of the strain maps of the front face, particularly those labeled g, h, and i, highlights a localized deformation, which is much larger on the advancing side than on the retreating one.

To show a very representative evolution in the strain field measured on the front face, two cross-sections of the maps at points b, e, and i along the $\vec{x}$- and the $\vec{y}$-direction, labeled P_1P_2 and P_3P_4 respectively,



a) Linear localization of AE events as a function of the applied macroscopic tensile stress



b) Map of AE events concentration with respect to macroscopic tensile stress

Fig. 16. Acoustic emission activity map during the tensile test.

are shown in Fig. 15. First, Fig. 15-a shows the strain field evolutions along the $\vec{x}$-direction (cross − section P_1 between P_2) at different values of the time. The curve deduced from map b is fairly regular whereas the curves from maps e and i are more heterogeneous. Sharp strain peaks appear as the FSW specimen is close to failure. This graphical representation highlights once again the existence of a strip of AA7075. It corresponds to the portion of the strain fields measured along the loading direction and on the front face is close to zero. Fig. 15-b puts in evidence the strain field evolution along the $\vec{y}$-direction (cross-section between P_3 and P_4). Even though the strain curve deduced from map b

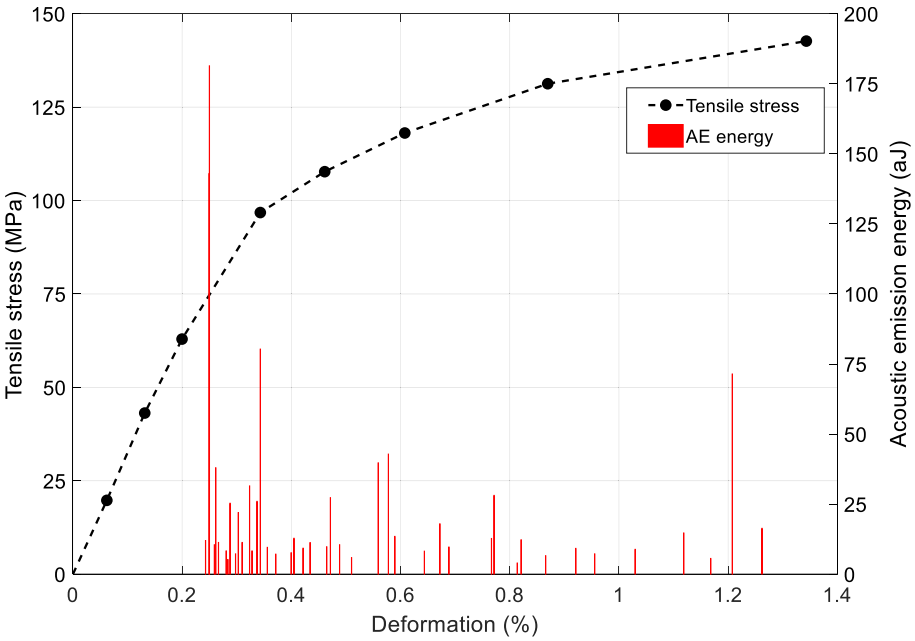


Fig. 17. AE energy analysis to detect the yield strength of the welded joint.

remains constant and small, one can see that the one from map i exhibits values ranging between 1.5% (in the vicinity of the point P_3) and 4.5% (in the vicinity of the point P_4). A linear trend is observed. This evolution along the $\vec{y}$-direction can be linked to that of the *Y porosity* (y) curve shown in Fig. 6-b. It can be seen from this figure that the value of the *Y porosity* (y) is about 0.2% and 1.4% in the vicinity of the points P_3 and P_4, respectively. This evolution of *Y porosity* (y) could locally reduce the effective cross-section of the specimen, thus leading an important part of the tensile loading to be transferred through the AA6061 and AA2024 alloy sheets. This is especially true in the vicinity of the point P_4. These results show once again how it is complex and difficult to investigate this type of welding configuration by using classic measurement tools and standard approaches.

3.4. Acoustic emission activity

The AE activity during the tensile test is first analyzed by focusing on the localization of AE events within the FSW joint (Fig. 16). The results show that cracking starts in the lower half of the joint before spreading throughout the assembly. The very first AE events appear for a stress value equal to 73 MPa.

For better visualization of the zones of the welded joint featuring a high concentration of cracks, the AE event distribution along the weld is plotted in Fig. 16 as a function of the tensile stress. It can be seen from this map that the first zone with a high crack concentration is detected when the FSW joint is subjected to a tensile stress of 77 MPa. Fig. 16-b) also shows that the zones with a high crack concentration appear at various levels of the tensile stress, and these "hot" areas may be associated with crack nucleation.

4. Correlation between results

4.1. Mechanical behavior versus AE activity

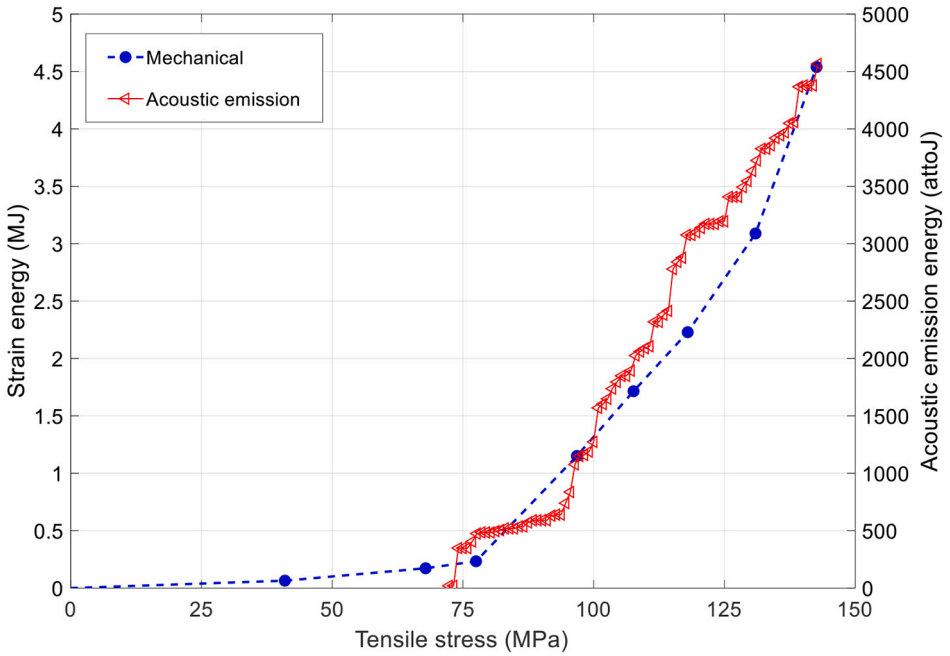
In this section, the macroscopic mechanical behavior of the welded joint is compared to the AE activity generated during the test. The evolution of the energy level associated with each AE event is plotted as a function of the longitudinal deformation (Fig. 17).

It can be seen from this comparison that the very first AE events occur well after the test has started. These results also point out that the highest released acoustic energy level is detected at a stress level of 75 MPa, and at the testing time at which the first crack concentration is detected and localized (see Fig. 16). As successfully experienced in a previous study [41], acoustic energy is a feature that helps evaluate, through its evolution, the yield strength of a material or a joint in the present study. Indeed, as long as the yield strength of the material or the assembly is not reached, the latter continues to store mechanical energy. Once reached, the released strain energy is accompanied by transient elastic waves that are highly energetic, which can be related to permanent strain or micro-damage within the material. During the test, the AE software records the wave signals and instantaneously computes and plots the corresponding acoustic energy value. It allows for real-time monitoring of acoustic energy evolution. Based on this evolution plotted in Fig. 17, one can point out that the second-highest acoustic energy value is detected when the slope of the macroscopic mechanical behavior curve drastically changes, thus for a tensile stress value of 96 MPa and a longitudinal deformation value of 0.34%.

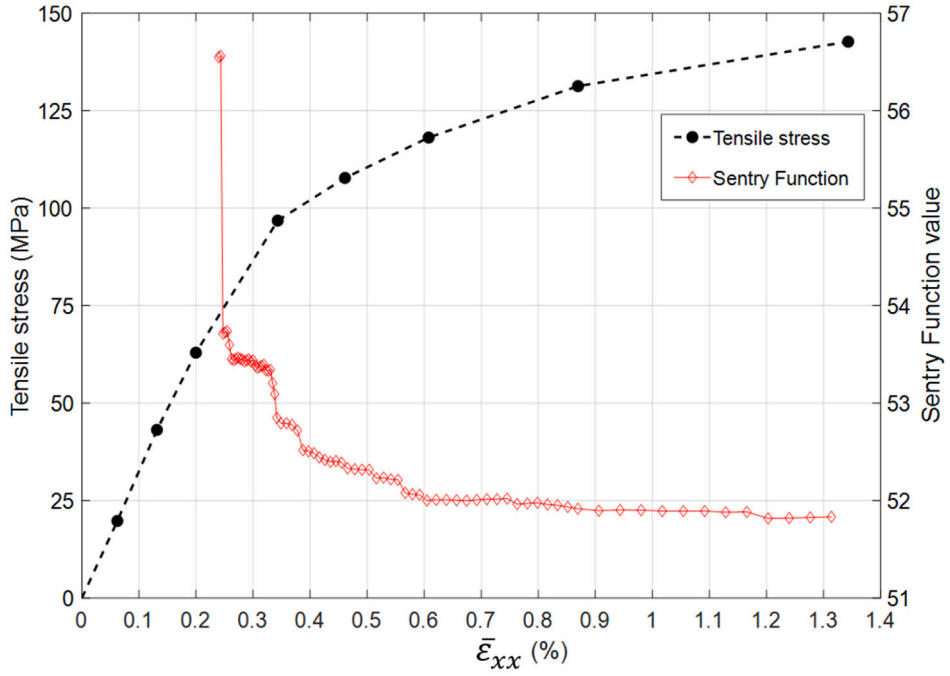
By comparing the results plotted in Fig. 17 and Figure Fig. 16, it can be observed that this radical change of slope is accompanied by the detection of crack concentration. In this study, the analysis of the AE activity shows that beyond the detection of first mechanical damage (crack concentration accompanied with AE events highly energetic), the FSW joint continues to store mechanical energy before reaching its yield strength. This analysis methodology may be used to compare the mechanical efficiency of several welding configurations by evaluating the impact of an early appearance of mechanical damage within the joint on its capacity to have an elastic response.

The evolutions of the mechanical and acoustic emission energies are compared in Fig. 18 to investigate in deep the welded joint behavior, in particular beyond its yield strength. One can see in Fig. 18-a that for a tensile stress value greater than 78 MPa, the evolutions of the two types of energy show the same trend. There is a ratio of about 1.10^{21} between these two quantities.

As successfully experienced in a previous study [42], the so-called Sentry function allows analyzing in-depth the mechanical behavior of the joint, since it combines both mechanical and acoustic energies. This function is given in eq. (6). It involves the logarithm of the ratio between the strain energy $E_s(x)$ and the acoustic energy $E_a(x)$, where x is the test-driving variable (usually displacement or strain).



a) Comparison between the evolution of both the strain energy and the acoustic emission energy during the tensile test

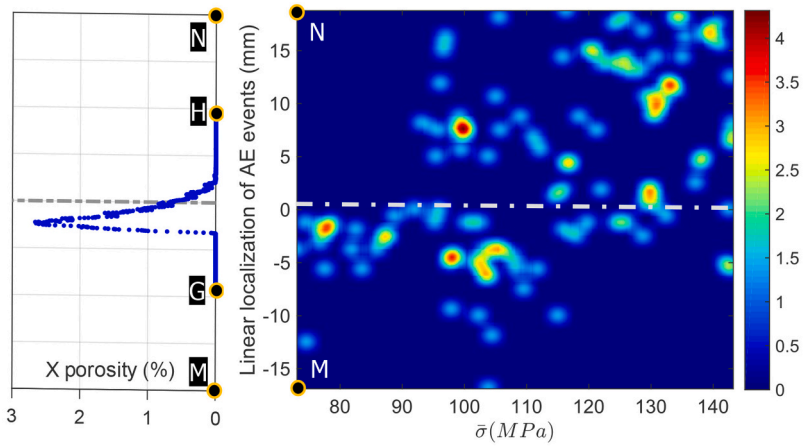


b) Use of the Sentry function to highlight the dependency between the strain energy and the acoustic emission energy during the tensile test

Fig. 18. Sentry function: Dependency between mechanical behavior and AE activity.

$$f(x) = ln\left[\frac{E_s(x)}{E_a(x)}\right] \quad (6)$$

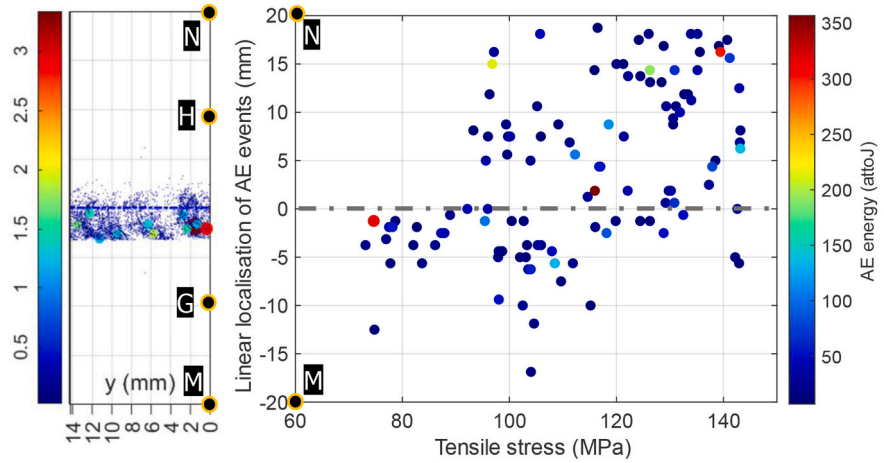
The Sentry function f(x) is divided into four distinct portions, and each one describes a particular signature of the mechanical behavior of the material (or the joint in the present study). Additional information on this Sentry function can be found in [42,44]. By analyzing the results from Fig. 18-b, it can be seen that the first stage of the Sentry function is characterized by the sudden release of the strain energy. Following this stage, one can notice some abrupt drops in the Sentry function. Each of them is associated with a sudden release of one part of the strain energy that was stored previously. This sudden release of mechanical energy is



a) Porosity distribution along the $\vec{x}$-direction

b) Linear localization of AE events concentration as a function of applied tensile stress

Fig. 19. X-ray microtomography versus AE: Localization of initial defects versus very first AE events.



a) Initial defects distribution projected in the XY plane

b) Mono-parametric analysis of AE activity during the tensile test: linear localization of AE events as a function of acoustic energy of the AE signal

Fig. 20. X-ray microtomography vs AE: Localization of initial defects versus AE energy of the very first events.

accompanied by the generation of acoustic waves with a high level of energy. These results also show that before each abrupt drop in the Sentry function, the joint exhibits an energy-storing phase.

4.2. Initial state of the internal structure versus localization of the AE events

In this section, the main objective is to highlight the correlation between the initial state of the FSW joint and the localization of the very first cracks. In practice, it consists in comparing the results of the X-ray microtomography analysis with those obtained with acoustic emission (see Fig. 19).

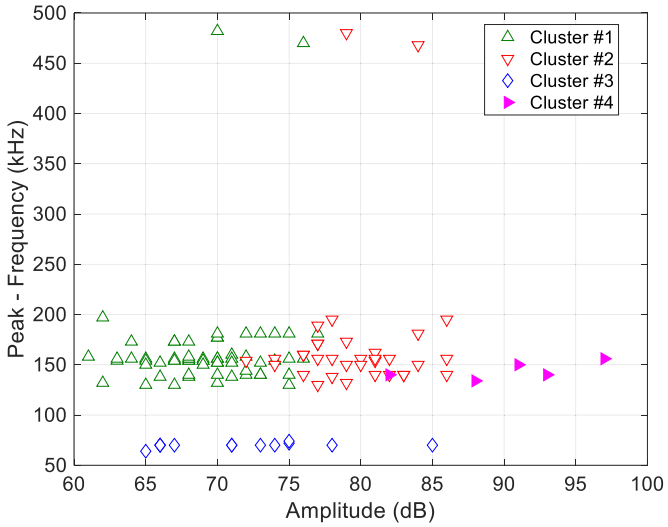
Results from the X-ray microtomography analysis show a high concentration of initial defects close to the center of the specimen (along the longitudinal axis). As stated in Section 3.4 above, the results from the AE activity (Fig. 19-b) show that the very first crack sources are located in the lower half of the joint. This good correlation between the results allows stating that the first crack sources are caused by the weakness zones detected in the initial state of the welded joint.

In addition to the previous analysis of the experimental results (see Fig. 19), the size effect of the initial defect (Fig. 20-a) on the acoustic signature of the resulting event is analyzed. This signature is expressed in terms of AE energy (Fig. 20-b). The results lead us to state that the bigger the initial defect, the higher the corresponding AE energy level.

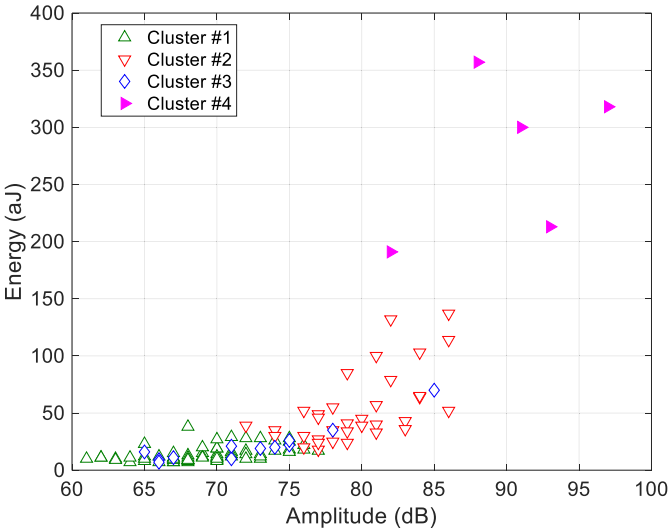
4.3. AE signature of damage mechanisms

As successfully experienced in previous studies [41–43] the k-means++ clustering algorithm is used to perform an unsupervised classification of the AE events to allow the number of cracking mechanisms (based on the optimal number of clusters) and their crack acoustic signatures to be identified. The optimal number of clusters is statistically determined based on the values of two clustering evaluation indices [42,43]: the Davies-Bouldin index (DB) and the Silhouette Coefficient (SC).

In the present study, seven AE features (amplitude, rise-time, counts, energy, duration, centroid frequency, and peak frequency) were selected in the clustering process. This optimal number of clusters led to a value of 0.61 for the DB index and 0.71 for the SC index. With these values, the clusters are dense and well separated, which corresponds to the standard



a) Cracking signatures based on the values of peak frequency and amplitude of the AE signal



b) Cracking signatures based on the values of energy and amplitude of the AE signal

Fig. 21. AE signatures of the cracking mechanisms.

concept of cluster. In general, an SC index value greater than 0.6 ensures that the clustering is of sufficient quality. As a result of the clustering process, similar AE events in terms of features can be statistically gathered into four clusters. This means that four cracking mechanisms with different acoustic signatures can be identified from the AE activity of the welding joint.

Fig. 21 proposes a projection of the four clusters onto a two-dimensional plot. The cluster analysis of the AE events enables us to represent the four clusters either in the peak frequency-amplitude coordinate system (see Fig. 21-a) or in the energy-amplitude one (see Fig. 21-b), the idea being to get the best separation of the clusters. One can conclude from these results that three main clusters (#1, #2, and #4) can be selected. They are comprised of AE events with a peak frequency value lying between 100 and 250 kHz. This interval falls within the frequency range where the AE sensors that were used are very sensitive. The bounds of these clusters are consequently deduced from the amplitude levels of the AE events.

To complete this analysis of the cracking mechanisms within the FSW joint, the clusters that were previously identified are used in the plot of the linear localization of the AE events (between the two sensors and along the x-axis, Fig. 1) as a function of the tensile stress (Fig. 22).

It can be seen from Fig. 22 that the very first AE events that are detected belong to clusters #2 and #4. They are characterized by an amplitude greater than around 77 dB and an energy level greater than around 35 aJ (attojoule). Based on the localization of these two first events and by comparing Fig. 22 and Fig. 20, one can see that the AE event of cluster#4 is certainly caused by the cracking of the biggest initial defect.

Fig. 21 shows that cluster#4 gathers all AE events that exhibit an acoustic energy level greater than around 200 aJ. The linear localization of these events (Fig. 22) is in good agreement with the acoustic analysis presented in Fig. 20 (focused on events with an energy level greater than 200 aJ). Besides, one can see by comparing Fig. 20, Fig. 22, and Fig. 17 that the AE events of cluster #4 appear at specific moments of the joint mechanical response. They can be due to macroscopic changes in the internal structure of the welded joint.

Fig. 22 shows the nucleation of AE events with low amplitude (cluster#1) in the vicinity of those of cluster#2. In the current state of the AE analysis, results from Fig. 22 tend to show that at any location in the welded joint AE events of cluster#2 appear before those of

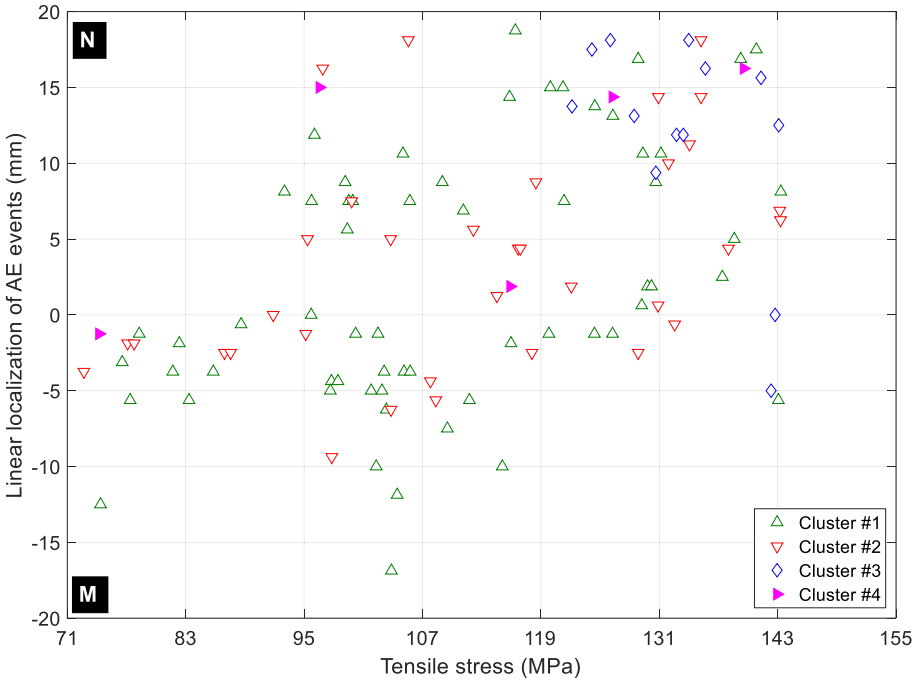


Fig. 22. 1D-localization of cracking mechanisms within the welded joint and during the tensile test.

cluster#1. Based on these analyses, the AE events of cluster#1 could be due to micro-cracking and, those of cluster#2 be related to macro cracking or crack nucleation. Events of cluster#4 could be associated with crack initiation.

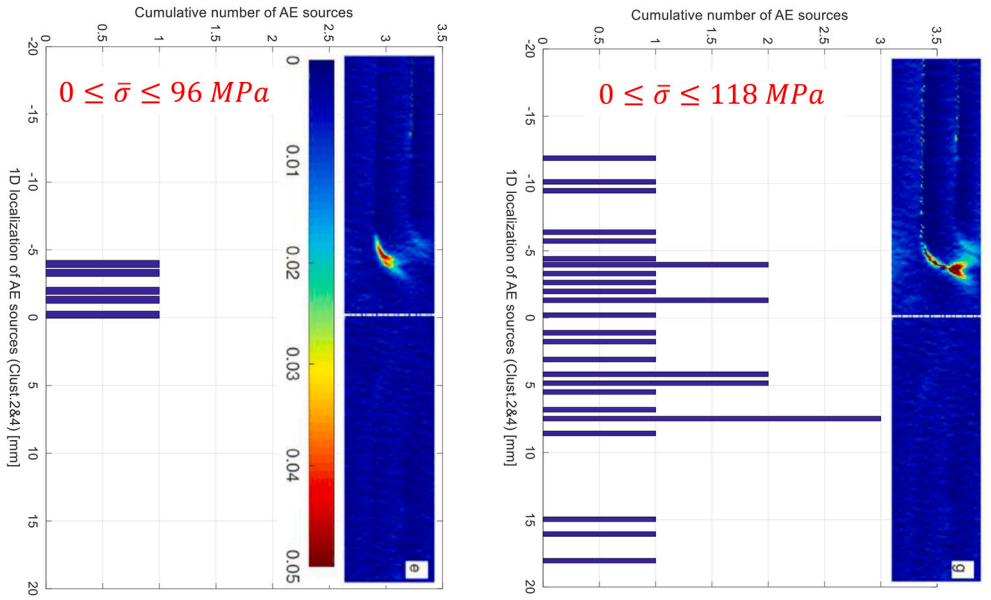
Fig. 23 shows how the monitoring of AE events that are characterized by particular acoustic signatures (clusters #2 and #4) can help to predict where the failure zone of the specimen will potentially be located. It provides information about the evolution of the cracked area as a function of the applied tensile stress. As previously highlighted by the analysis of both the strain fields (Fig. 13) and AE activity (Fig. 20) the very first concentration of deformation is located less than 5 mm from the center (welding line) of the specimen and exhibits the very first AE events (Fig. 22 and Fig. 23-a) that are characterized by particular acoustic signatures in terms of amplitude, energy, and peak frequency levels (Fig. 21). The monitoring of these particular AE events during the test allows showing how the cracked length (based on projected AE events localizations) spreads over the welding line delimited by the two AE sensors (Fig. 23). Fig. 23-b and Fig. 23-c show that some AE events are located in areas where no notable deformations are detected on both investigated surfaces. These AE events are probably due to cracks located either within the specimen volume or on the surface of the aluminum alloy sheet AA2024 since the AE sensors are fitted on this material.

Fig. 24 shows, that when the joint fails, the strain field (ε_{xx}) distribution on both the lateral and the front faces as well as the AE events (all clusters) localizations along the welded joint. The presence of a band perpendicular to the sample with very low ε_{xx} value (dark blue) is visible. This can be explained as follows: looking in Fig. 5-a, one can see that during the mixing of the three alloy sheets, the AA7075 alloy moved to the contact with the tool shoulder, removing thus the part of the AA6061 alloy located in the vicinity of the pin. When analyzing Fig. 11, one can see that the AA7075 and AA6061 alloys exhibit very different mechanical behavior. Thus, based on the macroscopic stress level of our welded sample, the AA7075 alloy remains in its elastic domain (very small deformation ε_{xx}) while the AA 6061 one is fully in its plastic domain, with a stress value in the x-direction of about 65 MPa. This confirms the good correlation between the experiment results. Since the AE technique allows real-time monitoring of the cracking mechanisms it could be helpful in further experimental works for the identification of the optimal welding process parameters.

5. Conclusions

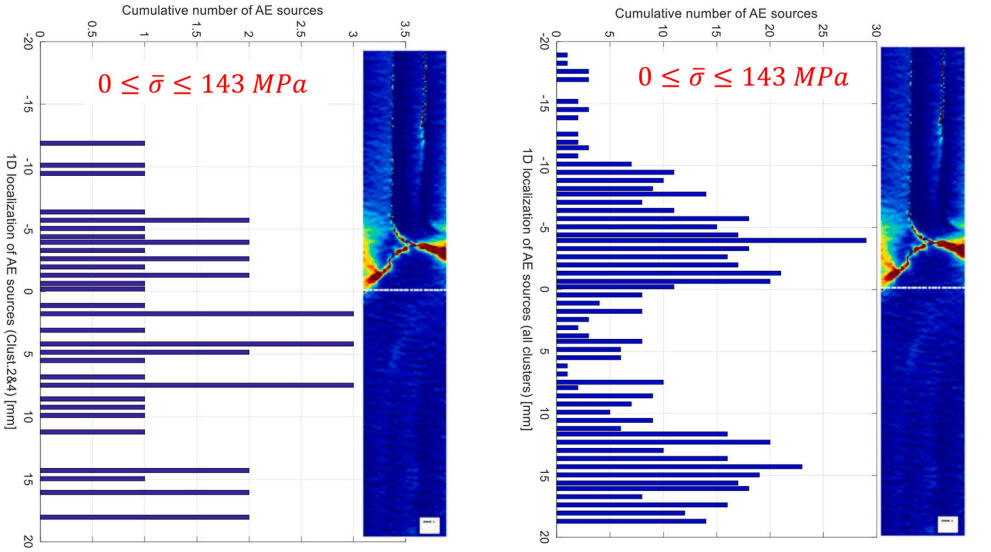
FSW process was used to weld three superimposed aluminum alloy sheets, namely AA6061, AA7075, and AA2024 (from top to bottom). Three samples were tested with good repeatability but results from only one sample were presented due to the richness of the experimental data. The experimental results show that under tensile loading, the strength of the welded assembly is about 40% lower than that of the configuration made up of three superimposed but non-welded alloy sheets. This relatively low effectiveness compared to that of butt-welded joints is mainly caused by the defects created during the assembling process. Even though the current work is not aimed at identifying the optimal parameters of the welding process, it brings to light how important it is to simultaneously use various experimental techniques for a better understanding of the phenomena that occur during the mechanical loading of the joint.

The use of X-ray micro-computed tomography seems to be essential for a good understanding of the internal structure of the joint before being subjected to mechanical loading. Indeed, it highlighted the mixing of the alloy sheets after manufacturing on the one hand and enabled us to evaluate both the distribution and the dimensional characteristics (shape, location, etc.) of the defects on the other hand. This analysis shows that the majority of the defects are characterized by an equivalent diameter lower than 0.2 mm and a rather spherical shape (sphericity rates larger than 0.5). The defects that are characterized by both a rate of sphericity lower than 0.4 and an equivalent diameter greater than 0.6 mm have a very particular shape. Such defects have been already observed in previous studies. In the present study, results show that their locations are correlated with micro-cracks initiation and damage evolution. Two perpendicular faces of the specimen were marked by using periodic patterns, namely a checkerboard, in order to ensure a high quality of the displacement and strain fields measurement by processing the pattern images shot during the test by a spectral method like the Localized Spectrum Analysis. The experimental results confirm the ability of this non-contact measurement technique to detect very early



a) Monitoring of AE events with specific signatures and comparison with strain field (ε_{xx} [in ***μdef***])

b) Monitoring of AE events with specific signatures and comparison with strain field (ε_{xx} [in ***μdef***])



c) Monitoring of AE events with specific signatures and comparison with strain field(ε_{xx} [in ***μdef***]) at specimen failure

d) Monitoring of AE events and comparison with strain map (ε_{xx} [in ***μdef***]) at specimen failure

Fig. 23. Monitoring of AE events and comparison with the corresponding local strain field during the tensile test. The color bar associated with Fig. 23-a remains valid for all the deformation maps (ε_{xx} [in ***μdef***]) shown in the other figures (b, c, d).

the appearance of strain concentrations on the two surfaces of the specimen that were investigated at the same time. The findings highlight a good correlation between the strain concentration zones and those characterized by a high density of defects, as also observed from the microtomography results analysis. Moreover, the presence of a significant density of defects within the FSW joint is undoubtedly the cause of the early cracking of the assembly, and thus also the cause of the quite low strength of the weld.

By analyzing the localization of AE events within the FSW joint, it can be seen that cracking starts at the lower half of the joint before spreading throughout the assembly. Moreover, the monitoring of the acoustic energy evolution during the mechanical test helped evaluate the yield strength of the welded joint. AE results were also compared with those obtained with the computed microtomography analysis in order to highlight the correlation between the initial state of the FSW joint and the localization of the very first cracks. This comparison allowed stating that the first crack sources were caused by the weakness zones detected at the initial state of the welded joint. In a deep analysis of the AE results, the k-means++ clustering algorithm was used to perform an unsupervised classification of the AE events, which led the number of cracking mechanisms and their crack acoustic signatures to be identified. The findings were that three main mechanisms governed

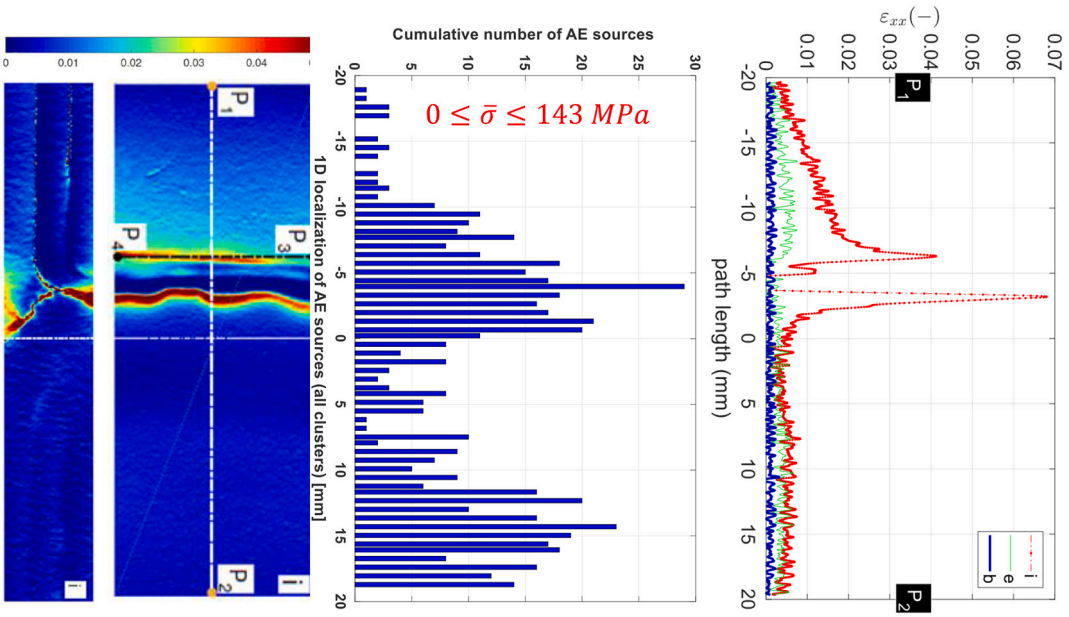


Fig. 24. Specimen fracture: strain field map (ε_{xx} [in ***μdef***]) compared with AE events distribution.

the damage evolution of the studied FSW joint. The acoustic signature of each cracking mechanism was defined by a pair of values (peak frequency, amplitude), each within a specific range. The results highlight a good correlation between the AE results with those from the strain analysis. Thus, the ability of the AE technique to provide real-time results should be helpful to identify the optimal welding process parameters in further experimental studies. It should also be relevant to investigate the evolution of the defects distribution in the bulk of such FSW joints by performing microtomography analysis at several levels of the mechanical loading. The experimental strategy developed in the framework of this study will be followed in our future works to identify the optimal welding parameters, thus optimizing the in-service life of the joint.

Declaration of Competing Interest

The authors declare that they have no known competing financial interests or personal relationships that could have appeared to influence the work reported in this paper.

References

[1] France: CO2 Country Profile. https://ourworldindata.org/co2/country/france.

[2] N. Leconte, B. Bourel, F. Lauro, C. Badulescu, E. Markiewicz, Strength and failure of an aluminum/PA66 self-piercing riveted assembly at low and moderate loading rates: experiments and modeling, Int. J. Impact Eng. 142 (2020), https://doi.org/10.1016/j.ijimpeng.2020.103587.

[3] G. Zhang, H. Zhao, X. Xu, G. Qiu, Y. Li, Z. Lin, Metallic bump assisted resistance spot welding (MBaRSW) of AA6061-T6 and bare DP590: part II-joining mechanism and joint property, J. Manuf. Process. 44 (2019) 19–27, https://doi.org/10.1016/j.jmapro.2019.05.041.

[4] W.M. Thomas, E.D. Nicholas, J.C. Needham, M.G. Murch, P. Temple-Smith, C. J. Dawes, Friction Welding, United States Pat, 1991, p. 5,460,317. https://patents.google.com/patent/US5460317.

[5] D. Camilleri, D. Micallef, P. Mollicone, Thermal stresses and distortion developed in mild steel DH36 friction stir-welded plates: an experimental and numerical assessment, J. Therm. Stresses 38 (5) (2015) 485–508, https://doi.org/10.1080/01495739.2015.1015856.

[6] T. Liyanage, J. Kilbourne, A.P. Gerlich, T.H. North, Joint formation in dissimilar Al alloy/steel and mg alloy/steel friction stir spot welds, Sci. Technol. Weld. Join. 14 (2009) 500–508, https://doi.org/10.1179/136217109X456960.

[7] R.P. Mahto, S.K. Pal, Friction stir lap welding of thin AA6061-T6 and AISI304 sheets at different values of pin penetrations, ASME 2018 13th Int, Manuf. Sci. Eng. Conf. MSEC 2018 (2018), https://doi.org/10.1115/MSEC2018-6590.

[8] Z. Shen, Y. Chen, M. Haghshenas, T. Nguyen, J. Galloway, A.P. Gerlich, Interfacial microstructure and properties of copper clad steel produced using friction stir welding versus gas metal arc welding, Mater. Charact. 104 (2015) 1–9, https://doi.org/10.1016/j.matchar.2015.02.022.

[9] Almigdad B. Ibrahim, Fadi Al-Badour, Akeem Yusuf Adesina, Nesar Merah, Effect of process parameters on microstructural and mechanical properties of friction stir diffusion cladded ASTM A516–70 steel using 5052 Al alloy, J. Manuf. Process. 34 (2018) 451–462, https://doi.org/10.1016/J.JMAPRO.2018.06.020.

[10] Noor Zaman Khan, Arshad Noor Siddiquee, Zahid A. Khan, Suha K. Shihab, Investigations on tunneling and kissing bond defects in FSW joints for dissimilar aluminum alloys, J. Alloys Compd. 648 (2015) 360–367, https://doi.org/10.1016/j.jallcom.2015.06.246.

[11] Raju Prasad Mahto, Ravi Kumar, Surjya Kanta Pal, characterizations of weld defects, intermetallic compounds and mechanical properties of friction stir lap welded dissimilar alloys, Mater. Charact. 160 (2020), https://doi.org/10.1016/j.matchar.2019.110115.

[12] Monica Daniela Iordache, Claudiu Badulescu, Malick Diakhate, Marius Adrian Constantin, Eduard Laurentiu Nitu, Younes Demmouche, Matthieu Dhondt, Denis Negrea, A numerical strategy to identify the FSW process optimal parameters of a butt-welded joint of quasi-pure copper plates: modeling and experimental validation, Int. J. Adv. Manuf. Technol. 115 (2021) 2505–2520, https://doi.org/10.1007/s00170-021-07296-9.

[13] Y.C. Lim, Mechanical properties and microstructural characterization of a multilayered multipass friction stir weld in steel, in: R. Mishra, M.W. Mahoney, Y. Sato, Y. Hovanski, R. Verma (Eds.), Friction Stir Welding and Processing VII, Springer, Cham, 2013, https://doi.org/10.1007/978-3-319-48108-1_9.

[14] M. Geyer, V. Vidal, T. Pottier, C. Boher, F. Rézaï-Aria, Investigations on the material flow and the role of the resulting hooks on the mechanical behaviour of dissimilar friction stir welded Al2024-T3 to Ti-6Al-4V overlap joints, J. Mater. Process. Technol. 292 (2021), https://doi.org/10.1016/j.jmatprotec.2021.117057 yyy-yyy.

[15] Kaifeng Wang, Haris Ali Khan, Zhiyi Li, Sinuo Lyu, Jingjing Li, Micro friction stir welding of multilayer aluminum alloy sheets, J. Mater. Process. Technol. 260 (2018) 137–145, https://doi.org/10.1016/j.jmatprotec.2018.05.029.

[16] J Summerscales, Non-Destructive Testing of fibre-reinforced plastics composites, Elsevier Appl. Sci. 2 (1990) 208–209.

[17] M. Dhondt, I. Aubert, N. Saintier, J.M. Olive, Mechanical behavior of periodical microstructure induced by friction stir welding on Al–cu–Li 2050 alloy, Mater. Sci. Eng. A,644 (2015) 69–75, https://doi.org/10.1016/j.msea.2015.05.072.

[18] D. Texier, F. Atmani, P. Bocher, F. Nadeau, J. Chen, Y. Zedan, N. Vanderesse, V. Demers, Fatigue performances of FSW and GMAW aluminum alloys welded joints: competition between microstructural and structural-contact-fretting crack initiation, Int. J. Fatigue 116 (2018) 220–233, https://doi.org/10.1016/j.ijfatigue.2018.06.020.

[19] S.A. Nikulin, S.V. Dobatkin, V.G. Khanzhin, S.O. Rogachev, S.A. Chakushin, Submicrocrystalline structure and inclusions on the deformation and failure of aluminum alloys and titanium, Met. Sci. Heat Treat. 51 (2009) 208–217.

[20] S. Senthil Kumar, S. Denis Ashok, Development of acoustic emission and motor current based fuzzy logic model for monitoring weld strength and nugget hardness of FSW joints, Procedia Eng. 97 (2014) 909–917, https://doi.org/10.1016/j.proeng.2014.12.366.

[21] A. Rastegaev, M.L. Linderov, D.L. Merson, M.A. Afanasyev, A.V. Danyuk, Monitoring of fracture of welded joints in hazardous facilities by acoustic emission under static and cyclic loadings, Indian J. Sci. Technol. 8 (35) (2015) 1–7, https://doi.org/10.17485/ijst/2015/v8i36/90555.

[22] A. Boşneag, M.A. Constantin, E.L. Nitu, Numerical simulation of friction stir welding of three dissimilar aluminium alloys, IOP Conf. Ser.: Mater. Sci. Eng. 564 (2019), 012033, https://doi.org/10.1088/1757-899X/564/1/012033.
[23] A. Boşneag, M.A. Constantin, E. Niţu, M. Iordache, Friction stir welding of three dissimilar aluminium alloy used in aeronautics industry, in: IOP Conf. Series: Materials Science and Engineering 252, 2017, p. 012041, https://doi.org/10.1088/1757-899X/252/1/012041.
[24] J.-Y. Buffière, E. Maire, J. Adrien, J.-P. Masse, E. Boller, In situ experiments with X ray tomography: an attractive tool for experimental mechanics, Exp. Mech. 50 (2010) 289–305.
[25] C. Petit, E. Maire, S. Meille, J. Adrien, Two-scale study of the fracture of an aluminum foam by X-ray tomography and finite element modeling, Mater. Des. 120 (2017) 117–127.
[26] H. Toda, T. Ohgaki, K. Uesugi, T. Kobayashi, N. Kuroda, T. Kobayashi, M. Niinomi, T. Akahori, K. Makii, Y. Aruga, Quantitative assessment of microstructure and its effect on compressive behavior of aluminum foams via high-resolution synchrotron X-ray tomography, Metall. Mater. Trans. A 37 (2006) 1211–1219, https://doi.org/10.1007/s11661-006-1072-0.
[27] A.C. Kak, M. Slaney, Principles of Computerized Tomographic Imaging, Society for Industrial and Applied Mathematics, Philadelphia, 2001.
[28] M. Sutton, J.J. Orteu, H. Schreier, Image Correlation for Shape, Motion and Deformation Measurements, Theory and Applications. Springer, Basic Concepts, 2009.
[29] M. Grédiac, B. Blaysat, F. Sur, On the optimal pattern for displacement field measurement: random speckle and DIC, or checkerboard and LSA? Exp. Mech. 60 (4) (2020) 509–534, https://doi.org/10.1007/s11340-019-00579-z.
[30] J.L. Piro, M. Grédiac, Producing and transferring low-spatial-frequency grids for measuring displacement fields with moiré and grid methods, Exp. Tech. 28 (4) (2004) 23–26, https://doi.org/10.1111/j.1747-1567.2004.tb00173.x.
[31] F. Sur, B. Blaysat, M. Grédiac, Determining displacement and strain maps immune from aliasing effect with the grid method, Opt. Lasers Eng. 86 (2016) 317–328, https://doi.org/10.1016/j.optlaseng.2016.06.010.
[32] M. Grédiac, B. Blaysat, F. Sur, Extracting displacement and strain fields from checkerboard images with the localized spectrum analysis, Exp. Mech. 59 (2) (2019) 207–218, https://doi.org/10.1007/s11340-018-00439-2.
[33] NIH National Institute of Health, Image J [in line], Available on, http://imagej.nih.
[34] M. Sezgin, Survey over image thresholding techniques and quantitative performance evaluation, J. Electron. Imaging. 13 (2004) 146–165, https://doi.org/10.1117/1.1631315.
[35] A. Rosenfeld, P. De La Torre, Histogram concavity analysis as an aid in threshold selection, IEEE Trans. Syst. Man Cybern. 13 (1983) 231–235, https://doi.org/10.1109/TSMC.1983.6313118.
[36] N. Otsu, A threshold selection method from gray-level histograms, IEEE Trans. Syst. Man Cybern. 9 (1979) 62–66, https://doi.org/10.1109/TSMC.1979.4310076.
[37] R.F. Hamade, A.M.R. Baydoun, Nondestructive detection of defects in friction stir welded lap joints using computed tomography, Mater. Des. 162 (2019) 10–23, https://doi.org/10.1016/j.matdes.2018.11.034.
[38] Dimitri Jacquin, Gildas Guillemot, A review of microstructural changes occurring during FSW in aluminium alloys and their modelling, J. Mater. Process. Technol. 288 (2021), https://doi.org/10.1016/j.jmatprotec.2020.116706.
[39] G. Lehmann, D. Legland, U.M.R., Efficient N-dimensional surface estimation using Crofton formula and run-length encoding, Insight J. 2 (2012) 1–11.
[40] H. Wadell, Volume, shape, and roundness of quartz particles, J. Geol. 43 (3) (1935) 250–280, https://doi.org/10.1086/624298.
[41] J. Destouesse, M. Diakhate, C. Badulescu, D. Thévenet, M. Stackler, W. Albouy, N. Carrere, Cluster analysis of acoustic emission data to investigate the damage evolution in modified scarf joint under bi-axial loading, J. Adhes. 96 (2018) 969–987, https://doi.org/10.1080/00218464.2018.1552854.
[42] M. Diakhate, E. Bastidas-Arteaga, R. Moutou Pitti, F. Schoefs, Cluster analysis of acoustic emission activity within wood material: towards a real-time monitoring of crack tip propagation, Eng. Fract. Mech. 180 (2017) 254–267, https://doi.org/10.1016/j.engfracmech.2017.06.006.
[43] L. Li, S.V. Lomov, X. Yan, V. Carvelli, Cluster analysis of acoustic emission signals for 2D and 3D woven glass/epoxy composites, Compos. Struct. 116 (2014) 286–299, https://doi.org/10.1016/j.compstruct.2014.05.023.
[44] A.A. Bakhtiary Davijani, M. Hajikhani, M. Ahmadi, Acoustic emission based on sentry function to monitor the initiation of delamination in composite materials, Mater. Des. 32 (2011) 3059–3065, https://doi.org/10.1016/j.matdes.2011.01.010.

3.4 Etudes en cours et perspectives

Les études en cours, que je mène avec l'équipe constituée de chercheurs de l'ENSTA Bretagne, de l'IUT de Morlaix et de l'Université de Pitesti / Roumanie, sur la thématique de soudage par friction malaxage, s'articulent autour de trois axes principaux, avec une cohérence logique vis-à-vis des études réalisées précédemment.

Le premier axe a pour ambition d'augmenter la productivité du procédé de soudage sur des alliages de cuivre. Une première option pour augmenter la productivité (faire augmenter la vitesse de réalisation du cordon) s'oriente vers l'utilisation d'une source supplémentaire de chaleur de type Tungsten Inert Gas (TIG). Cette source de chaleur pourrait générer un champ de température proche de la température optimale au voisinage du pion, sans avoir besoin d'attendre que cette température soit atteinte par frottement et déformation. Des analyses expérimentales par thermographie infrarouge montrent clairement que l'utilisation d'une telle source de chaleur impose un champ volumique de température très différent du champ obtenu par le procédé de soudage sans source de chaleur supplémentaire. Naturellement, nous nous posons alors la question sur les jeux de paramètres à utiliser pour le procédé, afin d'obtenir un joint avec un minimum de défauts et une résistance mécanique proche de celui du matériau de base. Les paramètres optimaux sont d'abord estimés par une étude numérique, similaire à celle proposée dans le travail précédent [124]. Dans cette stratégie numérique, nous avons intégré la source de chaleur supplémentaire, au préalable modélisée et identifiée. Plus précisément, des mesures expérimentales ont été réalisées afin de caractériser la source de chaleur à utiliser. Premièrement, la source de chaleur a été appliquée sur une des faces d'une tôle en cuivre de 3 mm, et le champ de température sur l'autre face a été enregistré : autant pour une source fixe, que pour une source en mouvement. L'effet des différents paramètres de cette source a été investigué expérimentalement. Ces résultats on permis d'identifier, finement, un modèle mathématique de cette source de chaleur, permettant ainsi la construction robuste d'une stratégie numérique d'optimisation des paramètres.

Basées sur cette stratégie d'identification de paramètres optimaux, des études paramétriques ont été réalisées et ont permis d'identifier des zones dans le plan : vitesse de rotation (v_r [rot/min]) - vitesse d'avancement (v_a [mm/min]), pour lesquelles ces paramètres sont optimaux. Ces résultats numériques ont été confrontés et validés avec des résultats expérimentaux. Dans un cas particulier, pour une configuration de soudage composée de tôles en cuivre quasi pur, d'épaisseur égale à 3mm, assemblées bout-à-bout, on obtient une augmentation de la productivité avec un facteur 3, par rapport à un soudage FSW classique, tout en obtenant une résistance mécanique quasi-identique.

Des analyses locales par mesure de champs cinématiques de déformation, au voisinage du joint, ont pu être réalisées. Les cartographies de ces champs de déformation montrent principalement que pour une même résistance mécanique, des joints obtenus avec ou sans apport de chaleur, présentent des comportements mécaniques très différents, surtout dans la zone soudée. La confrontation essais-calcul, très encourageante, ouvre plusieurs pistes d'amélioration et beaucoup de perspectives. La forme de la source de chaleur, influencée par différents paramètres (intensité du courant, distance ente

l'extrémité de la source et l'échantillon, l'inclinaison de la source, etc) pourrait conduire à une distribution du champ volumique de la température moins étendue et qui n'affecte uniquement que la zone malaxée, diminuant ainsi la zone affectée thermiquement ou thermo-mécaniquement. Des analyses microscopiques de la microstructure, de la présence de différentes phases ainsi que leur évolution, méritent d'être réalisées pour approfondir la compréhension des mécanismes associés à l'apport supplémentaire de la chaleur. Enfin, des pistes d'amélioration sur la qualité du joint et la productivité, à travers l'utilisation d'autres sources de chaleur, représentent un point à aborder dans un futur proche.

Le deuxième axe concerne la minimisation des défauts sur des configurations soudées par friction malaxage complexes, caractérisés par *i)* des géométries de l'outil (pion fileté et/ou avec des formes géométriques complexes) ou bien *ii)* des configurations de soudage où l'assemblage est constitué d'un empilement de plus de deux tôles d'alliages différents. Plus précisément, l'investigation qui est en cours, est constituée de 3 couches d'alliages d'aluminium superposées. Le premier objectif est de proposer l'ordre d'empilement optimal permettant de minimiser la quantité de défauts de type pores. Il est également important de se poser la question sur l'origine des défauts engendrés. Cela dit, des défauts pourraient apparaître du fait d'une température de malaxage insuffisante pour transformer la matière en état pâteux optimal ou bien d'une température trop importante qui transformerait alors la matière en un état fluide générant ainsi des défauts d'une taille significative. Ce champ de température pourrait être mesuré à la surface de l'échantillon, mais pas à l'intérieur de celui-ci.

Il est alors question de mettre en place un modèle numérique, capable de prédire de manière satisfaisante, la distribution et l'évolution du champ de température au sein de l'assemblage. Ces distributions de champ de température apportent des informations précieuses permettant d'évaluer l'écart entre la température des différentes tôles assemblées et leurs valeurs spécifiques optimales, identifiées au préalablement par des analyses expérimentales plus simples. Si cette distribution de température est trop éloignée des valeurs optimales, on pourrait se focaliser sur *i)* l'optimisation de la géométrie du pion et éventuellement sur *ii)* les paramètres du procédé. L'aboutissement de ces investigations proposées pourrait conduire à l'obtention d'un champ de température qui peut satisfaire au mieux les températures optimales de chaque tôle.

Une deuxième piste qui pourrait réduire la quantité de défauts générés repose sur l'utilisation de sources de chaleur supplémentaires, destinées à modifier le champ de température déjà formé par le pion afin d'obtenir une distribution proche de celle considérée comme optimale. Cette stratégie nécessite, dans un premier temps, des investigations numériques afin de pouvoir statuer sur la faisabilité et l'efficacité d'une telle approche. Dans ce cas, des structures soudées par FSW constituées de 3 tôles superposées ont été analysées par tomographie aux rayons X afin de déterminer la distribution de défauts en fonction de différents paramètres. Ultérieurement, ces configurations seront analysées avec l'objectif d'identifier une correspondance entre le champ de température obtenu expérimentalement et la distribution de défauts afin de valider ou non la stratégie proposée précédemment. Ensuite il serait également intéressant de l'implémenter expérimentalement avec un certain nombre de verrous scientifiques à lever. Il se peut, pour

des configurations relativement complexes, qu'il ne soit pas toujours possible d'éliminer complètement la présence de défauts. Alors dans ce cas, il est légitime de se poser la question sur la préjudiciabilité des défauts vis-à-vis de la résistance mécanique ultime.

Le troisième axe investigué dans le cadre des essais de soudage par friction malaxage, **porte sur l'amélioration des soudures d'aciers à haute limite élastique**. La principale difficulté est liée à la durabilité de l'outil. Ces investigations se concentrent, dans un premier temps, sur la soudure par friction- malaxage de type point. Les alliages en acier à haute limite élastique en général, posent des difficultés relativement importantes sur le soudage par friction malaxage. Ces difficultés sont principalement liées à la conductivité thermique de l'acier qui est extrêmement réduite par rapport aux alliages en cuivre ou en aluminium. La conséquence directe liée à ce paramètre est la localisation trop importante de la température, limitant drastiquement l'échauffement d'un volume suffisamment important pour qu'ils puissent être malaxés. On constate que les zones de jonctions de ces matériaux sont nettement inférieures à celles obtenues avec les alliages d'aluminium ou de cuivre. En conséquence, des stratégies numériques ont d'abord été utilisées afin d'estimer les paramètres du procédé conduisant à des résistances mécaniques satisfaisantes.

La caractérisation expérimentale de tels assemblages repose souvent sur des essais de type simple recouvrement, générant globalement un état de cisaillement. Il y a bien des applications où l'état de sollicitation est très éloigné de cet état de cisaillement, auquel cas, il faudra adapter la nature de l'essai à utiliser pour la caractérisation expérimentale. Des échantillons spécifiques sont en cours de réalisation, conçus et réalisés de manière à pouvoir solliciter un tel assemblage avec un spectre balayant des états de sollicitation très divers : cisaillement, traction-cisaillement ou traction, et en s'appuyant sur un montage de type Arcan modifié. Cette méthodologie de caractérisation, déjà utilisée pour d'autres types d'assemblage, permettra d'accéder non seulement à la résistance mécanique ultime d'un tel joint, mais surtout de pouvoir identifier l'enveloppe de rupture, indispensable pour dimensionner de manière satisfaisante un tel assemblage.

CHAPITRE

4 Synthèse et présentation des projets à 4 ans

Sommaire

4.1 Principaux objectifs atteints . . . 310
4.1.1 Adhésifs structuraux époxy bi-composants . . . 310
4.1.2 Joints soudés par friction malaxage . . . 310
4.2 Principaux thèmes de développement . . . 311
4.2.1 Approfondissement de la caractérisation de l'effet de l'hygrométrie sur les joints collés avec de l'adhésif époxy bi-composants . . . 311
4.2.2 Utilisation des outils de mesure de champs, pour la compréhension fine de mécanismes de comportement élémentaires de joints de colle . . . 311
4.2.3 Compréhension de mécanismes de distribution des différents alliages en aluminium dans les joints FSW à l'aide de la tomographie aux rayons X . 311
4.3 Présentation des projets à 4 ans . . . 312
4.3.1 Caractérisation des défauts et de leur effet dans les assemblages multi-matériaux collés . . . 312
4.3.2 Identification expérimentale des mécanismes d'endommagement . . . 313
4.3.3 Caractérisation d'assemblages collés à base de bio-colles et colles auto-cicatrisantes . . . 314

Comme expliqué en préambule, ce document cherche à donner dans sa deuxième partie, plusieurs niveaux de lecture de mes activités de recherche. Les chapitres 6 et 8 dressent un panorama des points abordés dans le cas d'assemblages collés et soudés, mettant en avant les aspects d'instrumentation, l'effet de l'environnement, l'identification et l'effet des défauts sur le comportement mécanique de l'adhésif et/ou du joint soudé par friction malaxage. Chaque section propose, une vision détaillée des pistes en cours pour chacun des grands axes de recherche. Le chapitre 9 souhaite avant tout proposer une vision synthétique des points marquants développés au cours de ces travaux de recherche et des principaux thèmes de développement à poursuivre.

4.1 Principaux objectifs atteints

Avant de reprendre les différents résultats obtenus, je tiens à souligner qu'ils sont majoritairement issus, directement ou indirectement de la collaboration très efficace mise en place avec les partenaires industriels suivants : Safran Reosc, Safran Composites, Thales, l'ADEME et l'ANR, mais également au sein du Pôle Thématique de Recherche « Assemblages Multi-matériaux » de l'IRDL. Je tiens à souligner la très bonne collaboration avec le laboratoire MATEIS de l'INSA de Lyon, caractérisé d'une grande efficacité, et m'a permis d'avancer de manière significative sur ces thématiques de recherche.

4.1.1 Adhésifs structuraux époxy bi-composants

- Mise en place de protocoles de caractérisation expérimentale pour déterminer les contraintes résiduelles (voire thermiques) dans les assemblages structuraux au moyen de techniques sans contacts ou par l'utilisation de fibres optiques ;
- Développement de modèles de comportement mécanique phénoménologiques, intégrant les comportements :viscoélastique, élasto-plastique et élasto-viscoplastique prenant en compte la pression hydrostatique, l'effet de vitesse, etc ;
- Caracterisation et l'intégration des contraintes résiduelles dans la stratégie de modélisation et de dimensionnement d'assemblages structuraux multi-matériaux. Identification des paramètres des modèles en intégrant la présence de ces contraintes à l'état initial.
- Prise en compte dans la modélisation du comportement mécanique de l'effet de la température et du conditionnement en environnement humide sous l'hypothèse d'un adhésif homogène ;
- Caractérisation des défauts dans les assemblages collés, en utilisant la tomographie aux rayons X. Détermination quantitative du pourcentage de phases, distribution spatiale, morphologie de défauts ;
- Identification de l'origine des défauts de type pores et de l'effet du cycle de polymérisation sur la génération des défauts. Mise en place d'une stratégie expérimentale, au moyen d'essais mini-scarf et de la tomographie aux rayons X pour la caractérisation de l'effet du chargement mécanique sur l'évolution des défauts ;
- Mise en évidence des principaux mécanismes de dégradation dans les joints de colle, sous sollicitations mécaniques.

4.1.2 Joints soudés par friction malaxage

- Mise en place d'une stratégie numérique de simulation du procédé de soudage par friction malaxage, efficace et basée sur une approche de type CEL (Coupled Eulerian Lagrangien) et adaptée à des études paramétriques ou d'optimisation ;
- Proposition d'une stratégie numérique pour l'identification des paramètres optimaux du procédé de soudage par FSW, validée sur une configuration de soudage de type bout-à-bout en cuivre quasi-pur ;

- Évaluation quantitative de défauts dans des configurations complexes de joints FSW en utilisant la tomographie de rayons X ;
- Investigation de l'effet de défauts sur le comportement local d'un joint obtenu par friction- malaxage, en couplant la tomographie aux rayons X, l'émission acoustique et les mesures du champ.

4.2 Principaux thèmes de développement

4.2.1 Approfondissement de la caractérisation de l'effet de l'hygrométrie sur les joints collés avec de l'adhésif époxy bi-composants

- Mise en place d'une procédure expérimentale de détection du gonflement, à l'échelle locale, par des analyses tomographiques et mesures du champ de déformation locale volumique ;
- Prédiction des contraintes de gonflement dans les assemblages collés et leur prise en compte dans la stratégie de modélisation et dimensionnement ;
- Investigation de l'effet de sorption – désorption sur les adhésifs époxy, en utilisant la tomographie aux rayons X avec l'objectif de déterminer les éventuelles déformations résiduelles résultant de ces chargements hydriques ;
- Application de la stratégie de caractérisation des colles par la tomographie aux rayons X.

4.2.2 Utilisation des outils de mesure de champs, pour la compréhension fine de mécanismes de comportement élémentaires de joints de colle

- Détection sans contact et en surface de champs cinématiques à des échelles micrométriques (mesure sur MEB) sur des adhésifs structuraux présentant des défauts ;
- Étude des mécanismes élémentaires de dégradation (effet de la présence de charges) par utilisation des mesures de champs cinématiques à différentes échelles ;
- Compréhension du comportement de l'adhésif proche de l'interface colle-substrat, ainsi que l'effet du substrat sur son comportement mécanique.

4.2.3 Compréhension de mécanismes de distribution des différents alliages en aluminium dans les joints FSW à l'aide de la tomographie aux rayons X

- Compréhension de mécanismes de distribution des différents alliages d'aluminium dans les joints FSW à l'aide de la tomographie des rayons X ;

- Identification expérimentale par l'utilisation de la tomographie aux rayons X pour détecter l'écoulement de la matière autour du pion, sur une configuration complexe obtenue par superposition de trois alliages d'aluminium. Des observations au microscope électronique à balayage seront conduites pour compléter la compréhension de ces phénomènes ;
- Effet de la géométrie de l'outil sur la distribution de différents alliages au sein du joint soudé afin d'optimiser la qualité du joint ;
- Analyse par mesure locale des champs cinématiques et de l'effet de la distribution de la matière sur la tenue mécanique du joint ;
- Analyse de l'évolution des défauts au cours d'essais de traction, in situ, sous tomographe et de leur impact sur la dégradation du joint.

4.3 Présentation des projets à 4 ans

Les perspectives aux différentes actions présentées dans la section précédente sont bien évidemment nombreuses et motivantes. Nous allons nous appuyer essentiellement sur les études récentes ou qui vont démarrer prochainement, mettant ainsi en lumière les nouveaux verrous scientifiques associés. Mes activités de recherche dans les 4 prochaines années s'articuleront autour de plusieurs projets ou thématiques, et dont les détails sont donnés ci-dessous.

4.3.1 Caractérisation des défauts et de leur effet dans les assemblages multi-matériaux collés

La plupart des études sur l'investigation de joints et d'assemblages collés se sont limitées pour l'instant aux adhésifs structuraux considérés homogènes, isotropes et sans défauts. Ces hypothèses facilitent grandement les investigations associées et par conséquent les moyens de modélisation mis en jeu. Des investigations réalisées au cours de mes dernières études montrent clairement qu'en réalité ces joints présentent différents défauts tels les pores, de la colle mal mélangée, du moins pour les colles bi-composants, des inclusions ou autres. Mon ambition est de déterminer, de manière non destructive et quantitative de ces défauts, à différentes échelles, d'analyser leurs effets sur le comportement mécanique de l'assemblage et de les prendre en compte dans la stratégie de dimensionnement.

La première échelle s'étend sur quelques centaines de microns. Nous nous intéressons ici à la caractérisation fine des défauts à l'origine de la dégradation de l'adhésif et ensuite à la compréhension fine des mécanismes d'endommagement afin de mieux comprendre les phénomènes activés à l'échelle des défauts et des charges. Des mesures physiques de la microstructure seront réalisées (en particulier par micro-tomographie, dans un premier temps au laboratoire MATEIS). Ces investigations pourront être accompagnées par une caractérisation thermomécanique fine à l'aide d'une caméra infra-rouge et d'un objectif spécifique. Cette dernière étape est un réel challenge expérimental, qui

est en passe d'être relevé. En parallèle, une démarche de modélisation est en cours de développement pour permettre d'analyser les données expérimentales et de faire ressortir les mécanismes représentatifs du comportement mécanique provoquant une dégradation du joint (amorçage des microfissures, rupture d'interface charges-matrice adhésive, plasticité).

La deuxième échelle est celle des éprouvettes : un volume de quelques dizaines de mm^3, d'abord sur un échantillon massique et ensuite sur un assemblage adapté en termes de taille et d'état de sollicitation, afin de poursuivre à la fois, le développement de la technique de caractérisation par tomographie aux rayons X, mais également de comprendre l'effet des défauts sur un échantillon représentatif. De plus, ces essais seront couplés à un suivi de l'activité acoustique permettant ainsi d'instrumenter sur le long terme, les différents assemblages et d'être informé en temps réel de son évolution, en particulier lorsqu'il s'approche d'un seuil critique.

Dernière échelle d'investigation, la structure, qui nous permettra d'étudier les influences du procédé de collage (population de défauts, cuisson, géométrie de la structure, etc.) et de confronter les prédictions de la stratégie de dimensionnement dans le cas de structures de ce type, accompagnée de gradients de propriétés de paramètres mécaniques par le vieillissement hydrique ou gradient de température. Outre les mesures de thermographie évoquées plus haut, les mesures par tomographie pourront alimenter la description des effets des défauts.

4.3.2 Identification expérimentale des mécanismes d'endommagement

Identifier les défauts d'un joint de colle peut être considéré comme un objectif ambitieux et difficilement atteignable, surtout si les tailles caractéristiques de ces défauts sont petites. Les dernières études menées ouvrent des pistes plutôt encourageantes. Même si l'état initial des défauts, avant application de la sollicitation mécanique, suscite un grand intérêt, l'aboutissement de ces travaux a pour objectif de mieux comprendre les mécanismes de dégradation de la colle. La nature de la sollicitation de l'adhésif, incluant ces populations de défauts, différentes d'un cycle de polymérisation à un autre, peut conduire à des mécanismes d'amorçage et d'évolution d'endommagement difficiles à anticiper. Des échantillons spécifiques avec des populations de défauts différents et d'états de sollicitation (traction, traction-cisaillement, cisaillement) permettront, à travers une analyse de la microstructure, et à l'aide de la tomographie aux rayons X, de dégager des conclusions solides sur la description de ces mécanismes de dégradation. Par conséquent, une fois ces informations obtenues, elles faciliteront la construction de modèles plus robustes assurant non seulement une description fine du comportement jusqu'à rupture, mais permettant aussi d'estimer le niveau d'endommagement et la rupture de l'assemblage. Des éléments concrets dans ce sens sont déjà initiés durant le stage post-doctoral de Marina BUNEA que j'ai co-encadré. Par ailleurs, une proposition de thèse est en cours de rédaction afin d'investiguer ces aspects très importants tant pour le milieu académique qu'industriel.

4.3.3 Caractérisation d'assemblages collés à base de bio-colles et colles auto-cicatrisantes

Si les outils de caractérisation et de dimensionnement d'assemblages collés semblent avoir atteint un degré de maturité, il me semble opportun de mettre à l'épreuve ces développements en étudiant deux familles d'adhésifs : les bio-colles et les adhésifs cicatrisants. Le contexte actuel lié aux pollutions dues à différents agents chimiques impose une réflexion sur les matériaux à privilégier. Les bio-colles semblent être des matériaux d'avenir et surtout très encouragés de nos jours, et permettront ainsi de proposer de nouveaux produits « verts » sur le marché. Une caractérisation fine et des modélisations pertinentes de ces colles seront des éléments indispensables pour améliorer la confiance des industriels vis-à-vis de ces nouveaux produits.

Une première étape, dans cette direction d'étude, est de dresser un bilan consistant sur les résistances mécaniques de ces adhésives. Ensuite, il est nécessaire d'interroger ces adhésifs sur leur adéquation avec des milieux agressifs en termes de température et/ou l'humidité. Même si actuellement, leur performance mécanique reste nettement inférieure à celle des colles thermodurcissables époxy, un panel d'applications varié, rend susceptible l'intégration de ces adhésifs au sein de différents domaines industriels. L'optimisation du cycle de polymérisation, la caractérisation des défauts engendrés lors de la phase de collage ou de polymérisation sont autant d'inconnues qui à l'heure actuelle freinent largement leur utilisation. Des réponses précises et solides apportées à ces questions permettront d'élargir les champs d'application et aider à l'émergence de tels adhésifs dans les structures assemblées. Des discussions avec quelques partenaires académiques et industriels ont eu lieu sur ces aspects dans l'idée de développer ces thématiques de plus en plus d'actualité.

Les colles auto-cicatrisantes offrent un potentiel d'autoréparation dès l'apparition de défauts dans l'adhésif. Le développement de ces colles très convoitées passe tout d'abord par des innovations chimiques permettant ainsi à l'adhésif de détecter l'amorçage d'une fissure et par la suite de déclencher des mécanismes de cicatrisation. Les défis chimiques ont eu des avancées significatives ces dernières années, et il me paraît opportun d'investiguer finement cette famille de colles, afin de déterminer l'apparition de défauts au moyen de la tomographie de rayons X, le pouvoir de cicatrisation de la colle et finalement *"le regain"* de propriétés mécaniques suite au processus d'auto-réparation. Des discussions avec des partenaires américains et roumains ont eu lieu sur ces sujets.

Bibliographie

[1] K.K. SAIRAJAN, G.S. AGLIETTI et K.M. MANI. “A review of multifunctional structure technology for aerospace applications”. In : *Acta Astronautica* 120 (2016), p. 30-42. DOI : https://doi.org/10.1016/j.actaastro.2015.11.024.

[2] Hak Sung KIM et al. “Inkjet printed electronics for multifunctional composite structure”. In : *Composites Science and Technology* 69.7 (2009), p. 1256-1264. DOI : https://doi.org/10.1016/j.compscitech.2009.02.034.

[3] Mythili SUNTHARALINGAM et Susan R WENTE. “Peering through the pore : nuclear pore complex structure, assembly, and function”. In : *Developmental cell* 4.6 (2003), p. 775-789.

[4] XUE ZHIHUI et al. “Review of in-space assembly technologies”. In : *Chinese Journal of Aeronautics* 34.11 (2021), p. 21-47.

[5] JD BOOKER, KG SWIFT et NJ BROWN. “Designing for assembly quality : strategies, guidelines and techniques”. In : *Journal of Engineering design* 16.3 (2005), p. 279-295.

[6] Anooshe Rezaee JAVAN et al. “Mechanical behaviour of composite structures made of topologically interlocking concrete bricks with soft interfaces”. In : *Materials & Design* 186 (2020), p. 108347.

[7] Nicolas LECONTE et al. “Strength and failure of an aluminum/PA66 self-piercing riveted assembly at low and moderate loading rates : Experiments and modeling”. In : *International Journal of Impact Engineering* 142 (2020), p. 103587.

[8] Justine DELOZANNE et al. “Thermal ageing of bonded assemblies. Effect of adhesive curing degree”. In : *The Journal of Adhesion* 99.6 (2023), p. 911-929.

[9] Claudiu BADULESCU et al. “Analysis of the low temperature-dependent behaviour of a ductile adhesive under monotonic tensile/compression–shear loads”. In : *International journal of adhesion and adhesives* 36 (2012), p. 56-64.

[10] A INVERNIZZI et al. “ELT secondary mirror manufacturing progress at Safran Reosc”. In : *Advances in Optical and Mechanical Technologies for Telescopes and Instrumentation IV*. T. 11451. SPIE. 2020, p. 81-94.

[11] Roberto TAMAI et al. “The ESO’s ELT construction status”. In : *Ground-based and Airborne Telescopes VII*. T. 10700. SPIE. 2018, p. 333-343.

[12] Vincent DUMONT. “On the durability of structural adhesive bonds in thermal environments : application to space-oriented optical systems”. Thèse de doct. ENSTA Bretagne-École nationale supérieure de techniques avancées Bretagne, 2020.

[13] Roland GEYL et al. “Freeform optics design, fabrication and testing technologies for Space applications”. In : *International Conference on Space Optics—ICSO 2018*. T. 11180. SPIE. 2019, p. 274-283.

[14] Ryan S MCCLELLAND et al. “Design and analysis of an x-ray mirror assembly using the meta-shell approach”. In : *Space Telescopes and Instrumentation 2016 : Ultraviolet to Gamma Ray*. T. 9905. SPIE. 2016, p. 2091-2099.

[15] Songnian TAN et al. “Micro-stress bonding analysis of high precision and lightweight mirrors”. In : *Optics Express* 29.21 (2021), p. 33665-33678.

[16] Asier LARRINGAN et al. “The final design for the Extremely Large Telescope prefocal stations”. In : *Ground-based and Airborne Telescopes VIII*. T. 11445. SPIE. 2020, p. 315-332.

[17] Odeh DABABNEH et Timoleon KIPOUROS. “A review of aircraft wing mass estimation methods”. In : *Aerospace Science and Technology* 72 (2018), p. 256-266.

[18] Ilan KROO. “Nonplanar wing concepts for increased aircraft efficiency”. In : *VKI lecture series on innovative configurations and advanced concepts for future civil aircraft* (2005).

[19] Frida ANDERSSON et al. “Design for manufacturing of composite structures for commercial aircraft–the development of a DFM strategy at SAAB aerostructures”. In : *Procedia Cirp* 17 (2014), p. 362-367.

[20] P MCMULLEN. “Fibre/resin composites for aircraft primary structures : a short history, 1936–1984”. In : *Composites* 15.3 (1984), p. 222-230.

[21] SP PANTELAKIS et KI TSERPES. “Adhesive bonding of composite aircraft structures : Challenges and recent developments”. In : *Science China Physics, Mechanics and Astronomy* 57 (2014), p. 2-11.

[22] FS WANG et al. “Experimental and numerical study on residual strength of aircraft carbon/epoxy composite after lightning strike”. In : *Aerospace Science and Technology* 75 (2018), p. 304-314.

[23] Paolo FERABOLI. “Composite materials strength determination within the current certification methodology for aircraft structures”. In : *Journal of Aircraft* 46.4 (2009), p. 1365-1374.

[24] Sonell SHROFF, Ertan ACAR et Christos KASSAPOGLOU. “Design, analysis, fabrication, and testing of composite grid-stiffened panels for aircraft structures”. In : *Thin-Walled Structures* 119 (2017), p. 235-246.

[25] F-X IRISARRI et al. “Progressive damage and failure of mechanically fastened joints in CFRP laminates–Part II : Failure prediction of an industrial junction”. In : *Composite Structures* 94.8 (2012), p. 2278-2284.

[26] Aurélien DOITRAND et al. “Dynamic crack initiation assessment with the coupled criterion”. In : *European Journal of Mechanics-A/Solids* 93 (2022), p. 104483.

[27] “La réglementation REACH”. In : *https ://www.ecologie.gouv.fr/reglementation-reach* (2018).

[28] “La réglementation EURO6”. In : *https ://www.ecologie.gouv.fr/normes-euros-demissions-polluants-vehicules* (2013).

[29] Kotaro KAWAJIRI, Michio KOBAYASHI et Kaito SAKAMOTO. “Lightweight materials equal lightweight greenhouse gas emissions ? : A historical analysis of greenhouse gases of vehicle material substitution”. In : *Journal of Cleaner Production* 253 (2020), p. 119805.

[30] Sofia POULIKIDOU et al. “A material selection approach to evaluate material substitution for minimizing the life cycle environmental impact of vehicles”. In : *Materials & design* 83 (2015), p. 704-712.

[31] S BUDHE et al. “An updated review of adhesively bonded joints in composite materials”. In : *International Journal of Adhesion and Adhesives* 72 (2017), p. 30-42.

[32] P HU et al. “Research on the static strength performance of adhesive single lap joints subjected to extreme temperature environment for automotive industry”. In : *International Journal of Adhesion and Adhesives* 41 (2013), p. 119-126.

[33] Robert W MESSLER. *Joining of materials and structures : from pragmatic process to enabling technology*. Butterworth-Heinemann, 2004.

[34] Zheng YAN et al. “Mechanical assembly of complex, 3D mesostructures from releasable multilayers of advanced materials”. In : *Science advances* 2.9 (2016), e1601014.

[35] Valérie ZILLE. “Modélisation et évaluation des stratégies de maintenance complexes sur des systèmes multi-composants”. Thèse de doct. Troyes, 2009.

[36] Georgio RIZK et al. “Durability of composite assemblies under extreme conditions : Thermomechanical damage prediction of a double-lap bonded composite assembly subject to impact and high temperature”. In : *Composite Structures* 213 (2019), p. 58-70.

[37] Melanie BORDES et al. “Prediction of long term strength of adhesively bonded steel/epoxy joints in sea water”. In : *International journal of adhesion and adhesives* 29.6 (2009), p. 595-608.

[38] Mohsen HESHMATI, Reza HAGHANI et Mohammad AL-EMRANI. “Effects of moisture on the long-term performance of adhesively bonded FRP/steel joints used in bridges”. In : *Composites Part B : Engineering* 92 (2016), p. 447-462.

[39] Marleine MORCOS et al. “Impact strength of thermally aged double lap adhesively bonded joints”. In : *International Journal of Adhesion and Adhesives* 112 (2022), p. 103029.

[40] AD CROCOMBE, ADAMS et RD. “Influence of the spew fillet and other parameters on the stress distribution in the single lap joint”. In : *The Journal of Adhesion* 13.2 (1981), p. 141-155.

[41] CSP BORGES et al. “Review on the effect of moisture and contamination on the interfacial properties of adhesive joints”. In : *Proceedings of the Institution of Mechanical Engineers, Part C : Journal of Mechanical Engineering Science* 235.3 (2021), p. 527-549.

[42] KL MITTAL. “The role of the interface in adhesion phenomena”. In : *Polymer Engineering & Science* 17.7 (1977), p. 467-473.

[43] Sally J MARSHALL et al. “A review of adhesion science”. In : *Dental materials* 26.2 (2010), e11-e16.

[44] Wei XU et Yueguang WEI. “Strength and interface failure mechanism of adhesive joints”. In : *International journal of adhesion and adhesives* 34 (2012), p. 80-92.

[45] Ludovic DUFOUR et al. “A viscoelastic-viscoplastic model with non associative plasticity for the modelling of bonded joints at high strain rates”. In : *International Journal of Adhesion and Adhesives* 70 (2016), p. 304-314.

[46] Alin ILIONI et al. “A viscoelastic-viscoplastic model to describe creep and strain rate effects on the mechanical behaviour of adhesively-bonded assemblies”. In : *International Journal of Adhesion and Adhesives* 82 (2018), p. 184-195.

[47] N CARRERE et al. “Theoretical study based on 2D assumptions of the influence of small pores on crack initiation in adhesively bonded joints”. In : *International Journal of Adhesion and Adhesives* 111 (2021), p. 102979.

[48] Vincent DUMONT et al. “On the influence of mechanical loadings on the porosities of structural epoxy adhesives joints by means of in-situ X-ray microtomography”. In : *International Journal of Adhesion and Adhesives* 99 (2020), p. 102568.

[49] Andreea TINTATU et al. “Understanding of water uptake mechanisms in an epoxy joint characterized by pore-type defects”. In : *The Journal of Adhesion* (2023), p. 1-33.

[50] Mauro OVEREND, Qian JIN et James WATSON. “The selection and performance of adhesives for a steel–glass connection”. In : *International Journal of Adhesion and Adhesives* 31.7 (2011), p. 587-597.

[51] G JEEVI, Sanjay Kumar NAYAK et M ABDUL KADER. “Review on adhesive joints and their application in hybrid composite structures”. In : *Journal of Adhesion Science and Technology* 33.14 (2019), p. 1497-1520.

[52] AQ BARBOSA et al. “Methods to increase the toughness of structural adhesives with micro particles : An overview with focus on cork particles : Methoden zur erhöhung der zähigkeit von strukturklebern mit mikropartikeln : Ein Überblick mit dem fokus auf kork”. In : *Materialwissenschaft und Werkstofftechnik* 47.4 (2016), p. 307-325.

[53] Sadik OMAIREY, Nithin JAYASREE et Mihalis KAZILAS. “Defects and uncertainties of adhesively bonded composite joints”. In : *SN Applied Sciences* 3.9 (2021), p. 769.

[54] Rosanna TAMBORRINO et al. “Assessment of the effect of defects on mechanical properties of adhesive bonded joints by using non destructive methods”. In : *Composites Part B : Engineering* 91 (2016), p. 337-345.

[55] Meysam GHASEMVAND, Bashir BEHJAT et Shabnam EBRAHIMI. “Experimental investigation of the effects of adhesive defects on the strength and creep behavior of single-lap adhesive joints at various temperatures”. In : *The Journal of Adhesion* 99.7 (2023), p. 1227-1243.

[56] Vincent DUMONT et al. “On the effect of the curing cycle on the creation of pores in structural adhesive joints by means of X-ray microtomography”. In : *The Journal of Adhesion* 97.12 (2021), p. 1073-1106.

[57] PA STEINMANN, Y TARDY et HE HINTERMANN. “Adhesion testing by the scratch test method : the influence of intrinsic and extrinsic parameters on the critical load”. In : *Thin solid films* 154.1-2 (1987), p. 333-349.

[58] Anna ELIADES et al. “Self-adhesive restoratives as pit and fissure sealants : a comparative laboratory study”. In : *Dental materials* 29.7 (2013), p. 752-762.

[59] José BARUCHEL, Jean-Yves BUFFIERE et Eric MAIRE. “X-ray tomography in material science”. In : (2000).

[60] Eric MAIRE et Philip John WITHERS. “Quantitative X-ray tomography”. In : *International materials reviews* 59.1 (2014), p. 1-43.

[61] Luc SALVO et al. “X-ray micro-tomography an attractive characterisation technique in materials science”. In : *Nuclear instruments and methods in physics research section B : Beam interactions with materials and atoms* 200 (2003), p. 273-286.

[62] J -Y BUFFIERE et al. “In situ experiments with X ray tomography : an attractive tool for experimental mechanics”. In : *Experimental mechanics* 50 (2010), p. 289-305.

[63] Patricia WILS. “Tomographie par rayons X : correction des artefacts liés à la chaıne d’acquisition”. Thèse de doct. Lyon, INSA, 2011.

[64] Vincent DUMONT et al. “Experimental investigation of porosities evolution in a bonded assembly by means of X-ray tomography”. In : *The Journal of Adhesion* 97.6 (2021), p. 528-552.

[65] Sheriff O OLAJIDE et Benedicta D ARHATARI. “Recent progress on damage mechanisms in polymeric adhesively bonded high-performance composite joints under fatigue”. In : *International Journal of Fatigue* 95 (2017), p. 45-63.

[66] Yao QIAO et al. “A study of adhesive bonding in metal-metal, metal-CFRP, and CFRP-CFRP material combinations under shear deformation : Fracture morphologies and damage mechanisms”. In : *International Journal of Adhesion and Adhesives* (2023), p. 103511.

[67] Dimitrios ZAROUCHAS et Danny VAN HEMELRIJCK. “Mechanical characterization and damage assessment of thick adhesives for wind turbine blades using acoustic emission and digital image correlation techniques”. In : *Journal of adhesion science and technology* 28.14-15 (2014), p. 1500-1516.

[68] Wendel K BELVIN et al. “In-space structural assembly : Applications and technology”. In : *3rd AIAA Spacecraft Structures Conference*. 2016, p. 2163.

[69] Stephen Richard HARTSHORN. *Structural adhesives : chemistry and technology*. Springer Science & Business Media, 2012.

[70] Maxwell DAVIS et David BOND. “Principles and practices of adhesive bonded structural joints and repairs”. In : *International journal of adhesion and adhesives* 19.2-3 (1999), p. 91-105.

[71] B TISSINGTON, G POLLARD et IM WARD. “A study of the influence of fibre/resin adhesion on the mechanical behaviour of ultra-high-modulus polyethylene fibre composites”. In : *Journal of materials science* 26 (1991), p. 82-92.

[72] Rolf MAHNKEN et Michael SCHLIMMER. “Simulation of strength difference in elasto-plasticity for adhesive materials”. In : *International journal for numerical methods in engineering* 63.10 (2005), p. 1461-1477.

[73] Julien MAURICE et al. “Characterization and modelling of the 3D elastic–plastic behaviour of an adhesively bonded joint under monotonic tension/compression-shear loads : influence of three cure cycles”. In : *Journal of adhesion science and technology* 27.2 (2013), p. 165-181.

[74] Jean-Yves COGNARD et al. “Experimental analysis of the influence of hydrostatic stress on the behaviour of an adhesive using a pressure vessel”. In : *The Journal of Adhesion* 87.7-8 (2011), p. 804-825.

[75] Jean-Yves COGNARD, Laurent SOHIER et Peter DAVIES. “A modified Arcan test to analyze the behavior of composites and their assemblies under out-of-plane loadings”. In : *Composites Part A : Applied science and manufacturing* 42.1 (2011), p. 111-121.

[76] Jean-Yves COGNARD et al. “Analysis of the nonlinear behavior of adhesives in bonded assemblies—Comparison of TAST and Arcan tests”. In : *International Journal of Adhesion and Adhesives* 28.8 (2008), p. 393-404.

[77] Leonardo ALFONSO, Claudiu BADULESCU et Nicolas CARRÈRE. “Use of the modified Arcan fixture to study the strength of bonded assemblies for automotive applications”. In : *International Journal of Adhesion and Adhesives* 80 (2018), p. 104-114.

[78] C BERNOLIN et al. “Assessment of the fracture properties of adhesively bonded joints submitted to fatigue loads using the Arcan fixture”. In : *Fatigue & Fracture of Engineering Materials & Structures* 46.3 (2023), p. 784-797.

[79] Romain CRÉAC'HCADEC, Jean-Yves COGNARD et Th HEUZÉ. “On modelling the non-linear behaviour of thin adhesive films in bonded assemblies with interface elements”. In : *Journal of adhesion science and technology* 22.13 (2008), p. 1541-1563.

[80] Romain CREAC'HCADEC. “Analyse et modélisation du comportement non-linéaire d'assemblages collés pour application marine”. In : (2008).

[81] Nicolas CARRERE et al. “3D models of specimens with a scarf joint to test the adhesive and cohesive multi-axial behavior of adhesives”. In : *International Journal of Adhesion and Adhesives* 62 (2015), p. 154-164.

[82] Jaime DESTOUESSE et al. “Cluster analysis of acoustic emission data to investigate the damage evolution in modified scarf joint under bi-axial loading”. In : *The Journal of Adhesion* (2018).

[83] Jean-Yves COGNARD et al. “A study of the non-linear behaviour of adhesively-bonded composite assemblies”. In : *Composite Structures* 76.1-2 (2006), p. 34-46.

[84] Louise BLYBERG et al. “Adhesive joints for structural timber/glass applications : Experimental testing and evaluation methods”. In : *International Journal of Adhesion and Adhesives* 35 (2012), p. 76-87.

[85] Anna RUDAWSKA. “The influence of curing conditions on the strength of adhesive joints”. In : *The Journal of Adhesion* 96.1-4 (2020), p. 402-422.

[86] EAS MARQUES et al. “Adhesive joints for low-and high-temperature use : an overview”. In : *The Journal of Adhesion* 91.7 (2015), p. 556-585.

[87] FS JUMBO et al. “Thermal residual stress analysis of epoxy bi-material laminates and bonded joints”. In : *International Journal of Adhesion and Adhesives* 30.7 (2010), p. 523-538.

[88] Abdulmohsen ALBEDAH et al. “Effects of adhesive disbond and thermal residual stresses on the fatigue life of cracked 2024-T3 aluminum panels repaired with a composite patch”. In : *International Journal of Adhesion and Adhesives* 87 (2018), p. 22-30.

[89] Abdul Khadar SYED et al. “An experimental study of residual stress and direction-dependence of fatigue crack growth behaviour in as-built and stress-relieved selective-laser-melted Ti6Al4V”. In : *Materials Science and Engineering : A* 755 (2019), p. 246-257.

[90] Matıas R VIOTTI et al. “Residual stress measurement using a radial in-plane speckle interferometer and laser annealing : preliminary results”. In : *Optics and lasers in engineering* 42.1 (2004), p. 71-84.

[91] Hong-Bing WANG et al. “Assessment of residual stresses during cure and cooling of epoxy resins”. In : *Polymer Engineering & Science* 35.23 (1995), p. 1895-1898.

[92] Lucas FM DA SILVA et RD ADAMS. “Stress-free temperature in a mixed-adhesive joint”. In : *Journal of Adhesion Science and Technology* 20.15 (2006), p. 1705-1726.

[93] Yong LU et al. “Reduction of composite deformation based on tool-part thermal expansion matching and stress-free temperature theory”. In : *The International Journal of Advanced Manufacturing Technology* 88 (2017), p. 1703-1710.

[94] Romain LÉGER, A ROY et JC GRANDIDIER. “A study of the impact of humid aging on the strength of industrial adhesive joints”. In : *International Journal of Adhesion and adhesives* 44 (2013), p. 66-77.

[95] Nicolas ARNAUD et al. “Analysis of the moisture effect on the mechanical behaviour of an adhesively bonded joint under proportional multi-axial loads”. In : *Journal of Adhesion Science and Technology* 29.21 (2015), p. 2355-2380.

[96] Alin ILIONI et al. “Prediction of mechanical behaviour of a bulk epoxy adhesive in a marine environment”. In : *The Journal of Adhesion* 95.1 (2019), p. 64-84.

[97] R.D. ADAMS et al. “The effect of temperature on the strength of adhesive joints”. In : *International Journal of Adhesion and Adhesives* 12.3 (1992), p. 185-190.

[98] Willard D BASCOM et Robert L COTTINGTON. “Effect of temperature on the adhesive fracture behavior of an elastomer-epoxy resin”. In : *The Journal of Adhesion* 7.4 (1976), p. 333-346.

[99] Vincent DUMONT et al. “Investigation of the influence of the temperature on the fracture properties of adhesive joints using the Arcan device”. In : *Engineering Fracture Mechanics* 269 (2022), p. 108524.

[100] Peter DAVIES et Guy EVRARD. “Accelerated ageing of polyurethanes for marine applications”. In : *Polymer degradation and stability* 92.8 (2007), p. 1455-1464.

[101] A LE GUEN-GEFFROY et al. “Physical ageing of epoxy in a wet environment : Coupling between plasticization and physical ageing”. In : *Polymer Degradation and Stability* 168 (2019), p. 108947.

[102] Harris G CARTER et Kenneth G KIBLER. “Langmuir-type model for anomalous moisture diffusion in composite resins”. In : *Journal of composite materials* 12.2 (1978), p. 118-131.

[103] MP ZANNI-DEFFARGES et MER SHANAHAN. “Diffusion of water into an epoxy adhesive : comparison between bulk behaviour and adhesive joints”. In : *International Journal of Adhesion and Adhesives* 15.3 (1995), p. 137-142.

[104] Amandine CÉLINO et al. “Characterization and modeling of the moisture diffusion behavior of natural fibers”. In : *Journal of Applied Polymer Science* 130.1 (2013), p. 297-306.

[105] H Ramezani DANA et al. “Characterisation of the hygro-thermo-mechanical behaviour of organic matrix composites instrumented with optical fibres : A study of interfacial bonding”. In : *International Journal of Adhesion and Adhesives* 77 (2017), p. 63-71.

[106] Ting ZHANG et al. “The influence of adhesive porosity on composite joints”. In : *Composites Communications* 15 (2019), p. 87-91.

[107] Hugo Leonardo Alfonso MEDINA. “Characterization and modeling of multi-material assemblies under mixed quasi-static loadings for the design of automotive structures”. Thèse de doct. Université de Bretagne occidentale-Brest, 2016.

[108] Claudiu BADULESCU et al. “Characterization and modelling of the viscous behaviour of adhesives using the modified Arcan device”. In : *Journal of Adhesion Science and Technology* 29.5 (2015), p. 443-461.

[109] Lucas Filipe Martins DA SILVA et Andreas ÖCHSNER. *Modeling of adhesively bonded joints*. Springer, 2008.

[110] P JOUSSET et M RACHIK. “Implementation, identification and validation of an elasto-plastic-damage model for the finite element simulation of structural bonded joints”. In : *International Journal of Adhesion and Adhesives* 50 (2014), p. 107-118.

[111] Jean-François MAIRE. “Etudes théorique et expérimentale du comportement de matériaux composites en contraintes planes”. Thèse de doct. Besançon, 1992.

[112] Alin ILIONI. “Influence of seawater ageing on the behaviour of adhesives : a rapid characterization of the evolution of mechanical properties of bonded joints”. Thèse de doct. Université de Bretagne occidentale-Brest, 2017.

[113] Wayne Morris THOMAS et al. *Improvements relating to friction welding*. 1993.

[114] Akbar HEIDARZADEH et al. “Friction stir welding/processing of metals and alloys : A comprehensive review on microstructural evolution”. In : *Progress in Materials Science* 117 (2021), p. 100752.

[115] Rajiv S MISHRA et ZY MA. “Friction stir welding and processing”. In : *Materials science and engineering : R : reports* 50.1-2 (2005), p. 1-78.

[116] Matthieu B LEZAACK et Aude SIMAR. “Avoiding abnormal grain growth in thick 7XXX aluminium alloy friction stir welds during T6 post heat treatments”. In : *Materials Science and Engineering : A* 807 (2021), p. 140901.

[117] Xiaocong HE, Fengshou GU et Andrew BALL. “A review of numerical analysis of friction stir welding”. In : *Progress in Materials Science* 65 (2014), p. 1-66.

[118] Mustafa Kemal BILICI et Ahmet Irfan YÜKLER. “Influence of tool geometry and process parameters on macrostructure and static strength in friction stir spot welded polyethylene sheets”. In : *Materials & Design* 33 (2012), p. 145-152.

[119] Vijay Shivaji GADAKH et Kumar ADEPU. “Heat generation model for taper cylindrical pin profile in FSW”. In : *Journal of Materials Research and Technology* 2.4 (2013), p. 370-375.

[120] Noor Zaman KHAN et al. “Investigations on tunneling and kissing bond defects in FSW joints for dissimilar aluminum alloys”. In : *Journal of alloys and Compounds* 648 (2015), p. 360-367.

[121] Paul KAH et al. “Investigation of weld defects in friction-stir welding and fusion welding of aluminium alloys”. In : *International Journal of Mechanical and Materials Engineering* 10.1 (2015), p. 1-10.

[122] Jinwen QIAN et al. “An analytical model to optimize rotation speed and travel speed of friction stir welding for defect-free joints”. In : *Scripta Materialia* 68.3-4 (2013), p. 175-178.

[123] P CAVALIERE, Antonino SQUILLACE et Francesco PANELLA. “Effect of welding parameters on mechanical and microstructural properties of AA6082 joints produced by friction stir welding”. In : *Journal of materials processing technology* 200.1-3 (2008), p. 364-372.

[124] Monica Daniela IORDACHE et al. “A numerical strategy to identify the FSW process optimal parameters of a butt-welded joint of quasi-pure copper plates : modeling and experimental validation”. In : *The International Journal of Advanced Manufacturing Technology* 115 (2021), p. 2505-2520.

[125] P PRASANNA, B Subba RAO et G Krishna Mohana RAO. “Finite element modeling for maximum temperature in friction stir welding and its validation”. In : *The International Journal of Advanced Manufacturing Technology* 51.9-12 (2010), p. 925-933.

[126] Pedro VILAÇA, Luısa QUINTINO et Jorge F dos SANTOS. “iSTIR—analytical thermal model for friction stir welding”. In : *Journal of materials processing technology* 169.3 (2005), p. 452-465.

[127] H SCHMIDT, Jesper HATTEL et John WERT. “An analytical model for the heat generation in friction stir welding”. In : *Modelling and simulation in materials science and engineering* 12.1 (2003), p. 143.

[128] Paolo FERRO et Franco BONOLLO. “A semianalytical thermal model for fiction stir welding”. In : *Metallurgical and Materials Transactions A* 41 (2010), p. 440-449.

[129] CM CHEN et R KOVACEVIC. “Finite element modeling of friction stir welding—thermal and thermomechanical analysis”. In : *International Journal of machine tools and manufacture* 43.13 (2003), p. 1319-1326.

[130] Mohammad Ali ANSARI et al. “An efficient coupled Eulerian-Lagrangian finite element model for friction stir processing”. In : *The International Journal of Advanced Manufacturing Technology* 101 (2019), p. 1495-1508.

[131] Murat TÜRKAN et Özler KARAKAŞ. “Numerical modeling of defect formation in friction stir welding”. In : *Materials Today Communications* 31 (2022), p. 103539.

[132] Bijan ABBASI-KHAZAEI, Abbas JAHANBAKHSH et Reza BAKHTIARI. “TLP bonding of dissimilar FSX-414/IN-738 system with MBF-80 interlayer : The effect of homogenizing treatment on microstructure and mechanical properties”. In : *Materials Science and Engineering : A* 651 (2016), p. 93-101.

[133] S HADIBEYK, Behrooz BEIDOKHTI et Seyed Abdolkarim SAJJADI. “Effect of bonding time and homogenization heat treatment on the microstructure and mechanical properties of the transient liquid phase bonded dissimilar GTD-111/FSX-414 TLP superalloys”. In : *Journal of Alloys and Compounds* 731 (2018), p. 929-935.

[134] Matthieu B LEZAACK et al. “Towards ductilization of high strength 7XXX aluminium alloys via microstructural modifications obtained by friction stir processing and heat treatments”. In : *Materialia* 20 (2021), p. 101248.

[135] Amlan KAR et al. “Effect of niobium interlayer in dissimilar friction stir welding of aluminum to titanium”. In : *Materials Characterization* 145 (2018), p. 402-412.

[136] EL NITU et al. “Analyzing defects and their effects on the strength of a three-layer FSW joint by using X-ray microtomography, localized spectrum analysis, and acoustic emission”. In : *Materials Characterization* 190 (2022), p. 112069.

[137] Florent HANNARD et al. “Ductilization of aluminium alloy 6056 by friction stir processing”. In : *Acta Materialia* 130 (2017), p. 121-136.

[138] AK LAKSHMINARAYANAN et V BALASUBRAMANIAN. “Process parameters optimization for friction stir welding of RDE-40 aluminium alloy using Taguchi technique”. In : *Transactions of Nonferrous Metals Society of China* 18.3 (2008), p. 548-554.

[139] Yahya BOZKURT. “The optimization of friction stir welding process parameters to achieve maximum tensile strength in polyethylene sheets”. In : *Materials & Design* 35 (2012), p. 440-445.

[140] Yingxin ZHAO et al. “Investigation of void formation in friction stir welding of 7N01 aluminum alloy”. In : *Journal of Manufacturing Processes* 37 (2019), p. 139-149.

[141] Atul Kumar CHOUDHARY et Rahul JAIN. “Numerical prediction of various defects and their formation mechanism during friction stir welding using coupled Eulerian-Lagrangian technique”. In : *Mechanics of Advanced Materials and Structures* 30.12 (2023), p. 2371-2384.

[142] B MEYGHANI et al. “Developing a finite element model for thermal analysis of friction stir welding by calculating temperature dependent friction coefficient”. In : *2nd international conference on mechanical, manufacturing and process plant engineering*. Springer. 2017, p. 107-126.

[143] Henrik B SCHMIDT et Jesper H HATTEL. “Thermal modelling of friction stir welding”. In : *Scripta Materialia* 58.5 (2008), p. 332-337.

[144] Veeresh MURTHY et al. “Application of image processing and acoustic emission technique in monitoring of friction stir welding process”. In : *Materials Today : Proceedings* 4.8 (2017), p. 9186-9195.